Summary of Report

WRI Project No. 1097701

EMR Contract No. 23440-6-9168/01-ST

R.J. Pick

D.H.B. Mok

Department of Mechanical Engineering
University of Waterloo
Waterloo, Ontario
Canada N2L 3G1

1988

1. Introduction

Since 1981 the Department of Mechanical Engineering at the University of Waterloo has studied techniques for the numerical prediction of residual stresses resulting from welding. Under contract to CANMET, Energy, Mines and Resources, Ottawa, a program was set up at the University of Waterloo to develop a numerical model to predict residual stresses induced by the welding process and apply it to multi-pass welds. In conjunction, Dr. G. Roy of CANMET undertook experimental measurements to support the multi-pass studies.

In the multi-pass study, a finite element model was developed by Leung for the analysis of multi-pass weld configurations [1, 2][These Numbers refer to References in the Report]. For a single pass weld Mair [4] showed that Leung's model was quite accurate compared to very detailed experimental measurements of residual stress. However confirmation of Leungs work for multi-pass welds has remained outstanding. Concurrently as part of a study of the fatigue of offshore steel structures in Canada, a series of T-joint specimens were used to study crack shape development and thickness effects under fatigue loading [5-7]. These fatigue tests were undertaken on the T-joint specimens in the as welded condition and a question has arisen regarding the role of the high weld residual stresses on the results of the fatigue testing. EMR chose to undertake experimental measurement of the weld residual stresses. This provided an opportunity to confirm the analysis techniques of Leung and to give greater detail of the residual stress distribution than could be expected from experimental measurements. This is a summary of a contract report prepared for EMR on prediction of the weld residual stress in the multi-pass weld of the T-Joint Fatigue Specimen. The results of this study were submitted as part of the requirements for a MASc

Degree by Danny H.B. Mok.

1.1 Objectives

The objectives of the study were:

(a) to investigate the effect of allotropic phase transformations on the weld residual stresses in the T-joint specimen.

(b) to calculate the residual stresses induced by welding during manufacture of a 26 mm T-joint fatigue specimen and determine the effect of the mechanical loading of the fatigue test on the residual stress field.

(c) to determine the agreement between experimental measurements made at EMR and the finite element predictions.

2. Phase Transformation Effect

In the first part of the study, a model based on Leung's single weld pass model [1] was developed to determine the effect of allotropic phase transformations and the accompanying volumetric strains on welding residual stress.

The welding residual stress was predicted using a transformation strain of 0.5% and transformation temperature of 650°C; values which were indicated in dilatation tests. The results were compared to an analysis without the phase transformation effect and only a very small difference in the predicted welding residual stresses was observed.

A parametric study of the effects of transformation temperature was carried out with transformation temperatures of 450°C, 650°C and 850°C. The results of the analyses with phase transformations at 650°C and 850°C were identical. The predicted residual stresses were lower by less than 10 MPa in the analysis with a phase transformation at 450°C.

The effect of the magnitude of the volumetric strain was also studied. Volumetric strains of 0.5% and 2.0% were used with the transformation taking place at 650°C. The predicted welding residual stresses for the analysis with the higher volumetric strain were lower by about 20 MPa.

Based on the results of this study, it can be concluded that the phase transformation effect is very small when realistic volumetric strains and transformation temperatures for ferritic steels are used. Furthermore, the transformation temperature affects the residual stress magnitude only in the fusion region where the transformation takes place. Transformations at high temperature appear to have no significant effect on residual stress. However, a small decrease in the residual stress magnitude can be expected for transformations at lower temperatures. Only when the volumetric strain is comparable to the thermal contraction strain (which is unrealistic), will a significant decrease in the magnitude of residual stress occur. When a transformation reduces residual stresses, the general trend of the stress distribution does not change, but the overall distortion of the welded structure may be affected. Small local perturbations in the residual stress may occur in the HAZ, however this is a function of both the phase transformation and local metallurgy.

It can be further concluded that the model developed by Leung [1,2] for stainless steel is adequate for predicting welding residual stress for most ferritic steels and other materials that exhibit allotropic phase transformations, providing that the volumetric expansion is small compared to the thermal contraction strain.

3. Analysis Of The 26 mm T-Joint Specimen

In the second part of the study, the welding residual stresses in a 26 mm T-joint fatigue specimen were predicted and the effect of mechanical loading on the welding residual stresses investigated.

The T-joint fatigue specimens being analysed were fabricated by AMCA International Limited of steel specified according to the Lloyds LT60 Specification and supplied by Algoma Steel. After welding, 2.54 cm (1 inch) was milled from each edge in an effort to remove any end effects due to the starting and stopping of the electrode on the fatigue behavior. The final dimensions of a typical specimen used are shown in Figure 5.1. [The figures are attached but the figure numbers correspond to those of the final report].

According to DeGarmo et al. [77], a weld bead length of 18 to 20 inches is required to develop sufficient differential shrinkage between the weld metal and the restraining parent metal to generate the maximum residual stress in the longitudinal direction of a flat plate. For the T-joint specimens, the welding length is only 254 mm (10 inches) and therefore the residual stresses in the specimen will not be fully developed. To determine the residual stresses accurately the analysis must be three-dimensional but the cost of such an analysis would be extreme. The calculated results of a planar (2-D) analysis would constitute an upper bound of the actual welding residual stresses and were undertaken at a much lower cost. For improved accuracy the stress field was modelled with a pseudo 3-D analysis in which generalized plane strain elements were used instead of plane strain element [3].

The residual stress distribution of a fillet welded 'T' shape is basically symmetrical about the center line [56]. Since a balanced welding sequence was used, a symmetric stress distribution is expected and this can be used to further reduce computing costs. Calculations were made to determine the validity of this assumption and its acceptability was shown.

The dimensions and coordinate system shown in Figure 5.1 were used throughout the study. The X-axis (or transverse direction) is defined as in the plane of the horizontal plate. The Y-axis is defined as the direction along the vertical plate. The Z-axis (or longitudinal direction) is parallel to the direction of the welds.

The weld of the T-joint specimen is made up of a number of passes (Figure 5.2). The residual stresses in such a weldment are very complex and result from the build up of thermal stress as each new pass is deposited. One method to predict the residual stresses due to welding is to apply a numerical model for single pass welds in a repetitive manner such that the transient thermal stresses for each pass are calculated. This method is affordable if the weld joint is made up of relatively few passes. Unfortunately the 26 mm T-joint specimen required an average of 26 passes which would require enormous computing to simulate every weld pass.

It was decided that it was reasonable to analysis only the final layer of weld passes or the capping passes of the full penetration weld. However, the residual stress from previous passes must be accounted for. One method is to input the previous residual stress as an initial stress before the capping passes are deposited. This method requires knowledge of the previous residual stress distribution. Unfortunately, at the beginning of this study, only the longitudinal stress distribution along the surface of a similar T-shape was found in the literature [56]. This was insufficient for an accurate prediction of residual stresses. Therefore the initial analyses were made of the capping passes without any previous residual stresses. After studying the development of residual stresses in the capping passes subsequent analyses were then undertaken with a more informed estimate of previous residual stresses.

There are four capping passes in the specific T-joint specimen being modelled. Further saving of computation can be made if passes can be grouped. Leung [2] found that in a layer of weld passes, the transverse residual stress is not fully developed until the last pass is deposited. Therefore, a layer of passes can be modelled in two analyses. The first analysis combines all the passes in the layer except the last pass by combining the various temperature histories with an envelope technique. The different thermal histories are first set to a common time frame. The temperature at any time is represented by the highest temperature from the different histories. In this study, the four capping passes were combined into three analyses with the second and third passes grouped. The first pass was not grouped as suggested by Leung's scheme because this pass would form the weld toe region which is of particular interest in the next phase of this study, i.e. loading of the T-joint specimen.

In the first stage the welding residual stresses due to the capping passes alone were calculated and in the last stage the residual stresses from previous passes were included in the results.

3.1 Heat Transfer Analysis

In the heat transfer analysis, the thermal history for the capping passes of the T-joint specimen were calculated. The heat input from the electrode was simulated using a modified version of Goldak's double ellipsoidal heat source model [48]. Convective and radiative heat transfer were assumed on all surfaces except on the surface of the weld pool which was assumed to be insulated. Half of the horizontal plate was not modelled in order to reduce computation time. The heat flow into the other half of the specimen was replaced by surface convection. The temperature distribution before the laying of the first capping pass was assumed to be room temperature which would introduce some error in the predicted thermal history because an interpass temperature of 230°C was reportedly maintained during welding.

Based on the results, this model appeared to predict the temperature history quite accurately. The predicted weld pool shapes compared reasonably well with measurements and the fast cooling rate expected in the fillet weld was also observed.

3.2 Welding Residual Stress Prediction

The predicted temperature history was supplied to the stress analysis as thermal loading. A two-dimensional analysis was carried out with generalized plane strain elements capable of modelling longitudinal displacements. During the analysis it was assumed that the T-joint specimen was free to distort due to the welding. Strain hardening and the Bauschinger effect were modelled using a kinematic hardening model and a time independent, thermo-elastic-plastic constitutive model was assume

Initially the welding residual stresses due to the four capping passes were predicted without the inclusion of residual stresses from previous passes, since the exact stress distribution resulting from the previous passes was not known. In order to estimate the previous stresses the results from the capping pass analysis were used as the basis for an assumed distribution. The residual stress distributions predicted for the capping passes were remapped to be closer to the center line of the specimen and were treated as initial stresses. Steps were taken to assure that equilibrium was achieved before the residual stress calculations were begun. The assumed stress distributions are shown in Figures 7.47 to 7.50.

3.2.1 Effect of Previous Weld Passes

Since the sequence of residual stress build up in the capping passes was known, only the first capping pass was analyzed to determine the effect of the assumed residual stress on the final residual stress distributions.

The residual stress contours due to the first capping pass are shown in Figures 7.51 to 7.54 and contain the assumed residual stress (designated as A.R.S.). The stress distributions along the surfaces and through the plate thickness of the bottom plate are plotted in Figures 7.55 to 7.63. These figures show stress distributions including the assumed residual stress and excluding the assumed residual stress (designated as WITHOUT A.R.S.).

After the first capping pass was deposited, no dramatic changes to the assumed residual stresses were observed except in the region where the new weld pass was deposited (compare Figures 7.47 to 7.50 with Figures 7.51 to 7.54). In the area away from the first capping pass, the residual stresses take on the values of the stresses already existing in the specimen. This is especially true for the transverse stress and the longitudinal stress as seen in Figures 7.56 and 7.62. In the area surrounding the new fusion zone, the residual stresses of previous passes appeared to be removed by the high welding temperatures and the new weld pass is responsible for the final residual stresses in this region. This effect can be seen clearly in Figures 7.55, 7.58 and 7.61 in which the residual stresses on the top surface of the bottom plate are plotted. The predicted stresses at the weld toe were nearly identical for the analyses with and without assumed stresses. The assumed Y-residual stress appears to have little or no effect on the final stress (see Figures 7.58 to 7.60).

As indicated above, the welding residual stresses around the weld toe region are mainly due to the layer of capping passes. Since the predicted residual stresses around the weld toe between analyses with and without inclusion of previous stresses are essentially identical, the final residual stress in this region can be calculated without assuming previous residual stresses in passes below the capping passes. In the next section the results of these analyses will be given and it will be shown that the predicted welding residual stress achieved reasonable agreement with measured results. The differences are small enough that the predicted results can be used in the consideration of the fatigue loading of the T-joint specimen.

In regions away from the weld zone, the predicted results were found to be slightly closer to the measurements with the inclusion of previous residual stresses. However the differences were small and for clarity it was decided to predict the residual stresses in the capping passes without the inclusion of the residual stresses from previous passes.

3.2.2 Residual Stresses Due To The Remaining Passes

The residual stresses resulting from the first capping pass can be assummed to be distributions shown in Figures 7.51 to 7.63. The residual stress contours for the combined second and third passes are plotted in Figures 7.39 to 7.42. The contours for the last pass are shown in Figures 7.43 to 7.46. There were no dramatic changes to the residual stress distributions after the first capping pass except a gradual build up as each pass was deposited, especially the Y-stress component. This trend of stress build up agrees with observations by other researchers [1, 2, 30, 31, 66, 67]. The zone of high residual stress expands and encloses each new weld pass. After the whole cavity was filled, a high stress gradient zone similar to the one in the bottom plate was formed at the weld toe of the vertical plate.

The surface stresses and the stresses below the weld toe are plotted in figures 7.29 to 7.37 for each of the weld passes.

Transverse Or X-Residual Stress

The transverse residual stress at the weld toe became more tensile as each pass was added. A maximum residual stress of 480 MPa was predicted on the top surface (Figure 7.29). On the bottom surface, the same trend of stress build up was observed (see Figure 7.30). A tensile stress of 250 MPa was predicted near the center line of specimen. These surface stresses decreased to zero about 40 mm from the center line. The zone of compressive stress was observed to expand up into the vertical plate (Figures 7.39 and 7.43). The maximum compressive stress at the weld toe was about 300 MPa, 8 mm below the top surface (Figure 7.31).

Y-Residual Stress

The Y-residual stress component built up significantly with each new pass, especially at the weld toe of the vertical plate. The vertical restraint in this region is similar to the transverse restraint at the weld toe of the bottom plate. Therefore, the Y-stress contours for the weld toe region of the vertical plate are similar to the transverse stress contours at the weld toe of the bottom plate (see Figures 7.43 and 7.44). The stresses along the surfaces of the bottom plate were zero as expected (Figures 7.32 and 7.33). The through thickness stress becomes more tensile near the top surface of the plate due to increasing vertical constraint by the weld passes (see Figure 7.34). A maximum tensile stress of about 100 MPa was predicted as deep as 6 mm below the top surface. This stress decreased to zero about one third into the plate thickness.

Longitudinal Or Z-Residual Stress

A zone of high tensile stress can be seen to enclose each new weld pass. After the cavity was filled, the stress contours around the weld region are almost symmetrical about the capping passes (Figure 7.45). The highest tensile stress is observed at the weld toes of both the vertical plate and the bottom plate. The stress along the top surface, near the weld toe did not increase significantly as the weld passes were deposited (see Figure 7.35). A maximum tensile stress of 480 MPa was predicted at the weld toe. On the bottom surface, a build up of compressive residual stress was observed in Figure 7.36. This could be the result of the growing tensile zone as each pass was deposited. In order to achieve equilibrium, the surrounding material becomes more compressive. Below the weld toe, the tensile stress due to the first capping pass was reduced as each additional pass was laid (see Figure 7.37). This could be caused by relaxation due to the high temperature of the additional weld passes.

Plastic Zone Size

The plastic zone (region in which the Von Mises stress is greater than the room temperature yield strength of the material, i.e., 350 MPa) extends to about 5 mm below the surface in the first three capping passes. After the last pass was deposited, the plastic zone can be seen to move up along the capping passes and only encloses the final three passes. This zone also extended deeper below the surface (see Figure 7.46) as the restraint increased as the cavity was filled.

3.3 Comparison With Measured Residual Stresses

3.3.1 Measurements Of Residual Stresses In 26 mm T-Joint Specimen By Holden et al.

The welding residual stresses in the 26 mm T-joint specimen were measured by Holden et al. [63] of Atomic Energy of Canada Limited, Chalk River, with the neutron diffraction technique. The residual stress components below the weld toe are shown in Figure 5.8. These results were calculated by Holden using an isotropic stress strain relationship. Dr. G. Roy of CANMET obtained similar results by assuming an anisotropic stress, strain relationship for the materials in the weld pool and in the HAZ [65]. Holden et al. suggested that the calculated residual stresses are accurate to ±100 MPa. The residual stress distributions near the surfaces (within 2.5 to 4.5 mm) of the horizontal plate (see Figures 5.9 and 5.10) were calculated by the authors from the strain measurements provided by Holden et al. The isotropic stress strain relationship was used.

As seen in Figure 5.8, the X-residual stress just below the toe of the weld is about 400 MPa which is close to the room temperature yield strength of this steel. This transverse stress becomes compressive about one third through the plate thickness and a maximum compressive value of 100 MPa was measured near the center of the plate. Tensile residual stress is observed near the bottom surface with a maximum value of about 225 MPa. One observation is that the measured transverse residual stress distribution below the weld toe is not in equilibrium. This resulted from difficulty by Holden et al. in determining the zero strain state. It appears that equilibrium would be achieved if the transverse stress distribution is lowered by about 50 MPa. From Figure 5.9, a tensile X-residual stress was measured along the top surface with a very high gradient near the toe of the weld. This stress component decreases to nearly zero about 60 mm from the center line of the specimen. A similar stress distribution was observed along the bottom surface (Figure 5.10) except the residual stress becomes slightly compressive about 60 mm from the center line.

The Y-residual stress component through the plate thickness is lower than the X or Z-stresses (Figure 5.8). A maximum value of about 200 MPa was measured just below the toe of the weld. As expected, the Y-residual stress becomes less tensile away from the top surface as the restraint in the vertical direction decreases near the bottom surface. However, the measured Y-residual stress is greater near the bottom surface than in the interior of the plate. A high stress gradient was observed for the Y-residual stress at the weld toe near the top surface (Figure 5.9). The magnitude of the residual stress decreased to a constant level of approximately 30 MPa at 60 mm from the center line of the specimen. A low compressive Y-residual stress was measured near the bottom surface (Figure 5.10) with a maximum value of about 50 MPa, 60 mm from the center of the specimen. The measured Y-residual stresses were small (less than

50 MPa) away from the weld toe regions and near the bottom surface, however the actual values should be zero. This indicates some of the uncertainty involved in the experimental technique.

The Z-residual stress is tensile below the weld toe (Figure 5.8) and a maximum value of over 400 MPa was measured. The Z-residual stress becomes less tensile and eventually becomes compressive midway through the plate thickness. The stress near the bottom surface is about 120 MPa in compression. The Z-residual stress gradient along the top surface is very high near the toe of the weld (Figure 5.9) and decreases to less than 50 MPa, 20 mm away from the weld toe. Along the bottom surface (Figure 5.10), a compressive Z-residual stress was observed. The stress is highest, over 100 MPa, near the center line of the specimen. The Z-residual stress distributions along the surfaces of the bottom plate are similar to those measured by Tall et al. [56-58].

These measured values described above are compared to the predicted residual stresses in Figures 7.29 to 7.37.

Transverse Or X-Residual Stress

On the top surface, the predicted stress agreed well with the measured value in the area of the weld toe region but was somewhat lower away from the weld toe region (Figure 7.29). The largest difference is about 75 MPa. On the bottom surface, excellence agreement was observed with the largest difference being less than 30 MPa (Figure 7.30). The stress distribution through the plate thickness achieved fair agreement with the measured distribution (see Figure 7.31). The predicted compressive stress zone below the weld region was larger and the values were greater than measured. However, the measured stress distribution was not in equilibrium through the plate thickness. This was caused by difficulty in determining the zero strain state in the T-joint specimen during the neutron diffraction measurements. In order to achieve equilibrium, the measured curve would have to be lowered by about 50 MPa and much better agreement would be observed.

Y-Residual Stress

The predicted stress distribution has the same trend as the measured distribution (Figures 7.32 to 7.34), but no agreement in actual values was obtained. This may be because the stress from previous passes were not included in the analysis. On the top surface and bottom surface, the calculated values are generally lower by about 50 MPa, with a larger difference at the weld toe. Note however that the measured distributions shown in Figures 7.32 and 7.33 were measured below the surface. This is the reason for the values not being zero as would be expected. Through the plate thickness (Figure 7.34), the largest difference between the numerical and measured results is about 100 MPa.

Longitudinal Or Z-Residual Stress

The predicted stress on the top surface agreed well with the measured results, especially at the weld toe (Figure 7.36). The numerical values are about 50 MPa lower away from this region. On the bottom surface (Figure 7.36), a difference of about 100 MPa was observed between the numerical and measured results near the center line of the specimen. However, better agreement was achieved in region further away. The difference was about 50 MPa at 50 mm from the center line. Good agreement was observed for the stress distribution through the plate thickness (Figure 7.37). The analysis predicted compressive stresses appearing about one third into the plate thickness while compressive stresses were measured only in the bottom half of the plate.

In general, the predicted residual stress without inclusion of residual stress from previous passes achieved reasonable agreement with results measured by the neutron diffraction technique. The small differences, usually less than 50 MPa, are most likely caused by neglecting the existing stresses in the specimen before the capping passes were deposited.

4. Effects Of Loading On The Welding Residual Stresses

4.1 Effect of Fatigue Loading

The stress-strain relationship used in this study is for monotonic loading. After the first load cycle, any subsequent loading will result in elastic loading and the results will be the same. Ideally to provide the most accurate model of a fatigue test, the cyclic stress strain curve should be used. However this degree of accuracy is beyond the scope of this report. Therefore, only the first loading cycle was analyzed which consisted of one load application and the subsequent unloading.

In the fatigue test, the load applied through the load cell was approximately 20000 lb. but the exact load was not recorded because the loading was adjusted to give a desired 'hot spot' stress which was measured with strain gauges. A number of loading cases were analyzed with a relatively coarse mesh to determine a suitable load for the final analyses. Based on these results, a evenly distributed load of 25 MPa applied along the top of the vertical plate would provide an equivalent 'hot spot' stress of approximately 250 MPa which would fall in the stress range used in the testing. In addition, an applied load of 50 MPa ('hot spot' stress of about 500 MPa) was analyzed to determine the effect of greater applied loads.

Since the depth of the specimen is over 200 mm, a plane strain condition exists in most parts of the specimen, except near the front and rear edges. Thus a plane strain condition was assumed and a two-dimensional analysis undertaken.

A stress concentration will always exist at the weld toe, the severity of which depends upon the weld radius of the first capping pass. Due to the high degree of variability in the welding process, the weld radius is not constant along the weldment and a wide range of radii can occur. To model the weld radius very accurately, a very fine mesh around the weld toe region is required which would lead to very high computing costs. It was believed that this degree of accuracy was not required in this analysis because the stress concentration effect is localized in a region of high welding residual stress. Local plasticity is expected when loaded and therefore, an approximate representation of the stress concentration should be sufficient. The same mesh used in the residual stress calculations was adopted and no weld radius was considered.

Mechanical loading of the 26 mm T-joint specimen was simulated in both the stress free and as welded conditions. The load was applied through the vertical plate of the T-joint specimen which loaded the horizontal plate in a three point bending configuration. This loading configuration is symmetrical about the center-line and plane strain exists in most part of the specimen. By applying a load similar to that of the fatigue test, 25 MPa ('hot spot' stress of

250 MPa), in the stress free condition, some yielding was predicted at the weld toe which left a small region of compressive residual stress when the load was removed. A stress concentration factor of 2.3 was predicted at the weld toe. This is smaller than values reported in the literature which indicates the finite element mesh used near the weld toe was not fine enough to capture the stress gradient.

In the simulation of loading in the as welded condition, the results showed that the welding residual stress is dominant in the weld zone and the bending stress is dominant in the rest of the specimen. Shakedown of the residual stress was observed. However, this effect was found only in the weld toe region and not through the whole plate thickness as assumed by some researchers. With an applied load of 25 MPa, tensile transverse residual stress still exists near the weld toe after shakedown. This tensile residual stress can lead to faster fatigue crack growth than a specimen that has been stress relieved.

There are very few studies in the literature on the effect of fatigue loading on welding residual stresses. Gurney [68] has shown the 'shakedown' of residual stresses in a simple theoretical model based on an elastic perfectly plastic material assumption and idealized residual stress distribution. To the author's knowledge, no attempts have been made to study the effect of loading on welding residual stresses with numerical techniques. The reason for this is that only recently researchers have become confident with the accuracy of the numerical models. Furthermore these numerical models are only economical for simple geometry. For complex welded structures, the computing cost is still very high.

Welding residual stresses are very difficult and laborious to measured experimentally. In addition, most techniques are destructive and fatigue testing of the specimen after the initial measurements is impossible. Only a handful of measuring methods, neutron diffraction and X-ray diffraction, are capable of measuring the residual stresses in a specimen before and after fatigue testing. Allen et al. of Harwell Laboratory [70] have measured the residual stresses of a similar T-joint specimen at different stages of the fatigue test. After shakedown (1000 load cycles) only small changes from the as welded residual strain measurements were observed with the neutron diffraction technique. The most significant changes occurred at the weld toe. This indicates that after initial loading, only localize plastic yielding occurs at the stress concentration. Upon elastic unloading, the high residual stresses are relaxed to a much lower level and further loading will always be elastic.

4.2 Loading In The As Welded Condition

In this analysis, the T-joint specimen was loaded after application of the predicted welding residual stress. Since some of the residual stresses were higher than the yield strength of the steel at room temperature, any loading would result in an increased amount of plasticity. Therefore, the mechanical load was applied in an incremental fashion with the automatic time stepping scheme provided in ABAQUS [3]. Unloading would occur elastically, and only one increment was required.

The stress contours with the 25 MPa load are shown in Figures 8.15 to 8.18. For most of the T specimen, particularly the bottom plate, the resultant transverse or X-stress distribution (Figure 8.15) is the superposition of the welding residual stress (Figure 7.43) and the applied bending stress. In regions away from the weld toe and low welding residual stresses, the bending stress is predominant; while the welding residual stress is the dominate component around the weld toe region. The compressive stresses in the lower half of the horizontal plate due to the applied load were observed to join up with the zone of compressive residual stress below the weld zone. At the weld toe, extremely high tensile stresses were observed as a result of both high tensile welding residual stresses and high tensile stresses resulting from the applied load.

For the Y-stress (Figure 8.16) and the longitudinal or Z- stress (Figure 8.17), only minor changes to the welding residual stress (Figures 7.44 and 7.45) were observed because the applied bending load is in the transverse direction. The changes in both the Y and Z stresses occurred in the weldment where high residual stresses already existed. The changes were caused by yielding of the material and the subsequent stress redistribution. From Figure 8.18, the plastic zone was observed to surround the whole weld region and penetrate to about half of the plate thickness.

The contours of the residual stress after the removal of the load are shown in Figures 8.19 to 8.22. Comparing these with Figures 7.43 to 7.46, it can be seen clearly that most of the welding residual stresses remain after the first loading cycle. Some stress reductions in both the transverse stress and the longitudinal stress were observed at the weld toe region where yielding had occurred with the application of the load. After the first load cycle, the zone in which the Von Mises stress exceeded the yield strength (350 MPa) was found to occur only around the weld toe of the vertical plate (Figure 8.22) whereas the Von Mises stress in the entire region of the capping passes zone exceeded yield after welding (Figure 7.46).

The analysis with 50 MPa applied load resulted in similar stress contours as those for the analysis with 25 MPa applied stress. As expected, the resultant stresses were much higher and the zones of high stresses were larger. Also, the welding residual stresses are less dominant below the weld region. The amount of stress reduction were much higher, especially around the weld toe where a great deal of yielding had occurred. In fact, compressive transverse residual stresses were resulted around the weld toe after the first load cycle.

The stresses through the thickness for both loading cases are presented in Figure 8.33. The predicted welding residual stresses are also plotted and indicated as W.R.S. Reduction of the transverse or X-residual stress after one loading cycle was observed in both analyses (see Figure 8.33). The tensile transverse residual stress at the weld toe decreased to less than 100 MPa after application of the 25 MPa load while a compressive residual stress was predicted after application of the 50 MPa load.

4.3 Discussion Of The Results

4.3.1 Finite Element Mesh

Considering the applied loading without residual stress, the highest calculated stress concentration factor was about 2.3 which is lower than the values of 3 or greater reported in the literature [68]. The main reason for the low stress concentration factor is that the mesh used is not fine enough at the weld toe region to capture the high gradient of stress at the toe. In addition, the analysis is an elastic-plastic model which takes yielding and strain hardening into account, whereas the values reported in the literature are usually based on elastic analysis. This effect is most evident in the analysis with the higher applied load.

The region of very high stress gradient is very small and is located where high welding residual stress occurs. With the applied load superimposed on the residual stress, the material yields and flows plastically. The stress gradient would be contained within the plastic zone and its effect would be decreased. Therefore, although the mesh used cannot model the high local stress gradient it should be reasonable for the purpose of studying the effect of loading on welding residual stress.

4.3.2 Effect Of loading On Welding Residual Stress

If the T-joint specimen was stress-relieved before the fatigue test, the specimen would be essentially loaded elastically by the load levels applied. Very localized yielding at the weld toe occurs as a result of the high stress concentration. Since this zone is very small and the plastic strain is contained by surrounding elastic material, the strain effectively returns to zero upon unloading. Compressive residual stress is the result as shown in the analyses. Clearly, further loadings create only elastic stresses. This process is known as 'shakedown'.

Since the T-joint specimen was tested in the as welded condition with residual stress of yield strength magnitude around the weld zone, any loading would cause yielding in a greater amount of material. The effect of shakedown is more wide spread as seen in the analyses. However, the welding residual stress is not totally relaxed after shakedown as assumed by some researchers. The same effect is also observed by Allen et al. [70] in their neutron diffraction measurement of similar T-joint specimen.

The largest reduction of stress occurs in a very localized region within 3 to 4 mm of the weld toe. This is also the region where significant plastic yielding has occurred. In areas that remain elastic throughout the loading, residual stress is also reduced to re-establish equilibrium, but the magnitude of reduction is much smaller. The amount of stress relaxation depends on the applied load with greater reductions resulting from higher loads. For loading greater than 25 MPa on the 26 mm specimen, the transverse tensile residual stress near the weld toe can be reduced to zero or to compression while the longitudinal residual stress can be reduced by a half.

4.3.3 Effect On Fatigue Life Of The T-joint Specimen

Fatigue predictions for the T-joint specimen are beyond the scope of this thesis, however, based on the results of this study, qualitative comments can be made on the possible effects of welding residual stresses on the fatigue behavior of the T- joint specimen.

Effect On Initiation Life

The formation of a fatigue crack is a complex process. It is believed that the shearing action of the cyclic loads causes dislocations to entangle [80]. Since the material surface is usually weaker than the interior, notches (intrusions) and ridges (extrusions) of atomic scale are formed. Under the action of the cyclic stresses, these surface defects eventually deepen to form microcracks. With further cyclic loading, these microcracks coalesce to form one dominant surface crack (macrocrack). The point at which initiation of the fatigue crack is considered finished and propagation has begun is arbitrary, but for typical steel components, initiation usually makes up the majority of the total fatigue life. However, for welded components and structures, initiation is usually a very small portion of the total life. Weld defects such as undercuts and porosities along the toe of the weld are perfect sites for the initiation of fatigue cracks. In fact, some researchers have considered fatigue of welded structures as a propagation problem only.

Since initiation is a result of the cyclic shearing action, residual stress which only modifies the mean stress, is thought to have only a small effect. A compressive mean stress tends to prevent microcracks from opening. This retards microcracks from growing into fatigue cracks. Of course, the opposite is true with tensile mean stress which tends to open microcracks and accelerates the formation of macrocracks. As observed in the results of the analysis using similar loading range as in the fatigue test, tensile transverse residual stresses still exist on the surface near the weld toe after shakedown. The residual stress is small (about 50 MPa) on the surface, so the effect on initiation is probably small. However, if an overload is used for shakedown, high compressive residual stress can be set up on the surface and delay the initiation of fatigue cracks.

Effect On Propagation Of A Fatigue Crack

A fatigue crack can propagate in three modes, Mode I (opening or tensile), Mode II (in-plane shear) and Mode III (out- of-plane shear). For the T-joint specimen in three point bending, the dominant mode of crack propagation is Mode I. The propagation rate of a fatigue crack can be predicted reasonably well with linear elastic fracture mechanics. The simplest model is the direct integration of the Paris equation [81],

$$\frac{da}{dN} = C(\triangle K)^m \tag{4.1}$$

where da/dN is the change of crack depth per load cycle; C and m are experimentally determined material properties; $\triangle$K is the stress intensity factor range which is a function of the stress range.

Some researchers have used shakedown to explain the effect (or no effect) of welding residual stresses on the fatigue life of welded structures. The usual assumption is that welding residual stresses of tensile yield stress level exist near the weld and are constant through the thickness. Thus, any tensile loading will cause yielding of the material and reduce the residual stresses to a lower level upon unloading. Further cyclic loading will be elastic up to but not beyond the yield stress. The actual stress level will be different from the nominal applied stress, however, the stress range will be the same which will give the same stress intensity factor range. The values of the material properties, C and m, are modified to compensate for the higher mean stress.

The above assumption of constant stress through the plate thickness, is probably true for thinner specimens or for full penetration butt welds. However, as observed in this study and similar results of Holden et al. [63] and Allen et al. [70], the residual stress in the direction normal to crack growth (transverse) is not constant through the horizontal plate thickness in the 26 mm T-joint specimen. In fact, about one third through the plate thickness, the residual stress is compressive. Shakedown does not occur throughout the plate thickness. Therefore, shakedown of the welding residual stresses through the whole plate thickness at the weld toe would not occur. As observed in the analysis, shakedown only affects the welding residual stresses in the top 1 mm around the weld toe and relatively high residual stresses remain elsewhere. These observations are contrary to the theory described above and the welding residual stresses can have various effects on fatigue crack propagation depending on the size of the crack. Since the transverse residual stresses are tensile in the top third of the plate, the crack growth rate could be faster than if the T-joint specimen had been heat treated to relief the welding residual stresses. The crack growth rate could decrease or even arrest when compressive residual stresses exists, but this was not observed in the fatigue tests [5-6] when the fatigue crack has penetrated into the transverse compressive residual stress zone. The reason for this is because the crack would be about 8 to 10 mm deep when it reached the compressive stress zone. A crack this size would probably have altered the whole stress field and removed any residual stresses. Therefore, the compressive residual stresses do not have any beneficial effect on crack growth.

One interesting observation in the fatigue test [6] was that the surface crack in the 26 mm and thinner specimens did not reach the edges and only grew as a semi-elliptical crack; while for thicker specimens, flat fronted cracks across the whole width developed very early. One suggested explanation is that compressive transverse residual stresses still existed at the edges in the thinner specimens even though one inch was removed from each end after welding. These compressive residual stresses prevented cracks from growing across the whole plate. Unfortunately, the present study cannot predict the residual stresses in this region of the specimen due to the three dimensional effects near the ends of the weld.

Effects On Final Fracture

After a large number of loading cycles, the fatigue crack may have grown to a point at which the remaining uncracked section cannot support the applied stress and final fracture of the component occurs. According to fracture mechanics, final fracture occurs after the stress intensity factor, K, which is a function of the geometry, loading condition and crack size, reaches the critical fracture toughness, K_{Ic}, of the material. K is directly proportional to the applied stress, and therefore, the maximum stress controls the fracture process. Tensile residual stresses which increase the actual stress in the component tend to cause fast fracture earlier than a stress free component; while the opposite is true for a compressive residual stress.

In the fatigue test of the 26 mm T-joint specimen [5, 6], final fracture did not occur till the fatigue crack penetrated over half of the plate thickness which is well within the transverse compressive residual stress zone. As mentioned in the last section, the welding residual stresses are most likely being relaxed by the large propagating crack. Therefore, the residual stresses probably have little or no effect on fast fracture. However, the residual stresses may have a significant role in the thicker specimens in which fast fracture occurred when the crack is very shallow, especially with a low applied stress [5-7]. Assuming the through thickness residual stress distribution is similar for both thin and thick specimens. With low applied stress, will cause only small reductions in residual stresses during shakedown. The high tensile residual stress near the weld toe can raise the actual stress in the specimen to a very high level and cause fast fracture to occur even with a very shallow crack.

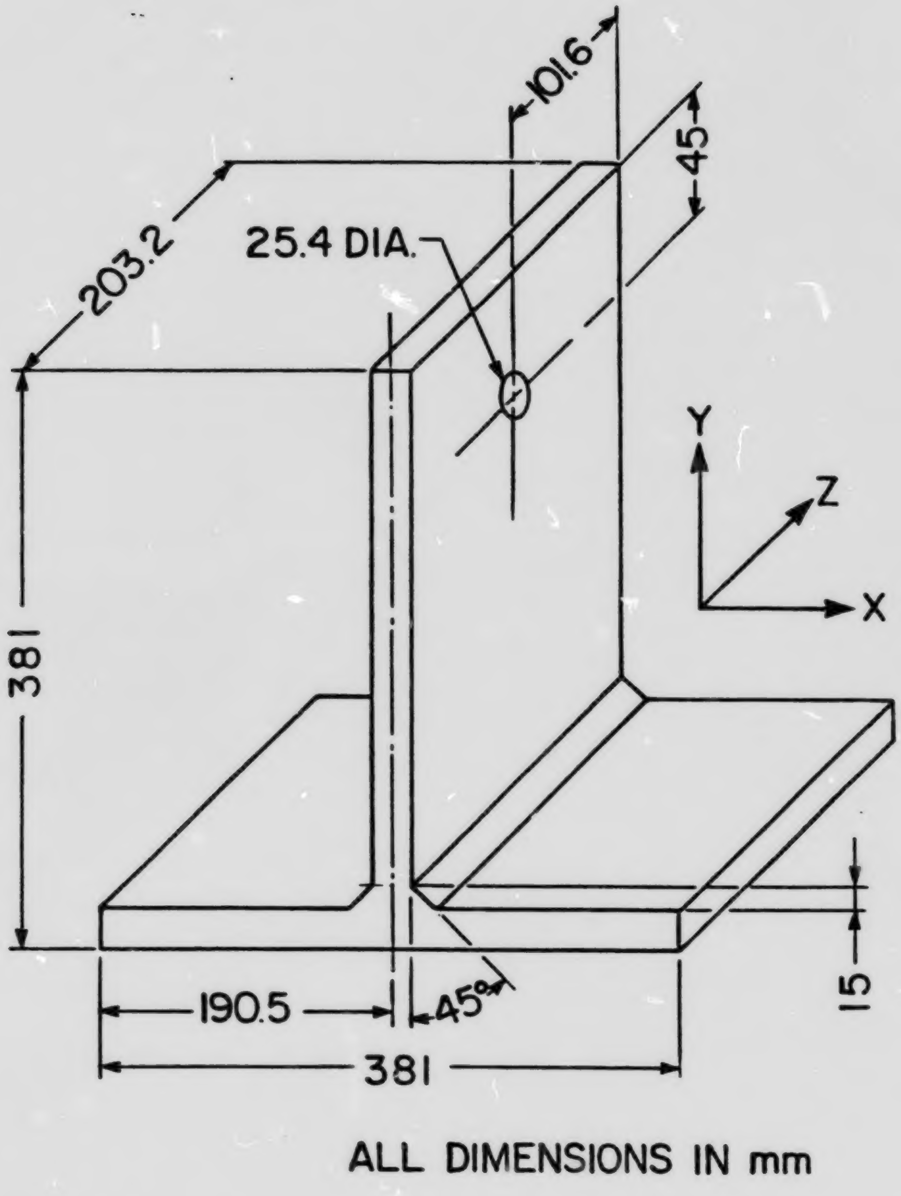
101.6
45
203.2
25.4 DIA.
Y
Z
X
381
15
190.5
45°
381
ALL DIMENSIONS IN mm

Figure 5.1: Dimensions of the 26 mm T-joint Specimen

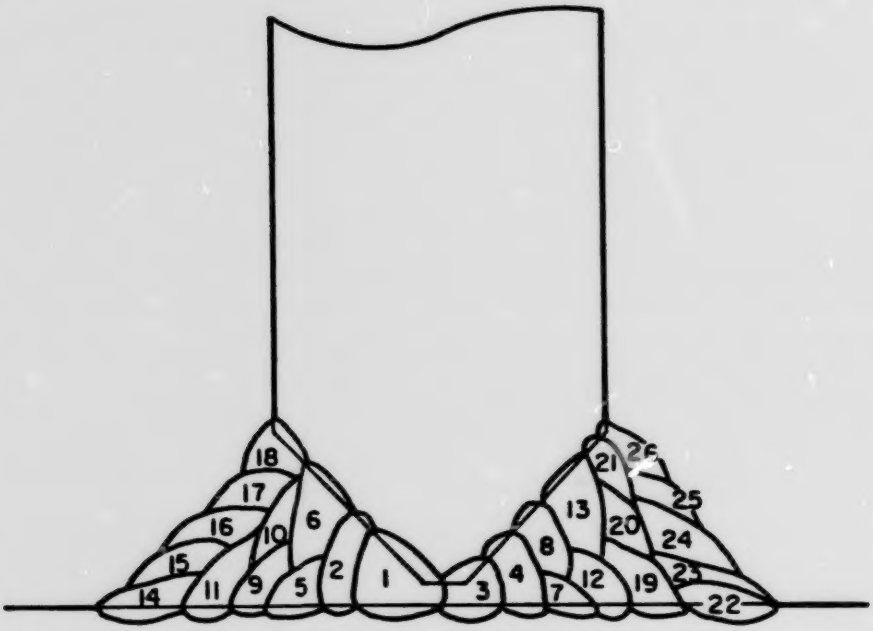
18
26
21
17
25
13
6
16
10
20
24
8
15
2
1
4
12
23
19
14
11
9
5
3
7
22

Figure 5.2: Welding sequence for the 26 mm T-joint specimen

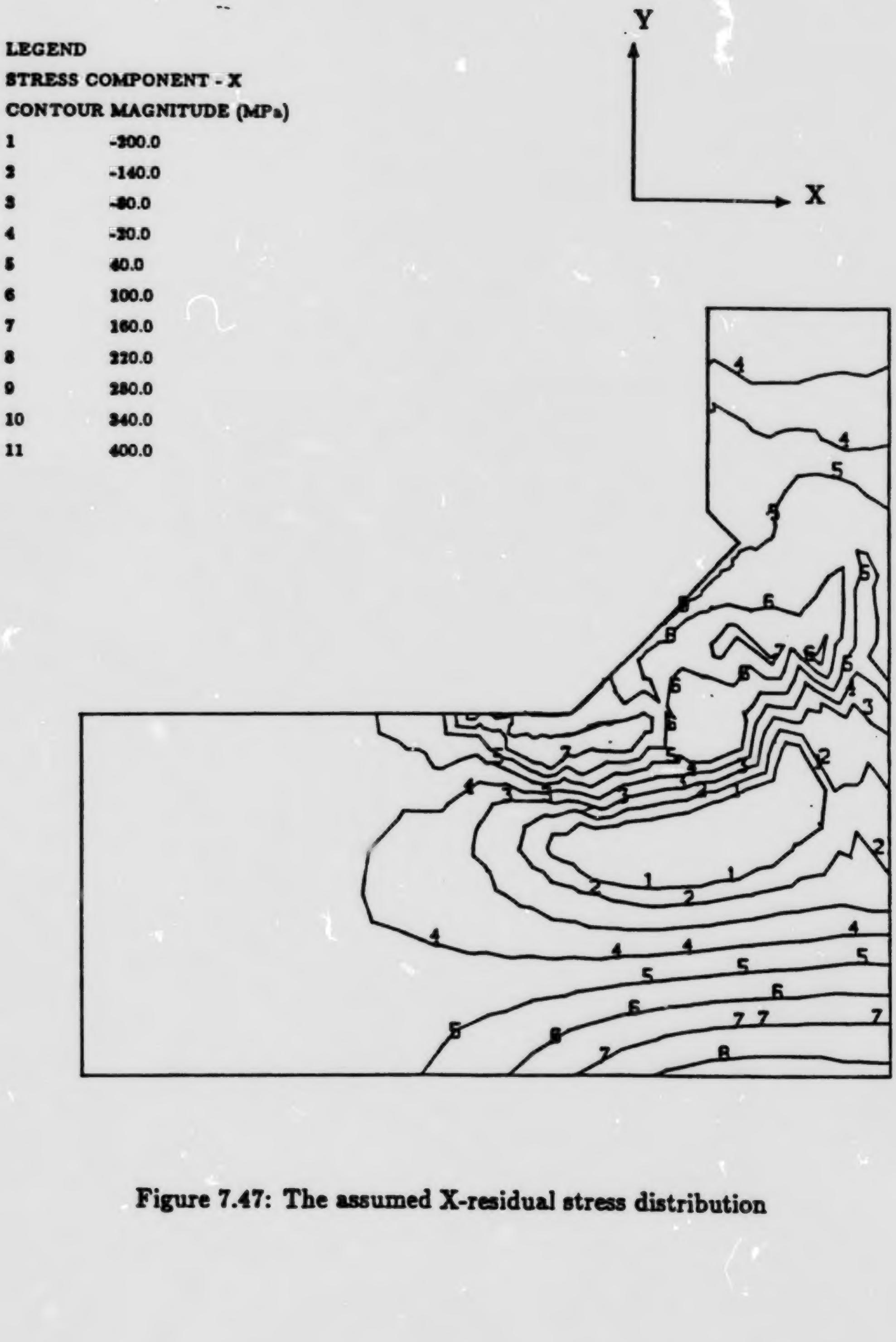

Figure 7.47: The assumed X-residual stress distribution

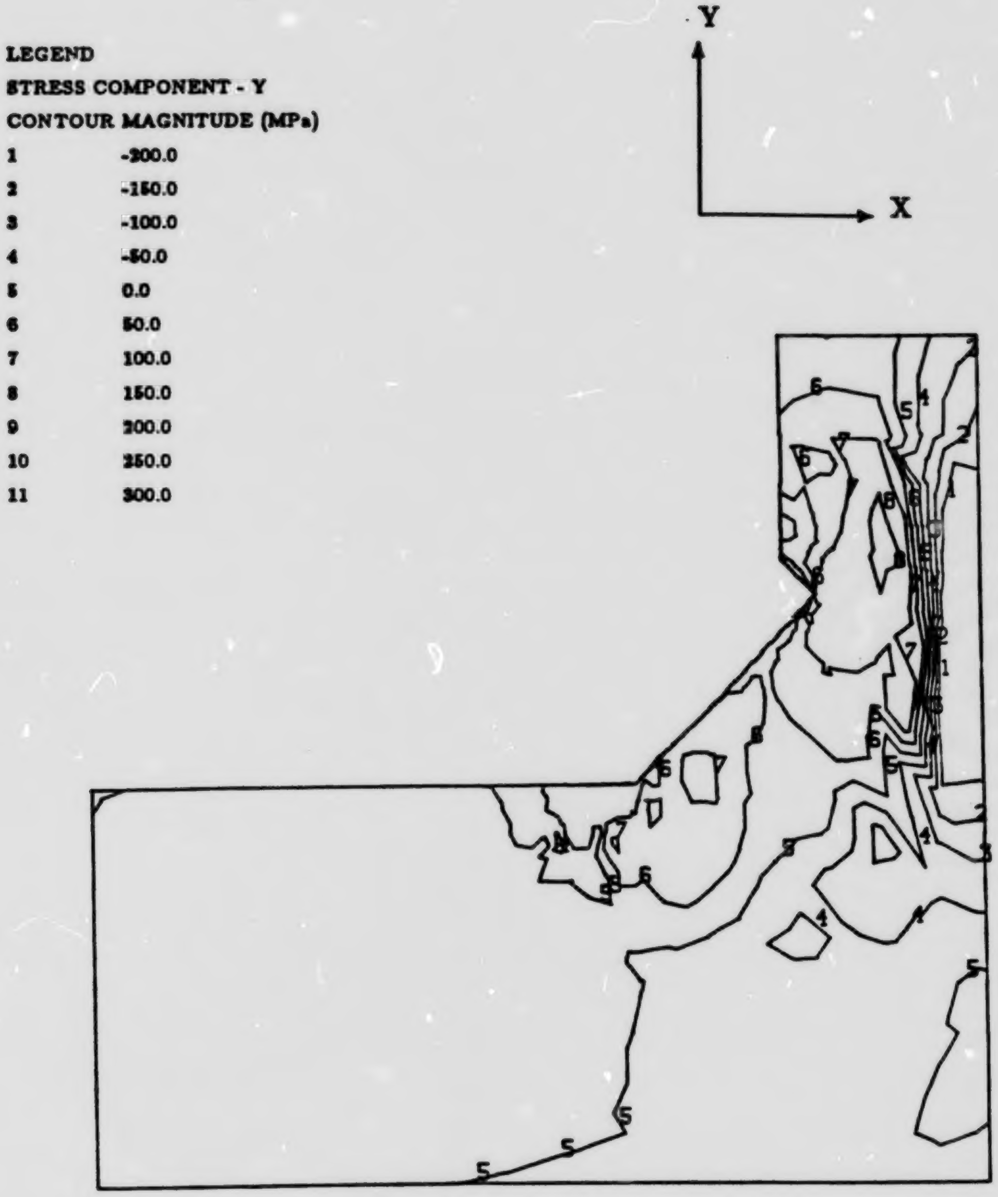

Figure 7.48: The assumed Y-residual stress distribution

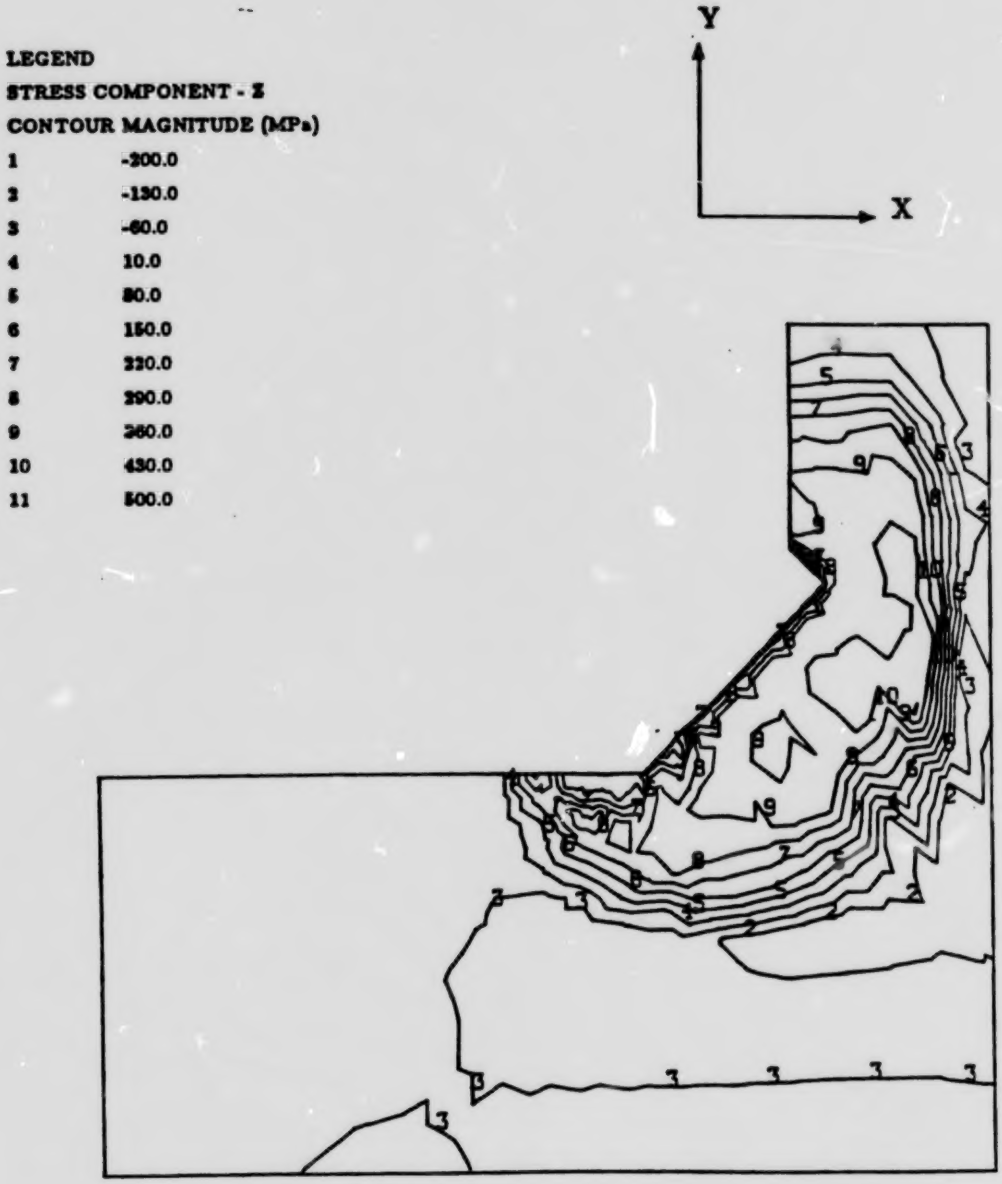

Figure 7.49: The assumed Z-residual stress distribution

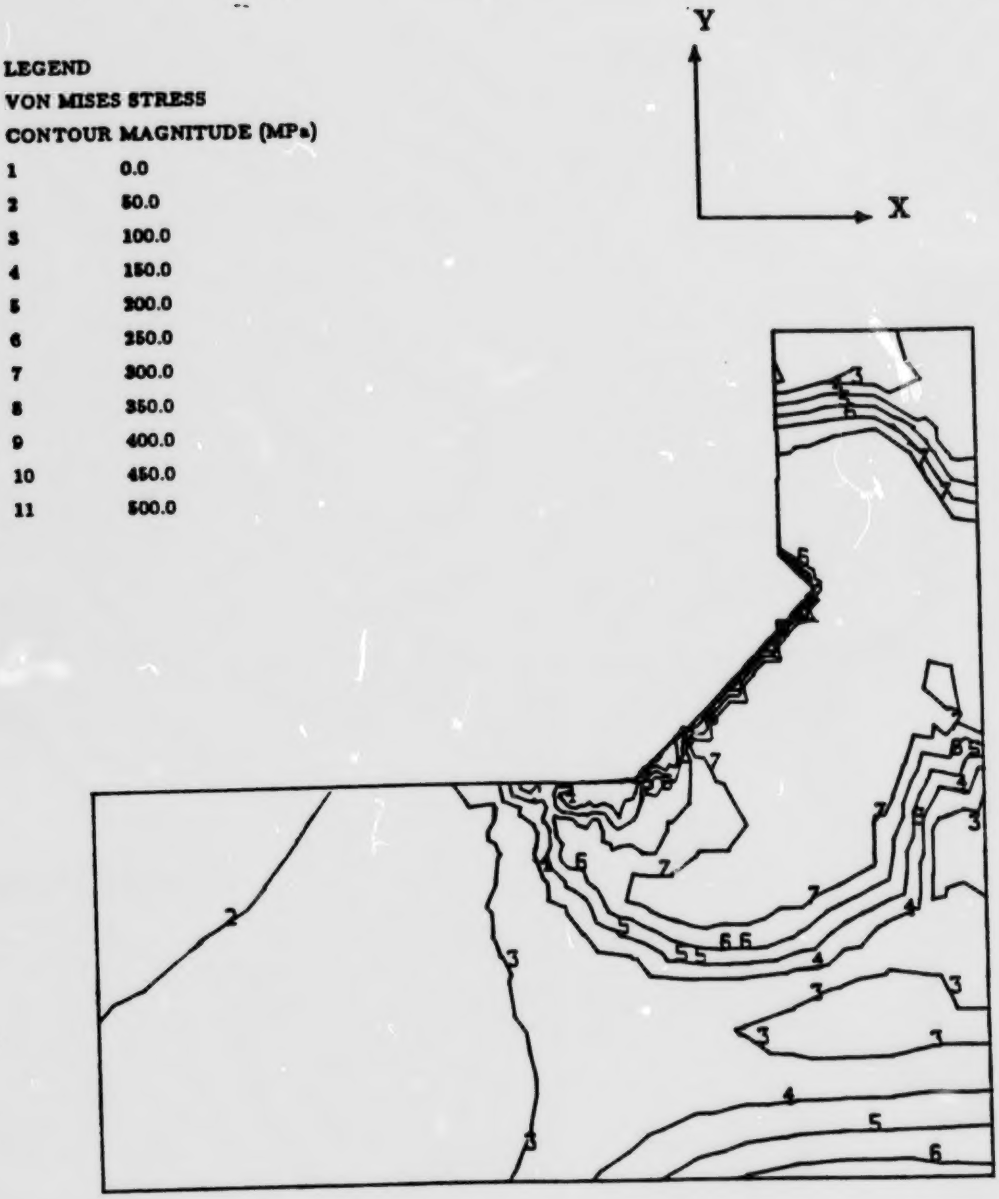

Figure 7.50: The assumed Von Mises equivalent stress distribution

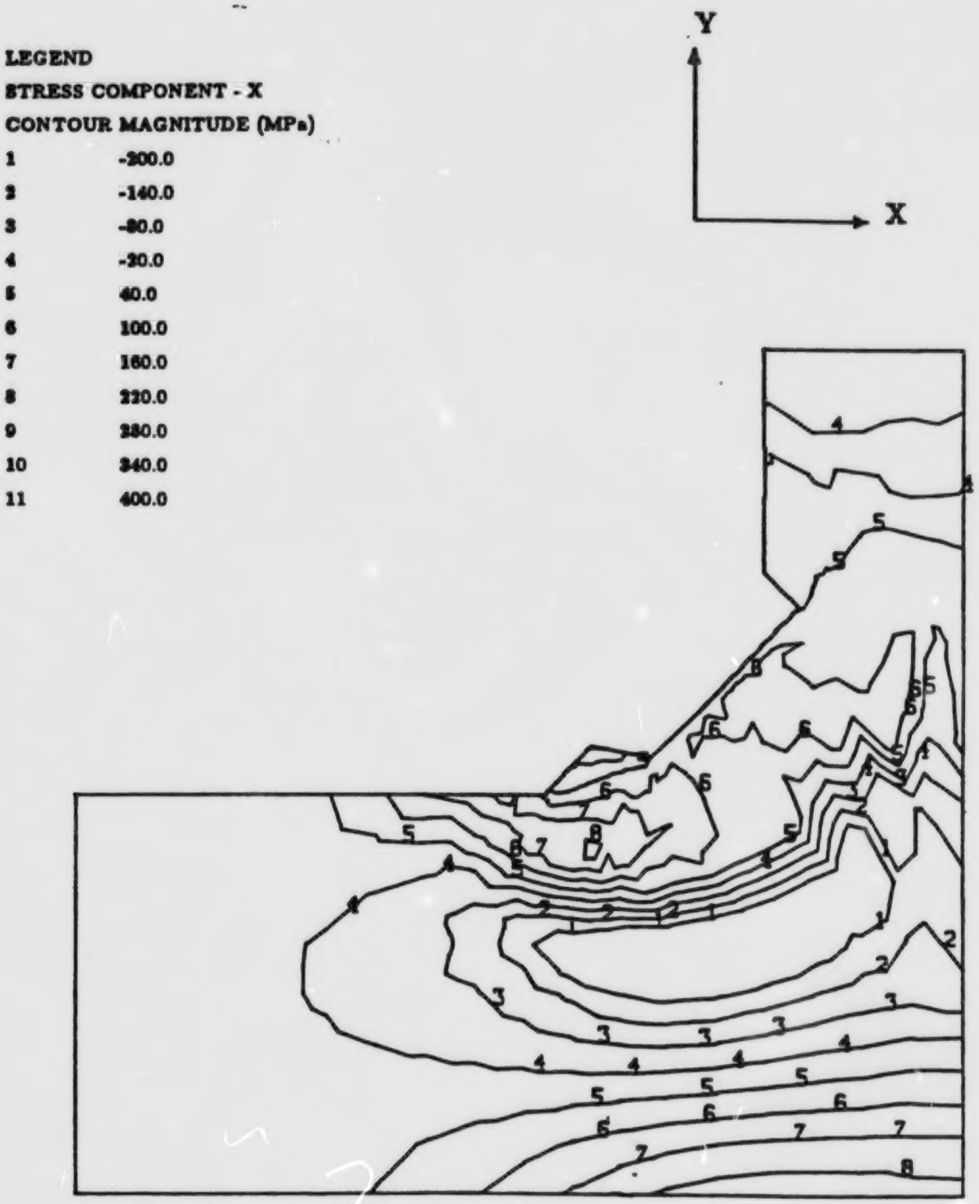

Figure 7.51: X-residual stress distribution with A.R.S - PASS 1

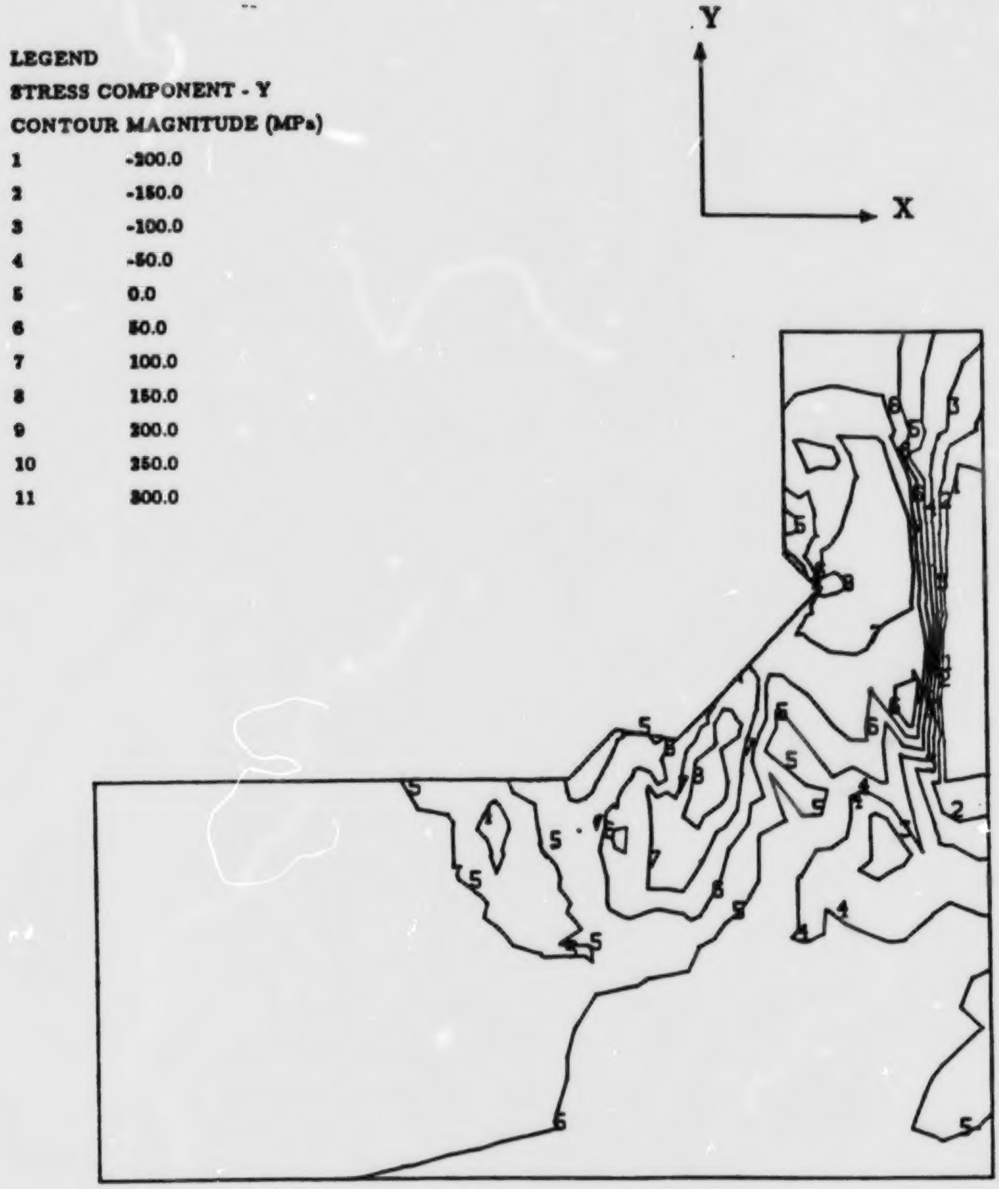

LEGEND

STRESS COMPONENT - Y

CONTOUR MAGNITUDE (MPa)

1	-200.0
2	-150.0
3	-100.0
4	-50.0
5	0.0
6	50.0
7	100.0
8	150.0
9	200.0
10	250.0
11	300.0

Figure 7.52: Y-residual stress distribution with A.R.S - PASS 1

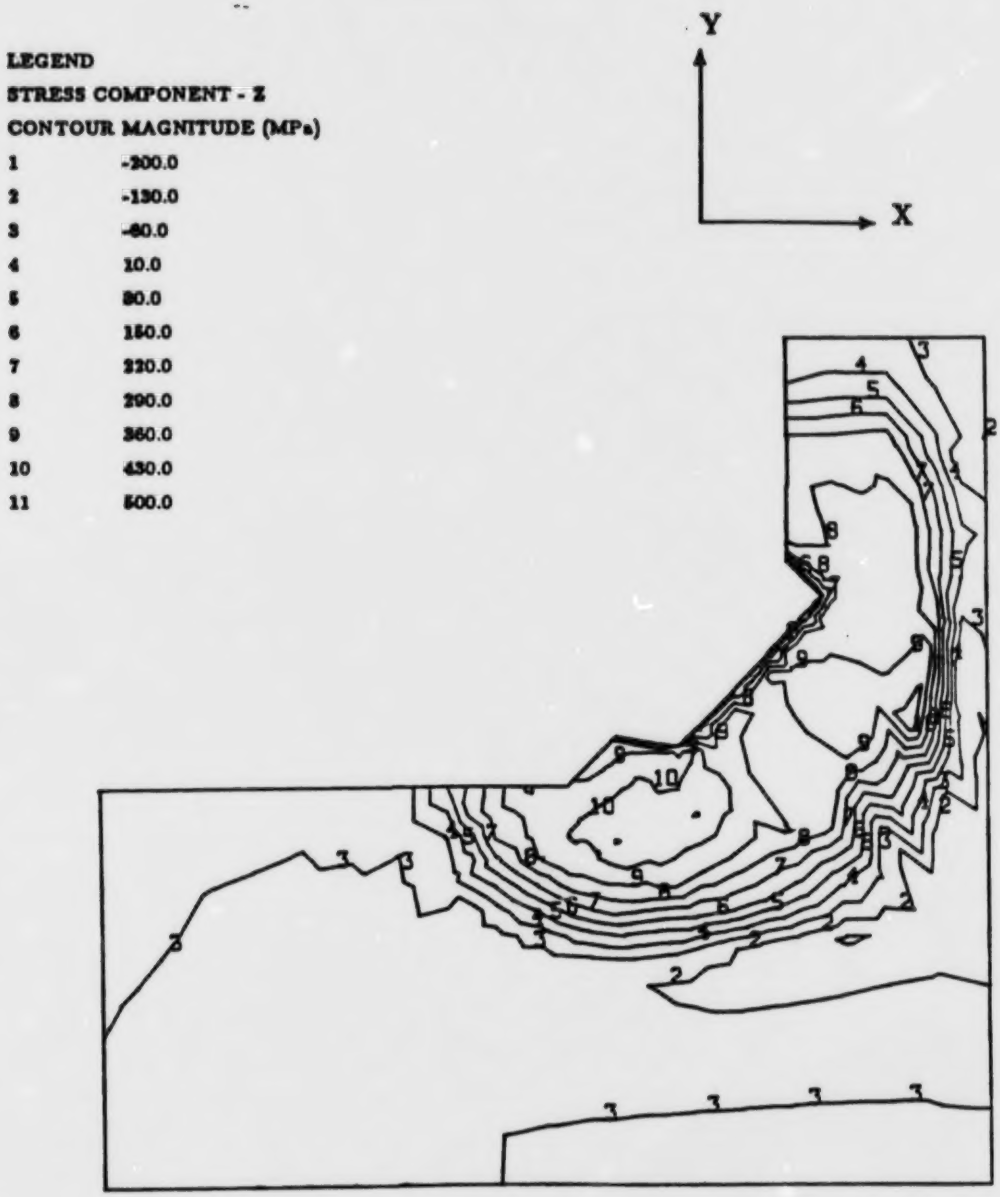

Figure 7.53: Z-residual stress distribution with A.R.S - PASS 1

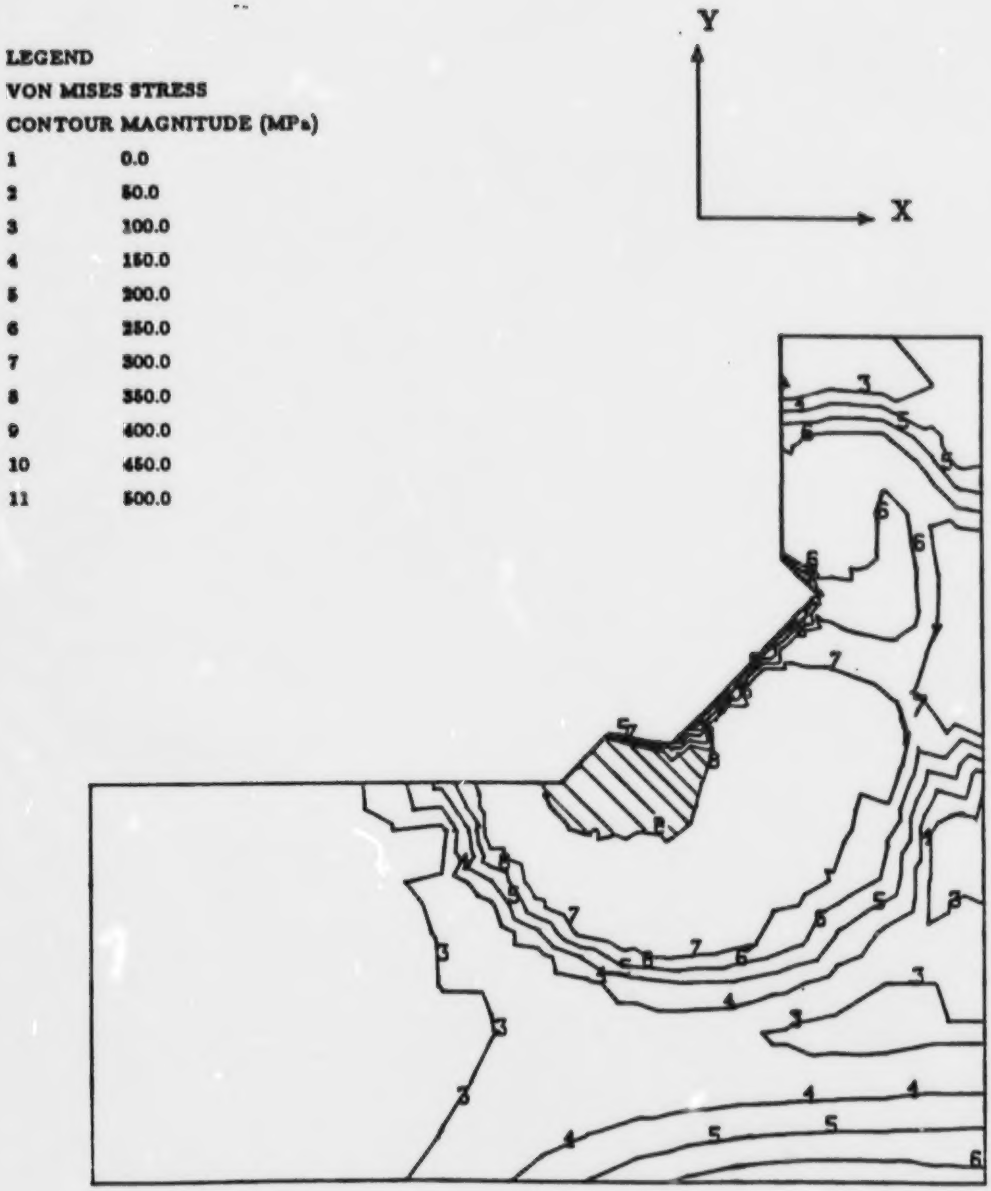

Figure 7.54: Von Mises stress distribution with A.R.S - PASS 1

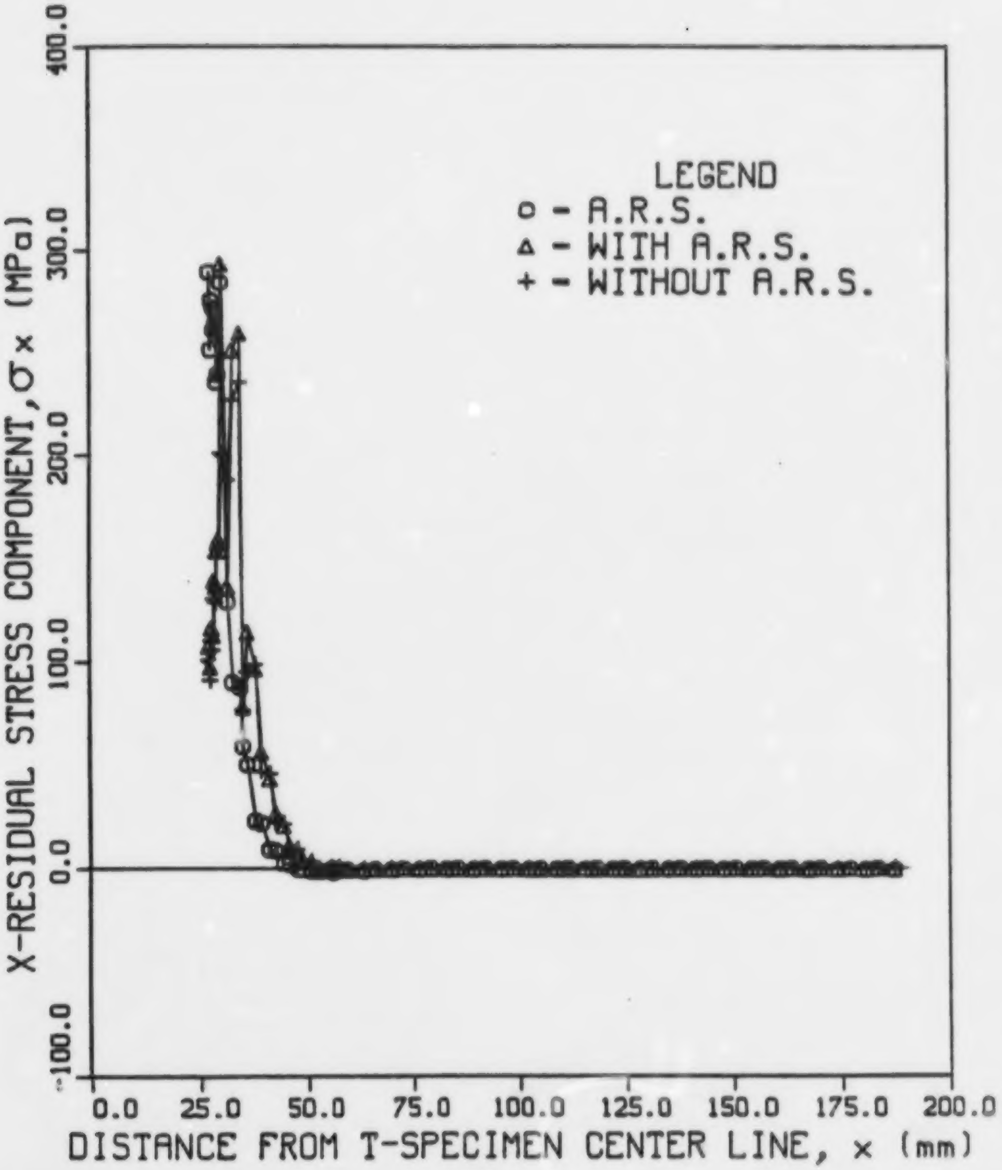

Figure 7.55: Distribution of the X-residual stress component along the top surface after the first pass

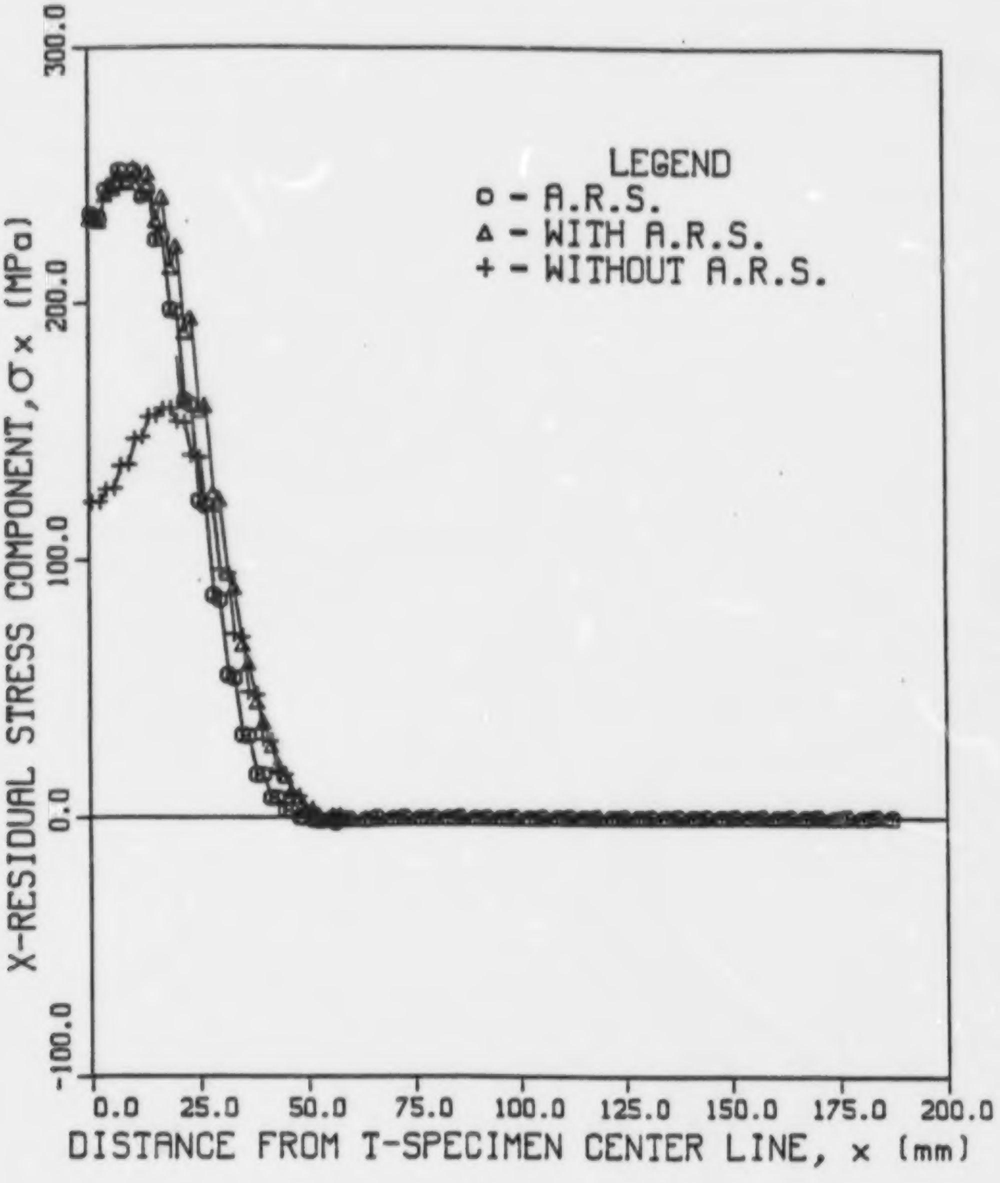

Figure 7.56: Distribution of the X-residual stress component along the bottom surface after the first pass

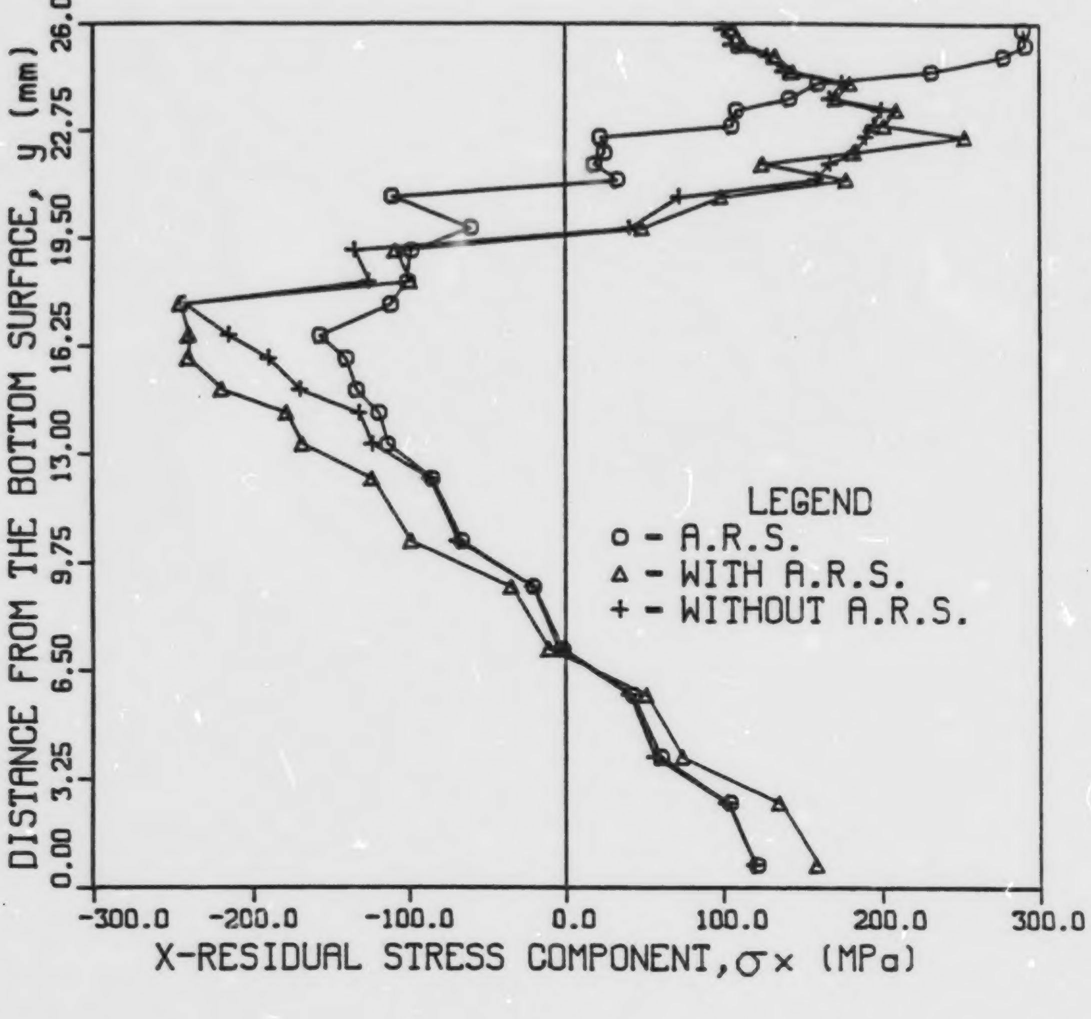

Figure 7.57: Distribution of the X-residual stress component through the plate thickness below the weld toe after the first pass

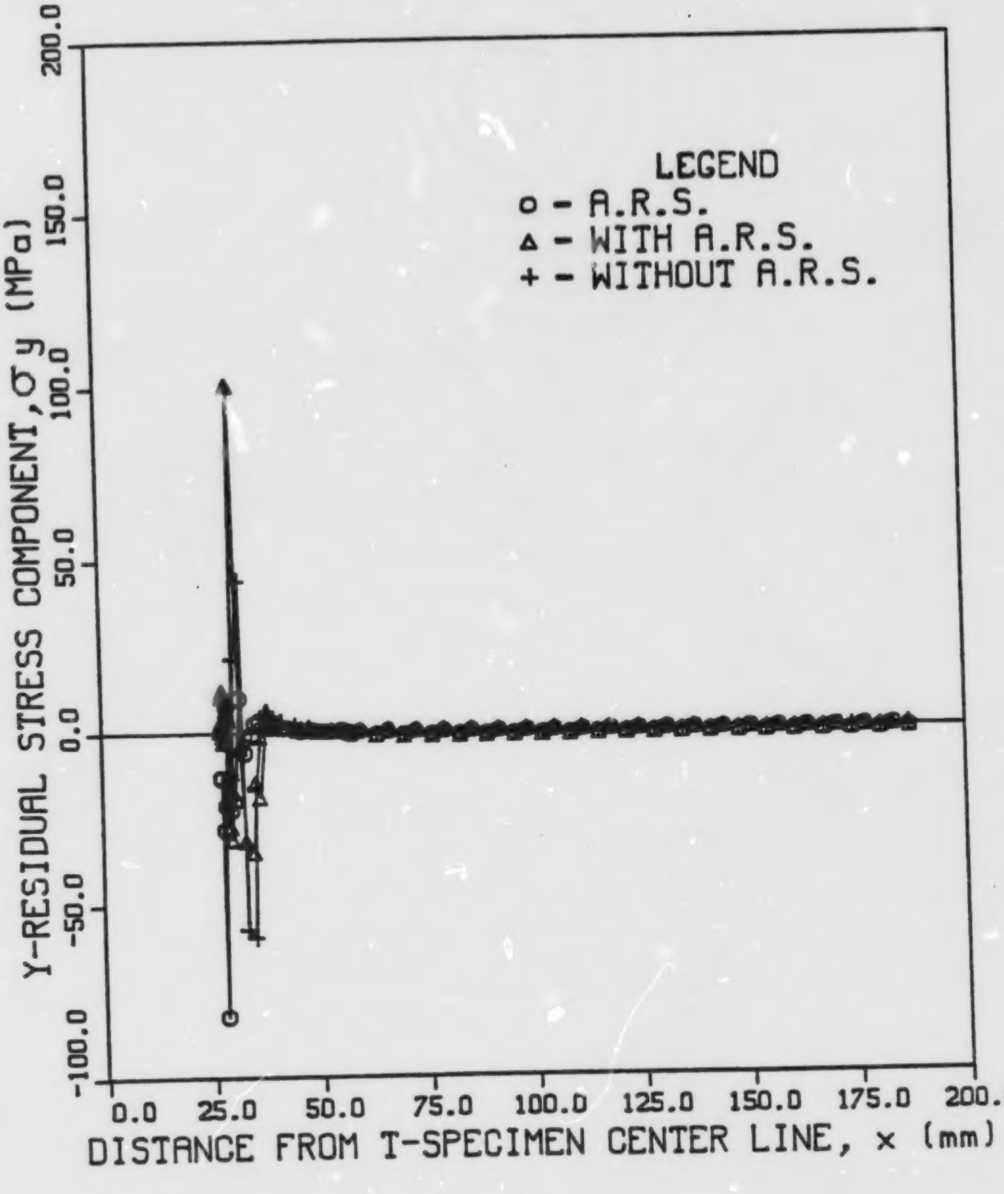

Figure 7.58: Distribution of the Y-residual stress component along the top surface after the first pass

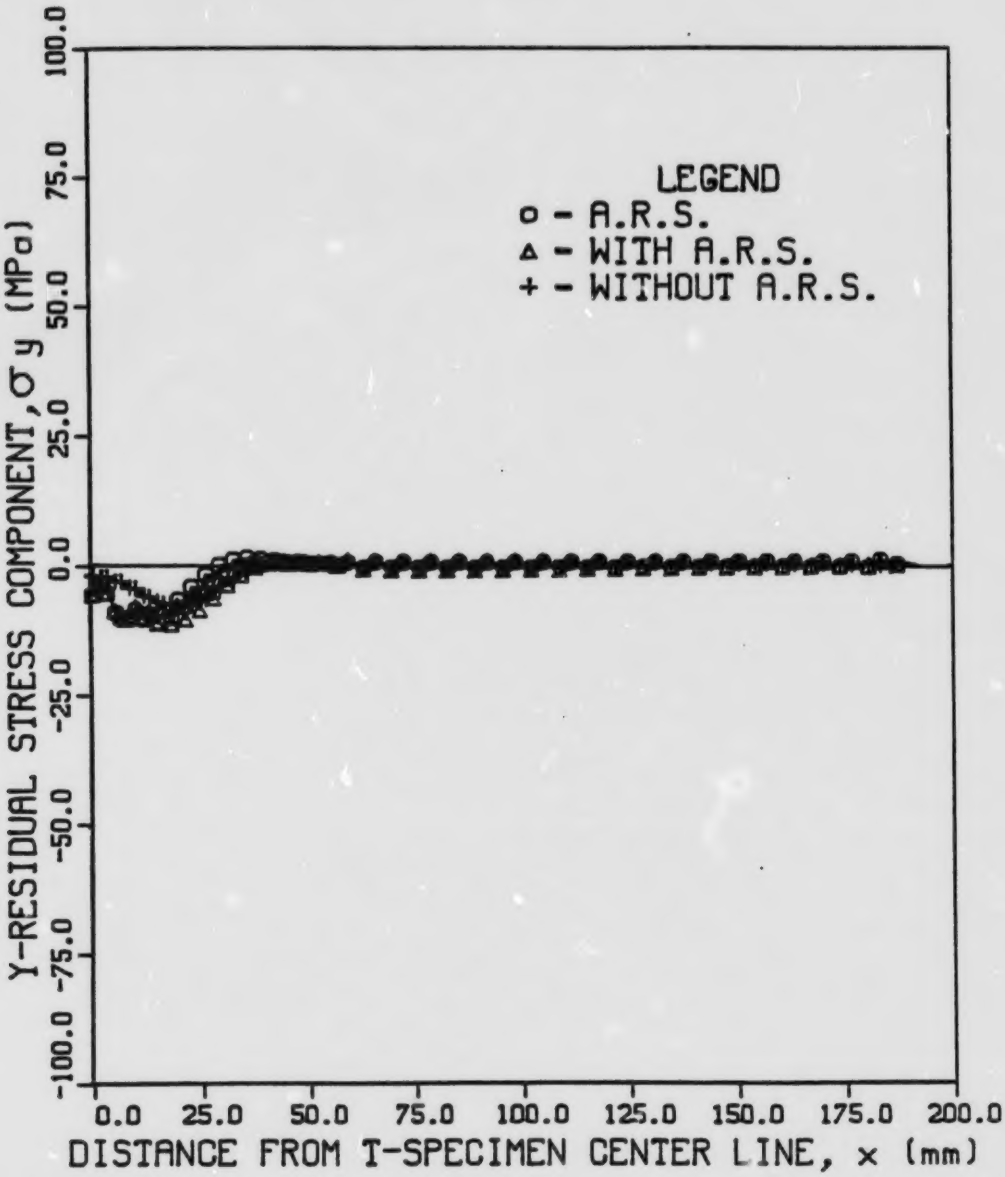

Figure 7.59: Distribution of the Y-residual stress component along the bottom surface after the first pass

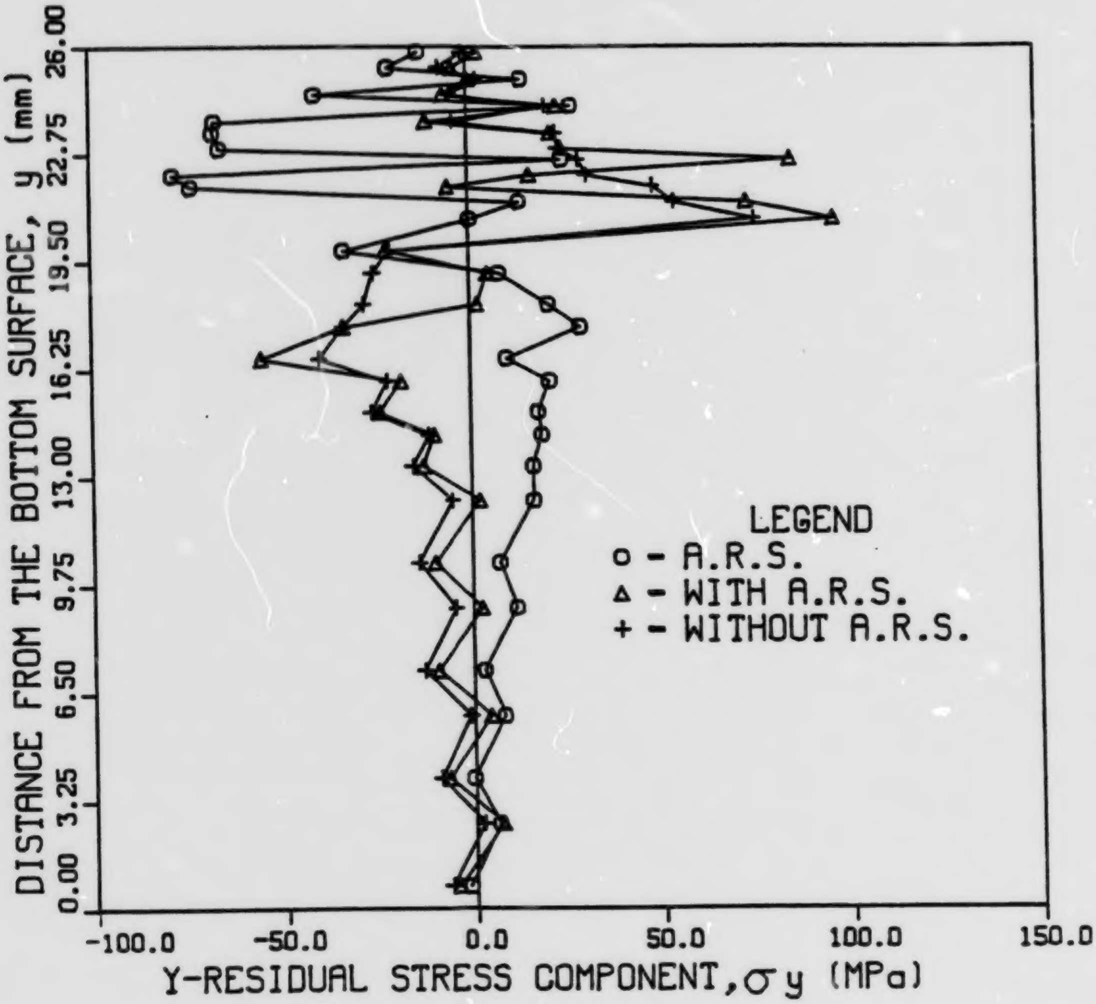

Figure 7.60: Distribution of the Y-resiudal stress component through the plate thickness below the weld toe after the first pass

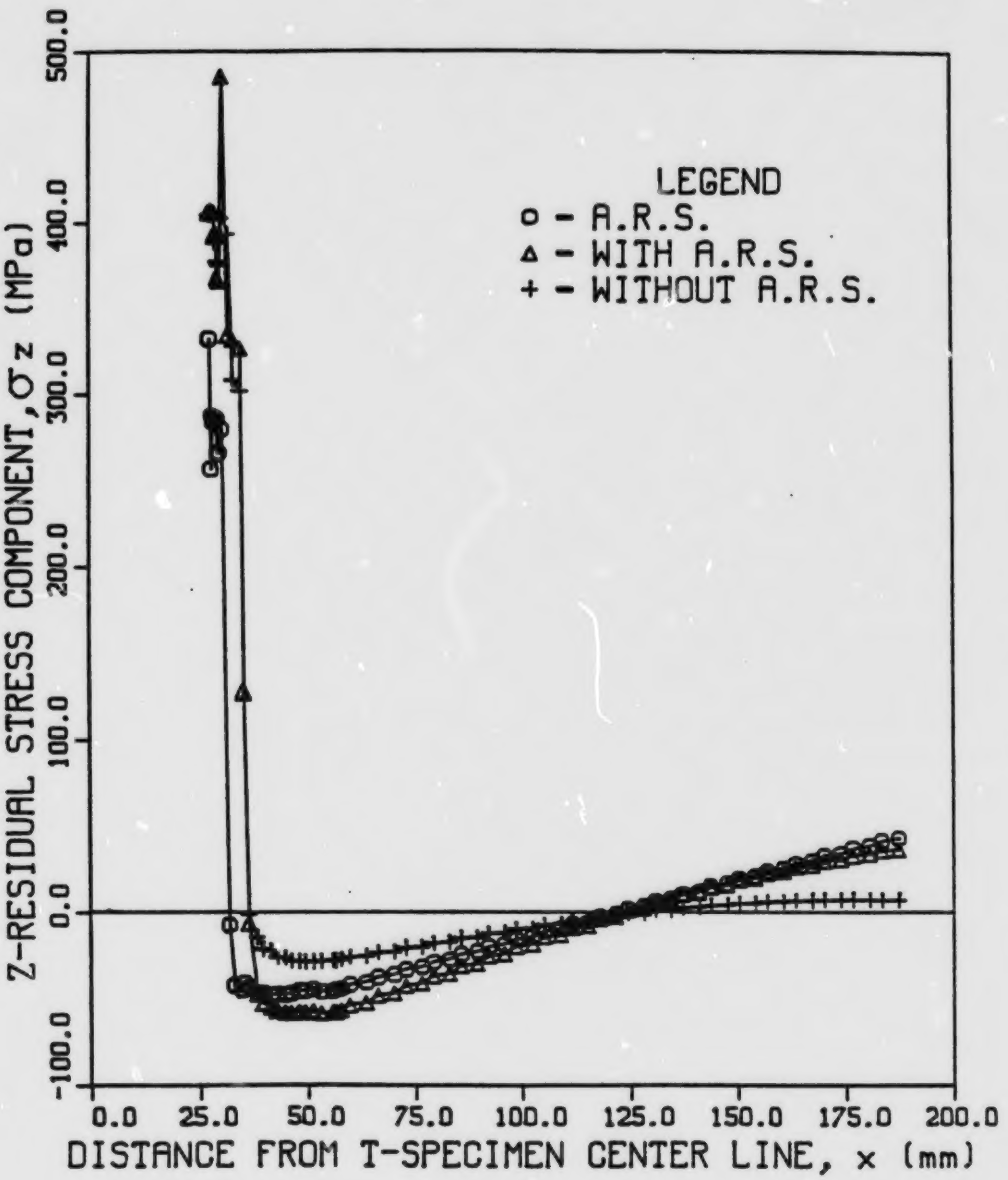

Figure 7.61: Distribution of the Z-residual stress component along the top surface after the first pass

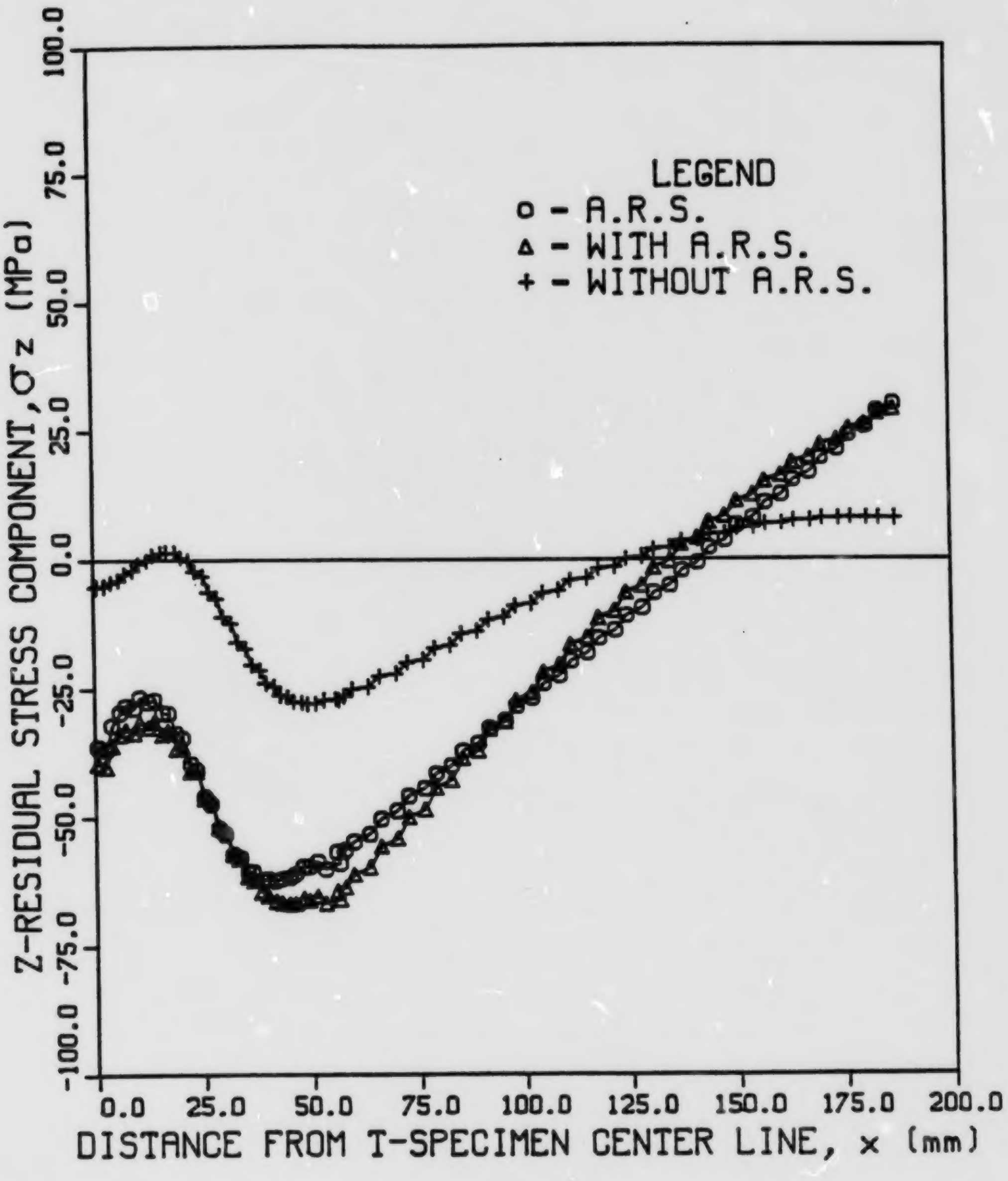

Figure 7.62: Distribution of the Z-residual stress component along the bottom surface after the first pass

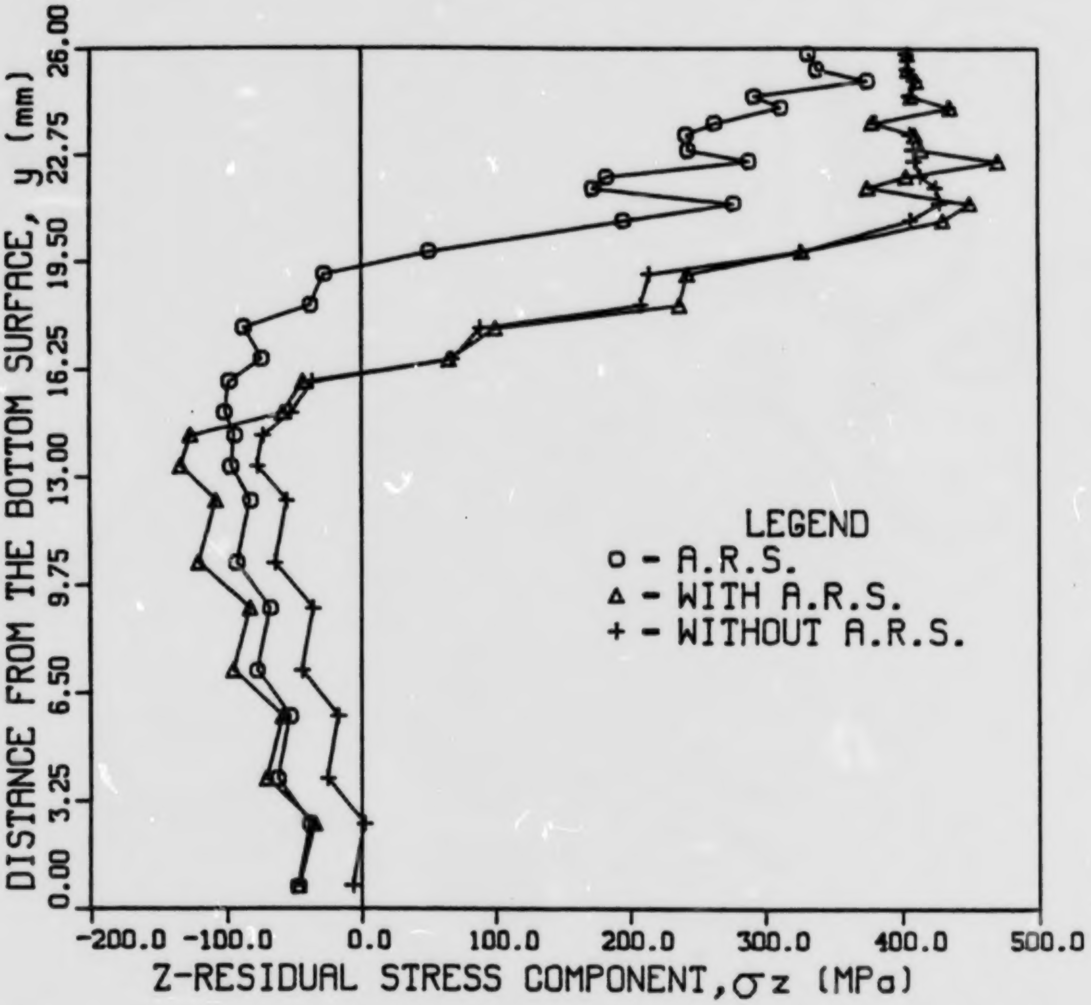

Figure 7.63: Distribution of the Z-residual stress component through the plate thickness below the weld toe after the first pass

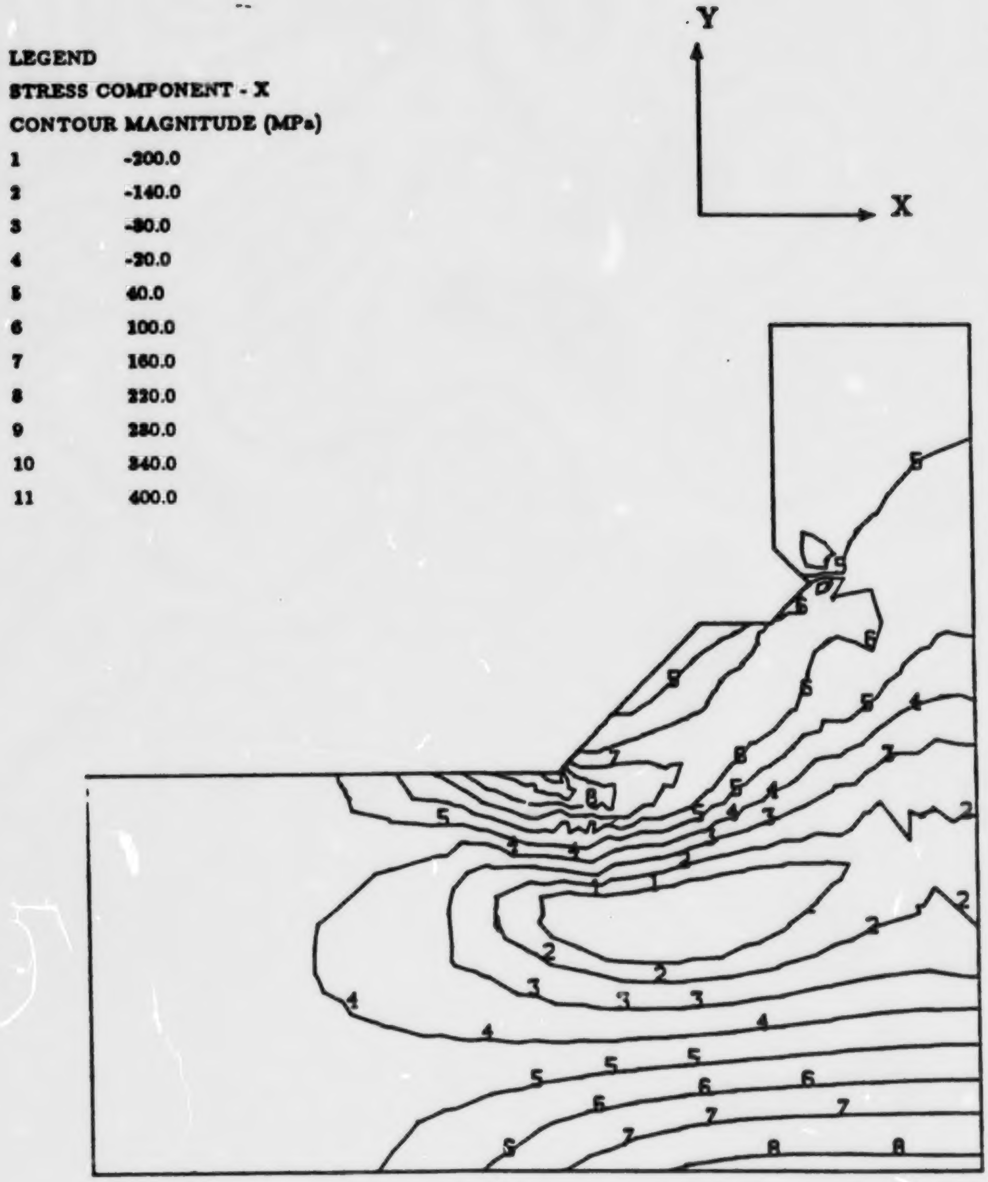

Figure 7.39: X-residual stress distribution - PASS 2&3

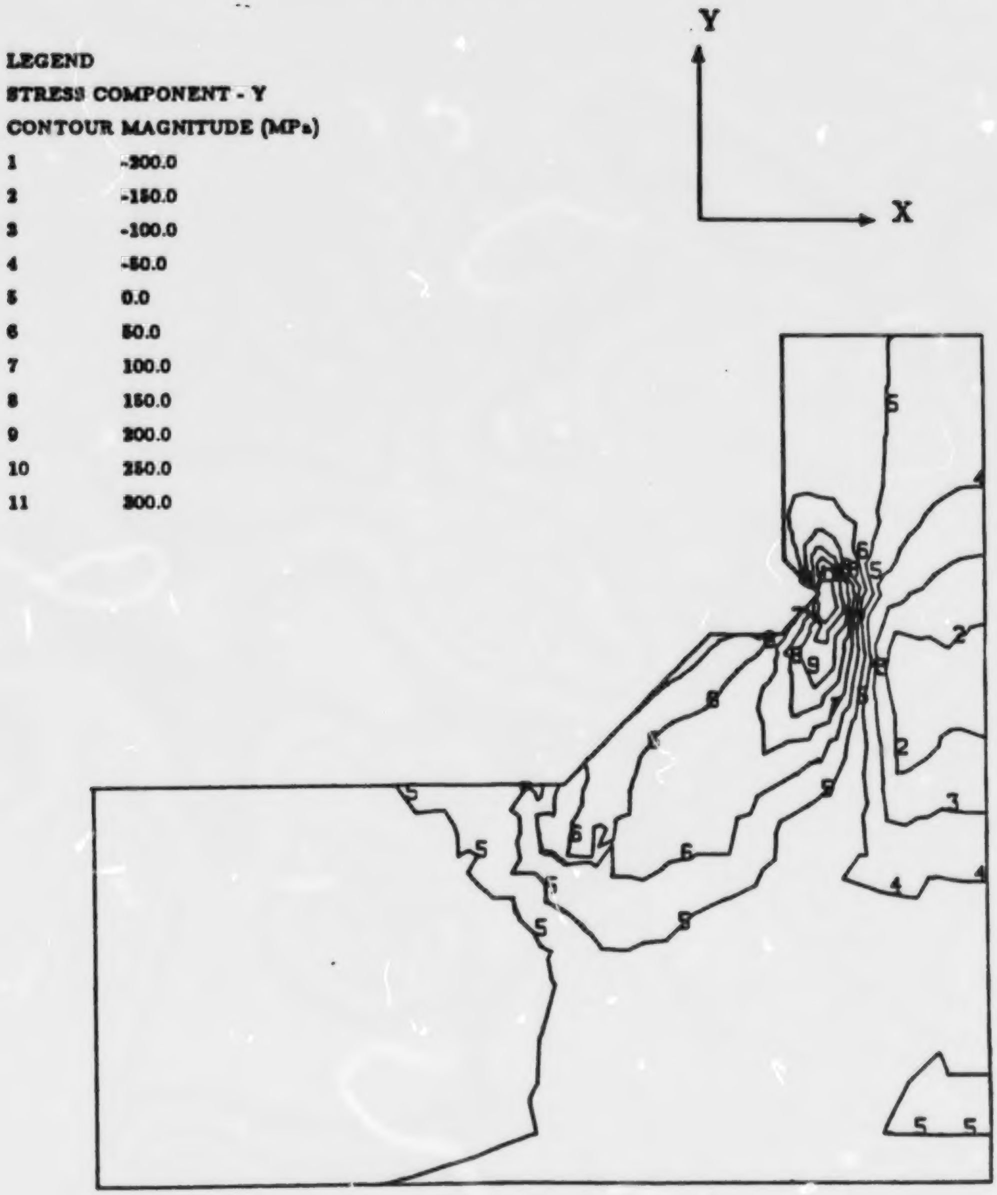

Figure 7.40: Y-residual stress distribution - PASS 2&3

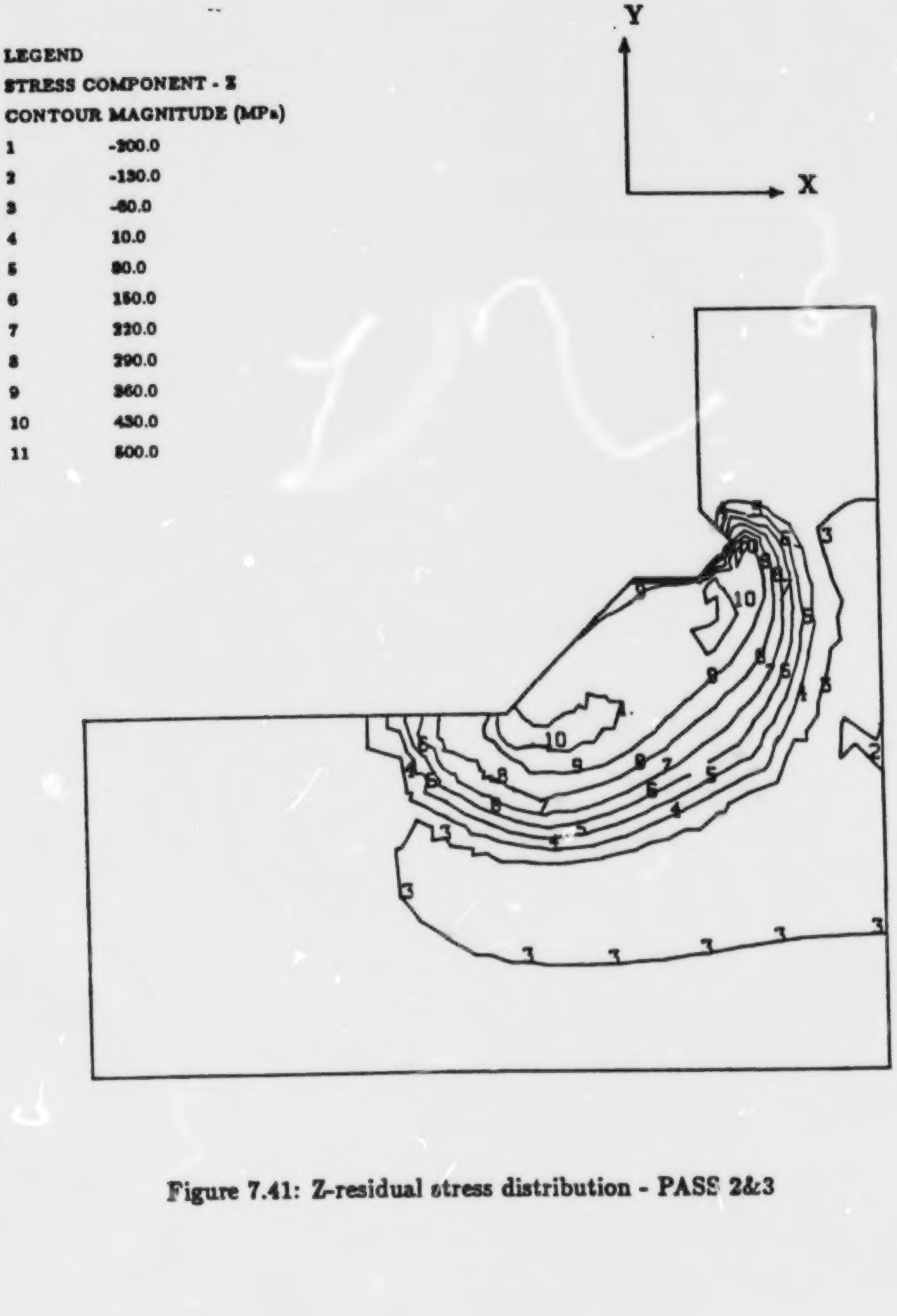

Figure 7.41: Z-residual stress distribution - PASS 2&3

LEGEND

VON MISES STRESS

CONTOUR MAGNITUDE (MPa)

1	0.0
2	50.0
3	100.0
4	150.0
5	200.0
6	250.0
7	300.0
8	350.0
9	400.0
10	450.0
11	500.0

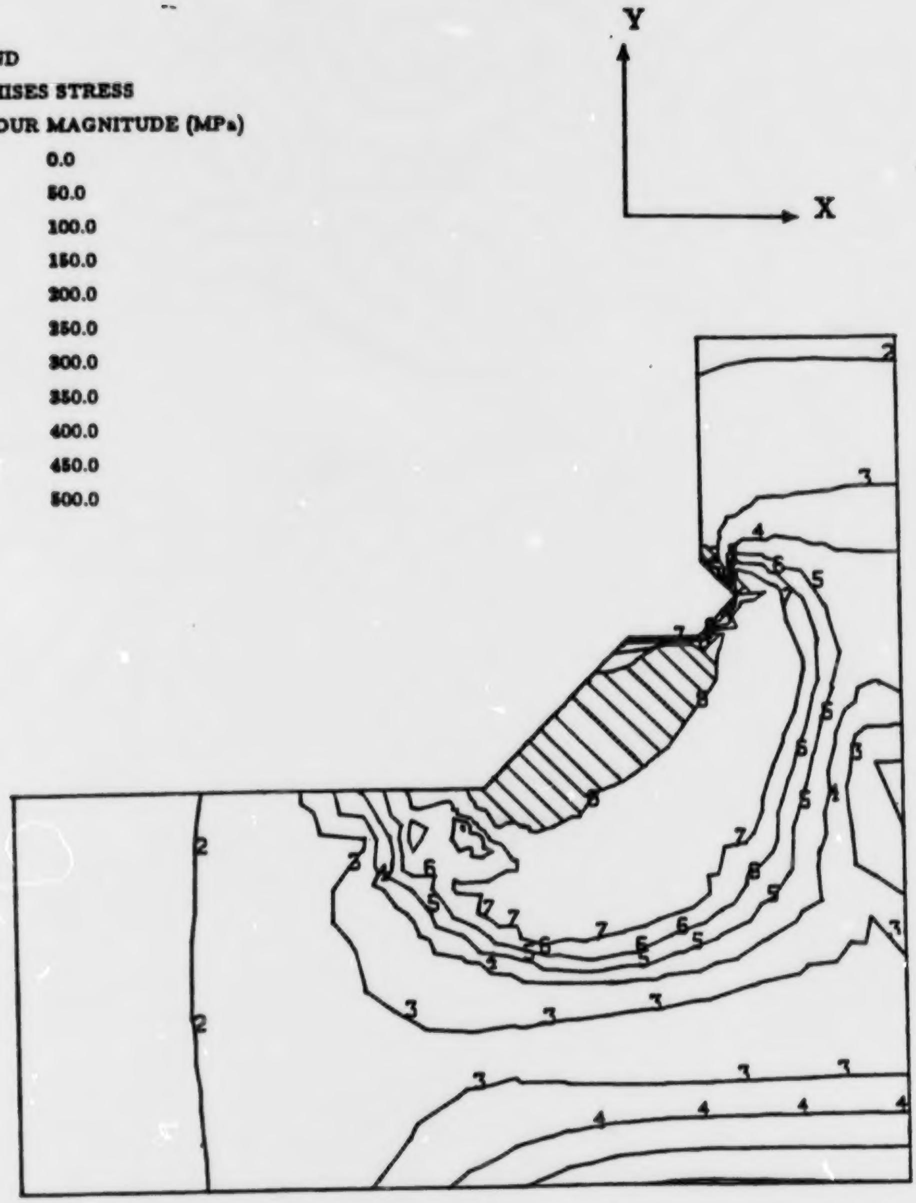

Figure 7.42: Von Mises residual stress distribution - PASS 2&3

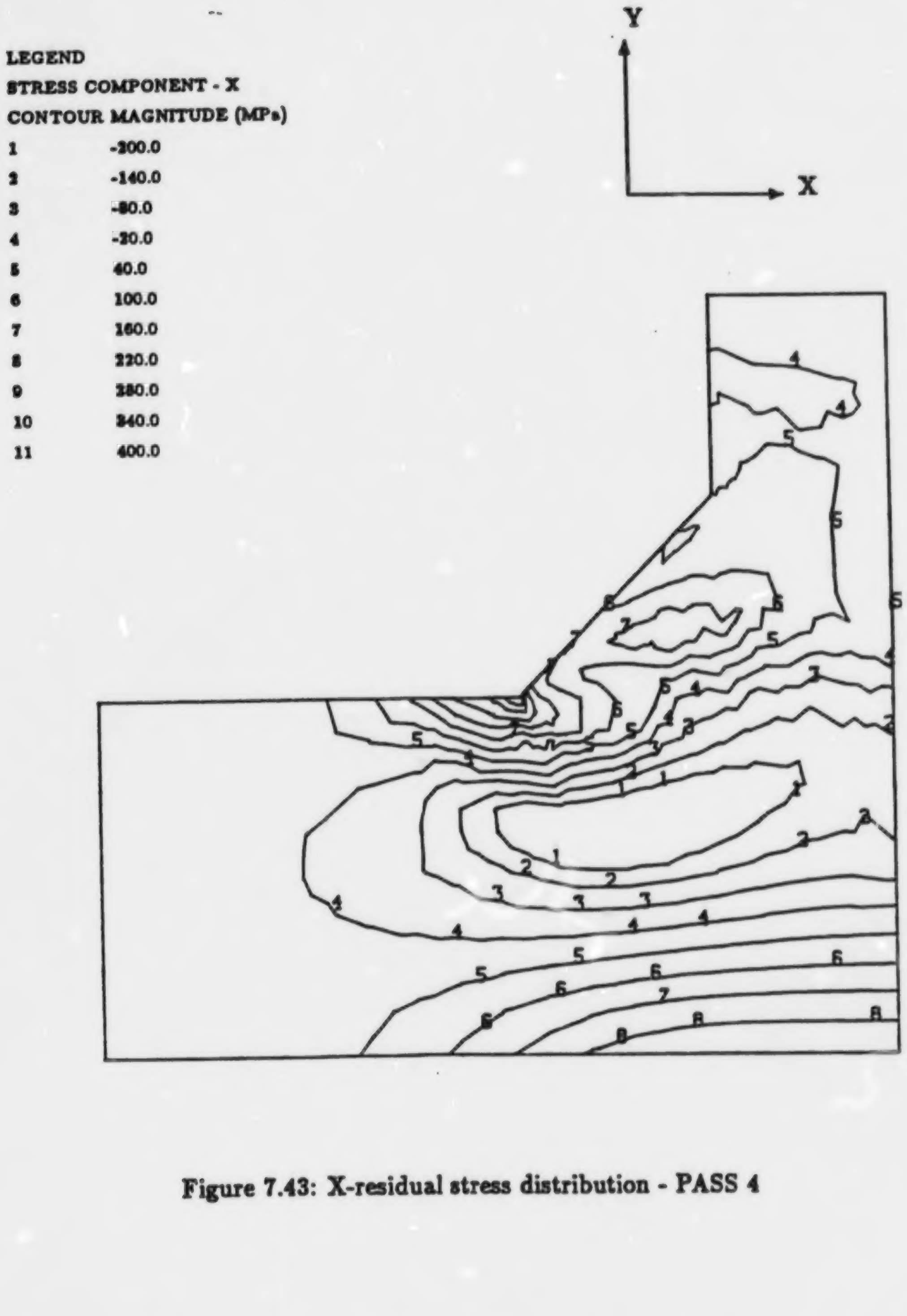

Figure 7.43: X-residual stress distribution - PASS 4

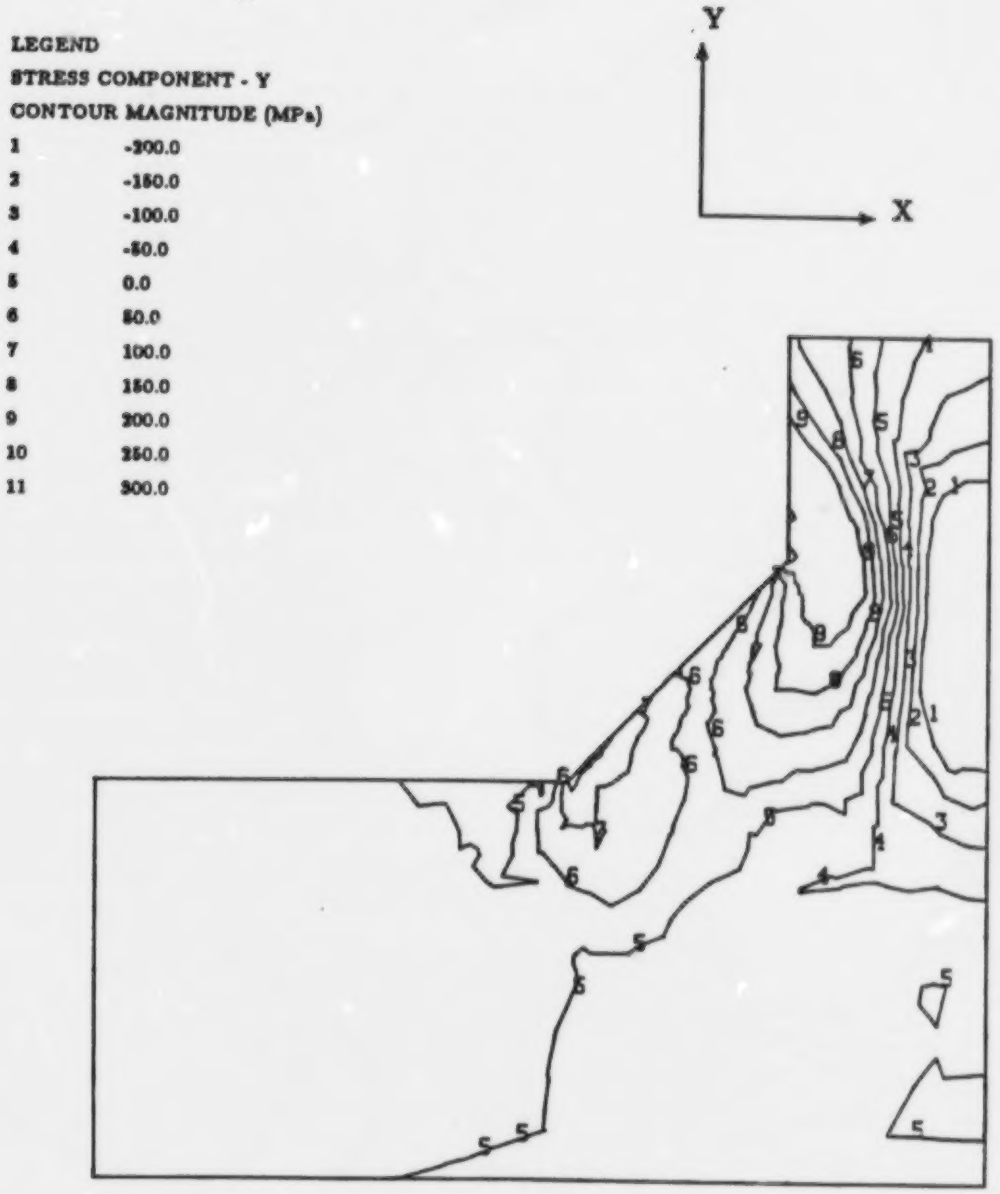

Figure 7.44: Y-residual stress distribution - PASS 4

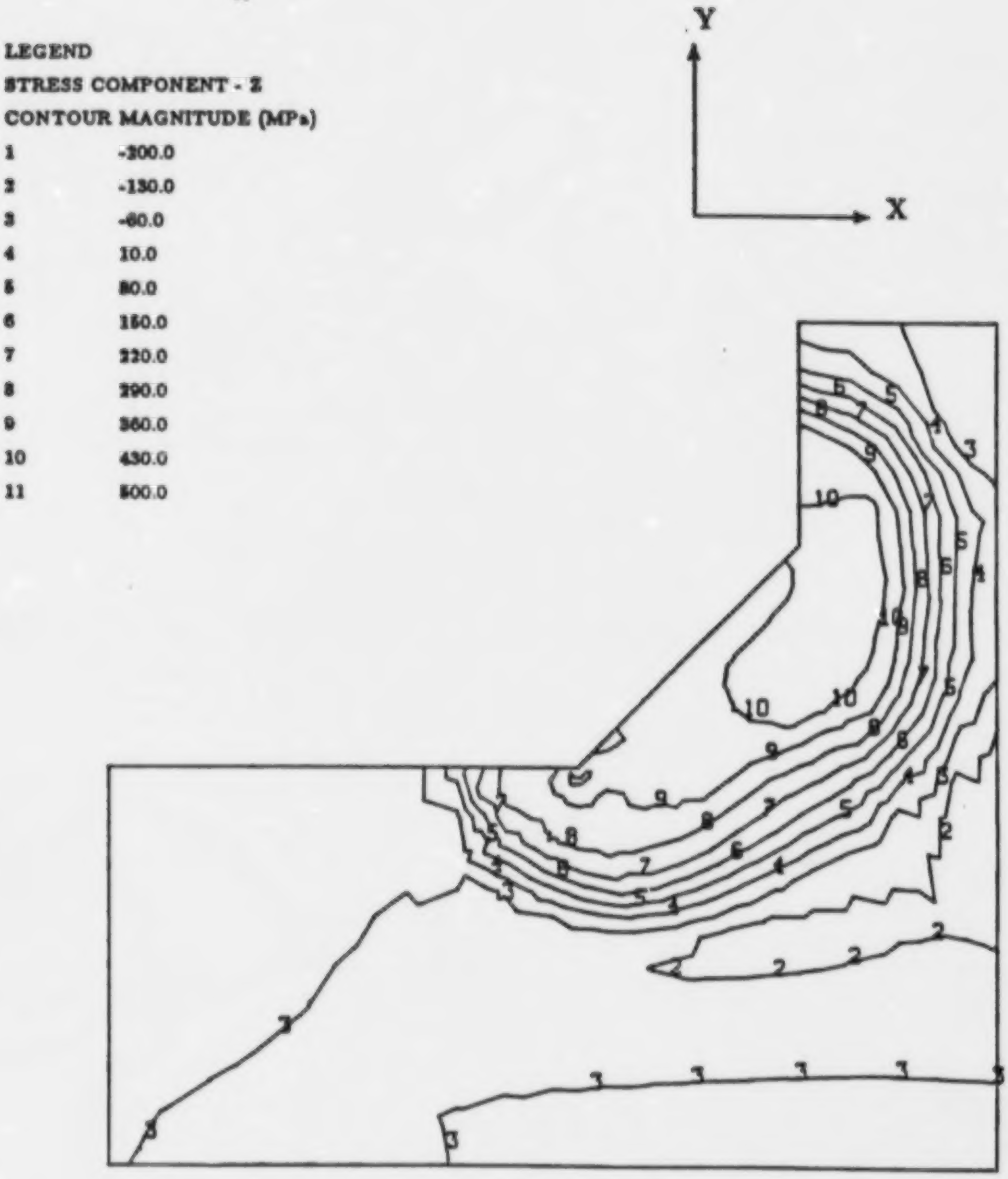

Figure 7.45: Z-residual stress distribution - PASS 4

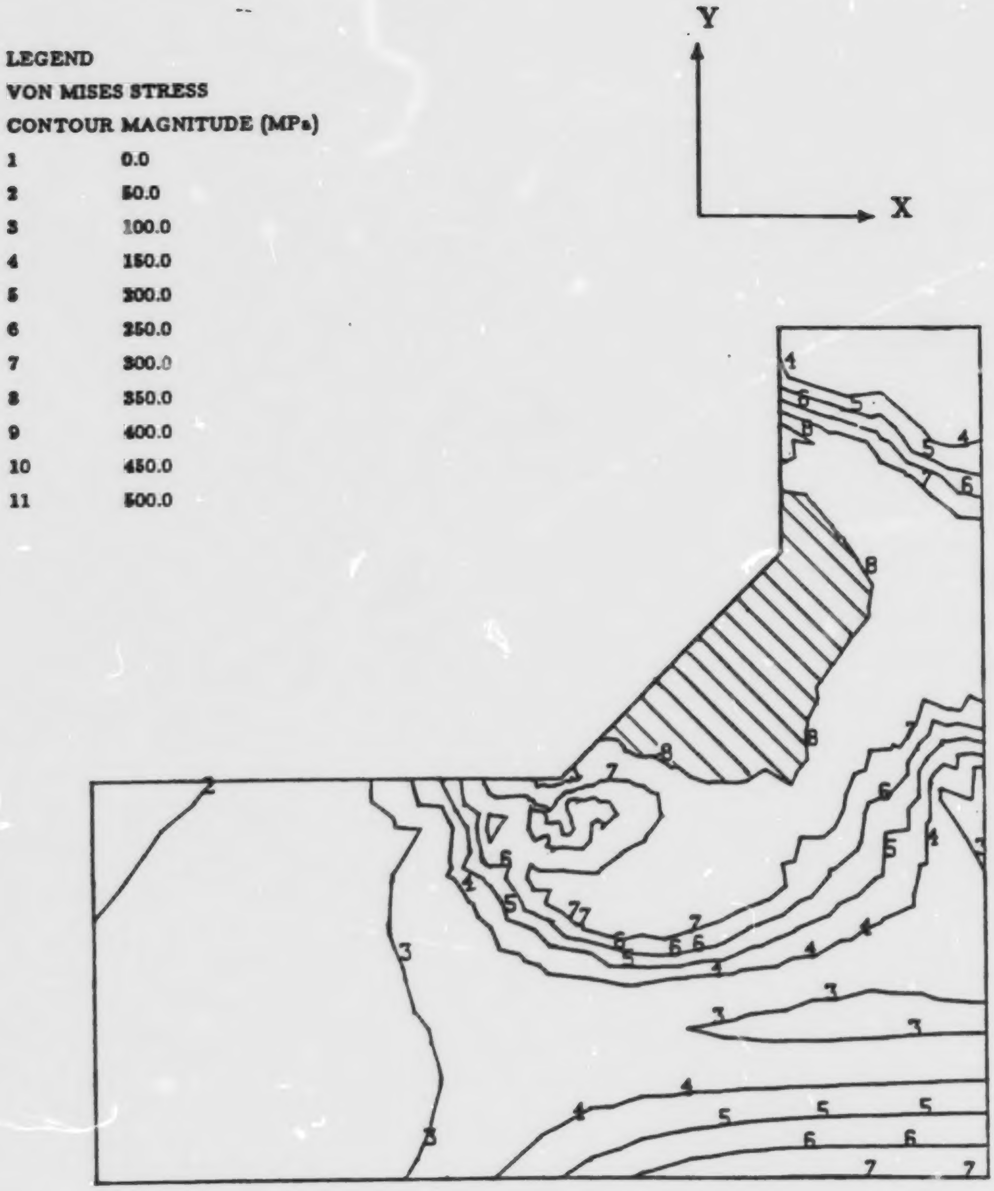

Figure 7.46: Von Mises residual stress distribution - PASS 4

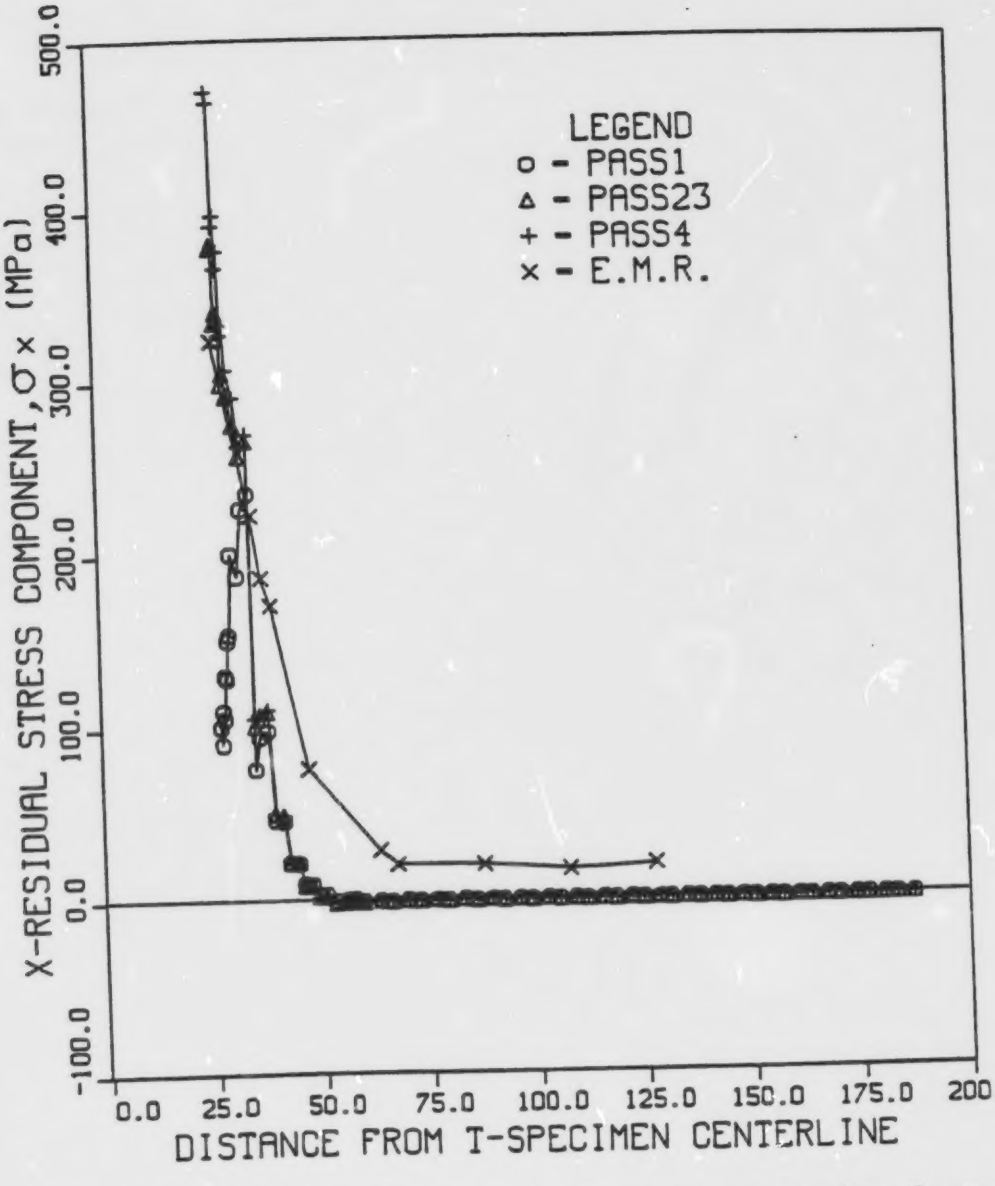

Figure 7.29: Distribution of the X-residual stress component along the top surface (without previous residual stresses)

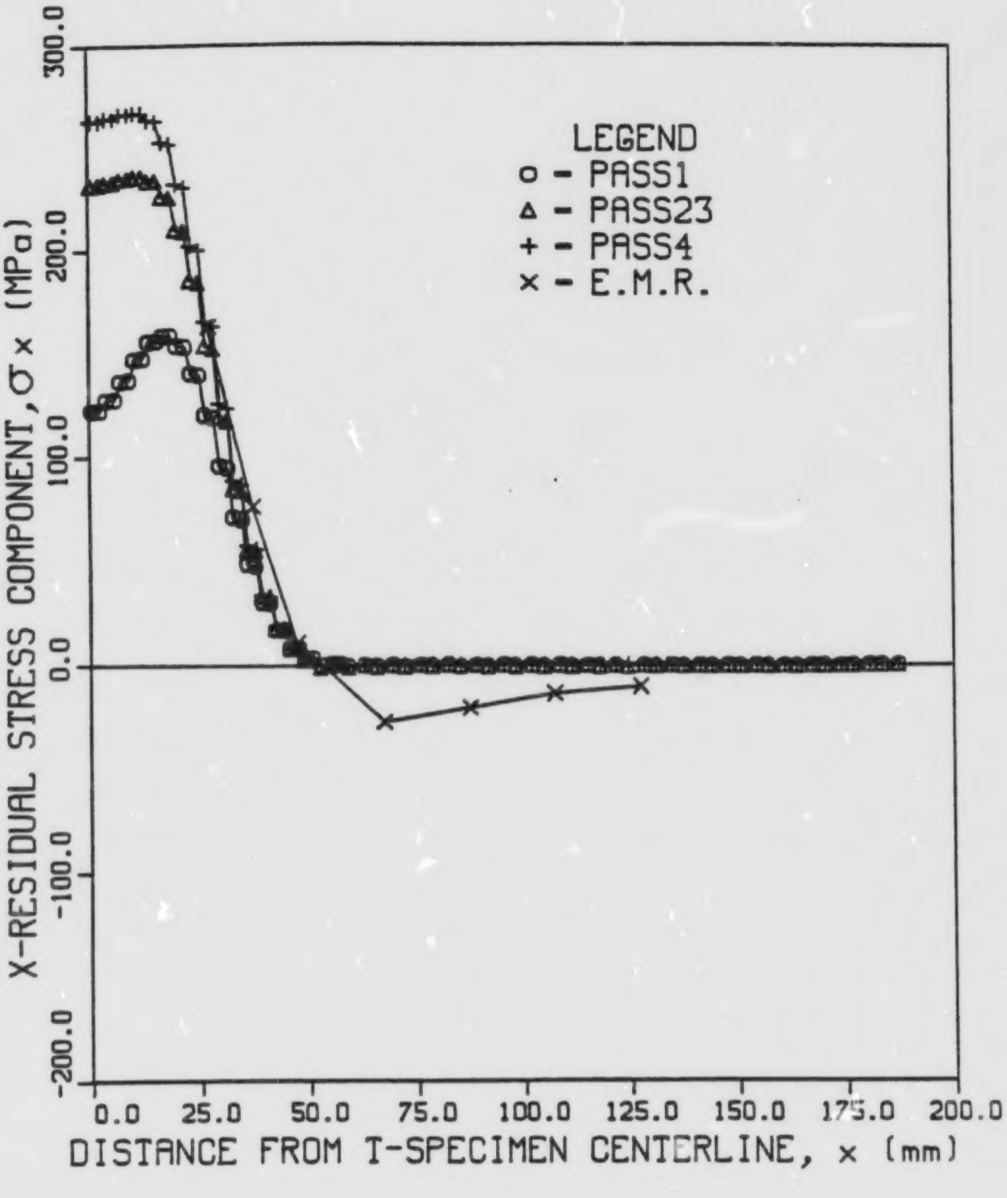

Figure 7.30: Distribution of the X-residual stress component along the bottom surface (without previous residual stresses)

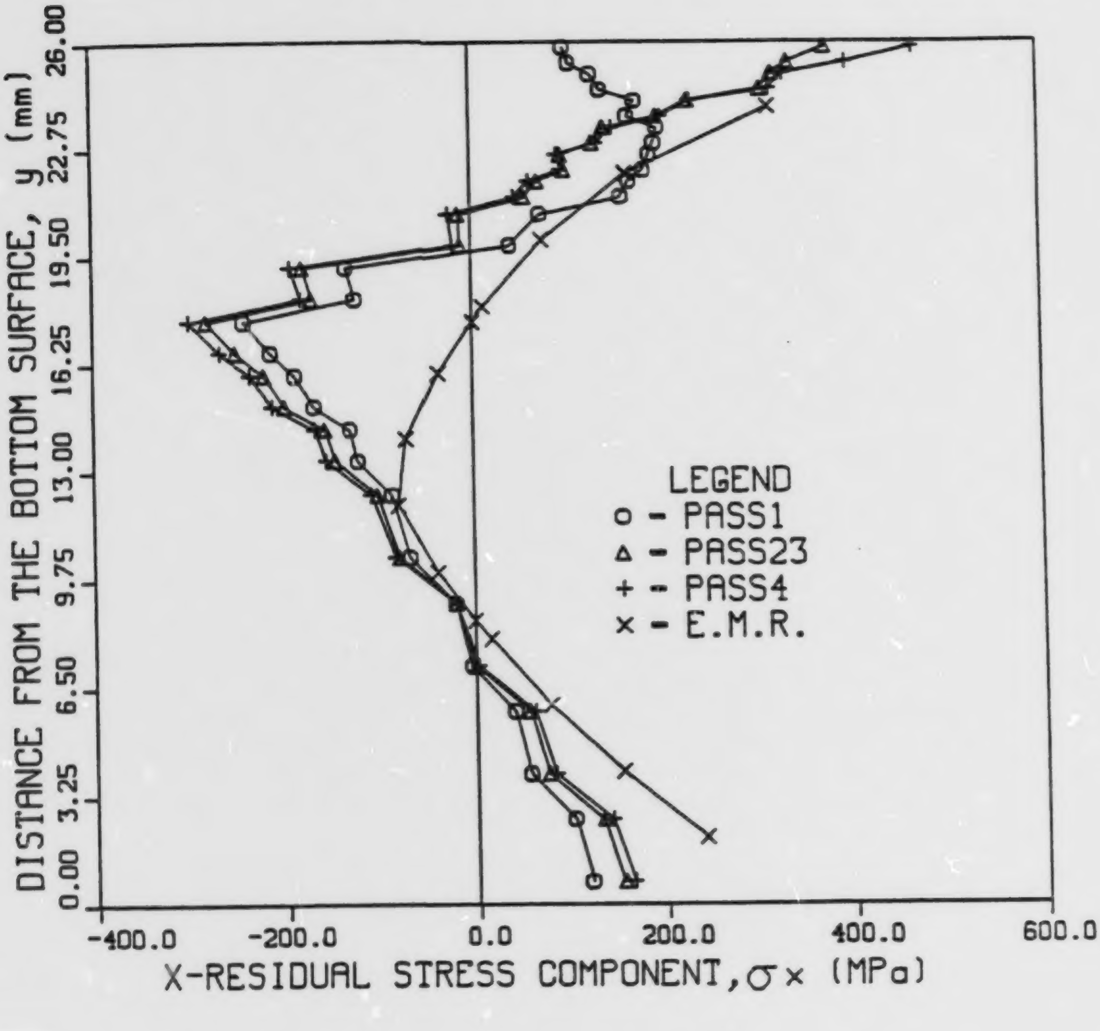

Figure 7.31: Distribution of the X-residual stress component through the plate thickness below the weld toe (without previous residual stresses)

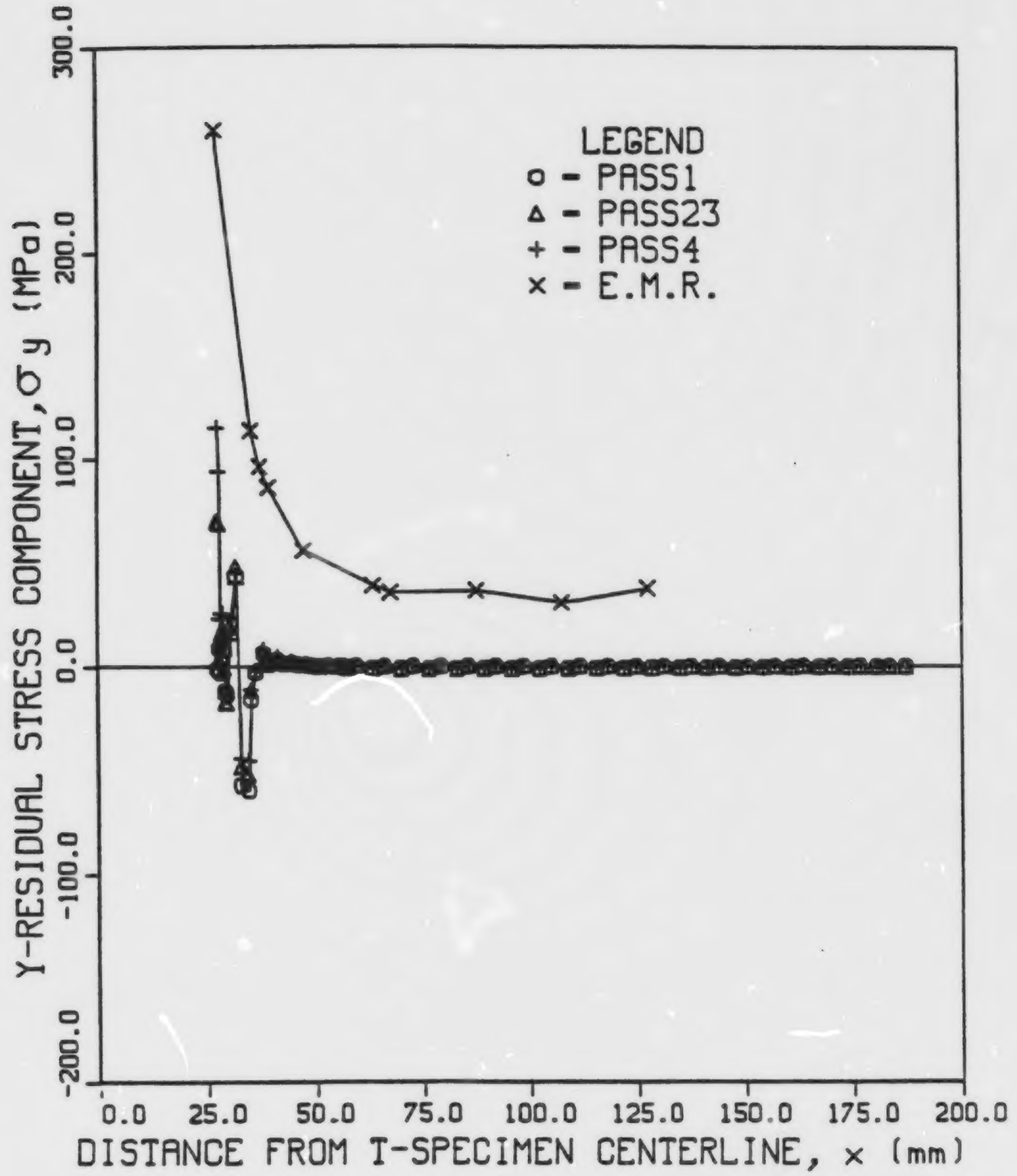

Figure 7.32: Distribution of the Y-residual stress component along the top surface (without previous residual stresses)

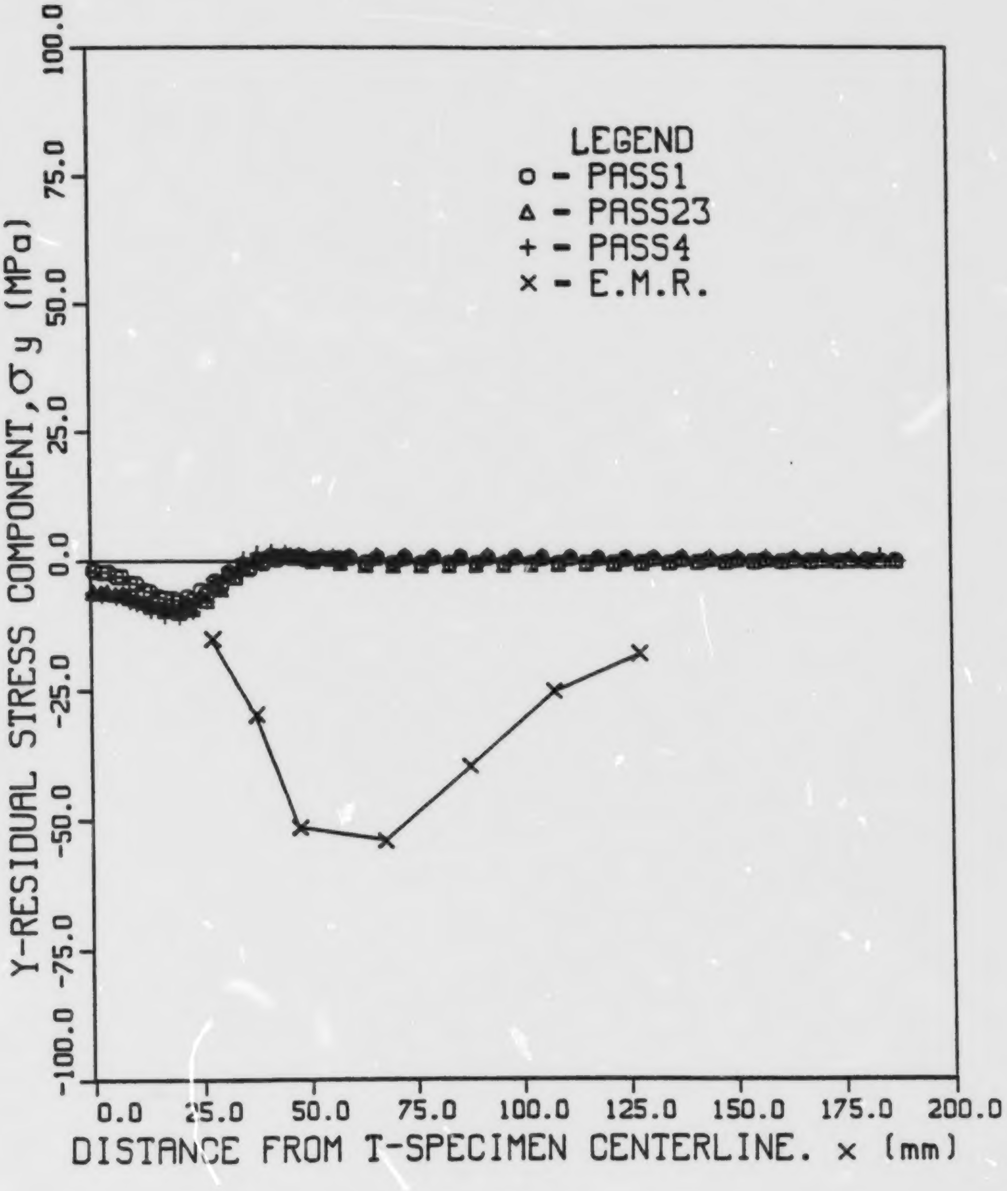

Figure 7.33: Distribution of the Y-residual stress component along the bottom surface (without previous residual stresses)

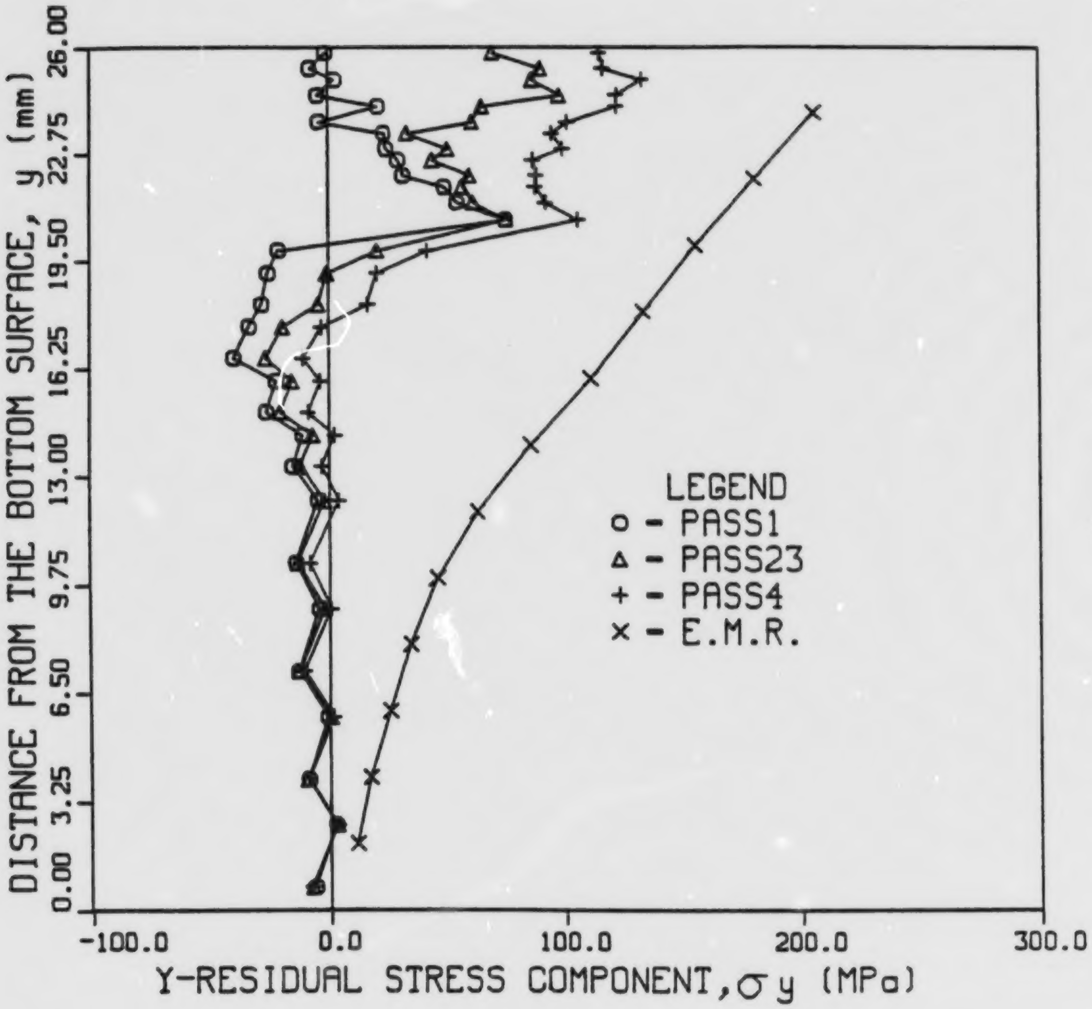

Figure 7.34: Distribution of the Y-residual stress component through the plate thickness below the weld toe (without previous residual stresses)

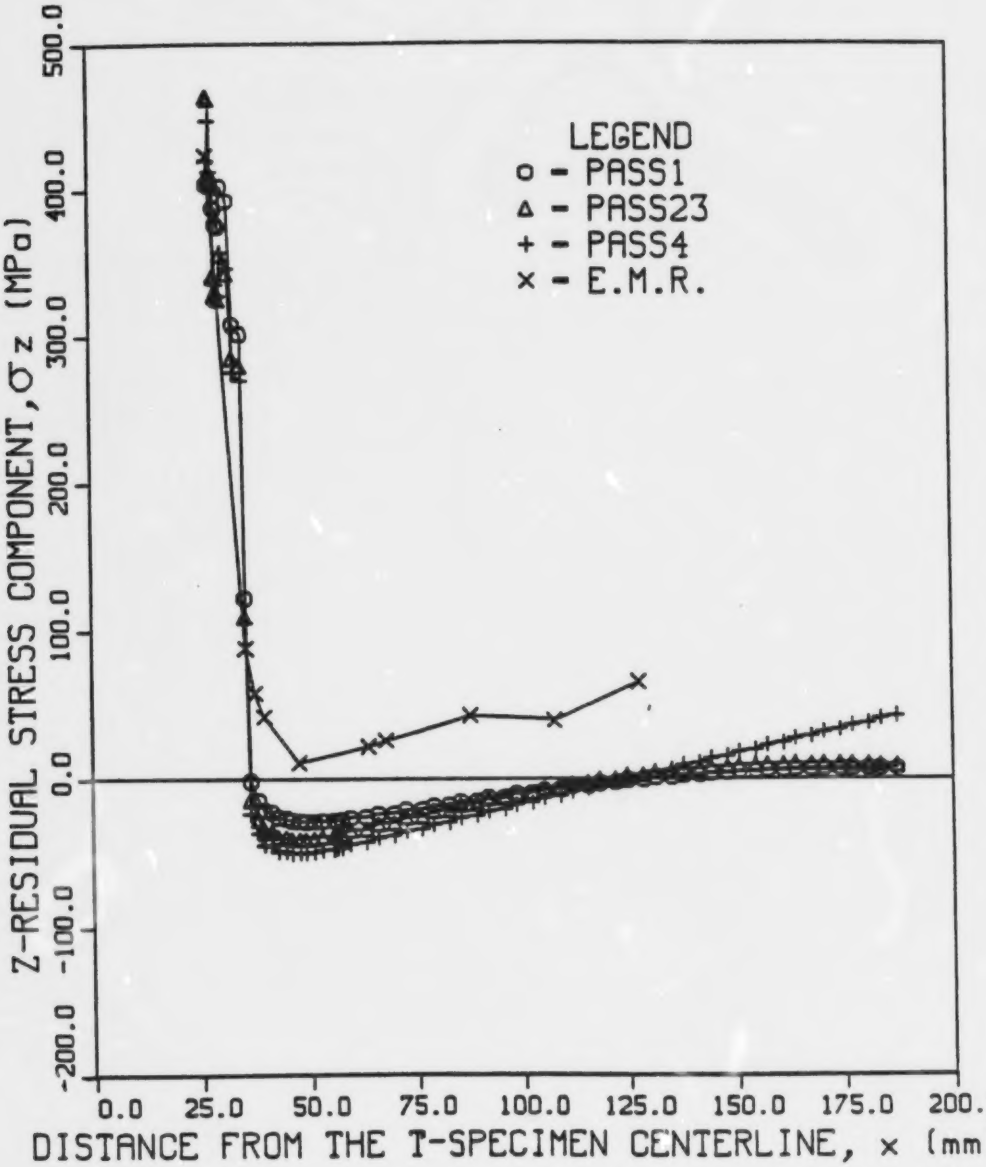

Figure 7.35: Distribution of the Z-residual stress component along the top surface (without previous residual stresses)

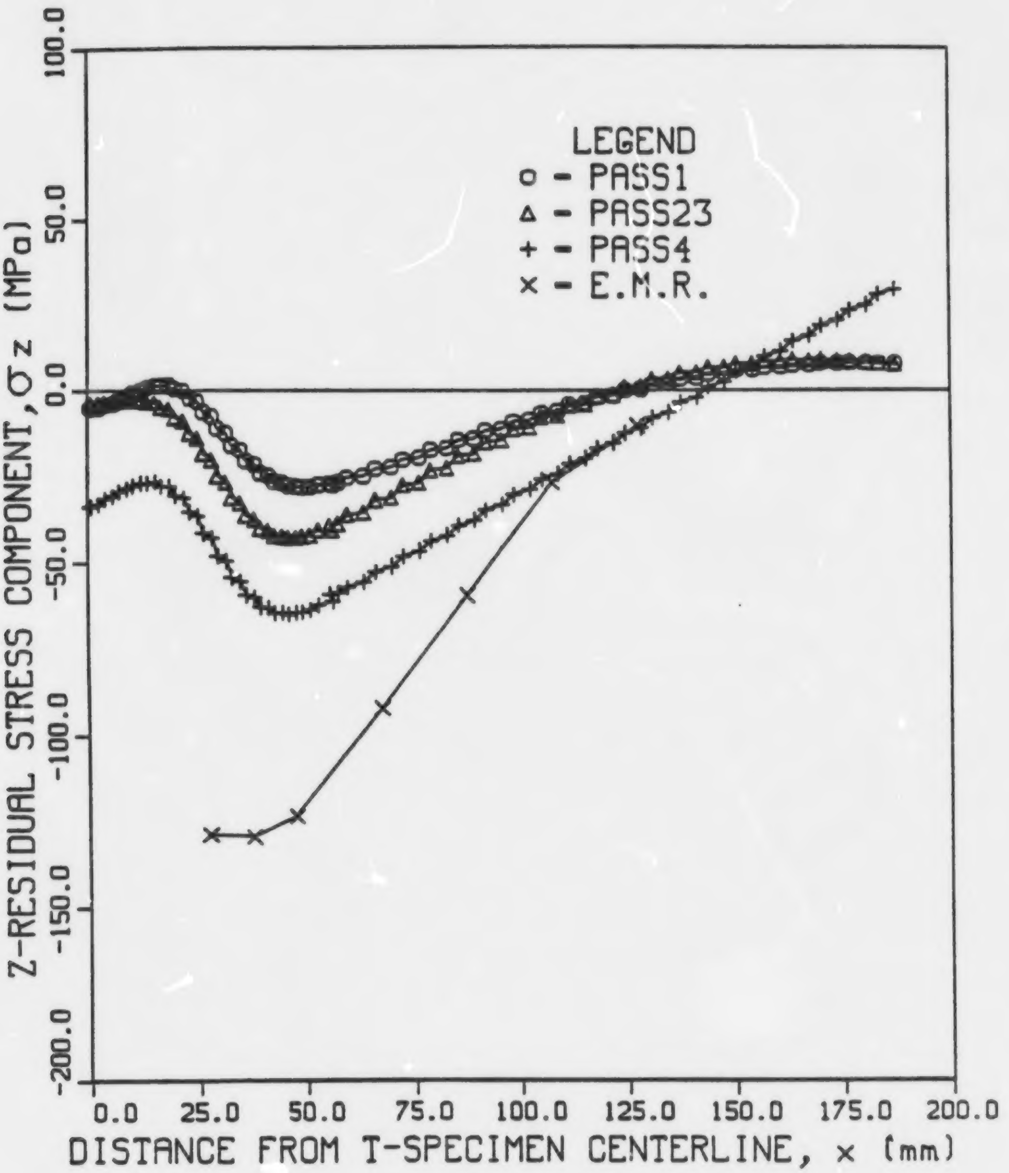

Figure 7.36: Distribution of the Z-residual stress component along the bottom surface (without previous residual stresses)

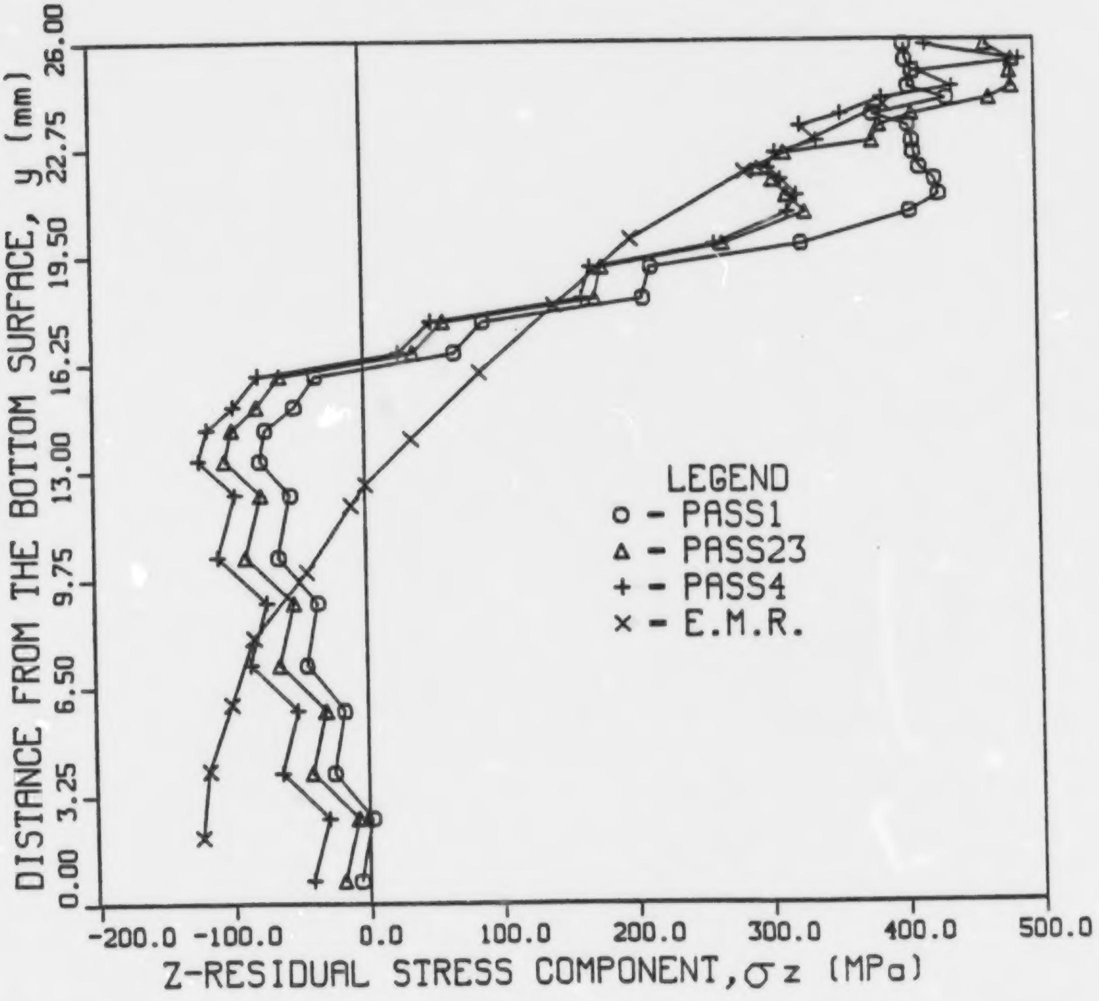

Figure 7.37: Distribution of the Z-residual stress component through the plate thickness below the weld toe (wihtout previous residual stresses)

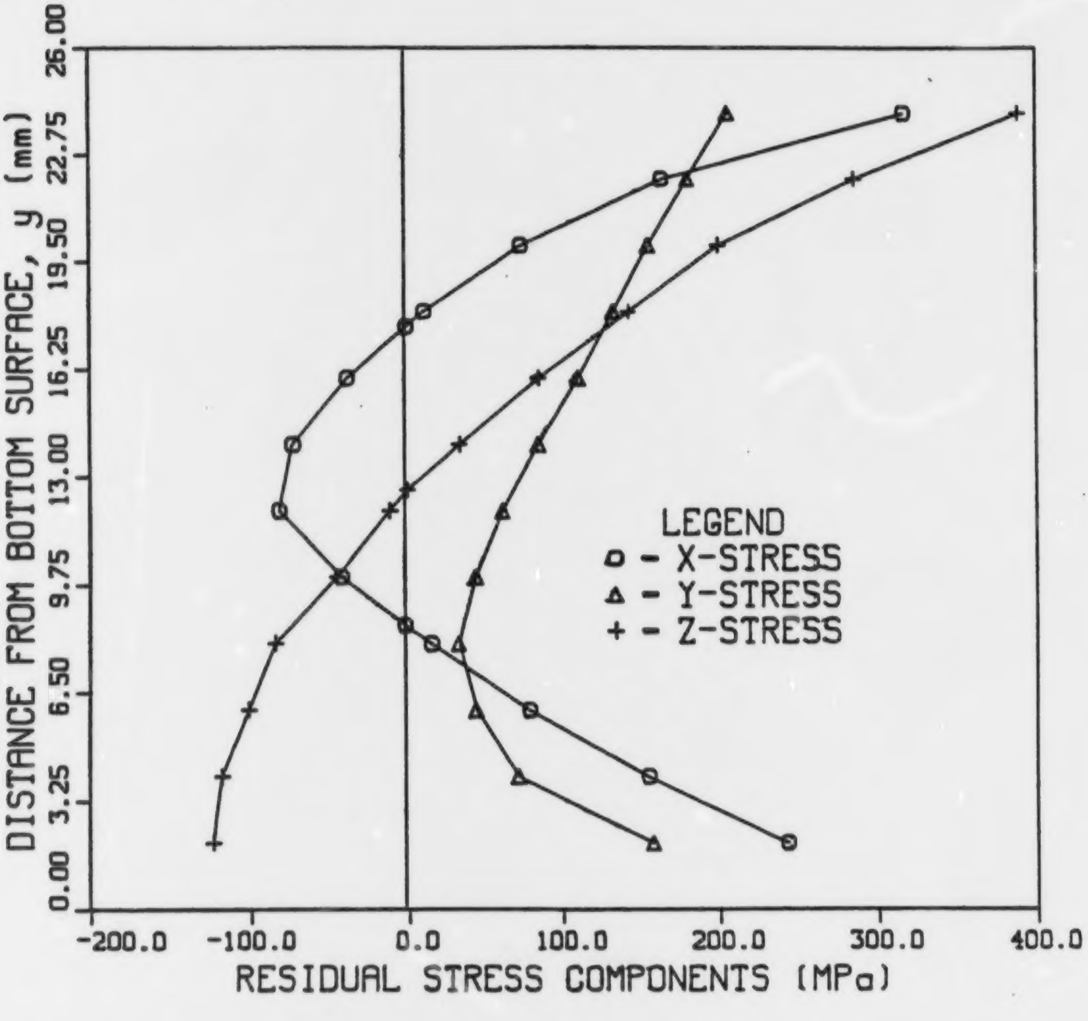

Figure 5.8: Residual stress distributions through the plate thickness below the weld toe as measured by Holden et al. [63]

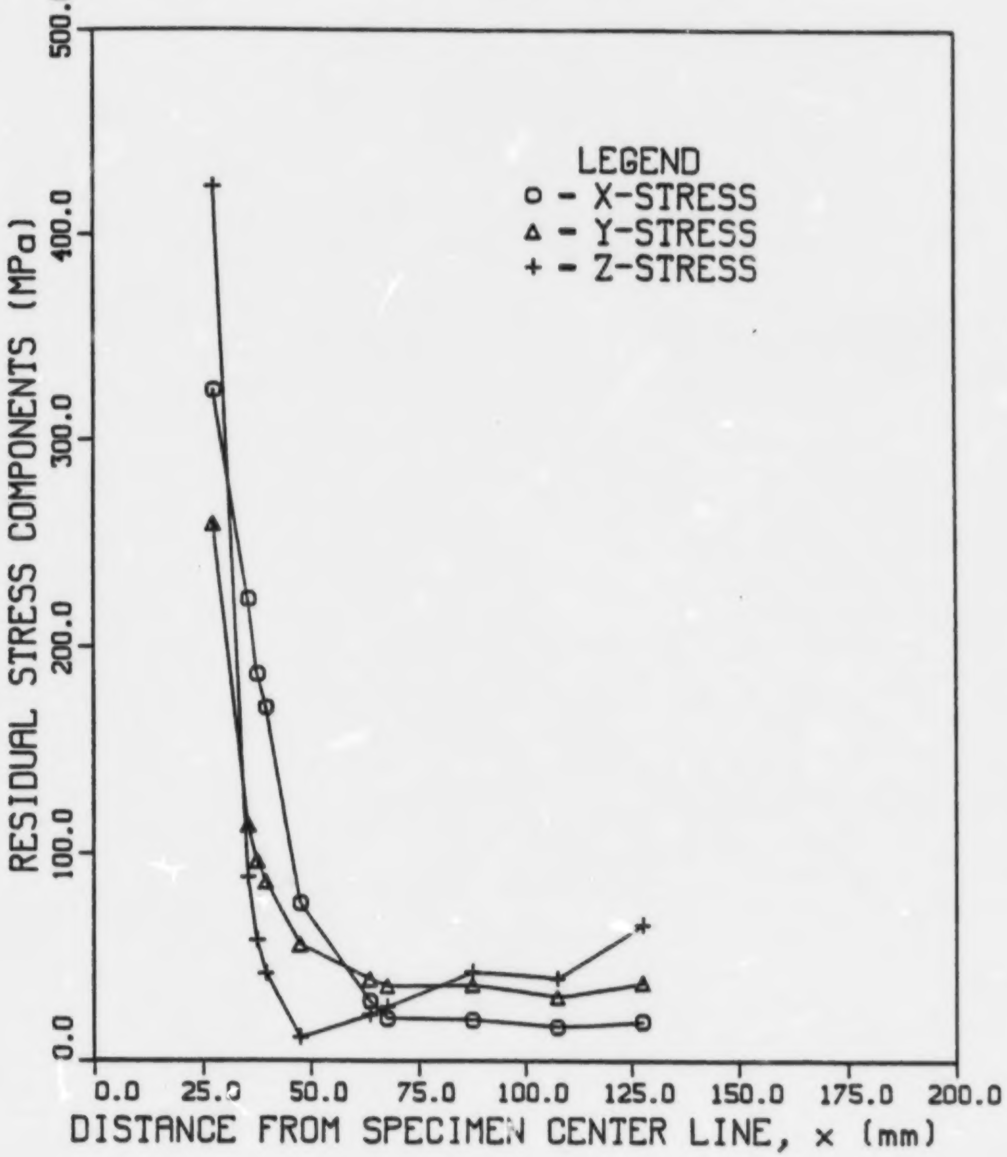

Figure 5.9: Residual stress distributions along the top surface as measured by Holden et al. [63]

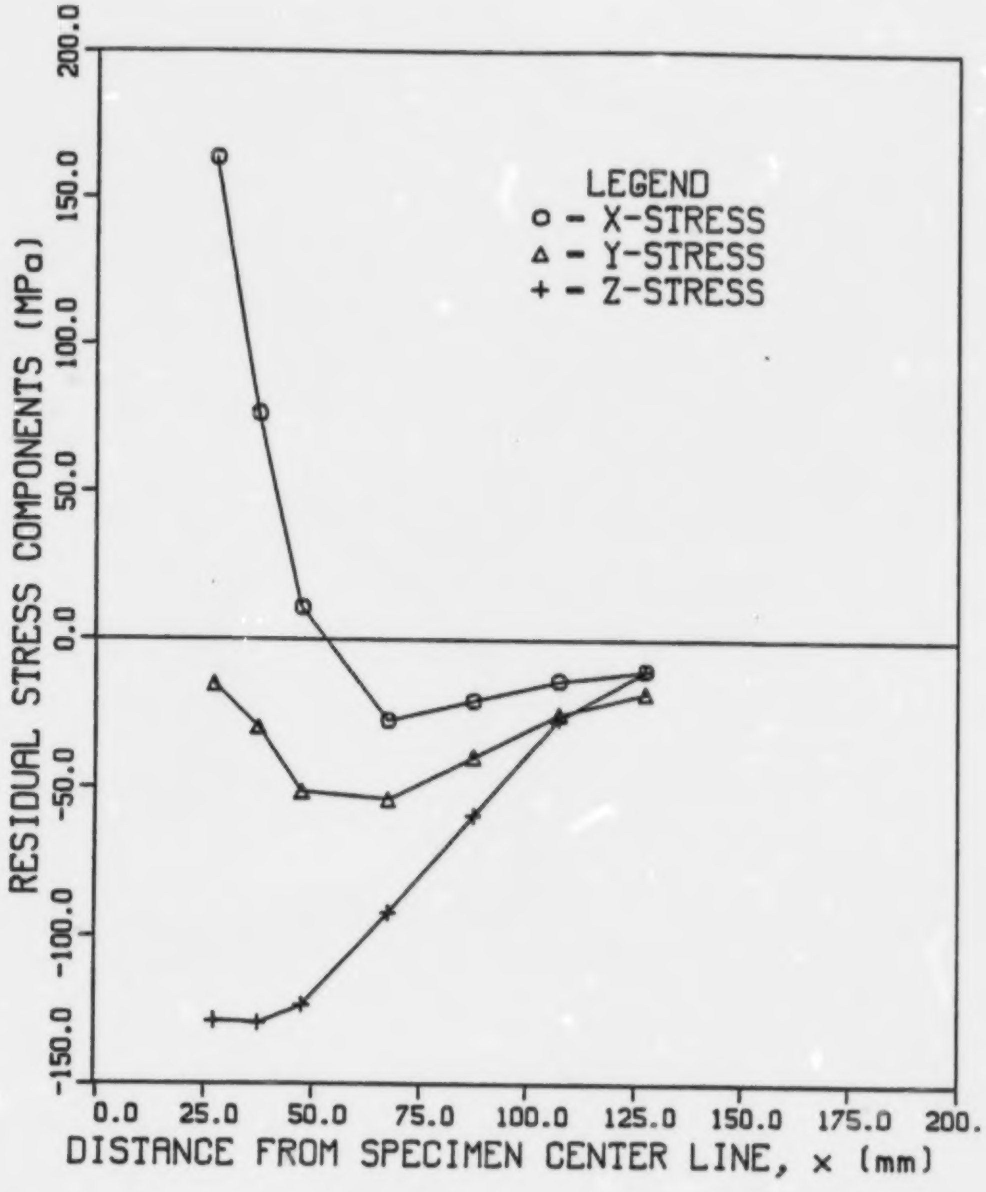

Figure 5.10: Residual stress distributions along the bottom surface as measured by Holden et al. [63]

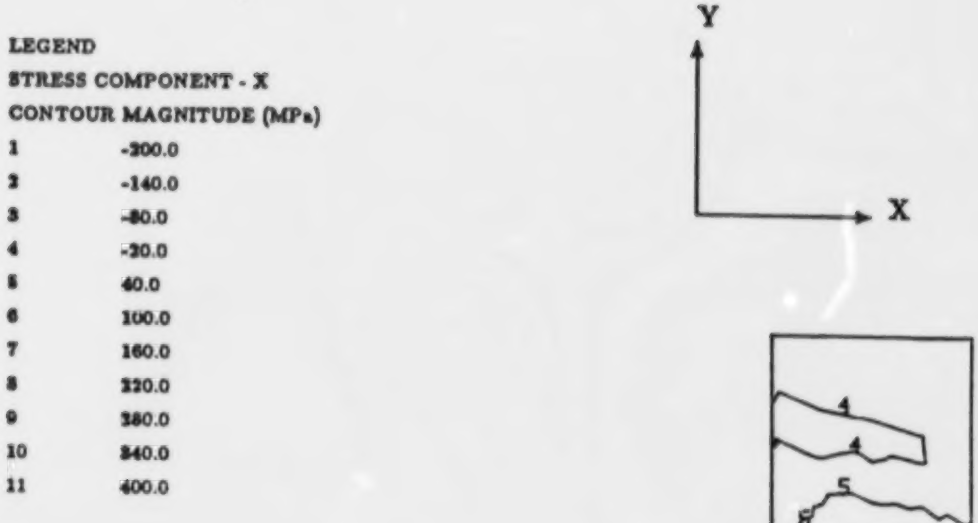

LEGEND

STRESS COMPONENT - X

CONTOUR MAGNITUDE (MPa)

1	-200.0
2	-140.0
3	-80.0
4	-20.0
5	40.0
6	100.0
7	160.0
8	220.0
9	280.0
10	340.0
11	400.0

Figure 8.15: X-stress distribution with 25 MPa load (as welded condition)

LEGEND

STRESS COMPONENT - Y

CONTOUR MAGNITUDE (MPa)

1	-200.0
2	-150.0
3	-100.0
4	-50.0
5	0.0
6	50.0
7	100.0
8	150.0
9	200.0
10	250.0
11	300.0

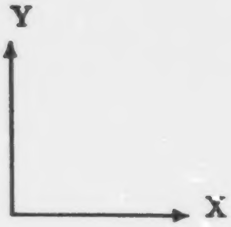

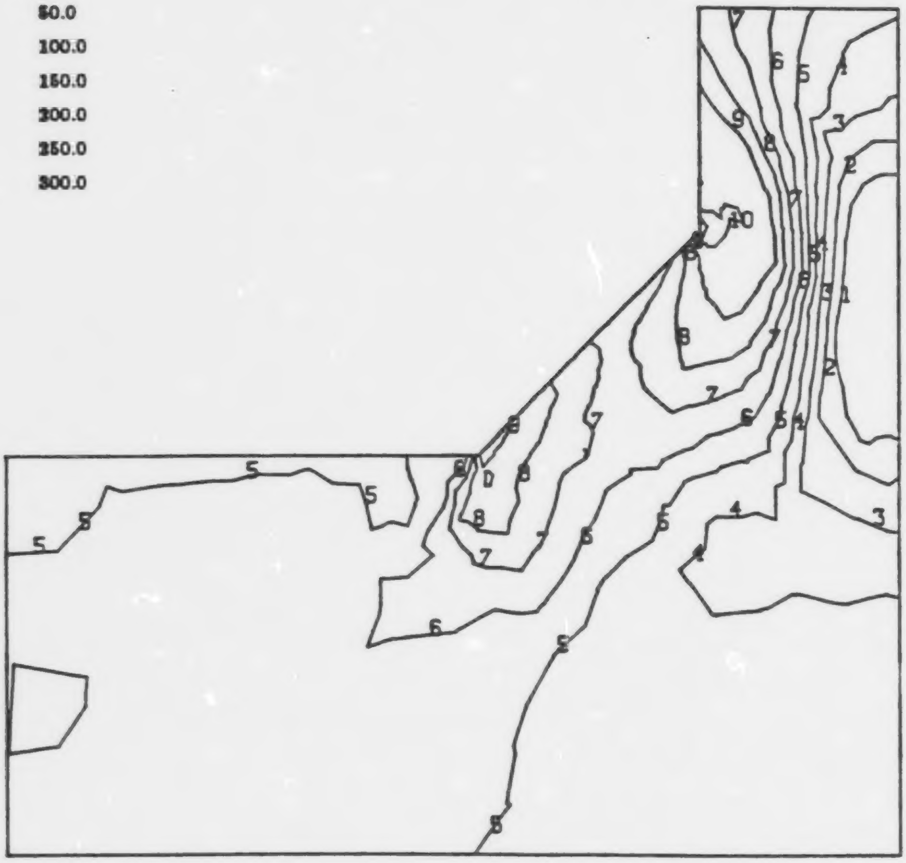

Figure 8.16: Y-stress distribution with 25 MPa load (as welded condition)

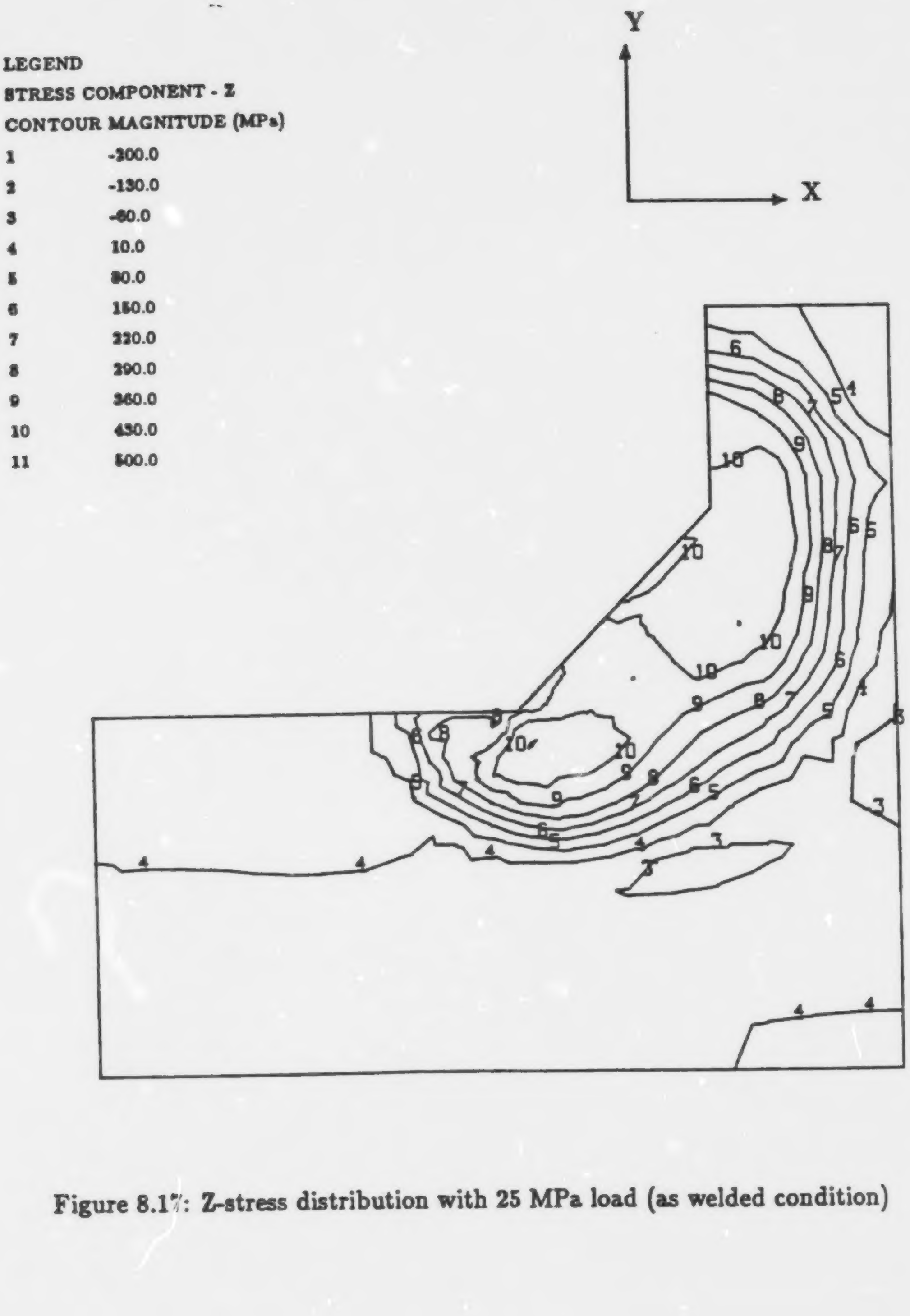

Figure 8.17: Z-stress distribution with 25 MPa load (as welded condition)

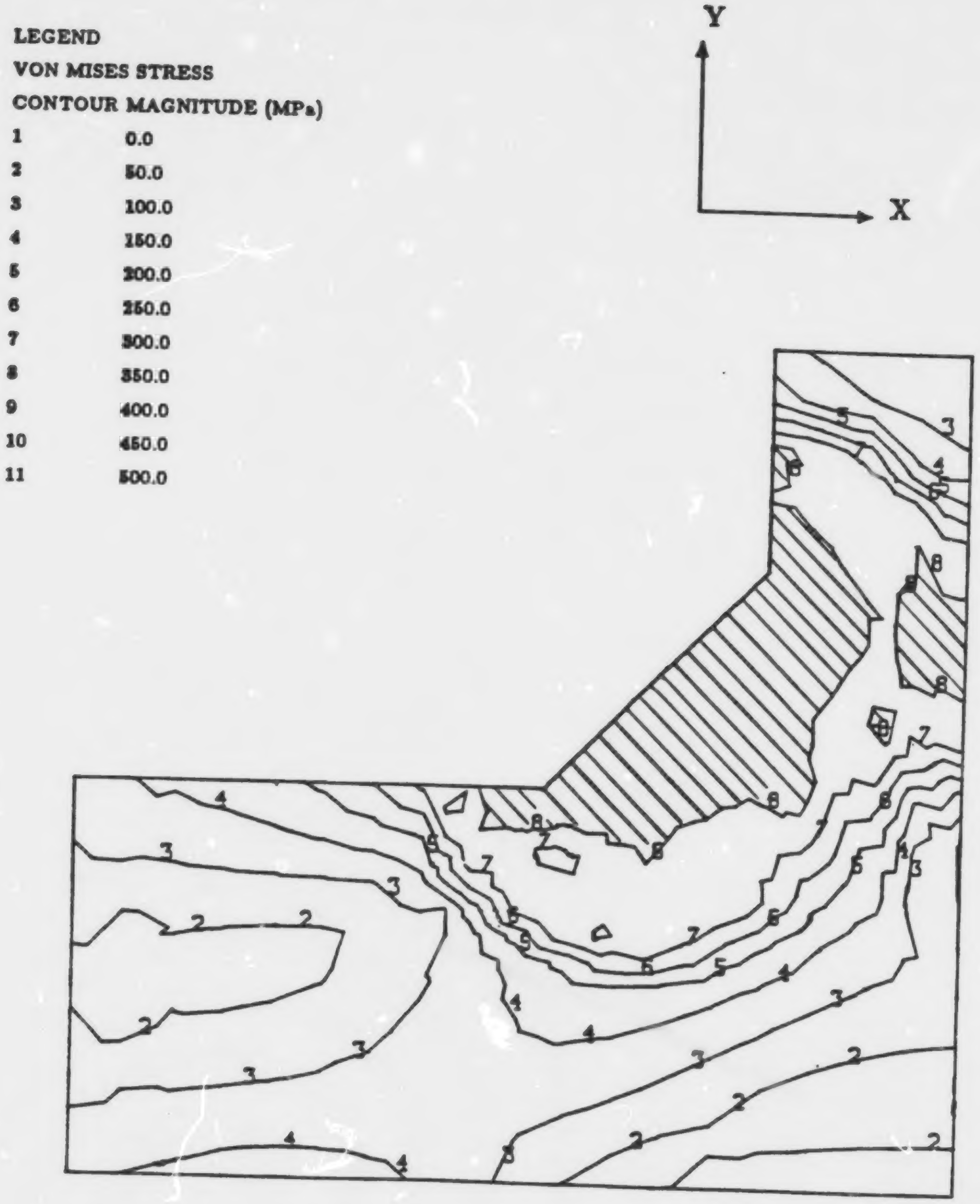

Figure 8.18: Von Mises stress distribution with 25 MPa load (as welded condition)

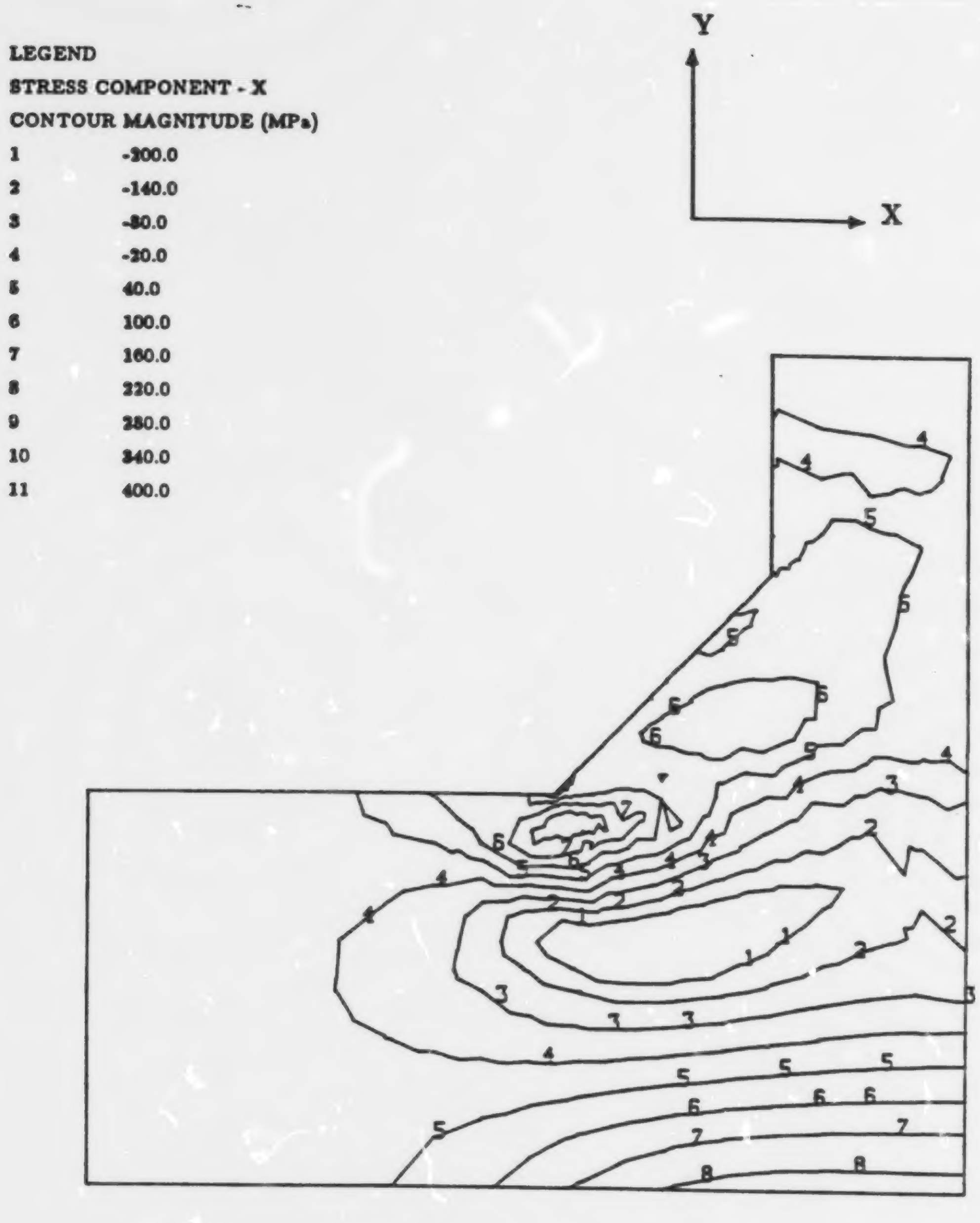

Figure 8.19: X-stress distribution after one 25 MPa loading cycle (as welded condition)

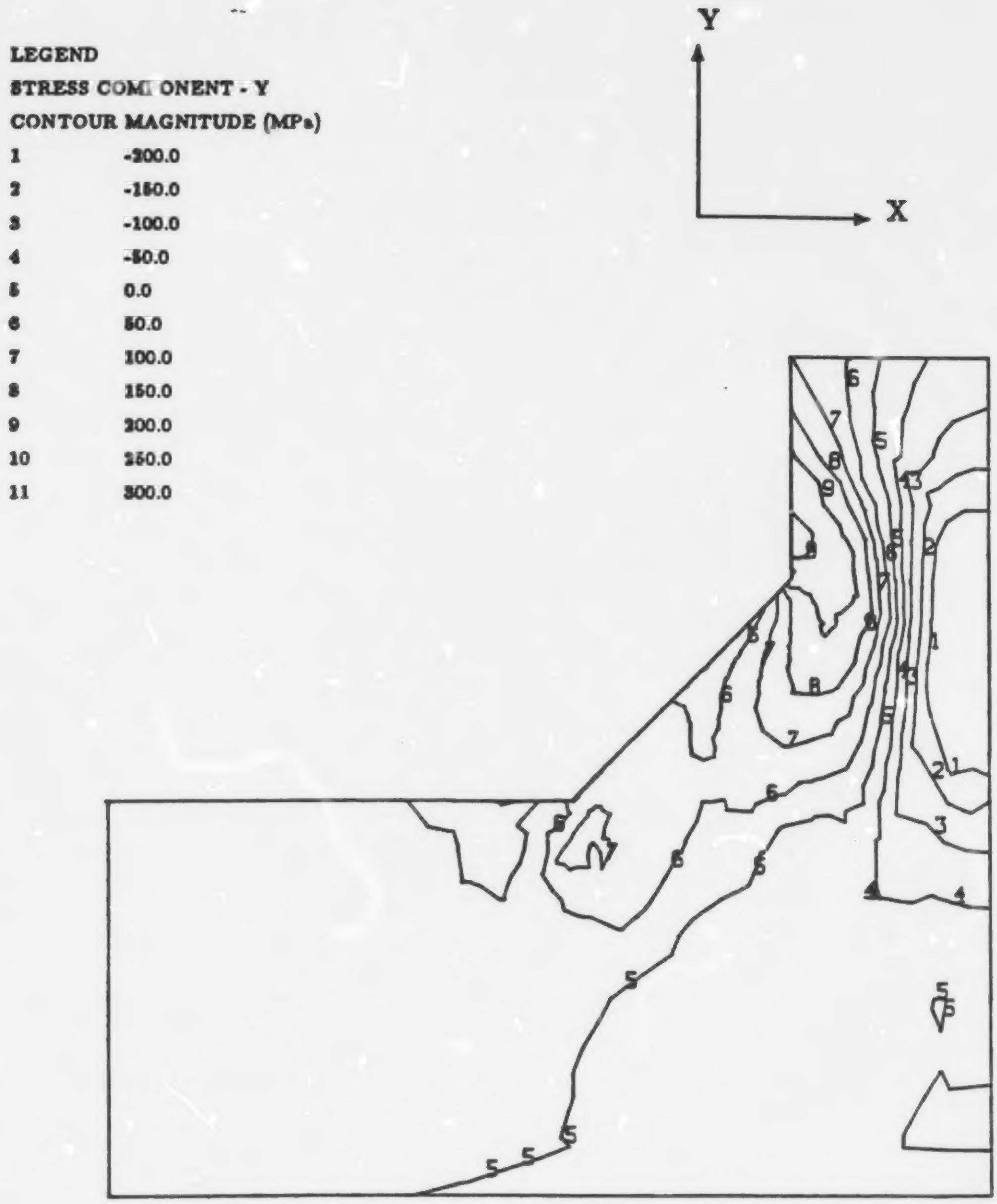

Figure 8.20: Y-stress distribution after one 25 MPa loading cycle (as welded condition)

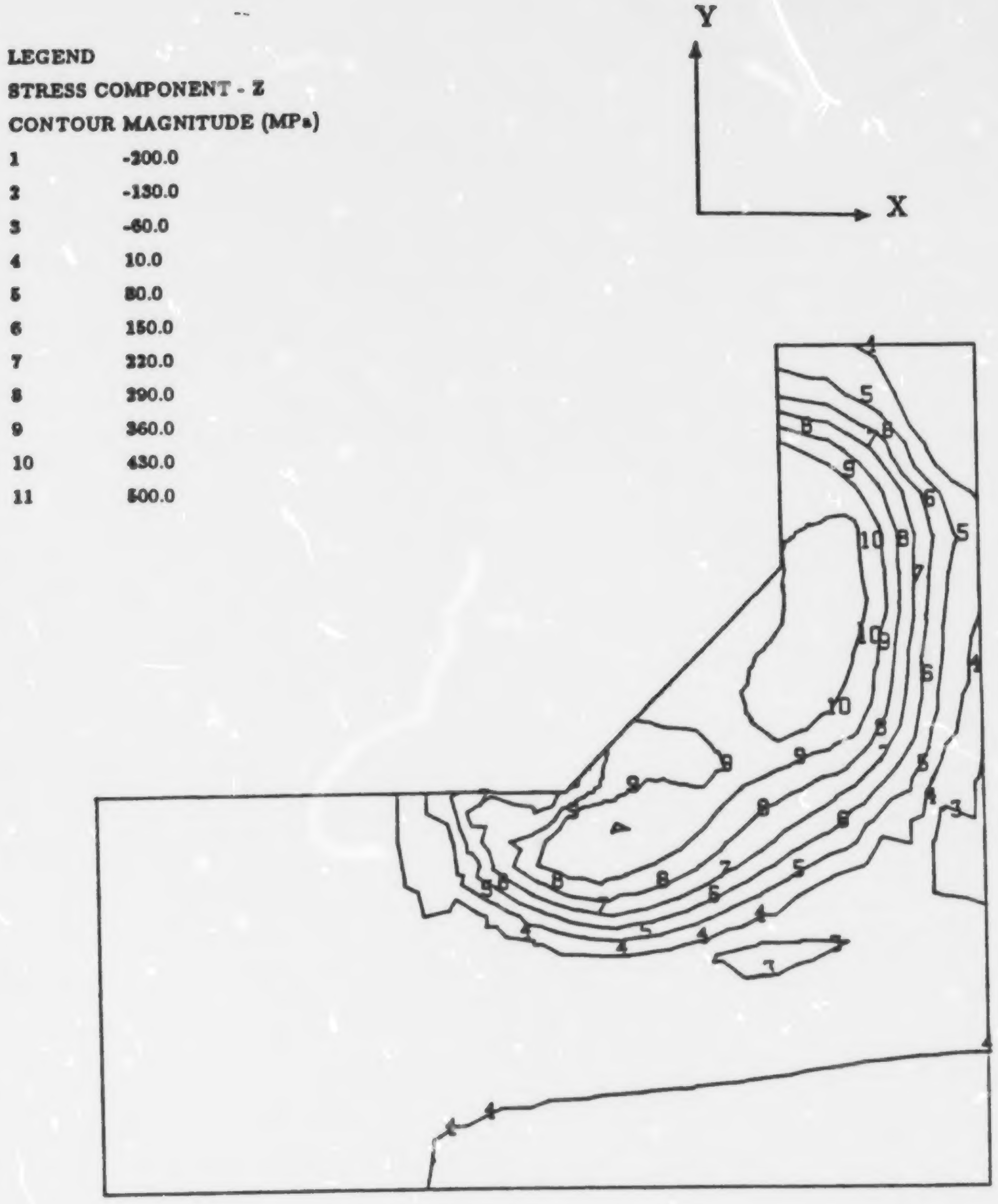

Figure 8.21: Z-stress distribution after one 25 MPa loading cycle (as welded condition)

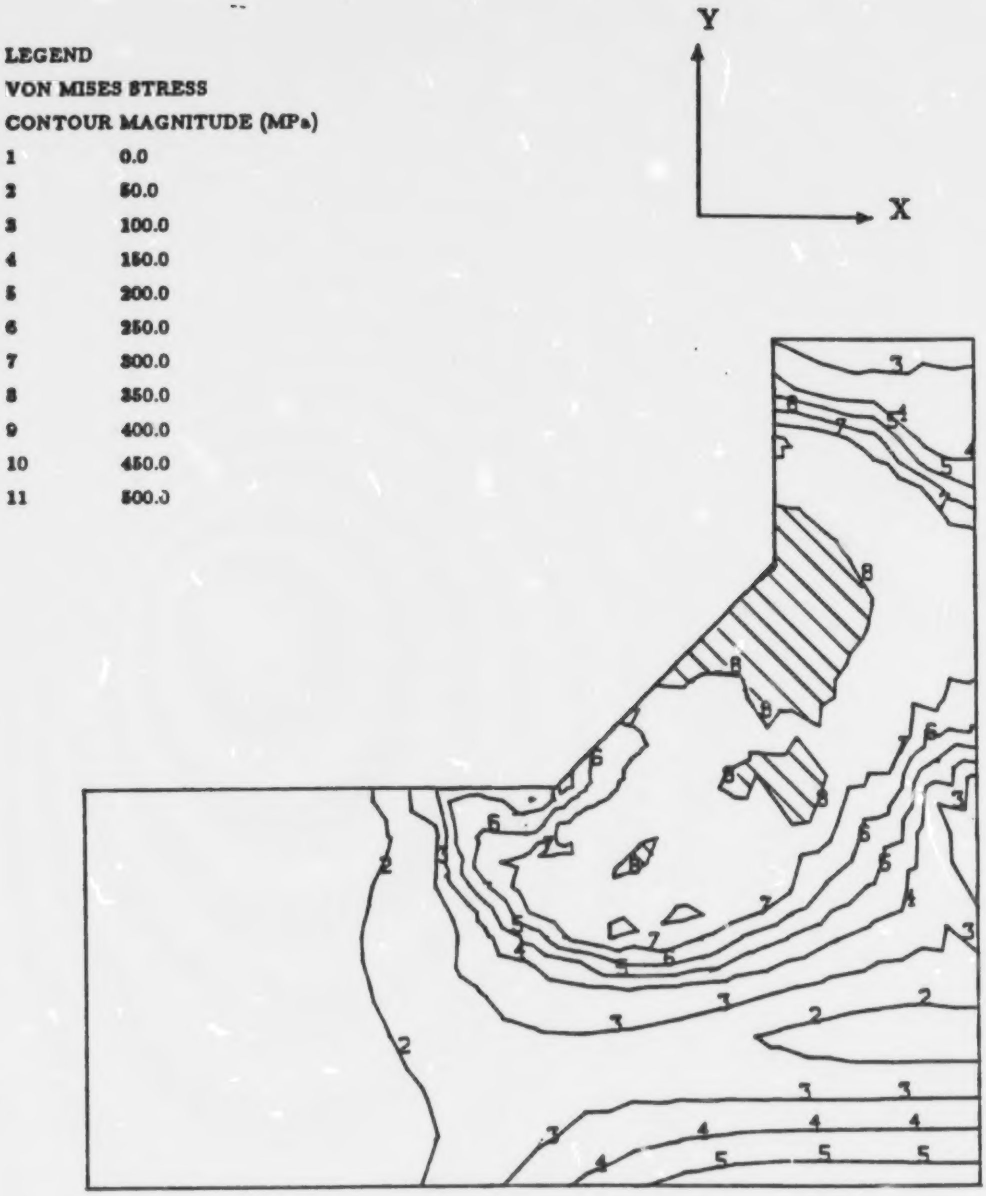

Figure 8.22: Von Mises stress distribution after one 25 MPa loading cycle (as welded condition)

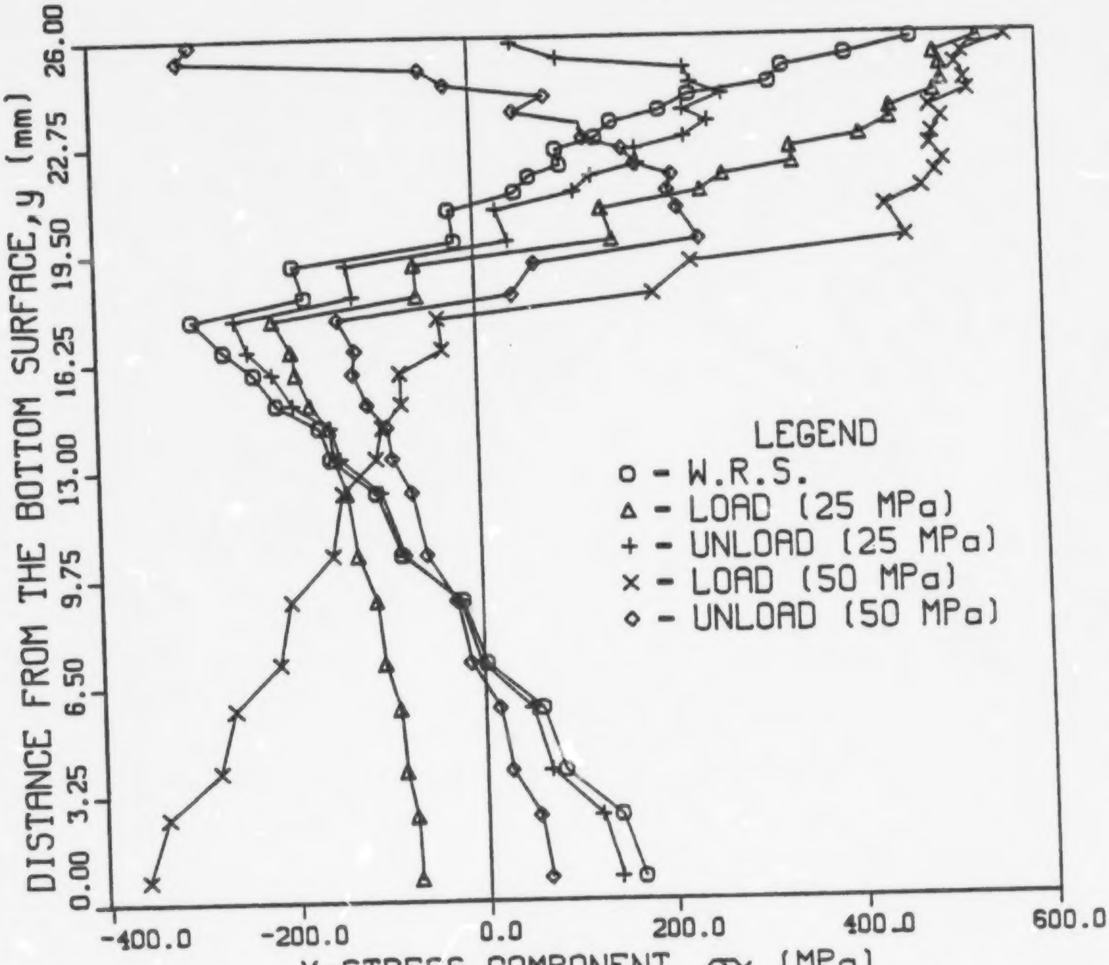

Figure 8.33: Distribution of the X-stress component through the plate thickness below the weld toe (as welded condition)

Final Report
A Finite Element Study of Residual Stresses In A Welded T-Joint Specimen

WRI Project No. 1097701
EMR Contract No. 23440-6-9168/01-ST

D.H.B. Mok   R.J. Pick

Department of Mechanical Engineering
University of Waterloo
Waterloo, Ontario
Canada N2L 3G1

1988

Abstract

The objective of this study was to determine the effect of mechanical loading on the welding residual stresses in a T-joint fatigue specimen.

Most ferritic steels undergo allotropic phase transformation when experiencing an extreme thermal history. The phase transformation produces a volumetric strain which influences residual stresses produced by welding. This volumetric expansion and its effect on welding residual stresses was studied using the finite element technique. The results showed that the phase transformation induced strain has a very small effect and in most cases may be neglected in welding residual stress predictions.

The welding residual stresses in a 26 mm T-joint specimen were determined using a numerical model based on the finite element method. The results were compared to measurements by the neutron diffraction technique and reasonable agreement was shown.

Loading of a T-joint specimen as in a fatigue test was simulated to determine the effect of mechanical stresses on the welding residual stresses. After one loading cycle, shakedown of the residual stress was observed near the weld toe region. This produced relatively high tensile residual stresses which may promote faster fatigue crack growth than in a stress free specimen.

Acknowledgements

The author wishes to acknowledge the Department of Energy, Mines and Resources, Canada, for their financial support under contract 2340-6-9168/01-ST with the University of Waterloo and for providing the experimental measurements for comparison in this study.

The author would also like to thank Kin Leung for providing the background and insight into predicting welding residual stresses; and to Mike Worswick for making his program available to post process the finite element results.

Contents

Abstract ii

Acknowledgements iii

Chapter 1

Introduction 1

1.1 Background 1

1.2 Objectives 2

1.3 Report Outline 3

Chapter 2

Literature Review - Phase Transformation Effects 5

2.1 Sources Of Residual Stress In Welding 5

2.2 Allotropic Phase Transformation Process 7

2.2.1 Allotropic Phase Transformation Model 8

2.3 Phase Transformation Effects In Welding 9

2.3.1 Phase Transformation Models In Welding 10

Chapter 3

Computer Model Including Phase Transformation Effects 15

3.1 Leung's Model 16

3.1.1 Heat Transfer Analysis 17

3.1.2 Thermal Stress Analysis 18

3.2 Volumetric Expansion Model 20

3.3 Heat Transfer Analysis 21

3.3.1 Results Of The Heat Transfer Analysis 22

3.4 Thermal Stress Analysis 22

3.4.1 Results Of The Thermal Stress Analyses 23

Chapter 4

Discussion Of Results Including Phase Transformation Effect 68

4.1 Allotropic Phase Transformation Effect 68

4.2 Effect Of Transformation Temperature 69

4.3 Effect Of Volumetric Strain Magnitude 70

4.4 Significance Of Allotropic Phase Transformations 70

Chapter 5

Analysis Of The T-joint Specimen 72

5.1 Fabrication Procedures [51] 73

5.2 Loading Condition In The Fatigue Test 74

5.3 Literature Review 75

5.3.1 Welding Temperatures In A T-Joint Specimen 76

5.3.2 Welding Residual Stresses In A T-Joint Specimen 77

5.3.3 Modelling Of 'T' Weld Shapes 80

5.3.4 Loading Of T-Joint Specimen 85

Chapter 6

Heat Transfer Analysis Of The T-Joint Specimen **100**

6.1 Computer Model For The Heat Transfer Analysis 100

6.1.1 Geometric Model 101

6.1.2 Finite Element Mesh 103

6.1.3 Heat Input Model 104

6.1.4 Thermal Boundary Conditions 104

6.1.5 Weld Pool Convection 105

6.1.6 Thermal Material Properties 105

6.1.7 Solution Strategy 106

6.2 Calculated Thermal History 108

Chapter 7

Thermal Stress Analysis Of The T-Joint Specimen **125**

7.1 Computer Model For The Thermal Stress Analysis 126

7.1.1 Geometry Considerations 126

7.1.2 Finite Element Mesh 127

7.1.3 Kinematic Boundary Conditions 128

7.1.4 Material Modelling 128

7.1.5 Mechanical Material Properties 129

7.1.6 Solution Strategy 131

7.2 Verification Of Symmetry Assumption 133

7.3 Residual Stress Due To The Capping Passes 134

7.3.1 Residual Stresses Due To The First Capping Pass 134

7.3.2 Residual Stresses Due To The Remaining Passes 137

7.3.3 Comparison With Measured Residual Stresses 139

7.4 Effect Of Previous Welding Stress 141

7.4.1 Residual Stress Distribution Of Previous Passes 141

7.4.2 Residual Stress Due To The First Capping Pass 142

Chapter 8

Loading Of The T-Joint Specimen 211

8.1 Mechanical Loading Of The 26 mm T-Joint Specimen 211

8.1.1 Loading Of The T-Joint Specimen In The Stress Free Condition 213

8.1.2 Loading In The As Welded Condition 214

8.2 Discussion Of The Results 217

8.2.1 Finite Element Mesh 217

8.2.2 Effect Of loading On Welding Residual Stress 218

8.2.3 Effect On Fatigue Life Of The T-joint Specimen 219

Chapter 9

Conclusions 263

9.1 Phase Transformation Effect 263

9.2 Analysis Of The 26 mm T-Joint Specimen 265

9.2.1 Heat Transfer Analysis 265

9.2.2 Welding Residual Stress Prediction 266

9.2.3 Loading Of The T-Joint Specimen 267

References 269

Appendix A

Test Problem For Volumetric Expansion Model 282

A.1 Test Problem 283

A.1.1 Analytical Solution 283

A.1.2 FEM Solution 284

A.1.3 Comparisons Of Results 284

References 285

Appendix B

ABAQUS Input Data And Subroutines For Heat Transfer Analysis 290

B.1 ABAQUS Input Data 291

B.1.1 First Capping Pass 291

B.1.2 Second Capping Pass 304

B.1.3 Third Capping Pass 306

B.1.4 Last Capping Pass 308

B.2 User Defined Subroutines 310

Appendix C

ABAQUS Input Data For Residual Stress Calculation **313**

C.1 First Capping Pass 314

C.2 Second And Third Capping Pass 325

C.3 Last Capping Pass 328

List of Tables

3.1 Welding parameters [1] 28

3.2 Maximum vertical displacement after welding 28

5.1 Chemical composition for Lloyds LT60 steel [5] 87

5.2 Chemical composition for E48018 welding electrode [52] 88

5.3 Typical welding parameters for a 26 mm T-joint specimen [51] (refer to figure 5.2) 89

6.1 Dimensions of weld pool for double ellipsoidal heat source model 110

6.2 Origins of heat sources 110

6.3 Chemical composition for manganese steel [76] 111

7.1 Chemical composition for steel used by Andersson [38] 144

List of Figures

3.1 Longitudinal butt-weld configuration [1] 29

3.2 Thermal conductivity for AISI 316L stainless steel 30

3.3 Specific heat for AISI 316L stainless steel 31

3.4 Parameters for double ellipsoidal heat source model 32

3.5 Thermal boundary conditions for submerged arc welding 33

3.6 Convective heat transfer coefficient for welding model 34

3.7 Young's modulus for AISI 316L stainless steel 35

3.8 Poisson's ratio for AISI 316L stainless steel 36

3.9 Yield strength for AISI 316L stainless steel 37

3.10 Tangent modulus for AISI 316L stainless steel 38

3.11 Linear thermal expansion coefficient for AISI 316L stainless steel 39

3.12 Temperature-dilatation curves [39] 40

3.13 Phase transformation induced volumetric strain at T_s = 680°C (PHTRAN) 41

3.14 Finite element mesh of a) welded plate; b) weld region for heat transfer analysis 42

3.15 Temperature contours around weld pool 43

3.16 Finite element mesh of a) welded plate; b) weld region for stress analysis 44

3.17 Classification of transformation zone 45

3.18 In-plane kinematic constraint for simply supported plate assumption 45

3.19 Phase transformation induced volumetric strain a) at T_s = 830°C (HITEM); b) AT T_s = 480°C (LOTEM); c) high strain magnitude at T_s = 680°C (HIVOL) 46

3.20 a) Displaced plate geometry; b) displaced mesh near weld region (NOPHASE) 48

3.21 Longitudinal residual stress distribution along the top surface (NOPHASE vs. PHTRAN) 49

3.22 Longitudinal residual stress distribution along the bottom surface (NOPHASE vs. PHTRAN) 50

3.23 Longitudinal residual stress distribution along the weld centerline (NOPHASE vs. PHTRAN) 51

3.24 Transverse residual stress distribution along the top surface (NOPHASE vs. PHTRAN) 52

3.25 Transverse residual stress distribution along the bottom surface (NOPHASE vs. PHTRAN) 53

3.26 Transverse residual stress distribution along the weld centerline (NOPHASE vs. PHTRAN) 54

3.27 Displaced mesh near weld region (PHTRAN) 55

3.28 Longitudinal residual stress distribution along the top surface - different transformation temperatures 56

3.29 Longitudinal residual stress distribution along the bottom surface - different transformation temperatures 57

3.30 Longitudinal residual stress distribution along the weld centerline - different transformation temperatures 58

3.31 Transverse residual stress distribution along the top surface - different transformation temperatures 59

3.32 Transverse residual stress distribution along the bottom surface - different transformation temperatures 60

3.33 Transverse residual stress distribution along the weld centerline - different transformation temperatures 61

3.34 Longitudinal residual stress distribution along the top surface - different volumetric strains 62

3.35 Longitudinal residual stress distribution along the bottom surface - different voluemtric strains 63

3.36 Longitudinal residual stress distribution along the weld centerline - different volumetric strains 64

3.37 Transverse residual stress distribution along the top surface - different volumetric strains 65

3.38 Transverse residual stress distribution along the bottom surface - different volumetric strains 66

3.39 Transverse residual stress distribution along the weld centerline - different volumetric strains 67

5.1 Dimensions of the 26 mm T-joint Specimen 90

5.2 Welding sequence for the 26 mm T-joint specimen 91

5.3 Dime test used for weld toe profile 92

5.4 Loading configuration in the fatigue test 93

5.5 Heat conduction in butt weld of flat plate 94

5.6 Heat conduction in fillet weld 95

5.7 Typical surface longitudinal residual stress and distortion of welded 'T' shape 96

5.8 Residual stress distributions through the plate thickness below the weld toe as measured by Holden et al. [63] 97

5.9 Residual stress distributions along the top surface as measured by Holden et al. [63] 98

5.10 Residual stress distributions along the bottom surface as measured by Holden et al. [63] 99

6.1 Finite element mesh of a) T-joint specimen; b) weld region for heat transfer analysis 112

6.2 Thermal boundary conditions for T-joint specimen analysis . . . 113

6.3 Convective film coefficient for T-joint specimen analysis 114

6.4 Thermal conductivity for T-joint specimen analysis 115

6.5 Specific heat for T-joint specimen analysis 116

6.6 Temperature contours around the weld pool of the first capping pass 117

6.7 Temperature contours around the weld pool of the second capping pass 118

6.8 Temperature contours around the weld pool of the third capping pass 119

6.9 Temperature contours around the weld pool of the last capping pass 120

6.10 Temperature history at various locations of the T-joint specimen 121

6.11 Weld pool shape of the capping passes 124

7.1 Finite element mesh of a) T-joint specimen; b) weld region for stress analysis (without symmetry) 145

7.2 Finite element mesh of a) T-joint specimen; b) weld region for stress analysis (with symmetry) 146

7.3 Kinematic boundary conditions for analysis without symmetry . 147

7.4 Kinematic boundary conditions for analysis with symmetry . . . 148

7.5 Elastic modulus for T-joint specimen analysis 149

7.6 Poisson's ratio for T-joint specimen analysis 150

7.7 Linear thermal expansion coefficient for T-joint specimen analysis 151

7.8 Yield strength for T-joint specimen analysis 152

7.9 Tangent modulus for T-joint specimen analysis 153

7.10 Displaced T-joint specimen geometry (a) and displaced mesh around the weld region (b) after PASS 1 (without symmetry) 154

7.11 Displaced T-joint specimen geometry (a) and displaced mesh around the weld region (b) after PASS 1 (with symmetry) 156

7.12 X-residual stress distribution - PASS 1 (without symmetry) . . . 158

7.13 Y-residual stress distribution - PASS 1 (without symmetry) . . . 159

7.14 Z-residual stress distribution - PASS 1 (without symmetry) . . . 160

7.15 Von Mises residual stress distribution - PASS 1 (without symmetry) . . . 161

7.16 X-residual stress distribution - PASS 1 (with symmetry) 162

7.17 Y-residual stress distribution - PASS 1 (with symmetry) 163

7.18 Z-residual stress distribution - PASS 1 (with symmetry) 164

7.19 Von Mises residual stress distribution - PASS 1 (with symmetry) 165

7.20 Distribution of the X-residual stress component along the top surface after the first pass (comparison for symmetry assumption) 166

7.21 Distribution of the X-residual stress component along the bottom surface after the first pass (comparison for symmetry assumption) 167

7.22 Distribution of the X-residual stress component through the plate thickness below the weld toe after the first pass (comparison for symmetry assumption) . . . 168

7.23 Distribution of the Y-residual stress component along the top surface after the first pass (comparison for symmetry assumption) 169

7.24 Distribution of the Y-residual stress component along the bottom surface after the first pass (comparison for symmetry assumption) 170

7.25 Distribution of the Y-residual stress component through the plate thickness below the weld toe after the first pass (comparison for symmetry assumption) . . . 171

7.26 Distribution of the Z-residual stress component along the top surface after the first pass (comparison for symmetry assumption) . 172

7.27 Distribution of the Z-residual stress component along the bottom surface after the first pass (comparison for symmetry assumption) 173

7.28 Distribution of the Z-residual stress component through the plate thickness below the weld toe after the first pass (comparison for symmetry assumption) 174

7.29 Distribution of the X-residual stress component along the top surface (without previous residual stresses) 175

7.30 Distribution of the X-residual stress component along the bottom surface (without previous residual stresses) 176

7.31 Distribution of the X-residual stress component through the plate thickness below the weld toe (without previous residual stresses) 177

7.32 Distribution of the Y-residual stress component along the top surface (without previous residual stresses) 178

7.33 Distribution of the Y-residual stress component along the bottom surface (without previous residual stresses) 179

7.34 Distribution of the Y-residual stress component through the plate thickness below the weld toe (without previous residual stresses) 180

7.35 Distribution of the Z-residual stress component along the top surface (without previous residual stresses) 181

7.36 Distribution of the Z-residual stress component along the bottom surface (without previous residual stresses) 182

7.37 Distribution of the Z-residual stress component through the plate thickness below the weld toe (wihtout previous residual stresses) 183

7.38 Displaced T-joint specimen geometry (a); displaced mesh around weld region (b) after PASS 4 184

7.39 X-residual stress distribution - PASS 2&3 186

7.40 Y-residual stress distribution - PASS 2&3 187

7.41 Z-residual stress distribution - PASS 2&3 188

7.42 Von Mises residual stress distribution - PASS 2&3 189

7.43 X-residual stress distribution - PASS 4 190

7.44 Y-residual stress distribution - PASS 4 191

7.45 Z-residual stress distribution - PASS 4 192

7.46 Von Mises residual stress distribution - PASS 4 193

7.47 The assumed X-residual stress distribution 194

7.48 The assumed Y-residual stress distribution 195

7.49 The assumed Z-residual stress distribution 196

7.50 The assumed Von Mises equivalent stress distribution 197

7.51 X-residual stress distribution with A.R.S - PASS 1 198

7.52 Y-residual stress distribution with A.R.S - PASS 1 199

7.53 Z-residual stress distribution with A.R.S - PASS 1 200

7.54 Von Mises stress distribution with A.R.S - PASS 1 201

7.55 Distribution of the X-residual stress component along the top surface after the first pass 202

7.56 Distribution of the X-residual stress component along the bottom surface after the first pass 203

7.57 Distribution of the X-residual stress component through the plate thickness below the weld toe after the first pass 204

7.58 Distribution of the Y-residual stress component along the top surface after the first pass 205

7.59 Distribution of the Y-residual stress component along the bottom surface after the first pass 206

7.60 Distribution of the Y-resiudal stress component through the plate thickness below the weld toe after the first pass 207

7.61 Distribution of the Z-residual stress component along the top surface after the first pass 208

7.62 Distribution of the Z-residual stress component along the bottom surface after the first pass 209

7.63 Distribution of the Z-residual stress component through the plate thickness below the weld toe after the first pass 210

8.1 Kinematic boundary conditions for loading analysis 224

8.2 X-stress distribution with 25 MPa load (stress free condition) . . 225

8.3 Y-stress distribution with 25 MPa load (stress free condition) . . 226

8.4 Z-stress distribution with 25 MPa load (stress free condition) . . 227

8.5 Von Mises stress distribution with 25 MPa load (stress free condition) 228

8.6 X-stress distribution along the top surface after one loading cycle (stress free condition) 229

8.7 X-stress distribution along the bottom surface after one loading cycle (stress free condition) 230

8.8 X-stress distribution through the palte thickness below the weld toe after one loading cycle (stress free condition) 231

8.9 Y-stress distribution along the top surface after one loading cycle (stress free condition) 232

8.10 Y-stress distribution along the bottom surface after one loading cycle (stress free condition) 233

8.11 Y-stress distribution through the plate thickness below the weld toe after one loading cycle (stress free condition) 234

8.12 Z-stress distribution along the top surface after one loading cycle (stress free condition) 235

8.13 Z-stress distribution along the bottom surface after one loading cycle (stress free condition) 236

8.14 Z-stress distribution through the plate thickness below the weld toe after one loading cycle (stress free condition) 237

8.15 X-stress distribution with 25 MPa load (as welded condition) . . 238

8.16 Y-stress distribution with 25 MPa load (as welded condition) . . 239

8.17 Z-stress distribution with 25 MPa load (as welded condition) . . 240

8.18 Von Mises stress distribution with 25 MPa load (as welded condition) 241

8.19 X-stress distribution after one 25 MPa loading cycle (as welded condition) 242

8.20 Y-stress distribution after one 25 MPa loading cycle (as welded condition) 243

8.21 Z-stress distribution after one 25 MPa loading cycle (as welded condition) 244

8.22 Von Mises stress distribution after one 25 MPa loading cycle (as welded condition) 245

8.23 X-stress distribution with 50 MPa load (as welded condition) . . 246

8.24 Y-stress distribution with 50 MPa load (as welded condition) . . 247

8.25 Z-stress distribution with 50 MPa load (as welded condition) . . 248

8.26 Von Mises stress distribution with 50 MPa load (as welded condition) 249

8.27 X-stress distribution after one 50 MPa loading cycle (as welded condition) 250

8.28 Y-stress distribution after one 50 MPa loading cycle (as welded condition) 251

8.29 Z-stress distribution after one 50 MPa loading cycle (as welded condition) 252

8.30 Von Mises stress distribution after one 50 MPa loading cycle (as welded condition) 253

8.31 Distribution of the X-stress component along the top surface (as welded condition) 254

8.32 Distribution of the X-stress component along the bottom surface (as welded condition) 255

8.33 Distribution of the X-stress component through the plate thickness below the weld toe (as welded condition) 256

8.34 Distribution of the Y-stress component along the top surface (as welded condition) 257

8.35 Distribution of the Y-stress component along the bottom surface (as welded condition) 258

8.36 Distribution of the Y-stress component through the plate thickness below the weld toe (as welded condition) 259

8.37 Distribution of the Z-stress component along the top surface (as welded condition) 260

8.38 Distribution of the Z-stress component along the bottom surface (as welded conditon) 261

8.39 Distribution of the Z-stress component through the plate thickness below the weld toe (as welded condition) 262

A.1 Test problem configuration 286

A.2 Finite element mesh for test problem 287

A.3 Kinematic constraints for test problem 287

A.4 Comparison between analytical and FEM solution (radial stress distribution) 288

A.5 Comparison between analytical and FEM solution (tangential stress distribution) 289

Chapter 1

Introduction

1.1 Background

Since 1981 the Department of Mechanical Engineering at the University of Waterloo has studied techniques for the numerical prediction of residual stresses resulting from welding. Such stresses have been predicted with numerical models developed by various researchers around the world, however, the majority of these models have for single pass welds. Under contract to CANMET, Energy, Mines and Resources, Ottawa, a program was set up at the University of Waterloo to develop a numerical model to predict residual stresses induced by the welding process and to apply it to multi-pass welds. In conjunction, Dr. G. Roy of CANMET undertook experimental measurements to support the multi-pass studies.

In the multi-pass study, a finite element model was developed by Leung for the analysis of multi-pass weld configurations [1, 2]. The model made use of a commercially available finite element package called ABAQUS [3] which contained most of the features required to simulate the welding process. For a single pass weld Mair [4] showed that Leung's model was quite accurate compared to very detailed experimental measurements of residual stress. However, confirmation of Leung's work for multi-pass welds remained outstanding.

Concurrently as part of a study of the fatigue of offshore steel structures in Canada, a series of T-joint fatigue specimens were used to study crack shape development and thickness effects under fatigue loading [5-7]. These fatigue tests were undertaken on the T-joint specimens in the as welded condition and a question has arisen regarding the role of the high weld residual stresses on the results of the fatigue testing. EMR/CANMET chose to undertake experimental measurement of the weld residual stresses. This provided an opportunity to confirm the analysis techniques of Leung and to provide greater detail of the residual stress distribution than could be expected from experimental measurements.

In 1986 a contract was let to the Department of Mechanical Engineering at the University of Waterloo to predict the weld residual stress in the multi-pass weld of the T-Joint Fatigue Specimen. This study was undertaken as part of the requirement for a MASc Degree by Danny H.B. Mok and is reported herein.

1.2 Objectives

The objective of this study was to calculate the residual stresses induced by welding during manufacture of a 26 mm T-joint fatigue specimen and determine the effect of the mechanical loading of the fatigue test on the residual stress field.

Unfortunately Leung's model was developed for Austenitic steels and does not include allotropic phase transformations. The manganese steel used for the T-joint specimen would undergo such phase transformations during welding and the effect of these transformations on welding residual stress is not known. Therefore an additional objective of this study was to investigate the effect of phase transformations on welding residual stresses and if necessary include it in the T-joint specimen modelling.

Finally, in keeping with previous studies, it was desired to determine the agreement between experimental measurements made at EMR/CANMET and the finite element predictions. This was to confirm both the experimental measurements and support the finite element techniques developed by Leung [1, 2].

1.3 Report Outline

This Report is divided into two parts. In the first part, the effects of allotropic phase transformations on welding residual stresses were studied. A literature review of studies of phase transformations effects is presented in Chapter 2. The numerical model used in this study and the results of the analyses are described in Chapter 3. A discussion of the results is presented in Chapter 4.

In the second part of this Report, the 26 mm T-joint specimen was modelled. The welding procedures used in the fabrication of the 26 mm T-joint specimen and the loading conditions used in the fatigue test are described in Chapter 5. In addition, a review of the literature on topics relating to welding residual stresses in 'T' shapes is also presented. The heat transfer analysis and the welding residual stresses calculations are described in Chapter 6 and Chapter 7 respectively. Modelling of the first loading cycle of the fatigue test, along with a discussion of the possible effects of the welding residual stresses on the fatigue

behavior are presented in Chapter 8. Finally, the conclusions of this study are summarized in Chapter 9.

Chapter 2

Literature Review - Phase Transformation Effects

2.1 Sources Of Residual Stress In Welding

According to Macherauch and Wohlfahrt [8], there are three main sources of residual stress that result from welding. The first is due to the difference in shrinkage of nonuniformly heated and cooled parts of a welded joint. The fusion region is initially subjected to temperatures above the material's melting point, while the rest of the material experiences a much less severe thermal history. The fusion region will contract more due to higher temperatures at solidification. As the metal cools, it contracts and regains some of its strength. This contraction is hindered by the rest of the parent material which subjects the fusion zone to a large tensile stress in the longitudinal direction of the weld. This contraction also causes transverse stress normal to the weld but generally at a lower level due to less severe restraint conditions. High residual stresses occur in materials that have a large product of Young's modulus and the linear thermal expansion coefficient.

The second source of residual stress is due to the more rapid cooling of the weld surface than the interior. Thus, a temperature gradient is created through the thickness which causes inhomogeneous plastic deformation upon further cooling. The residual stress is expected to be compressive at the surface of the fusion region, with equilibrating tensile stress in the interior. The maximum stresses would be found for thick plates with rapid surface cooling.

The third source of residual stress is due to solid-solid phase transformations and their accompanying volumetric growth during cooling. For most structural steels, this transformation is from austenite to ferrite, bainite, or martensite, depending on the cooling rate and chemical composition. The expansion of the transforming material is restrained by the untransformed material, thus creating residual stress. The transformed material is forced into compression while the surrounding material is placed in tension. Transformation induced residual stresses are higher if the yield stress is high at the transformation temperature.

The overall welding residual stresses can be approximated by the superposition of the above three sources. As a result, there is usually a local minima in the stress distribution along the surfaces at the fusion zone. Depending on the magnitude of each source, the residual stresses in the fusion zone can be in compression while the adjacent material in the HAZ is in tension. These oscillations in the residual stress distribution have also been observed experimentally in simulated welds [8-10].

2.2 Allotropic Phase Transformation Process

Most ferritic steels undergo solid-solid phase transformations when subjected to thermal history in which the temperature passes through the A_1 to A_3 temperature range. Usually accompanying this transformation is a volumetric change as the crystallographic structure of the steel changes [11]. This volumetric change depends on the thermal history. Consider a hypoeutectoid steel being heated from below the A_1 temperature (eutectoid temperature for hypoeutectoid carbon steel). When the steel reaches the A_{c1} temperature (the subscript c stands for non-equilibrium heating), it begins to transform into austenite. The transformation process is completed when the A_{c3} temperature (temperature that separates the austenite phase and austenite plus ferrite phase) is reached. The reverse sequence will occur if this steel is being cooled from above the A_3 temperature. Depending on the cooling rate and steel composition, the austenite phase will transform into pearlite, bainite or martensite at the A_{r3} temperature (subscript r stands for non-equilibrium cooling). Completion of the transformation is achieved at the A_{r1} temperature.

Pearlite, bainite and martensite are alpha phase iron alloys which have a body center cubic (BCC) crystallographic structure. Austenite is a gamma phase iron alloy which is face center cubic (FCC). Since the volume of a BCC iron unit cell is larger than that of FCC iron, there is a volume change in the steel during the FCC to BCC allotropic phase transformation. The specific volume will shrink during heating and will expand during cooling. If this volume change is restrained, significant stresses can be developed.

2.2.1 Allotropic Phase Transformation Model

During heat treatment processes such as quenching, the whole component undergoes allotropic phase transformations as the cooling front passes through the component. Thus, significant residual stresses can be induced. A number of researchers have developed theoretical models based on continuum mechanics for calculating the phase transformation induced residual stresses during heat treatment processes [12-19]. A thermo-elastic-plastic material behavior is usually used with a constitutive equation (in incremental form):

$$d\epsilon^{t} = d\epsilon^{E} + d\epsilon^{th} + d\epsilon^{P} + d\epsilon^{Tr} \tag{2.1}$$

where $d\epsilon^{t}$ is the total strain; $d\epsilon^{E}$, $d\epsilon^{th}$ and $d\epsilon^{P}$ are the elastic strain, thermal strain and plastic strain respectively, and $d\epsilon^{Tr}$ is the strain due to phase transformation. The first three terms on the right hand side of equation 2.1 are defined in classical plasticity theory. The phase transformation term can further be separated into two components,

$$d\epsilon^{Tr} = d\epsilon^{TrV} + d\epsilon^{TrP} \tag{2.2}$$

where $d\epsilon^{TrV}$ is the strain due to the volumetric change associated with the phase transformations and $d\epsilon^{TrP}$ is the plastic strain as a result of plastic flow of the material under stress lower than the yield strength when the phase transformation takes place. The volumetric change is usually combined into the thermal strain using dilatation curves [12,17-19]. A number of researchers have modelled the effect of transformation plasticity by lowering the yield strength of the material artificially [13] and achieved some success. However, most researchers used a semi-empirical approach in which the effective plastic strain component is calculated by an empirical formula [14-19]. Denis et al. [18] have observed significant differences in calculated quenching stresses with and without the inclusion of transformation plasticity. Although these models were developed for heat treatment processes, they are applicable to welding residual stress calculations.

2.3 Phase Transformation Effects In Welding

In the welding process, the material around the fusion zone experiences extreme temperature changes, ranging from room temperature to above the melting point and back down to room temperature, while most of the parent material is being heated only to a moderate temperature. In the weld region, a solid-solid phase transformation will occur. During the heating cycle, phase transformation effects are not important because any accumulated damage is relieved at temperatures near the melting point. But this is not the case during cooling. Initially, the metal contracts according to the linear thermal expansion coefficient. As the temperature drops below the A_{r3} temperature, the phase transformation occurs and the metal that has transformed will expand. This expansion alleviates tension in the HAZ caused by the contraction and the magnitude of the residual stress is reduced. This reducing effect during cooling has been observed by Jones and Alberry [20, 21]. The extend of this stress reduction depends on the transformation temperature and the change in specific volume. If the transformation occurs at high temperature when the material is relatively weak, the effect will be small. If the volumetric expansion is small compared to the thermal contraction, the effect will also be small. Jones and Alberry [12, 13] have suggest that a significant residual stress build-up will only occur during cooling from the finish of the transformation to ambient temperature. For the purpose of calculation of residual stress, the stress accumulation after the completion of the phase transformation is the only stress which needs to be considered.

2.3.1 Phase Transformation Models In Welding

The first two sources of welding residual stresses described in Section 2.1 have been predicted quite accurately by various researchers using numerical techniques. In these analyses, the phase transformation effect is usually not considered [22-25] or the material is chosen such that no phase transformation occurs during welding [1, 2, 26-32]. However, the models to predict welding residual stress for metals that undergo allotropic phase transformation are very similar to models with no transformation. Since comprehensive reviews on models for prediction of welding residual stresses can be found in Leung's study of multipass welds [1, 2] and in the book by Masubuchi [33], a review will not be presented here. Instead, the following discussion will describe studies that include phase transformation effects.

Heat Transfer Analysis

The thermal, metallurgical and mechanical behavior of a metal during welding are interrelated. However, the thermal problem is normally assumed uncoupled from the residual stress analysis and the microstructure calculations. Hibbitt [34, 35] suggested that the coupling effect between thermal and mechanical response is weak when the dimensional changes are small and the strain rate effect is small compared to the temperature effect. Argyris et al. [36] attempted to include the weakly coupled thermomechanical effect by using a staggered solution procedure in which the strain energy due to mechanical strain was supplied to the heat transfer analysis as heat input. The authors found that the maximum temperature difference between coupled and uncoupled solutions was about 2°C.

The latent heat of allotropic phase transformation can be integrated into a temperature dependent specific heat value and a constant enthalpy formulation can be used. However, these are ignored in most studies because the values are usually unavailable in the literature. Dubois et al. [37] have included the latent heats of all phase transformations and achieved improved agreement with measurement, especially for lower temperatures during the bainitic transformation. However, the error is expected to be small if the latent heats for allotropic phase transformations are neglected because these are usually small.

Metallurgical Changes In Welding

When modelling welding of a metal that undergoes allotropic phase transformation, knowledge of the phase transformation kinetics which determine the final microstructure and the magnitude of volumetric change is required.

Since prediction of the final microstructures is not the goal of this study, it will not be reviewed in detail. The transformation kinetics of steel is very complex. It depends on the chemical composition, peak temperature and cooling rate. The process can be followed with the aid of a continuous cooling transformation (CCT) diagram. Unfortunately, the CCT diagram is not always available in handbooks, especially for cooling rates that are typical in welding.

The magnitude of volumetric changes can be determined from dilatation-temperature curves. Unfortunately, dilatation curves are rarely published although they are commonly used to determine the transformation temperatures for the construction of CCT diagrams. Therefore, the best approach to obtain data on the transformation kinetic and volumetric changes is to conduct one's own experiment. This is generally a laborious and expensive task.

Residual Stress Analysis

Hibbitt and Marcal [35] were pioneers in including an allotropic phase transformation effect in the study of residual stress. These authors have included the volumetric expansion by modifying the thermal linear expansion coefficient with a delta function at the transformation temperature. Distinction between different possible phase transformations that different parts of a weld would undergo was not made. Considering both weld metal and parent metal were the same, a parametric study was conducted with various transformation temperatures. No significant difference was observed in the residual stresses predicted for different transformation temperatures.

Andersson [38] has included this distinction in his model and separated the HAZ into three different zones classified by their peak temperature in the thermal history. It was assumed that each zone would follow a specific dilatation curve. The results showed that both longitudinal and transverse residual stress distributions on the surface were similar to those found in an analysis without a transformation effect, except there was an oscillation in the longitudinal stress distribution at the interface between fusion zone and parent metal. In a later study on the same weld [39] a plane stress condition was assumed and the oscillation was not observed. Ueda [40] also suggested a similar approach. However, the author did not indicate the effect of phase transformation on the predicted residual stresses. Josefson applied Andersson's model to study the welding and annealing of thin-walled pipes [41, 42] and thick-walled pipes [43]. He also included transformation plasticity in the HAZ by lowering the yield stress [42]. A very small increase in residual stress within the fusion zone was observed for butt welding of thin plates. The opposite effect was observed for butt welding of thin-walled pipe. The author found that the welding residual stress distribution for thick-walled pipe with phase transformations was similar to that without the transformation. Jonsson [44] studied the transverse distortion of a butt weld during welding. Using Andersson's model, he refined the HAZ into six zones instead of three. Reasonable agreement with experimental results were achieved. However, in this study, Jonsson did not perform the analyses without the transformation effect to determine the difference.

Argyris et al. [36] included transformation plasticity by lowering the yield stress and modifying the linear expansion coefficient similar to the model of Hibbitt and Marcal [36]. The authors found that the thermal stress histories are different for analyses with and without phase transformations. The largest difference in the predicted residual stress was about 100 MPa in the transverse direction. However, the differences were observed only in the fusion zone. The difference was negligible when using the Von Mises equivalent stress.

Papazoglou [45, 46] has developed a comprehensive model that followed the transformation kinetics to determine the transformed phases. For each phase (i.e., ferrite, bainite, or martensite), he assigned a thermal expansion coefficient. The average thermal expansion coefficient at any temperature was calculated by the rule of mixtures. The author suggested that a small fluctuation in the surface stress distribution observed at the fusion zone interface was a phase transformation effect but no attempt was made to compare the results with an analysis that did not include phase transformations.

Wang and Inoue [47] have derived a visco-plastic constitutive relationship similar to those described in Section 2.2.1 that has included a phase transformation. The volumetric strain derived from dilatation curves was added to the total strain formulation. Residual stress distributions for a butt welded plate and a hole filling weld in circular plate showed typical residual stress distributions without any fluctuations and agreed well with measurements by x-ray diffraction technique. Again, the authors did not state the effect of phase transformation on residual stress. Dubois et al. [37] have also used a similar approach in an analysis of deposition of cladding on a flat plate. In this study, transformation plasticity was included, with the plastic strain due to this effect being calculated by an empirical formula. Due to the complexity of the problem, only the austenite-bainite transformation was modelled. A maximum difference of about 400 MPa in the longitudinal stress and about 200 MPa in the transverse stress was observed in the HAZ between analyses with and without transformation plasticity. In general, the residual stresses in the HAZ was less compressive in the analysis with transformation plasticity. The authors have suggested that the global effect of transformation plasticity is to increase the stress when it is compressive and decrease when it is tensile. Since the material in the HAZ was in compression during the bainitic transformation, transformation plasticity raised the overall stress, thus, a less compressive stress field was observed.

Chapter 3

Computer Model Including Phase Transformation Effects

From the literature survey, the effect of an allotropic phase transformation and the associated change in specific volume are expected to be small and local to the fusion zone. For residual stress predictions, a simple model similar to Andersson's [38] should be used instead of Papazoglou's [46] complex model unless the final microstructure is also of interest. Of course, with this model, transformation plasticity will not be considered.

To determine the importance of including volumetric changes due to phase transformations in the prediction of welding residual stresses, it was decided to use Leung's model of single pass, submerged arc weld of stainless steel [1, 2], which has been shown to accurately predict welding residual stress [4], as the basic analysis and artificially add a transformation strain. This approach creates an unrealistic material, i.e., 316L stainless steel with allotropic phase transformation. However, the transformation effect can be clearly identified when the results are compared to that of Leung's. The approach to implement the transformation strain was similar to that of Andersson's [38]. However, instead of combining the thermal strain and transformation strain, these were separated such that a parametric study of transformation temperatures and magnitudes of volumetric strain were carried out.

3.1 Leung's Model

In Leung's study of multipass welds [1, 2], the author's philosophy was that if single pass weld can be predicted accurately, then multipass welds can be modelled by applying the single pass model in a repetitive manner. Thus, a significant effort was spent on developing a single pass model. This model is summarized in this discussion.

The geometry of the plate used in Leung's study is shown in Figure 3.1. The steel chosen was 316L stainless steel because it is widely used in the nuclear industry and material property data is available. In addition, during the welding process only a small amount of the austenite undergoes a phase transformation and this effect can be neglected. A 'V' groove preparation was assumed along the center line of the plate and a submerged Arc welding (SAW) process was used to deposit weld metal of similar chemical composition to the parent plate. The welding parameters are listed in Table 3.1. The weld was laid with one edge of the plate clamped to the welding table; while the other edge was supported such that the plate could only rotate upward off the welding table.

3.1.1 Heat Transfer Analysis

The heat transfer analysis and the thermal stress analysis were uncoupled according to Hibbitt [34]. A commercially available finite element package called ABAQUS [3] was used in this study. Since the plate was sufficiently long and the weld speed was fast enough, a quasi-stationary state would be guaranteed in regions away from the start and stop of welding. A two-dimensional analysis was used to model a cross section plane at the midpoint of the plate with the weld pool moving through this plane. Assuming symmetry, only one half of the plane was modelled. The cross-sectional was discretized using 4-noded isoparametric elements (DC2D4) in the fusion zone to model the latent heat effect and 8-noded isoparametric elements (DC2D8) in the rest of the cross section.

The material properties required for the heat transfer analysis were the thermal conductivity, specific heat, mass density, latent heat of transformation and the associated transformation temperatures. The thermal conductivity and specific heat, as a function of temperature, are shown in Figures 3.2 and 3.3 respectively. Extrapolated values have to be used for properties close to the melting point because data are not available at such high temperatures. A constant mass density of 7952 kg/m^3 and a latent heat of fusion of 292 kJ/kg was assumed. The solidus and liquidus temperatures are 1375°C and 1400°C respectively. As mentioned the model assumed that the stainless steel does not undergo phase transformation, and therefore, no latent heat of phase transformation was used. The chemical compositions for both the weld metal and parent metal were assumed to be similar, and therefore, no distinction was made in the analysis.

The weld metal was assumed to be deposited instantaneously in this model. Goldak's double ellipsoidal heat source model [48] was used to simulate the heat input from the weld arc. The parameters used in Leung's analysis were obtained by measurement from the actual welded specimen and are shown in Figure 3.4. The weld pool convection was modelled by artificially increasing the thermal conductivity for temperatures greater than the melting point to five times the value at the solidus temperature. Since there are always power losses during welding, the actual heat input into the weld metal is less than the total power provided by the welding machine. This effect was taken into account by an arc efficiency. For submerged arc welding, arc efficiencies are usually very high because of the thick layer of flux used during welding. A value of 90% was assumed.

The thermal boundary conditions for submerged arc welding are shown in Figure 3.5. Convective and radiative heat losses were expected from all surfaces except in the areas covered by the flux where an adiabatic condition would exist. Convective heat loss was modelled by Newton's cooling law with the temperature dependent surface film coefficient shown in Figure 3.6. Radiative heat loss was modelled by the Stefan-Boltzmann power law with an average value of 0.55 for the surface emissivity.

3.1.2 Thermal Stress Analysis

After the heat transfer analysis was completed, the thermal history was supplied to the stress analysis as thermal loading. In order to avoid numerical problems, the thermal history was modified such that the maximum temperature never exceeded 1400°C within the weld pool.

Leung used a second mesh for his stress analysis due to the incompatibility of 4-noded and 8-noded elements for stress calculations. The cross-section was discretized using 4-noded isoparametric elements. In order to model the longitudinal displacement more accurately, a generalize plane strain element was used [3]. When the weld metal is in the melted state, the yield strength of the material is very low and large hydrostatic stresses can result. In order to avoid numerical problems, Leung used a hybrid element [3] in which the hydrostatic stress was formulated as a state variable (CGPE6H).

The constitutive model used in the stress analysis was a rate independent elastic-plastic model with temperature dependent material properties. The onset of yielding was predicted by the Von Mises's yield criterion and the associated flow rule by Prantl-Reuss was used to calculate the incremental plastic strain. A kinematic hardening model was adopted for modelling the Bauschinger effect of reverse plasticity which occurs during welding. The mechanical and physical properties required by the thermal stress analysis are Young's Modulus, Poisson's ratio, the virgin yield stress, the tangent modulus which describes the strain hardening and the average linear thermal expansion coefficient. The values used in Leung's study are shown in Figures 3.7 to 3.11. Creep was not modelled because the metal only remains at a high temperature for a very short time during welding.

As described earlier, the weld metal was deposited with one edge of the plate clamped to the welding table while the other edge was free to displace. Leung has modelled this support condition. He has also studied the effect of three other support (or restraint) conditions on the residual stress development. The first restraint condition examined was a plate simply supported on both edges with various other restraint conditions such as no uneven longitudinal shrinkage and no plate bowing. The second restraint condition studied was a plate clamped along both sides. The last restraint condition was a fully restrained plate.

3.2 Volumetric Expansion Model

Leung's model does not consider phase transformation effects. Therefore, a model to implement the volumetric expansion due to phase transformation was developed. This model is described in this discussion. A survey of the literature revealed that most researchers model the volumetric expansion due to allotropic phase transformations by modifying the thermal linear expansion coefficient [34, 46] or by combining the volumetric strain with the linear thermal expansion into a dilatation curve [38, 39]. In this model, these two effects are kept separate with the thermal strain being calculated from the average linear thermal expansion coefficient and the volumetric expansion specified as material swelling using the SWELLING option in the commercial code ABAQUS [3]. By separating the volumetric strains from the thermal strains, different starting transformation temperatures and different volumetric expansions can be studied. The SWELLING option was originally designed for volumetric swelling of material under radiation, which is both time and temperature dependent. However, the option was modified with a user defined subroutine such that it is only temperature dependent. With the SWELLING option, a VISCO (time and temperature dependent) analysis instead of a STATIC analysis (time independent) has to be used for stress calculations. This method was confirmed by solving a test problem that is described in Appendix A.

An approach similar to that of Andersson's [38] is used but only the phase transformation during cooling is included because the effect during heating would be relieved at high temperatures. The HAZ is divided into three zones where each zone followed an experimentally determined dilatation curve for a specific cooling rate to simulate the transformation from austenite into the different phases (Figure 3.12). Each zone is classified by the maximum temperature in the thermal history. The three classifications are as followed:

zone 1: $T_{max} \geq 1250°C$
zone 2: $1250°C \geq T_{max} \geq 1050°C$
zone 3: $1050°C \geq T_{max} \geq 850°C$

No transformation was assumed for areas where the maximum temperature did not reached 850°C. After the heat transfer analysis, a post-processing operation has to be performed in order to divide the whole plate into the different zones. The maximum temperature is based on average element values. Each zone is then assigned a different SWELLING characteristic for the thermal stress analysis. The volumetric strain for each zone was extracted from Andersson's dilatation curves for HT-36 steel which is a fine-grain manganese steel (Figure 3.13). As explained earlier, these dilatation curves are applied to the stainless steel model of Leung. This leads to a material which does not exist, however, the total package of material properties is not unlike typical ferritic steel and is accurate enough to show the effect of allotropic phase transformations.

3.3 Heat Transfer Analysis

In the heat transfer analysis, the thermal history was calculated with a much finer mesh than the one used by Leung [1, 2]. The cross-sectional plane was discretized into 386 4-noded isoparametric elements with a total of 442 nodes (Figure 3.14a-3.14b). The material properties, thermal boundary conditions and heat source model were the same as described in Section 3.1.1. As in Leung's analysis, no latent heat of transformation was used in the present study. This is assumed to be acceptable because the latent heat is believed to have only a small effect on the thermal history and therefore little effect on the residual stress calculation.

3.3.1 Results Of The Heat Transfer Analysis

The ABAQUS input file and the user defined subroutine for the double ellipsoidal heat source model can be found in [49] and will not be listed here.

The fusion zone size predicted by the analysis is shown in Figure 3.15. The weld pool shape and thermal history is very similar to that predicted by Leung [1, 2]. An unrealistic maximum temperature in the weld pool was observed and modified to 1400°C for the thermal stress analysis.

3.4 Thermal Stress Analysis

In the thermal stress analysis, the finite element mesh used in the heat transfer analysis was modified by combining four 4-noded elements into one 8-noded element. The cross-section was discretized into 93 elements with 336 nodes (Figures 3.16a-3.16b). Instead of the 4-noded generalized plane strain hybrid element (CGPE6H of ABAQUS [3]) used in Leung's analysis, the 8-noded generalized plane strain element (CGPE10R) was used because the hybrid element is not compatible with the analysis scheme as discussed in Section 3.2. The finite element mesh was divided into four zones according to the classification described above (see Figure 3.17).

For simplicity, the plate was assumed to be simply supported with the in-plane kinematic constraint shown in Figure 3.18. The longitudinal shrinkage was assumed to be even and no bowing of the plate was allowed.

The welding residual stress for the stainless steel plate without an allotropic phase transformation was determined so that a comparison can be made with an analysis including the transformation effect. A parametric study was undertaken to determine how the different phase transformation parameters affect the welding residual stress. The transformation temperature was varied in two other analyses (Figures 3.19a to 3.19b) to study the effect of transformation temperatures. The magnitude of the volumetric strain of phase transformation was increased (Figure 3.19c) to determine the relationship between volumetric strain and welding residual stress.

3.4.1 Results Of The Thermal Stress Analyses

The ABAQUS input files and the user defined subroutine for the volumetric expansion model are listed in [49] and are not repeated here.

No Phase Transformation Effect

The deformed plate after welding is shown in Figures 3.20a and 3.20b. The distortion in the weld pool region is a numerical problem due to the type of element used. In Leung's analysis, the hybrid element was used for which the hydrostatic stress is a state variable and therefore the solution technique is more stable. For the current analyses, the hybrid element could not be used due to an incompatibility with the VISCO analysis. Therefore, convergence of the solution is slower and large unrealistic displacement can occur in certain areas. However, these numerical errors occur at high temperatures for which the accumulated damage is small and is relieved. Thus, the effect on residual stress is minimal.

During the heating cycle, the metal in and around the fusion zone expands more than the rest of the plate. This expansion and the simply supported condition allows the plate to pivot about the supports, rising at the weld center-line. As the weld cools, the metal contracts, and, as before, the plate pivots about the supports with the weld center-line moving downwards to its final position. The predicted maximum downward deflection is about 3.5 mm.

The longitudinal stress distribution along the surfaces and through the thickness at the weld center-line are plotted in Figures 3.21 to 3.23 respectively. The transverse stress distributions at the same locations are presented in Figures 3.24 to 3.26. The predicted residual stresses are typical of a butt welded plate. The results for the analysis with phase transformation effects (described in the next section) are also presented. There is a zone of high longitudinal tensile stress (about 300 MPa) around the fusion zone on both the top and bottom surfaces. The tensile stress decreases away from the weld region and eventually becomes compressive to achieve equilibrium. The transverse residual stresses are much lower than the longitudinal stresses. On the top surface the stress is compressive in the fusion zone and is tensile just outside this zone. On the bottom surface, the transverse stress is all tensile. Through the thickness along the weld center-line, the stress oscillates between compressive and tensile to maintain equilibrium. In all cases the residual stress distributions agree well with Leung's results [1, 2].

Including Phase Transformation Effect

An analysis with phase transformation effects was undertaken and designated as PHTRAN. The allotropic phase transformation parameters used in this analysis were extracted directly from [38]. The starting transformation temperature (T_s) is at approximately 680°C. As mentioned in section 3.2, a VISCO analysis procedure is required for the SWELLING option. However, numerical problems were encountered during the analysis of the heating cycle such that excessive displacement in the weld zone was predicted. This problem was overcome by using the STATIC analysis procedure for the heating phase and the VISCO analysis procedure for the cooling phase. This approach is acceptable because no transformation effects are assumed for the heating phase, i.e., the VISCO analysis procedure is not required. Distortions similar to that without a phase transformation were observed (Figure 3.27). The maximum vertical deflection after welding occurs is about 2.9 mm which is slightly less than the case without phase transformation (Table 3.2). This indicates that the the thermal contraction is partially offset by the volumetric expansion during the phase change.

The longitudinal and transverse residual stress distributions along the surfaces and through the thickness along the weld center-line are presented in Figures 3.21 to 3.26 respectively along with the results without phase transformation effects. The residual stress distributions for both cases are very similar. The maximum difference in longitudinal stress is about 10 MPa and is less than 2 MPa for transverse stress.

Effect Of Starting Transformation Temperatures

Two other analyses were conducted with different transformation starting temperatures, T_s; 830°C (designated as HITEM) and 480°C (designated as LOTEM). The analyses were restarted from the end of the heating phase which was assumed to correspond to the previous analysis (PHTRAN). The maximum vertical distortions for the two analyses were almost identical to PHTRAN at 2.9 mm (summarized in Table 3.2).

The longitudinal residual stress distributions along the top surface, bottom surface and through the thickness at the weld center line are shown in Figures 3.28 to 3.30 for the two analyses and PHTRAN. The longitudinal residual stresses for the two higher T_s values are about the same. A very small decreased in stress level (3 MPa) is observed in the fusion zone for the lowest T_s analysis.

The transverse residual stress distributions are very similar for all three analyses (Figures 3.31 to 3.33). In general, the magnitude of the transverse residual stress is about 5 MPa lower for the lowest T_s case than the other two temperatures.

Effect Of Volumetric Strain Magnitude

To investigate the effect of the magnitude of the volumetric growth, the volumetric strain was increased to four times that of the PHTRAN analysis with the maximum volumetric strain at about 2%. The maximum vertical distortion for this analysis was found to be about 1.5 mm which is about half of the deflection of the other analyses with the phase transformation effect.

The residual stress distributions for the two analyses with different volumetric strain magnitudes are very similar. The distribution for the higher volumetric strain shows some oscillations in the transverse direction. In general, the magnitude of the residual stresses are lower for larger volumetric expansion with a maximum decrease of 20 MPa in both longitudinal and transverse directions. The longitudinal stress on the top surface, bottom surface and through the thickness along the weld center-line are presented in Figures 3.34 to 3.36 The transverse stresses are shown in Figures 3.37 to 3.39.

Table 3.1: Welding parameters [1]

Voltage	34 Volts
Current	440 - 450 Amps
Travel Speed	88.9 cm/min
Stick Out	2.54 cm
Wire Feed	3.175 cm/sec

Table 3.2: Maximum vertical displacement after welding

Analysis	Displacement (mm)
NOPHASE	3.49
PHTRAN	2.97
HITEM	2.99
LOTEM	2.96
HIVOL	1.46

- NOPHASE - no phase transformation effect.
- PHTRAN - phase transformation starts at 680°C.
- HITEM - phase transformation starts at 830°C.
- LOTEM - phase transformation starts at 480°C.
- HIVOL - volumetric strain is 3 times that of PHTRAN.

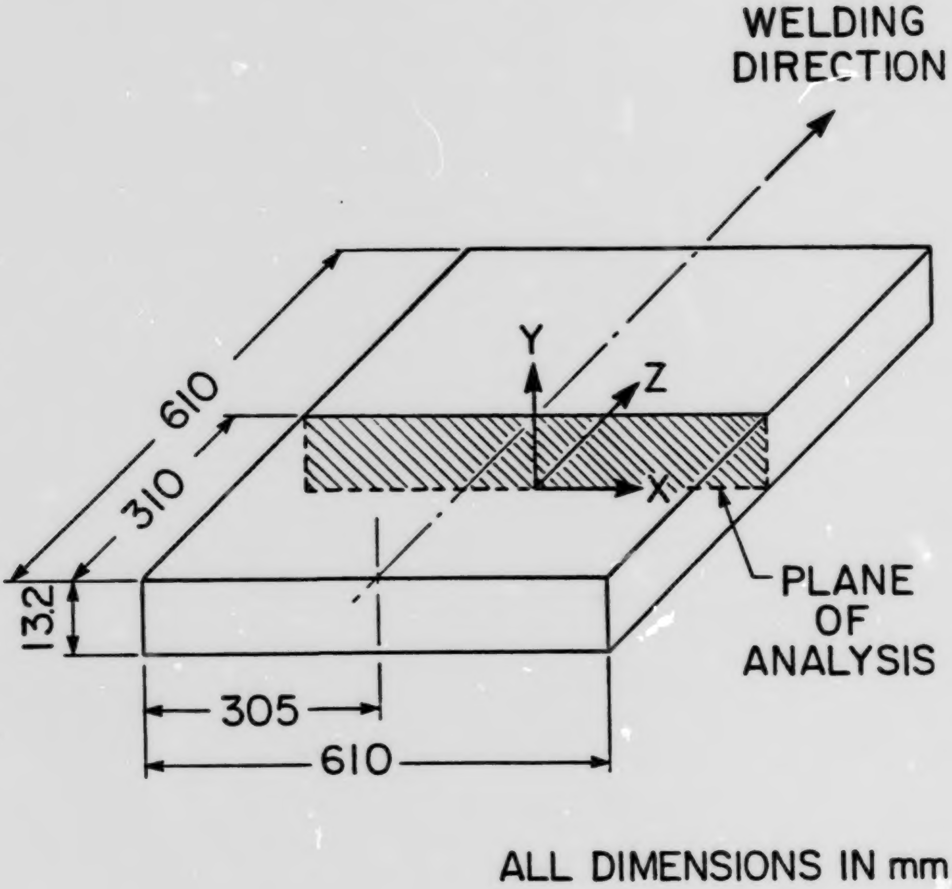
WELDING
DIRECTION
Y
Z
X
610
310
13.2
305
610
PLANE
OF
ANALYSIS
ALL DIMENSIONS IN mm

Figure 3.1: Longitudinal butt-weld configuration [1]

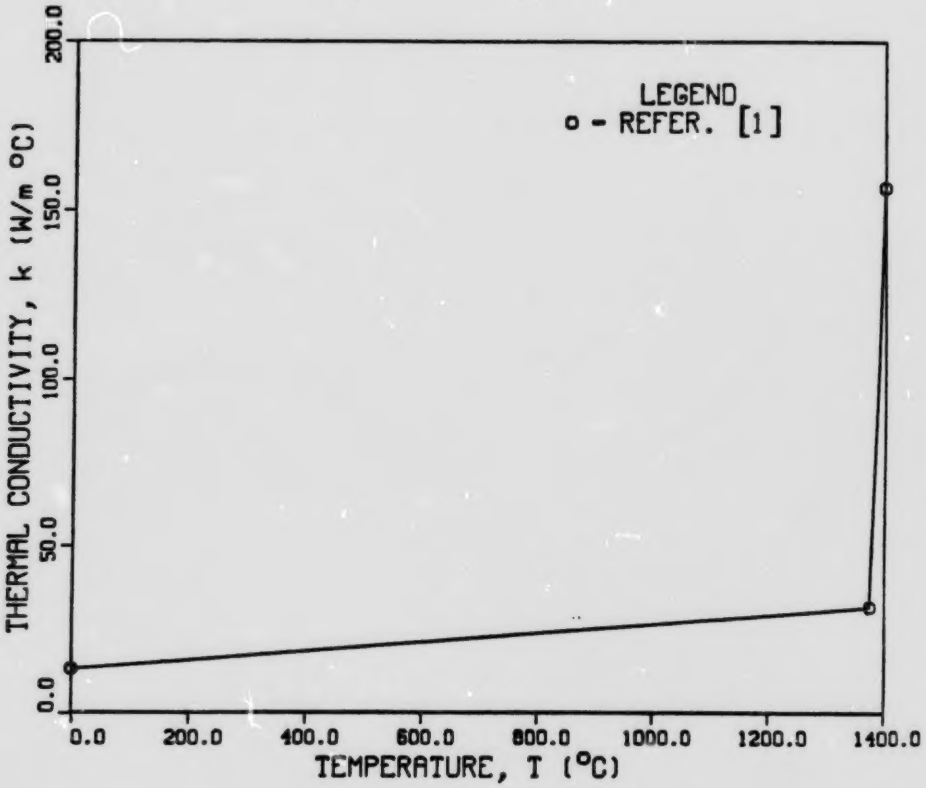

Figure 3.2: Thermal conductivity for AISI 316L stainless steel

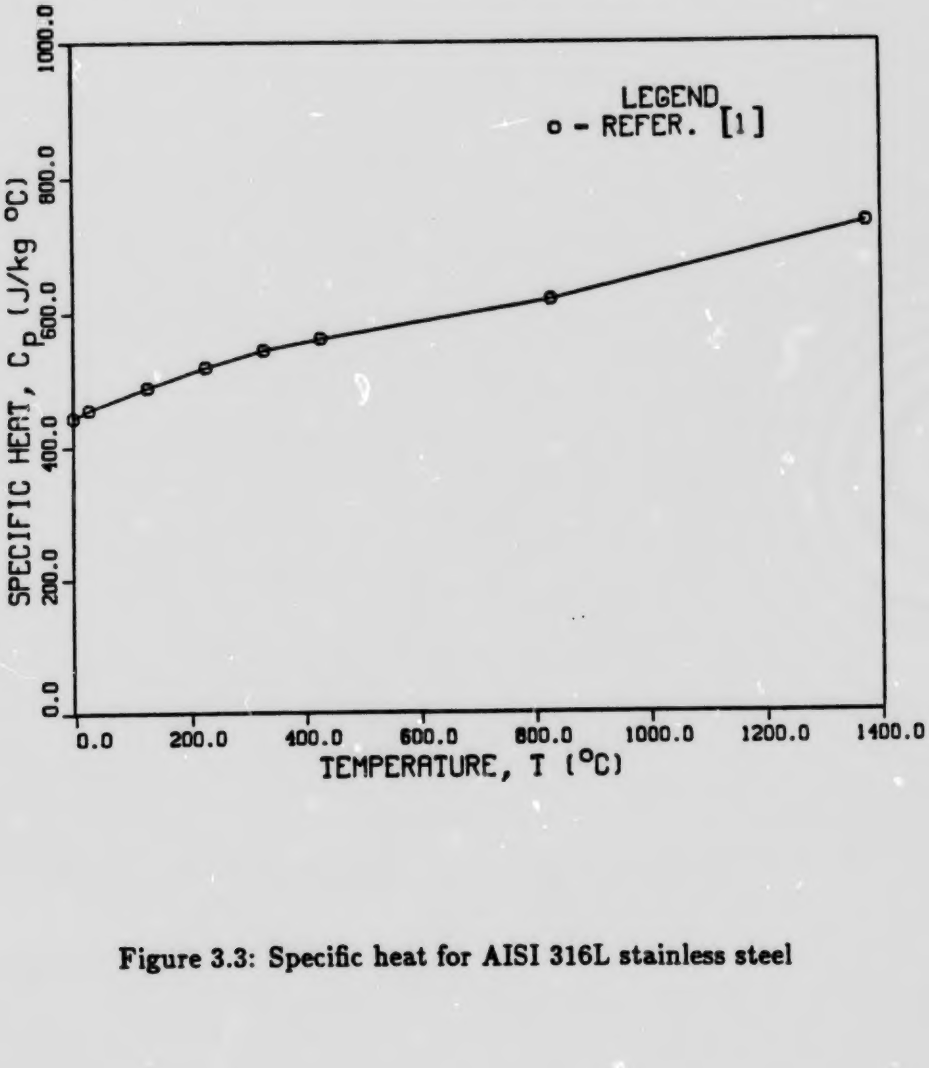

Figure 3.3: Specific heat for AISI 316L stainless steel

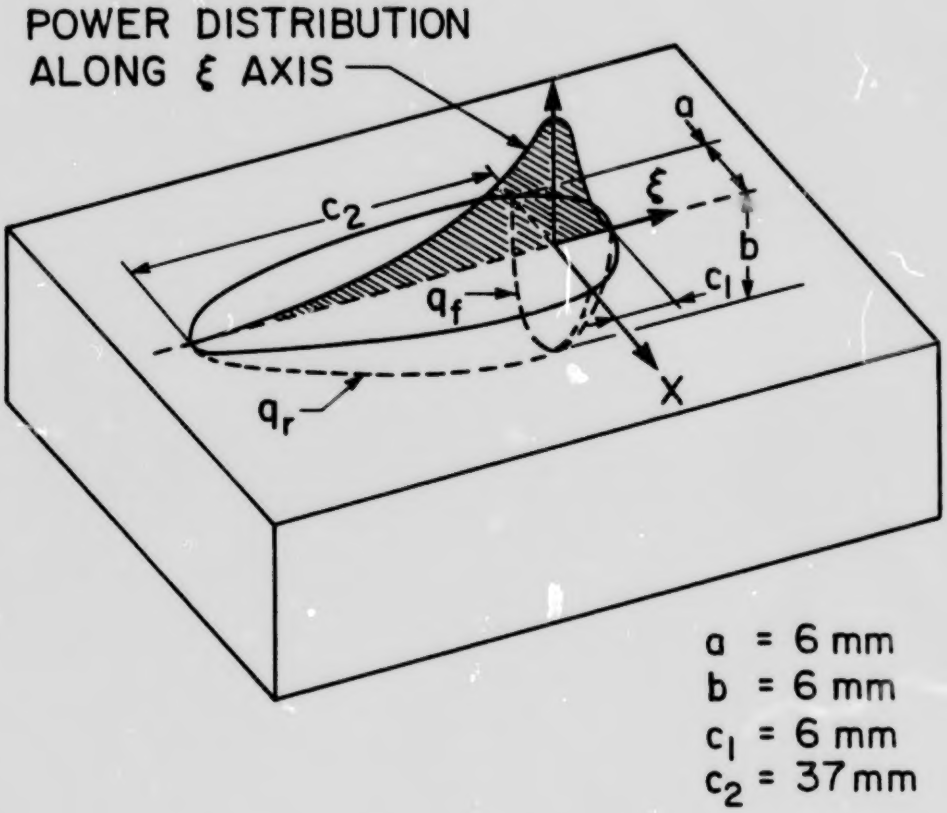
POWER DISTRIBUTION
ALONG ξ AXIS
a
ξ
b
c_2
c_1
q_f
q_r
X
a = 6 mm
b = 6 mm
c_1 = 6 mm
c_2 = 37 mm

Figure 3.4: Parameters for double ellipsoidal heat source model

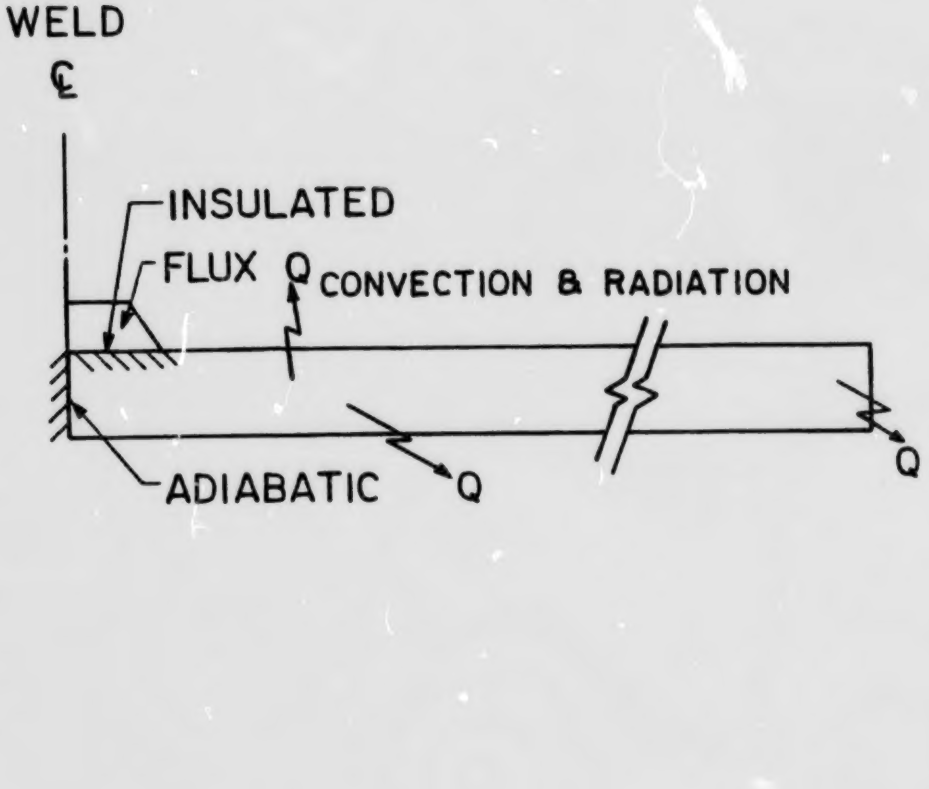
WELD
℄
INSULATED
FLUX
Q
CONVECTION & RADIATION
ADIABATIC
Q
Q

Figure 3.5: Thermal boundary conditions for submerged arc welding

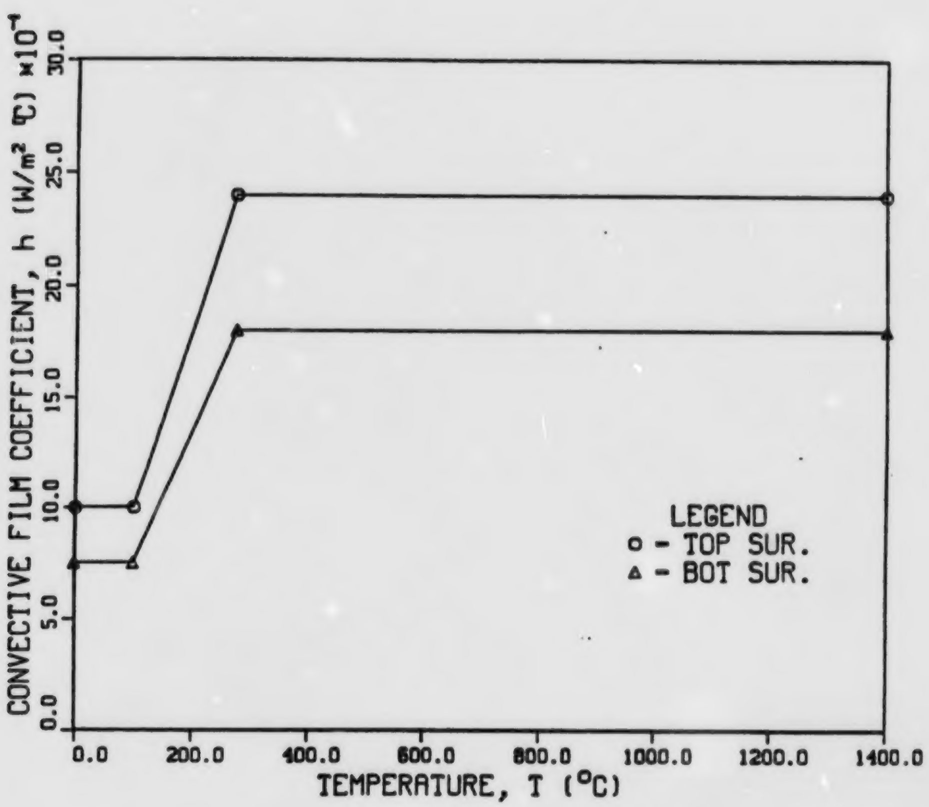

Figure 3.6: Convective heat transfer coefficient for welding model

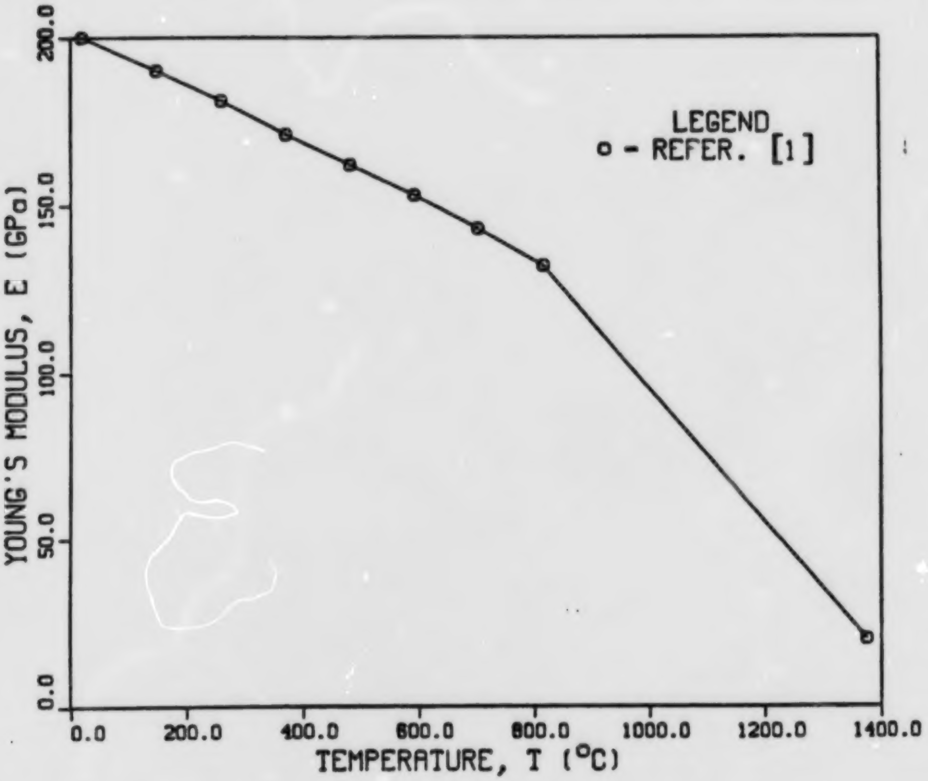

Figure 3.7: Young's modulus for AISI 316L stainless steel

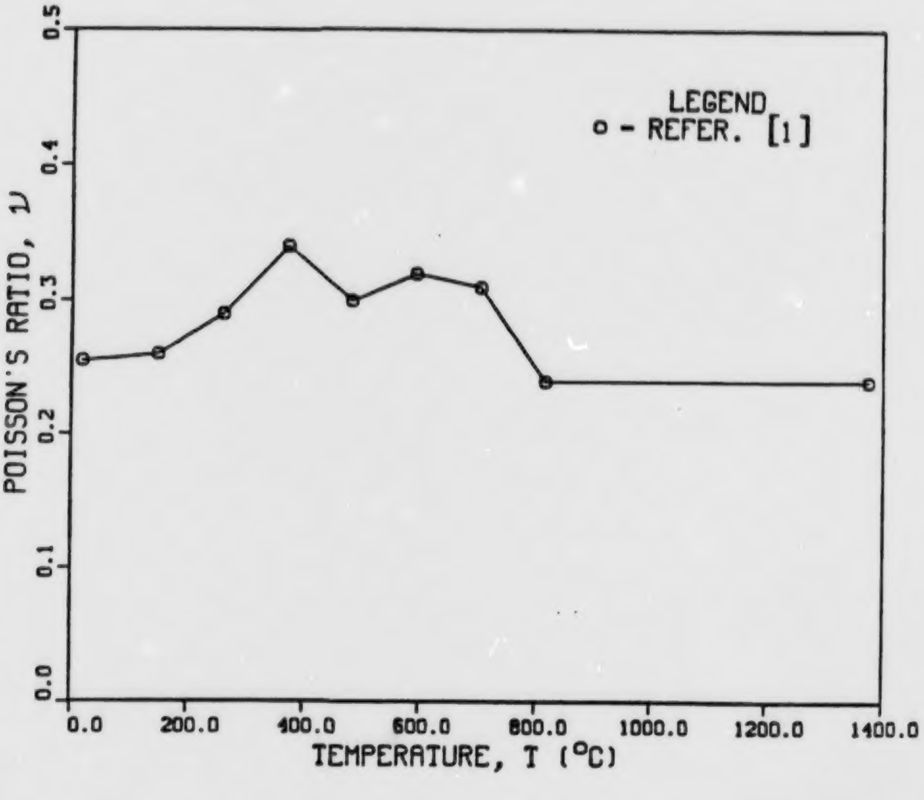

Figure 3.8: Poisson's ratio for AISI 316L stainless steel

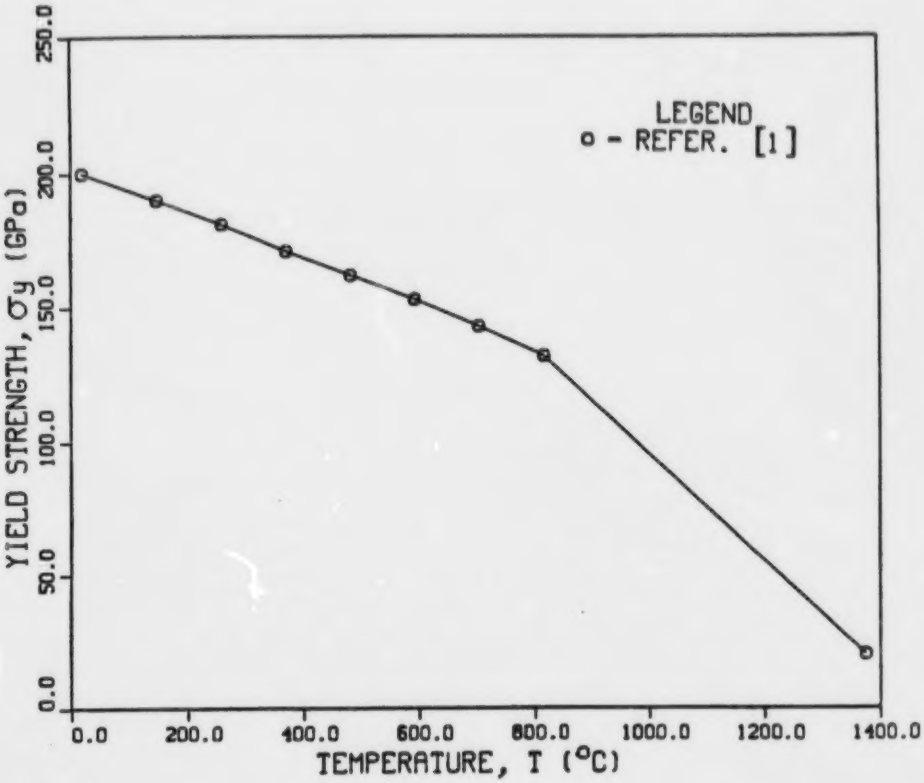

Figure 3.9: Yield strength for AISI 316L stainless steel

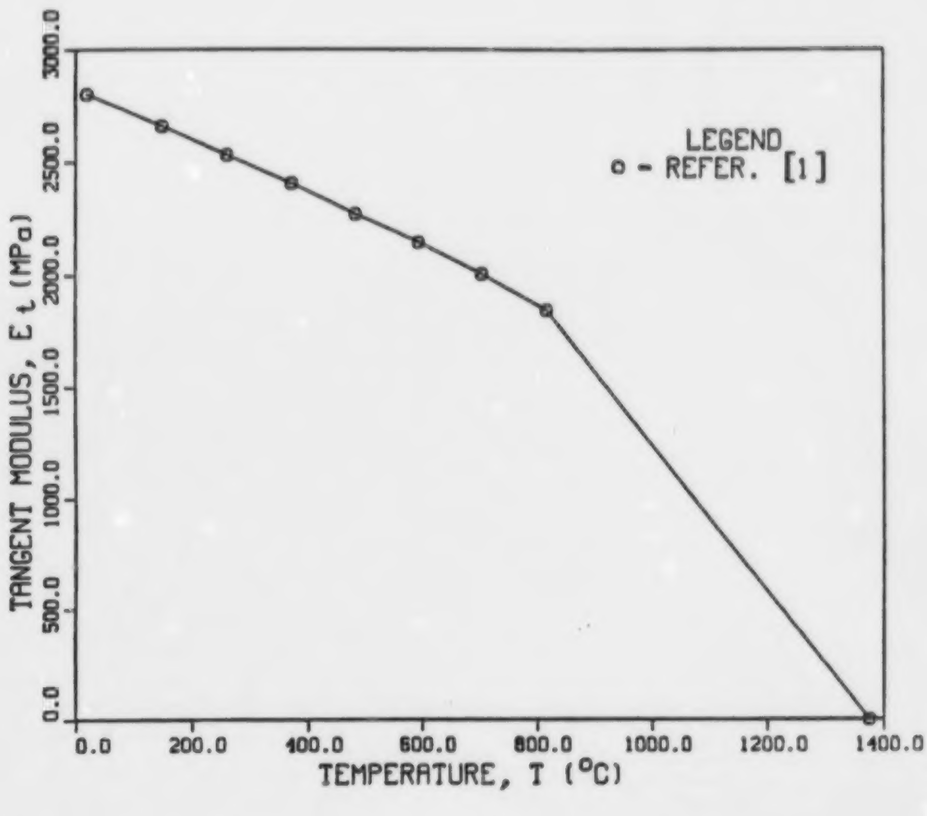

Figure 3.10: Tangent modulus for AISI 316L stainless steel

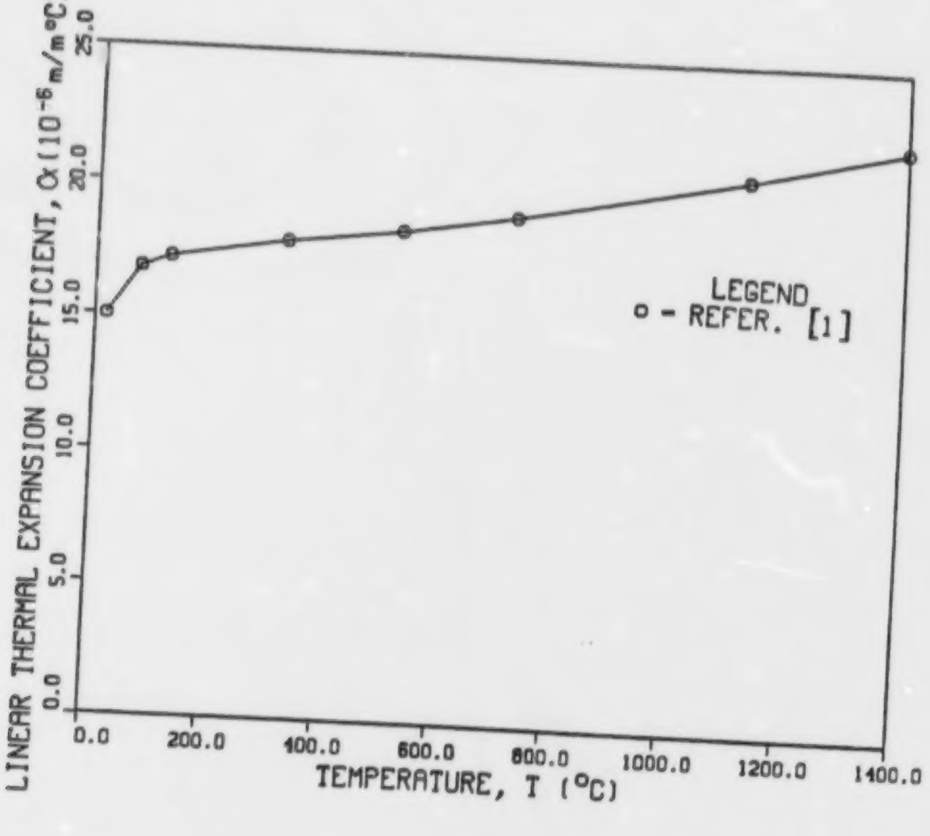

Figure 3.11: Linear thermal expansion coefficient for AISI 316L stainless steel

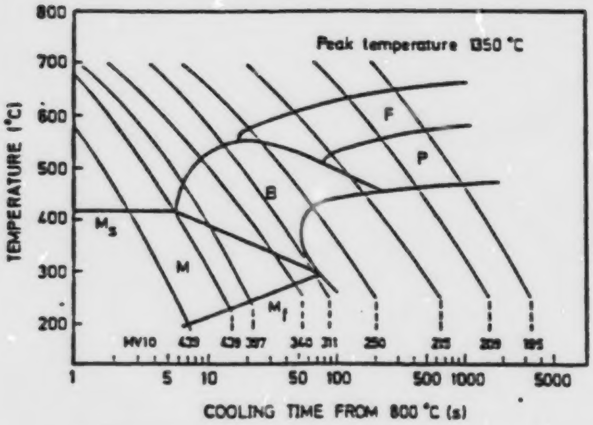

Continuous-cooling-transformation diagram

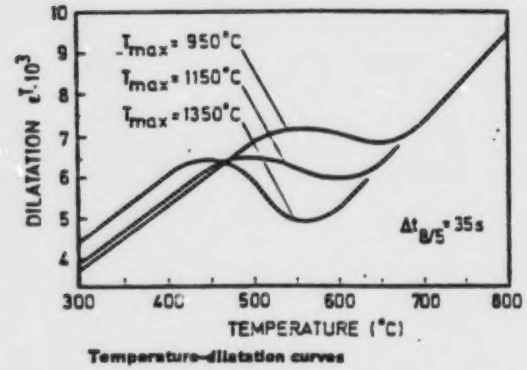

Temperature-dilatation curves

Figure 3.12: Temperature-dilatation curves [39]

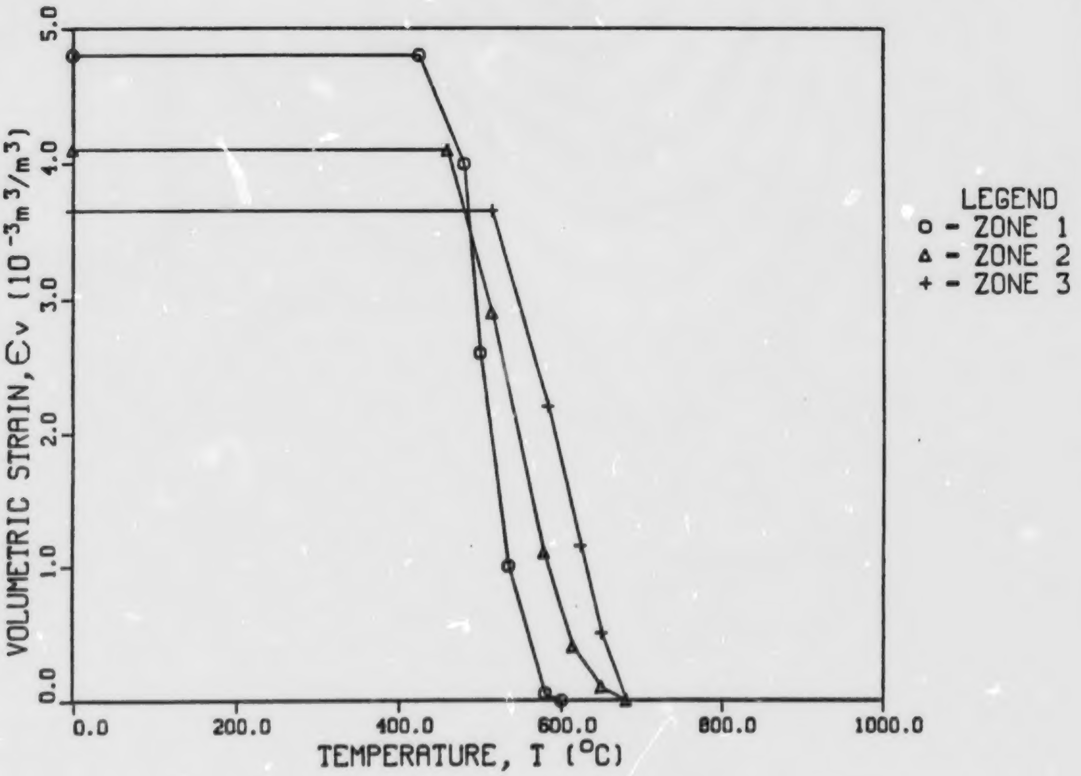

Figure 3.13: Phase transformation induced volumetric strain at T_s = 680°C (PHTRAN)

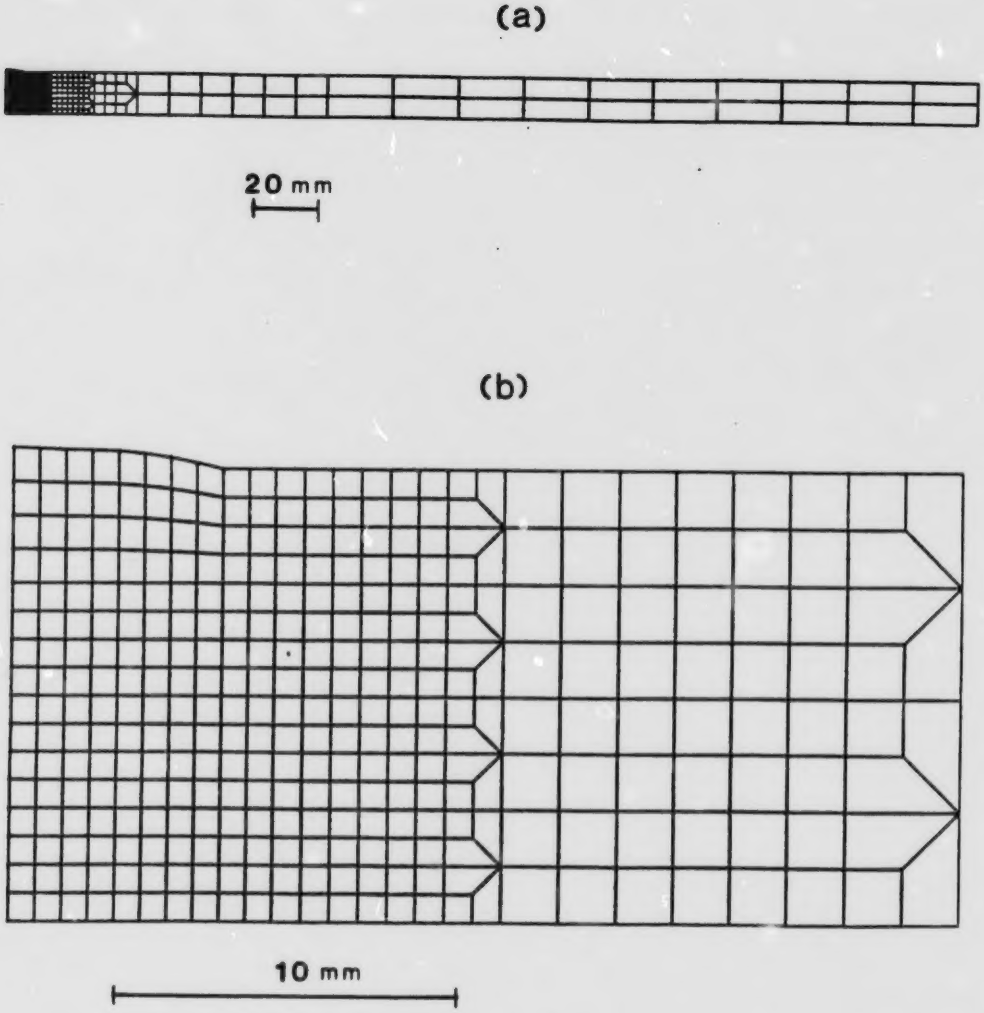
(a)
20 mm
(b)
10 mm

Figure 3.14: Finite element mesh of a) welded plate; b) weld region for heat transfer analysis

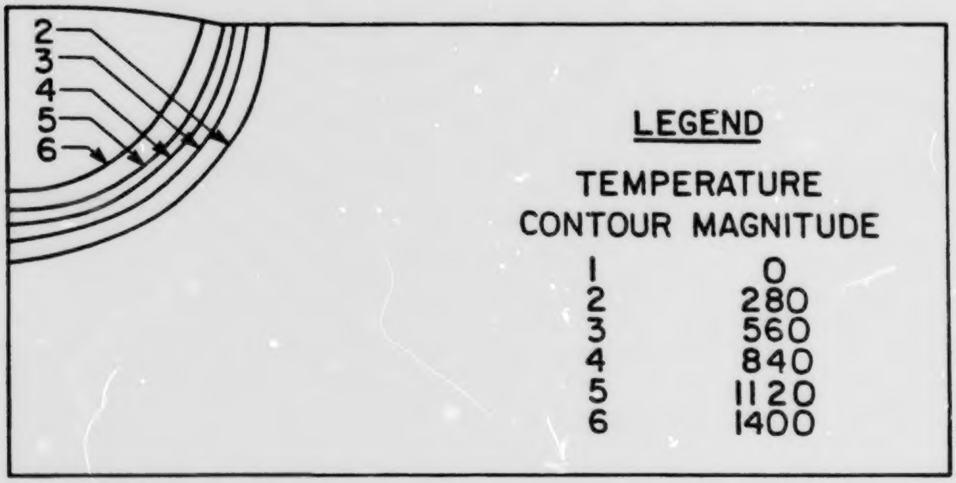
2
3
4
5
6
LEGEND
TEMPERATURE
CONTOUR MAGNITUDE
1 0
2 280
3 560
4 840
5 1120
6 1400

Figure 3.15: Temperature contours around weld pool

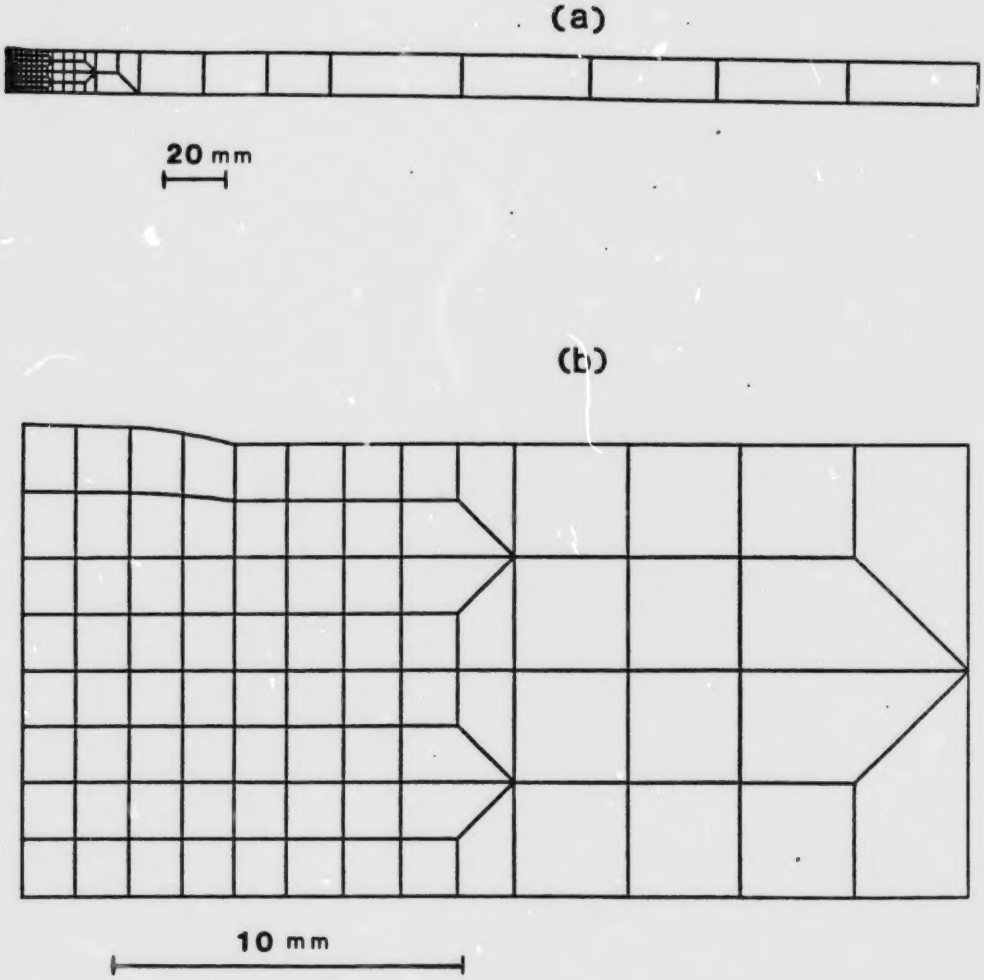
(a)
20 mm
(b)
10 mm

Figure 3.16: Finite element mesh of a) welded plate; b) weld region for stress analysis

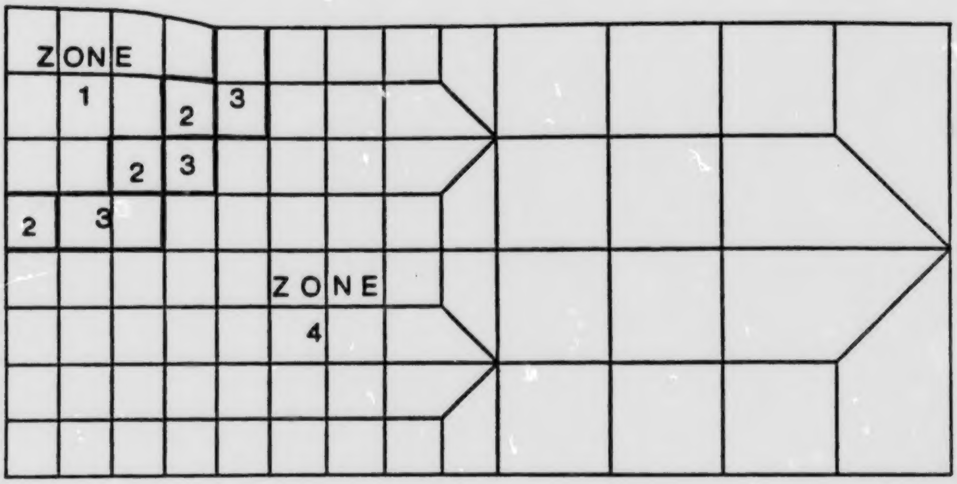
ZONE
1
2
3
2
3
2
3
ZONE
4

Figure 3.17: Classification of transformation zone

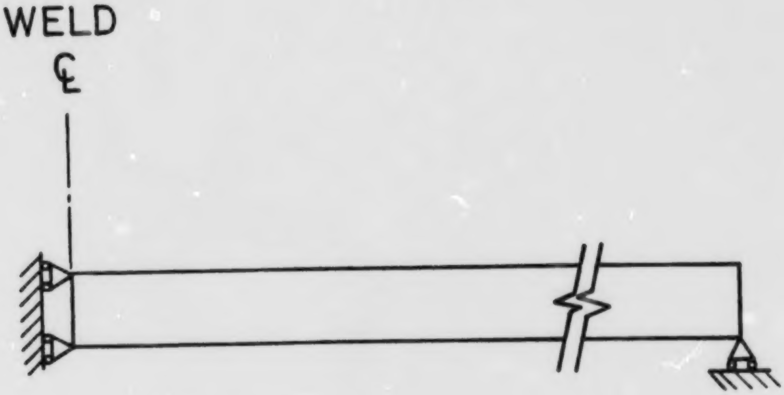

Figure 3.18: In-plane kinematic constraint for simply supported plate assumption

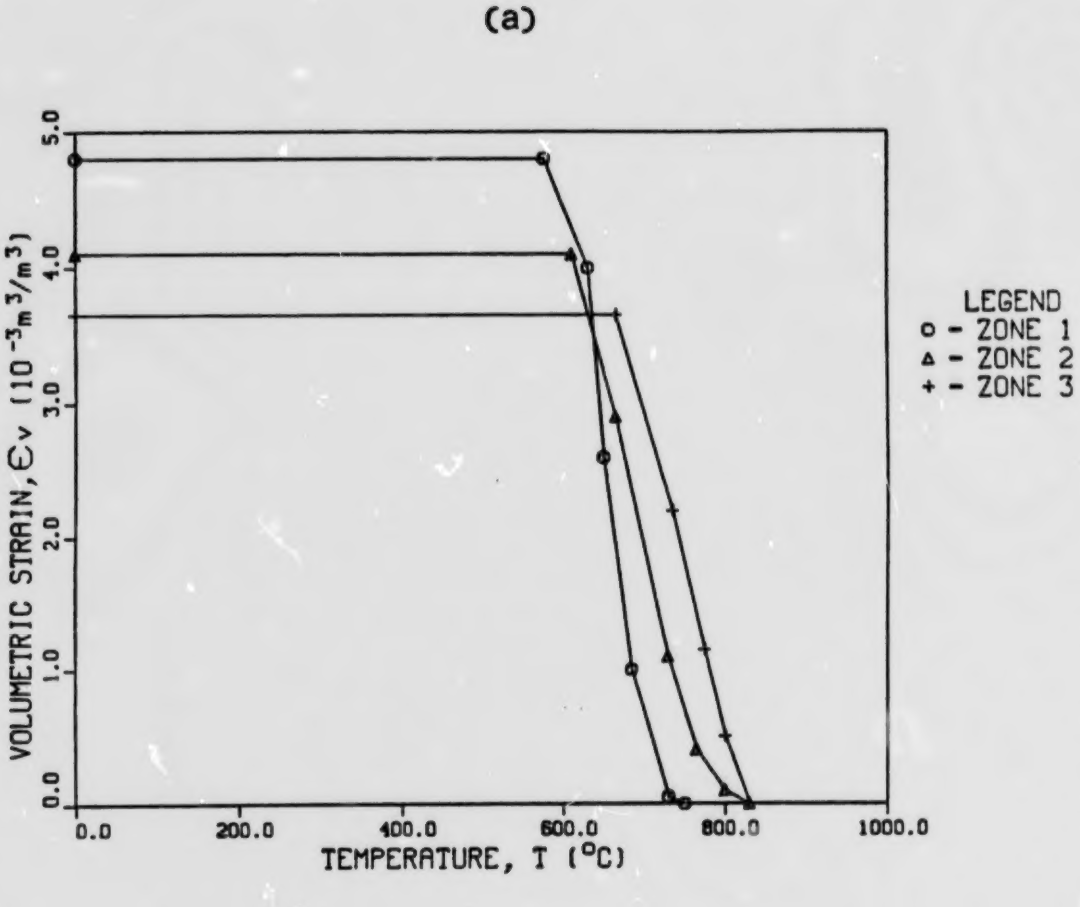

Figure 3.19: Phase transformation induced volumetric strain a) at T_s = 830°C (HITEM); b) AT T_s = 480°C (LOTEM); c) high strain magnitude at T_s = 680°C (HIVOL)

(b)

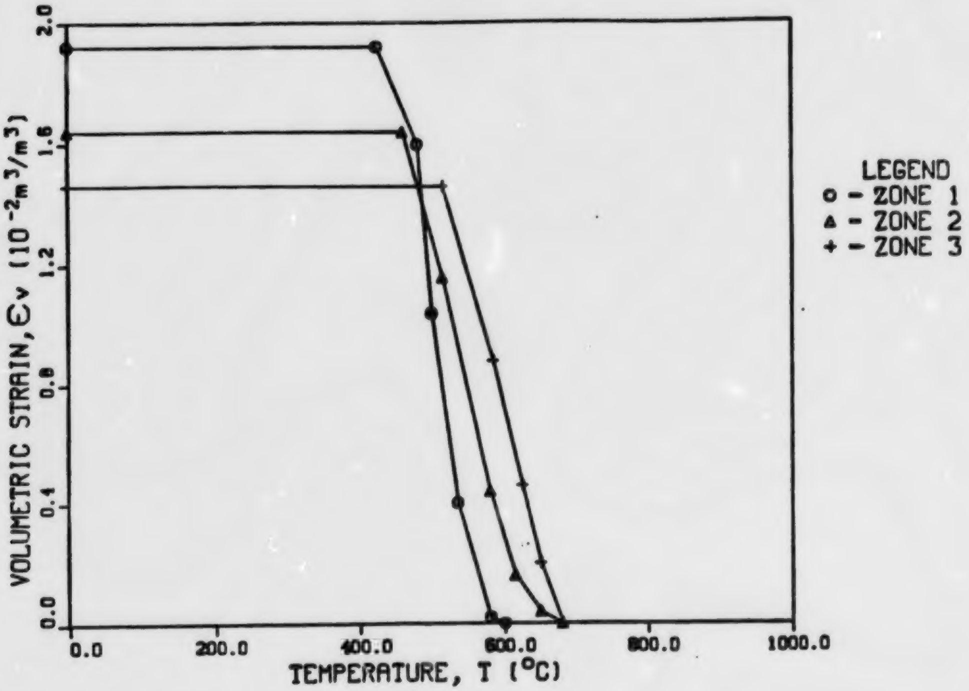
2.0
1.6
1.2
0.8
0.4
0.0
VOLUMETRIC STRAIN, Ɛv (10^{-2}m^3/m^3)
0.0
200.0
400.0
600.0
800.0
1000.0
TEMPERATURE, T (°C)
LEGEND
o - ZONE 1
▲ - ZONE 2
+ - ZONE 3

(c)

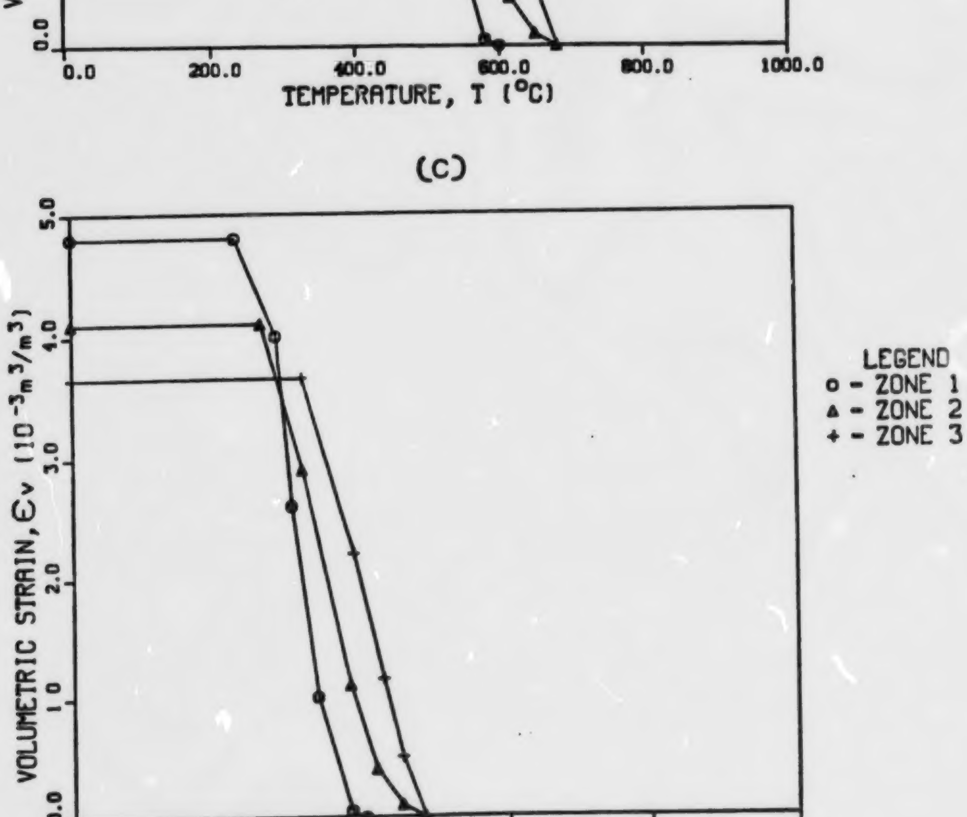
5.0
4.0
3.0
2.0
1.0
0.0
VOLUMETRIC STRAIN, Ɛv (10^{-3}m^3/m^3)
0.0
200.0
400.0
600.0
800.0
1000.0
TEMPERATURE, T (°C)
LEGEND
o - ZONE 1
▲ - ZONE 2
+ - ZONE 3

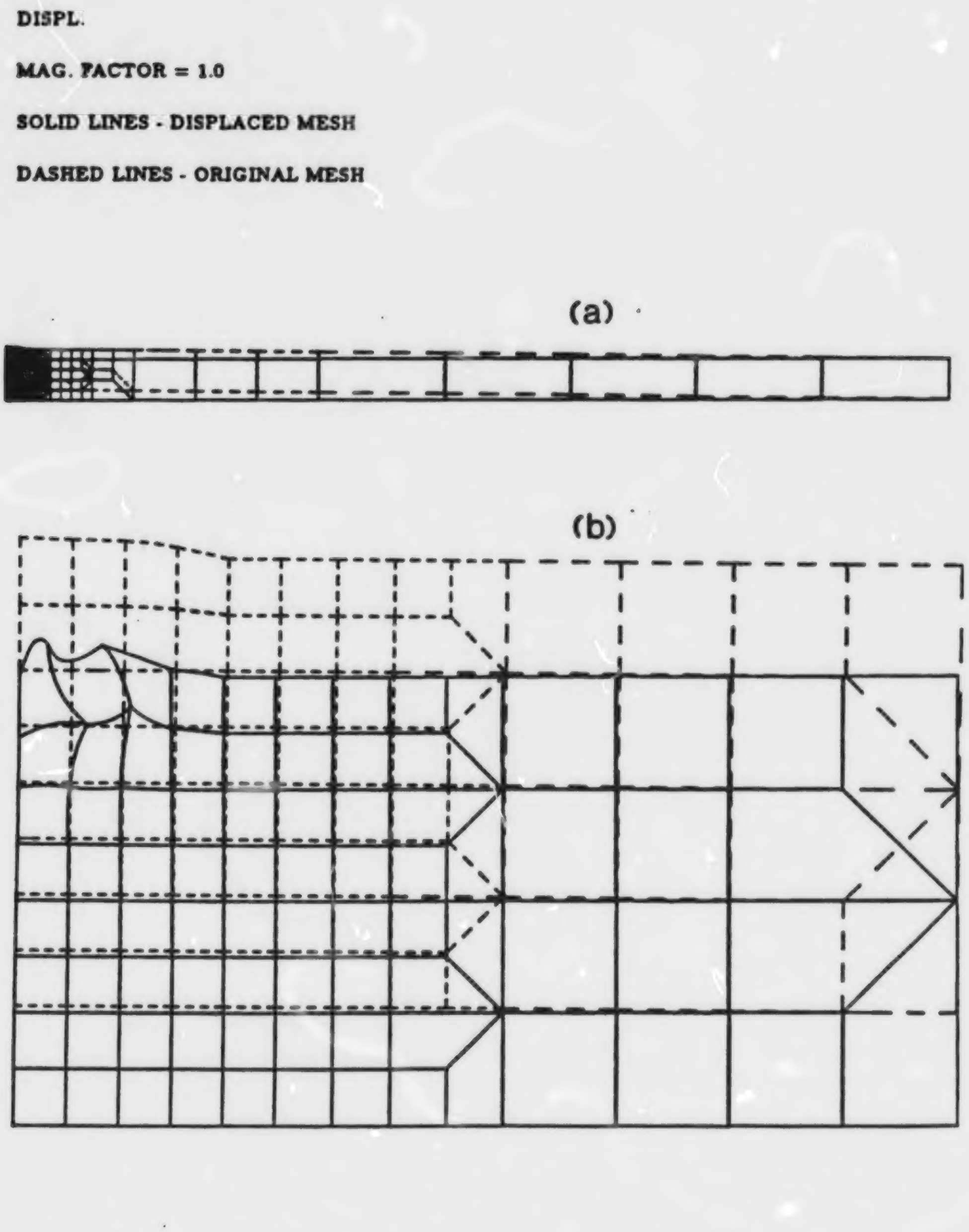
DISPL.
MAG. FACTOR = 1.0
SOLID LINES - DISPLACED MESH
DASHED LINES - ORIGINAL MESH
(a)
(b)

Figure 3.20: a) Displaced plate geometry; b) displaced mesh near weld region (NOPHASE)

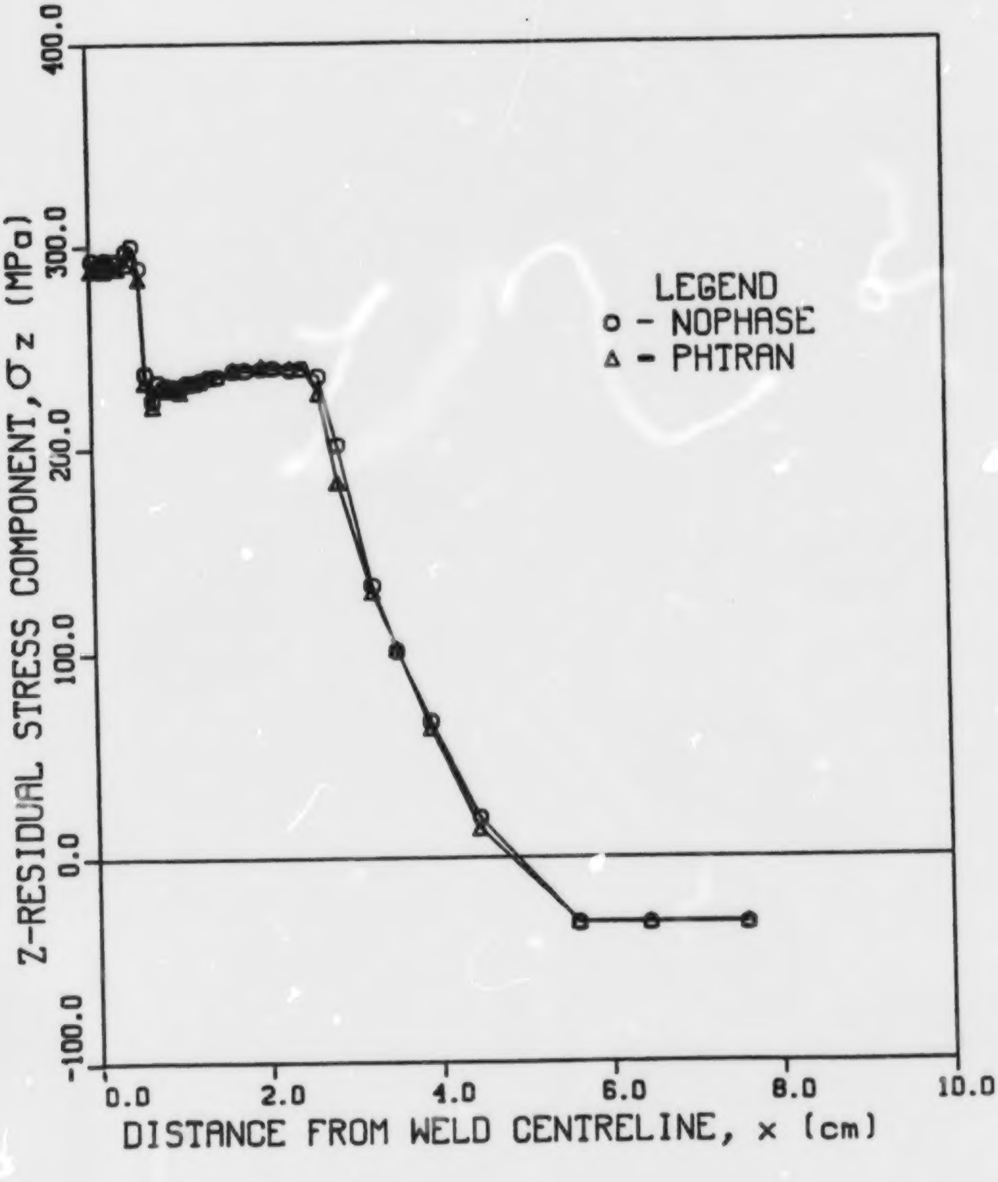

Figure 3.21: Longitudinal residual stress distribution along the top surface (NOPHASE vs. PHTRAN)

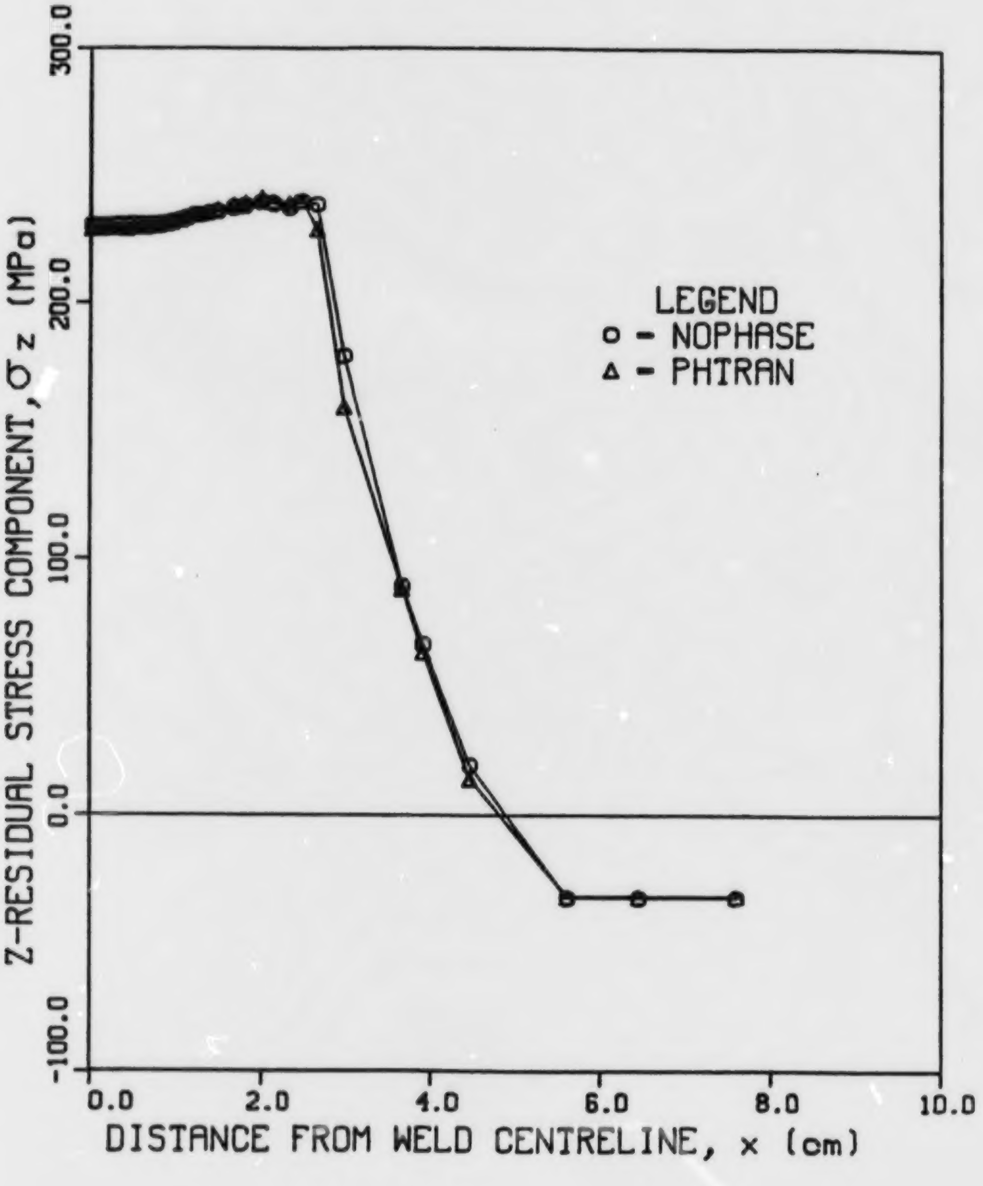

Figure 3.22: Longitudinal residual stress distribution along the bottom surface (NOPHASE vs. PHTRAN)

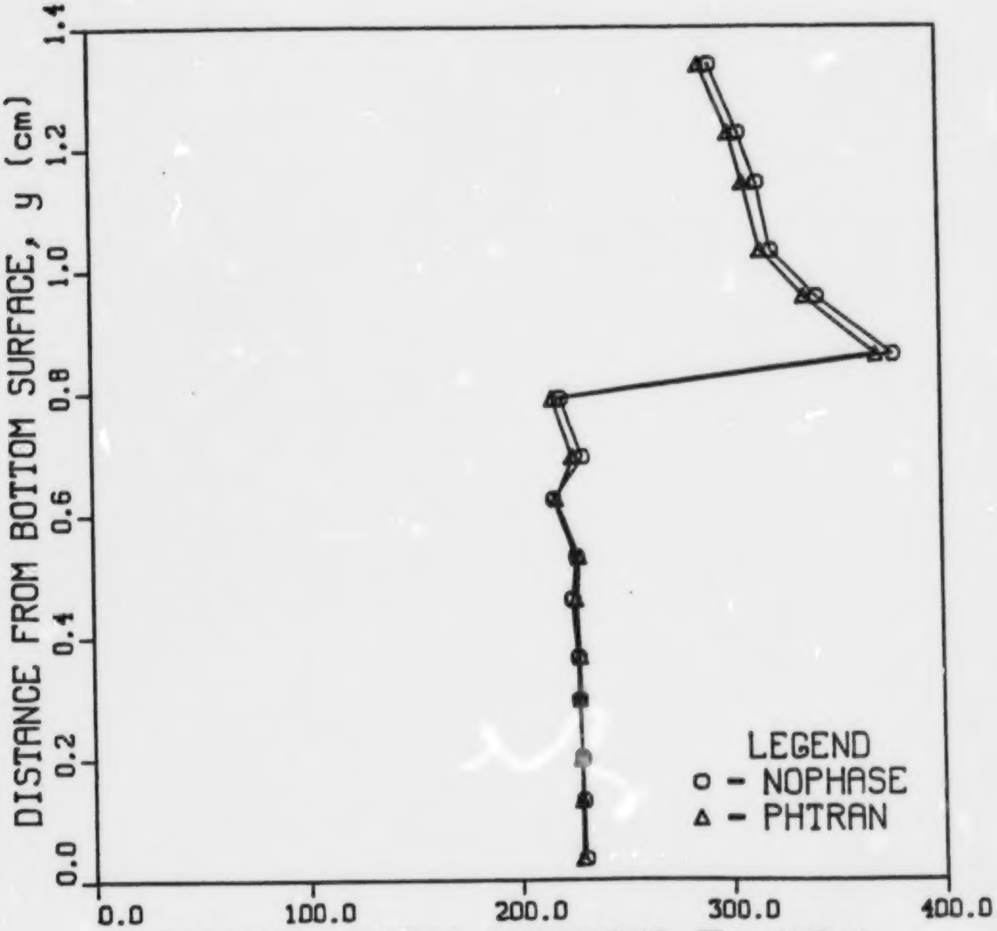

Figure 3.23: Longitudinal residual stress distribution along the weld centerline (NOPHASE vs. PHTRAN)

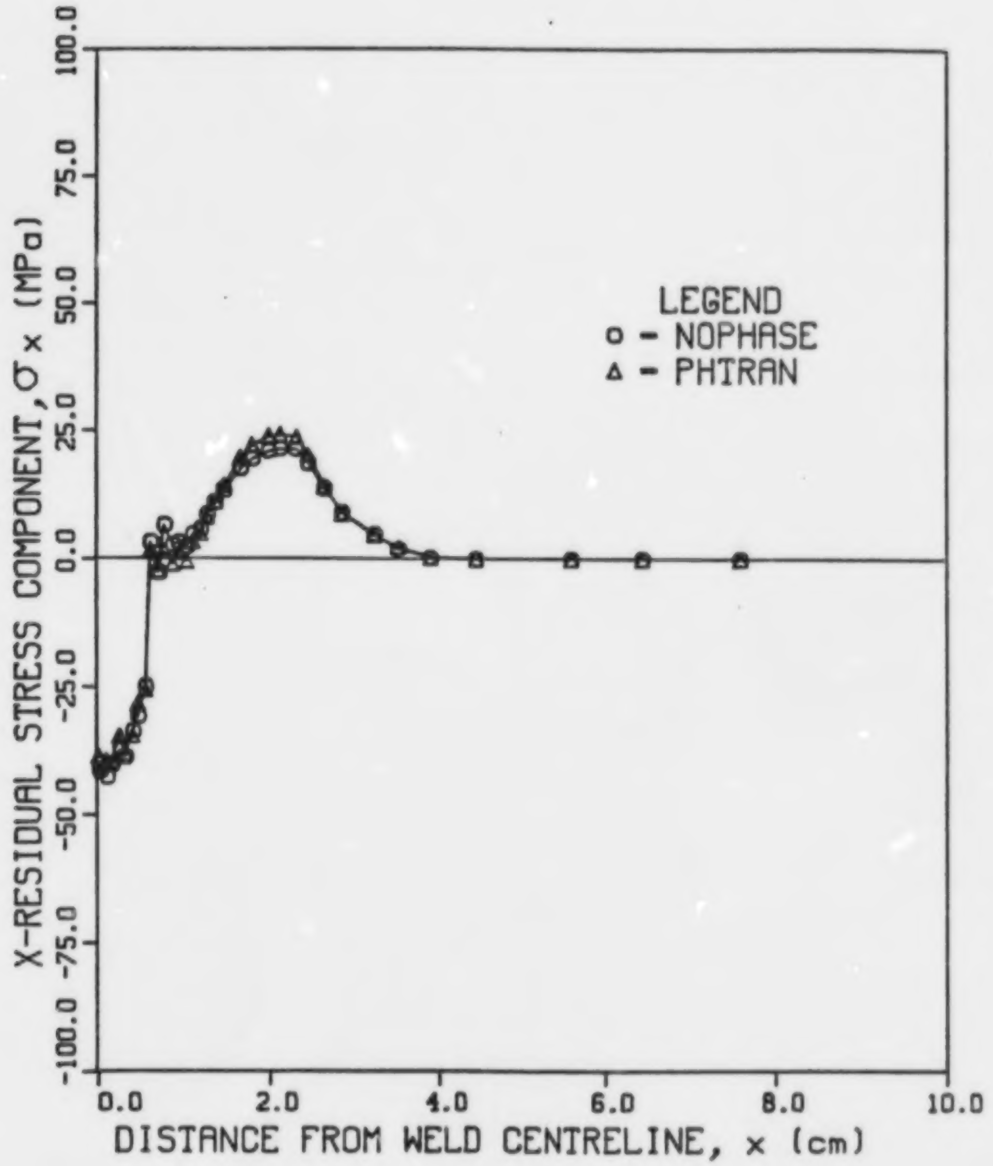

Figure 3.24: Transverse residual stress distribution along the top surface (NOPHASE vs. PHTRAN)

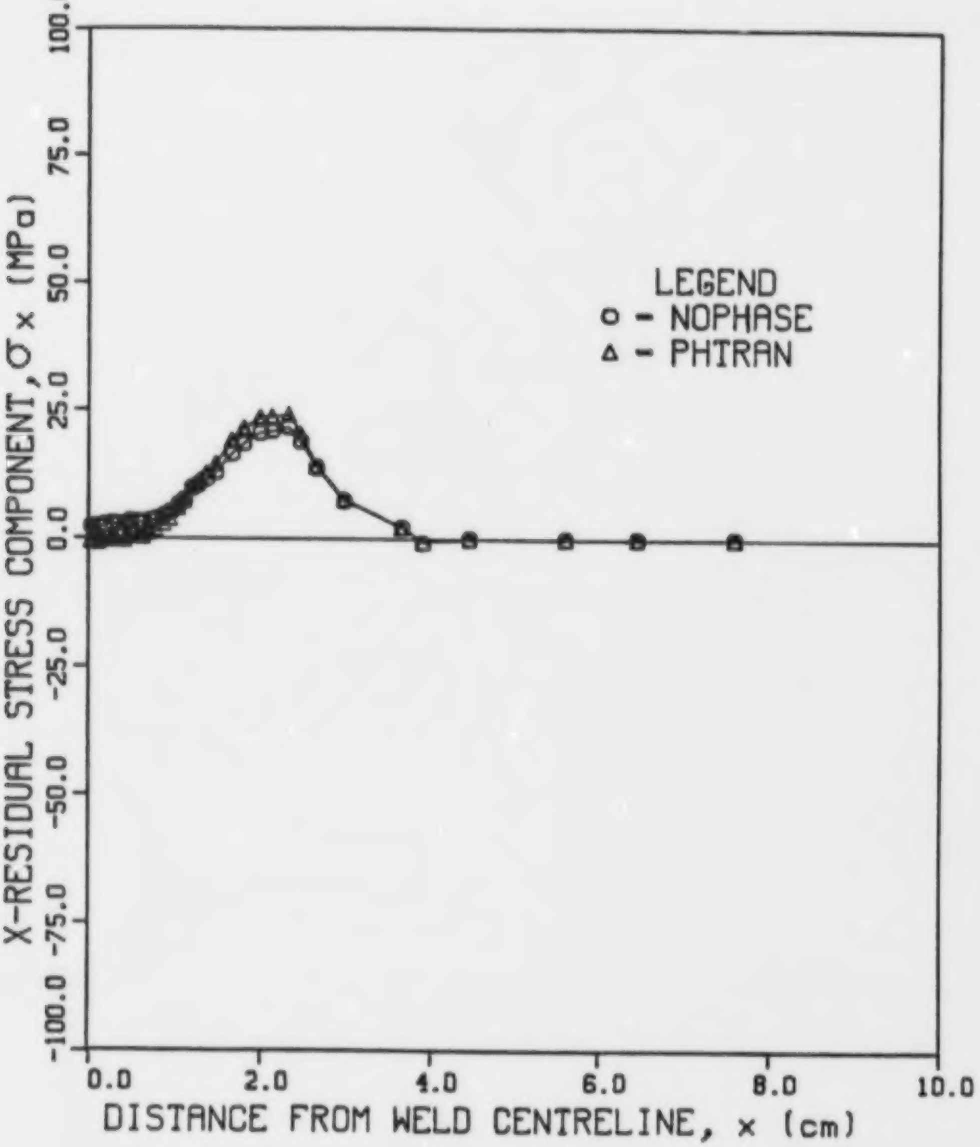

Figure 3.25: Transverse residual stress distribution along the bottom surface (NOPHASE vs. PHTRAN)

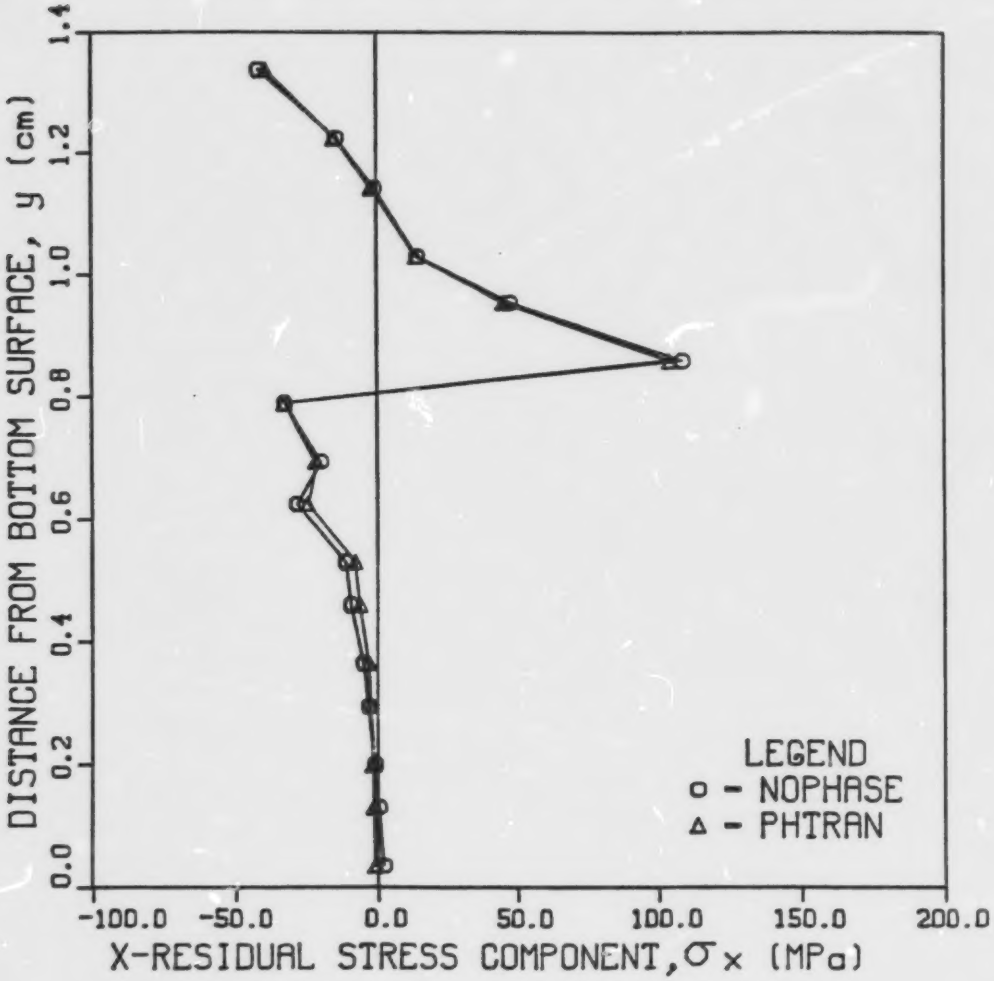

Figure 3.26: Transverse residual stress distribution along the weld centerline (NOPHASE vs. PHTRAN)

DISPL.

MAG. FACTOR = 1.0

SOLID LINES - DISPLACED MESH

DASHED LINES - ORIGINAL MESH

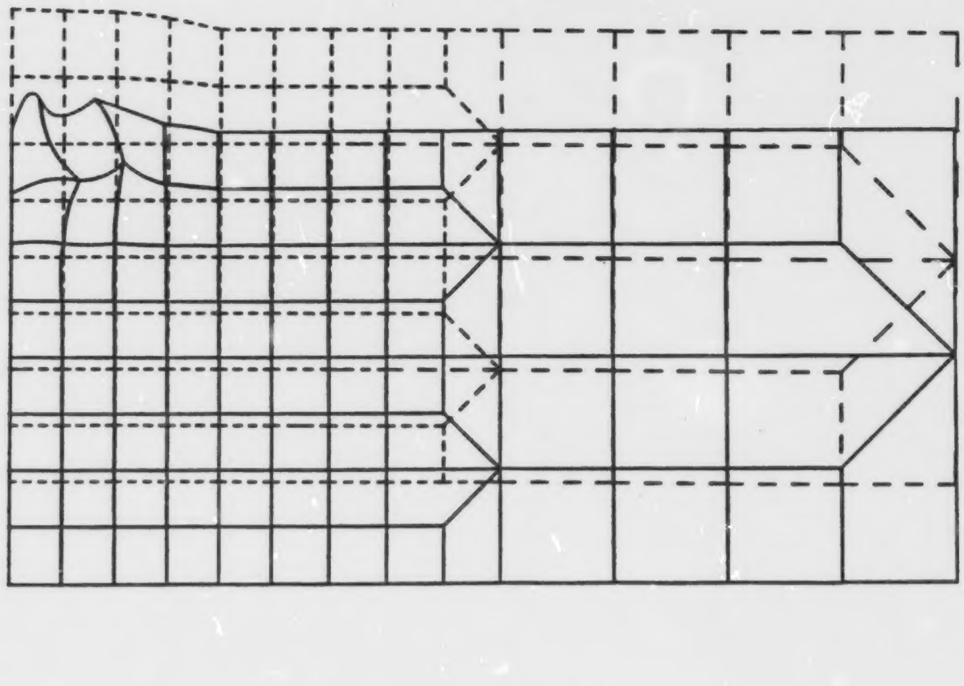

Figure 3.27: Displaced mesh near weld region (PHTRAN)

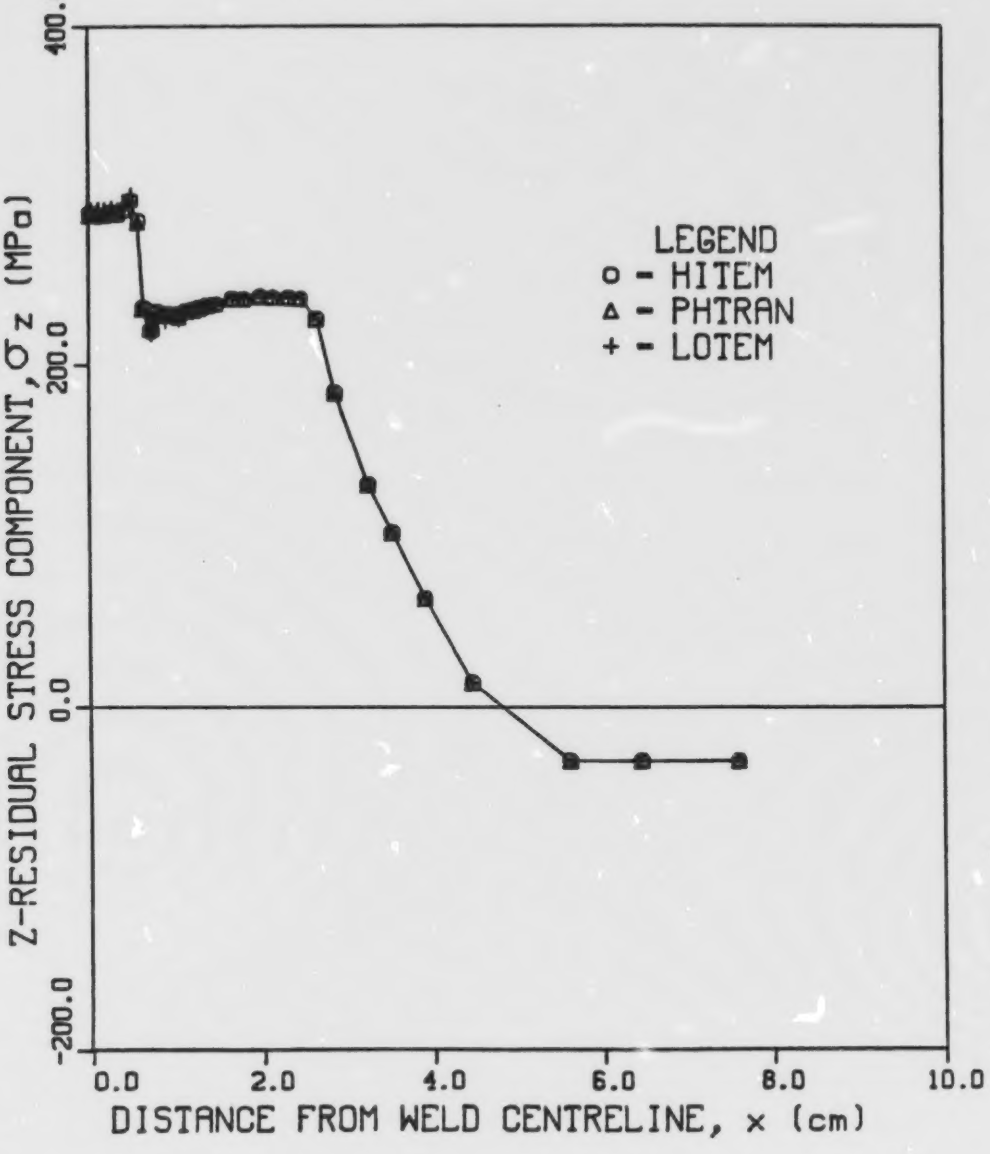

Figure 3.28: Longitudinal residual stress distribution along the top surface - different transformation temperatures

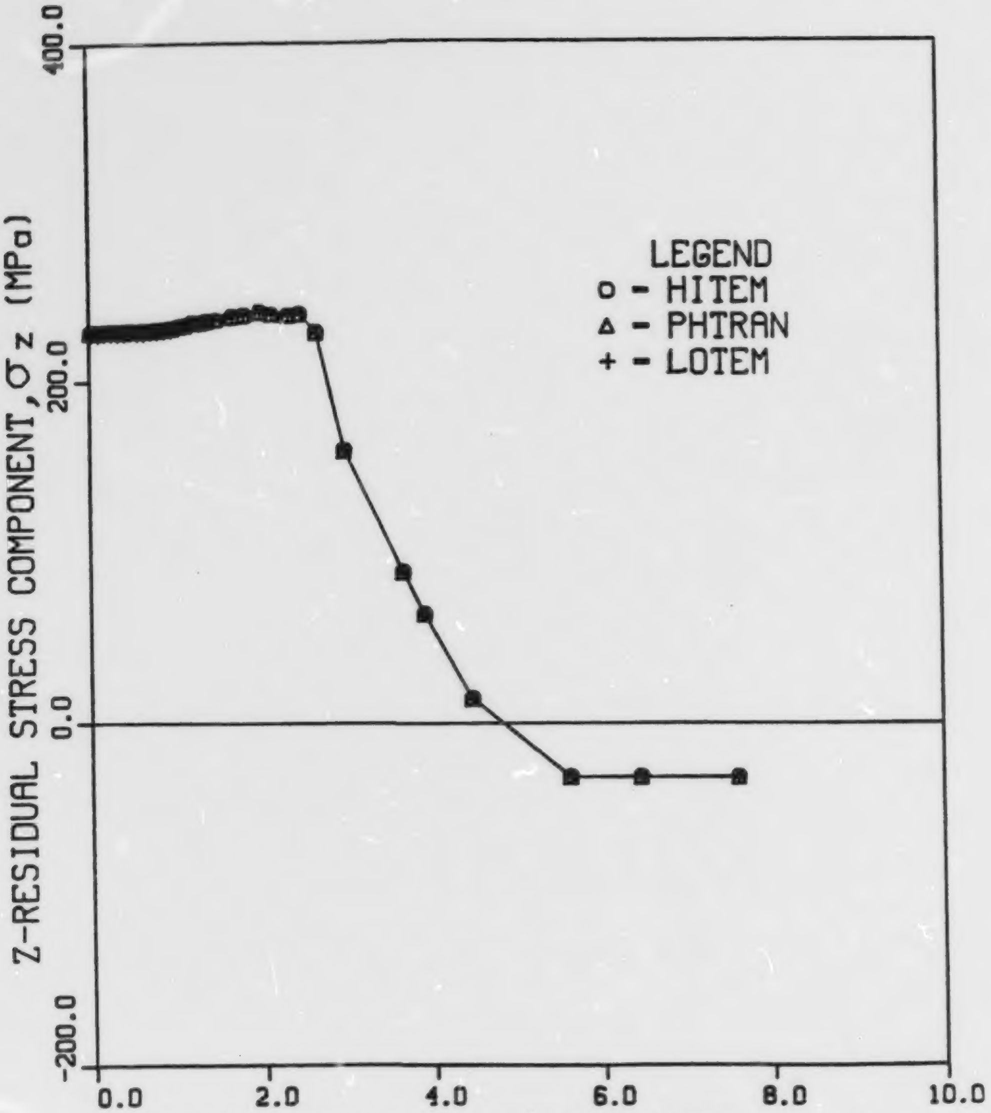

Figure 3.29: Longitudinal residual stress distribution along the bottom surface - different transformation temperatures

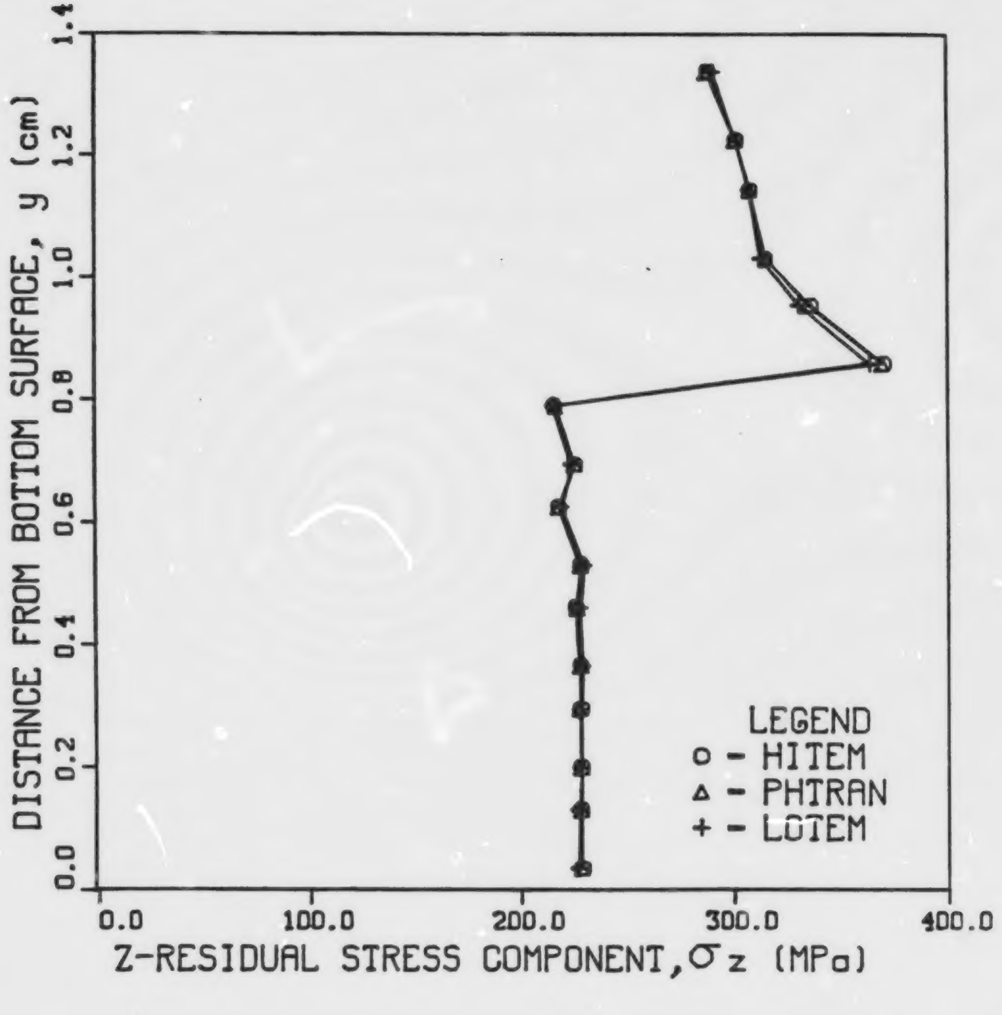

Figure 3.30: Longitudinal residual stress distribution along the weld centerline - different transformation temperatures

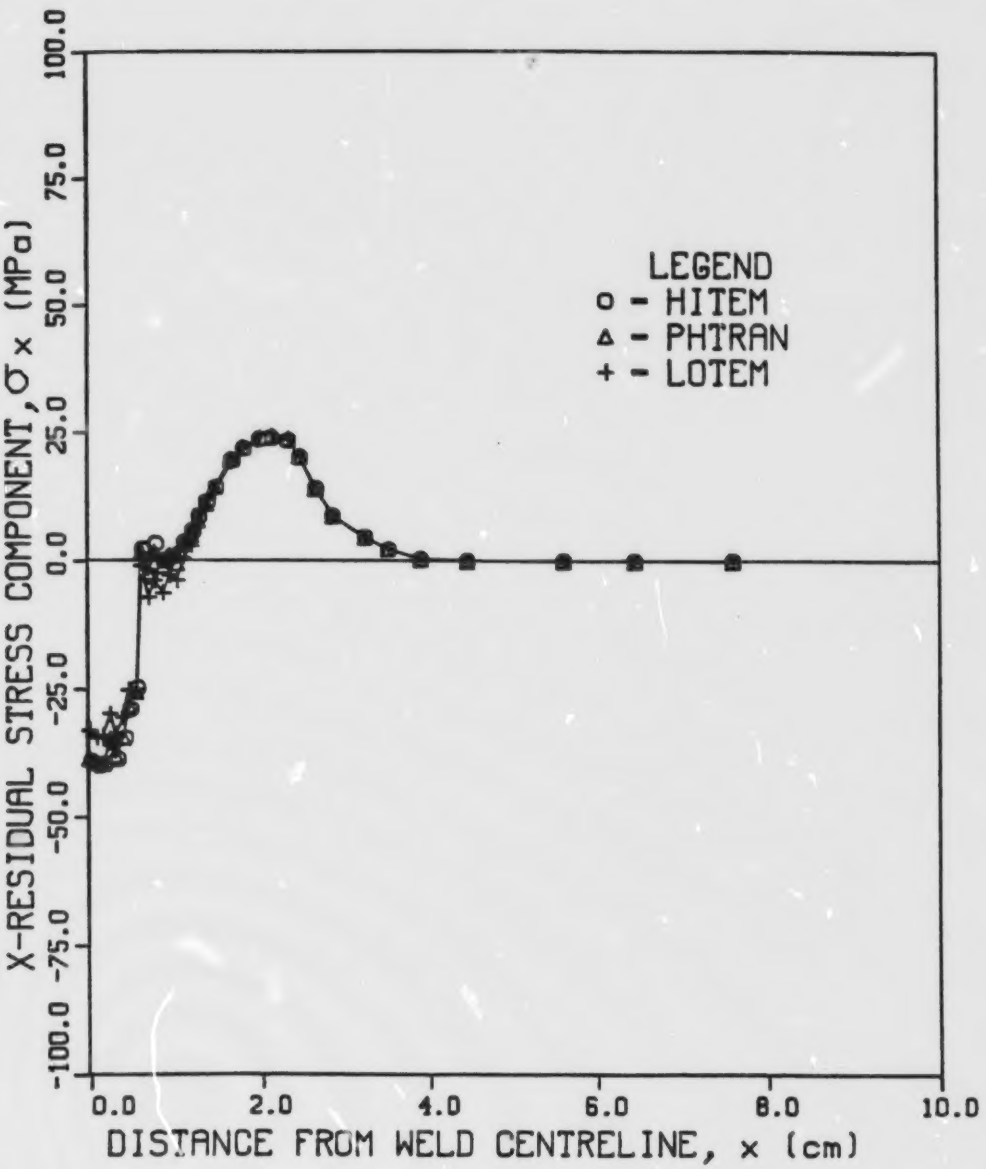

Figure 3.31: Transverse residual stress distribution along the top surface - different transformation temperatures

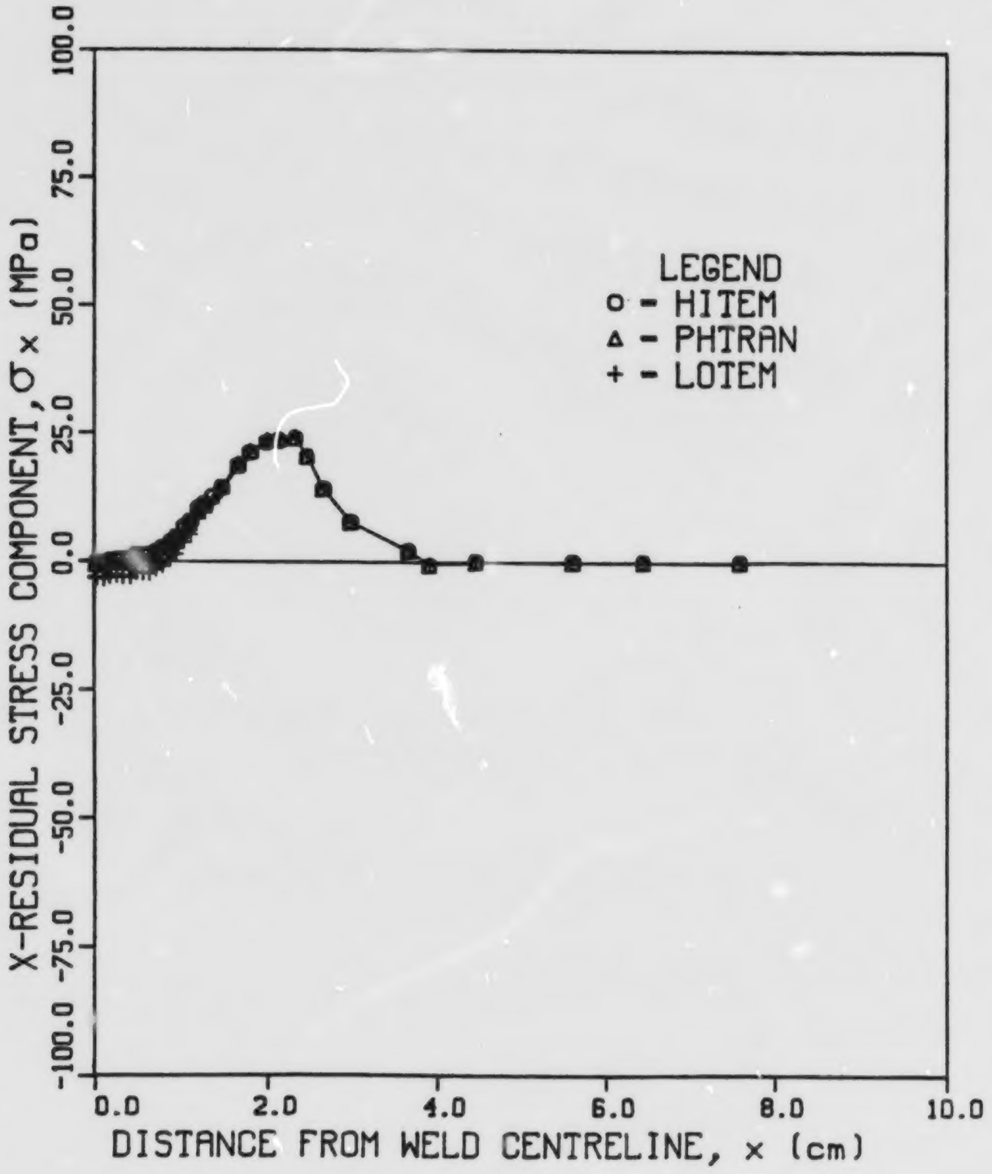

Figure 3.32: Transverse residual stress distribution along the bottom surface - different transformation temperatures

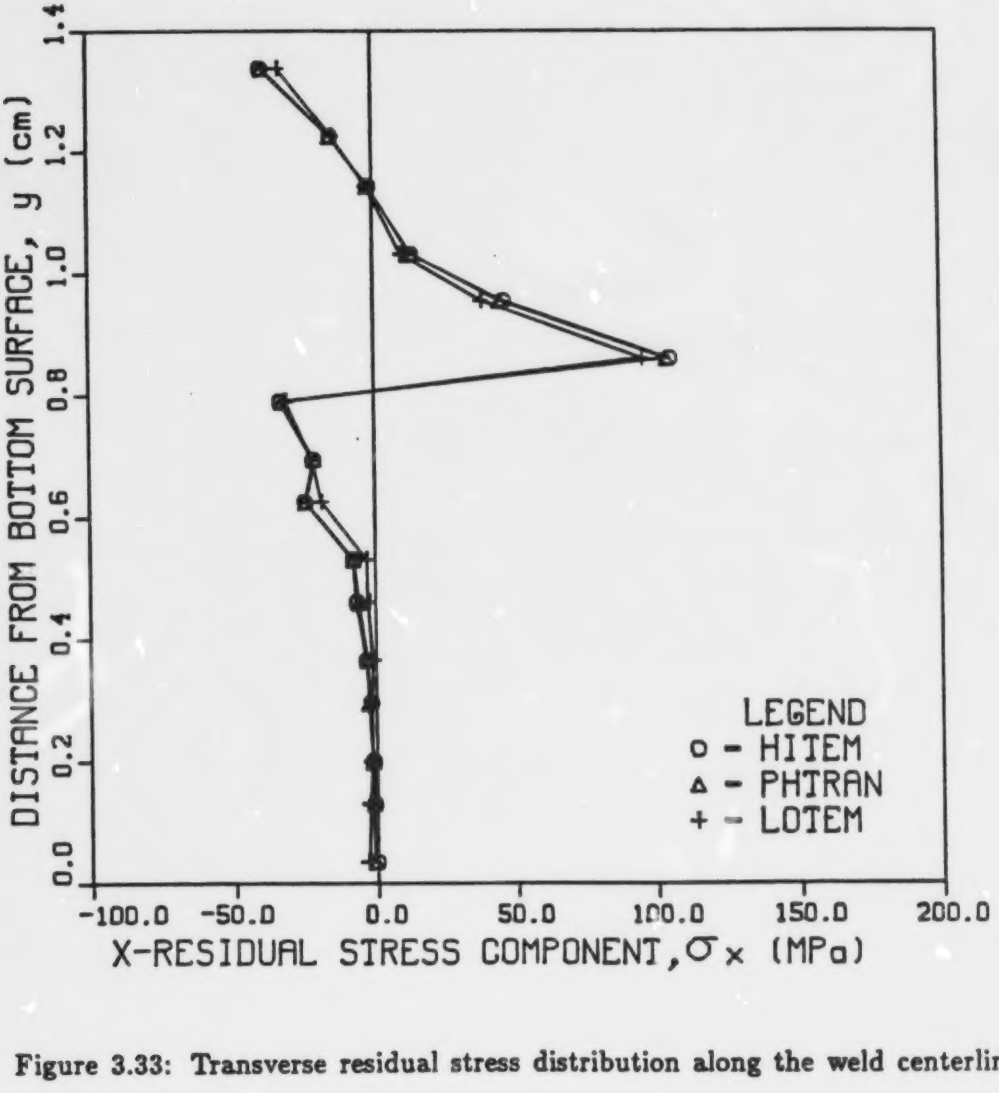

Figure 3.33: Transverse residual stress distribution along the weld centerline - different transformation temperatures

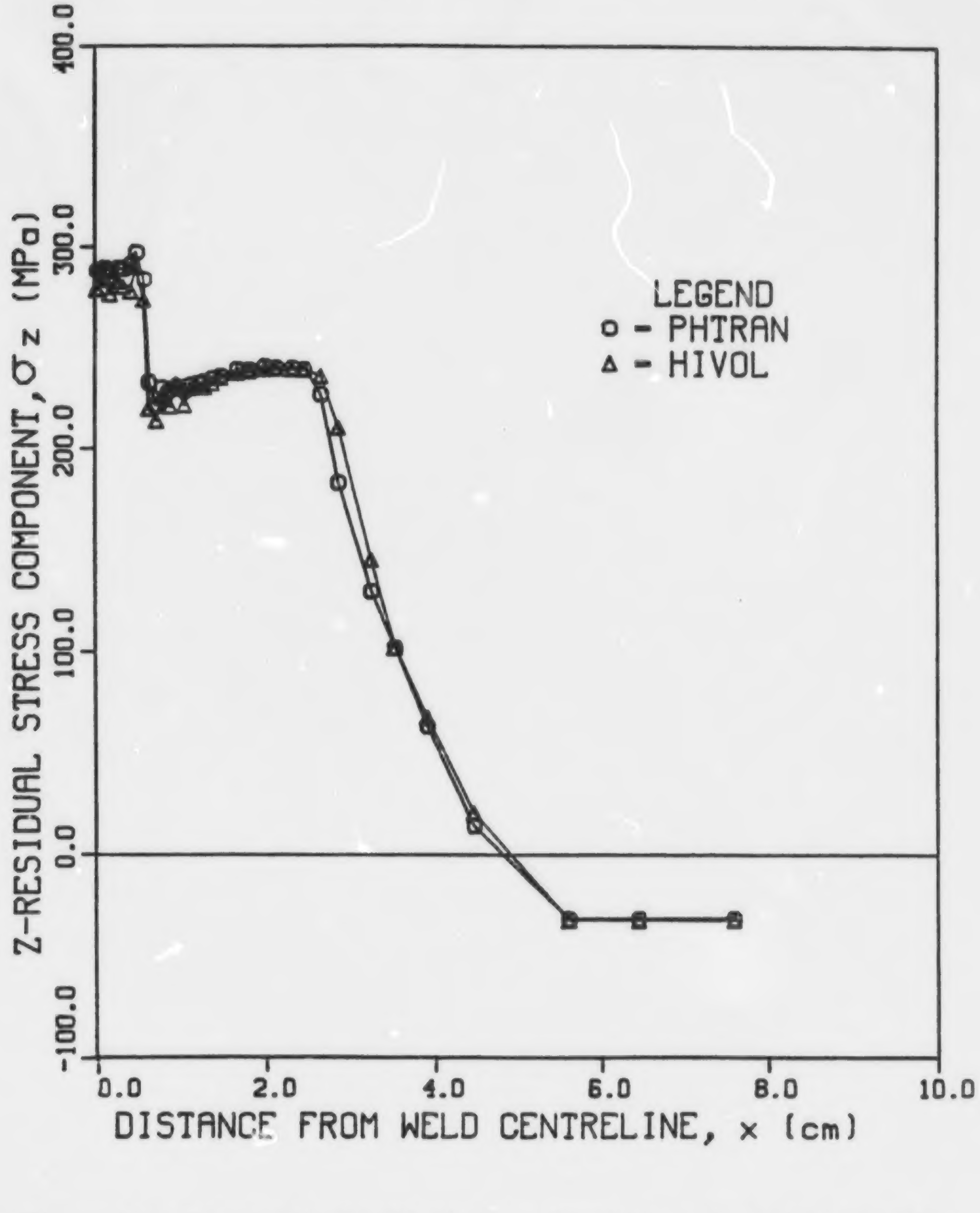

Figure 3.34: Longitudinal residual stress distribution along the top surface - different volumetric strains

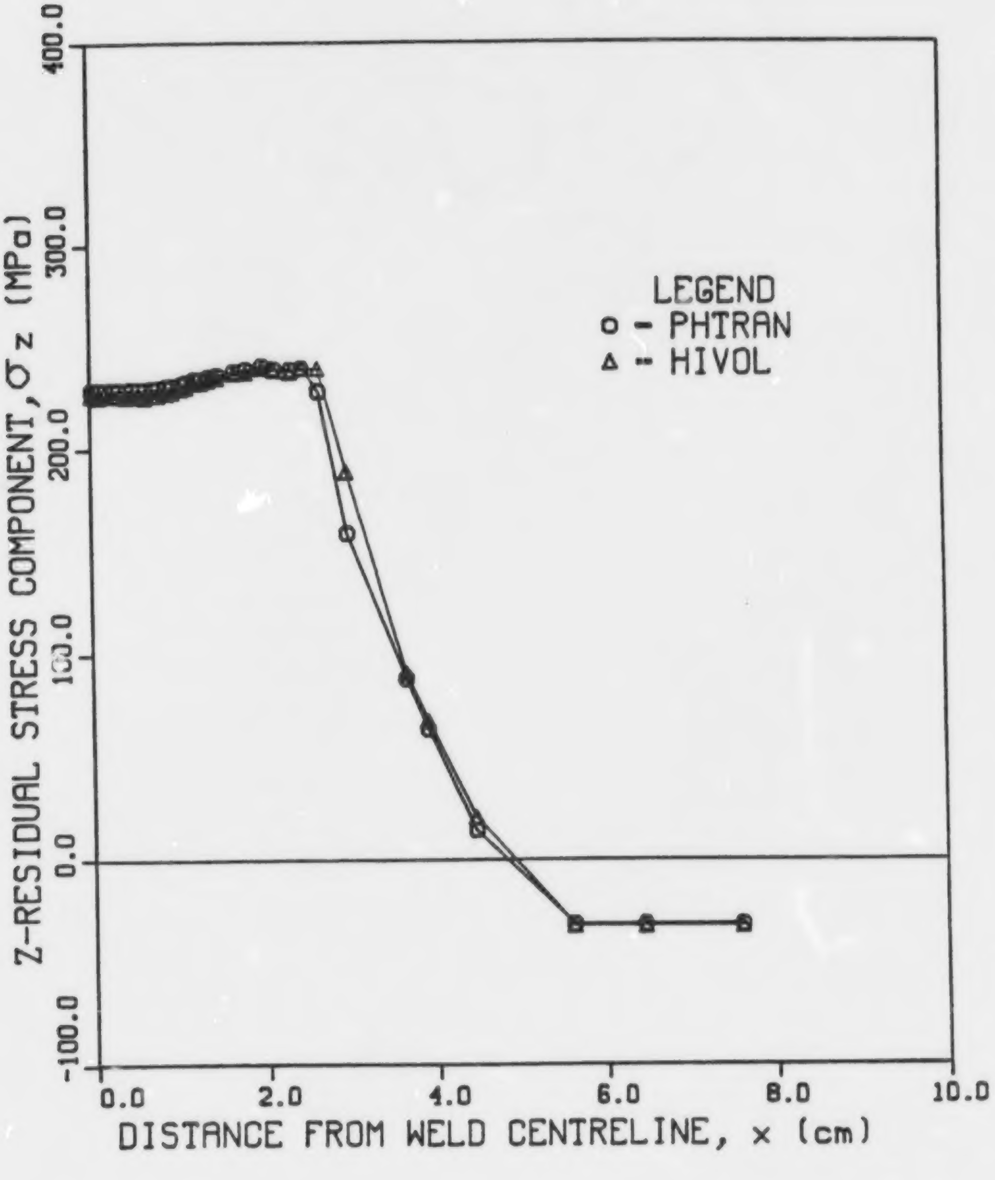

Figure 3.35: Longitudinal residual stress distribution along the bottom surface - different voluemtric strains

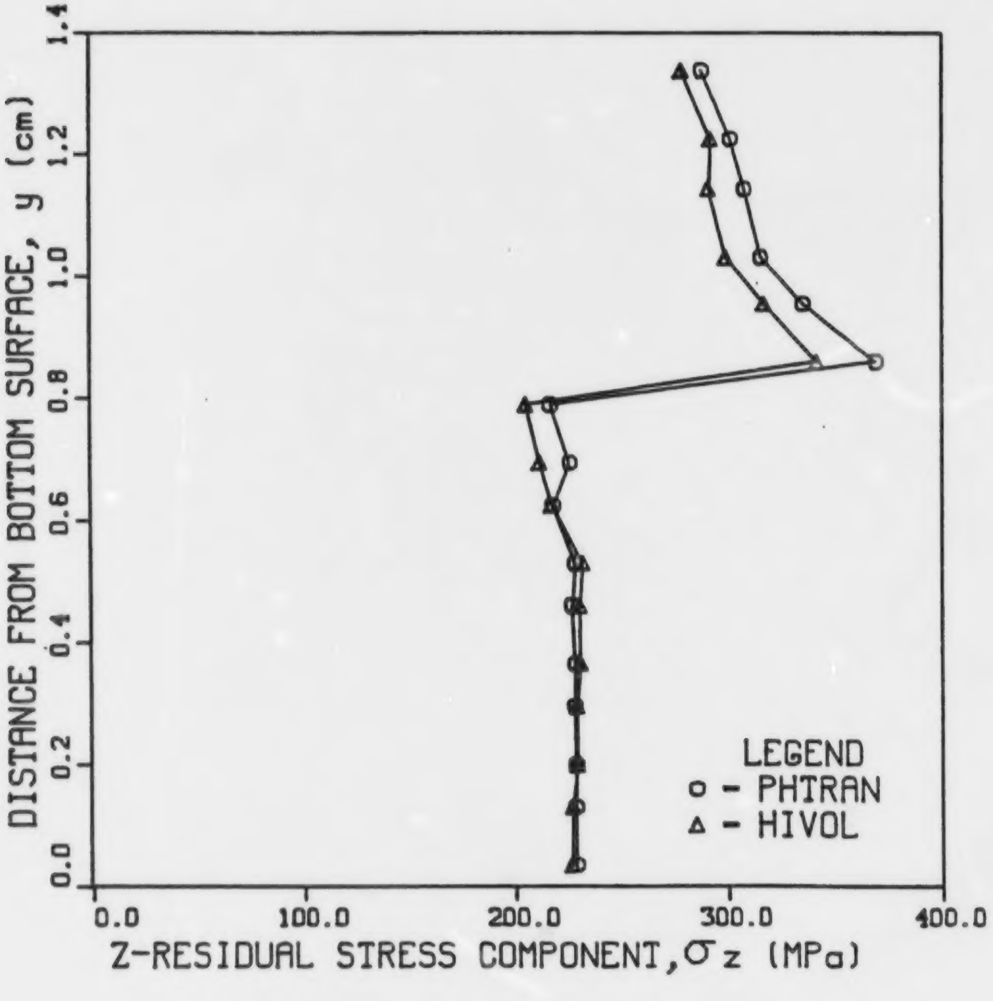

Figure 3.36: Longitudinal residual stress distribution along the weld centerline - different volumetric strains

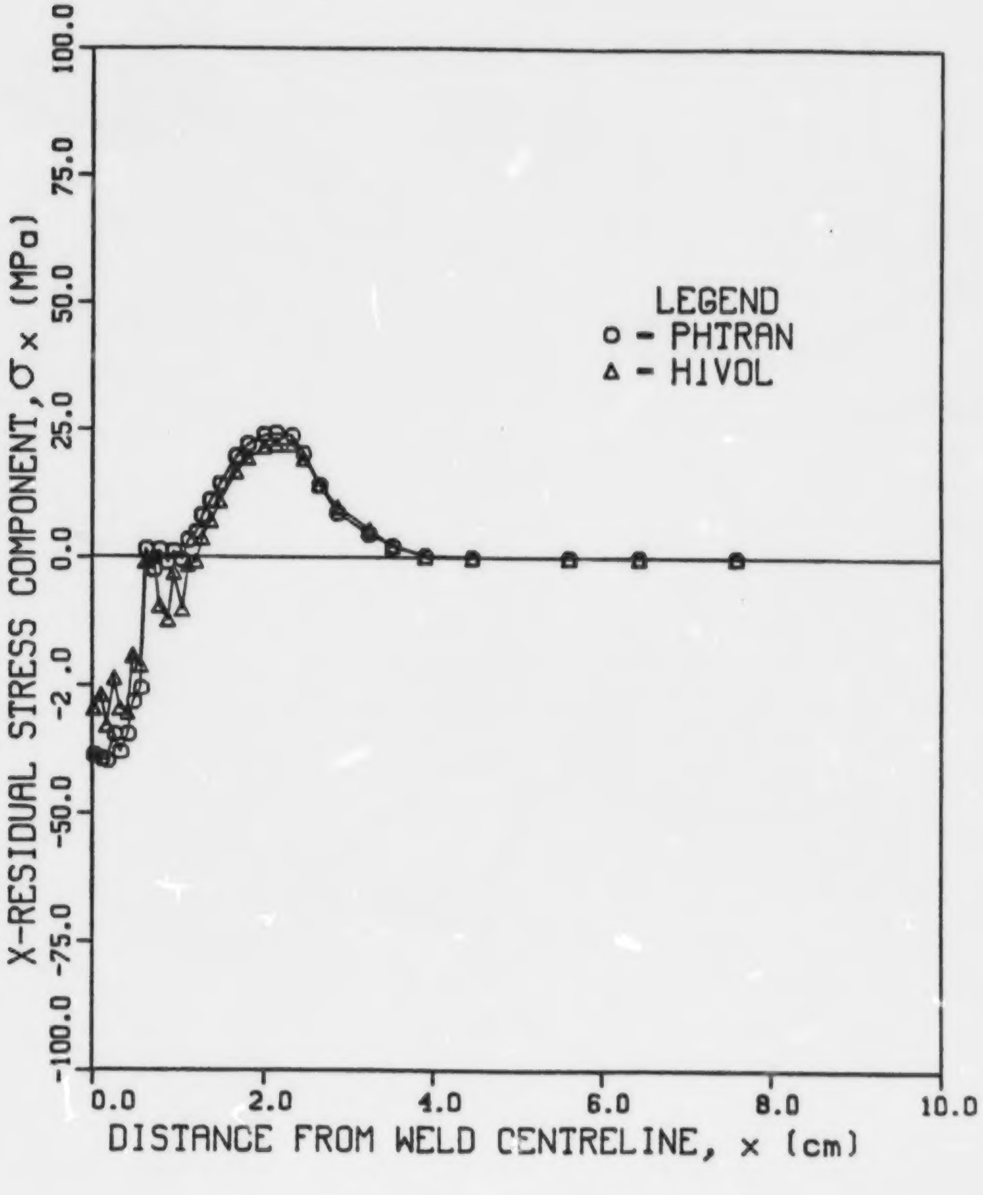

Figure 3.37: Transverse residual stress distribution along the top surface - different volumetric strains

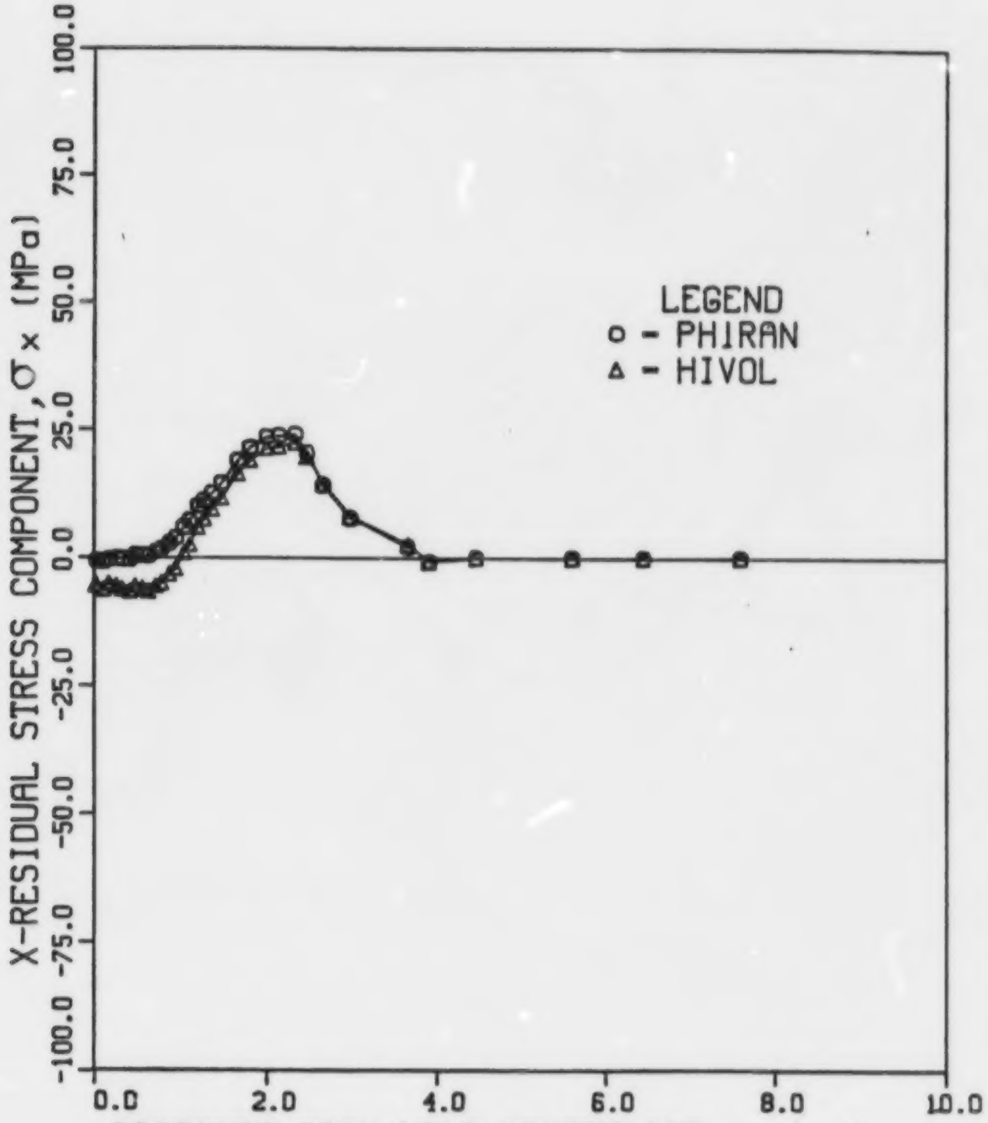

Figure 3.38: Transverse residual stress distribution along the bottom surface - different volumetric strains

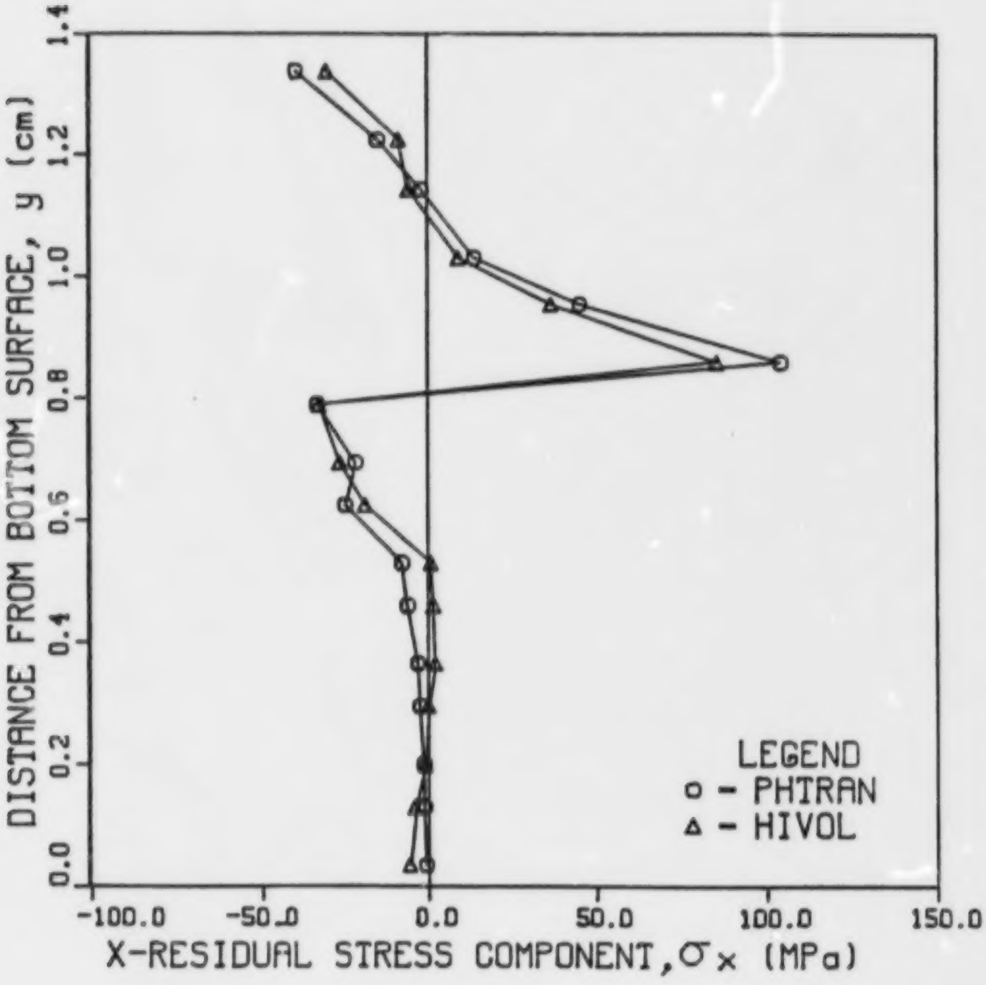

Figure 3.39: Transverse residual stress distribution along the weld centerline - different volumetric strains

Chapter 4

Discussion Of Results Including Phase Transformation Effect

4.1 Allotropic Phase Transformation Effect

The predicted residual stress distributions for the analysis without a phase transformation (NOPHASE) agrees very well with the analysis of Leung's [2] and can be assumed to be correct. Thus, different results in other analyses must be due to the effect of phase transformation.

As shown in Figures 3.30 to 3.35, a phase transformation has only a very small effect on the welding residual stress. In a private discussion with J. Bowker of Energy, Mines and Resources, Ottawa, [50], the volumetric strain values used for this analysis (about 0.5%) appears reasonable for most ferritic steels. Leung has suggested that the contracting strain during cooling is the dominant mechanism for creating welding residual stress and other variations in the welding process and material behavior may alter the magnitude of the residual stress but the general trend will remain. During a phase transformation, the thermal contraction strain is partially cancelled by the volumetric expansion of the phase transformation. Therefore, the residual stresses in the fusion zone are expected to be reduced slightly as the total contracting strain is lowered.

A simple method to assess the effect of phase transformations is to compare the thermal strain and volumetric strain. Consider that upon cooling of the weld, no strain or stress has been accumulated until the transformation starting temperature is reached and that the average expansion coefficient is constant with temperature. For cooling from T_s (about 700°C) to room temperature the thermal contraction strain is over 1%, while the linear transformation strain (1/3 of the volumetric strain) is approximately 0.16%. Clearly, the contraction strain is the dominant factor. Using the simple model presented by Leung (Eqn. 5.2 of [2]), the maximum longitudinal residual stress on the surface would be approximately 310 MPa as compared to 314 MPa without the phase transformation.

4.2 Effect Of Transformation Temperature

In the literature, there is a general suggestion that the effect of transformation would be larger if the transformation occurred at a lower temperature since the material would be stiffer. The transformation induced stress would offset a larger portion of the tensile stress induced by the thermal contraction. Using the opposite argument, the offsetting effect would be smaller for a higher transformation temperature. This behavior was observed in the analyses (HITEM and LOTEM), however, the lower transformation temperature only decreased the longitudinal stress and transverse stress by about 5 MPa (2% and 5% respectively) compared to the basic analysis (PHTRAN). The change in average thermal expansion coefficient is small between 700°C and 500°C, i.e., the thermal contraction is still dominant over the transformation expansion. Thus, the decrease is small.

For the higher transformation temperature analysis, no significant difference was observed. This is consistent with the assumption that the transformation effect is negligible at high temperatures.

4.3 Effect Of Volumetric Strain Magnitude

The magnitude of the volumetric strain can affect the welding residual stress significantly. This is quite evident in the analysis with the higher volumetric strain (HIVOL). The volumetric strain was four times larger than the basic analysis (PHTRAN). However, a volumetric strain of 2% is unrealistic for most ferritic steels. The maximum decrease in the longitudinal and transverse stress magnitude were about 20 MPa (6% and 20% respectively) when compared to the analysis with realistic properties (PHTRAN). The larger decrease in stress is due to a larger portion of the thermal contraction strain being cancelled by the transformation expansion.

4.4 Significance Of Allotropic Phase Transformations

As shown in the results of the parametric study, the effect of the transformation is very dependent on the magnitude of the volumetric strain and to a lesser extent the temperature of the transformation. By neglecting phase transformations in welding residual stress calculations, the error should be small for most ferritic steels. The calculated stresses would be conservative because they always over-estimate the values if phase transformation is included. The difference in the largest stress component (longitudinal) is only about 5%, which is well within the accuracy of the finite element model. The percentage difference in the transverse component is larger but the transverse stress is usually much smaller. Furthermore, the affected area is localize in the weld region which is usually small compared to the rest of the structure. Therefore, neglecting the phase transformation is a reasonable assumption, providing that the volumetric expansion is small compared to the thermal contraction strain.

Chapter 5

Analysis Of The T-joint Specimen

In the program of fatigue testing of offshore structures conducted at the University of Waterloo and at CANMET/PMRL of Energy, Mines and Resources of Canada in Ottawa, a series of T- butt sections with double sided, full penetration welds with reinforcing fillets were used as fatigue specimens. Specimens were prepared from five different plate thicknesses ranging from 15 to 100 mm with steels obtained from two different suppliers. However, in this study, only the 26 mm (1 inch) T-joint specimen was modelled. In this chapter, the fabrication procedure of these specimens and loading conditions in the fatigue test are described. A literature review on modelling of T-shapes is also given.

5.1 Fabrication Procedures [51]

All T-joint specimens used in the fatigue testing program were fabricated by AMCA International Limited of Kanata, Ontario. The 26 mm specimens were made of steel specified according to the Lloyds LT60 Specification and supplied by Algoma Steel. This steel is ingot cast with calcium additions. The chemical composition of this steel is presented in Table 5.1 [5].

The dimensions of a typical specimen used in the test program conducted at the University of Waterloo is shown in Figure 5.1. The final dimensions of the specimen (shown in Figure 5.1) are slightly different than before welding. The width of the plates (in the direction of weld) was approximately 25 cm (10 inches). After welding, 2.54 cm (1 inch) was milled from each edge in an effort to remove any effects on the fatigue behavior due to the starting and stopping of the electrode.

Note that the coordinate system shown in Figure 5.1 will be used throughout this Report. The X-axis (or transverse direction) is defined as in the plane of the horizontal plate. The Y-axis is defined as the direction along the vertical plate. The Z-axis (or longitudinal direction) is parallel to the direction of the welds.

The specimen was manually welded using the shielded metal arc (SMAW) process. The welding electrodes used were CLA E48018 which has the chemical composition shown in Table 5.2 [52]. Weld passes were laid in the vertical up (3G) welding position with no restraint. On average, each specimen required 26 weld passes to build up the correct weld profile. A balanced welding sequence was used to insure minimum distortion of the final geometry (see Figure 5.2 for a typical specimen). Two diameters of electrode were used. A smaller diameter electrode, 3.2 mm, was used for the root passes and the capping passes; while 4 mm diameter welding electrodes were used for filling. In order to assure similar weld-toe profiles between different specimens, the capping passes were laid down with the smaller diameter electrode such that it would pass the dime test (see Figure 5.3) according to specifications set by the United Kingdom Offshore Steels Research Program (UKOSRP). The welding parameters used in the fabrication of the 26 mm tee joints are listed in Table 5.3. The average electrode traveling speed was between 127 to 178 mm/min (5-7 in/min) depending on the weld pass being laid down. The average heat input was about 1.4 kJ/mm. No preheat was applied before welding but an interpass temperature of 230°C was maintained.

5.2 Loading Condition In The Fatigue Test

Fatigue testing of T-joint specimens was conducted in two laboratories, at the University of Waterloo and at CANMET in Ottawa. Details of these experiments are beyond the scope of this Report, but these along with the experimental results can be found in the paper by Mohaupt et al. [5]. Instead, the loading conditions used in the tests are reviewed here.

In the fatigue test, the T-joint specimens were cyclicly loaded with constant amplitude in a three point bending configuration. The cyclic loads were applied through the vertical attachment plate. In the test conducted at the University of Waterloo, the bottom plate was supported on rollers at about 120 mm from the specimen center line; while at CANMET, the ends of the bottom plate were firmly attached to the testing structure. A graphical representation of the loading and support conditions of the specimen is shown in Figure 5.4. A load cell was used to control the applied stress which was calibrated by linearly gauge measurements along the top surface of the horizontal plate. Depending on the specimen thickness, different loading ranges were used. For the 26 mm specimens, the 'hot spot' stress ranged between 80 and 300 MPa, with most of tests conducted between 100 and 200 MPa. A load ratio, R, of 0.05 was used such that the weld toe region was always in tension.

5.3 Literature Review

Research related to welding residual stress has been carried out by various researchers around the world. Pioneers in this area of research are Rosenthal [53], and Boulton and Lance Martin [54] in the 1930's. Tall and coworkers at Lehigh University conducted experimental measurements of welding residual stresses for various built-up shapes [55-60]. Hibbitt and Marcal [34-35] showed that the finite element method was a viable technique for welding residual stress predictions. Other significant work has been contributed by Masubuchi et al. at M.I.T. [22-24, 28, 29, 33, 47]; Rybicki et al. at the University of Tulsa [30, 31]; Andersson and colleagues at Chalmers University of Technology in Sweden [38, 39, 41-44]; Ueda et al. of Osaka University [32, 40]; Pick and Leung at the University of Waterloo [1, 2, 4]. Most of this work was confined to simple weld geometries and comprehensive reviews can be found in References [2, 33]. This review is confined to work that is relate to the modelling of 'T' shapes.

5.3.1 Welding Temperatures In A T-Joint Specimen

In a welding process, the major mode of heat flow away from the fusion zone is by conduction into the component. This heat flow characteristic is slightly different between build up shapes like 'T' or 'I' beams which are jointed together with fillet welds and butt weld of plates. In butt welds, heat is being conducted away from the fusion zone into the butted plates in the transverse direction, through the thickness and in the direction of the weld (see Figure 5.5). However, in a fillet weld, heat can also flow into the attachment plate (see Figure 5.6), increasing the heat flow rate significantly. This effect was observed experimentally by Kihara et al. [61]. The heat flow rate in a fillet weld was found to be about twice as fast as in a butt weld.

Since the heat flow found in welding of 'T' shapes is very complex, it is impossible to obtain an analytical solution of the welding temperature. Therefore, numerical solutions must be used. Numerical models described in the literature have been developed mainly for simple weld geometries such as butt welds in plates. However, these models, with some modifications, can be applied to calculate the temperature history for more complicated weld geometry such as fillet welds and full penetration welds. Paley and Hibbert [62] have shown that their three dimensional finite difference model is equally applicable for butt welds and fillet weld.

Goldak's three dimensional double ellipsoidal heat source model [48] was developed for welding of flat plates. Leung modified this model for planar analysis and for welding angles other than normal to the plate surface [1, 2]. This modified model is applicable to the T-joint analysis.

5.3.2 Welding Residual Stresses In A T-Joint Specimen

In order to evaluate the fracture behavior of a welded component correctly, an accurate description of the residual stresses due to welding is essential in the fracture calculation. In the case of the T-joint specimen loaded in three point bending, the residual stresses through the thickness below the weld toe are most critical because this is the region where fatigue cracks are most likely formed. The residual stress distribution can be determined either by experimental measurements or by calculation with a numerical model.

Measurements Of Residual Stress In Build Up Shapes By Tall et al.

Tall et al. at Lehigh University have measured the residual stresses for a number of weld shapes [55-60]. Typical longitudinal residual stress distributions along the surfaces and the distortion of a welded 'T' shape are shown in Figure 5.7. The residual stresses in the horizontal plate are similar to those of a weld bead on flat plate where high tensile residual stresses are found in the area of the weld metal and low compressive stresses in the rest of the plate. In the attachment plate, high tensile stresses are again found near the weld. Low compressive stress is usually found in the rest of the plate. From Tall's results, the stress variation through the plate thickness is small for plates up to about 0.5 inches. For greater plate thickness, compressive stresses are observed along the bottom surface of the horizontal plate. Unfortunately, the residual stresses in the other directions were not published.

Measurements Of Residual Stresses In 26 mm T-Joint Specimen By Holden et al.

The welding residual stresses in the 26 mm T-joint specimen were measured by Holden et al. [63] of Atomic Energy of Canada Limited, Chalk River, with the neutron diffraction technique. The authors [64] have also measured the welding residual stresses in the specimen used in Leung's study [1, 2]. Details about this technique can be found in Reference [4, 63, 64] and will not be discussed here. The residual stress components below the weld toe are shown in Figure 5.8. These results were calculated by Holden using an isotropic stress strain relationship,

$$\begin{bmatrix} \sigma_x \\ \sigma_y \\ \sigma_z \end{bmatrix} = \begin{bmatrix} 22.61 & 13.02 & 13.02 \\ 13.02 & 29.50 & 6.13 \\ 13.02 & 6.13 & 29.50 \end{bmatrix} \begin{bmatrix} \epsilon_x \\ \epsilon_y \\ \epsilon_z \end{bmatrix} \tag{5.1}$$

where the strains are expressed in units of 10^{-4} and the stresses in MPa. G. Roy of CANMET obtained similar results by assuming an anisotropic stress-strain relationship for the materials in the weld pool and in the HAZ [65]. Holden et al. suggested that the calculated residual stresses are accurate to ±100 MPa. The residual stress distributions near the surfaces (within 2.5 to 4.5 mm) of the horizontal plate (see Figures 5.9 and 5.10) were calculated by this author from the strain measurements provided by Holden et al. The isotropic stress strain relationship was used.

As seen in Figure 5.8, the X-residual stress just below the toe of the weld is about 400 MPa which is close to the room temperature yield strength of this steel. This transverse stress becomes compressive about one third through the plate thickness and a maximum compressive value of 100 MPa was measured near the center of the plate. Tensile residual stress is observed near the bottom surface with a maximum value of about 225 MPa. One observation is that the measured transverse residual stress distribution below the weld toe is not in equilibrium. This resulted from difficulty by Holden et al. in determining the zero strain state. It appears that equilibrium would be achieved if the measured transverse stress distribution through the plate thickness is lowered by about

50 MPa. From Figure 5.9, a tensile X-residual stress was measured along the top surface with a very high gradient near the toe of the weld. This stress component decreases to nearly zero about 60 mm from the center line of the specimen. A similar stress distribution was observed along the bottom surface (Figure 5.10) except the residual stress becomes slightly compressive about 60 mm from the center line.

The Y-residual stress component through the plate thickness is lower than the X or Z-stresses (Figure 5.8). A maximum value of about 200 MPa was measured just below the toe of the weld. As expected, the Y-residual stress becomes less tensile away from the top surface as the restraint in the vertical direction decreases near the bottom surface. However, the measured Y-residual stress is greater near the bottom surface than in the interior of the plate. A high stress gradient was observed for the Y-residual stress at the weld toe near the top surface (Figure 5.9). The magnitude of the residual stress decreased to a constant level of approximately 30 MPa at 60 mm from the center line of the specimen. A low compressive Y-residual stress was measured near the bottom surface (Figure 5.10) with a maximum value of about 50 MPa, 60 mm from the center of the specimen. The measured Y-residual stresses were small (less than 50 MPa) away from the weld toe regions and near the bottom surface, however the actual values should be zero. This indicates some of the uncertainty involved in the experimental technique.

The Z-residual stress is tensile below the weld toe (Figure 5.8) and a maximum value of over 400 MPa was measured. The Z-residual stress becomes less tensile and eventually becomes compressive midway through the plate thickness. The stress near the bottom surface is about 120 MPa in compression. The Z-residual stress gradient along the top surface is very high near the toe of the weld (Figure 5.9) and decreases to less than 50 MPa, 20 mm away from the weld toe. Along the bottom surface (Figure 5.10), a compressive Z-residual stress was observed. The stress is highest, over 100 MPa, near the center line of the specimen. The Z-residual stress distributions along the surfaces of the bottom plate are similar to those measured by Tall et al. [56-58].

These measured results were compared with the calculated residual stresses in Chapter 7.

5.3.3 Modelling Of 'T' Weld Shapes

To the author's knowledge, numerical predictions of welding residual stress found in the literature have been confined to simple weld geometries such as the butt weld of plates and pipes even though the numerical model used can be applied to complex weld geometries such as 'T' or 'I' shapes.

In the T-joint specimen and in most welded structures, the weld joints are made up of a number of passes. The residual stresses in such a structure are very complex and result from the build up of thermal stresses as new weld metal is deposited. One method to predict the residual stresses due to welding is to apply a numerical model for single pass welds in a repetitive manner such that the transient thermal stresses for each pass are calculated. The welding residual stresses are determined when all the weld passes have been simulated. This method is workable if the weld joint is made up of relatively few passes.

The 26 mm T-joint specimen as described in Section 5.1, required an average of 26 weld passes to build up the correct joint profile. The cost of computing would be enormous if every weld pass was simulated. Various researchers have developed techniques to simplify the analysis of multipass welds. Some of these techniques are applicable to the analysis of the T specimen and were reviewed.

Studies By Ueda et al.

Ueda et al. [40, 66] have study residual stresses resulting from multipass welds in the connection of pressure vessel components. The authors approximated a welded cylinder to head connection by the welding of thick plates. Plate thicknesses considered were 100, 200 and 300 mm with 7, 20 and 34 layers of weld passes respectively with a maximum of two passes per layer. In this model, temperature history of each weld pass was calculated. However, the transient thermal stresses were calculated only for the last pass of each layer. The predicted results achieved good agreement with measured values except in the vicinity of the weld metal of the thinnest specimen. The authors also observed that during welding, the transverse stress is always highest just below the weld metal of the newest layer. As the layers are deposited, the stresses in the earlier layers are relieved gradually and eventually become compressive. Furthermore, the highest tensile transverse residual stress is located just below the finishing bead.

Ueda et al. [67] have also modelled a twenty pass narrow gap arc weld in a 50 mm thick plate with the technique described above. Since the welding process is for a narrow gap, each layer consisted of only one pass. The analysis was carried out for every second weld pass only. The authors observed that the residual stresses near the finishing beads are induced by the last few layers or just the last weld pass alone.

The technique of analyzing only the last pass in a layer of weld passes is not very useful when considering the T specimen because some layers consist of more than two passes. However, Ueda's results show welding residual stresses in regions of the weld toe are induced by the finishing passes. This suggested that it is possible to predict the residual stresses near the weld toe by analyzing the capping passes only. In the T-joint specimen, the residual stresses in this region are the most critical in a fracture calculation.

Studies By Rybicki et al.

Rybicki et al. [30,31] have investigated residual stresses in multipass girth-butt welded pipes. Girth welds made up of 2, 7 and 30 passes were analyzed. In Rybicki's model, the temperature distribution for the pipe material was calculated using a moving heat source solution [53]. In residual stress predictions, the exact thermal history was not simulated. Instead, the weld was assumed to undergo one cooling phase and one heating phase for each pass. With this method, the temperature distribution at three different times during welding are required, one at a time just before the start of laying the weld metal, one at a critical time during welding, and one at some time after the weld was applied. The critical time during welding was chosen as the point at which the weld metal just regains its stiffness. Intermediate temperatures were interpolated linearly. When several passes are analyzed consecutively, the temperature distribution at the start of one pass is the same as the final temperature of the last pass. When weld passes are grouped in a layer, the 'envelope' method is used. The temperature distribution for each pass in the layer is calculated. The thermal history for each stress model element is examined to determine which pass caused that point to experience the highest temperature. These maximum temperatures are then used in the stress analysis as if the whole layer of passes was deposited simultaneously.

In the seven pass analysis, the authors used an assumption of symmetry and grouped the weld passes into four layers. The calculated residual stresses appear to underestimate the measured results. The authors also observed that the residual stresses are higher on the side of the pipe with the last pass.

In the thirty pass weld analysis, the weld passes were grouped into nine layers. The predicted residual stresses agreed reasonably well with the few measured values. The authors also grouped the thirty passes into three layers and no agreement with measurements was observed.

Rybicki et al. have showed that layering is a viable technique to reduce the computing cost in the analysis of multipass welds. This technique is also applicable to the T-joint specimen study, especially for the capping passes.

Study Of Multipass Welds By Leung

In Leung's study of multipass welds [1,2], three weld configurations were modelled. In the first configuration, two passes were laid vertically on top of each other in a 'V' weld preparation. In the second and third configuration, a layer of two and three passes were laid side by side in a rectangular weld preparation. The author carried out complete simulations in which every pass was analyzed. In addition, simulations were also carried out with simplified techniques to save computing cost. In the analysis with two passes laid vertically, the author observed that the area containing residual stress built up with the deposition of each new layer of weld passes. In addition, the magnitude of stresses near the top surface are nearly identical to that of analyzing only the capping pass which is very similar to Ueda's observation [67]. However, only analyzing the capping passes will lead to a significant under estimation of the residual stress below the capping layer.

In the analyses of weld passes in a layer, Leung observed that the transverse residual stresses do not fully develop until the whole layer is finished because the transverse constraint is highest when the cavity (or weld preparation) is filled. For the longitudinal residual stresses, gradual build up of the area of the residual stresses are observed regardless of the welding sequence. The author has shown that Rybicki's grouping technique is incorrect because it cannot predicted the skewing effect of residual stresses towards the last pass in a layer of welds. Instead, Leung suggests a grouping technique that requires two analyses per layer of weld passes. In this method, the temperature history for every pass is calculated. Then the thermal history for all passes except the last pass are grouped together using the 'envelope' approach suggested by Rybicki. The residual stresses for this group of weld passes are calculated in the first analysis. Then the placement of the last pass is simulated in the second analysis. Although the saving in computing cost is not as great as Rybicki's method, the predicted results appeared to be more accurate.

5.3.4 Loading Of T-Joint Specimen

The stresses experienced by a welded structure are very complex since the resultant stresses will be a combination of the applied stresses, local effects due to stress concentrations and residual stresses induced by the welding process.

Stress Concentration Factor

In a welded structure, stress concentrations are inevitably found around the weld joints. Considering the T-joint specimen, stress concentrations are located at the toe of the welds with the severity of the stress concentration depending on the weld angle and the weld radii at the toe. A nominal weld profile of 45° was maintained and the weld radii was controlled by conforming to the dime test. However due to the variability of the welding process, the shape of the weld bead is not constant. Thus the stress concentration factor can be expected to vary along the length of the weld toe.

Researchers have tried to determine the stress concentration factor (SCF) of 'T' weld shapes by finite element analyses and photoelasticity [68]. Values of 3 or higher have been reported, but these results are far from certain. Besides the variation due to the effects mentioned above, different values can be calculated depending on the finite element mesh used; a greater stress concentration factor can result from a finer mesh. Theoretically, infinitely small elements are needed to capture the stress gradient around the toe of the weld. Lawrence et al. have suggested that an element size of one tenth the weld toe radius should be used in the weld toe region in order to model the stress concentration [69].

Effects Of Loading On The Welding Residual Stresses

There are very few studies in the literature on the effect of fatigue loading on welding residual stresses. Gurney [68] has shown the 'shakedown' of residual stresses in a simple theoretical model based on an elastic perfectly plastic material assumption and idealized residual stress distribution. To the author's knowledge, no attempts have been made to study the effect of loading on welding residual stresses with numerical techniques. The reason for this is that only recently researchers have become confident with the accuracy of the numerical models. Furthermore these numerical models are only economical for simple geometry. For complex welded structures, the computing cost is still very high.

Welding residual stresses are very difficult and laborious to measured experimentally. In addition, most techniques are destructive and fatigue testing of the specimen after the initial measurements is impossible. Only a handful of measuring methods, neutron diffraction and X-ray diffraction, are capable of measuring the residual stresses in a specimen before and after fatigue testing. Allen et al. of Harwell Laboratory [70] have measured the residual stresses of a similar T-joint specimen at different stages of the fatigue test. After shakedown (1000 load cycles) only small changes from the as-welded residual strain measurements were observed with the neutron diffraction technique. The most significant changes occurred at the weld toe. This indicates that after initial loading, only localized plastic yielding occurs at the stress concentration. Upon elastic unloading, the high residual stresses are relaxed to a much lower level and further loading will always be elastic.

Table 5.1: Chemical composition for Lloyds LT60 steel [5]

Chemical Composition	Percentage %
C	0.12
Mn	1.39
Si	0.28
S	0.011
P	0.017
Al	0.027
Ni	0.15
Cr	0.17
Mo	< 0.01
Cu	0.15
V	0.053
Nb	0.041
Fe	balance

Table 5.2: Chemical composition for E48018 welding electrode [52]

Chemical Composition	Percentage %
C	0.12
Mn	0.90
Si	0.80
S	0.04
P	0.03
Mo	0.40-0.65
Fe	balance

- Electrode coating - basic, iron powder.

Table 5.3: Typical welding parameters for a 26 mm T-joint specimen [51] (refer to figure 5.2)

Pass No.	Electrode Size (mm)	Input Current (Amp)	Input Voltage (Volt)
1-2	3.2	115/125	20/23
3-4	3.2	115/125	20/23
5-6	4.0	160/175	20/23
7-8	4.0	160/175	20/23
9-10	4.0	160/175	20/23
11	3.2	115/125	20/23
12-13	4.0	160/175	20/23
14-18	3.2	115/125	20/23
19	4.0	160/175	20/23
20-26	3.2	115/125	20/23

1. The welding process used was the shielded metal arc process.
2. All welds were made in the vertical up (3G) welding position.
3. The type of electrode used was the CLA E48018 with DC+ polarity.
4. No preheat was used and the interpass temperature was 230°C.
5. The welding speed was about 127 mm/min (5 in/min).

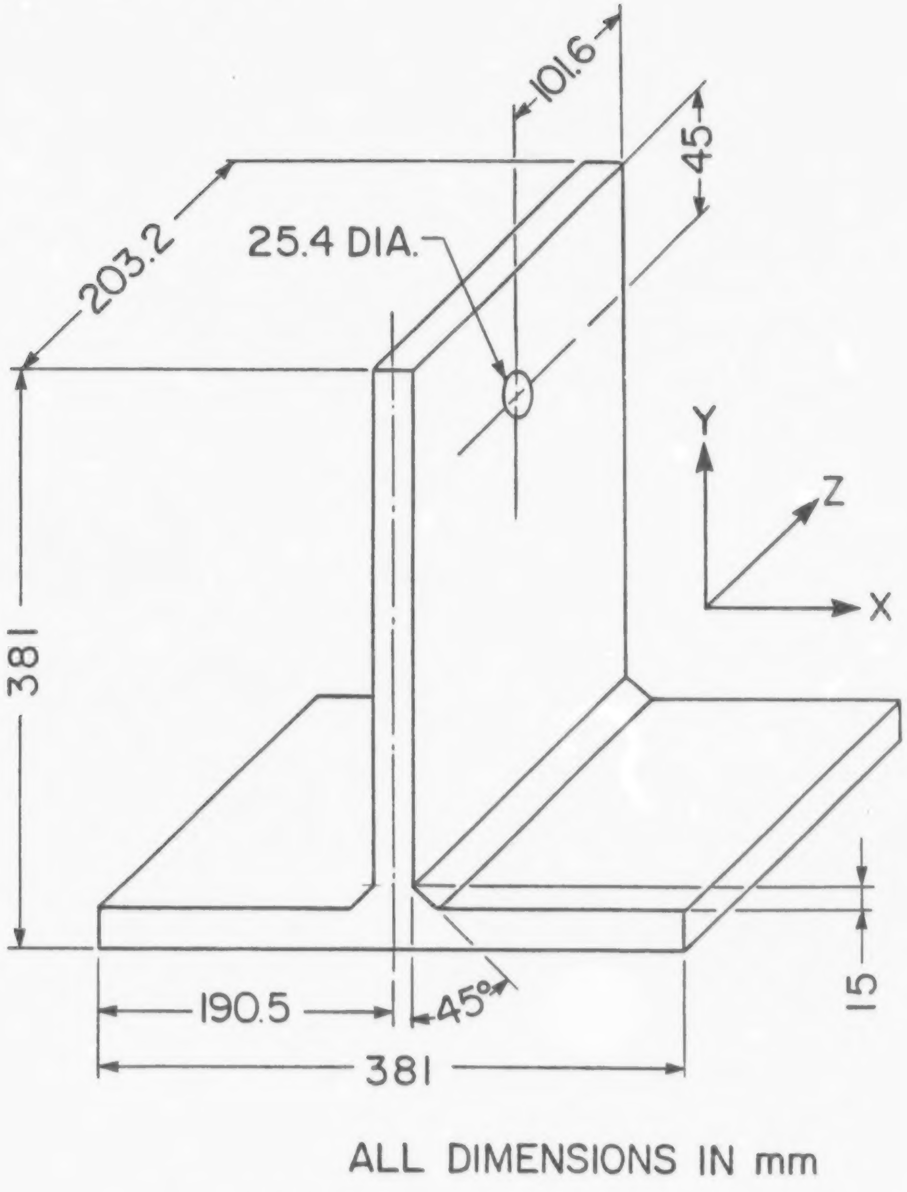
101.6
45
203.2
25.4 DIA.
Y
Z
X
381
15
190.5
45°
381
ALL DIMENSIONS IN mm

Figure 5.1: Dimensions of the 26 mm T-joint Specimen

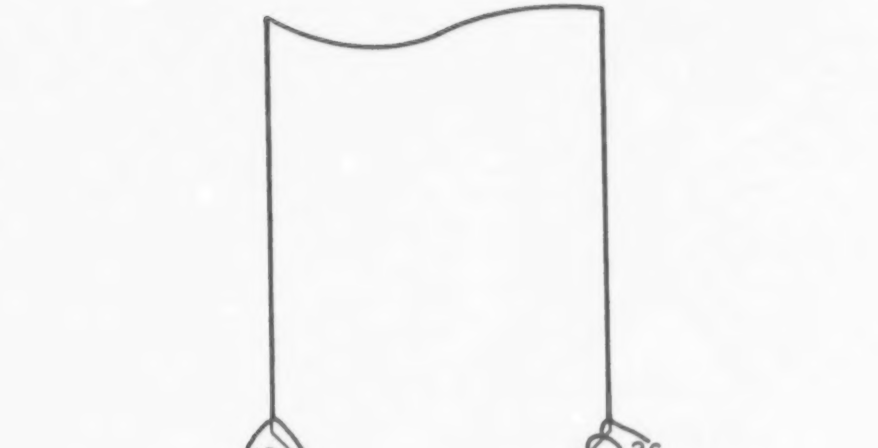
1
2
3
4
5
6
7
8
9
10
11
12
13
14
15
16
17
18
19
20
21
22
23
24
25
26

Figure 5.2: Welding sequence for the 26 mm T-joint specimen

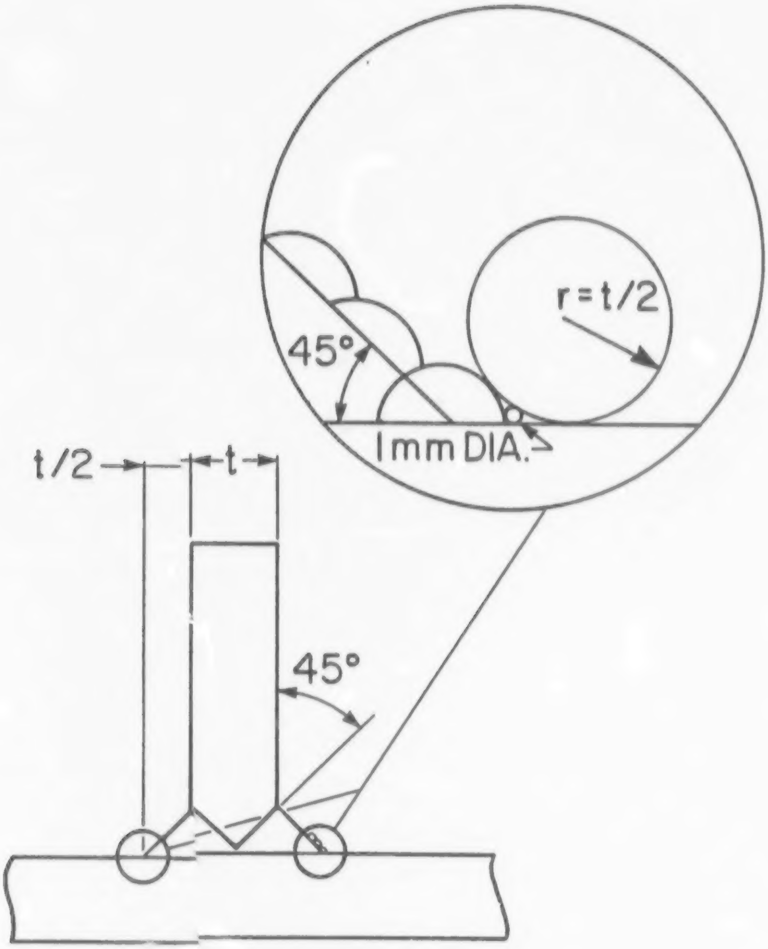
r = t/2
45°
1mm DIA.
t/2
t
45°

Figure 5.3: Dime test used for weld toe profile

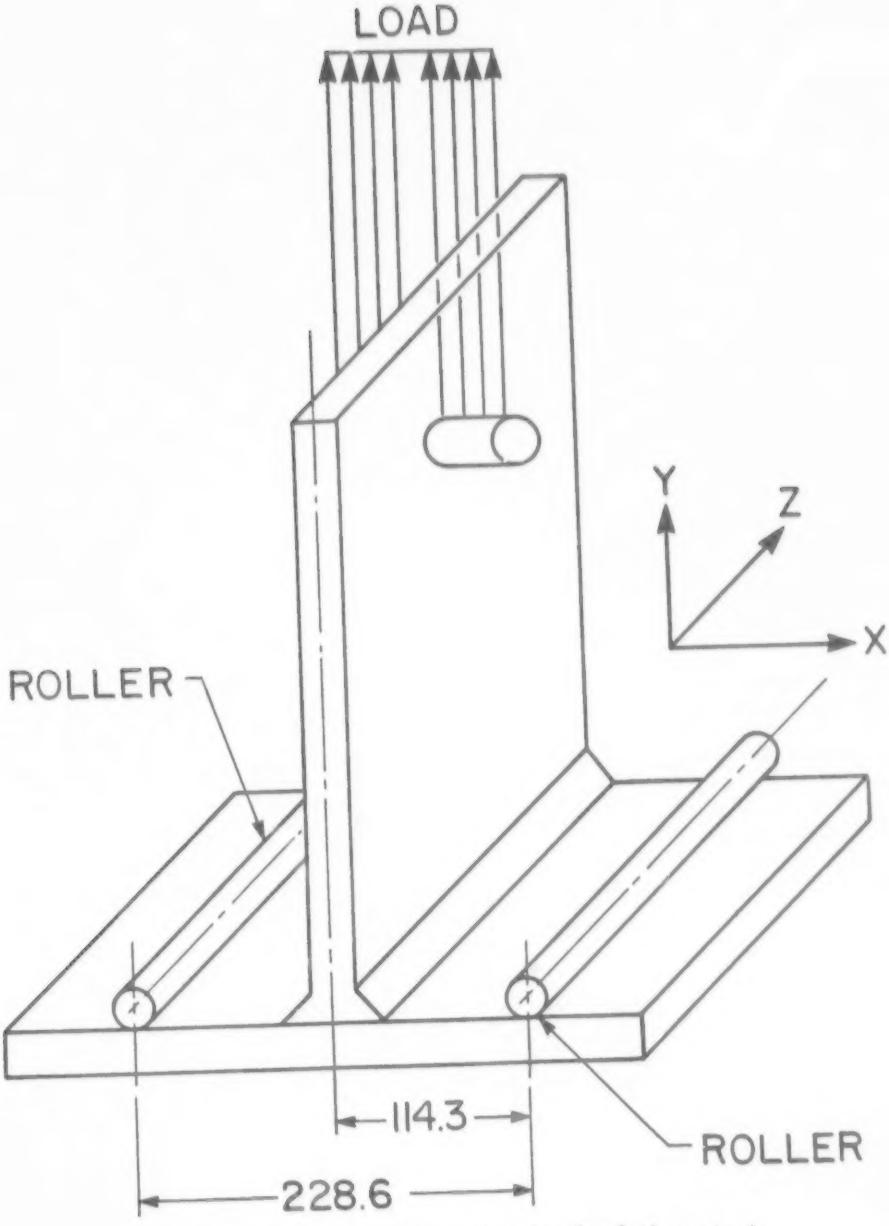
LOAD
Y
Z
X
ROLLER
ROLLER
114.3
228.6

Figure 5.4: Loading configuration in the fatigue test

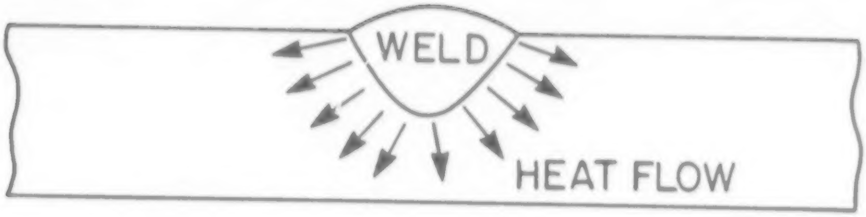
WELD
HEAT FLOW

Figure 5.5: Heat conduction in butt weld of flat plate

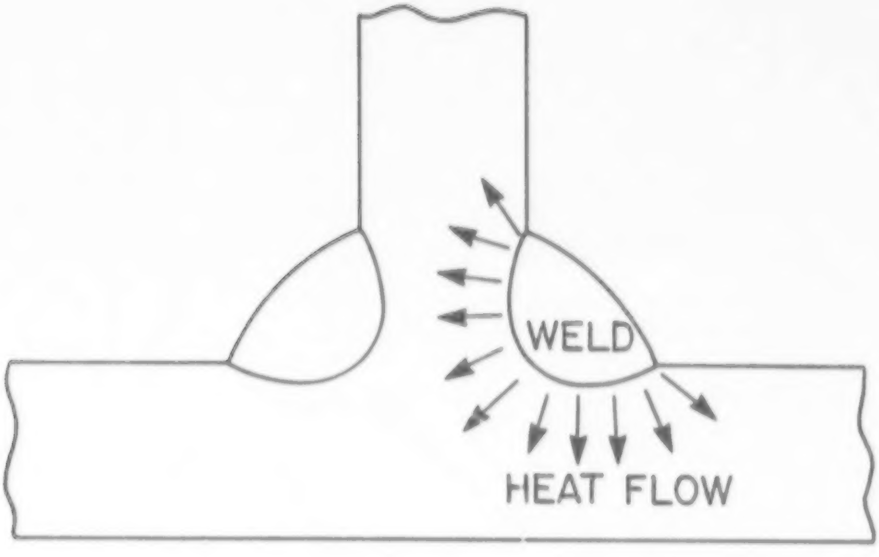
WELD
HEAT FLOW

Figure 5.6: Heat conduction in fillet weld

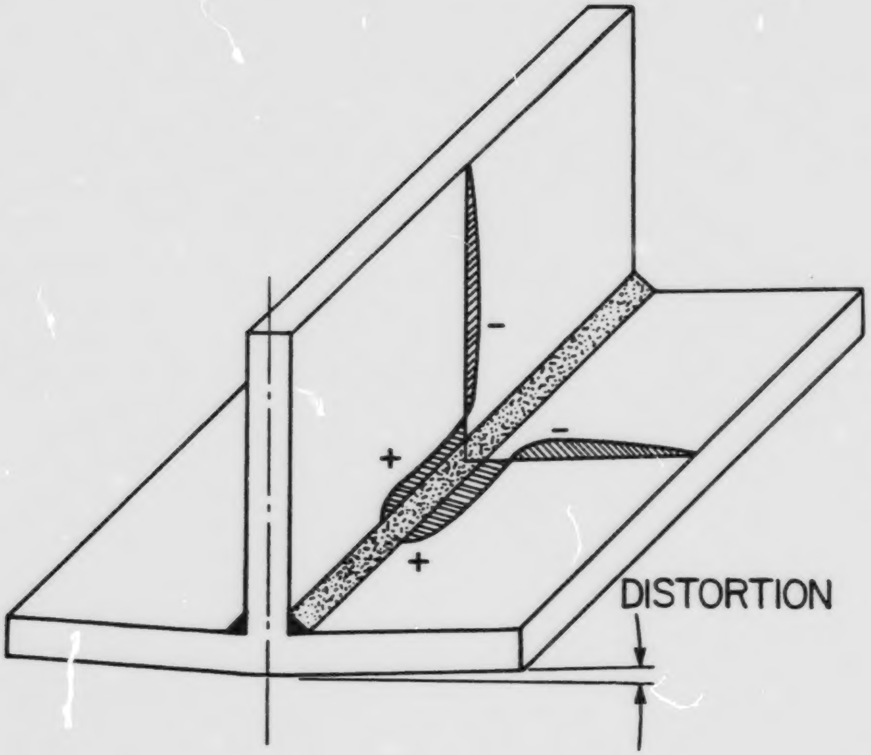
-
-
+
+
DISTORTION

Figure 5.7: Typical surface longitudinal residual stress and distortion of welded 'T' shape

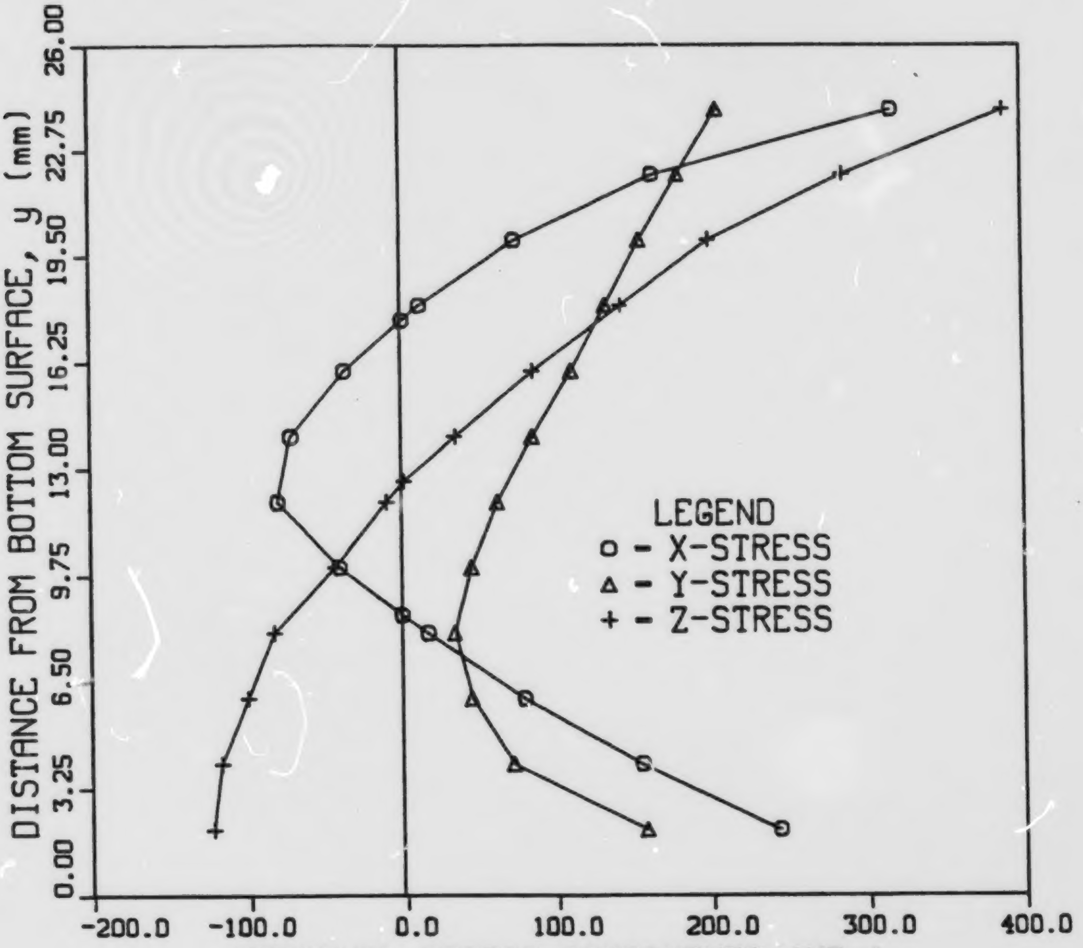

Figure 5.8: Residual stress distributions through the plate thickness below the weld toe as measured by Holden et al. [63]

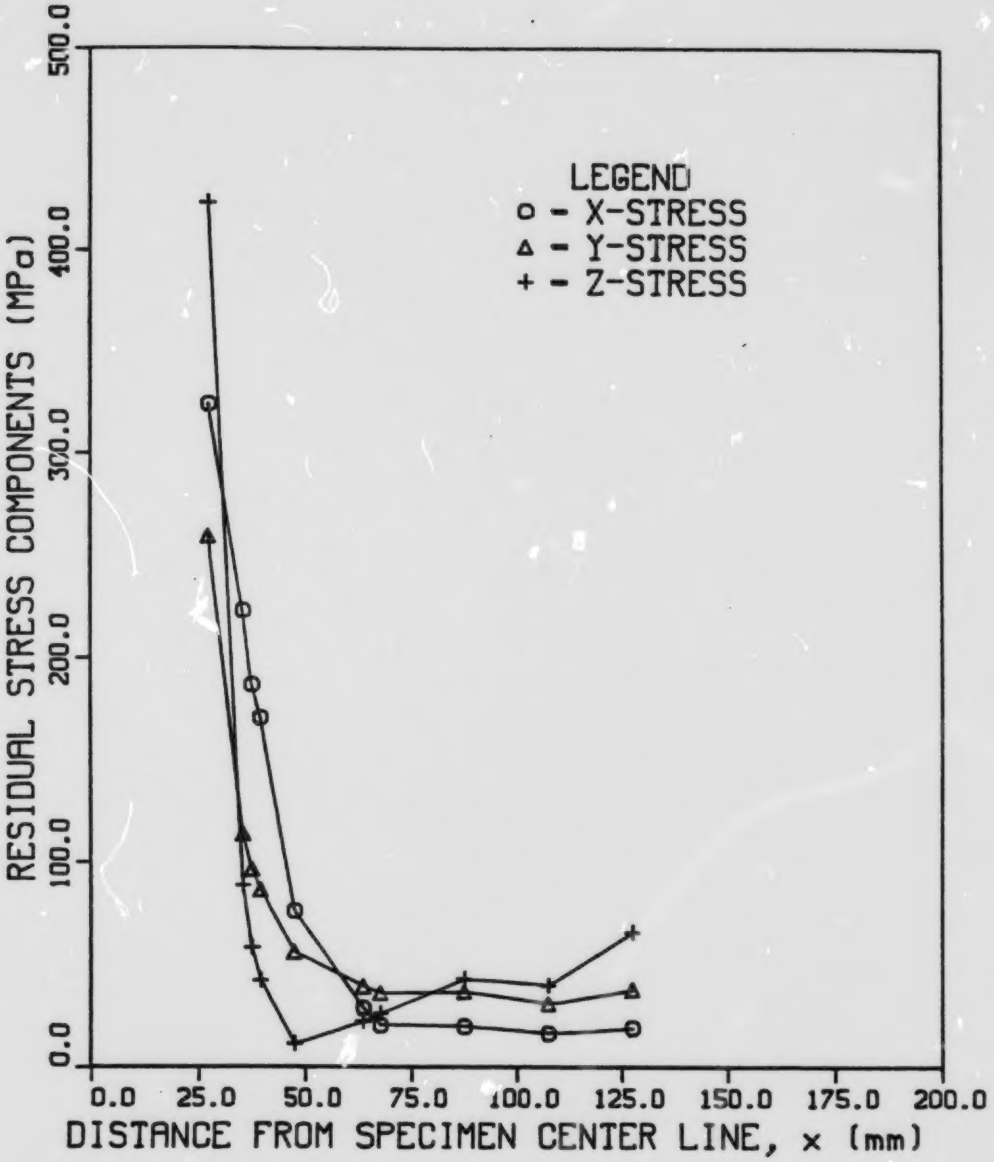

Figure 5.9: Residual stress distributions along the top surface as measured by Holden et al. [63]

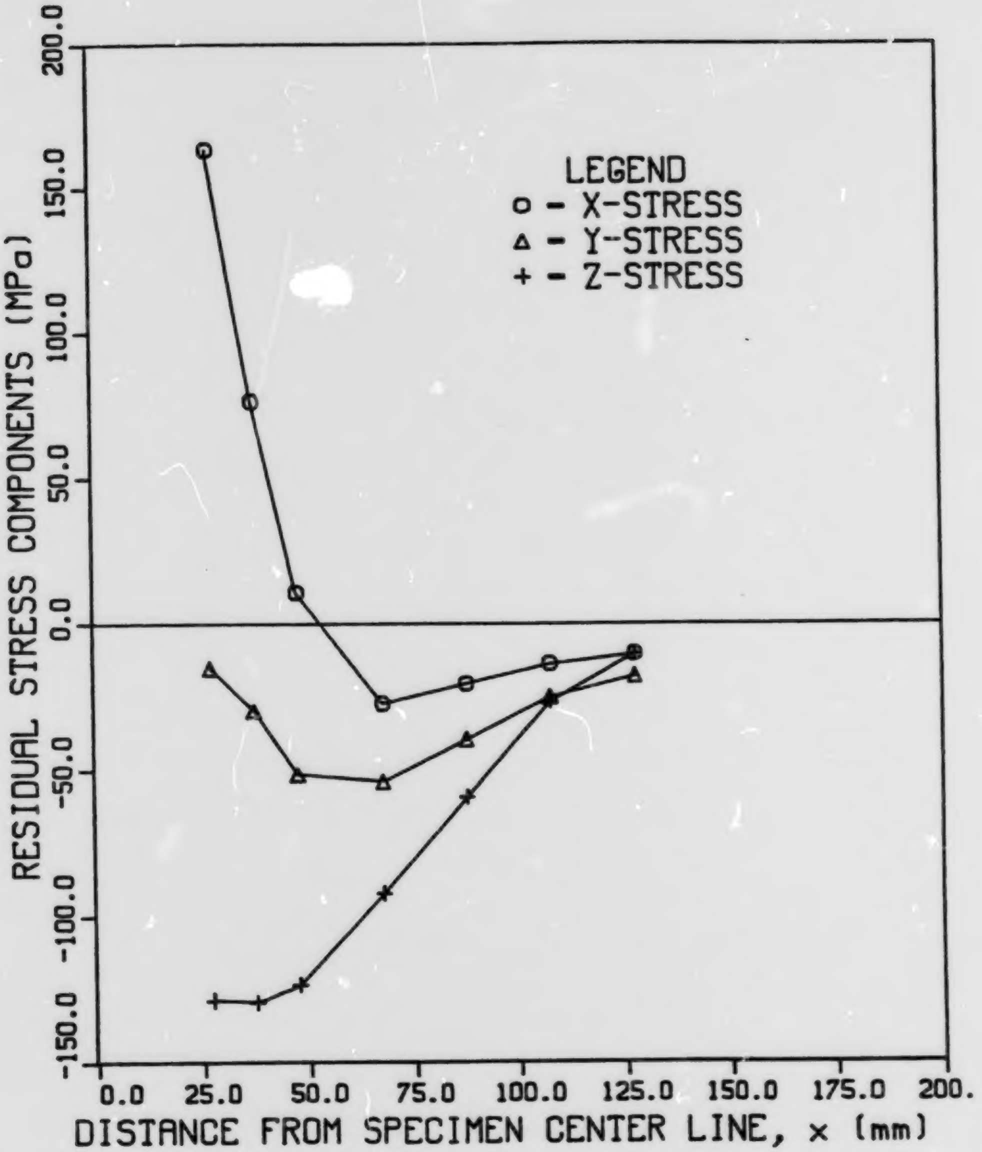

Figure 5.10: Residual stress distributions along the bottom surface as measured by Holden et al. [63]

Chapter 6

Heat Transfer Analysis Of The T-Joint Specimen

The welding sequence and the welding parameters used in the fabrication of the 26 mm T-joint specimen were described in Chapter 5. In this chapter, the temperature history of the T- joint specimen during welding is predicted such that the results can be used to calculate the residual stresses in the T-joint specimen during the welding process.

6.1 Computer Model For The Heat Transfer Analysis

The finite element method was used to determine the thermal history of the fabrication of the T-joint specimen. The model used is an extension of the butt weld model developed by Leung [2]. This model requires information about the geometry of the specimen, the heat source model, the thermal material properties and the thermal boundary conditions that are appropriate to the shielded metal arc welding process. The required parameters, along with the assumptions made, are described in the following sections.

6.1.1 Geometric Model

Based on experience with the butt weld model, the computer time required to model a full penetration weld was believed to be much higher since the geometry is more complicated. In addition, since each T-joint specimen has an average of 26 passes, the total cost of computing would be extremely high if every pass was modelled. Therefore, some assumptions were required to reduced the computation time to an acceptable level. For example, according to Goldak et al. [71], a full two-dimensional cross section analysis takes about 1/90th of the time of a full three-dimensional analysis.

The heat conduction of any welding process is three-dimensional in nature. However, under certain welding conditions, the dimensionality of the problem can be reduced to two dimensions. The heat flow in the welding direction can be neglected if the welding speed is fast compared to the thermal diffusivity of the material [72] or an internal heat generation term is used to compensate for the heat flow ahead of the electrode. Since the heat can be conducted away in all directions, the heat flow in the direction of the weld is not as important as in the direction perpendicular to the weld along the vertical and horizontal plates. Therefore, the heat flow in the weld direction has been neglected in the heat transfer analysis even though the traveling speed of the electrode is not very fast in this process (Table 5.3). The experimental results of Kihara et al. [61] suggested that a quasi-stationary state exists in the middle of welds longer than

100 mm. Therefore, a planar analysis (2-D) is used to model the T-joint specimen away from the edges. In this model, a three-dimensional heat source is assumed to travel across the plane of analysis to simulate the heat flow in the direction of welding.

In the welded T-joint specimen, fatigue cracks always initiate at the toe of the weld due to the stress concentration and possible weld defects. These cracks coalesce and grow below the weld toe. If welding residual stresses have any effect on the fatigue behavior, the residual stress distribution around the weld toe region would be most critical. From Leung's analyses of multipass welds laid on top of each other, the final residual stress near the reinforcement is not fully developed until the top layer of weld passes are laid [2]. Any previous residual stresses in the vicinity of the new weld layer are removed due to the high temperature. The final residual stress at the weld reinforcement results from placement of the top layer. For a T-joint specimen, the residual stress around the weld toe would mainly be due to the capping passes. Since this is the region that was of interest in this study, only the capping passes were modelled.

It can be shown that the welding residual stresses of a fillet welded T-joint specimen are essentially symmetrical about the center line of the vertical plate [56]. Since the specimens were fabricated using a balanced welding sequence, this symmetry assumption is expected to hold true. Thus, only one half of the specimen was modelled in the residual stress calculation which reduced the computing time by half. However, the heat flow is not symmetrical about the center line unless welds are laid on both sides simultaneously. A test problem was analyzed to determine the validity of a symmetry assumption for the temperature calculation in an effort to save computing time. A weld bead was laid on the top of a plate which has the same plate thickness as the T-joint specimen. In the first analysis, heat was allowed to flow freely in the thickness direction. In the second analysis, symmetry was assumed at mid-thickness. The results showed that heat conduction was impeded if symmetry was assumed and therefore in the T-joint specimen the whole vertical plate has to be included in order to model the heat flow out of the weld properly.

In preliminary analyses of the T-joint specimen considering welding of the first capping pass with the symmetry assumption, the temperature changes were minimal in the horizontal plate away from the weld zone. Therefore, since only the welding passes on one side were being modelled, the author decided to model the capping passes with the whole vertical plate and part of the horizontal plate (Figure 6.1). The heat flow to the other portion of the horizontal plate was replaced by convective heat transfer.

6.1.2 Finite Element Mesh

A cross-sectional plane was discretized using 622 4-noded two-dimensional isoparametric elements with a total of 698 nodes (see Figures 6.1a and 6.1b). The weld pool dimensions were measured from an actual specimen tested at the University of Waterloo. The specimen had only four capping passes instead of five as shown in Figure 5.2. Therefore, only four passes were modelled. The results are not expected to be any different than an analysis with five passes, since the same amount of weld metal was deposited.

6.1.3 Heat Input Model

The heat input model is the most important part of a welding analysis. Goldak's three-dimensional, double ellipsoidal heat source model [48] which Leung had modified for planar analysis was used [1,2]. The parameters for this model are the actual heat input to the weld metal and the weld pool dimensions.

The total heat input, calculated as the product of the arc current and the voltage, is higher than the actual heat being input to the weld metal due to losses between the arc and the environment and the resistive loss in the wire. This power loss is accounted for by a factor called the arc efficiency. For shielded metal arc welding, efficiencies between 65% and 85% are suggested in the literature [73]. The arc efficiency used in this study was 65%.

The weld pool dimensions were measured from a T-joint specimen tested at the University of Waterloo. The width of the weld pool was measured across the top of the weld bead. The depth was measured after the end was polished and etched. The length was estimated by the distance between ripples. The values used are summarized in Tables 6.1 and 6.2. Some trial and error was required to set the origin of the double ellipsoidal model for each weld pass.

6.1.4 Thermal Boundary Conditions

Natural convection and radiation were assumed to occur on all surfaces except on the surface of the weld metal (see Figure 6.2). On this surface, the flux deposited along with the weld metal was assumed to produce an insulating effect. Preliminary test problems showed no difference between analyses with insulated surfaces and analyses with free convection and radiation on the weld metal surface. These results indicated that the main mode of heat loss is conduction through the parent metal.

Newton's cooling law was used to model the heat loss due to surface convection. This requires knowledge of the film coefficient. The T-joint was welded together in the vertical up (3G) position. In this case, the convective film coefficient would be different from welding in the horizontal position. The film coefficient as a function of surface temperature was calculated using a method found in the heat transfer text book by Incropera and DeWitt [74]. These values are shown in Figure 6.3. The ambient temperature was assumed to be 20°C.

The Stefan-Boltzmann radiation law was used to model the radiative heat loss. The surface emissivity for this particular steel was not found in the literature. Values were found for steels with lower manganese content [75]. An average value of 0.83 was used in this analysis. The reference temperature assumed was 0°K and the ambient temperature 20°C.

6.1.5 Weld Pool Convection

The thermal energy dissipated through weld pool convection was modelled by artificially increasing the thermal conductivity at temperatures above the melting point. Similar to Leung's analyses, a conductivity of five times its value at the solidus temperature was used.

6.1.6 Thermal Material Properties

The thermal material properties required to calculate the temperature history of a welding process are the thermal conductivity, specific heat, mass density, latent heat of fusion and allotropic phase transformation and the corresponding transformation temperatures for both the parent metal and the weld metal. Since both the parent and weld metals have similar chemical compositions, they were assumed to be the same for the analyses.

Thermal properties for the manganese steel used were not available in the literature. However, properties for another manganese steel with a similar chemical composition (see Table 6.3 [76]) were considered sufficiently accurate for this analysis. The thermal conductivity and specific heat as a function of temperature are shown in Figures 6.4 and 6.5 respectively. The value for the thermal conductivity at temperatures greater than the solidus temperature was modified to compensate for the convection in the weld pool. The mass density of this steel is 7850 kg/m^3 at room temperature and is assumed to be independent of temperature.

The solidus and liquidus temperature for this steel are 1504°C and 1528°C respectively. The latent heat of fusion is 277 kJ/kg. The manganese steel used to make the T-joint specimens experiences allotropic phase transformations during heating and cooling. However, it was concluded in the first part of this study that the effect of phase transformation on welding residual stresses is small and can be neglected. Therefore, allotropic phase transformations were not modelled in the analyses.

6.1.7 Solution Strategy

In order to calculate the temperature history with the finite element method, the initial temperature of the T-joint specimen is required. Since it was decided to model only the capping passes, the temperature distribution before the first capping pass is deposited must be known. The interpass temperature during welding was 230°C as measured at the vicinity of the weldment; however, this temperature does not applied to the whole specimen. Instead of guessing an initial temperature distribution, the whole specimen was assumed to be at 15°C. This undoubtedly introduces errors in the calculated temperature history, but the error is expected to be small for the residual stress calculation.

The time required to apply a single pass was not recorded and had to be approximated. The welding speed was about 127 mm/min and the width of the plates were 254 mm. Thus at least two minutes per weld pass was required. The deposited flux had to be removed before the next pass could be welded. This operation was estimated to take one minute for a total time per pass of three minutes. After the last capping pass was deposited, the thermal history for the next fifty minutes was calculated to allow the specimen to return to room temperature.

The weld metal for each pass was assumed to be deposited instantaneously at the beginning of the weld pass (i.e., when the weld pool first reached the plane of analysis). Based on the weld speed and the estimated weld pool size, the heating cycle would last for 4.25 seconds. The cooling cycle would take up the remainder of the three minutes per weld pass. The temperature distribution at the end of three minutes would be the initial temperature for the next pass.

The ABAQUS input data files, the user defined subroutines for the heat source model and the convective film coefficient for the thermal history calculations for the four capping passes can be found in Appendix B.

6.2 Calculated Thermal History

The temperature contours at the point that the plane of analysis passed through the origin of the double ellipsoidal heat source of the capping passes are presented in Figures 6.6 to 6.9. Semi-circular isotherms similar to those of butt-welded plates were observed. The hottest temperatures were located at the fusion zone surrounded by high thermal gradients. High cooling rates for fillet welds similar to those observed by Kihara [61] were quite evident as shown in Figure 6.10 in which the thermal histories for a number of the nodes were plotted. Node 120 is located at the centerline of the specimen on the bottom surface; Node 16106 at the weld toe closest to the first capping pass; Nodes 16116, 16122 and 16128 at the top surface of capping pass 1, 2 and 3 respectively; Node 16134 at the weld toe of the vertical plate; and Node 22128 at the weld toe on the opposite side of the vertical plate.

The maximum temperature predicted was well over 2800°C. This maximum temperature would be lower if weld pool convection was modelled. However, an error in the residual stress calculation was not expected as a temperature ceiling was applied to the data prior to residual stress calculations. The assumption to neglect half of the bottom plate appeared valid. The temperatures along the face where the plate was cut did not change significantly indicating that the heat flow through this part of the plate was minimal.

The calculated weld pool shape determined by the melting temperature for each of the capping passes are superimposed in Figure 6.11. Some remelting of previous weld metal was observed (the intersection of two weld pools). The predicted weld pool shapes compared reasonable well with the shape measured on an actual T-joint specimen.

The best method to check the calculated thermal history is by comparison with measured values during welding. Unfortunately, no measurements were made during fabrication of the T-joint specimen. Therefore, it was impossible to determine the accuracy of the predicted temperature history. However, based on the reasonable agreement between the measured and the predicted weld pool shape, along with the fast cooling characteristic of fillet welds as observed by Kihara [61], the predicted temperature history was believed to be accurate enough for the purpose of residual stress calculations.

Table 6.1: Dimensions of weld pool for double ellipsoidal heat source model

Parameters	Front Quadrant	Rear Quadrant
Width, a_1	4.4	4.4
Depth, b_1	4.4	4.4
Length, c_1	4.0	6.0
Fraction of Heat	0.8	0.2

Table 6.2: Origins of heat sources

Capping	Origin of Heat Source		Angle of Heat Source
Pass No.	x (mm)	y (mm)	(deg. from vertical)
1	171.0	28.8	-25.0
2	174.0	31.9	-25.0
3	177.5	35.2	-25.0
4	180.5	38.25	-55.0

Table 6.3: Chemical composition for manganese steel [76]

Chemical Composition	Percentage %
C	0.23
Mn	1.51
Si	0.12
S	0.038
P	0.03
Ni	0.04
Cr	0.06
Cu	0.1
Fe	balance

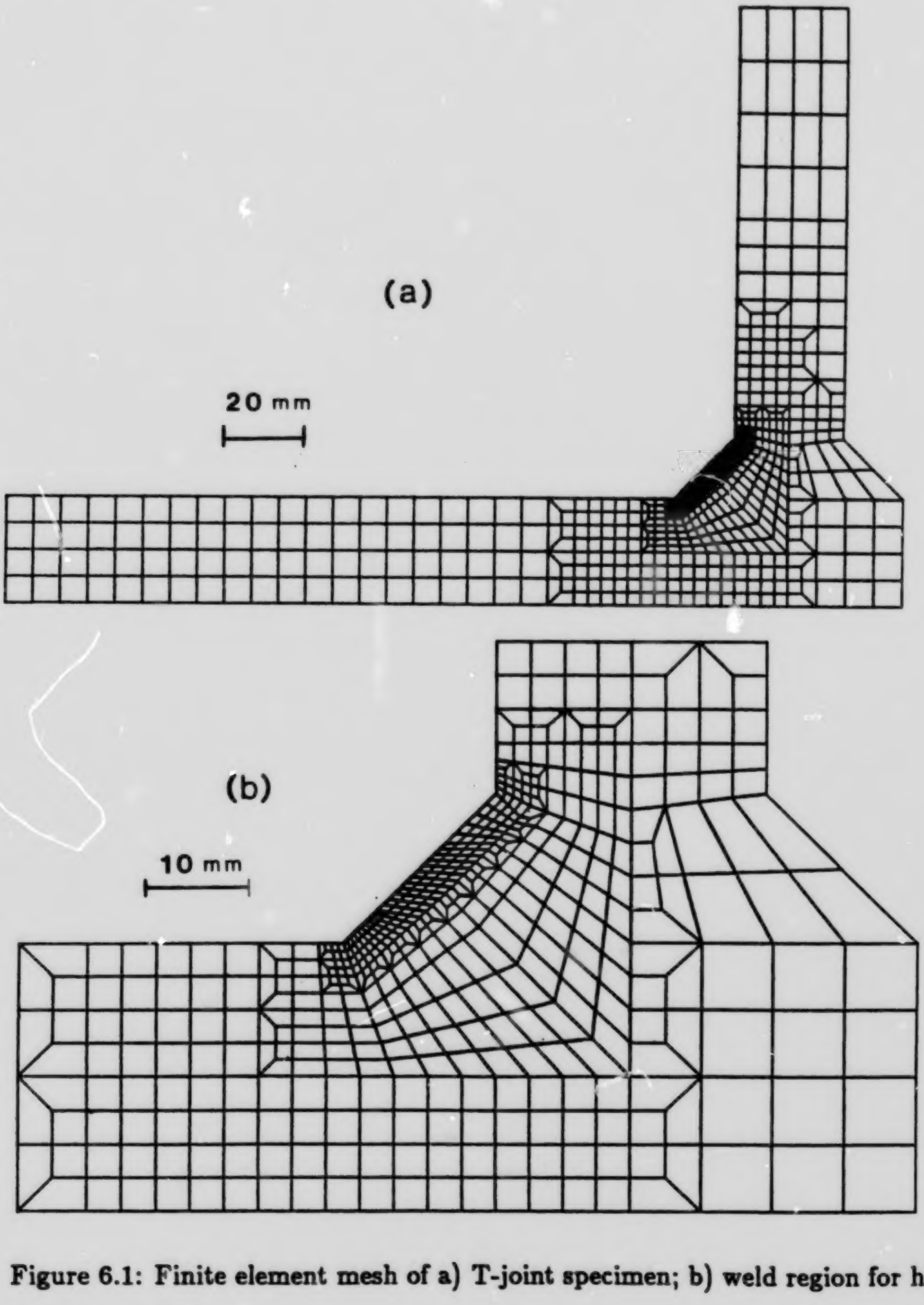
(a)
20 mm
(b)
10 mm

Figure 6.1: Finite element mesh of a) T-joint specimen; b) weld region for heat transfer analysis

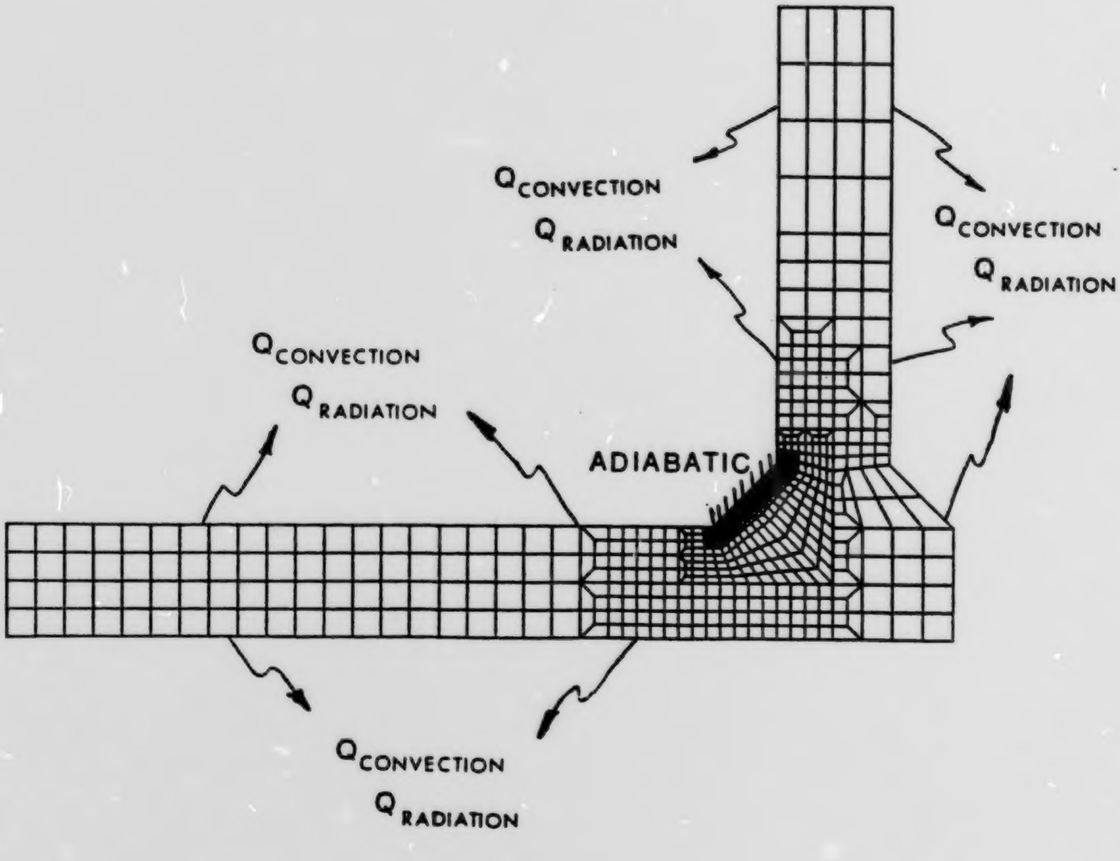
Q CONVECTION
Q RADIATION
Q CONVECTION
Q RADIATION
Q CONVECTION
Q RADIATION
ADIABATIC
Q CONVECTION
Q RADIATION

Figure 6.2: Thermal boundary conditions for T-joint specimen analysis

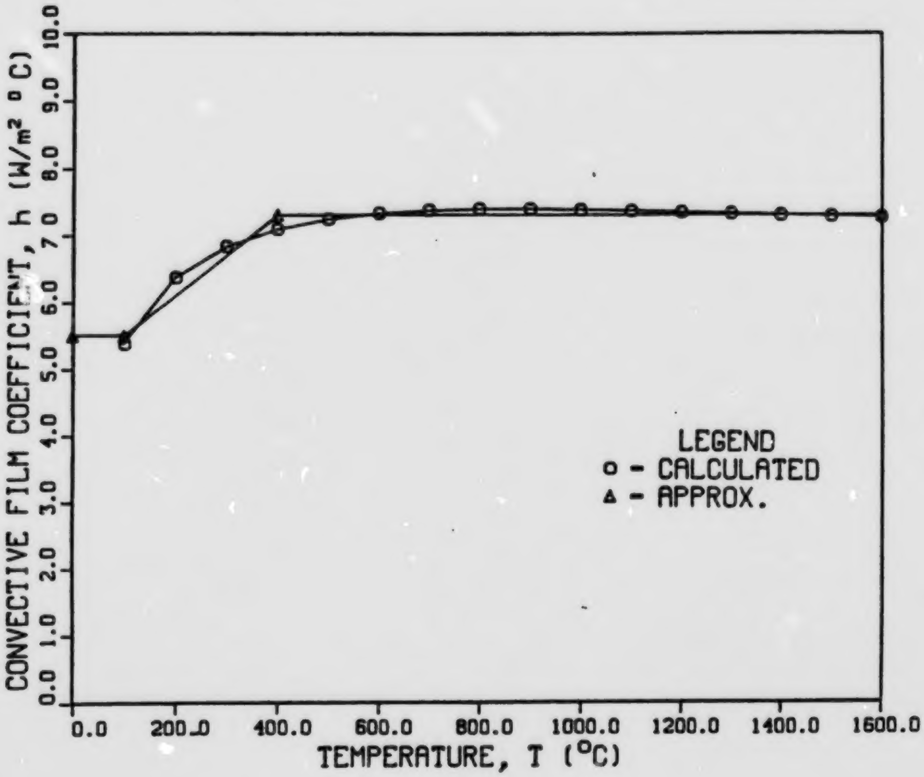

Figure 6.3: Convective film coefficient for T-joint specimen analysis

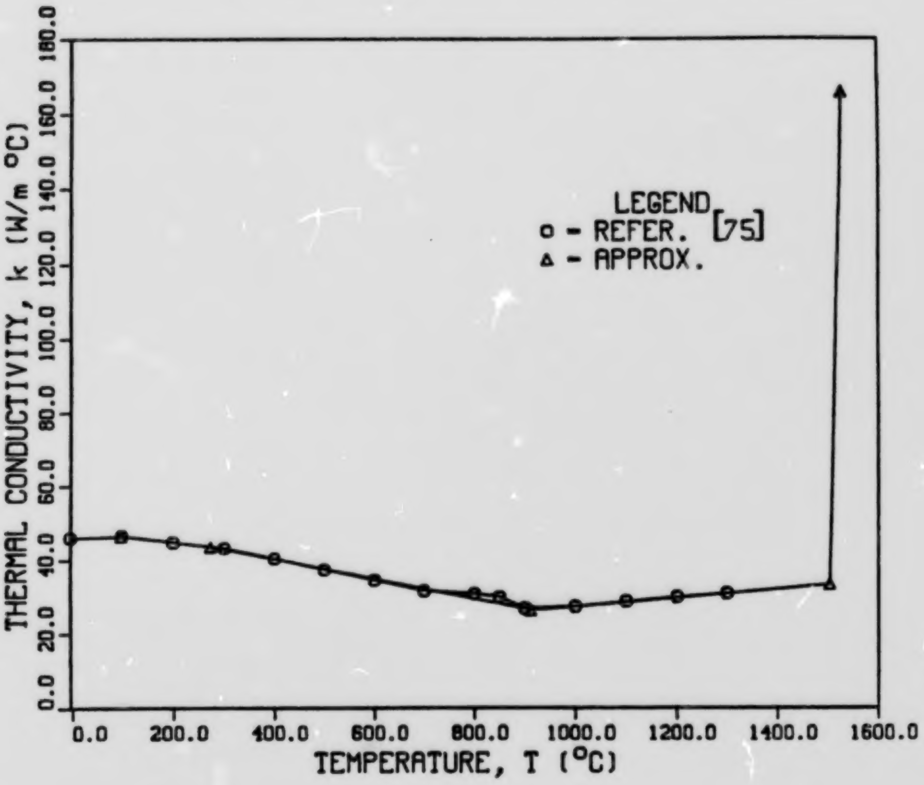

Figure 6.4: Thermal conductivity for T-joint specimen analysis

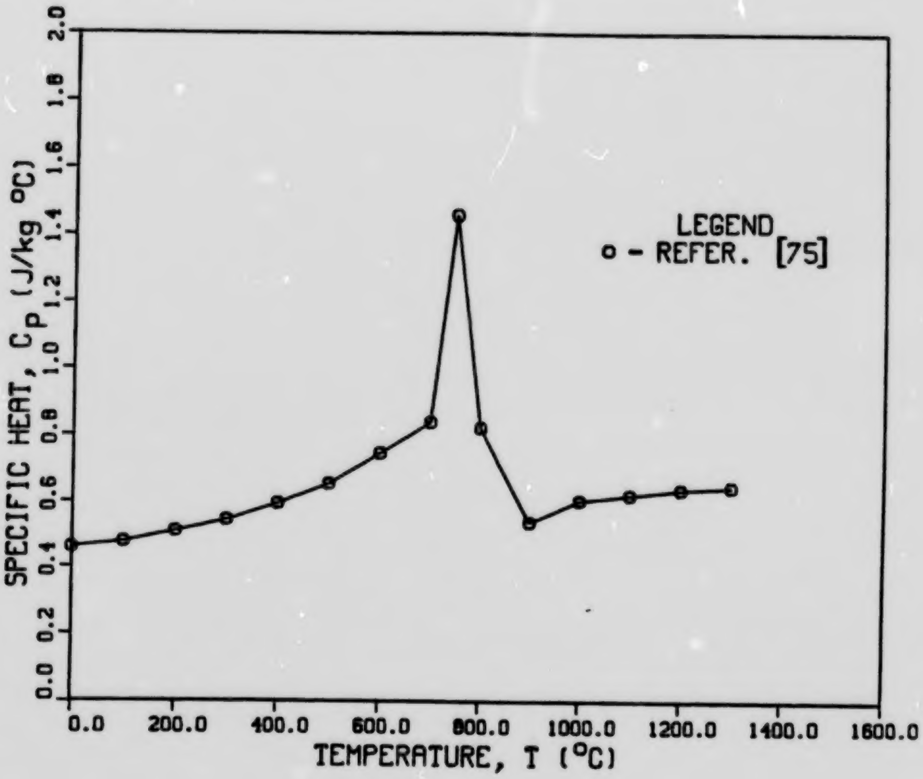

Figure 6.5: Specific heat for T-joint specimen analysis

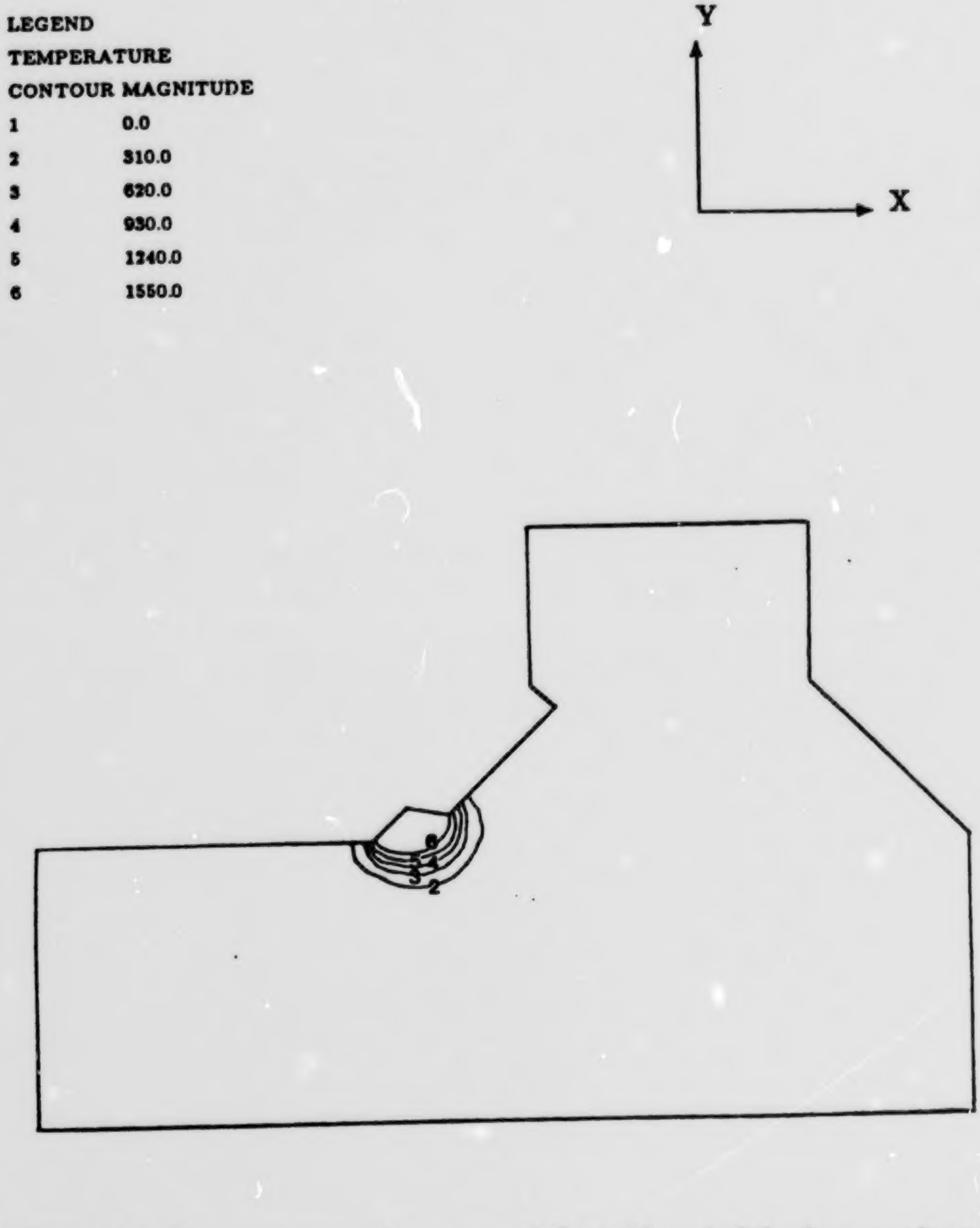

Figure 6.6: Temperature contours around the weld pool of the first capping pass

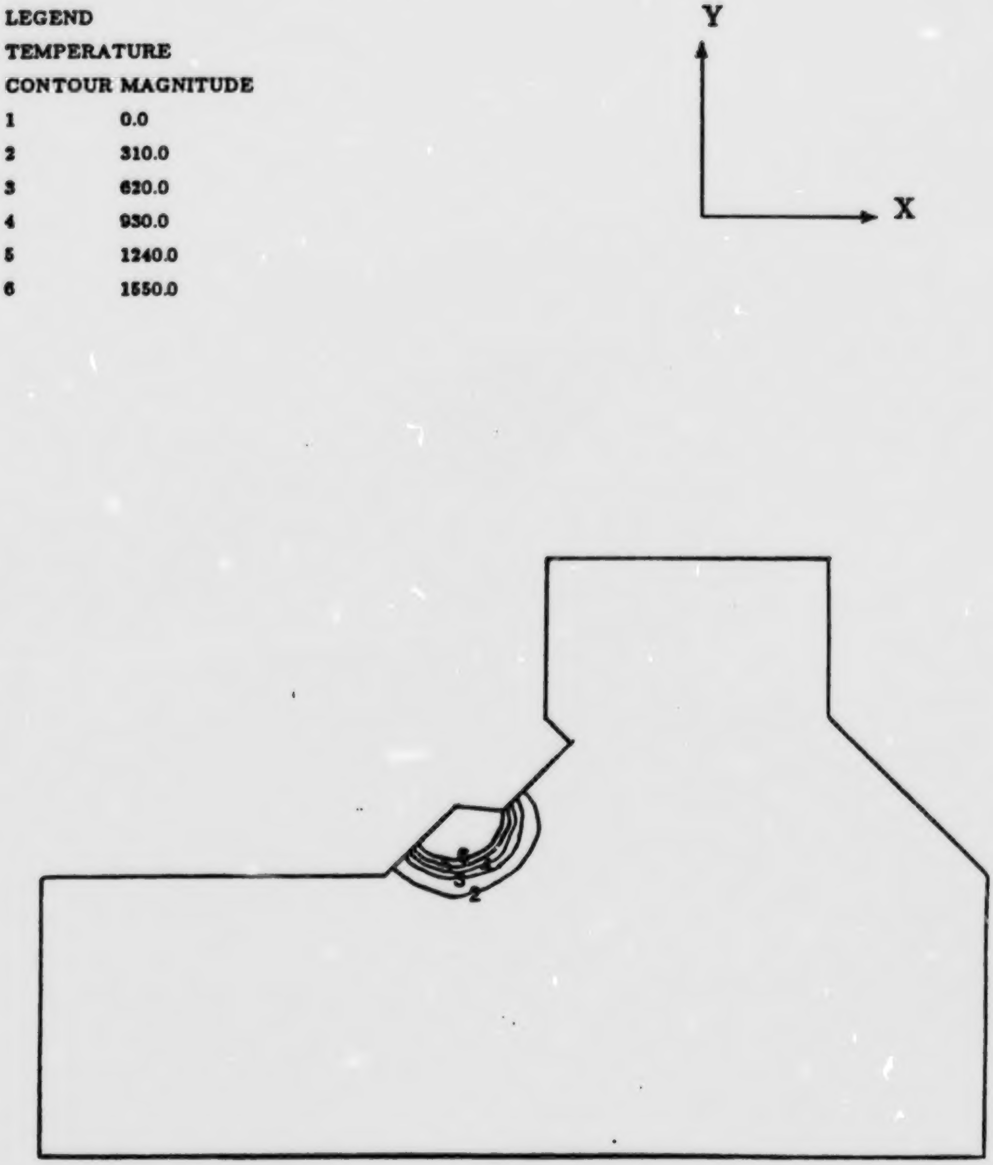

Figure 6.7: Temperature contours around the weld pool of the second capping pass

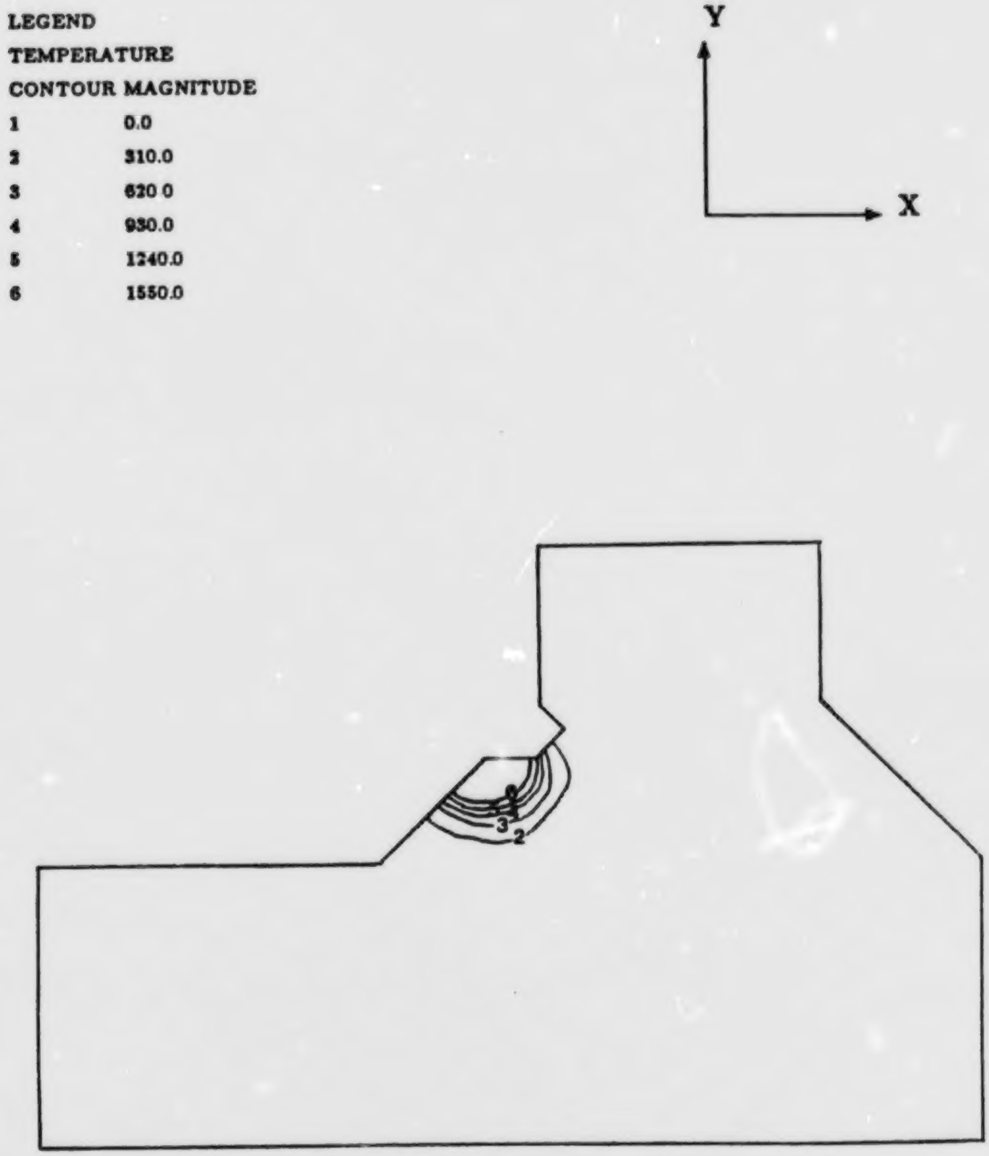

Figure 6.8: Temperature contours around the weld pool of the third capping pass

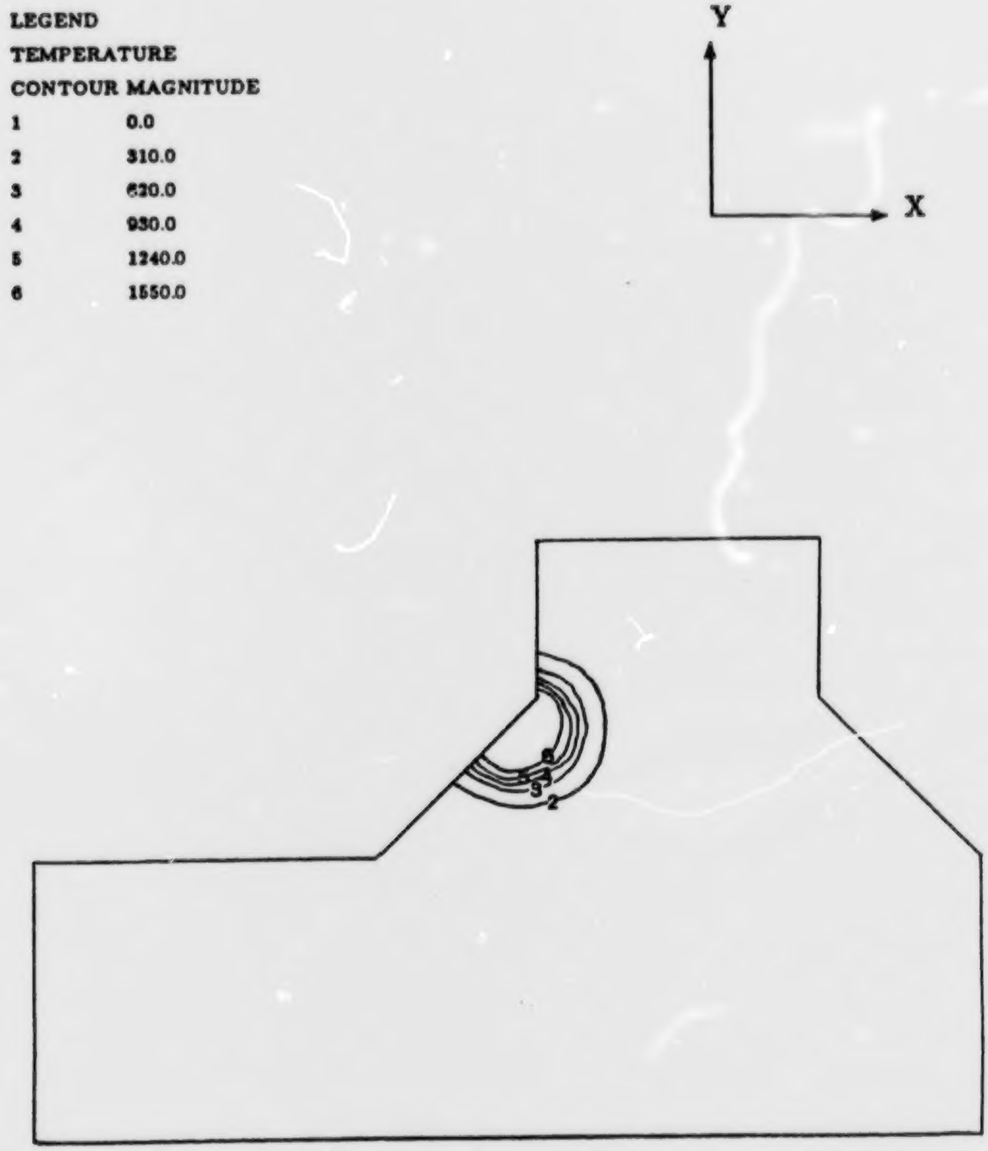

Figure 6.9: Temperature contours around the weld pool of the last capping pass

(a) NODE 120 AND 22128

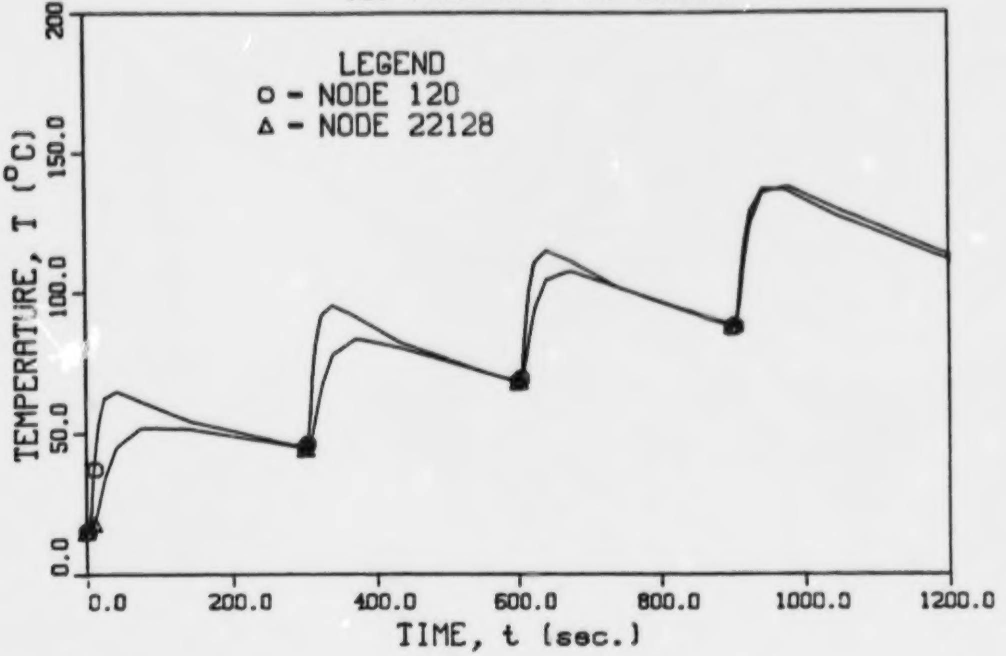

(b) NODE 16106

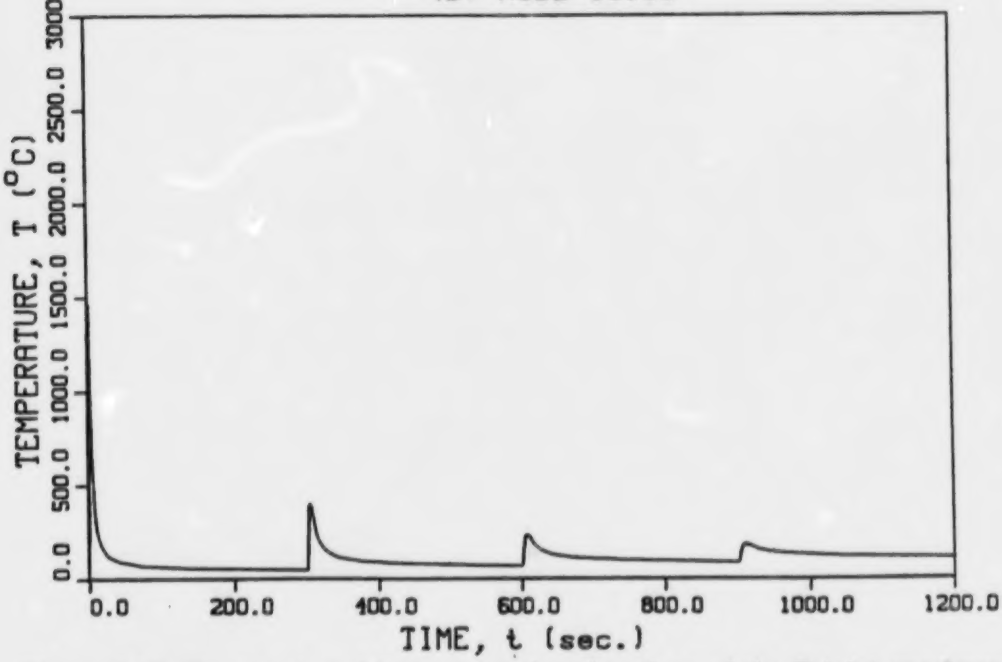

Figure 6.10: Temperature history at various locations of the T-joint specimen

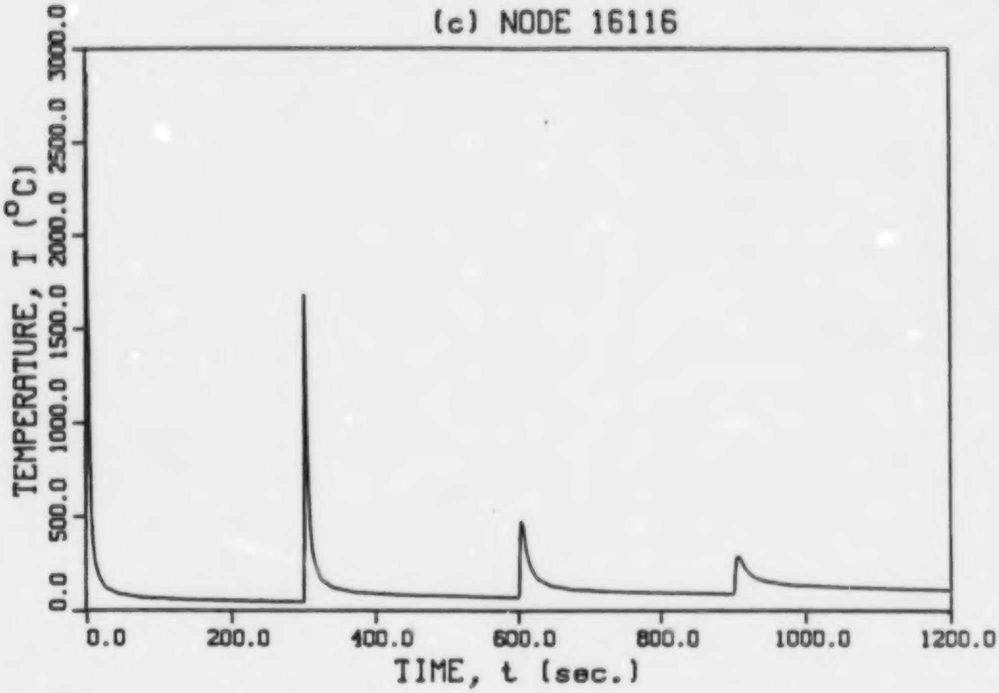

(c) NODE 16116

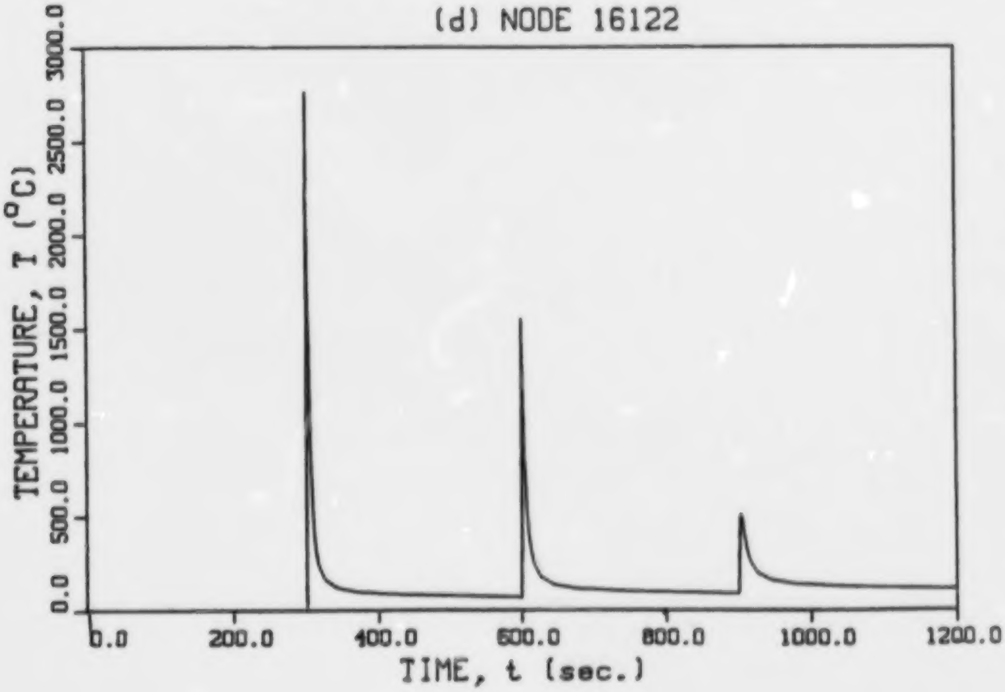

(d) NODE 16122

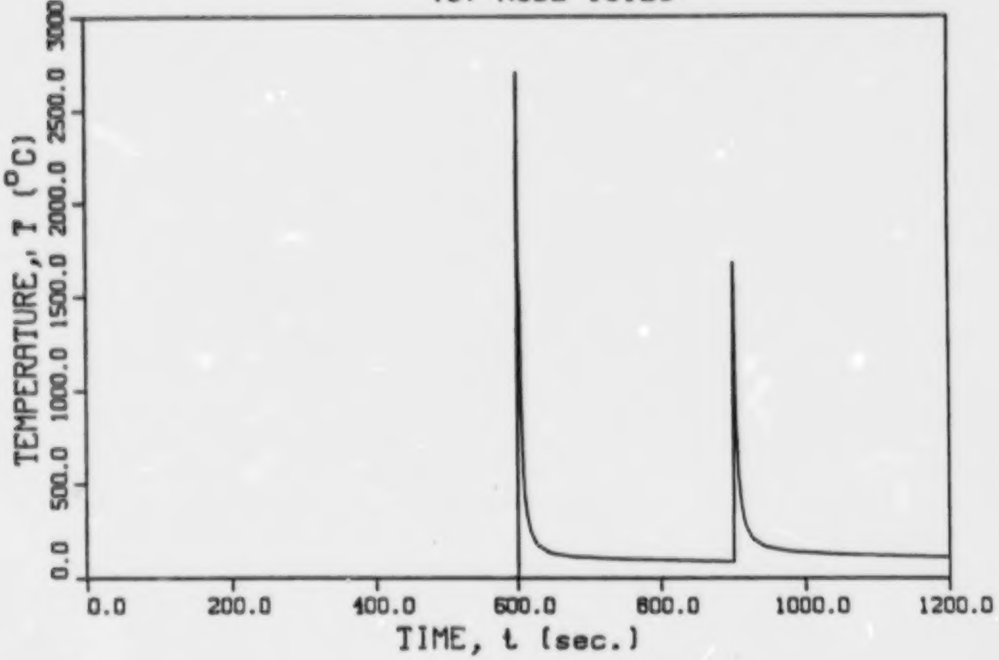
(e) NODE 16128

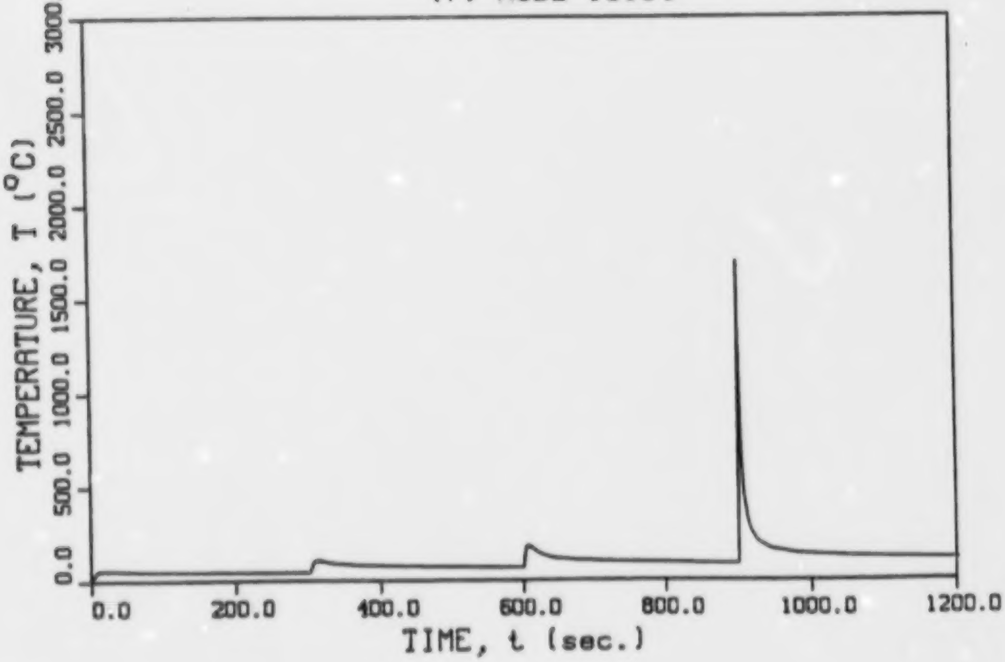
(f) NODE 16134

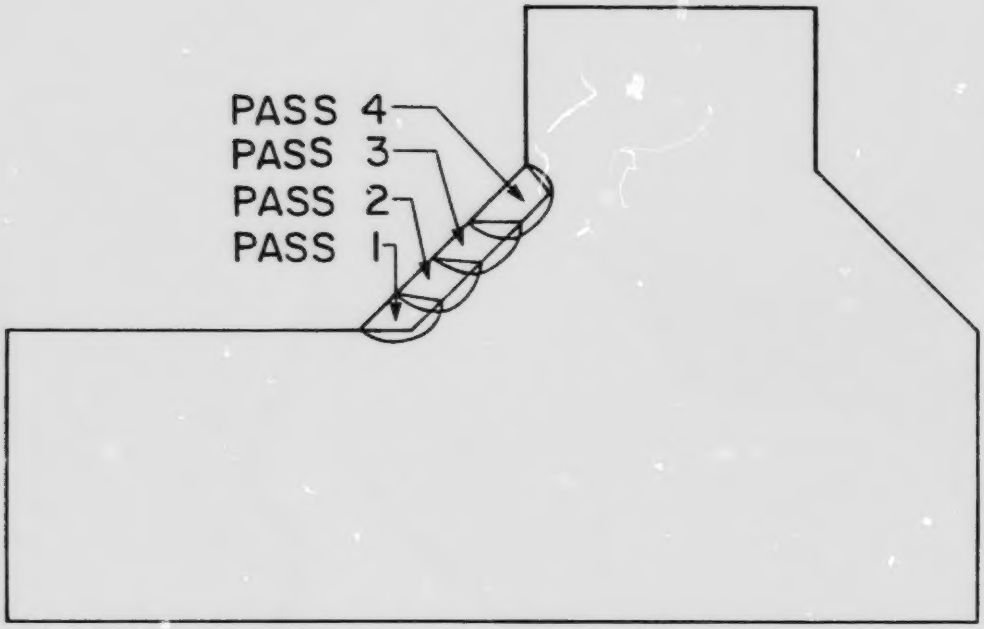
PASS 4
PASS 3
PASS 2
PASS 1

Figure 6.11: Weld pool shape of the capping passes

Chapter 7

Thermal Stress Analysis Of The T-Joint Specimen

As indicated in Chapter 5, numerical models of welding residual stress have generally been restricted to simple welding geometries. To the author's knowledge, analysis of more complex weld geometries such as full or partial penetrating fillet welds in built-up shapes has not been attempted. Furthermore, experimental measurements are also very difficult to find.

In general, the models used by most researchers are adaptable to fillet joints. The method developed by Leung [1,2] for calculating the welding residual stress of multipass butt welds is one such example. In this study, Leung's model was adopted for calculating the welding residual stress of the 26 mm thick, multipass, full penetrating, fillet T-joint specimen used in the fatigue program conducted jointly by the University of Waterloo and EMR/CANMET of Ottawa.

7.1 Computer Model For The Thermal Stress Analysis

The finite element method was used to determine the welding residual stresses from fabrication of the T-joint specimens. The thermal history predicted from chapter 6 was input as thermal loading. Required information such as model geometry, material properties, kinematic boundary conditions, along with the assumptions made, are described in the following sections.

7.1.1 Geometry Considerations

According to DeGarmo et al. [77], a weld bead length of 18 to 20 inches is required to develop sufficient differential shrinkage between the weld metal and the restraining parent metal to generate maximum residual stress in the longitudinal direction of a flat plate. For a weld of this length, the longitudinal residual stress remains constant in a region 9 inches from either end of the weld while the transverse residual stress appears to be independent of weld length. In Leung's analysis, the specimens used were 610 mm long (about 24 inches) in the welding direction, which would guarantee fully developed residual stress in the midplane region. Therefore, a two-dimensional analysis with generalized plane strain elements was carried out for a plane section normal to the welding direction to calculate the welding residual stress in the welded plate. For the T-joint specimens, the welding length is only 254 mm (10 inches) which is much shorter than the 18 inches recommended by DeGarmo. Therefore, it can be considered that the residual stress in the specimen will not be fully developed and that a three-dimensional analysis is desirable. Unfortunately, the cost of such an analysis would be extreme. However, the calculated results of a planar analysis would constitute an upper bound of the actual welding residual stresses and can be performed at a much lower cost. For improved accuracy, the three-dimensional stress field can be modelled with a pseudo 3-D analysis in which generalized plane strain elements are used instead of plane strain element [3].

As indicated before, the residual stress distribution of a fillet welded 'T' shape is basically symmetrical about the center line [56]. Since a balanced welding sequence was used, a symmetric stress distribution is expected and this can be used to reduce computing costs. Calculations were made to determine the validity of this assumption.

7.1.2 Finite Element Mesh

The 4-noded, isoparametric, generalized plane strain, hybrid finite elements (CGPE6H) contained within ABAQUS [3] were used. For the generalized plane strain element, additional degrees of freedom for the last two nodes of each element are used to define the longitudinal displacement and planar rotation of the cross section with respect to the other two axes. For the full analysis (without the symmetry assumption) the cross-section was discretized to the mesh used in the heat transfer analysis (see Figures 7.1a and 7.1b). For the symmetric analysis, only half of the cross section was modelled, i.e., only the left side of the above mesh was used (see Figures 7.2a and 7.2b). This finite element mesh has 544 elements and 1167 nodes.

7.1.3 Kinematic Boundary Conditions

Since the tee specimens were welded without any restraint, every degree of freedom in this problem should be free. However, such a problem is ill-conditioned and a solution will not be guaranteed. Some nodal degrees of freedom have to be fixed in order to prevent divergence of the displacement solution and allow overall equilibrium.

The kinematic boundary conditions are different for the analysis with symmetry and the analysis without symmetry. The boundary conditions for the analysis without symmetry are shown in Figure 7.3. The nodes on the left end of the bottom plate were fixed such that the whole cross section was allowed to rotate. For the analysis with symmetry, no transverse displacements were allowed along the center line (see Figure 7.4). This forced the vertical plate to remain vertical and only allowed the bottom plate to have in-plane rotation. The degrees of freedom corresponding to the longitudinal displacement and out-of-plane rotations calculated by the generalized plane strain element were all free but the longitudinal displacements were confined to remain on a plane.

7.1.4 Material Modelling

With a combination of high thermal loading and softening of the material at high temperatures, the material around the fusion zone will yield in compression during the heating cycle of the welding process. Upon cooling, reverse plasticity occurs as the metal contracts. The constitutive relationship must be able to model all the above effects. The material model used in the thermal stress calculation was a time-independent thermo-elastic-plasticity model with temperature dependent material properties. The Von Mises yield criterion and the associated flow rule were adopted. The material around the fusion zone behaves incompressibly when melted, and large hydrostatic stresses are created which can cause numerical problems. To overcome this, a hybrid element was used in which the hydrostatic stress was determined as an interpolated state variable.

After initial yielding of the material, the steel will strain harden. This hardening effect can be modelled by either an isotropic hardening model which allows the yield surface to expand after initial yielding or a kinematic hardening model which allows the yield surface to translate but not change in size. Since the material around the fusion zone can experience reverse plasticity during welding, the Bauschinger effect can be significant. This effect can be magnified in multipass welds. The actual material behavior is probably a combination of the two hardening models. However, the most important features can be modelled with the kinematic hardening model and this model was used in this study.

During the fabrication of the T-joint specimens, some material, especially near the weld, remains at a temperature much higher than room temperature through the combined effect of many weld passes (typically 26 passes for the 26 mm specimens) and a high interpass temperature (230°C). With these conditions, creep of the metal could occur. However, in this study, this effect was neglected, because the affected region was small compared to the whole specimen.

7.1.5 Mechanical Material Properties

For a thermal stress analysis, the material properties required are the elastic modulus (E), Poisson's ratio (ν) and the linear thermal expansion coefficient

(α). For the kinematic hardening model used in ABAQUS [3], a bi-linear stress strain curve is required for which the yield stress (σ_y) and the tangent modulus (E_t) are defined. The properties of the specific steel used (Table 6.1) was not found in the literature, but the steel used in Andersson's analysis [38] was of similar chemical composition (see Table 7.1) and room temperature strength. Therefore, the mechanical properties in Andersson's paper were used in this study.

The elastic modulus as a function of temperature is shown in Figure 7.5. The value at 1600°C was not set to zero, as in Andersson's paper, to avoid numerical problems. The values of Poisson's ratio are shown in Figure 7.6. Poisson's ratio should approach a value of 0.5 when the material melts to satisfy the criterion of incompressibility. However, this will cause numerical problems. Leung [2] found that the calculated residual stresses are not very sensitive to the values used. Therefore, a value of 0.3 was used at temperatures above room temperature in this analysis. The values for the linear thermal expansion coefficient were reported by Touloukian et al. [78] for manganese steel with a similar chemical composition (see Figure 7.7). These values were very close to those reported by Goldsmith et al. [79]. The yield stress and the tangent modulus are presented in Figures 7.8 and 7.9 respectively. Again, the values near melting were modified to avoid any numerical problems.

The material properties for temperatures below 15°C as shown in Figures 7.5 to 7.9 were fictitious and will be explained in the next section.

The manganese steel studied will experience allotropic phase transformations during both the heating and cooling cycle of the welding process. These transformations are accompanied by volumetric contraction and expansion. As concluded in the first part of this Report, this effect is believed to have only a minor effect on the welding stress. Therefore, phase transformation effects were neglected in this study.

7.1.6 Solution Strategy

As discussed in Chapter 6, only the final layer of capping passes were chosen to be analyzed in this study. However, the residual stress from previous passes must be accounted for. One method is to input the previous residual stress as an initial stress before the capping passes are deposited. This method requires knowledge of the previous residual stress distribution. Unfortunately, at the beginning of this study, only the longitudinal stress distribution along the surface of a similar T-shape was found in the literature [56]. This was insufficient for an accurate prediction of residual stresses. Therefore rather than guessing the stress distribution with only limited data, it was decided to initially analyze the capping passes without any previous residual stresses. Subsequent analyses could then be undertaken after studying the development of residual stresses in the capping passes of the T-joint specimen with a more informed estimate of previous residual stresses.

Another question that was addressed in the solution strategy was the assumption of symmetry. This was studied by analyzing the first capping pass with and without the symmetry assumption. If the two sets of calculated residual stress distributions differ significantly, then symmetry cannot be assumed and the whole cross section has to be modelled. However, if the differences are small, then the symmetry assumption can be made and the computation greatly reduced.

There are four capping passes in the specific T-joint specimen being modelled. Further saving of computation can be made if passes can be grouped. Leung [2] found that in a layer of weld passes, the transverse residual stress is not fully developed until the last pass is deposited. Therefore, a layer of passes can be modelled in two analyses. The first analysis combines all the passes in the layer except the last pass by combining the various temperature histories with an envelope technique. The different thermal histories are first set to a common time frame. The temperature at any time is represented by the highest temperature from the different histories. In this study, the four capping passes were combined into three analyses with the second and third passes grouped. The first pass was not grouped as suggested by Leung's scheme, because this pass would form the weld toe region which is of particular interest in the next phase of this study, i.e., loading of the T-joint specimen.

In his study of multi-pass welds, Leung found that if elements for the undeformed filler material of subsequent passes were introduced into the already deformed weld preparation, the calculated residual stress from previous passes would be modified significantly. He developed a scheme in which the elements were introduced with the yield strength of molten metal and applied the displacements of the interface nodes as boundary condition so that the elements would fit into the weld preparation without introducing any stress. This scheme was used in this study. The material properties as shown in Figures 7.5 to 7.9 for temperatures below 15°C were fictitious. The yield strength and the elastic modulus were assigned values equal to those above the melting temperature. The linear thermal expansion coefficient was set to zero. Various values of yield stress and elastic modulus were studied since if the material is too soft the solution will diverge.

As mentioned in Chapter 6, the calculated maximum temperature in the fusion zone was above 2800°C which is much higher than the melting temperature of this steel. This would cause numerical problems in the thermal stress calculation and therefore, the calculated thermal history was modified such that temperatures exceeding 1550°C were reduced to 1550°C.

The thermal stress analysis of the T-joint specimen was carried out in three stages. The first stage was to verify the symmetry assumption and the results are presented in Section 7.2. In the second stage the welding residual stresses due to the capping passes alone were calculated as described in Section 7.3. In the last stage the effect of residual stresses from previous passes was included in the results as described in Section 7.4. The ABAQUS input data files are listed in Appendix C.

7.2 Verification Of Symmetry Assumption

The symmetry assumption was verified by calculating the residual stress created as the first capping pass was deposited with and without the assumption of symmetry.

The displaced mesh for both analyses are shown in Figures 7.10 and 7.11. As can be seen there is very little distortion in the fusion zone. The end of the bottom plate was displaced by 0.5 mm in the analysis with the assumption of symmetry while the other analysis predicted almost no displacement.

The stress contours near the weld region of the analysis without the symmetry assumption are shown in Figures 7.12 to 7.15. The corresponding plots for the analysis with the symmetry assumption are shown in Figures 7.16 to 7.19. No significant differences were observed between the results of the two analyses.

The longitudinal compressive zone below the weld region is larger in the analysis with the assumption of symmetry which reflects the higher degree of restraint caused by this assumption.

The stress distributions along the top and bottom surface and through the plate thickness below the weld toe for both analyses are plotted in Figures 7.20 to 7.28. Again, no significant differences were observed. The transverse residual stress (X-component) along the bottom surface for the case with symmetry assumption is about 50 MPa higher than the other case. This is a direct consequence of the greater transverse restraint imposed by the symmetry assumption. However, the overall difference was sufficiently small to suggest that the symmetry assumption is reasonable.

7.3 Residual Stress Due To The Capping Passes

The thermal stress analysis with the symmetry assumption was continued with the RESTART option in ABAQUS [3]. The second and third capping passes were combined into one analysis. This was followed by the last capping pass.

7.3.1 Residual Stresses Due To The First Capping Pass

The stress contours of the first capping pass are shown in Figures 7.16 to 7.19. The surface stresses and the stresses below the weld toe are plotted in Figures 7.29 to 7.37 for each of the weld passes.

Transverse Or X-Residual Stress

Tensile stresses were observed near the top and bottom surface and in the weld region (see Figure 7.16). These zones occupy the top and bottom 6 mm of the plate, which correspond to about one quarter of the plate thickness from both surfaces (Figure 7.31). A zone of compressive stress was found in the center of the bottom plate. A high stress gradient was observed between the tensile and compressive stress zone. In the bottom plate the stress decreased to zero about 40 mm from the center line of the specimen. In the vertical plate away from the weld, the stress also decreases to zero.

This stress distribution is different from that created by a butt weld. The tensile stress zone along the bottom surface was caused by bending action due to the contraction of the weld metal during cooling. The tensile zone on top was due to the high degree of transverse restraint caused by the vertical brace plate which prevented the contraction of the weld metal. For equilibrium, a compressive zone was generated in the center of the plate.

Y-Residual Stress

In general, the Y-component of the residual stress was very small (Figure 7.17). The highest tensile stress, about 150 MPa, was found near the surface of the unwelded cavity. A small zone of low compressive stress was predicted in the weld region. The stresses along the top surface (Figure 7.32) and bottom surface (Figure 7.33) are approximately zero. A small zone of tensile stress was also predicted just below the surface at the weld toe (see Figure 7.34).

This component builds up in a series of steps as each layer of weld passes are deposited. Since no initial residual stress was assumed, this stress component was not expected to develop until all capping passes were deposited.

Longitudinal Or Z-Residual Stress

High longitudinal tensile stresses were predicted to surround the fusion zone of the first capping pass with a high stress gradient (see Figure 7.18). Compressive stresses were predicted in the bottom two thirds of the plate thickness (also see Figure 7.37). The stress on the top surface decreased very quickly from high tensile stress at the weld toe to slightly compressive at about 35 mm from the center line of the specimen (see Figure 7.35). On the bottom surface, zero stress was predicted directly below the vertical plate and about 120 mm from the center of the specimen with compression in between (see Figure 7.36).

This stress distribution is different from that created in a butt weld. Below the fusion zone, the residual stress changes from tensile to compressive through the plate thickness instead of being tensile throughout. This could be a result of the combined effect of greater longitudinal restraint of a T-shape and greater plate thickness. The contraction of the weld metal during cooling is restricted more effectively by the surrounding metal. Thus compressive stress results in the lower portion of the plate.

Plastic Zone Size

The plastic zone (region where the Von Mises equivalent stress is greater than the room temperature yield stress, 350 MPa) was observed to enclose a region of about 7 mm radius centered around the first capping pass (refer to Figure 7.19).

7.3.2 Residual Stresses Due To The Remaining Passes

The final deformed meshes of the T-joint specimen in the area of the weld region are shown in Figures 7.38a and 7.38b respectively. A vertical displacement of about 1 mm at the end of the bottom plate was predicted. However, this does not agree with measurements of distortion on the actual specimen (about 5 mm) because the accumulated distortion of the previous passes are not included.

The residual stress contours for the combined second and third passes are plotted in Figures 7.39 to 7.42. The contours for the last pass are shown in Figures 7.43 to 7.46. There were no dramatic changes to the residual stress distributions after the first capping pass except a gradual build up as each pass was deposited, especially the Y-stress component. This trend of stress build up agrees with observations by other researchers [1, 2, 30, 31, 66, 67]. The zone of high residual stress expands and encloses each new weld pass. After the whole cavity was filled, a high stress gradient zone similar to the one in the bottom plate was formed at the weld toe of the vertical plate.

Transverse Or X-Residual Stress

The transverse residual stress at the weld toe became more tensile as each pass was added. A maximum residual stress of 480 MPa was predicted on the top surface (Figure 7.29). On the bottom surface, the same trend of stress build up was observed (see Figure 7.30). A tensile stress of 250 MPa was predicted near the center line of specimen. These surface stresses decreased to zero about 40 mm from the center line. The zone of compressive stress was observed to expand up into the vertical plate (Figures 7.39 and 7.43). The maximum compressive stress at the weld toe was about 300 MPa, 8 mm below the top surface (Figure 7.31).

Y-Residual Stress

The Y-residual stress component built up significantly with each new pass, especially at the weld toe of the vertical plate. The vertical restraint in this region is similar to the transverse restraint at the weld toe of the bottom plate. Therefore, the Y-stress contours for the weld toe region of the vertical plate is similar to the transverse stress contours at the weld toe of the bottom plate (see Figures 7.43 and 7.44). The stresses along the surfaces of the bottom plate were zero as expected (Figures 7.32 and 7.33). The through thickness stress becomes more tensile near the top surface of the plate due to increasing vertical constraint by the weld passes (see Figure 7.34). A maximum tensile stress of about 100 MPa was predicted as deep as 6 mm below the top surface. This stress decreased to zero about one third into the plate thickness.

Longitudinal Or Z-Residual Stress

A zone of high tensile stress can be seen to enclose each new weld pass. After the cavity was filled, the stress contours around the weld region are almost symmetrical about the capping passes (Figure 7.45). The highest tensile stress is observed at the weld toes of both the vertical plate and the bottom plate. The stress along the top surface, near the weld toe did not increase significantly as the weld passes were deposited (see Figure 7.35). A maximum tensile stress of 480 MPa was predicted at the weld toe. On the bottom surface, a build up of compressive residual stress was observed in Figure 7.36. This could be the result of the growing tensile zone as each pass was deposited. In order to achieve equilibrium, the surrounding material becomes more compressive. Below the weld toe, the tensile stress due to the first capping pass was reduced as each additional pass was laid (see Figure 7.37). This could be caused by relaxation due to the high temperature of the additional weld passes.

Plastic Zone Size

The plastic zone extends to about 5 mm below the surface in the first three capping passes (see Figures 7.19 and 7.42). After the last pass was deposited, the plastic zone can be seen to move up along the capping passes and only encloses the final three passes. This zone also extended deeper below the surface (see Figure 7.46) as the restraint increased as the cavity was filled.

7.3.3 Comparison With Measured Residual Stresses

As described in Chapter 5, the welding residual stresses in the T-joint specimen were measured by Holden et al. [63] of Atomic Energy Of Canada Limited at Chalk River with a neutron diffraction technique. These measured values are shown along with the predicted residual stresses in Figures 7.29 to 7.37 for comparison.

Transverse Or X-Residual Stress

On the top surface, the predicted stress agreed well with the measured value in the area of the weld toe region but was somewhat lower away from the weld toe region (Figure 7.29). The largest difference is about 75 MPa. On the bottom surface, excellence agreement was observed with the largest difference being less than 30 MPa (Figure 7.30). The stress distribution through the plate thickness achieved fair agreement with the measured distribution (see Figure 7.31). The predicted compressive stress zone below the weld region was larger and the values were greater than measured. As described in Section 5.3.2, the measured stress distribution through the plate thickness was not in equilibrium due to difficulty in determining the zero strain state in the T-joint specimen during the neutron diffraction measurements. Equilibrium can be achieved if this stress distribution was lowered by about 50 MPa. Much better agreement would be observed between the predicted and measured results (not shown).

Y-Residual Stress

The predicted stress distribution has the same trend as the measured distribution (Figures 7.32 to 7.34), but no agreement in actual values was obtained. This may be because the stress from previous passes were not included in the analysis. On the top surface and bottom surface, the calculated values are generally lower by about 50 MPa, with a larger difference at the weld toe. Note, however, that the measured distributions shown in Figures 7.32 and 7.33 were measured below the surface. This is the reason for the values not being zero as would be expected. Through the plate thickness (Figure 7.34), the largest difference between the numerical and measured results is about 100 MPa.

Longitudinal Or Z-Residual Stress

The predicted stress on the top surface agreed well with the measured results, especially at the weld toe (Figure 7.36). The numerical values are about 50 MPa lower away from this region. On the bottom surface (Figure 7.36), a difference of about 100 MPa was observed between the numerical and measured results near the center line of the specimen. However, better agreement was achieved in region further away. The difference was about 50 MPa at 50 mm from the center line. Good agreement was observed for the stress distribution through the plate thickness (Figure 7.37). The analysis predicted compressive stresses appearing about one third into the plate thickness while compressive stresses were measured only in the bottom half of the plate.

In general, the predicted residual stress without inclusion of residual stress from previous passes achieved reasonable agreement with results measured by the neutron diffraction technique. The small differences, usually less than 50 MPa, are most likely caused by neglecting the existing stresses in the specimen before the capping passes were deposited. This effect is examined in the next section.

7.4 Effect Of Previous Welding Stress

In this section, the residual stress of the capping passes were calculated with the inclusion of existing stresses from the previous passes. In the first part, the residual stresses of the previous passes were introduced. In the second part, the residual stress of the first capping pass was calculated.

7.4.1 Residual Stress Distribution Of Previous Passes

Since the exact stress distribution resulting from the previous passes was not known, a distribution was assumed. In order to achieve the best estimate, the results from the analysis described above were used as the basis for the assumed distribution. The residual stress distributions reported above were remapped to be closer to the center line of the specimen and were treated as initial stresses. Steps were taken to assure that equilibrium was achieved before the residual stress calculations were begun. The assumed stress distributions are shown in Figures 7.47 to 7.50.

7.4.2 Residual Stress Due To The First Capping Pass

Since the sequence of residual stress build up in the capping passes was known, only the first capping pass was analyzed to determine the effect of the assumed residual stress on the final residual stress distributions.

The residual stress contours due to the first capping pass are shown in Figures 7.51 to 7.54. The stress distributions along the surfaces and through the plate thickness of the bottom plate are plotted in Figures 7.55 to 7.63. The stress distributions of the assumed residual stress (designated as A.R.S.) and the results of the analysis without the assumed residual stress (designated as WITHOUT A.R.S.) at the same locations, are also presented for comparison.

After the first capping pass was deposited, no dramatic change from the assumed residual stresses was observed except in the region where the new weld pass was deposited (compare Figures 7.47 to 7.49 with Figures 7.51 to 7.53). In the area away from the first capping pass, the residual stresses take on the values of the stresses already existing in the specimen. This is especially true for the transverse stress and the longitudinal stress as seen in Figures 7.56 and 7.62. In the area surrounding the new fusion zone, the residual stresses of previous passes appeared to be removed by the high welding temperatures and the new weld pass is responsible for the final residual stresses in this region (compare Figures 7.51 to 7.53 with Figures 7.16 to 7.18). This effect can be seen clearly in Figures 7.55, 7.58 and 7.61 in which the residual stresses on the top surface of the bottom plate are plotted. The predicted stresses at the weld toe were nearly identical for the analyses with and without assumed stresses. The assumed Y-residual stress appears to have little or no effect on the final stress (see Figures 7.58 to 7.60).

As suggested in Section 7.3, the welding residual stresses around the weld toe region is mainly due to the layer of capping passes. This is supported by the fact that there is little difference between the results of analyses with and without the inclusion of stress already existing in the specimen. In areas away from the weld toe, the predicted results with inclusion of previous stresses appears to be closer to the measured value than analysis without previous stresses. One interesting note is that the under estimation of the Y-residual stresses (described in Section 7.4.3) was believed to be due to the neglected stresses. However, as seen in the results, the assumed stress distribution appears to have little or no effect on the surface stresses and through the plate thickness below the weld toe. One possible explanation is that the assumed Y-stress distribution under estimated the actual stress. Thus, no significant improvement was observed.

Since the predicted residual stresses around the weld toe between analyses with and without inclusion of previous stresses are essentially identical, the final residual stress in this region will be similar to those described in Section 7.3. An accurate description of the residual stress distribution around the weld toe region is most important for inclusion in a fatigue calculations. As seen in Section 7.3, the predicted welding residual stress achieved reasonable agreement with measured results. The differences are small enough that the predicted results can be used in the next phase of this study, which is a consideration of loading of the T-joint specimen.

Table 7.1: Chemical composition for steel used by Andersson [38]

Chemical Composition	Percentage %
C	0.13
Mn	1.57
Si	0.20
Nb	0.024
Fe	balance

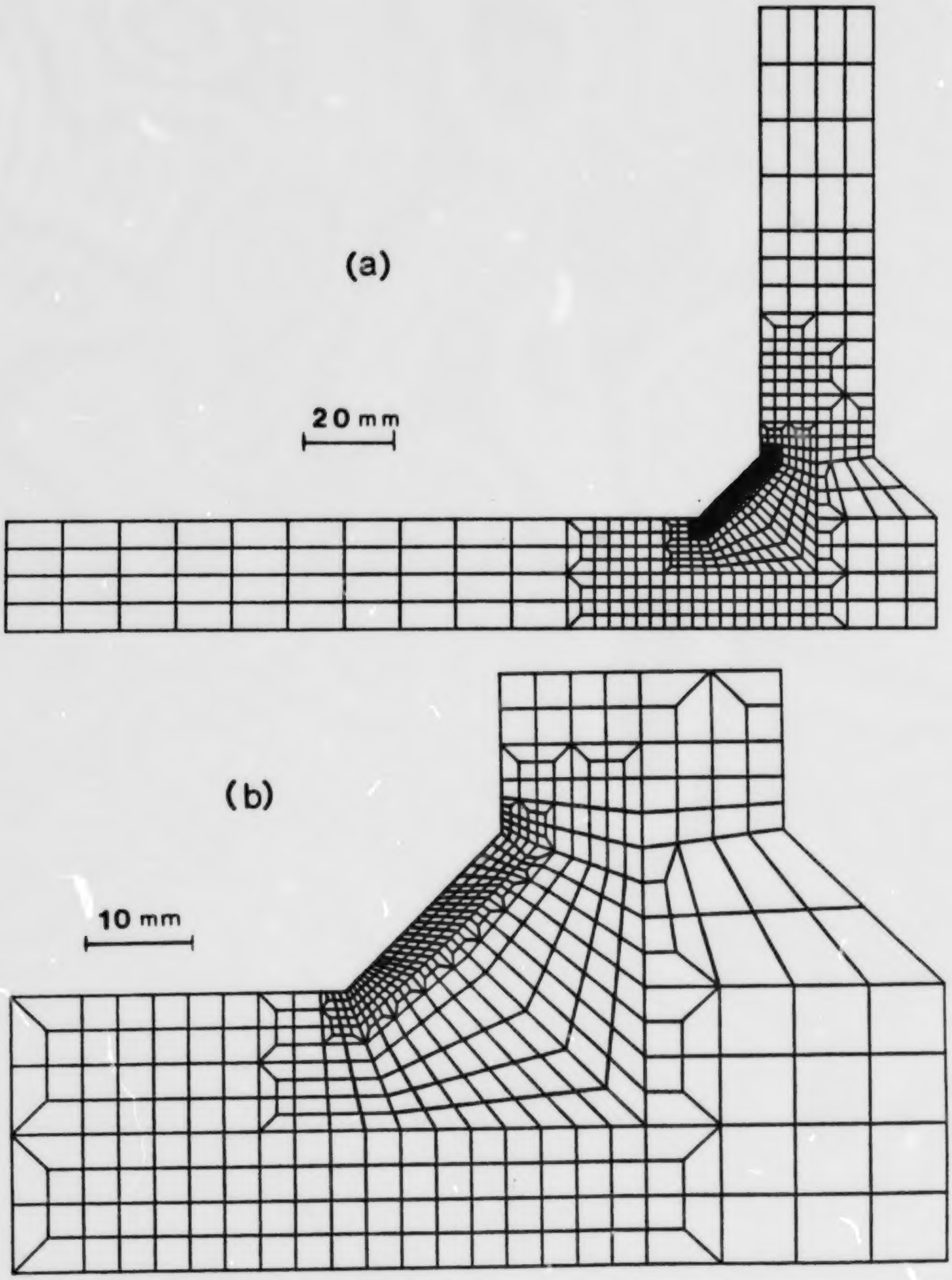
(a)
20 mm
(b)
10 mm

Figure 7.1: Finite element mesh of a) T-joint specimen; b) weld region for stress analysis (without symmetry)

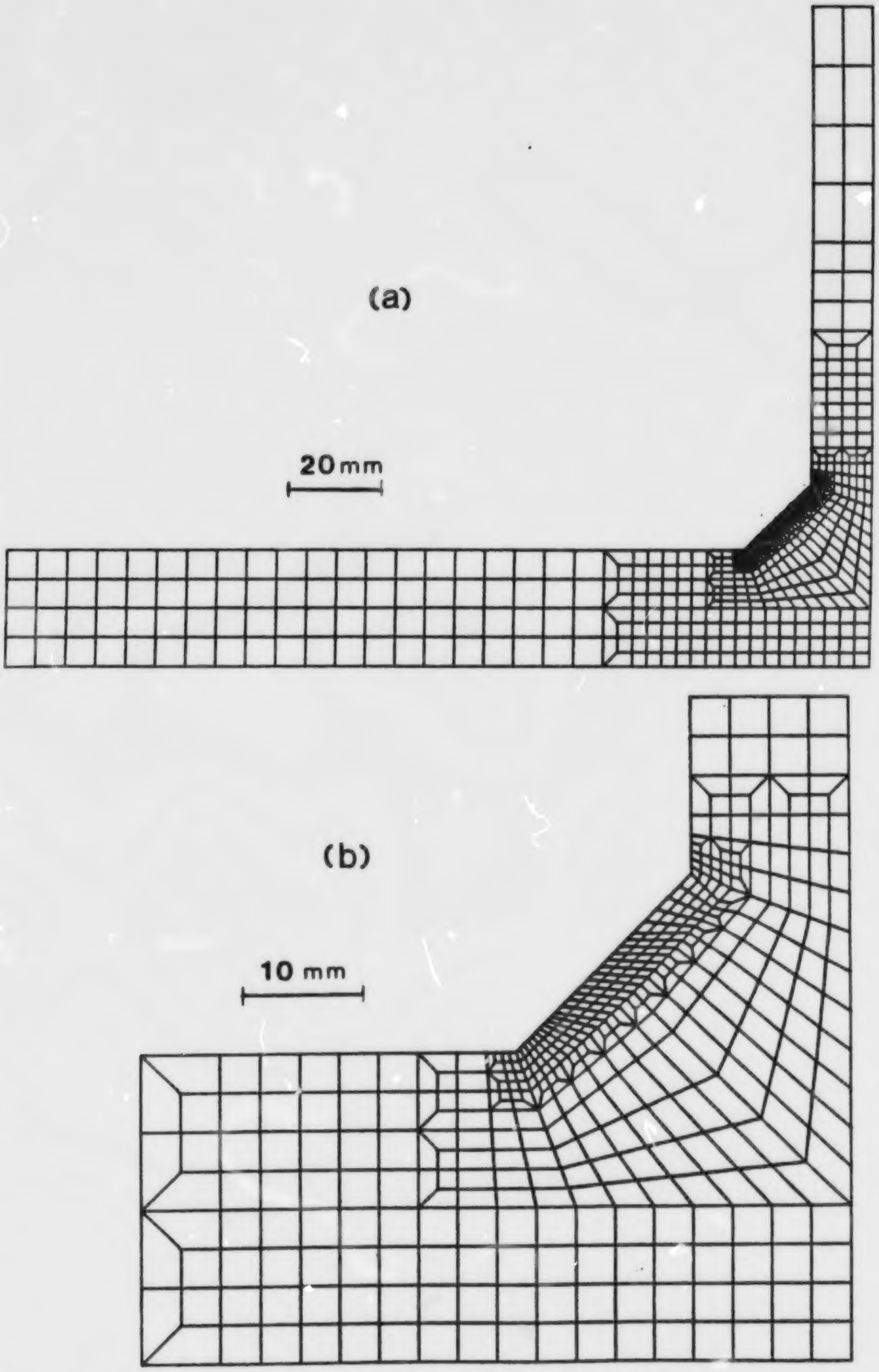
(a)
20mm
(b)
10 mm

Figure 7.2: Finite element mesh of a) T-joint specimen; b) weld region for stress analysis (with symmetry)

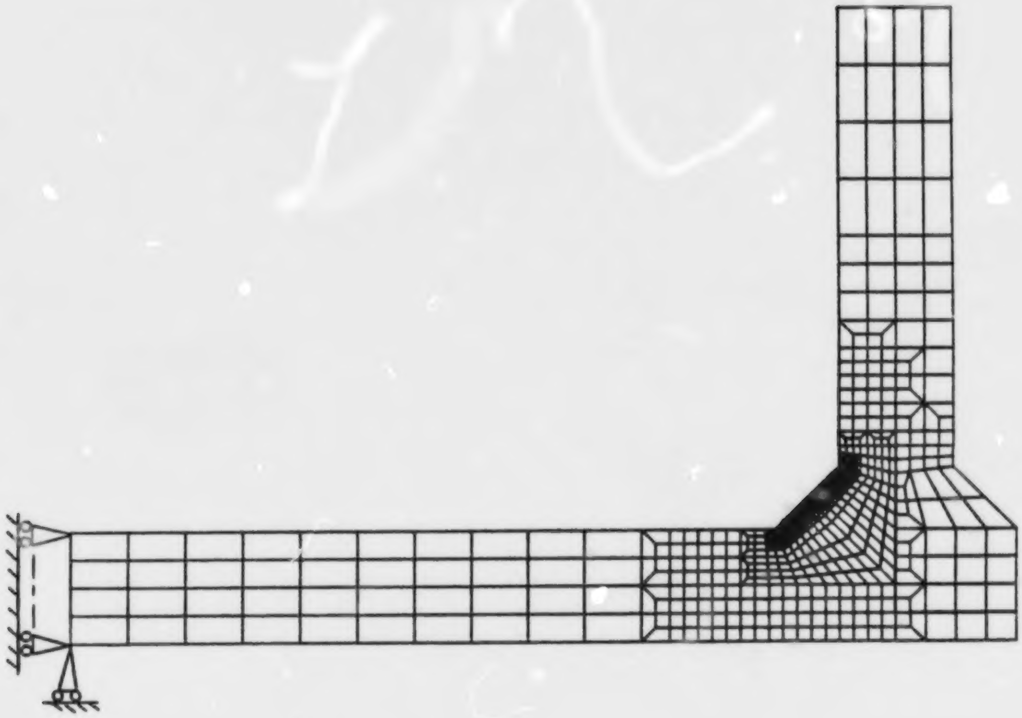

Figure 7.3: Kinematic boundary conditions for analysis without symmetry

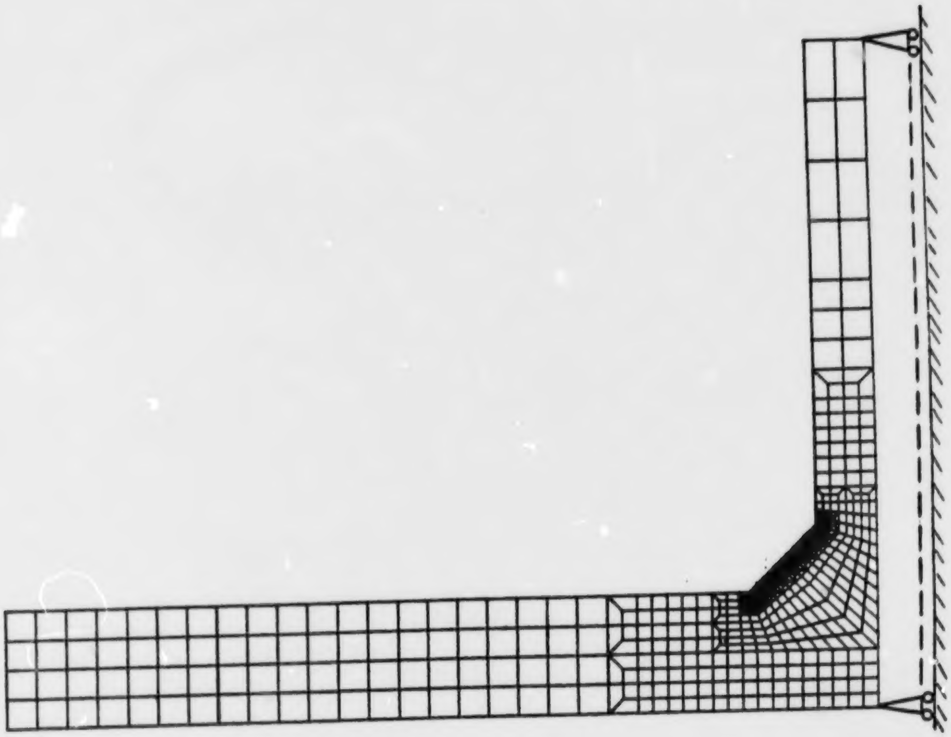

Figure 7.4: Kinematic boundary conditions for analysis with symmetry

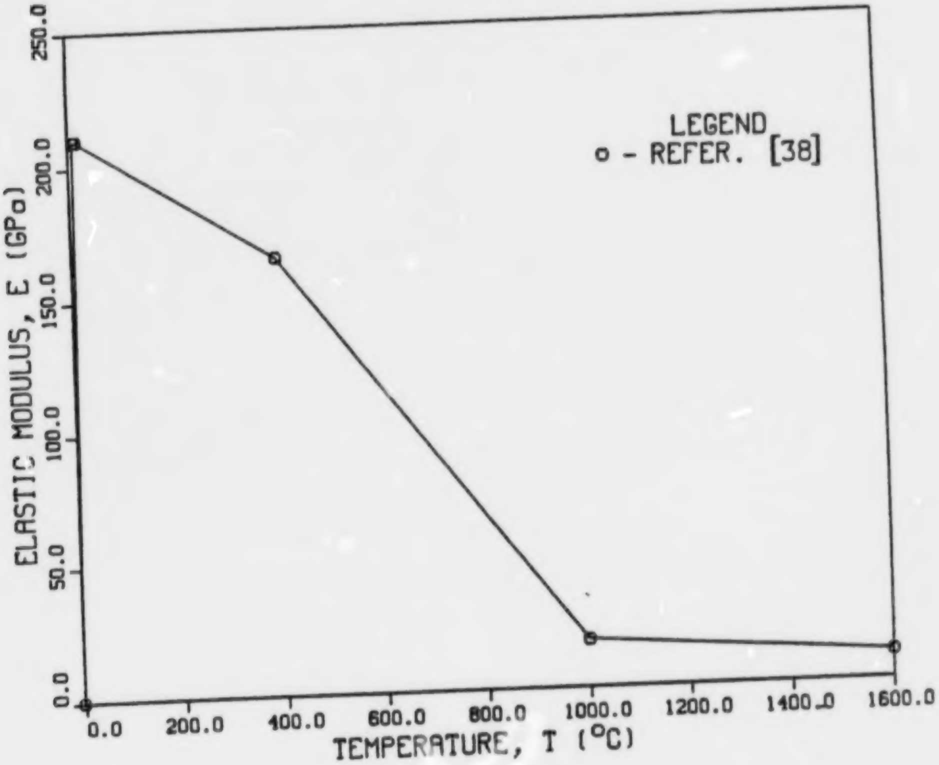

Figure 7.5: Elastic modulus for T-joint specimen analysis

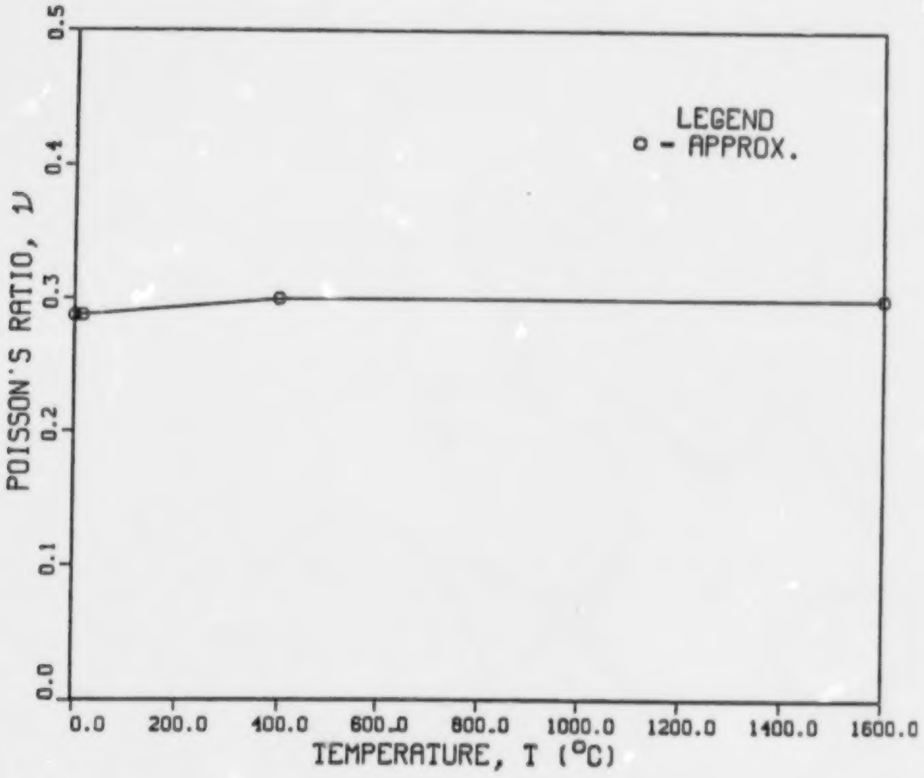

Figure 7.6: Poisson's ratio for T-joint specimen analysis

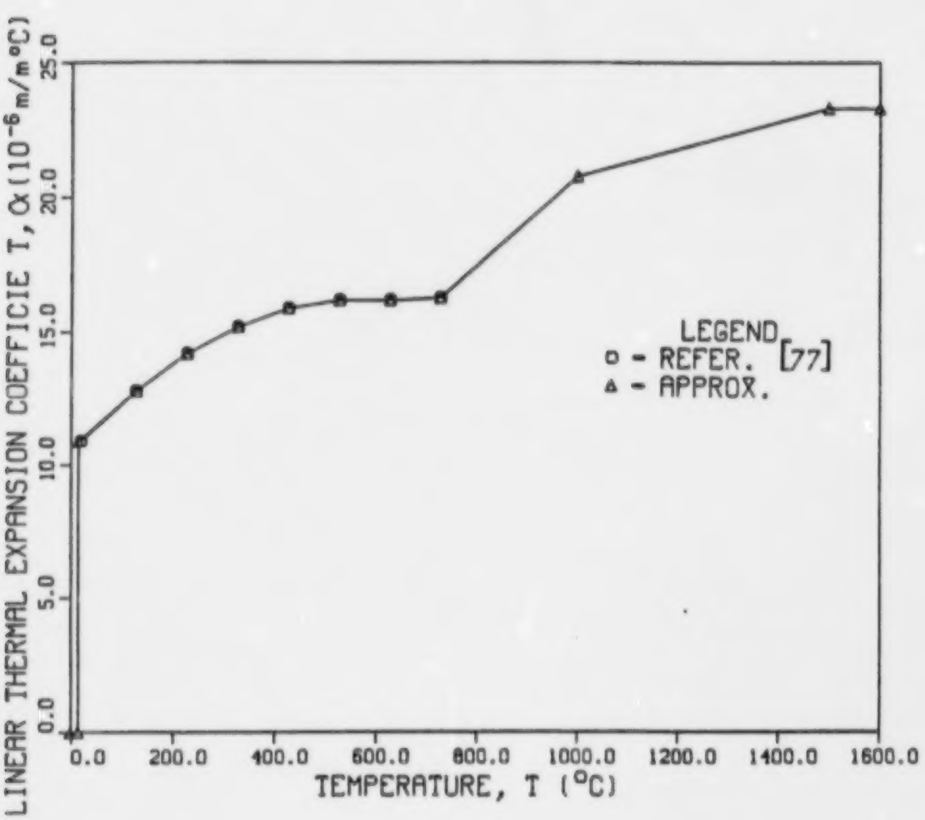

Figure 7.7: Linear thermal expansion coefficient for T-joint specimen analysis

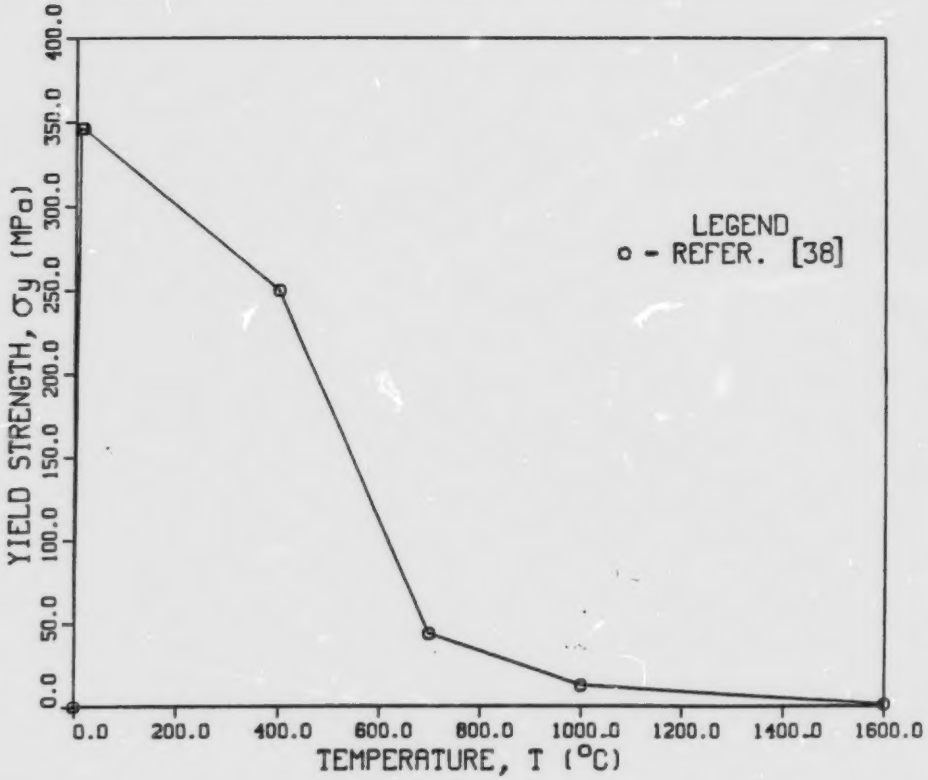

Figure 7.8: Yield strength for T-joint specimen analysis

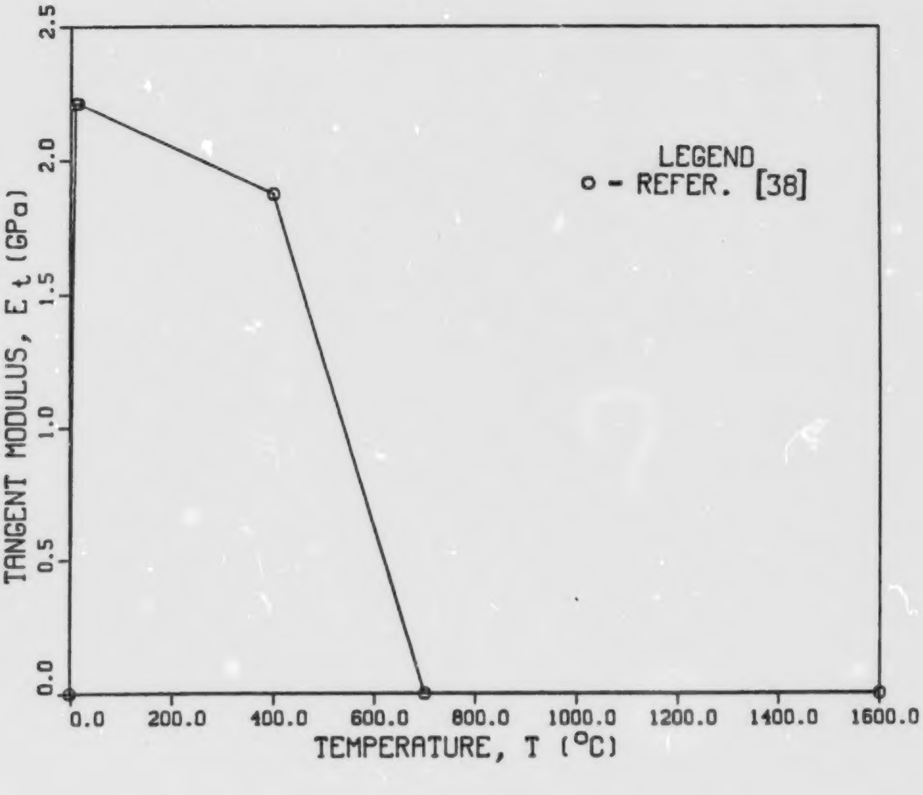

Figure 7.9: Tangent modulus for T-joint specimen analysis

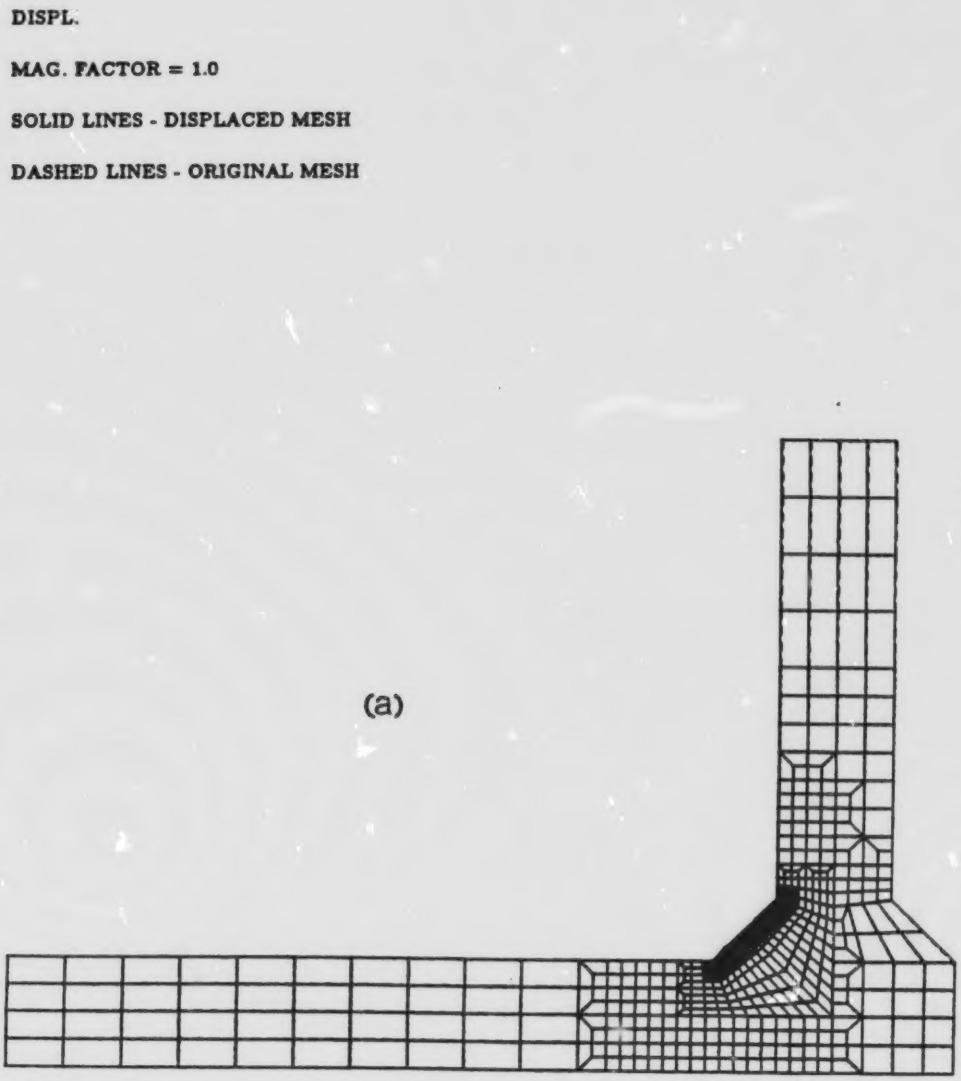
DISPL.
MAG. FACTOR = 1.0
SOLID LINES - DISPLACED MESH
DASHED LINES - ORIGINAL MESH
(a)

Figure 7.10: Displaced T-joint specimen geometry (a) and displaced mesh around the weld region (b) after PASS 1 (without symmetry)

DISPL.
MAG. FACTOR = 1.0
SOLID LINES - DISPLACED MESH

DASHED LINES - ORIGINAL MESH

(b)

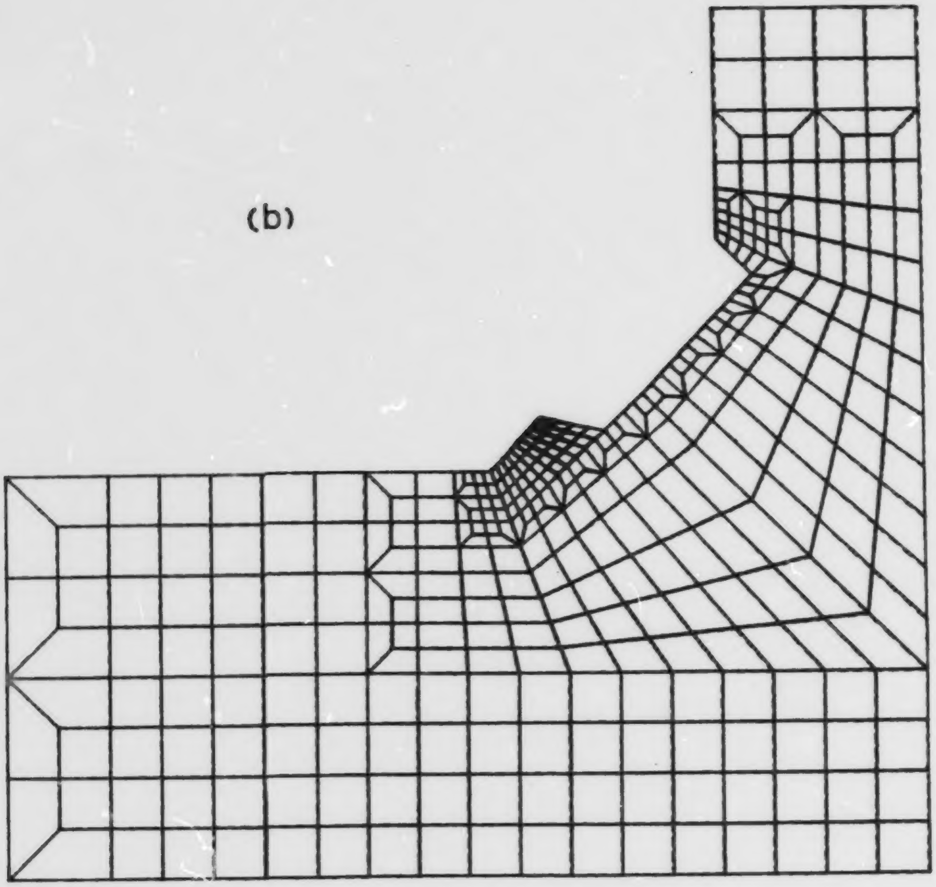

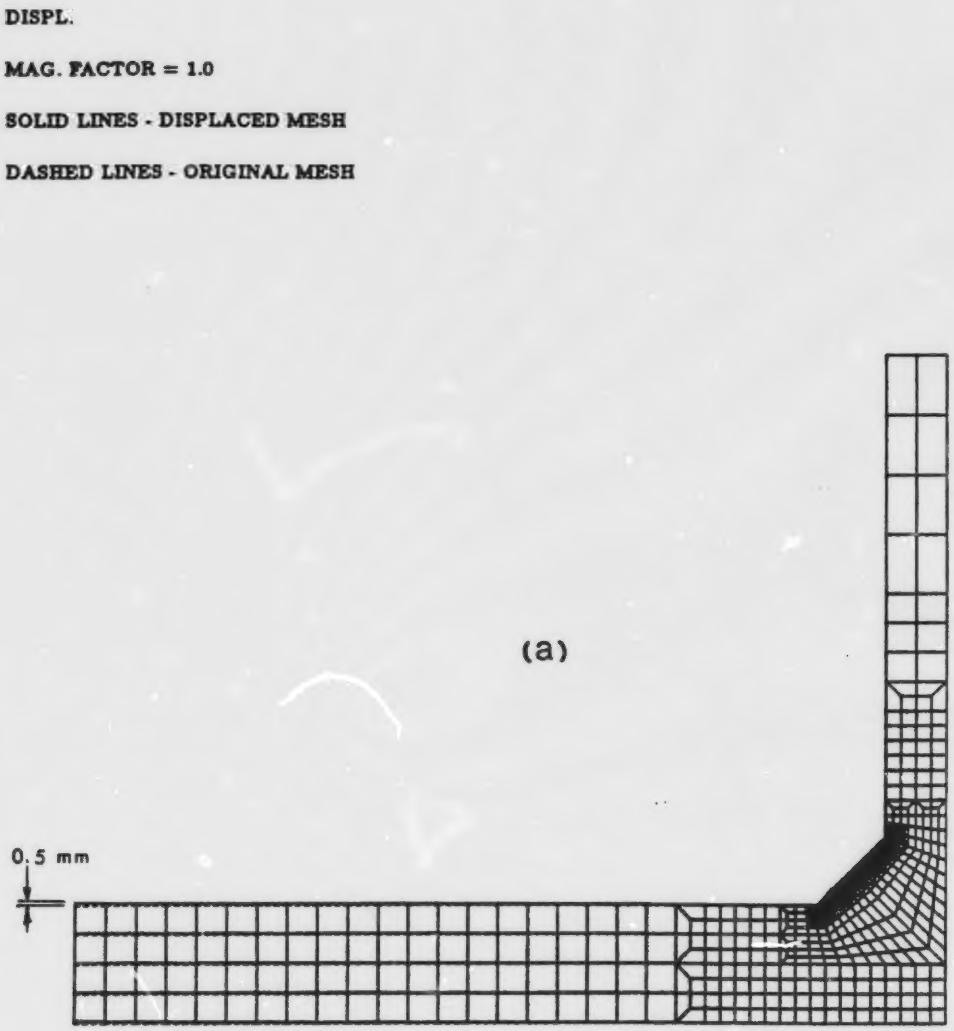
DISPL.
MAG. FACTOR = 1.0
SOLID LINES - DISPLACED MESH
DASHED LINES - ORIGINAL MESH
(a)
0.5 mm

Figure 7.11: Displaced T-joint specimen geometry (a) and displaced mesh around the weld region (b) after PASS 1 (with symmetry)

DISPL.
MAG. FACTOR = 1.0
SOLID LINES - DISPLACED MESH

DASHED LINES - ORIGINAL MESH

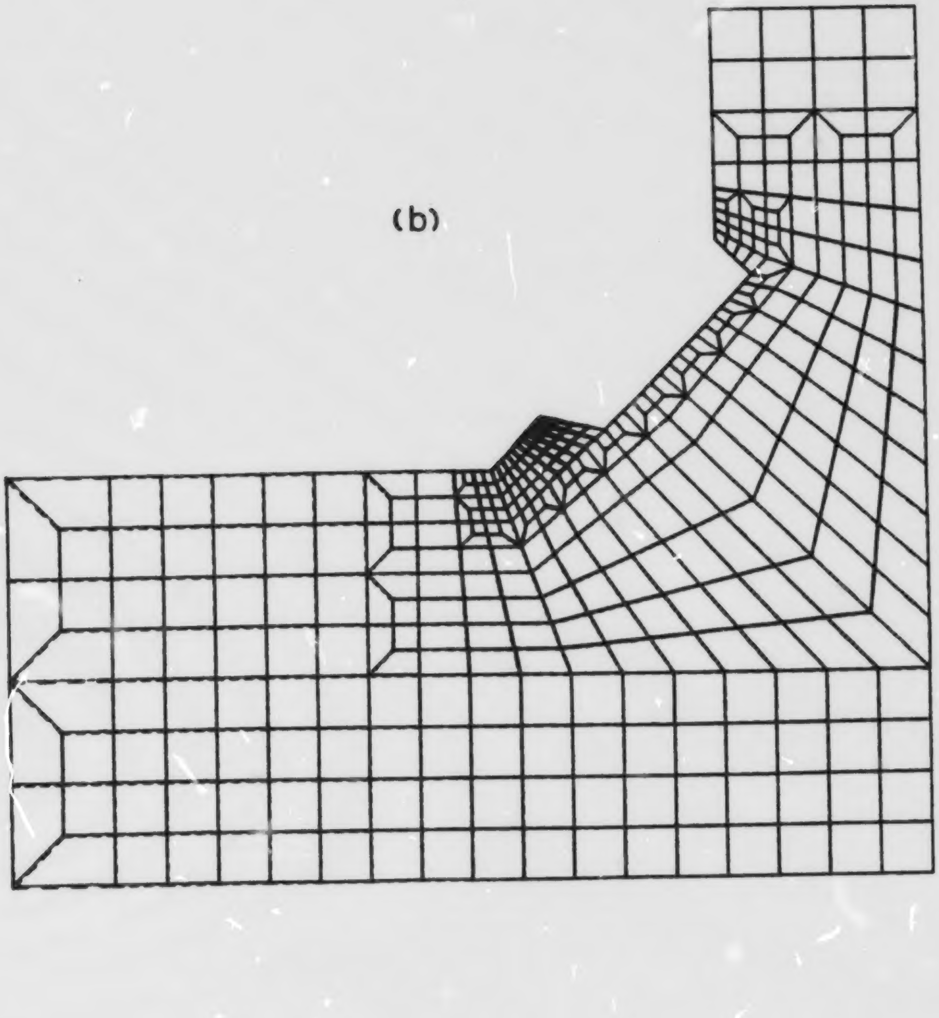

(b)

LEGEND

STRESS COMPONENT - X

CONTOUR MAGNITUDE (MPa)

1	-200.0
2	-140.0
3	-80.0
4	-20.0
5	40.0
6	100.0
7	160.0
8	220.0
9	280.0
10	340.0
11	400.0

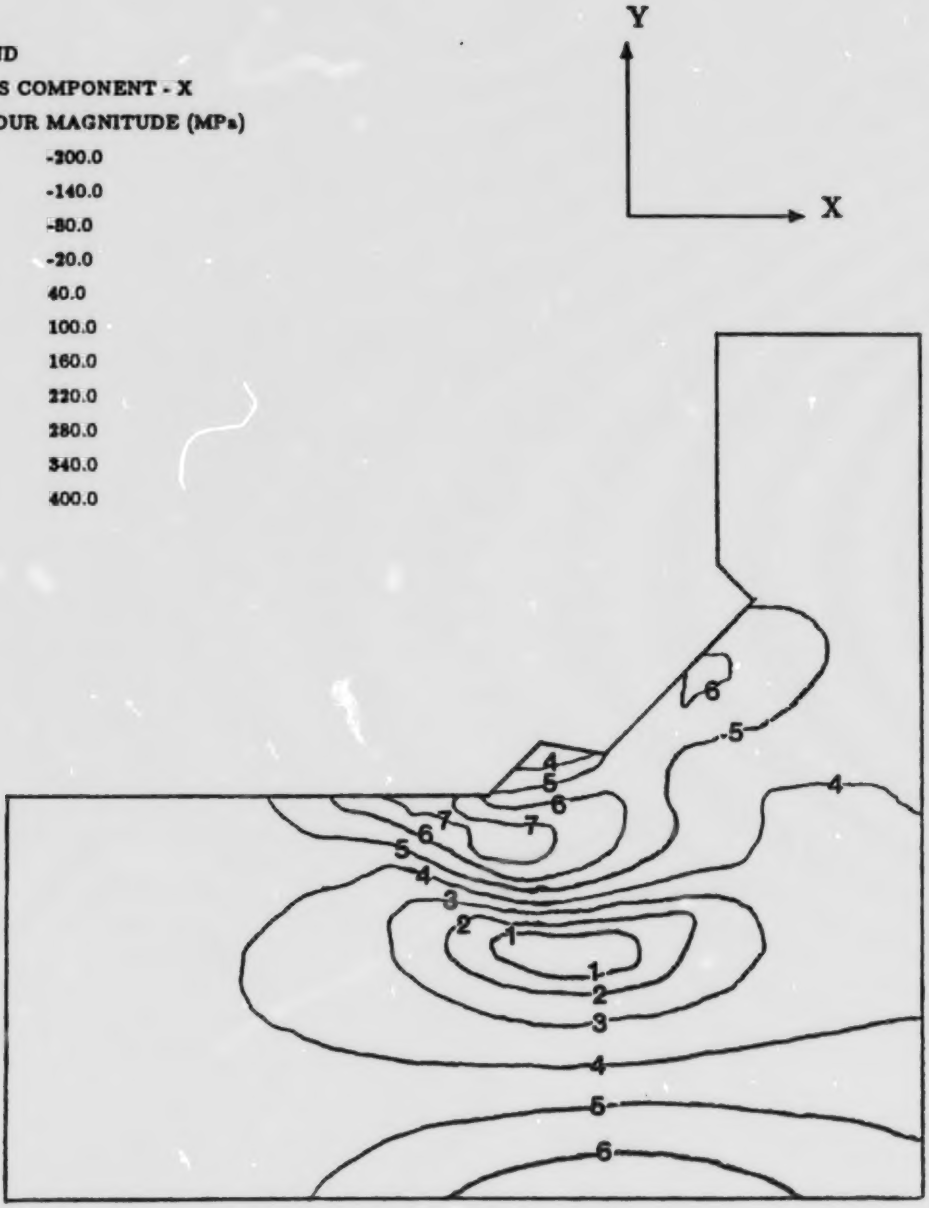

Figure 7.12: X-residual stress distribution - PASS 1 (without symmetry)

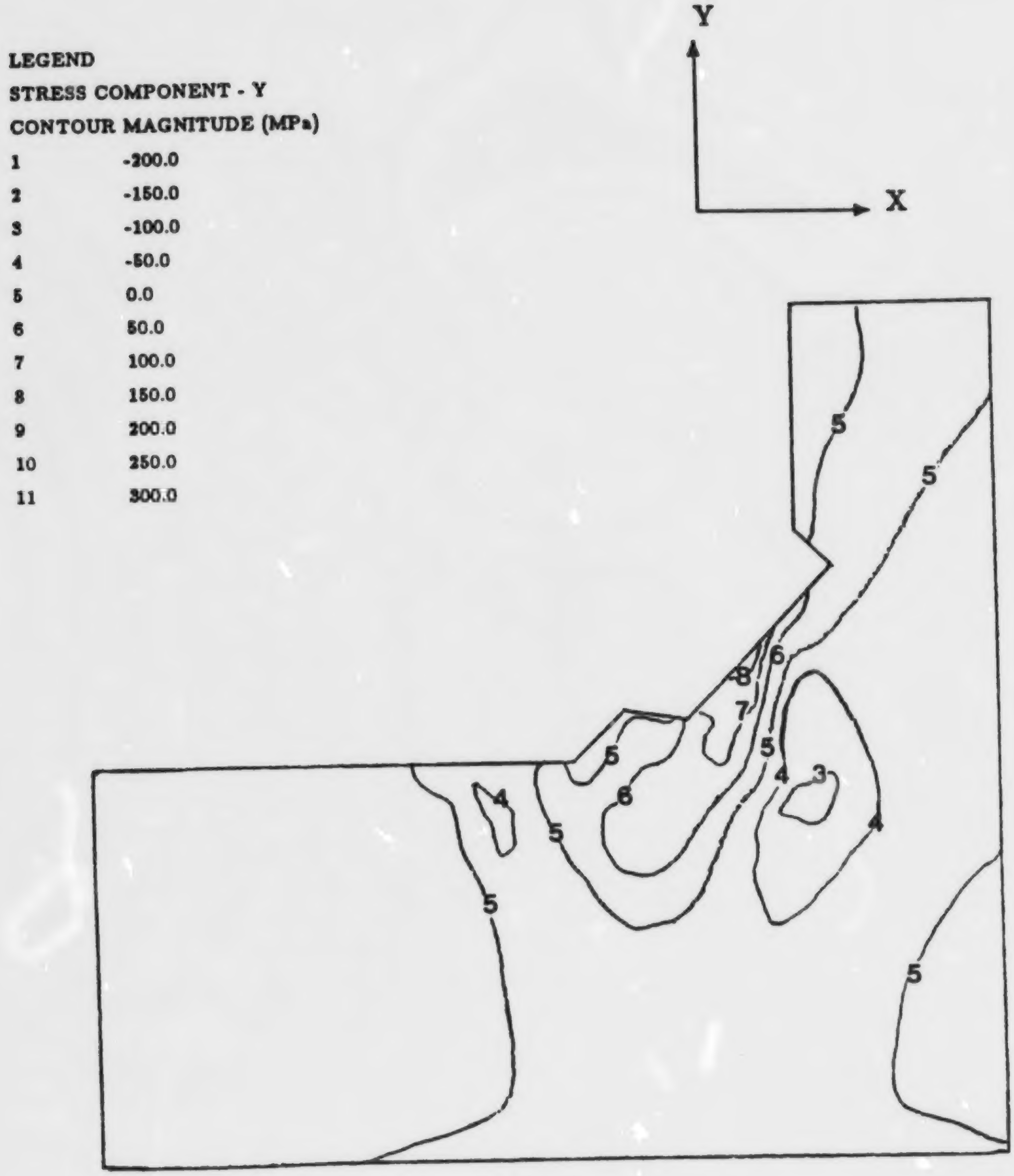

Figure 7.13: Y-residual stress distribution - PASS 1 (without symmetry)

LEGEND

STRESS COMPONENT - Z

CONTOUR MAGNITUDE (MPa)

1	-200.0
2	-130.0
3	-60.0
4	10.0
5	80.0
6	150.0
7	220.0
8	290.0
9	360.0
10	430.0
11	500.0

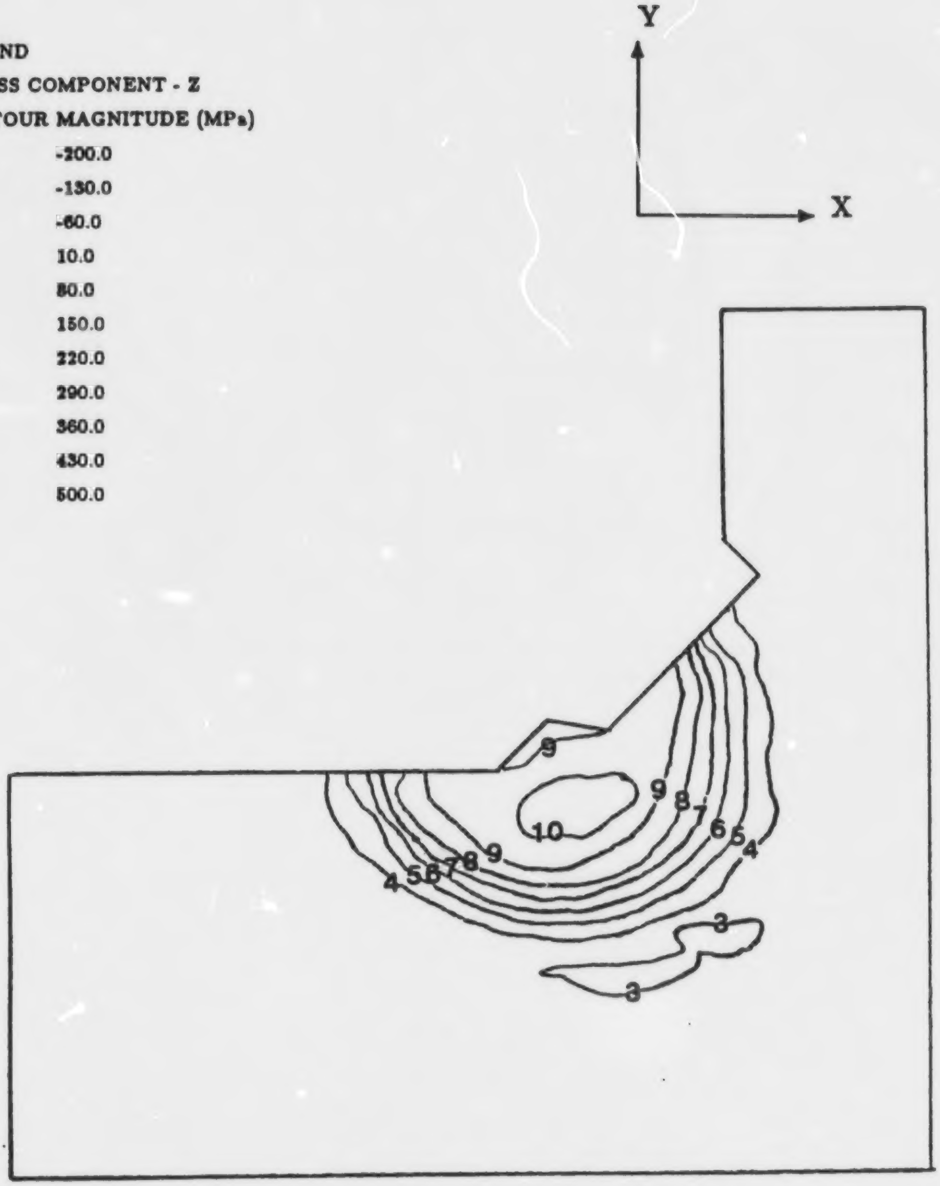

Figure 7.14: Z-residual stress distribution - PASS 1 (without symmetry)

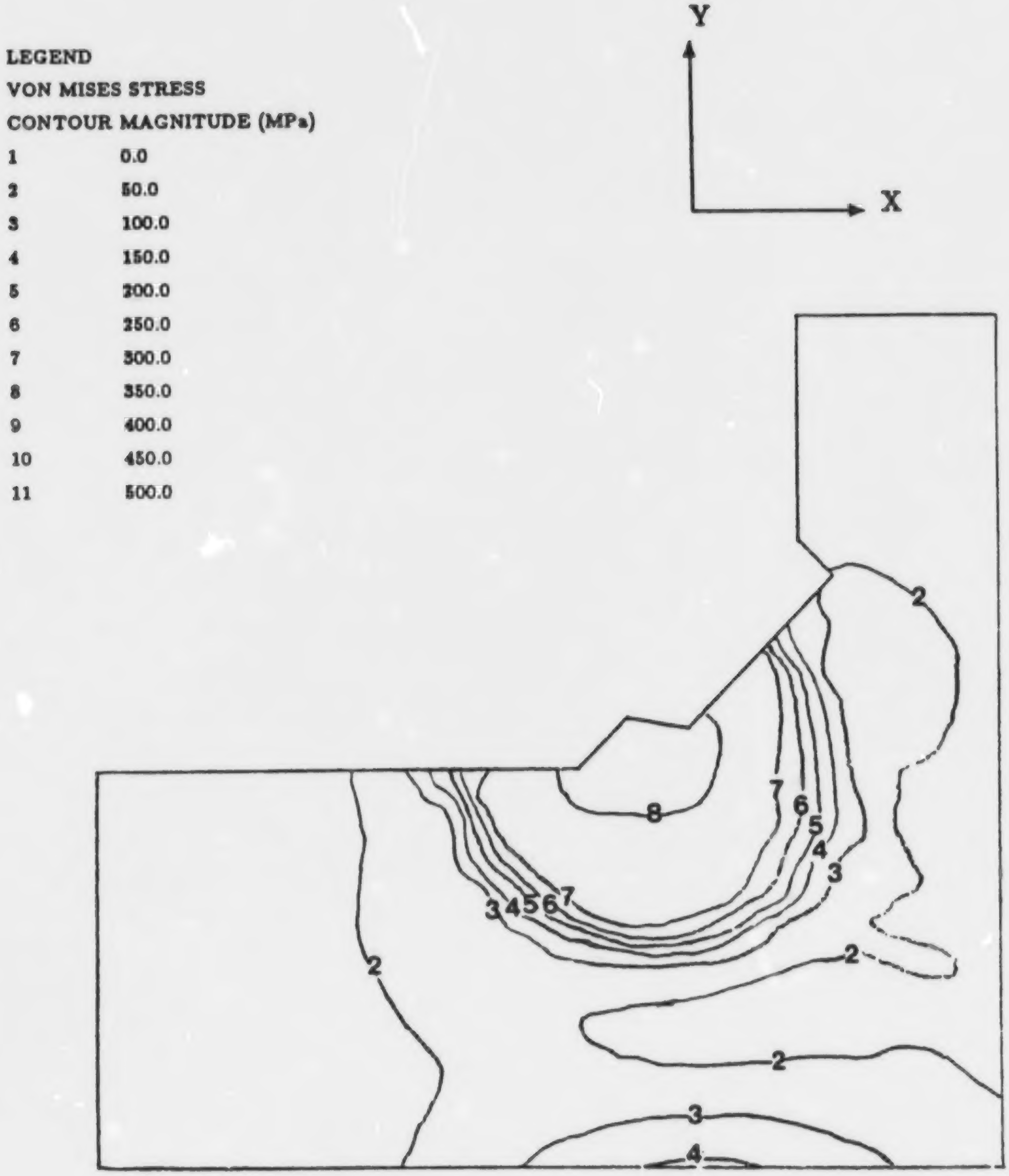

Figure 7.15: Von Mises residual stress distribution - PASS 1 (without symmetry)

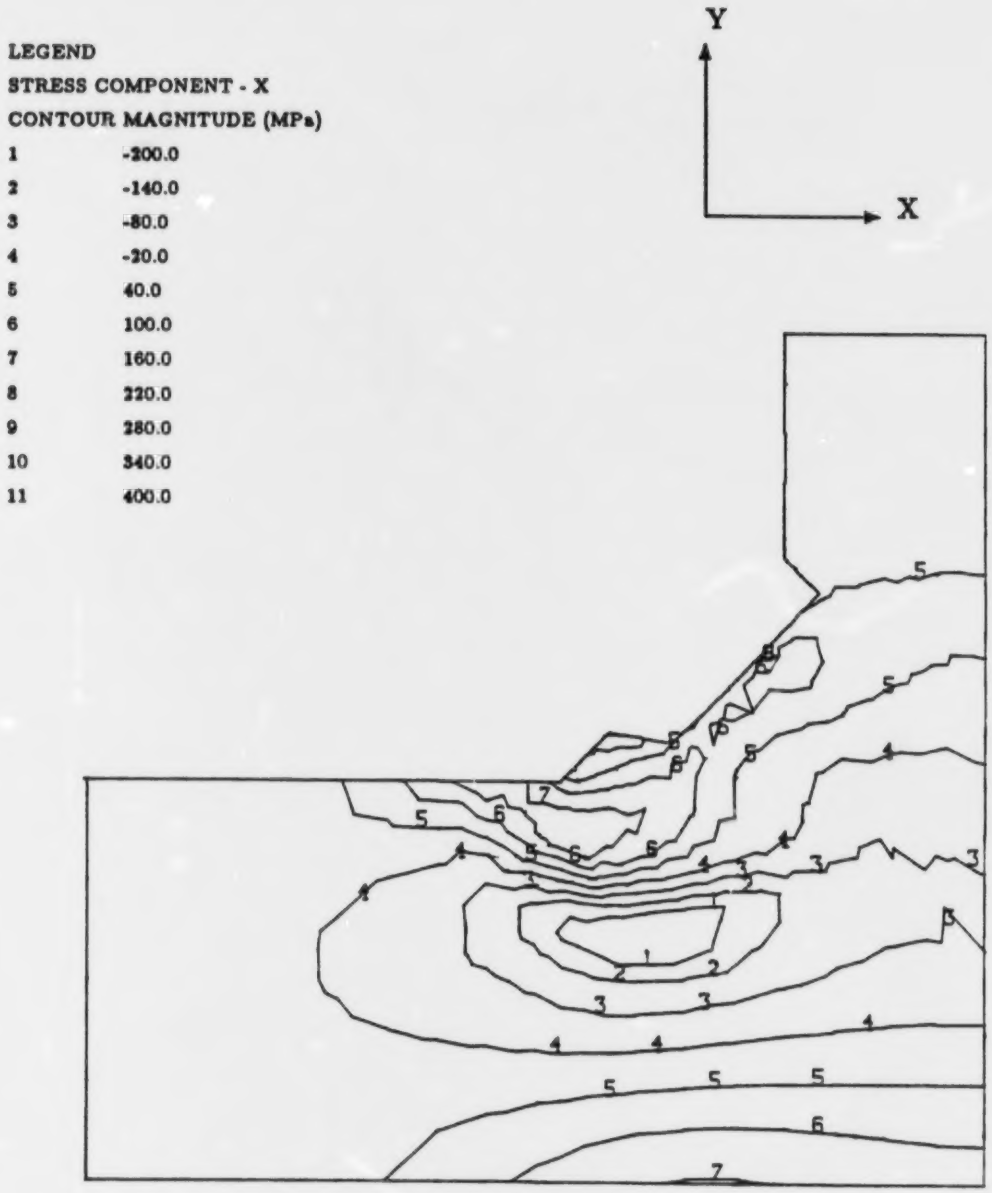

LEGEND
STRESS COMPONENT - X
CONTOUR MAGNITUDE (MPa)

1	-200.0
2	-140.0
3	-80.0
4	-20.0
5	40.0
6	100.0
7	160.0
8	220.0
9	280.0
10	340.0
11	400.0

Figure 7.16: X-residual stress distribution - PASS 1 (with symmetry)

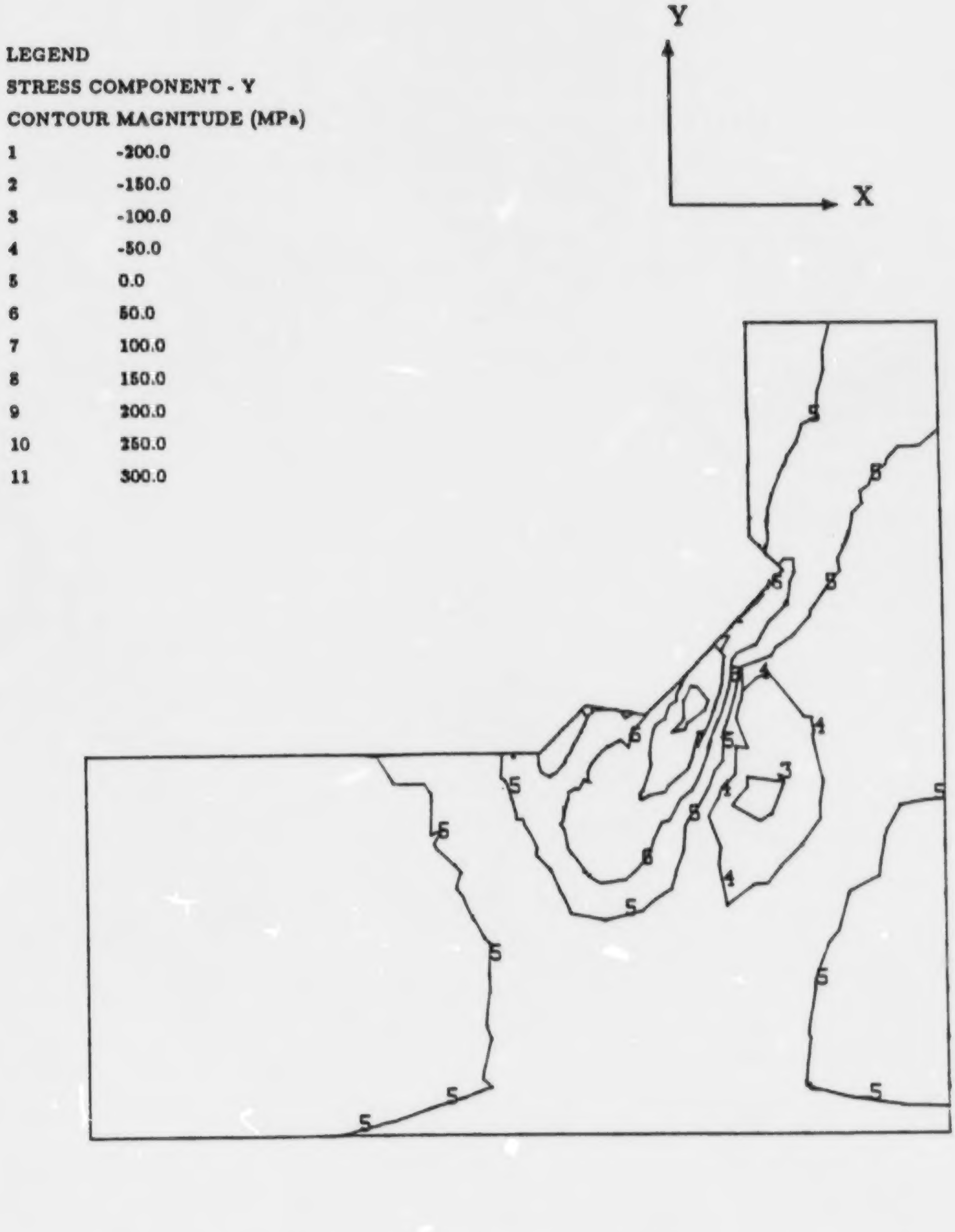

Figure 7.17: Y-residual stress distribution - PASS 1 (with symmetry)

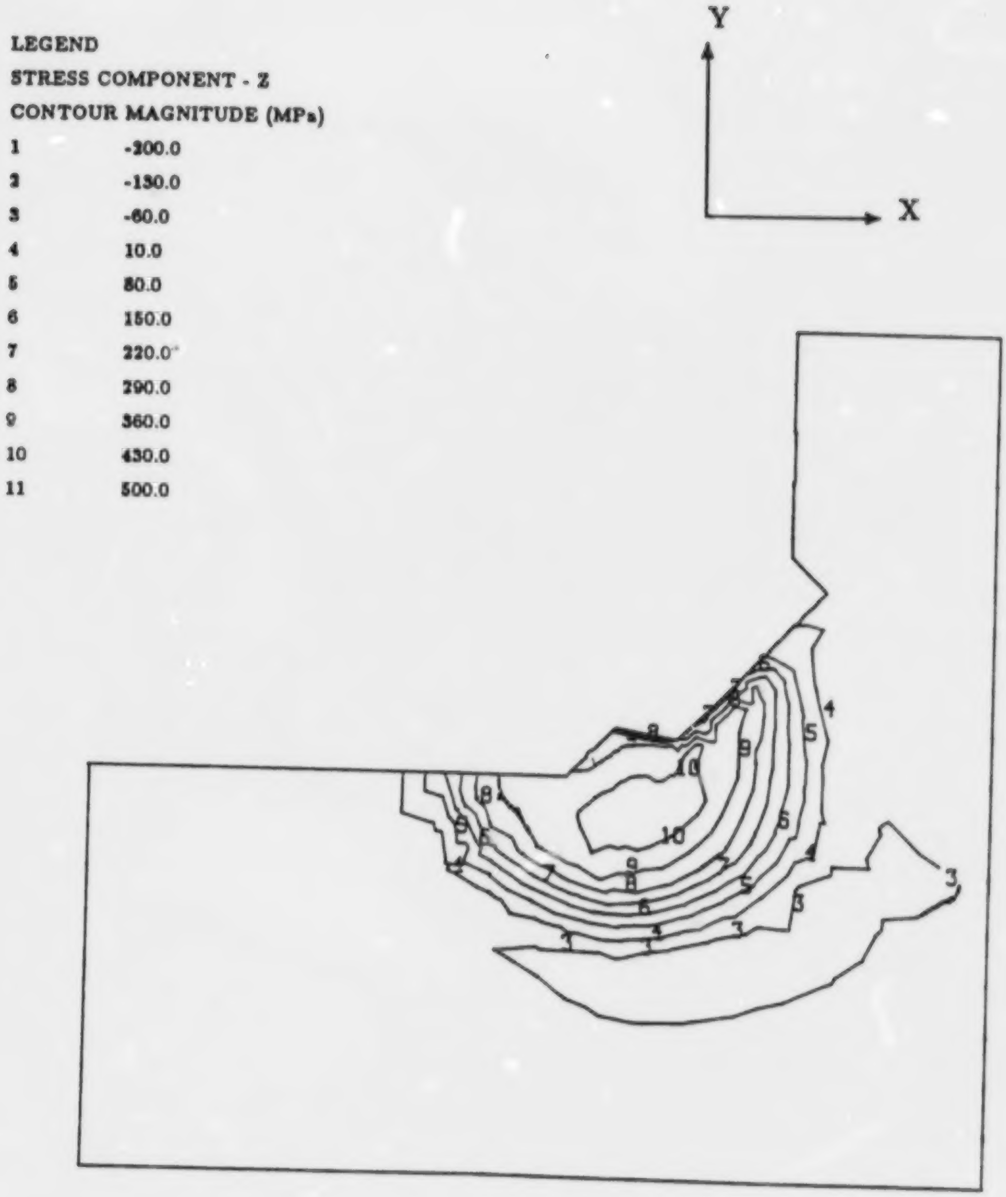

Figure 7.18: Z-residual stress distribution - PASS 1 (with symmetry)

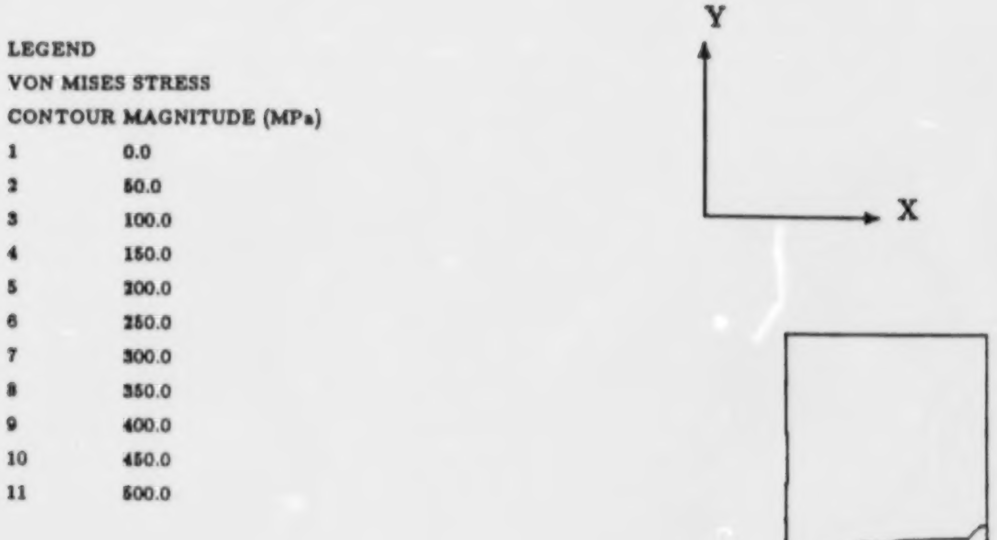

Figure 7.19: Von Mises residual stress distribution - PASS 1 (with symmetry)

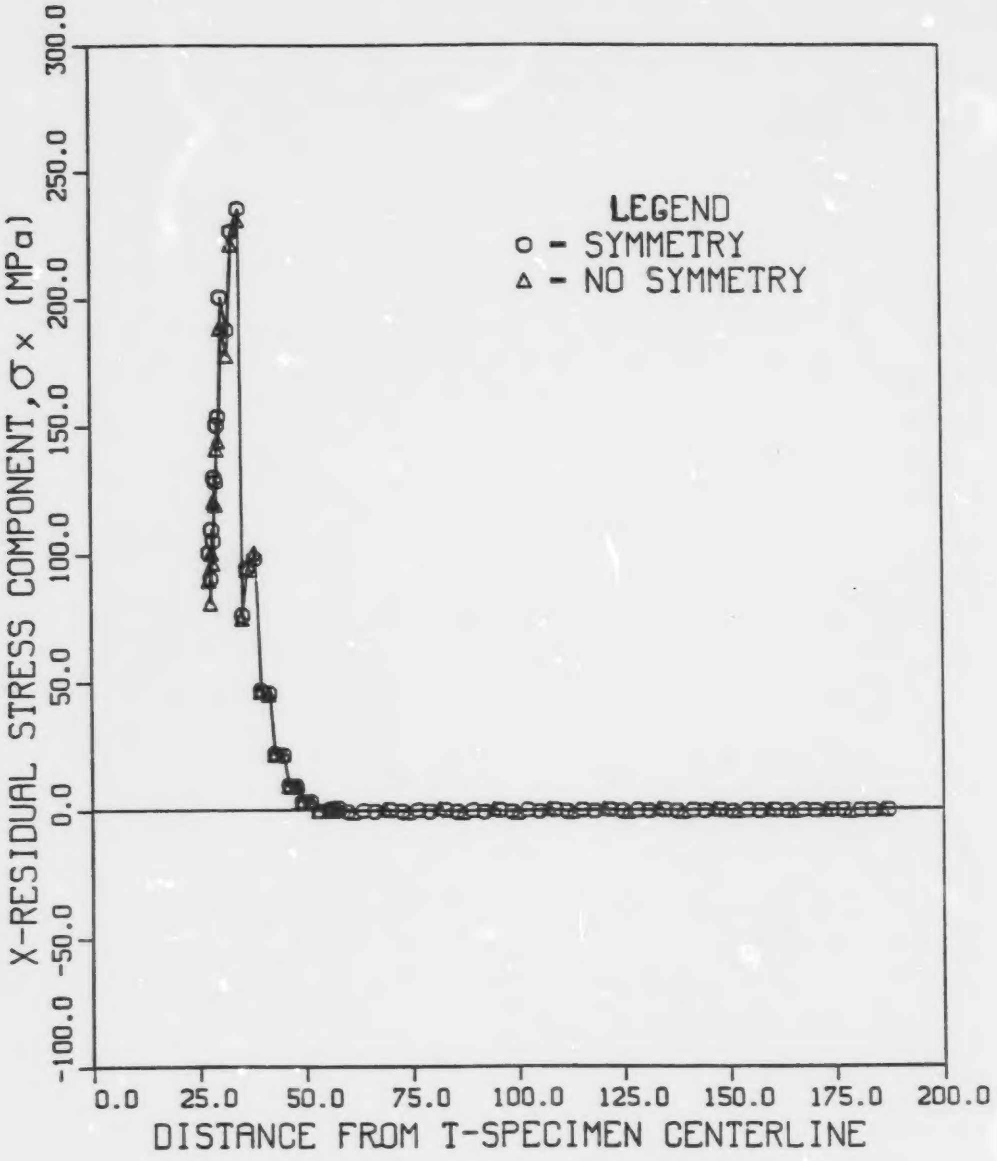

Figure 7.20: Distribution of the X-residual stress component along the top surface after the first pass (comparison for symmetry assumption)

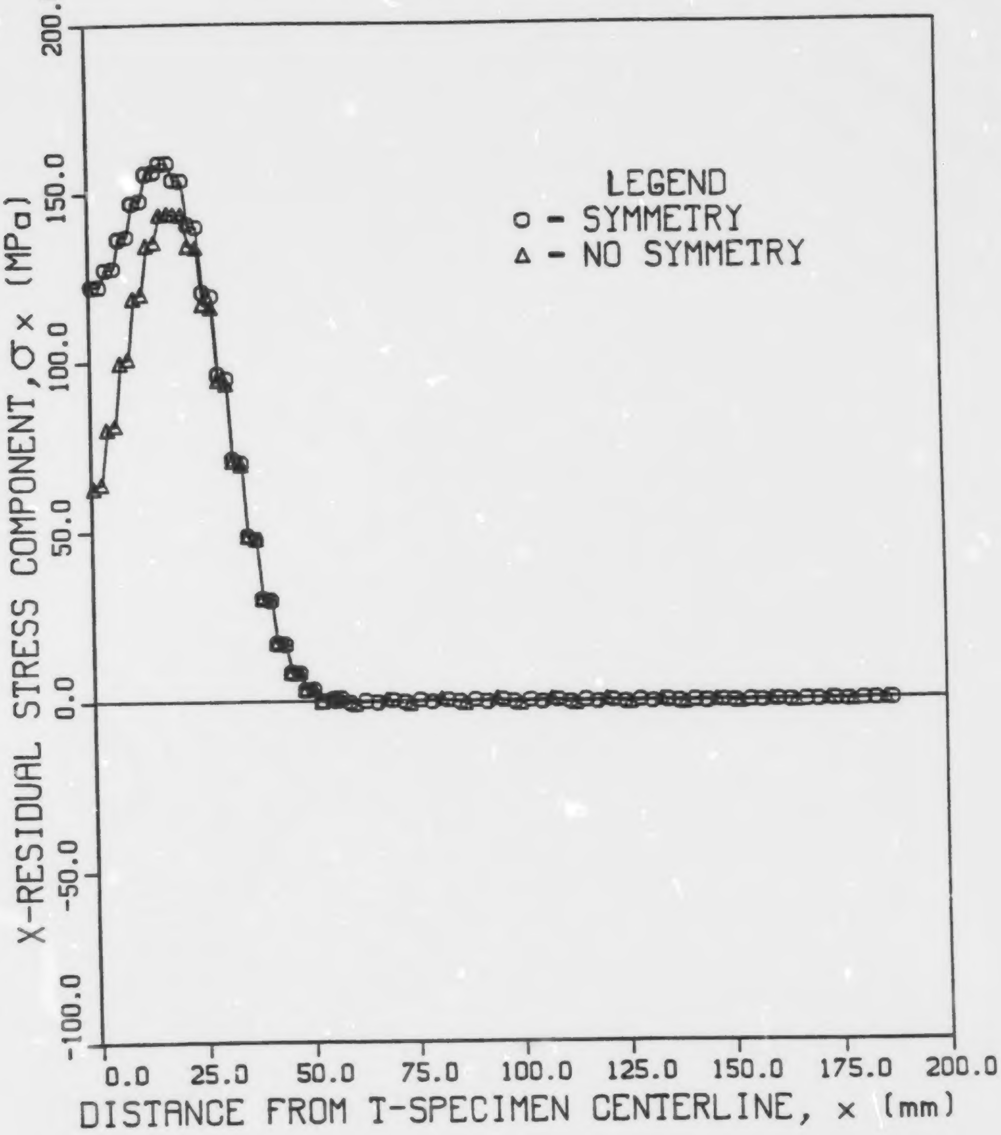

Figure 7.21: Distribution of the X-residual stress component along the bottom surface after the first pass (comparison for symmetry assumption)

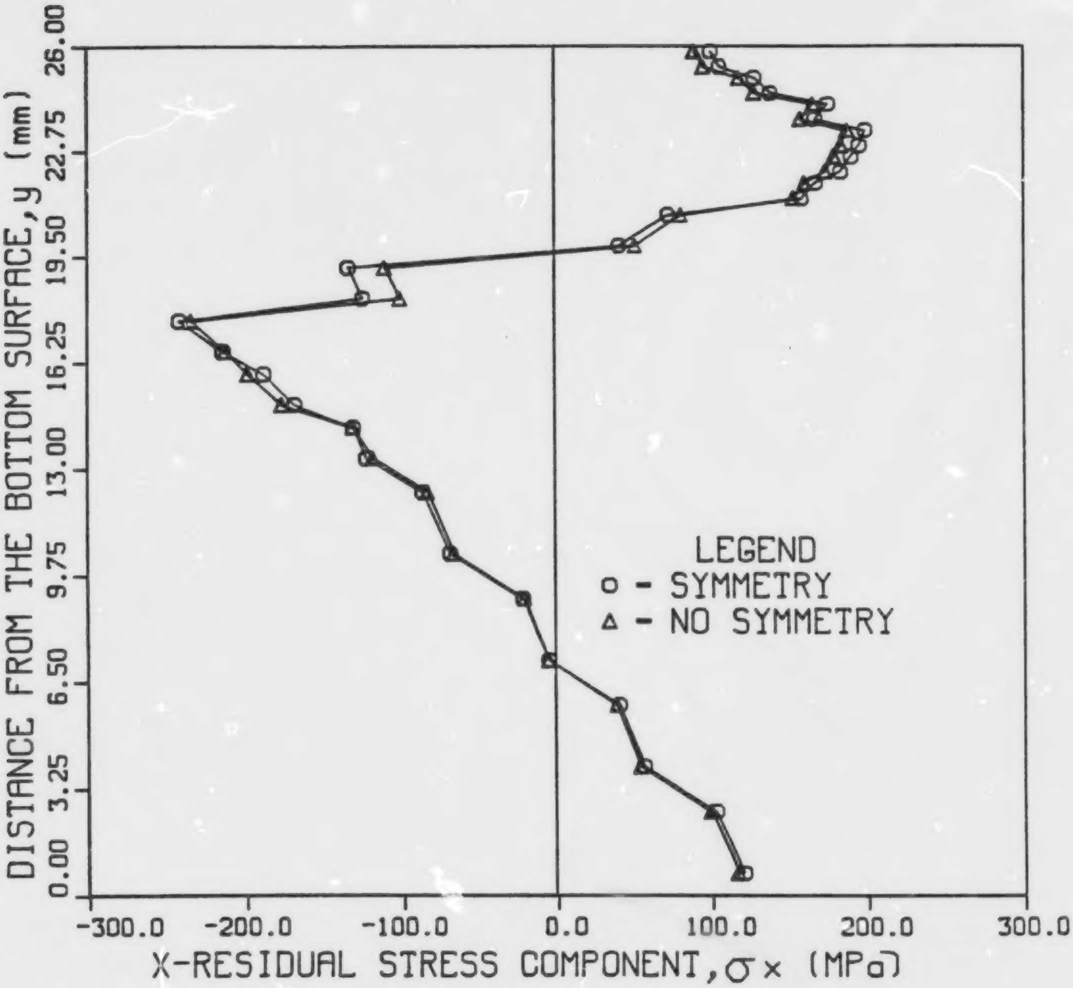

Figure 7.22: Distribution of the X-residual stress component through the plate thickness below the weld toe after the first pass (comparison for symmetry assumption)

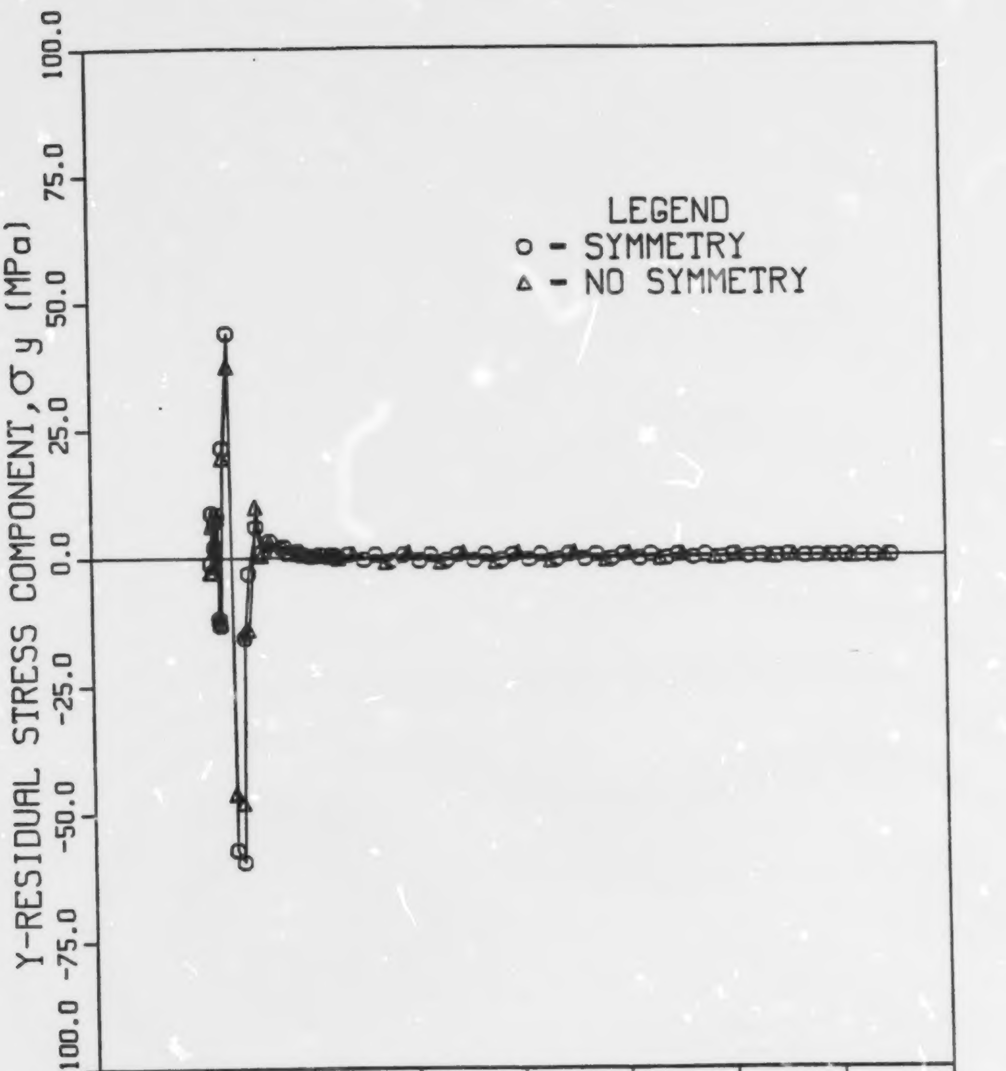

Figure 7.23: Distribution of the Y-residual stress component along the top surface after the first pass (comparison for symmetry assumption)

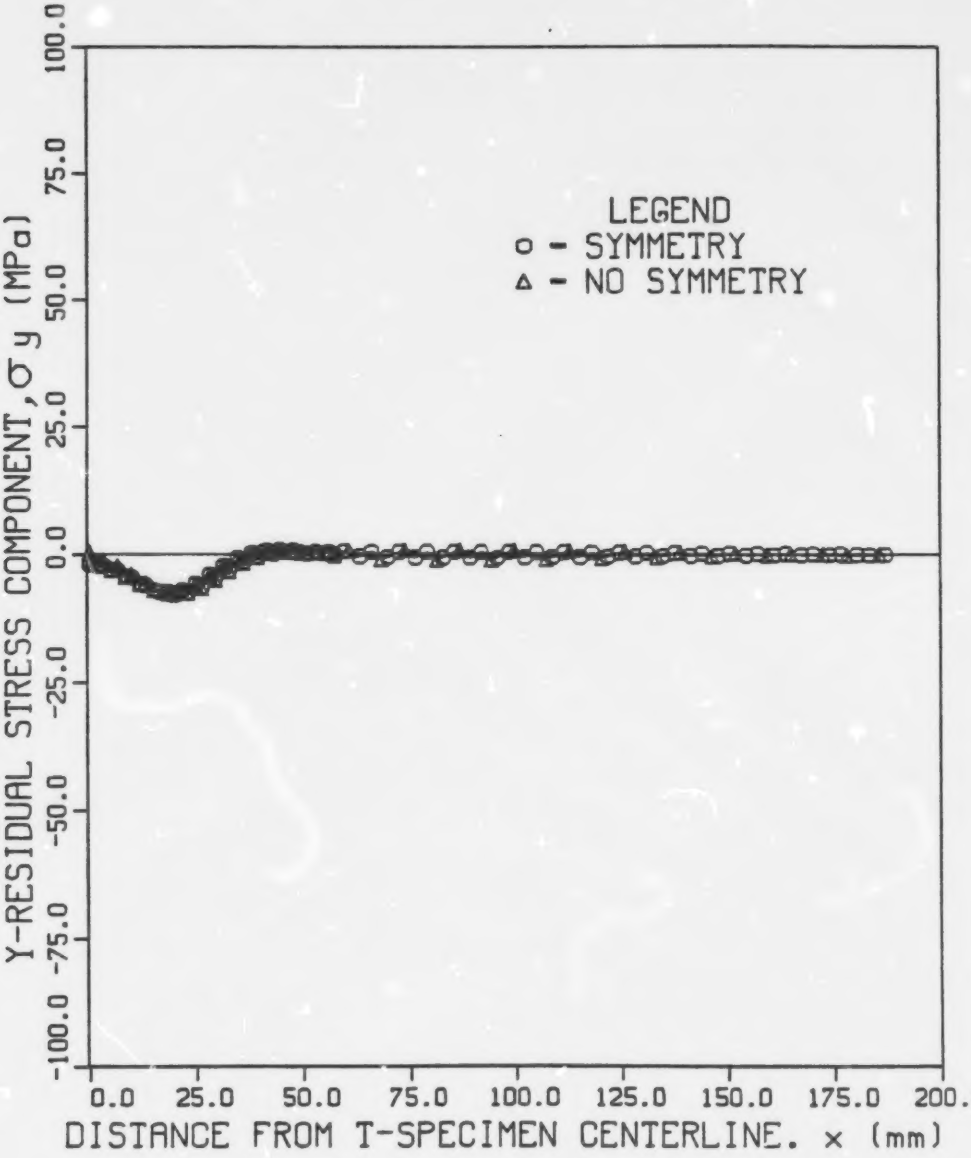

Figure 7.24: Distribution of the Y-residual stress component along the bottom surface after the first pass (comparison for symmetry assumption)

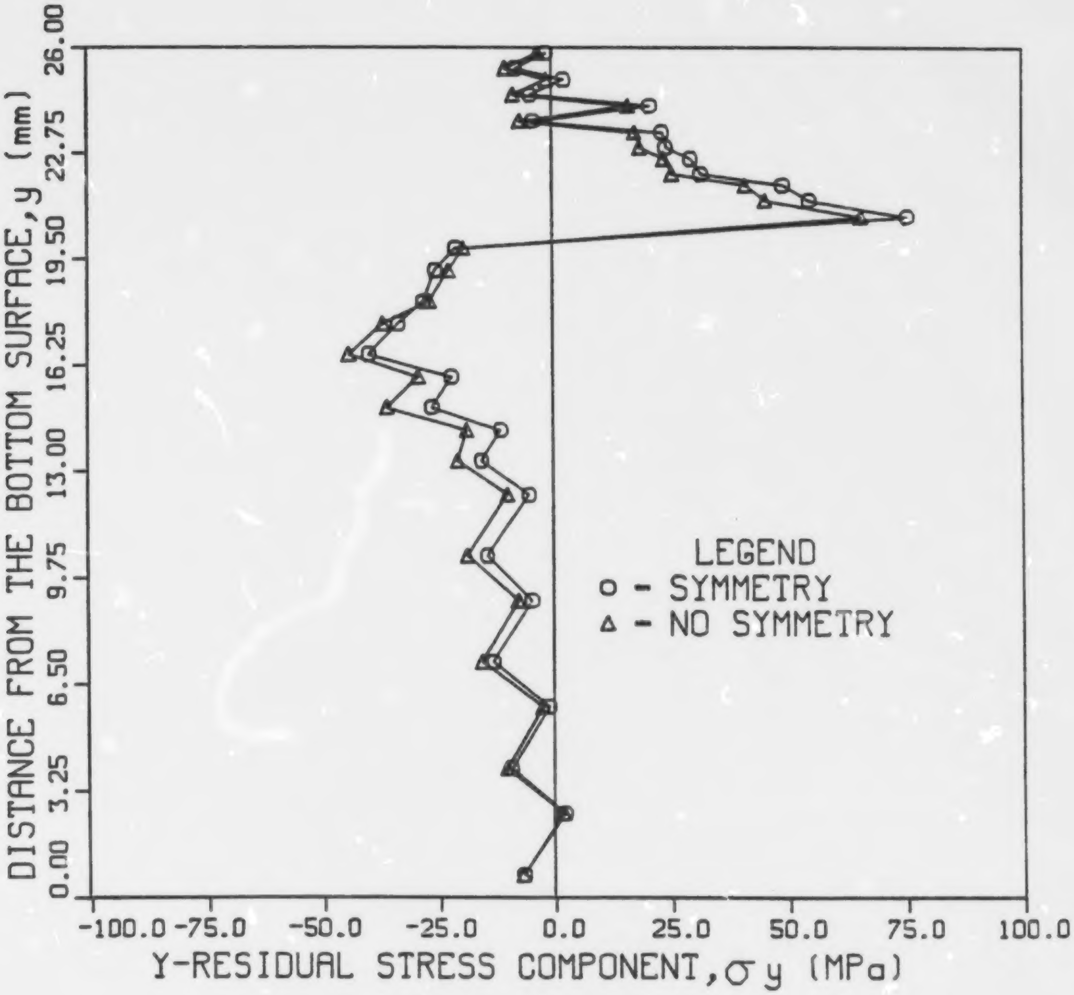

Figure 7.25: Distribution of the Y-residual stress component through the plate thickness below the weld toe after the first pass (comparison for symmetry assumption)

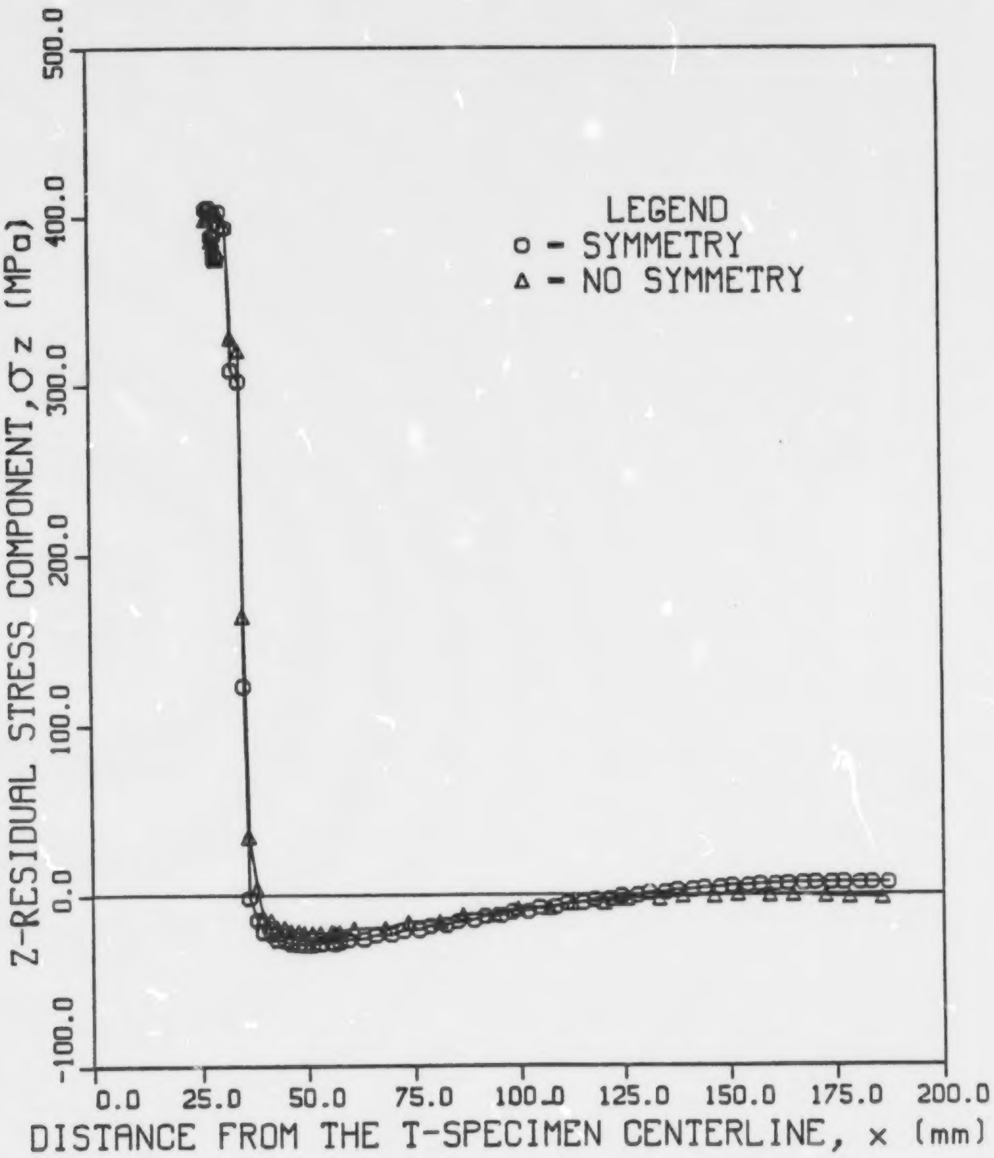

Figure 7.26: Distribution of the Z-residual stress component along the top surface after the first pass (comparison for symmetry assumption)

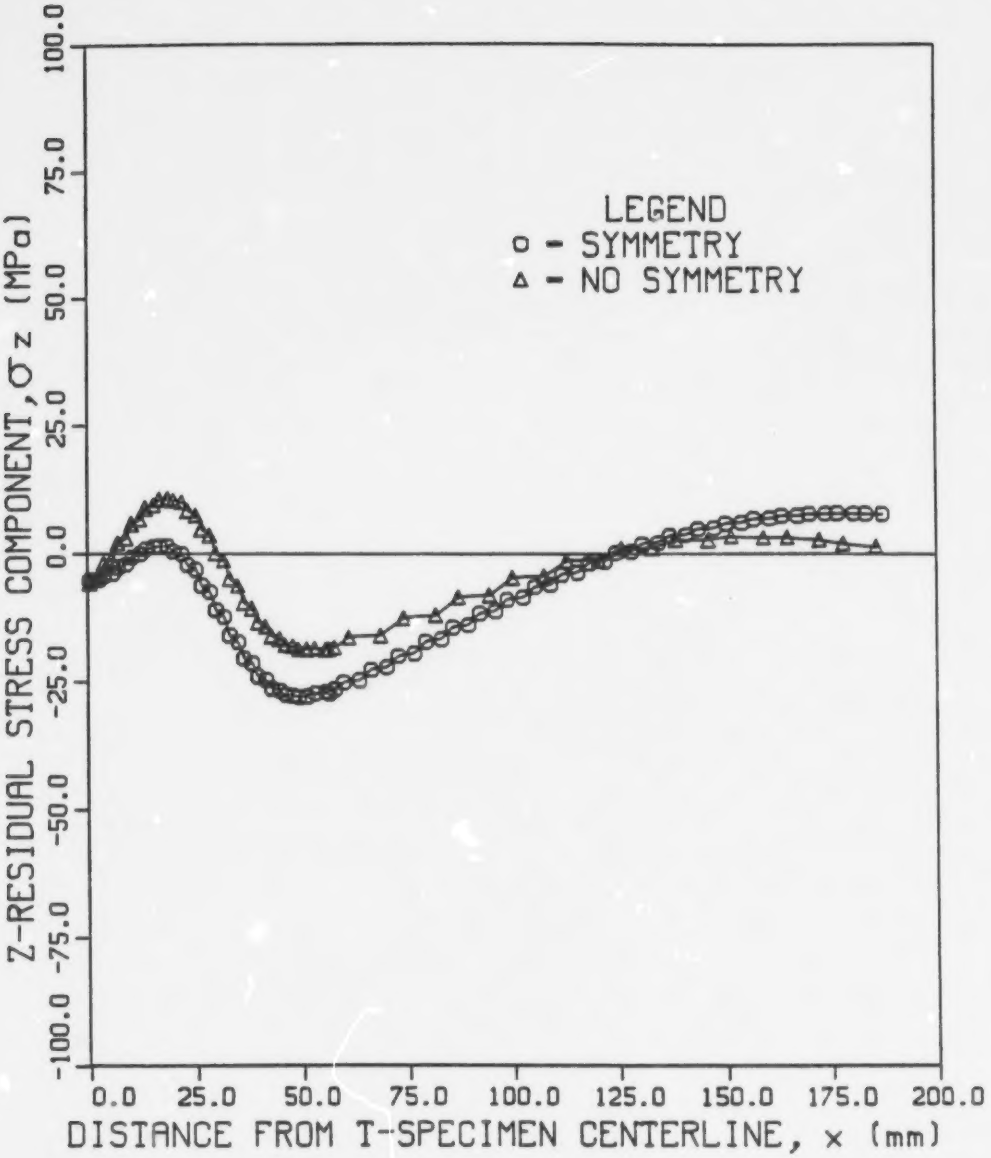

Figure 7.27: Distribution of the Z-residual stress component along the bottom surface after the first pass (comparison for symmetry assumption)

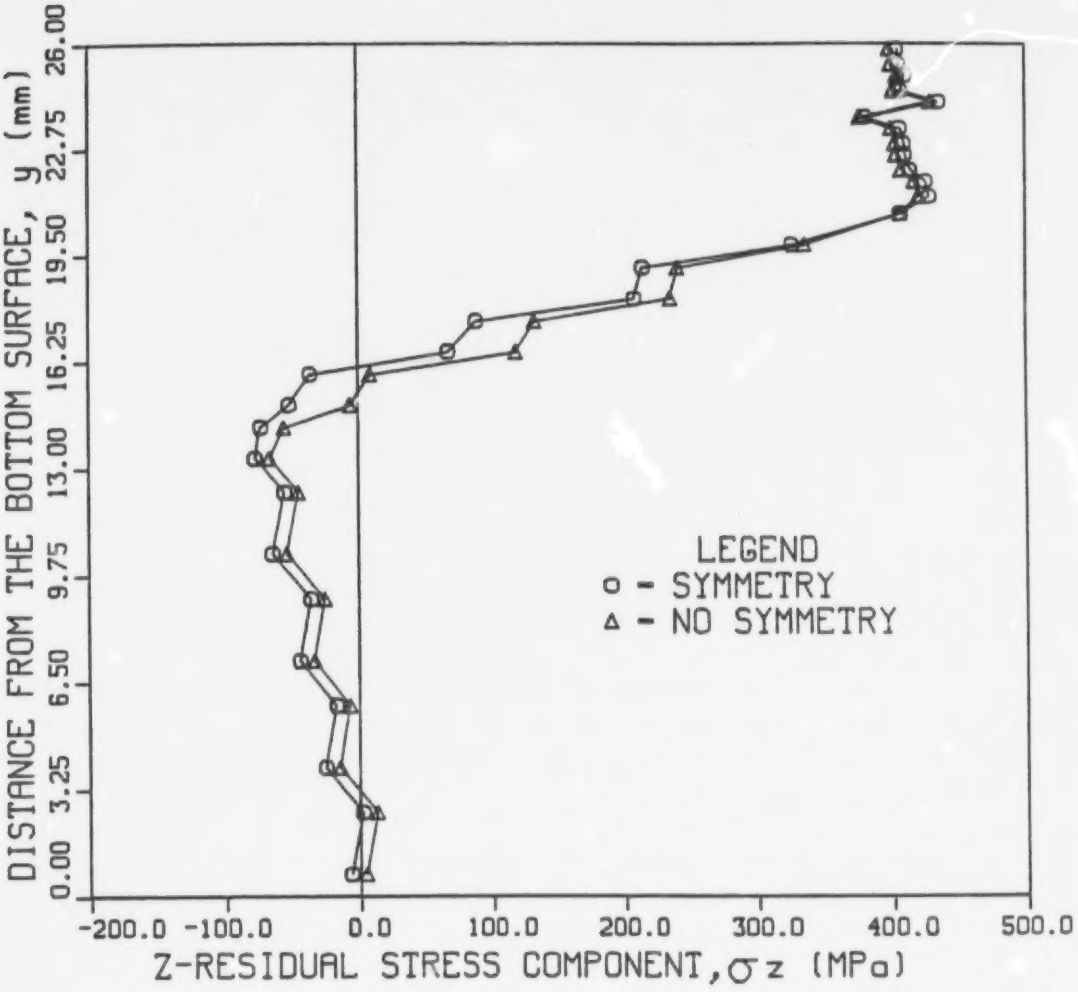

Figure 7.28: Distribution of the Z-residual stress component through the plate thickness below the weld toe after the first pass (comparison for symmetry assumption)

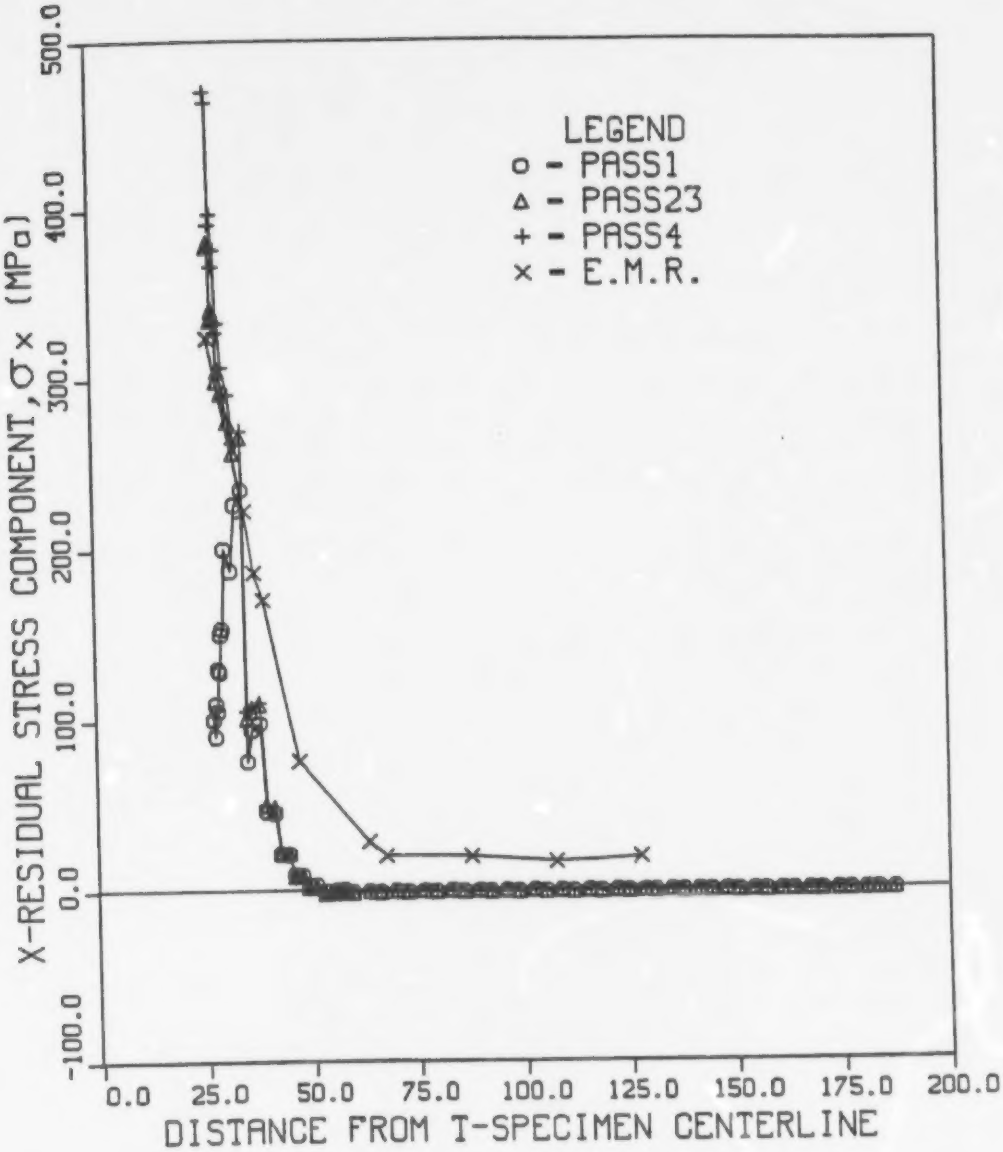

Figure 7.29: Distribution of the X-residual stress component along the top surface (without previous residual stresses)

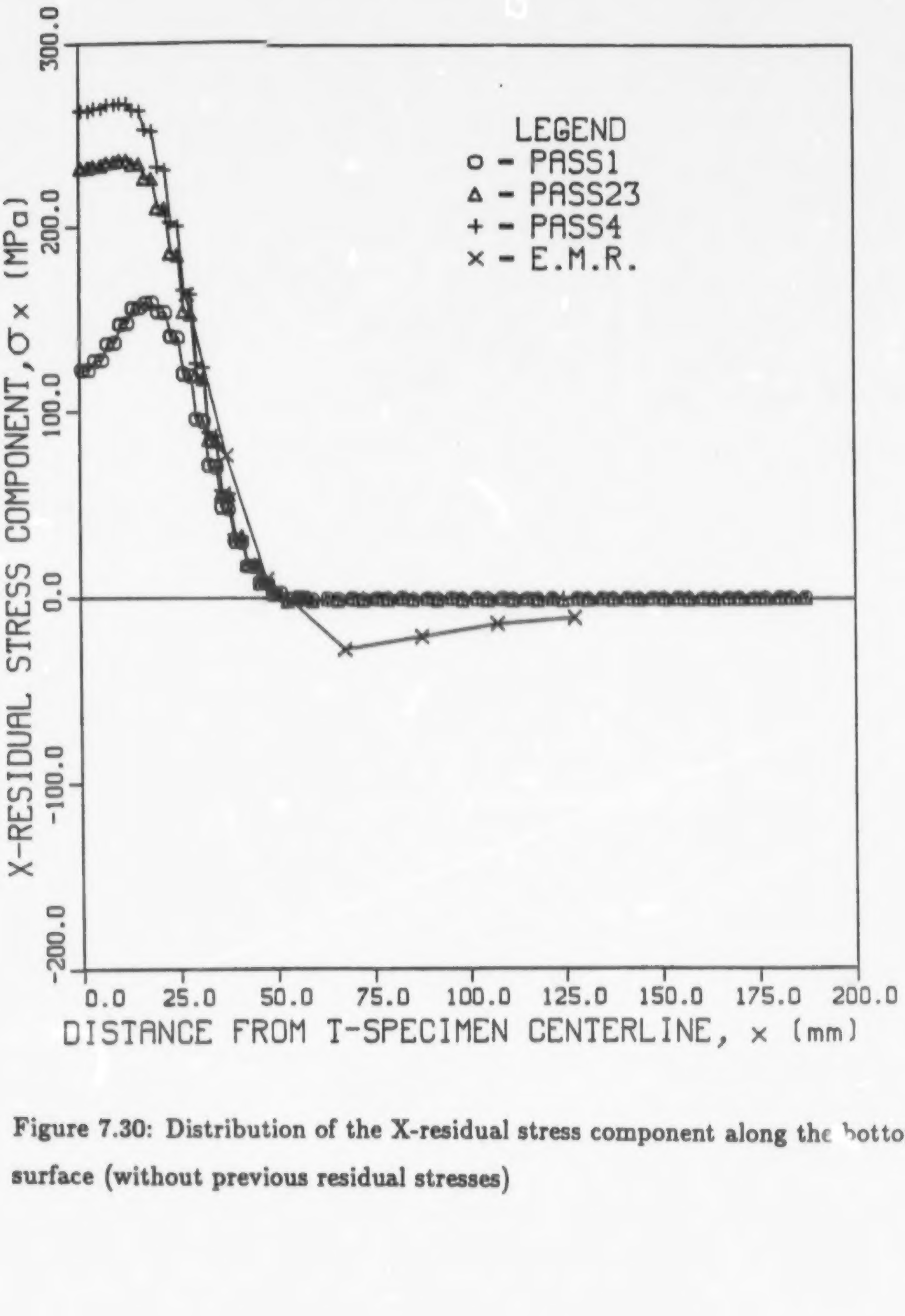

Figure 7.30: Distribution of the X-residual stress component along the bottom surface (without previous residual stresses)

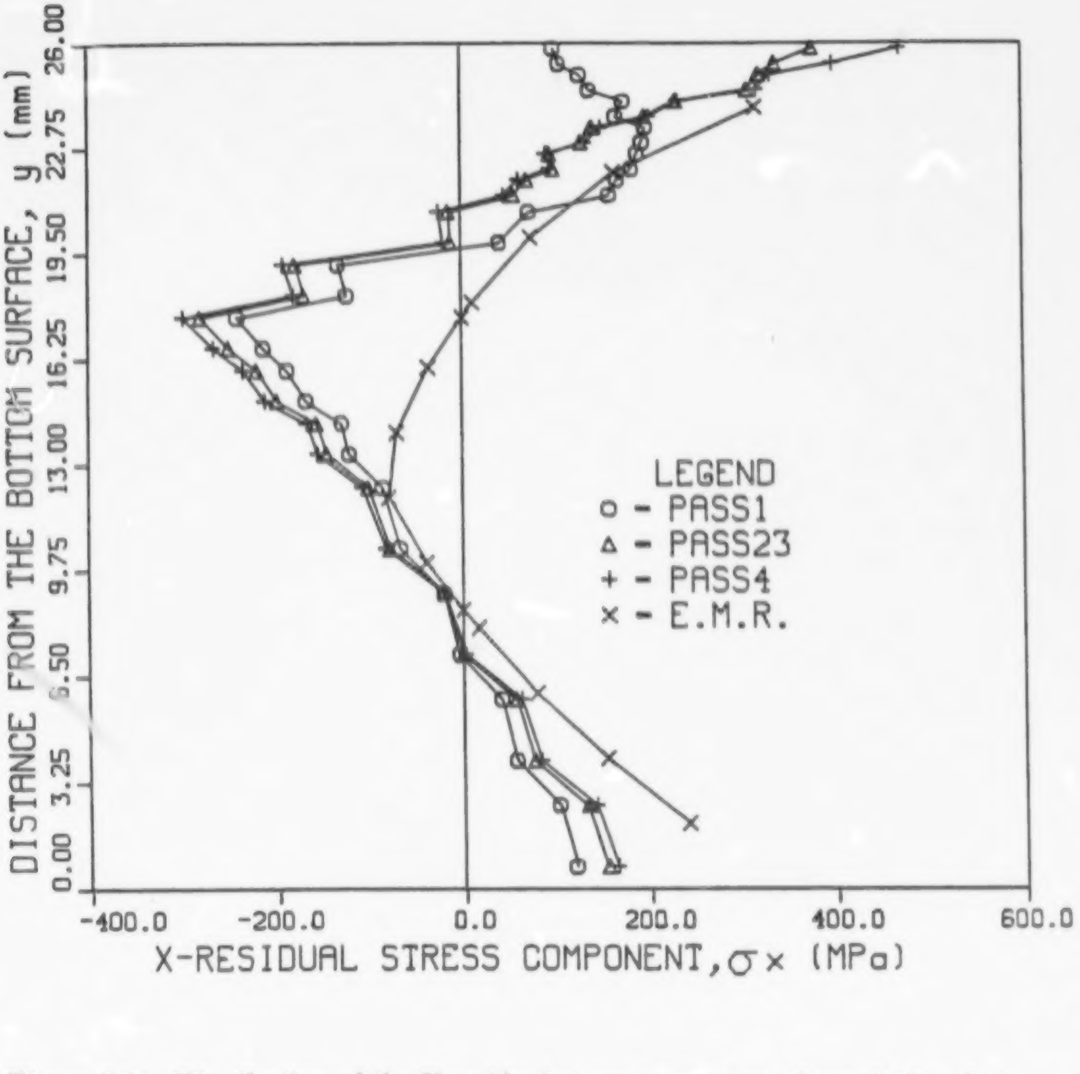

Figure 7.31: Distribution of the X-residual stress component through the plate thickness below the weld toe (without previous residual stresses)

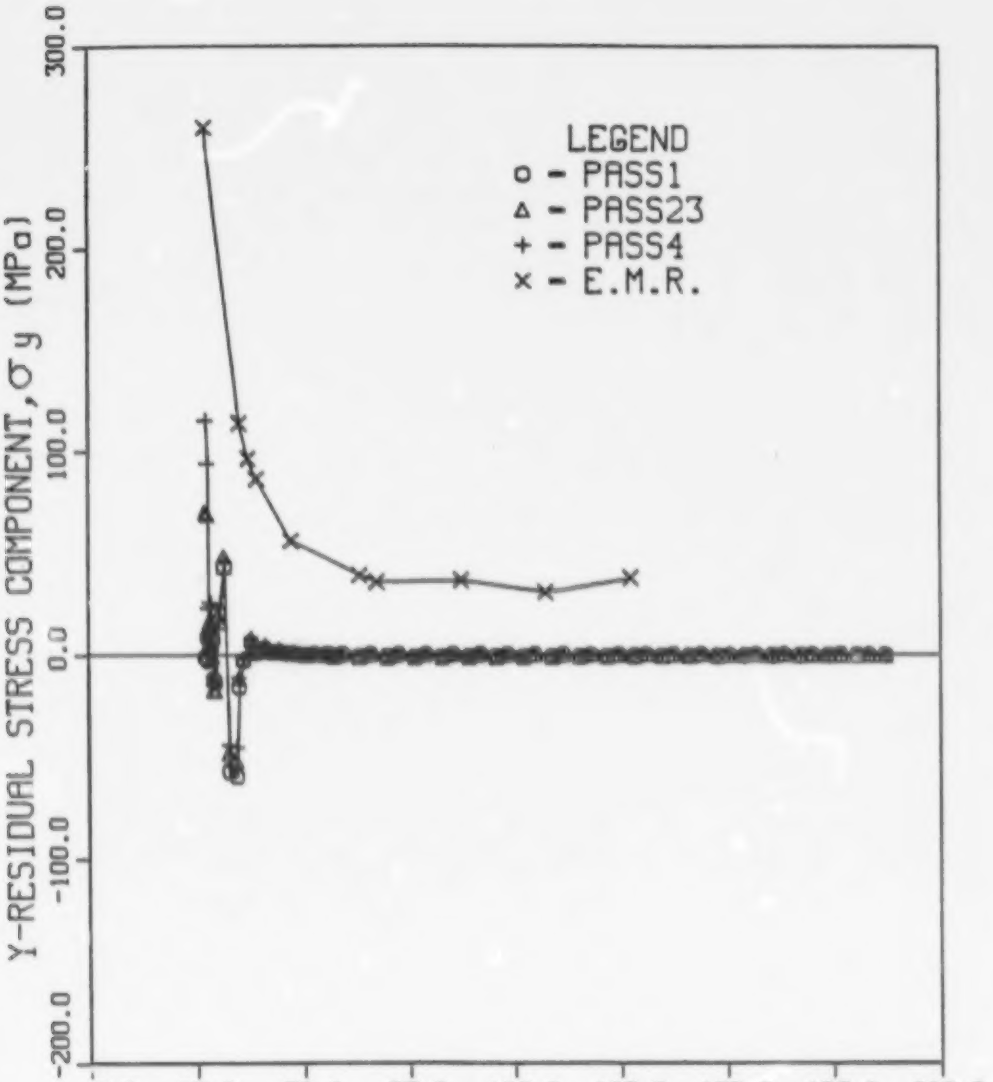

Figure 7.32: Distribution of the Y-residual stress component along the top surface (without previous residual stresses)

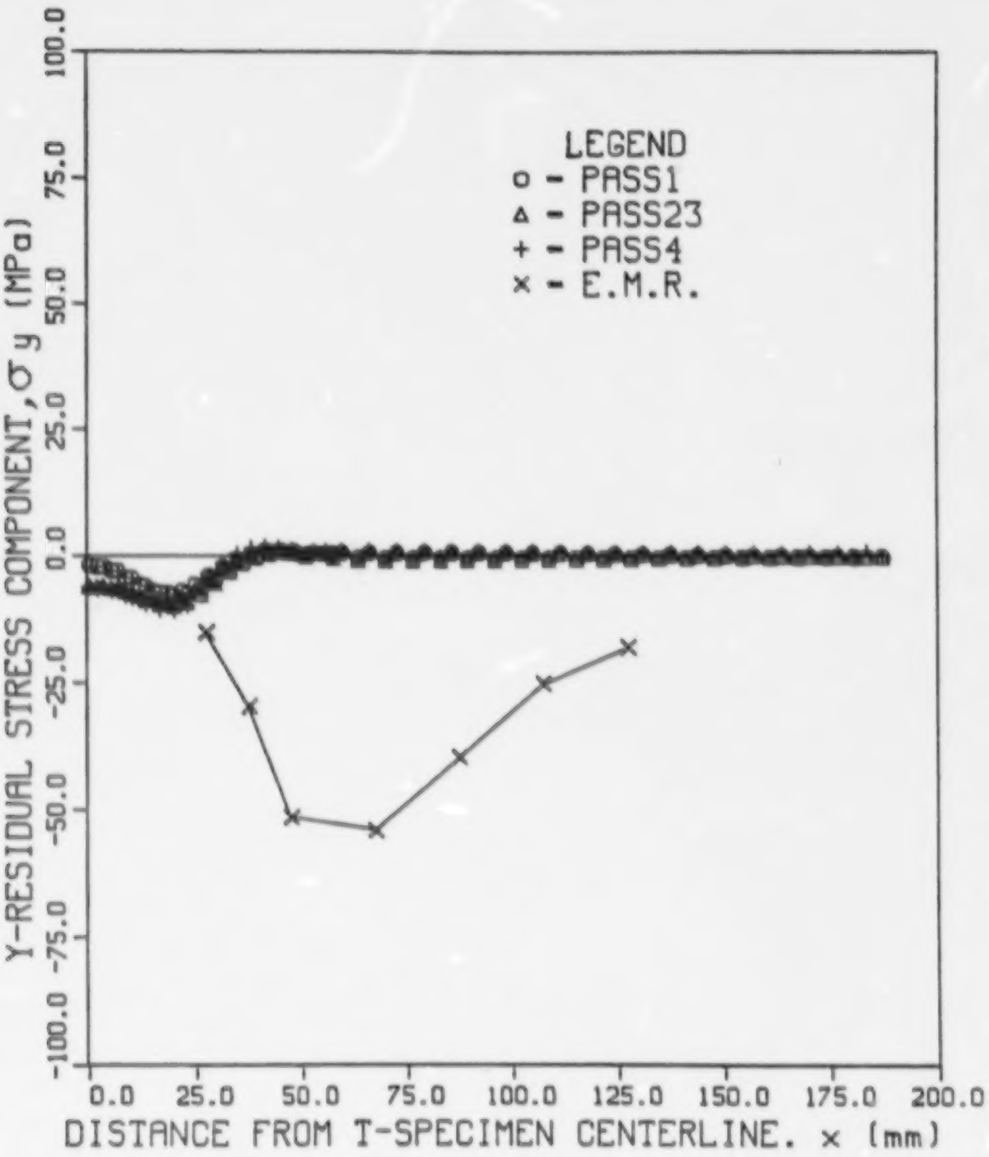

Figure 7.33: Distribution of the Y-residual stress component along the bottom surface (without previous residual stresses)

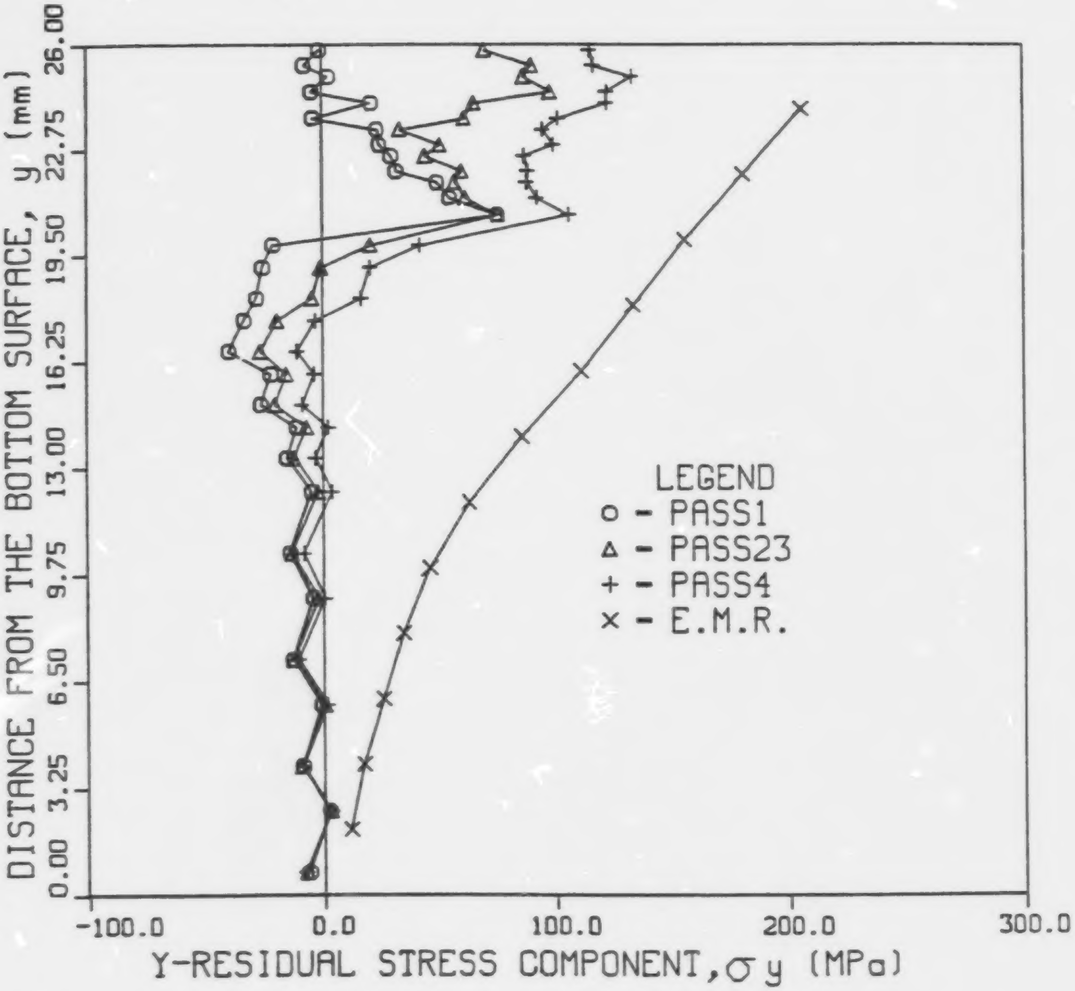

Figure 7.34: Distribution of the Y-residual stress component through the plate thickness below the weld toe (without previous residual stresses)

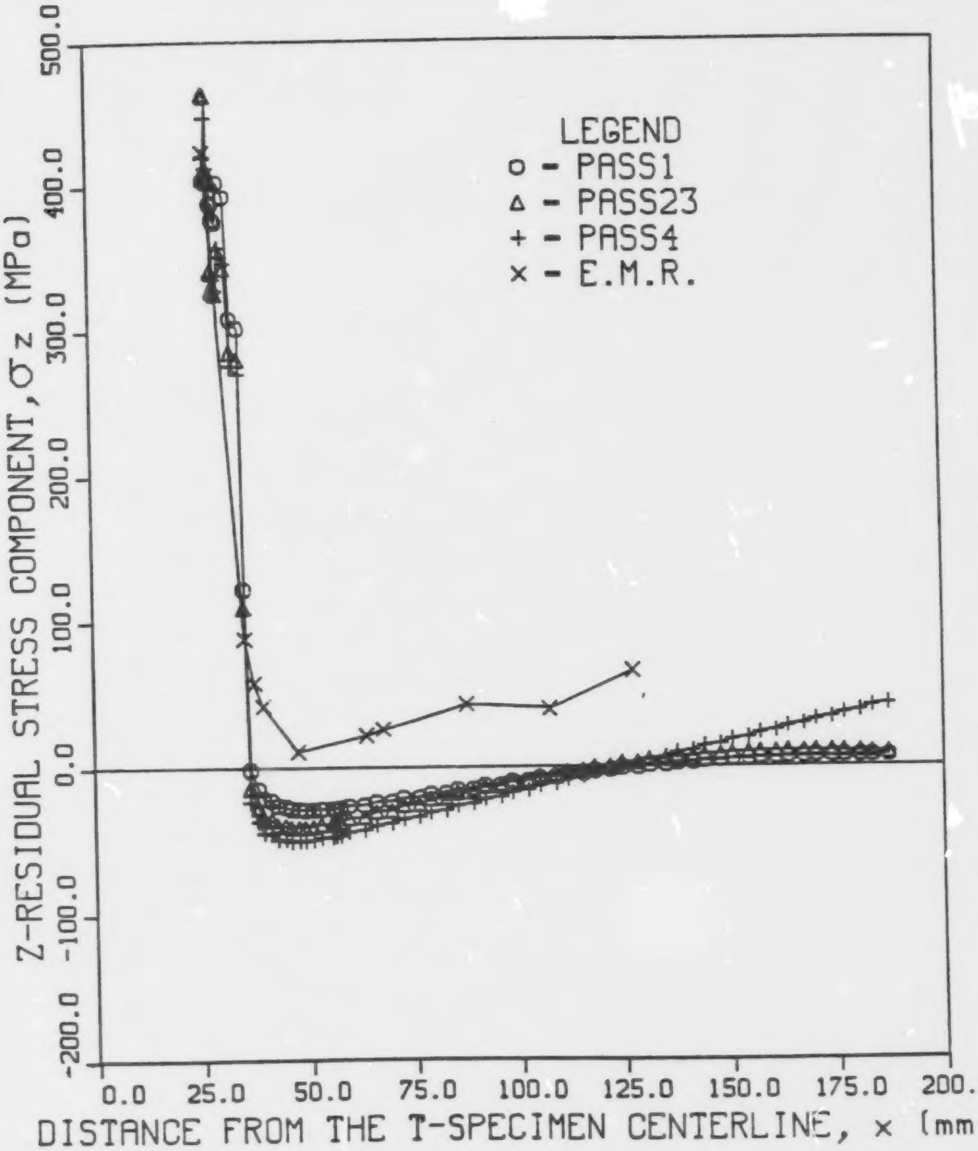

Figure 7.35: Distribution of the Z-residual stress component along the top surface (without previous residual stresses)

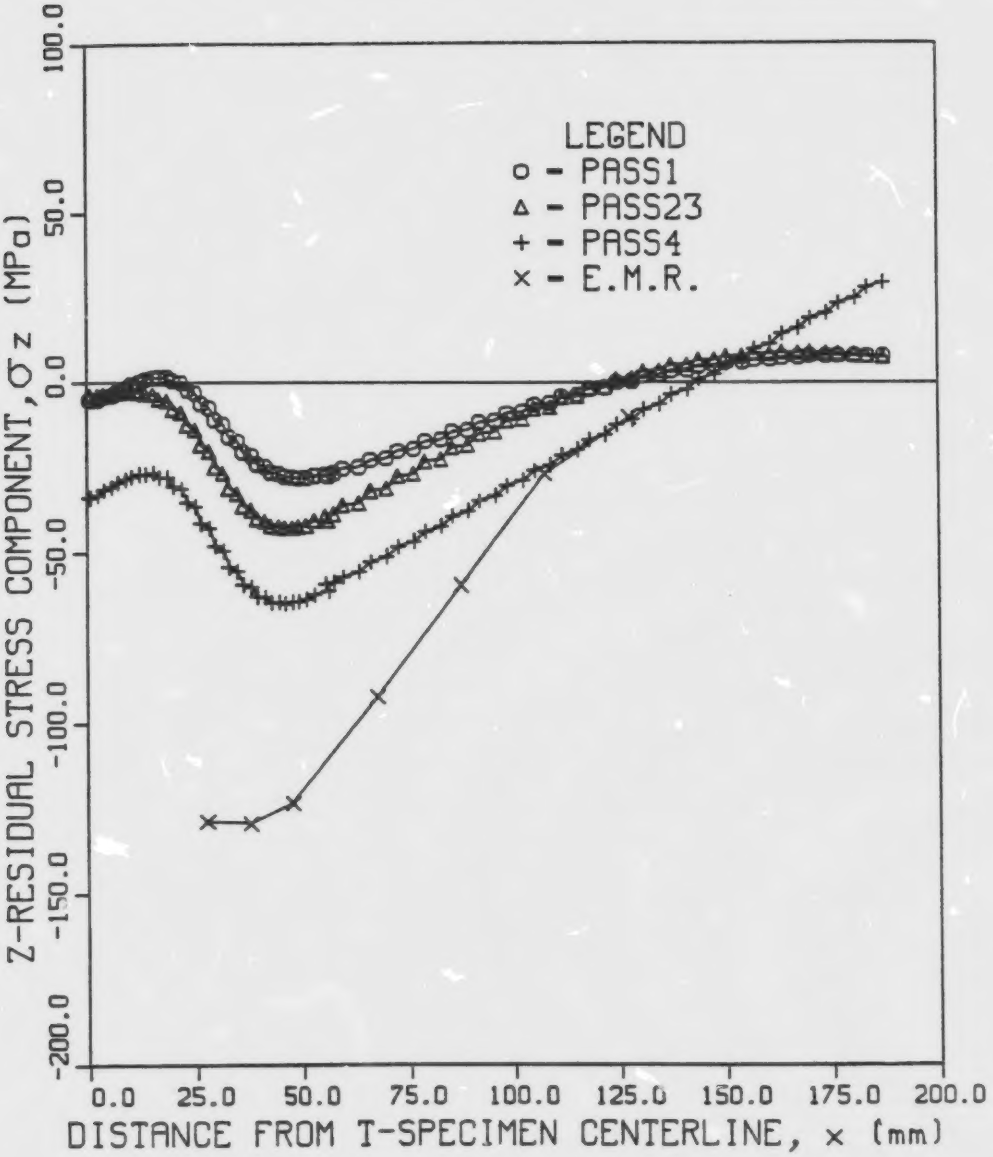

Figure 7.36: Distribution of the Z-residual stress component along the bottom surface (without previous residual stresses)

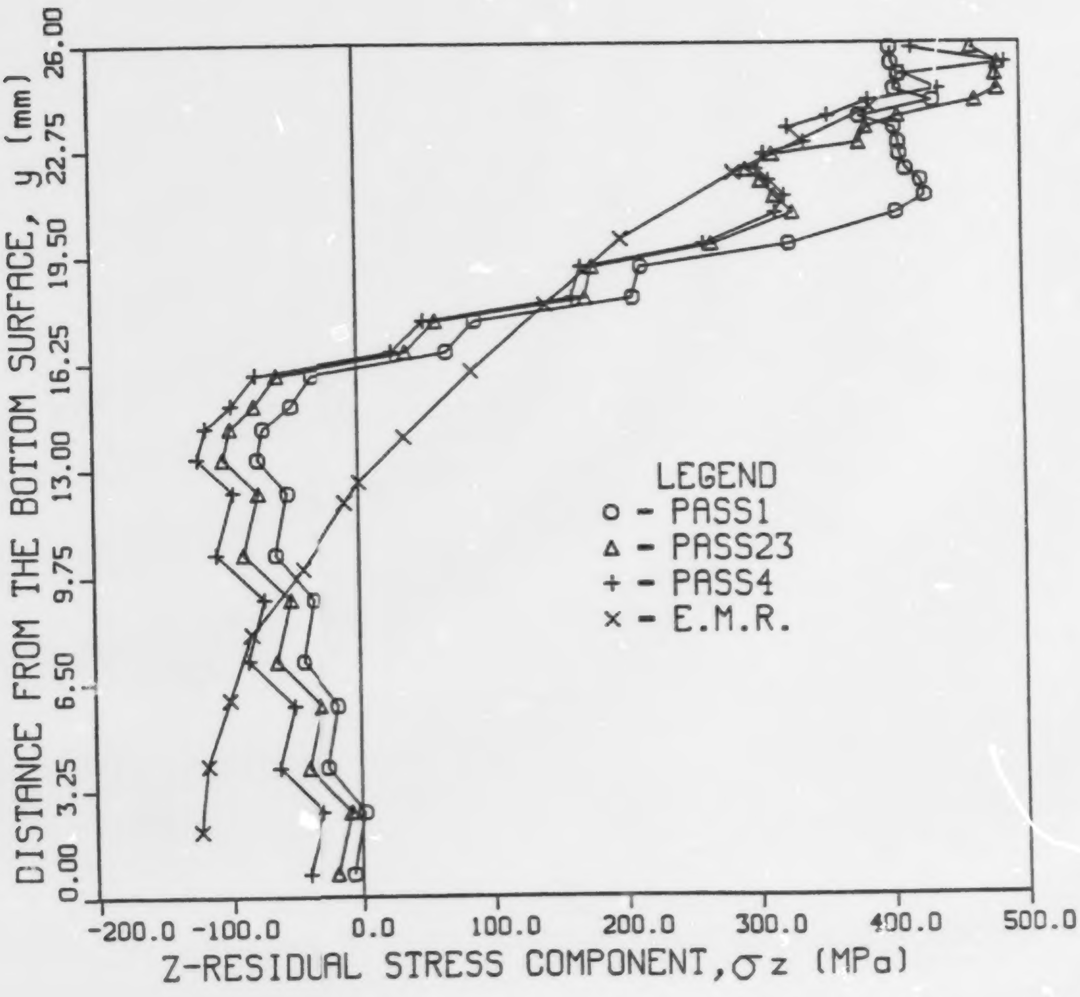

Figure 7.37: Distribution of the Z-residual stress component through the plate thickness below the weld toe (wihtout previous residual stresses)

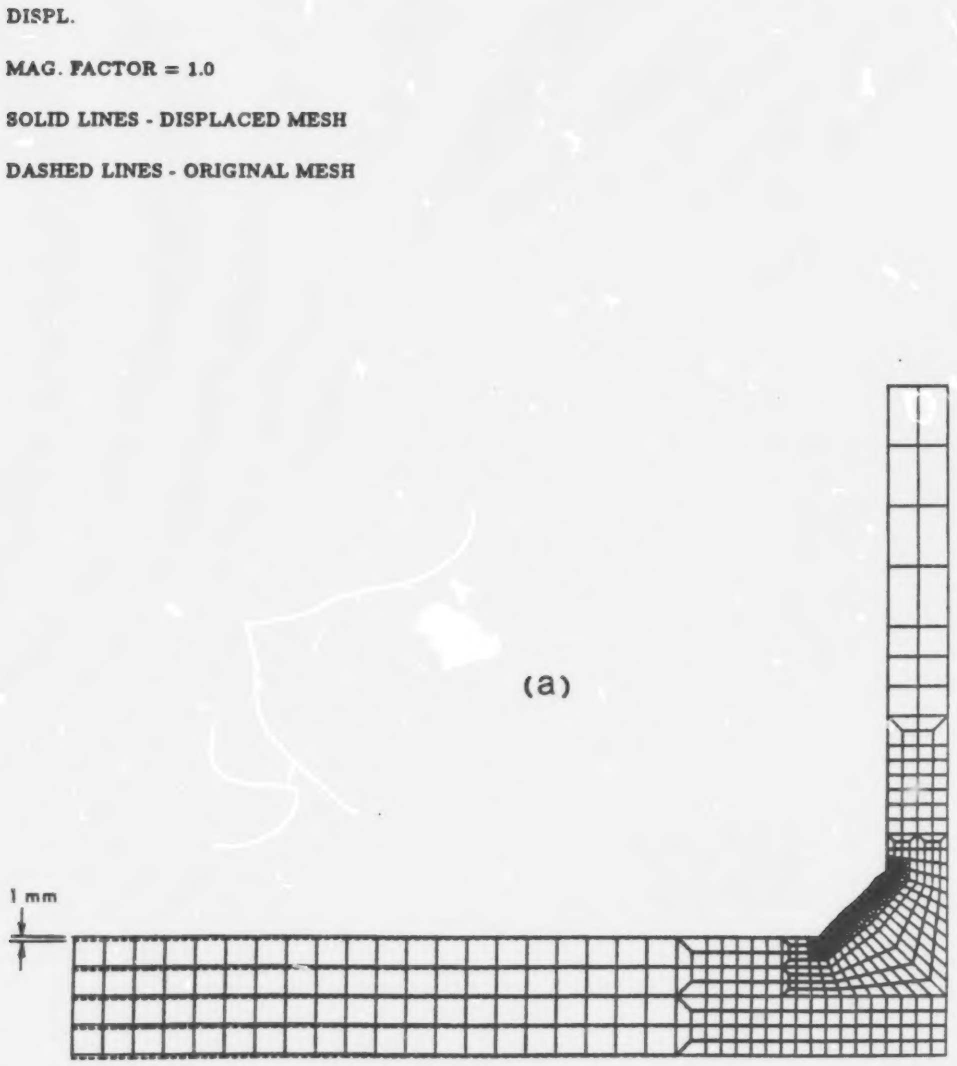
DISPL.
MAG. FACTOR = 1.0
SOLID LINES - DISPLACED MESH
DASHED LINES - ORIGINAL MESH
(a)
1 mm

Figure 7.38: Displaced T-joint specimen geometry (a); displaced mesh around weld region (b) after PASS 4

DISPL.
MAG. FACTOR = 1.0
SOLID LINES - DISPLACED MESH

DASHED LINES - ORIGINAL MESH

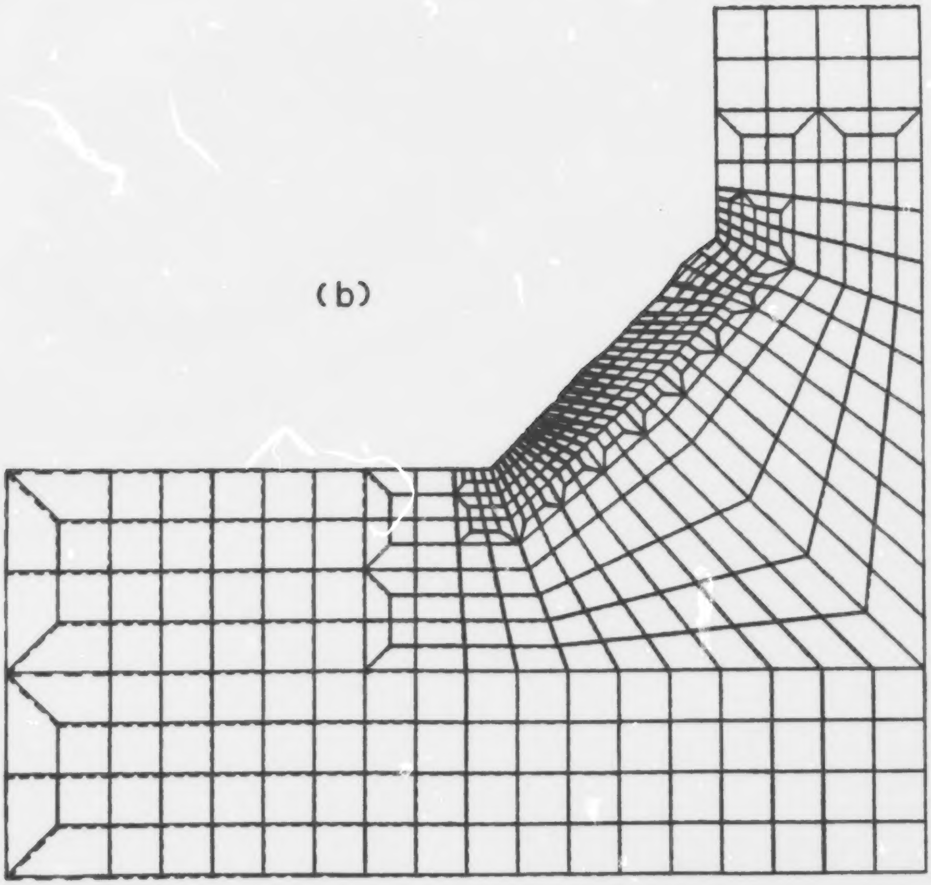

(b)

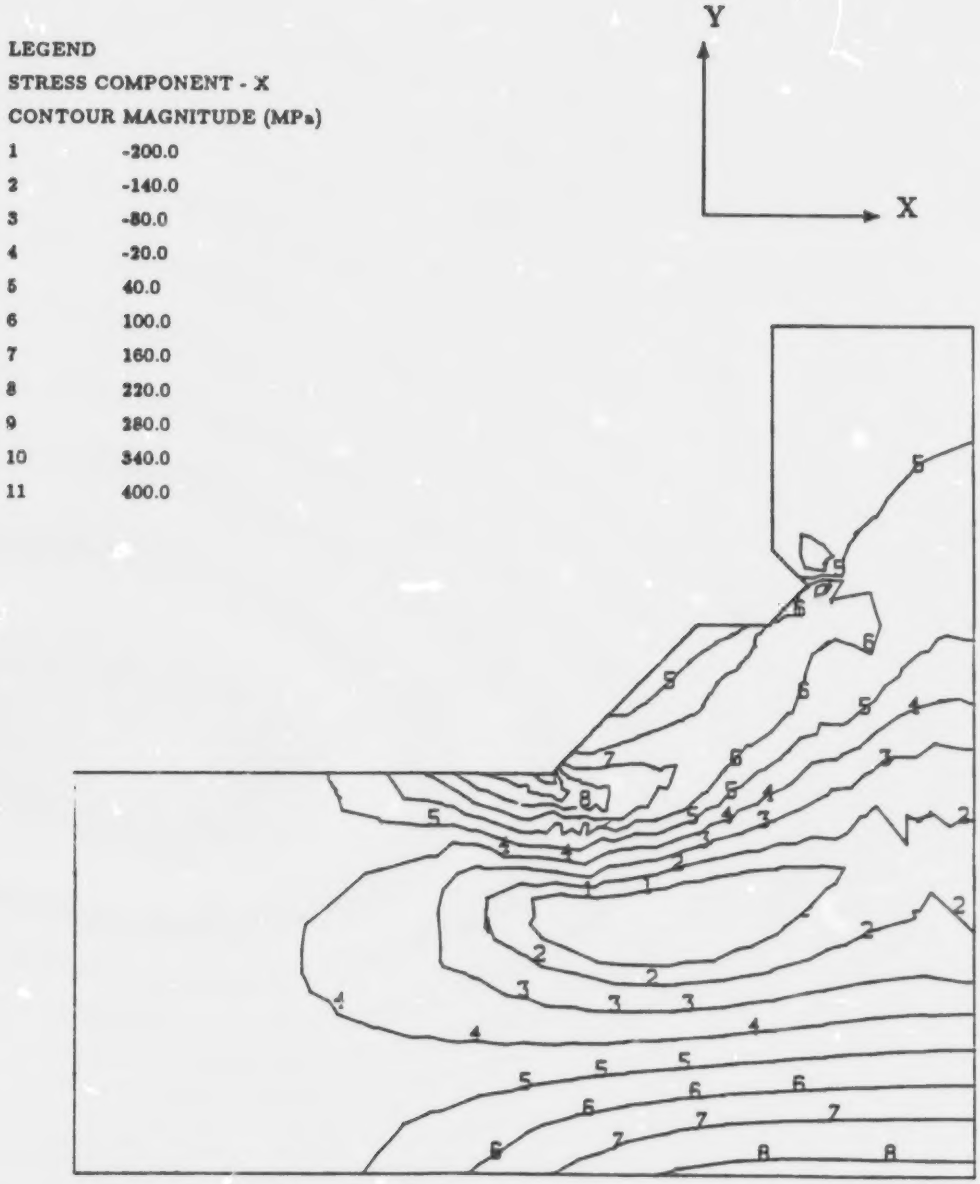

Figure 7.39: X-residual stress distribution - PASS 2&3

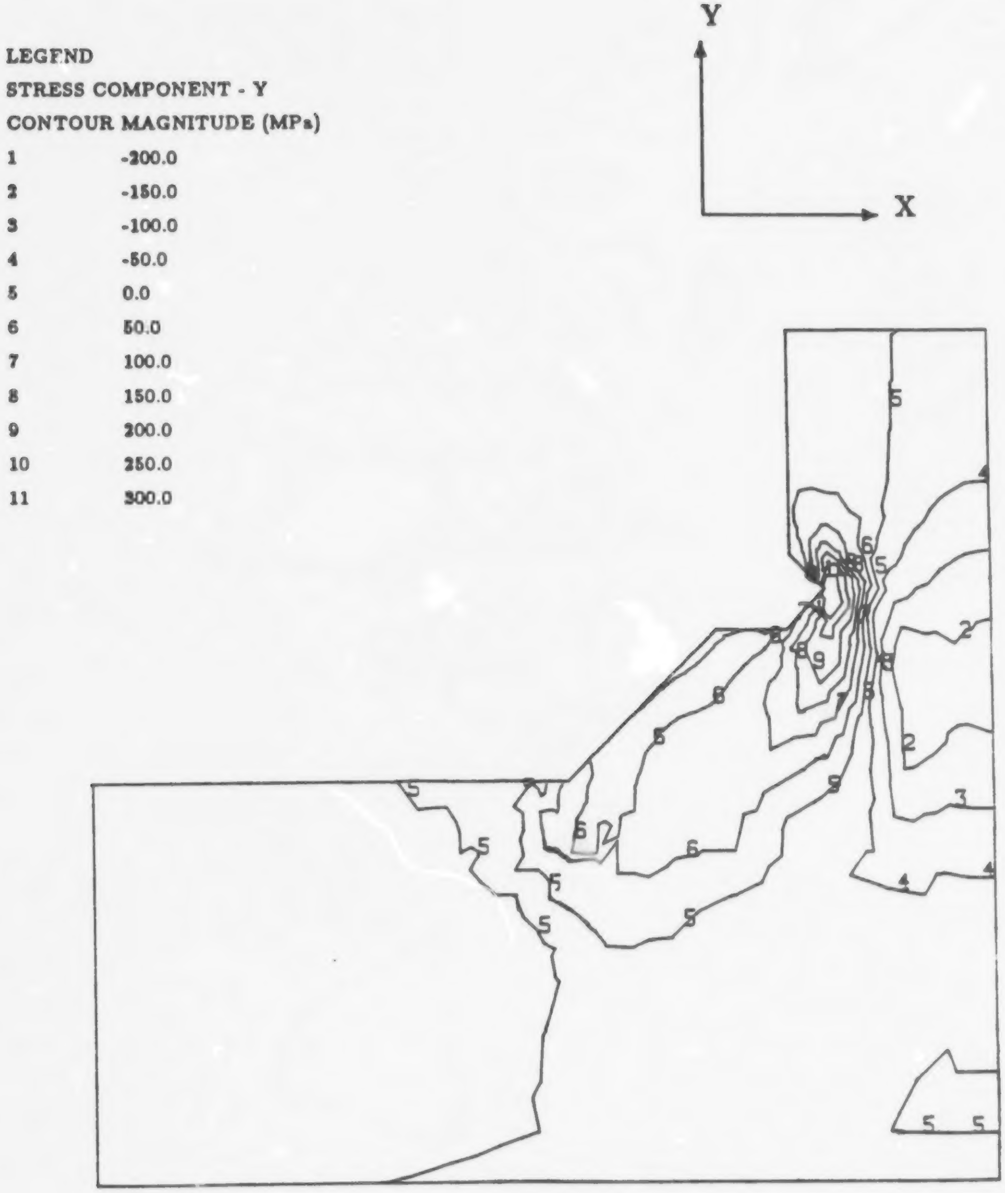

Figure 7.40: Y-residual stress distribution - PASS 2&3

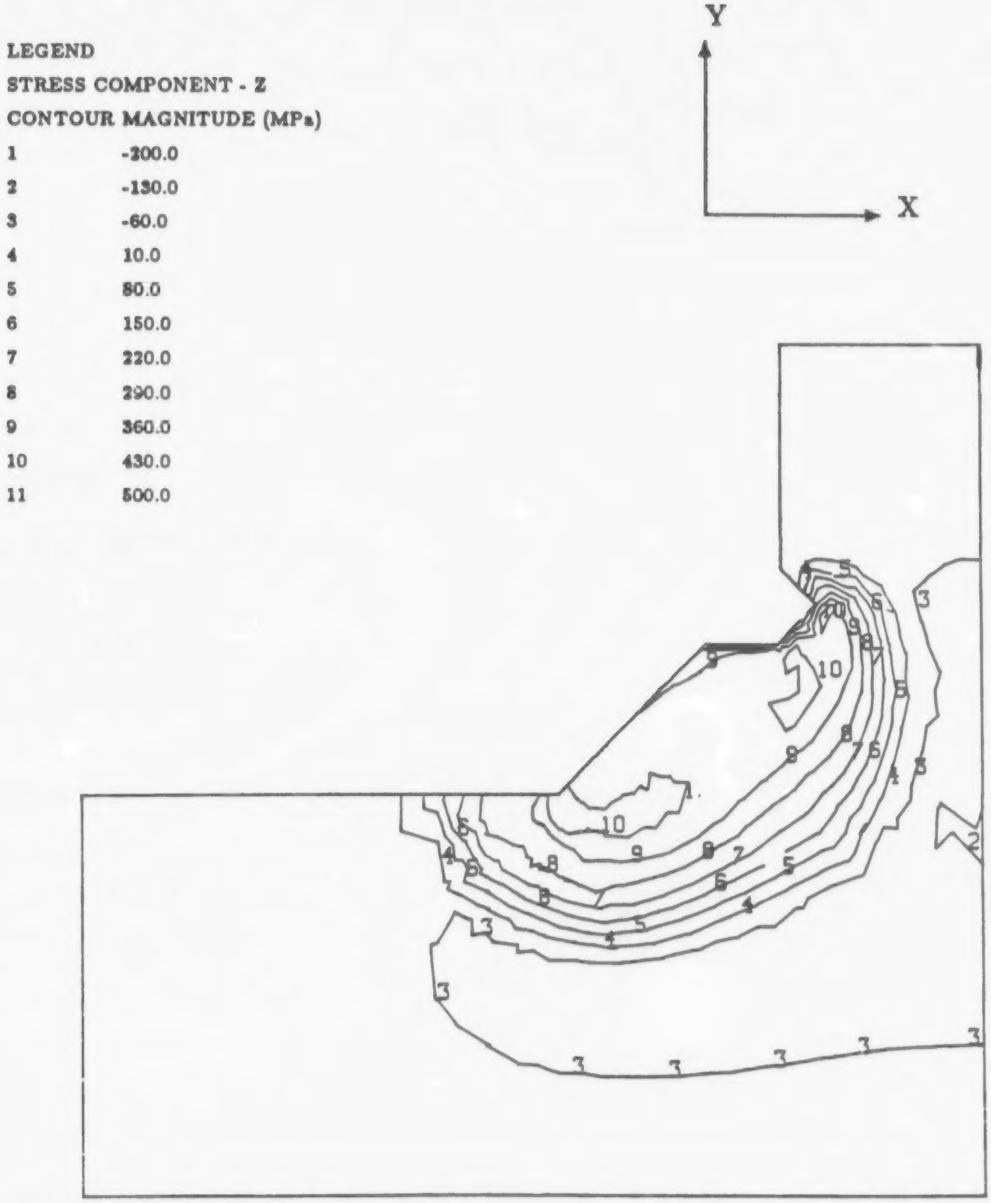

LEGEND

STRESS COMPONENT - Z

CONTOUR MAGNITUDE (MPa)

1	-200.0
2	-130.0
3	-60.0
4	10.0
5	80.0
6	150.0
7	220.0
8	290.0
9	360.0
10	430.0
11	500.0

Figure 7.41: Z-residual stress distribution - PASS 2&3

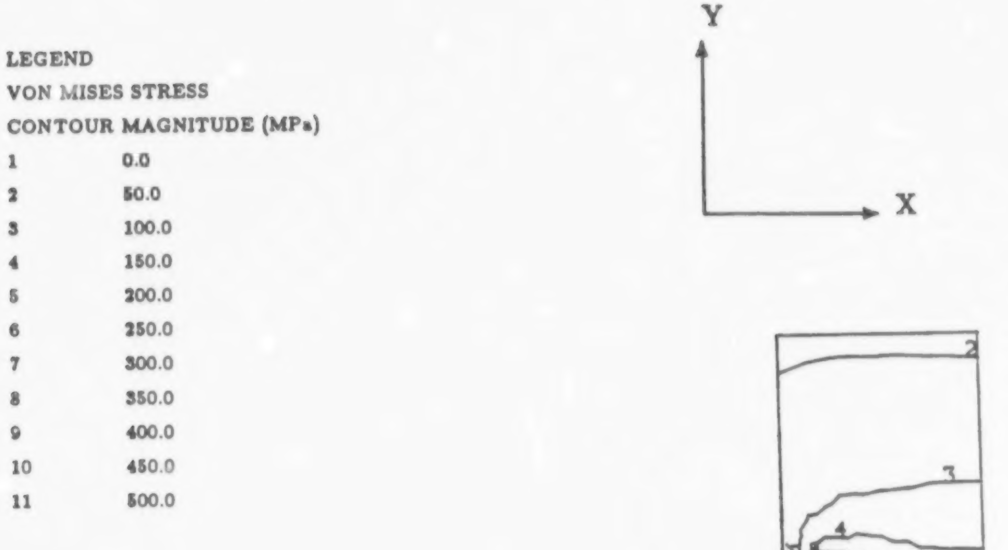

LEGEND
VON MISES STRESS

CONTOUR	MAGNITUDE (MPa)
1	0.0
2	50.0
3	100.0
4	150.0
5	200.0
6	250.0
7	300.0
8	350.0
9	400.0
10	450.0
11	500.0

Figure 7.42: Von Mises residual stress distribution - PASS 2&3

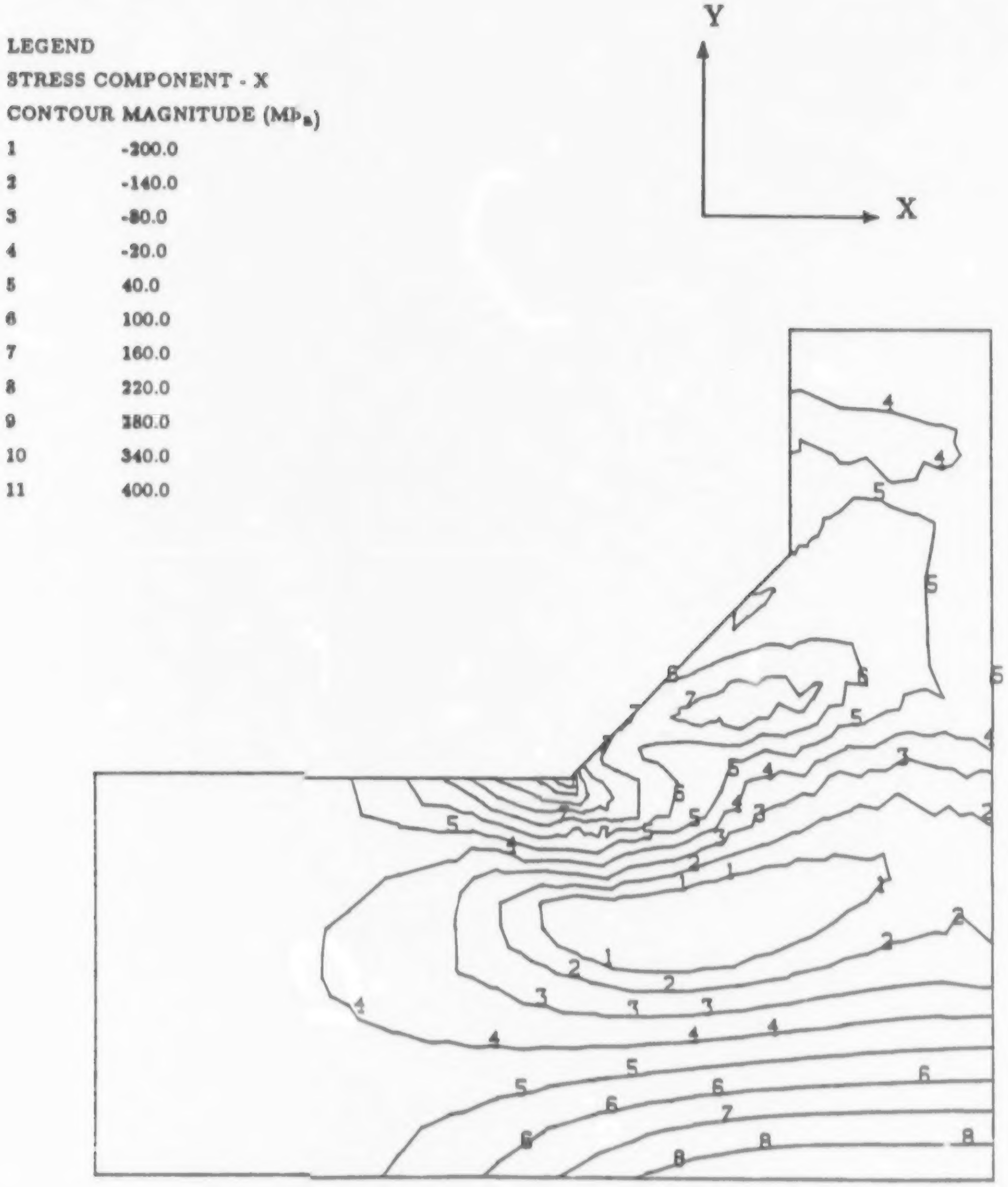

Figure 7.43: X-residual stress distribution - PASS 4

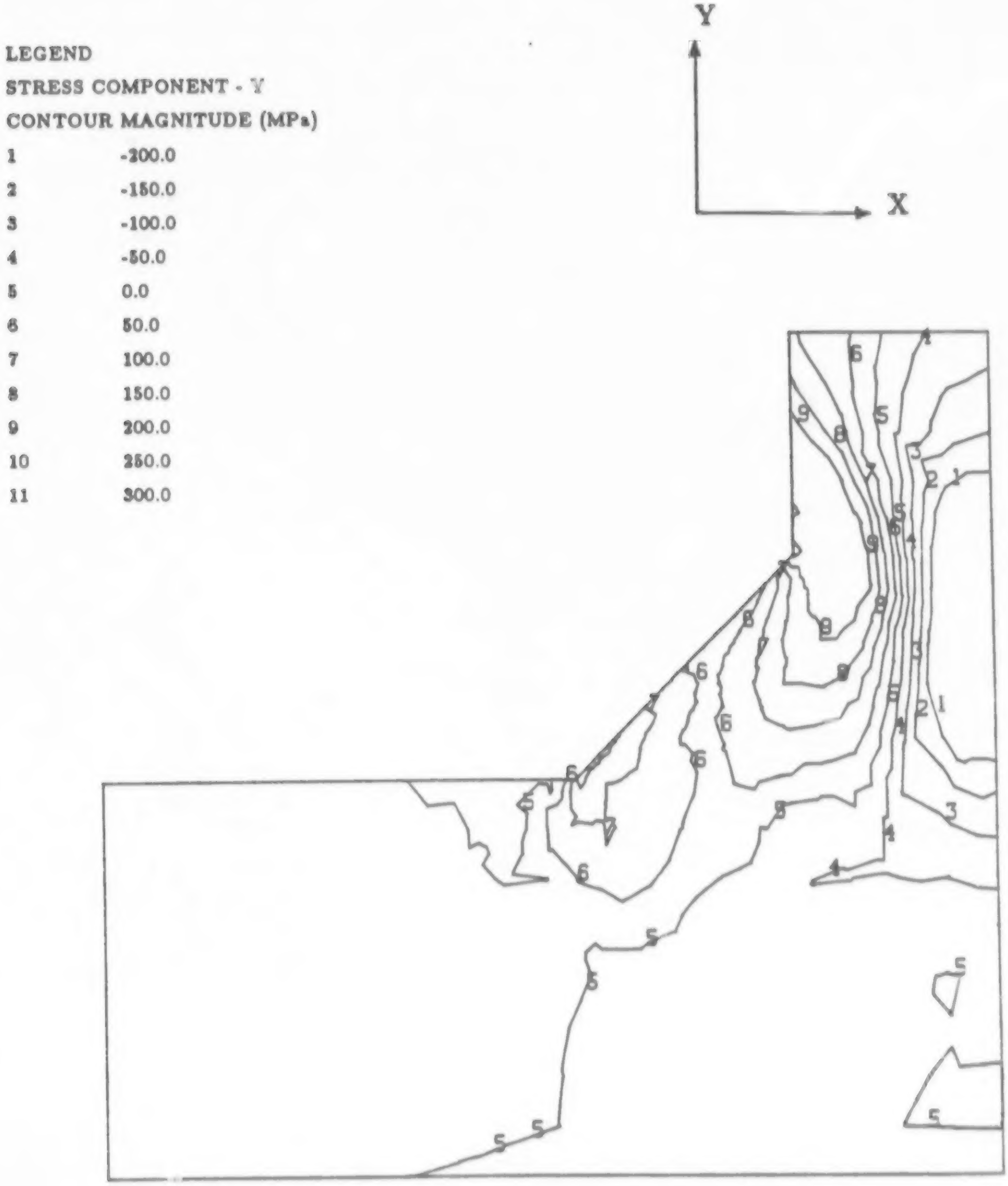

Figure 7.44: Y-residual stress distribution - PASS 4

LEGEND

STRESS COMPONENT - Z

CONTOUR MAGNITUDE (MPa)	
1	-200.0
2	-130.0
3	-60.0
4	10.0
5	80.0
6	150.0
7	220.0
8	290.0
9	360.0
10	430.0
11	500.0

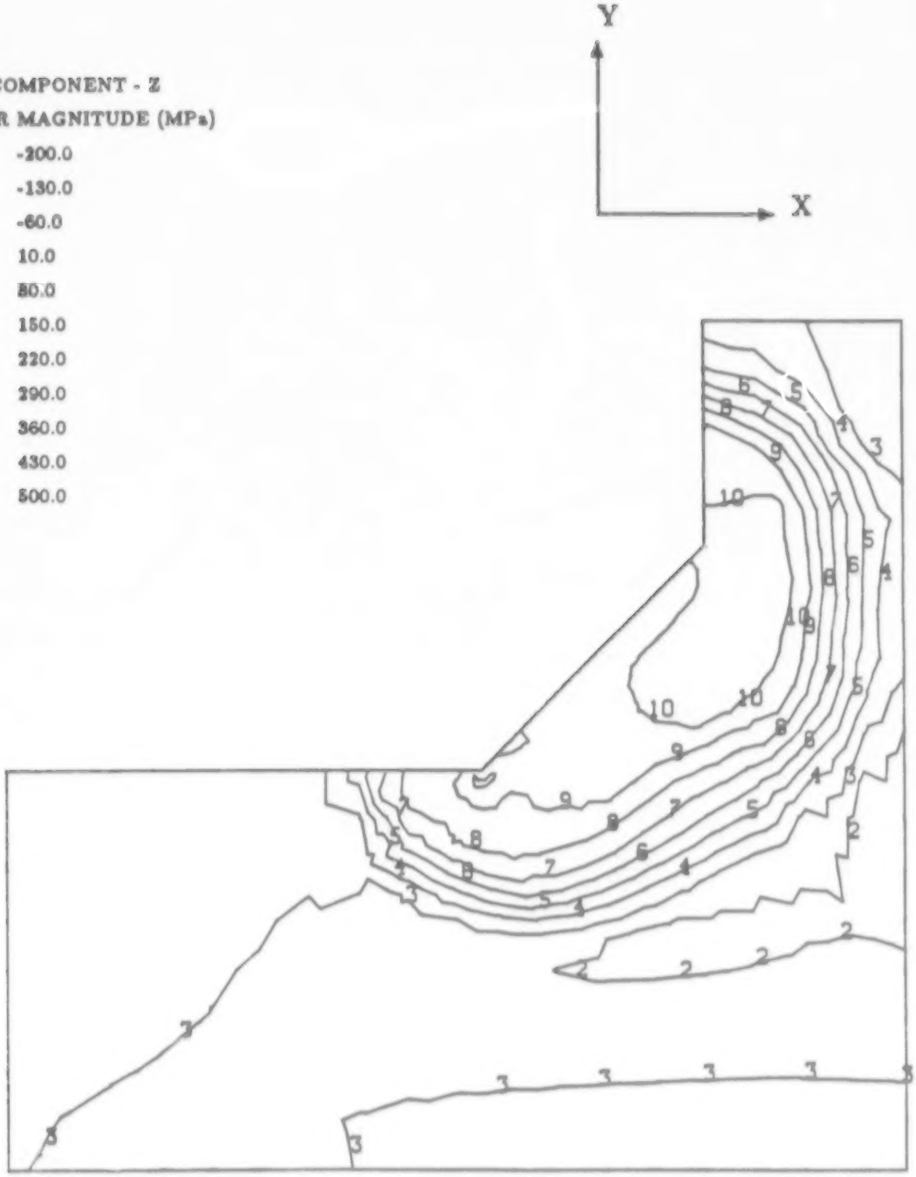

Figure 7.45: Z-residual stress distribution - PASS 4

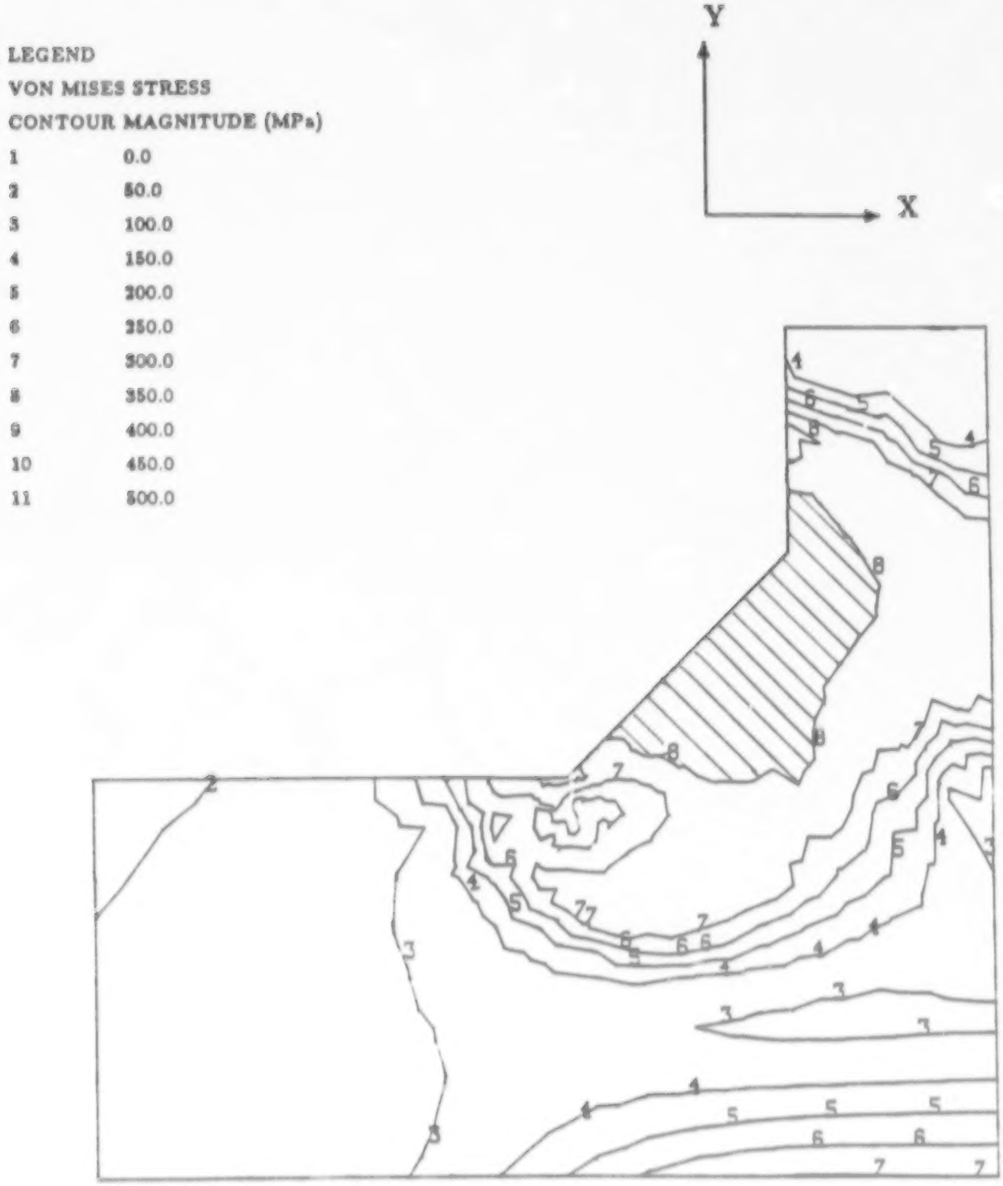

LEGEND
VON MISES STRESS

CONTOUR	MAGNITUDE (MPa)
1	0.0
2	50.0
3	100.0
4	150.0
5	200.0
6	250.0
7	300.0
8	350.0
9	400.0
10	450.0
11	500.0

Figure 7.46: Von Mises residual stress distribution - PASS 4

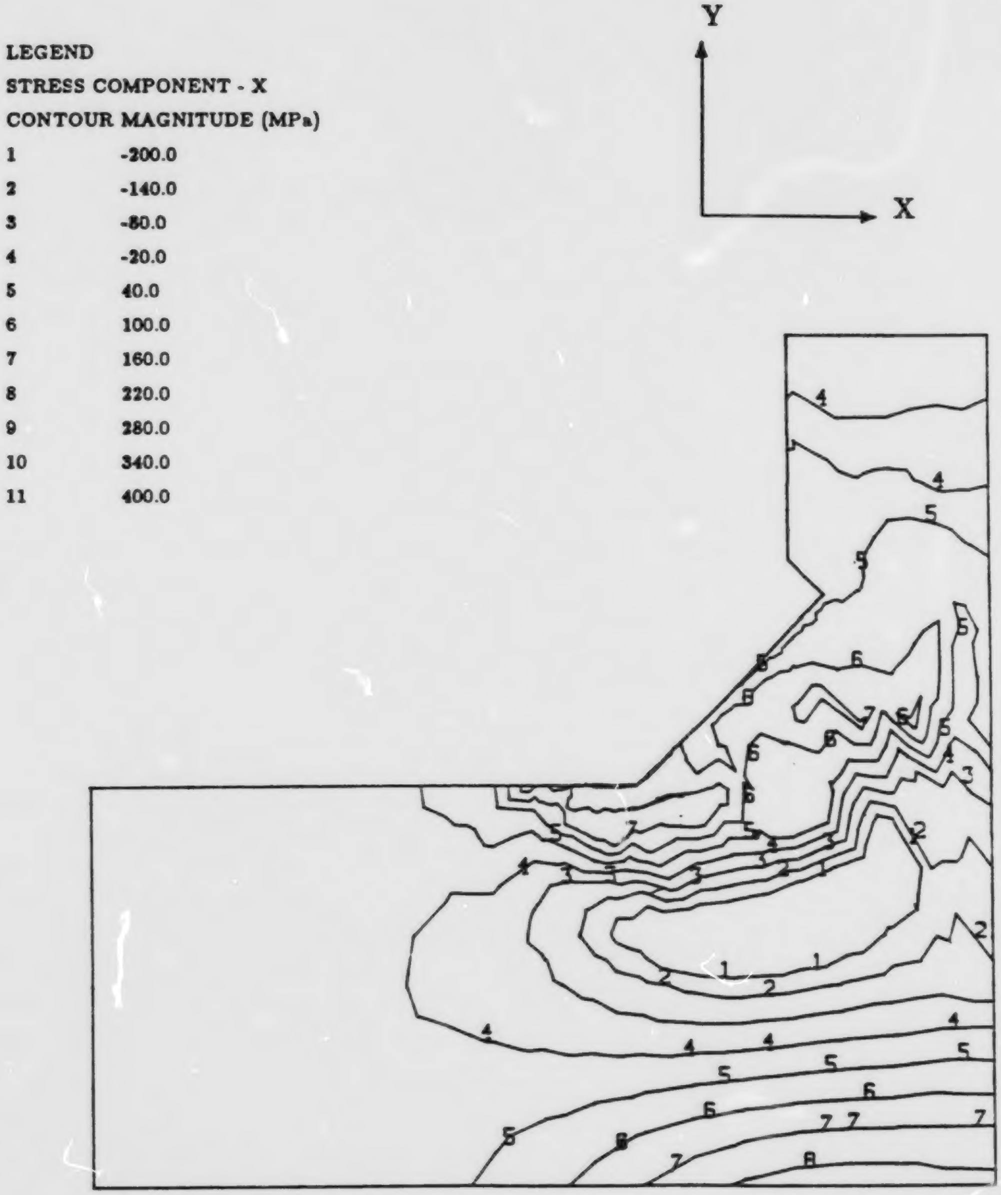

LEGEND

STRESS COMPONENT - X

CONTOUR	MAGNITUDE (MPa)
1	-200.0
2	-140.0
3	-80.0
4	-20.0
5	40.0
6	100.0
7	160.0
8	220.0
9	280.0
10	340.0
11	400.0

Figure 7.47: The assumed X-residual stress distribution

LEGEND

STRESS COMPONENT - Y

CONTOUR MAGNITUDE (MPa)

1	-200.0
2	-150.0
3	-100.0
4	-50.0
5	0.0
6	50.0
7	100.0
8	150.0
9	200.0
10	250.0
11	300.0

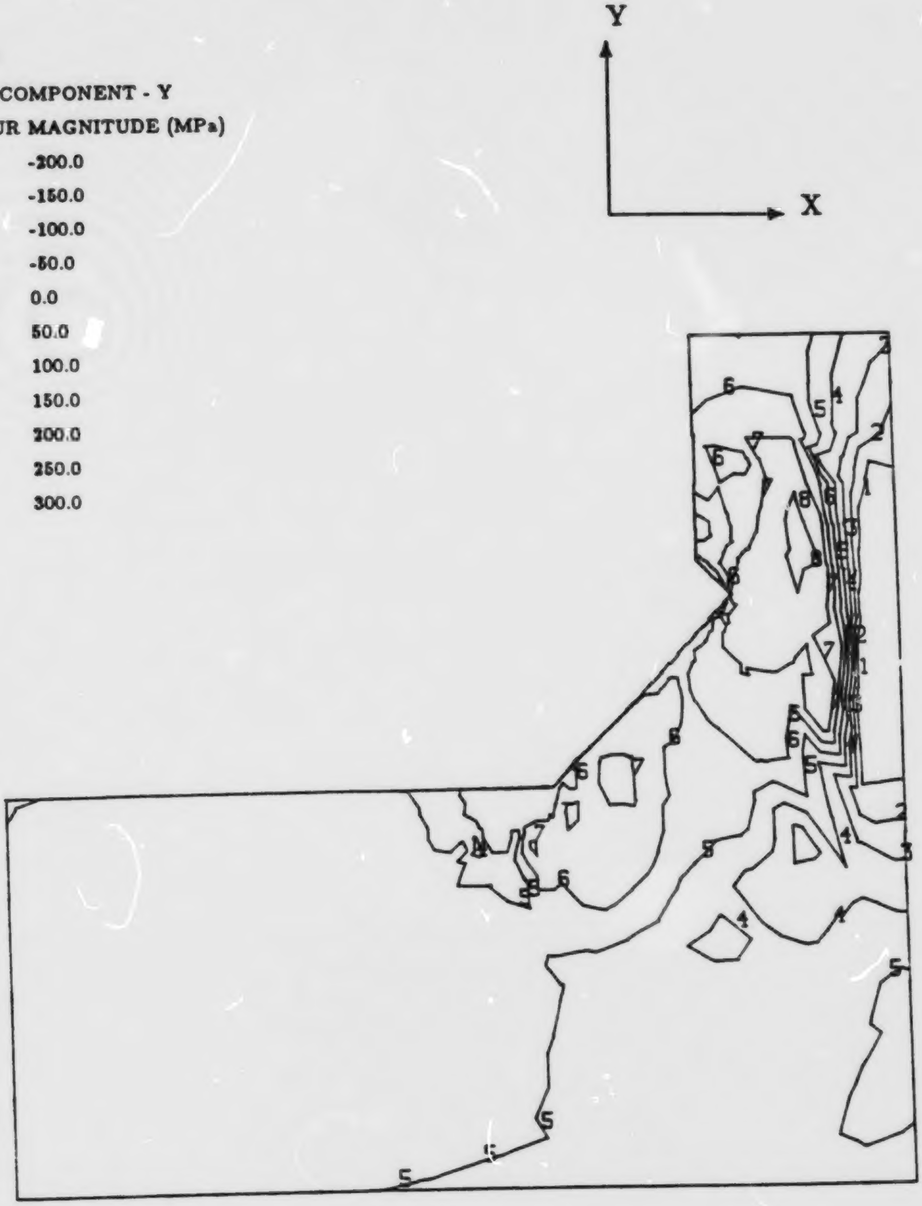

Figure 7.48: The assumed Y-residual stress distribution

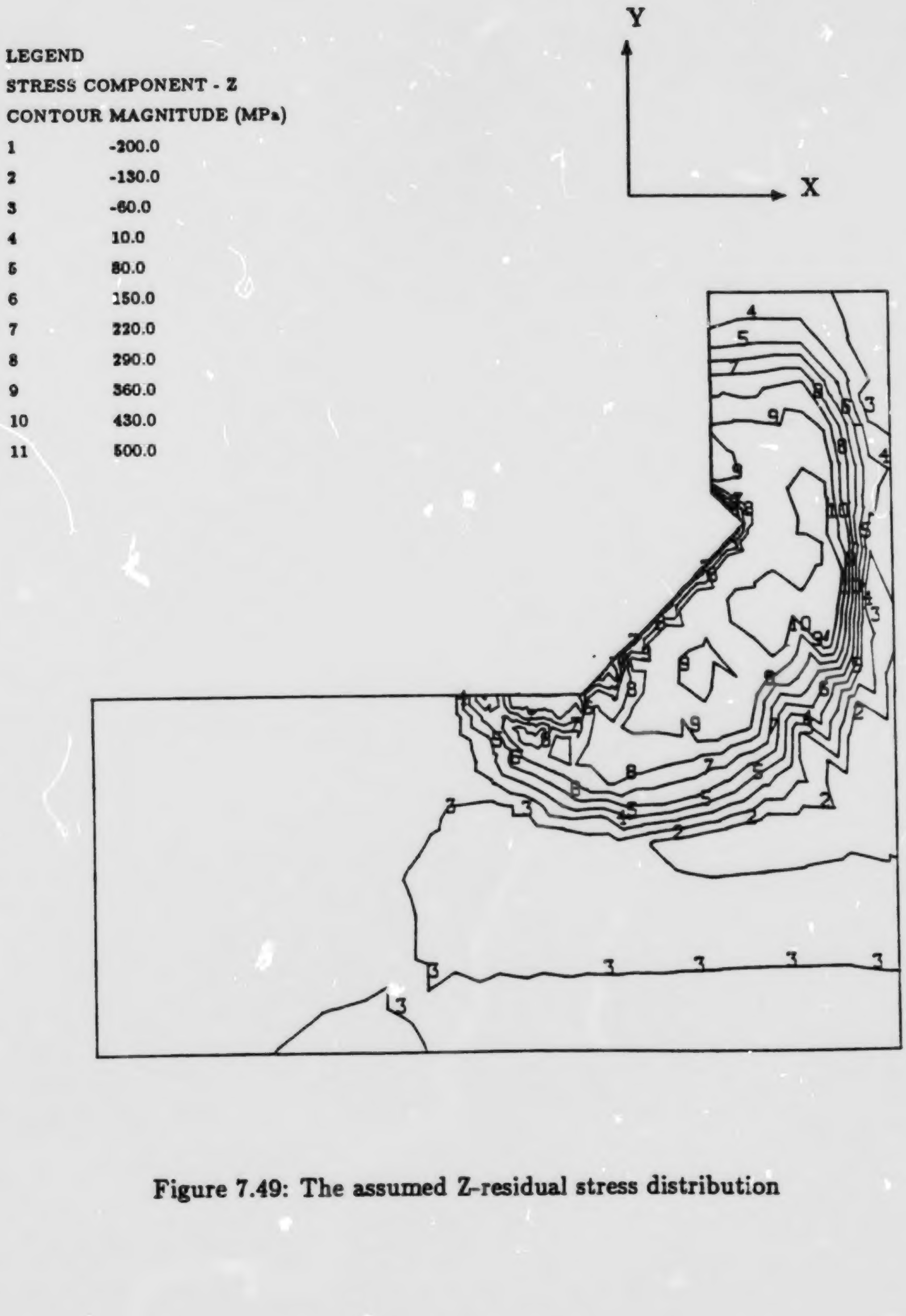

LEGEND

STRESS COMPONENT - Z

CONTOUR MAGNITUDE (MPa)

1	-200.0
2	-130.0
3	-60.0
4	10.0
5	80.0
6	150.0
7	220.0
8	290.0
9	360.0
10	430.0
11	500.0

Figure 7.49: The assumed Z-residual stress distribution

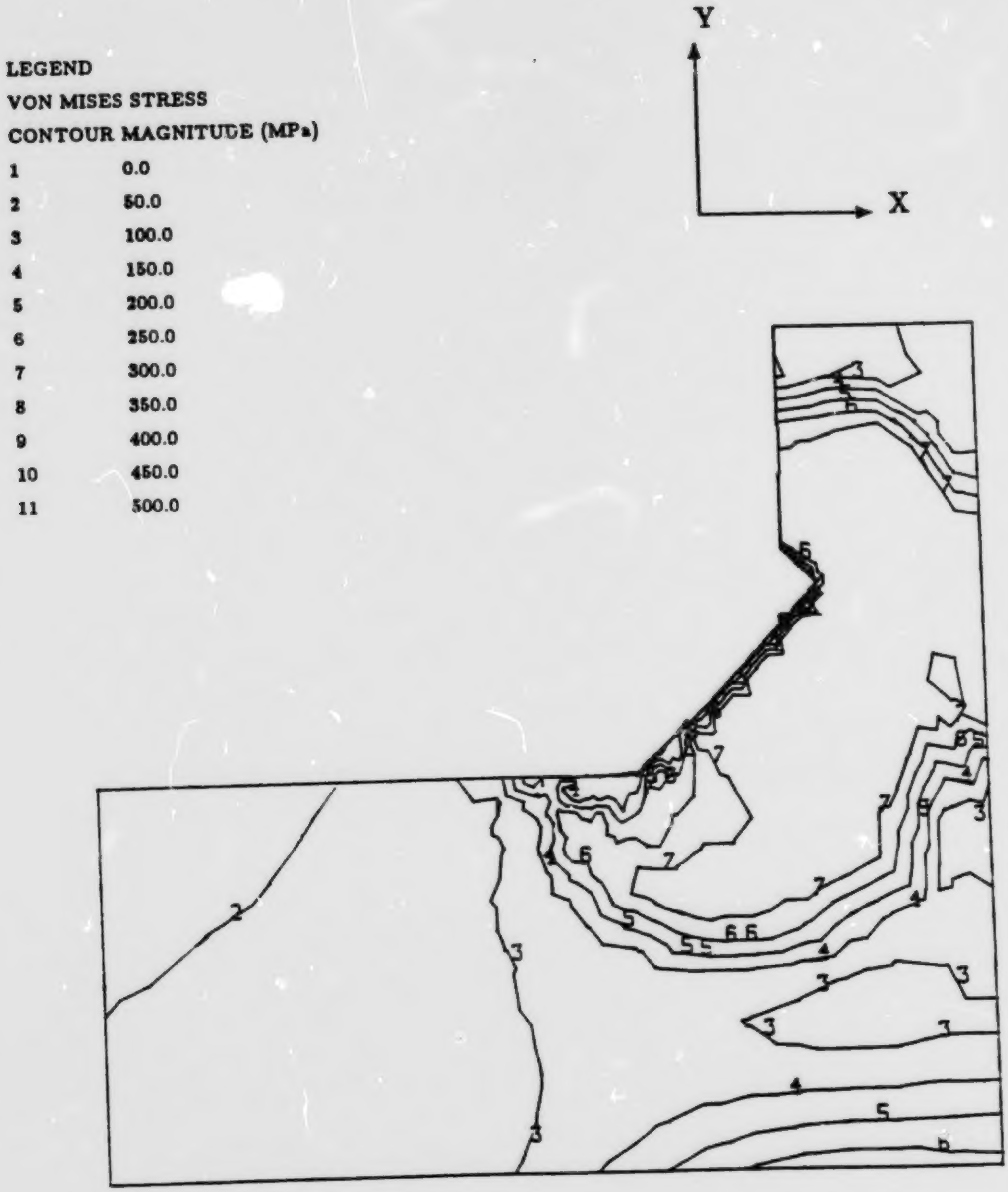

Figure 7.50: The assumed Von Mises equivalent stress distribution

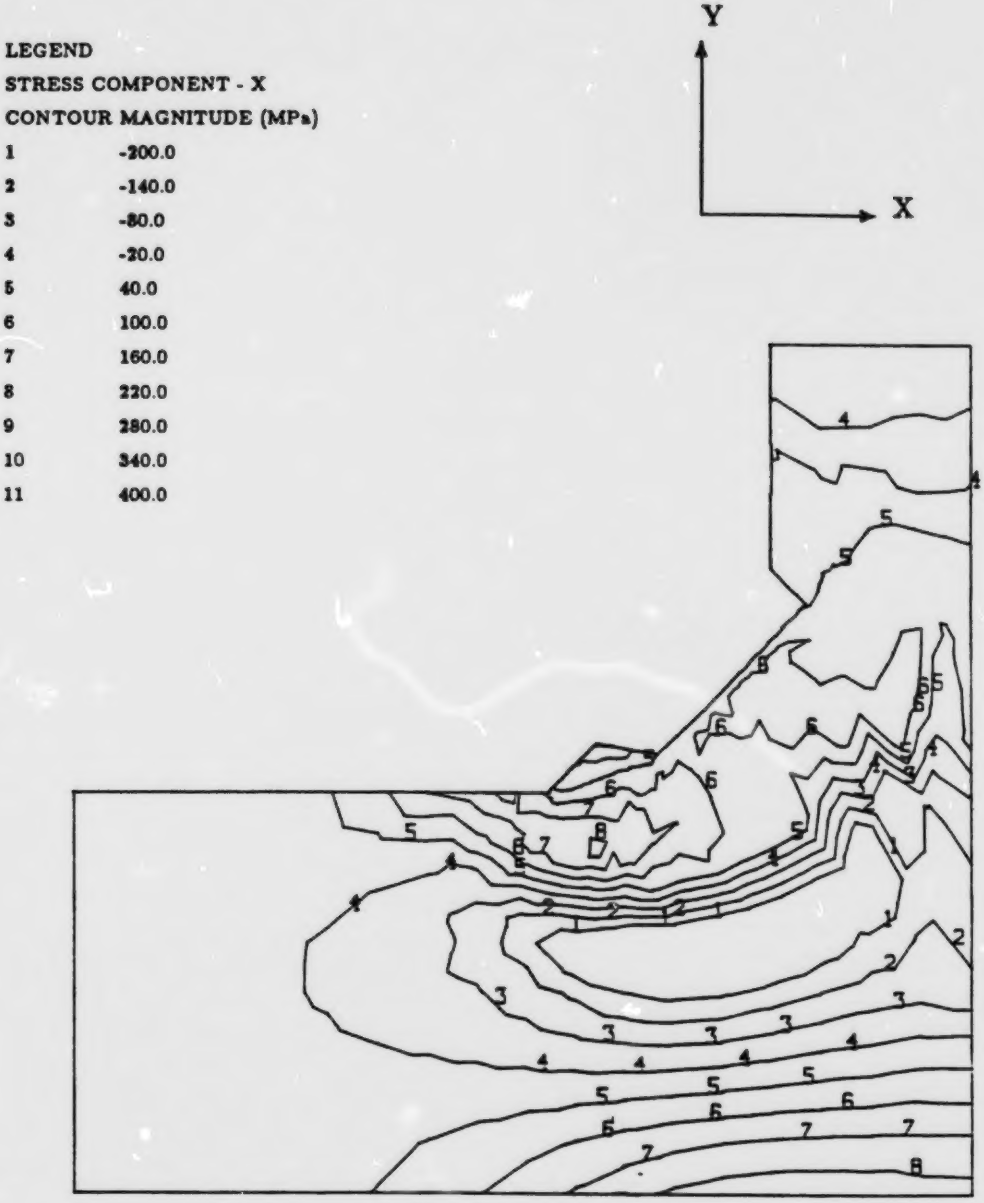

Figure 7.51: X-residual stress distribution with A.R.S - PASS 1

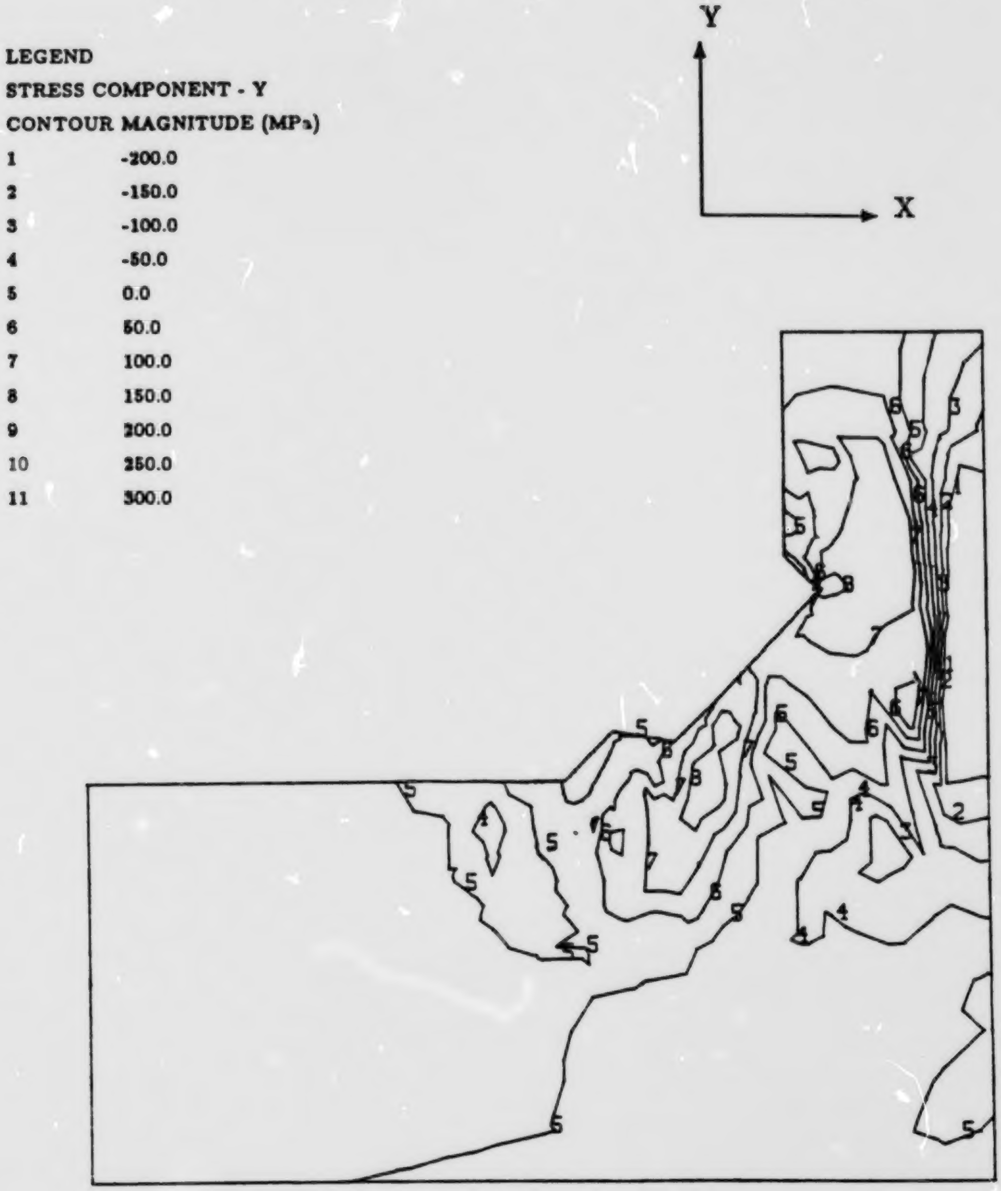

Figure 7.52: Y-residual stress distribution with A.R.S - PASS 1

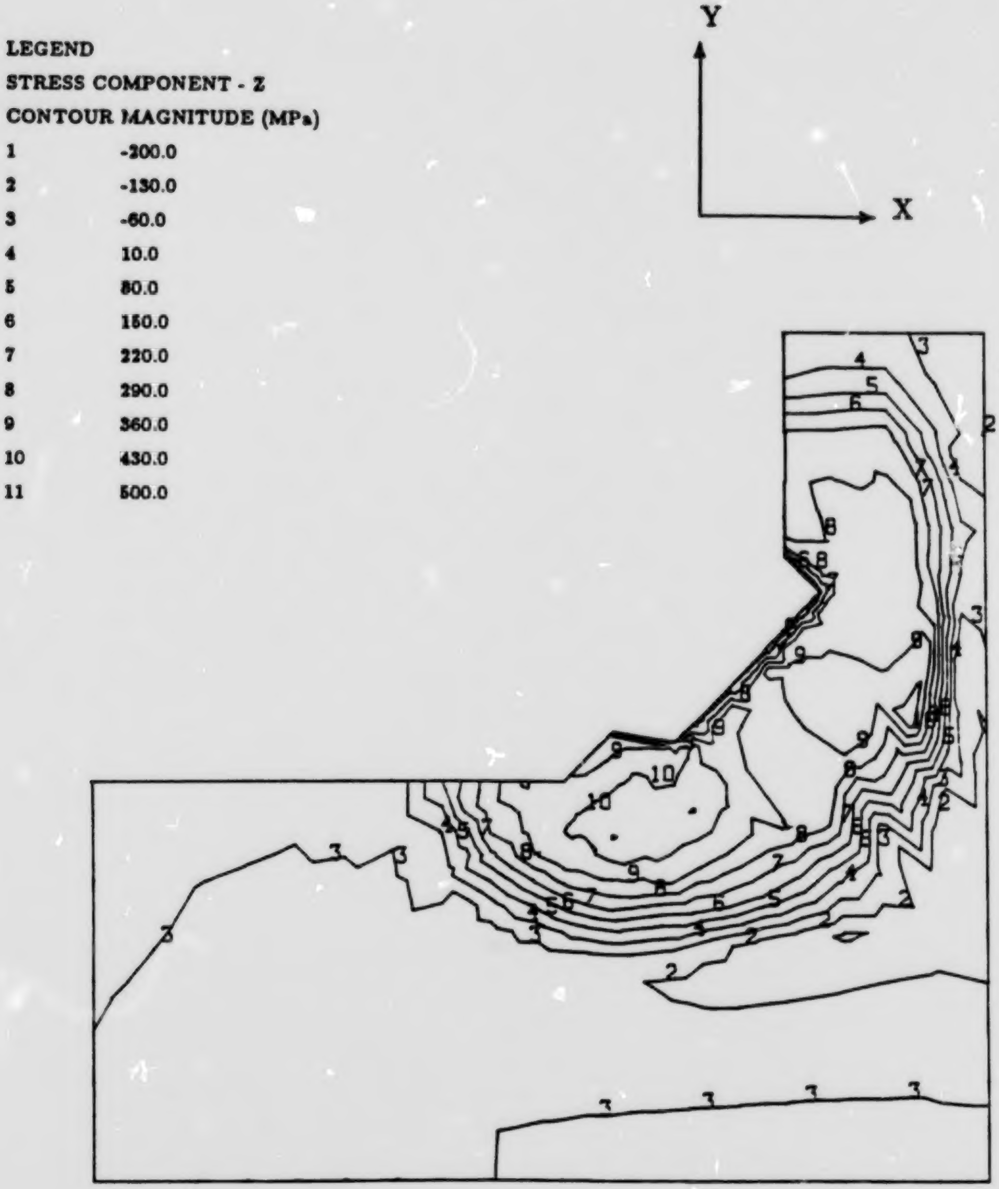

Figure 7.53: Z-residual stress distribution with A.R.S - PASS 1

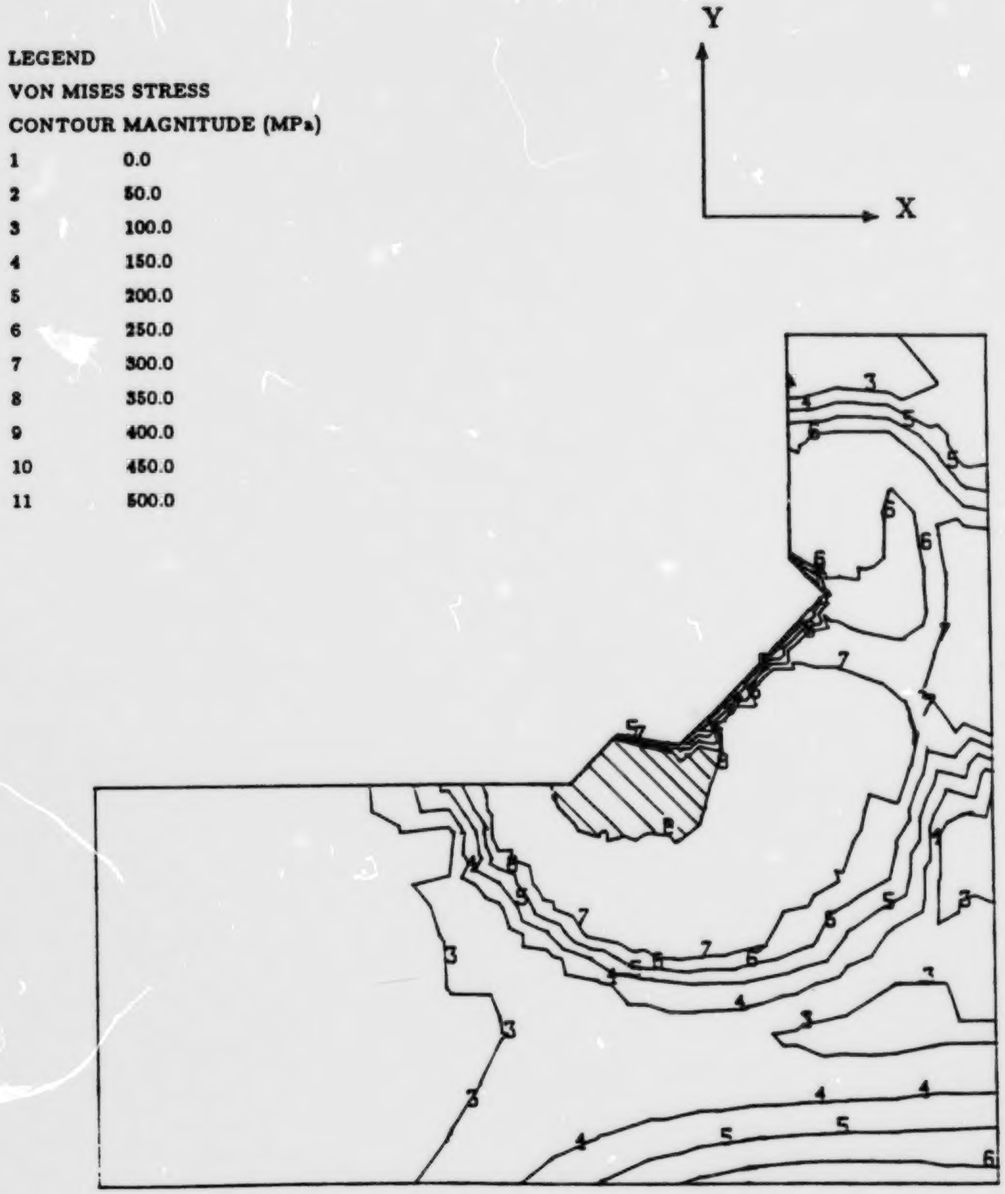

LEGEND

VON MISES STRESS

CONTOUR MAGNITUDE (MPa)

1	0.0
2	50.0
3	100.0
4	150.0
5	200.0
6	250.0
7	300.0
8	350.0
9	400.0
10	450.0
11	500.0

Figure 7.54: Von Mises stress distribution with A.R.S - PASS 1

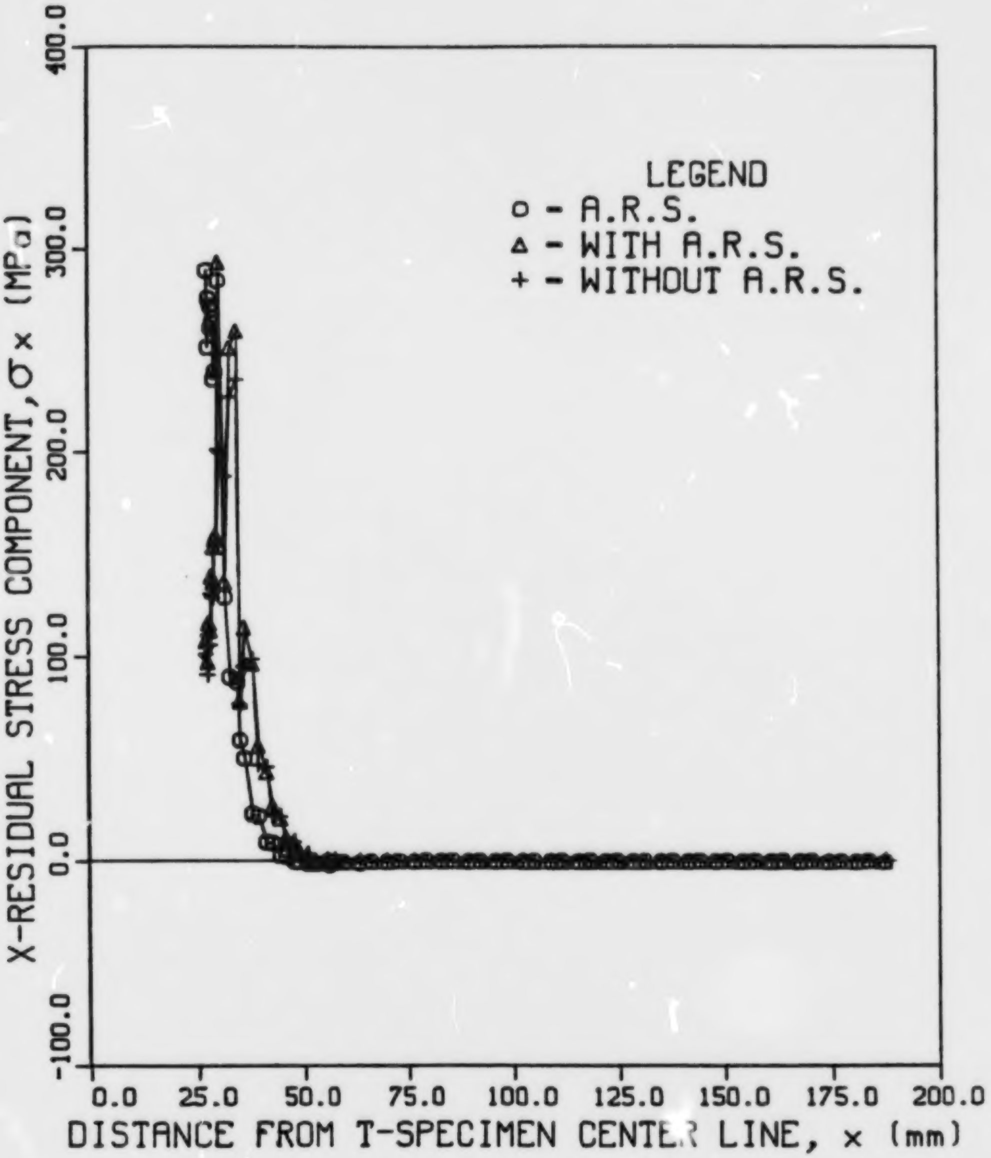

Figure 7.55: Distribution of the X-residual stress component along the top surface after the first pass

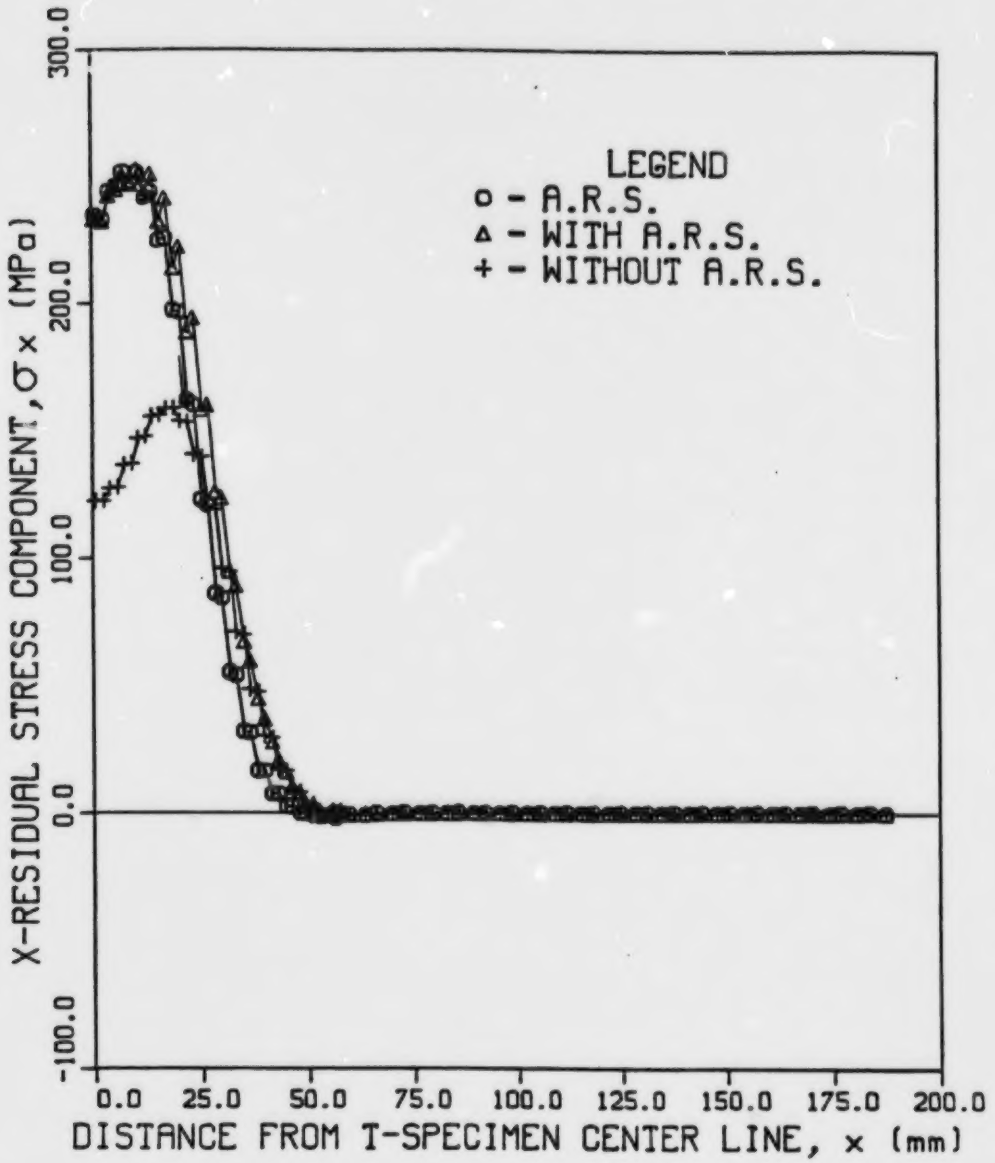

Figure 7.56: Distribution of the X-residual stress component along the bottom surface after the first pass

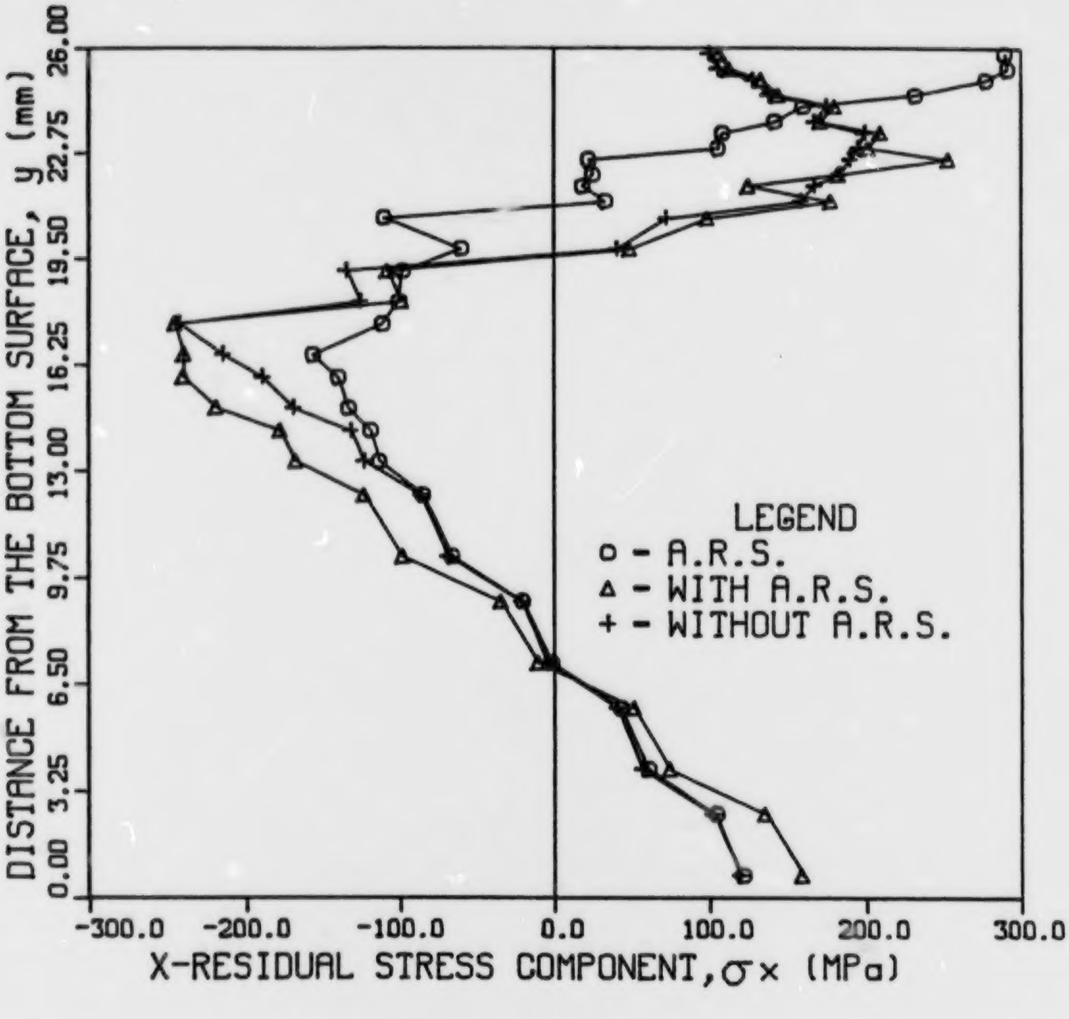

Figure 7.57: Distribution of the X-residual stress component through the plate thickness below the weld toe after the first pass

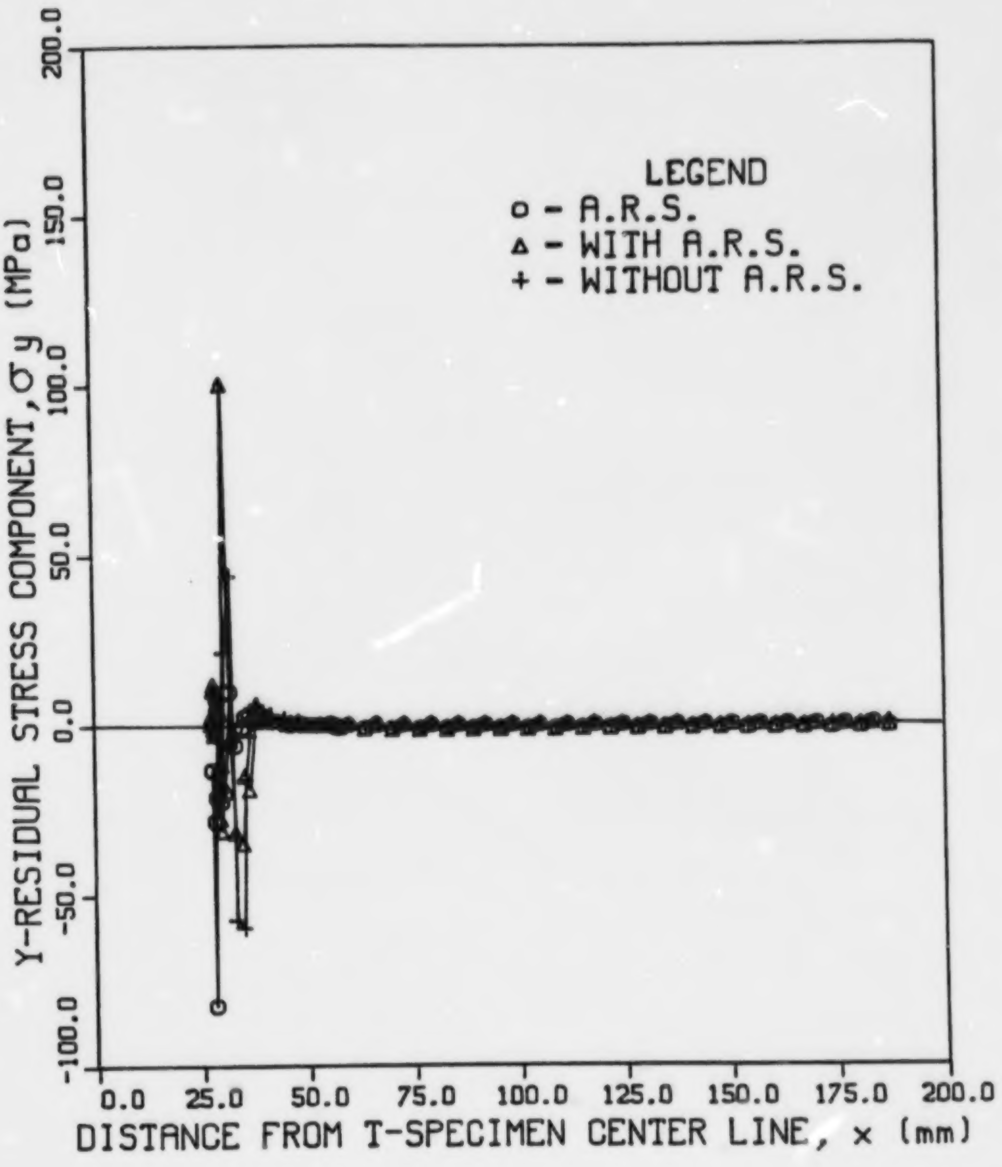

Figure 7.58: Distribution of the Y-residual stress component along the top surface after the first pass

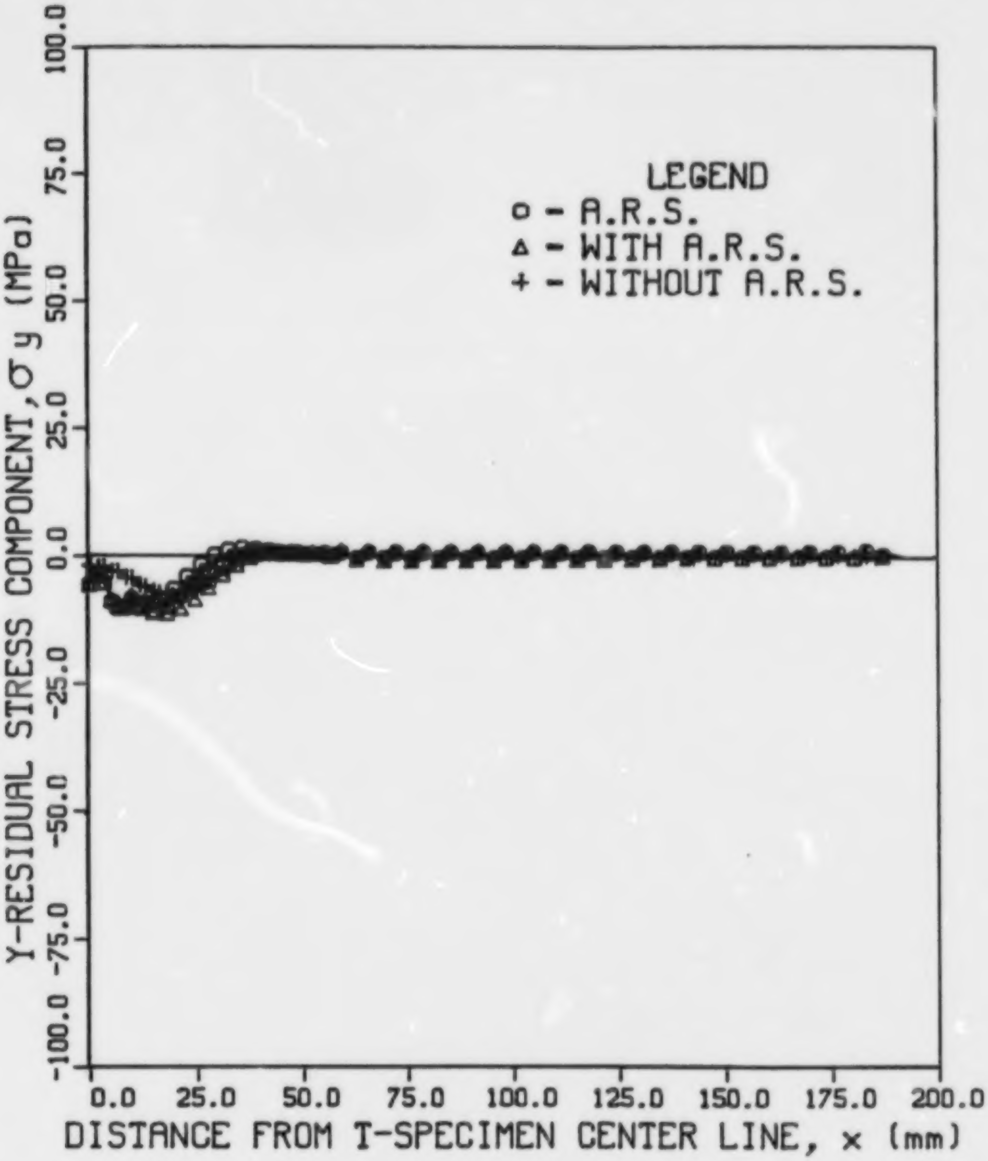

Figure 7.59: Distribution of the Y-residual stress component along the bottom surface after the first pass

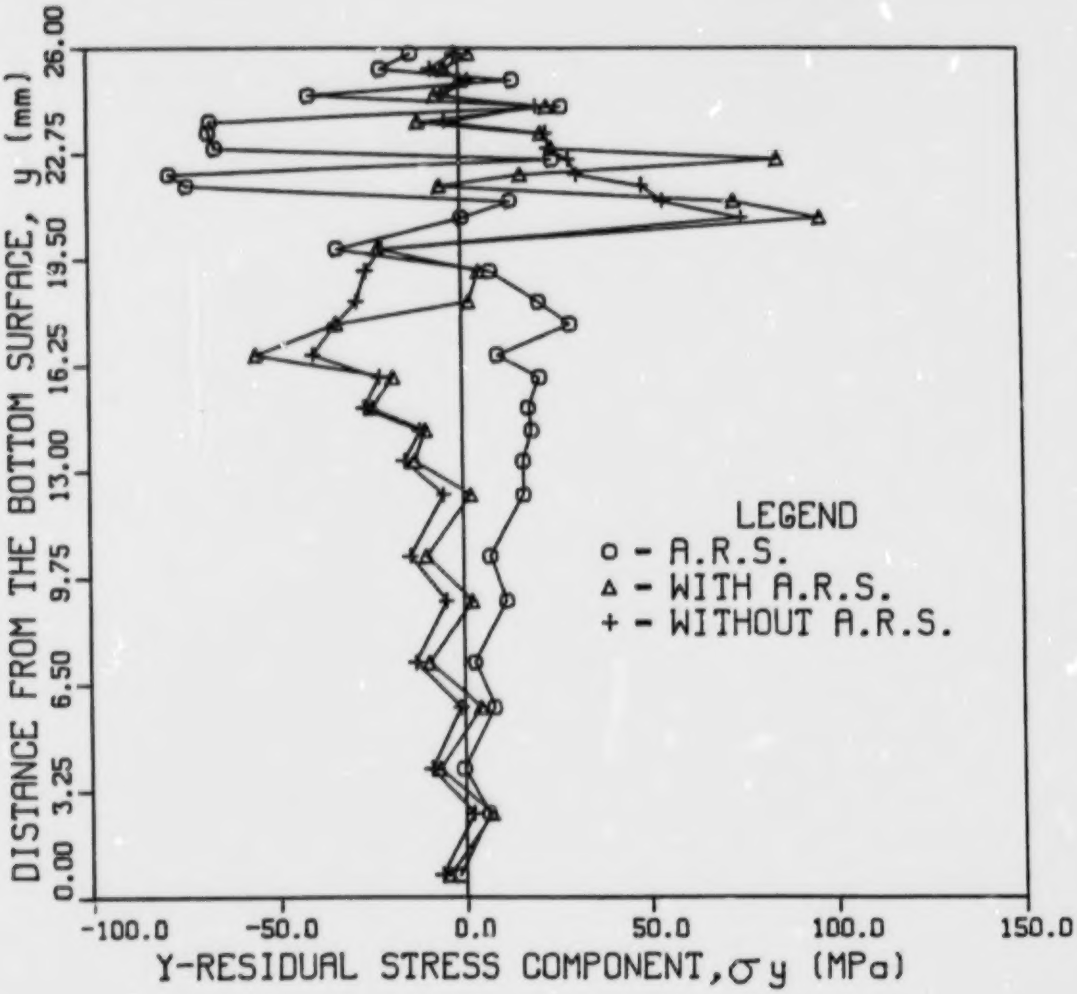

Figure 7.60: Distribution of the Y-resiudal stress component through the plate thickness below the weld toe after the first pass

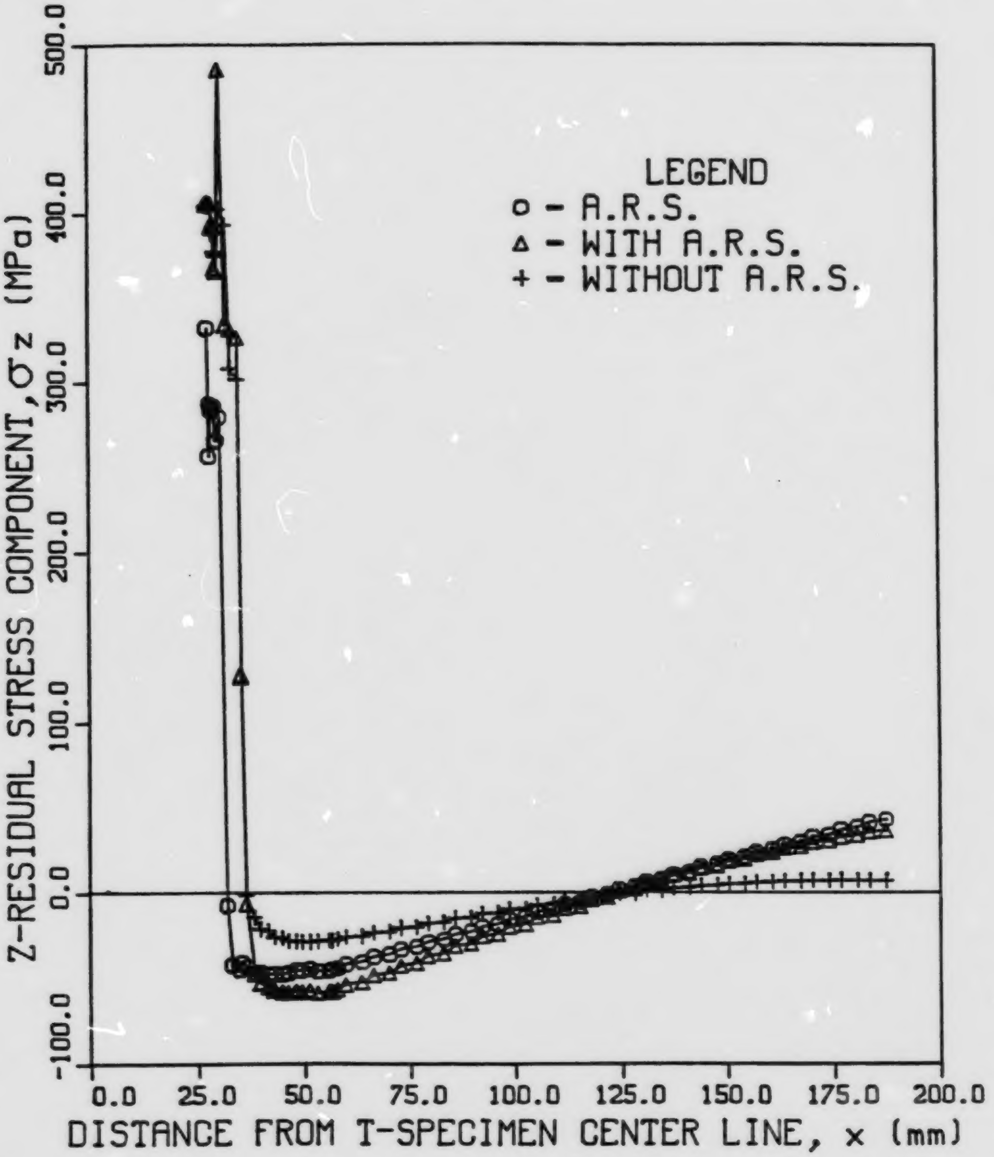

Figure 7.61: Distribution of the Z-residual stress component along the top surface after the first pass

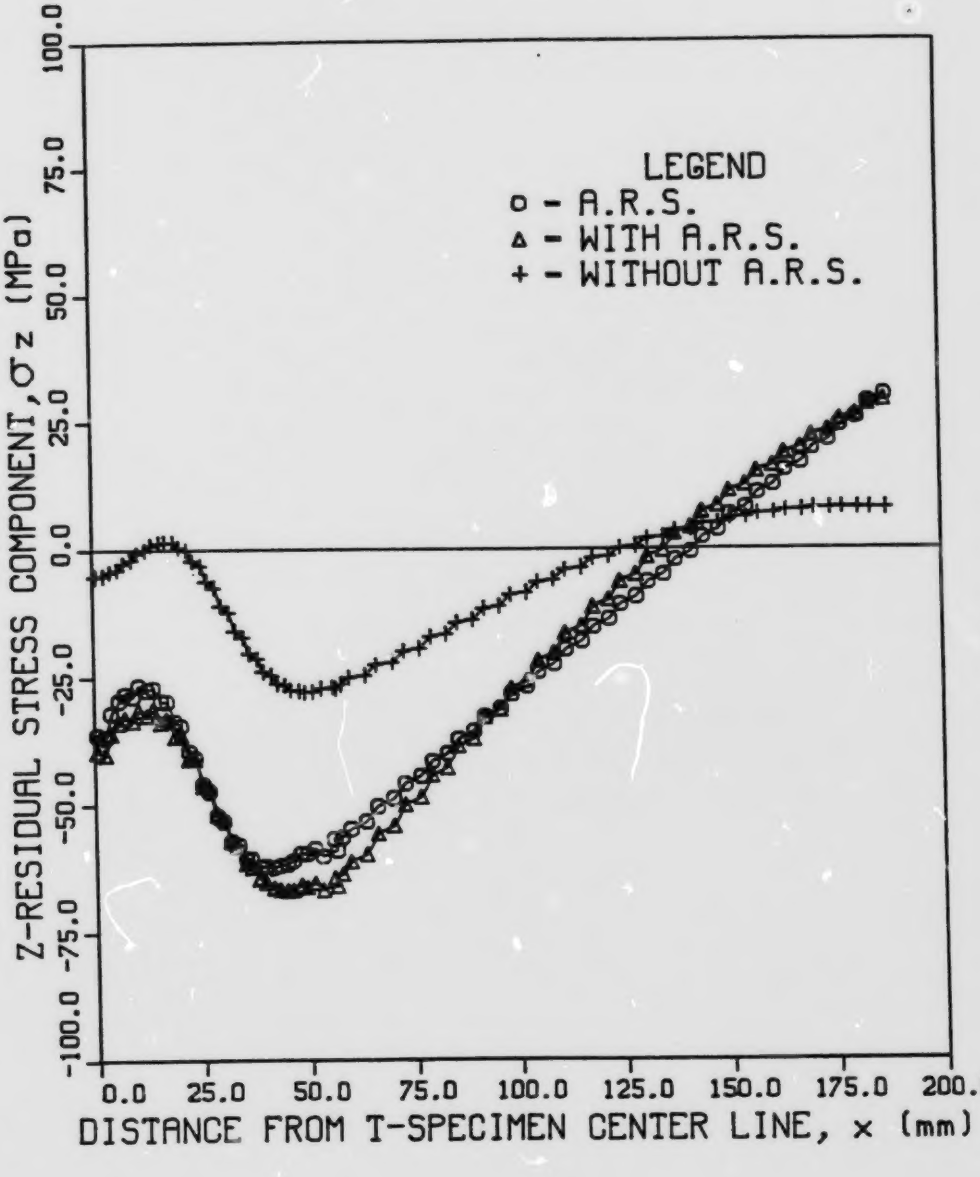

Figure 7.62: Distribution of the Z-residual stress component along the bottom surface after the first pass

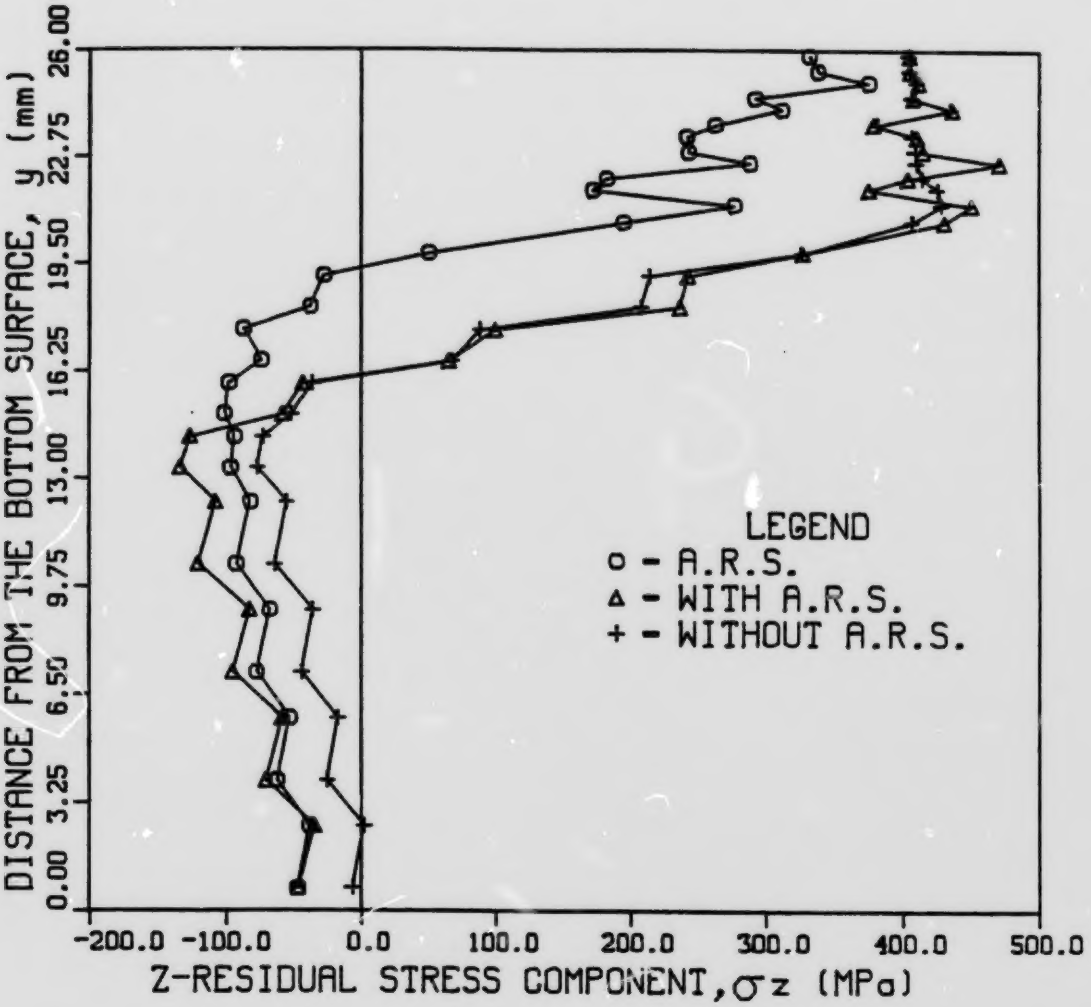

Figure 7.63: Distribution of the Z-residual stress component through the plate thickness below the weld toe after the first pass

Chapter 8

Loading Of The T-Joint Specimen

As explained in Chapter 5, one of the objectives of this study is to determine the effects of mechanical loading on the welding residual stresses in the T-joint specimen. This was accomplished by determining the stress distribution during and after the first loading cycle in the fatigue test. The loading conditions were those described in Chapter 5. In this chapter, the analyses and the calculated results are presented.

8.1 Mechanical Loading Of The 26 mm T-Joint Specimen

The stress strain relationship used in this study is for monotonic loading. After the first load cycle, any subsequent loading will result in elastic loading and the results will be the same. Ideally to provide the most accurate model of a fatigue test, the cyclic stress strain curve should be used. However, this degree of accuracy is beyond the scope of this study. Therefore, only the first loading cycle was analyzed which consisted of one load application and the subsequent unloading. The Bauschinger effect was believed to be small in this study because the mechanically induced plastic strain was not expected to be large. Since a kinematic hardening model can model the Bauschinger effect more accurately than an isotropic hardening model, it was used in this study.

In the fatigue test, the load applied through the load cell was approximately 20,000 lb. (89 kN), but the exact load was not recorded because the loading was adjusted to give a desired 'hot spot' stress which was measured with strain gauges. A number of loading cases were analyzed with a relatively coarse mesh to determine a suitable load for the final analyses. Based on these results, a evenly distributed load of 25 MPa applied along the top of the vertical plate would provide an equivalent 'hot spot' stress of approximately 250 MPa which would fall in the stress range used in the testing. In addition, an applied load of 50 MPa (equivalent 'hot spot' stress of 500 MPa) was analyzed to determine the effect of greater applied loads.

As seen in Figure 5.3, the loading condition is clearly symmetrical about the specimen center line. Therefore, a symmetry assumption was used to reduce the finite element mesh. The boundary conditions used in the analyses are shown in Figure 8.1. Since the depth of the specimen is over 200 mm, a plane strain condition exists in most parts of the specimen, except near the front and rear edges. Thus a plane strain condition was assumed and a two dimensional analysis undertaken.

A stress concentration will always exist at the weld toe, the severity of which depends upon the weld radius of the first capping pass. Due to the high degree of variability in the welding process, the weld radius is not constant along the weldment and a wide range of radii can occur. To model the weld radius very accurately, a very fine mesh around the weld toe region is required which would lead to very high computing costs. It was believed that this degree of accuracy was not required in this analysis because the stress concentration effect is localized in a region of high welding residual stress. Local plasticity is expected when loaded and therefore, an approximate representation of the stress concentration should be sufficient. The same mesh used in the residual stress calculations was adopted (see Figures 7.2a and 7.2b) and no weld radius was considered.

In order to gain a better understanding of the loading effect, the analyses were separated into two sections. In the first section, the effect of the loading alone was determined by loading the T-joint specimen without the inclusion of welding residual stresses. In the second section, the residual stresses predicted in Chapter 7 were included to simulate loading in the as welded condition.

8.1.1 Loading Of The T-Joint Specimen In The Stress Free Condition

For this analysis, all residual stresses were assumed to be relieved as though by a heat treatment. In the first analysis, the applied load was 25 MPa. The contours of the different stress components with the applied load are shown in Figures 8.2 to 8.5. The transverse stress away from the weld toe resembled that of a beam loaded in bending which is the loading condition used in the fatigue test. High tensile stresses and high stress gradients were observed around the weld toe region which is due to the stress concentration effect. The Y-stress and Z-stress were small and resulted from Poisson's effect. Only a small plastic zone was observed at the weld toe (see Figure 8.5). Similar stress contours but higher stress gradients were observed in the analysis with the applied load of 50 MPa (not shown).

The stress along the surfaces and through the thickness below the weld toe for both analyses are shown in Figures 8.6 to 8.14. By linearly extrapolating the top surface stress, the predicted 'hot spot' stress for the two analyses were approximately 235 and 470 MPa. By doubling the applied load, the 'hot spot' stress also doubled which indicates that most of the specimen is loaded elastically.

Using the ratio of maximum stress to the 'hot spot' stress, the stress concentration factors for the two analyses were about 2.3 and 1.5. From Figures 8.6 and 8.8, the stress concentration effect extended over a region of 4 mm radius about the weld toe.

In general, very small residual stresses were observed near the weld toe region after the load was removed. These residual stresses would have resulted from the local yielding of the material at the weld toe.

8.1.2 Loading In The As Welded Condition

In this analysis, the T-joint specimen was loaded after application of the welding residual stress predicted in Chapter 7. Since some of the residual stresses were higher than the yield strength of the steel at room temperature, any loading would result in an increased amount of plasticity. Therefore, the mechanical load was applied in an incremental fashion with the automatic time stepping scheme provided in ABAQUS [3]. Unloading would occur elastically, and only one increment was required.

The stress contours with the 25 MPa load (250 MPa 'hot spot' stress) are shown in Figures 8.15 to 8.18. For most of the T specimen, particularly the bottom plate, the resultant transverse or X-stress distribution (Figure 8.15) is the superposition of the welding residual stress (Figure 7.43) and the applied bending stress (Figure 8.2). In regions away from the weld toe and low welding residual stresses, the bending stress is predominant; while the welding residual stress is the dominate component around the weld toe region. The compressive stresses in the lower half of the horizontal plate due to the applied load were observed to join up with the zone of compressive residual stress below the weld zone. At the weld toe, extremely high tensile stresses were observed as a result of both high tensile welding residual stresses and high tensile stresses resulting from the applied load.

For the Y-stress (Figure 8.16) and the longitudinal or Z- stress (Figure 8.17), only minor changes to the welding residual stress (Figures 7.44 and 7.45) were observed because the applied bending load is in the transverse direction. The changes in both the Y and Z stresses occurred in the weldment where high residual stresses already existed. The changes were caused by yielding of the material and the subsequent stress redistribution. From Figure 8.18, the plastic zone (shaded area) was observed to surround the whole weld region and penetrate to about half of the plate thickness.

The contours of the residual stress after the removal of the load are shown in Figures 8.19 to 8.22. Comparing these with Figures 7.43 to 7.46, it can be seen clearly that most of the welding residual stresses remain after the first loading cycle. Some stress reductions in both the transverse stress and the longitudinal stress were observed at the weld toe region where yielding had occurred with the application of the load. After the first load cycle, i.e., after unloading, the zone in which the Von Mises stress exceeding the room temperature yield stress was found to occur only around the weld toe of the vertical plate (Figure 8.22) whereas the Von Mises stress in the entire region of the capping passes zone exceeded yield after welding (Figure 7.46).

The analysis with the higher applied load (500 MPa 'hot spot' stress) resulted in similar stress contours (Figures 8.23 to 8.26) as those for the analysis with 25 MPa applied stress. As expected, the resultant stresses were much higher and the zones of high stresses were larger. Also, the welding residual stresses are less dominant below the weld region. The residual stress contours after the load was removed are shown in Figures 8.27 to 8.30. The amount of stress reduction were much higher, especially around the weld toe where a great deal of yielding had occurred. In fact, compressive transverse residual stresses were resulted around the weld toe after the first load cycle (see Figure 8.27).

The stress along the surfaces of the horizontal plate and through the thickness for both loading cases are presented in Figures 8.31 to 8.39. The predicted welding residual stresses are also plotted and indicated as W.R.S. Reduction of the transverse or X-residual stress after one loading cycle was observed in both analyses (see Figures 8.31 to 9.33). The tensile transverse residual stress at the weld toe decreased to less than 100 MPa after application of the 25 MPa load while a compressive residual stress was predicted after application of the 50 MPa load (Figure 8.31). This zone of stress reduction extends 2 to 3 mm below the top surface. Only a moderate decrease in the tensile residual stress was observed on the bottom surface (Figure 8.32). The magnitude of the transverse compressive residual stress in the zone below the weld toe decreased slightly as a result of re-establishing equilibrium (Figure 8.33).

The loading caused only minor alternations to the Y-component of the welding residual stress in both analyses (Figures 8.34 to 8.36). The probable reasons for the small decrease are that the initial Y-residual stress is small, and that the load is in the transverse direction.

In the longitudinal (Z) direction, significant stress reduction was observed near the weld toe in a similar fashion to the transverse residual stress (Figures 8.37 to 8.39). A decrease of about 200 MPa was predicted with the smaller load and this decrease extended to about 3 mm below the top surface. With the larger load, a small compressive residual stress was predicted and the zone of large stress reduction was observed to extend to 5 mm below the top surface. On the bottom surface, the compressive residual stress became tensile after loading in both analyses (Figure 8.38).

8.2 Discussion Of The Results

8.2.1 Finite Element Mesh

Considering the applied loading without residual stress, the highest calculated stress concentration factor was about 2.3 which is lower than the values of 3 or greater reported in the literature [68]. The main reason for the low stress concentration factor is that the mesh used is not fine enough at the weld toe region to capture the high gradient of stress at the toe. In addition, the analysis is an elastic-plastic model which takes yielding and strain hardening into account, whereas the values reported in the literature are usually based on elastic analysis. This effect is most evident in the analysis with the higher applied load.

The region of very high stress gradient is very small and is located where high welding residual stress occurs. With the applied load superimposed on the residual stress, the material yields and flows plastically. The stress gradient would be contained within the plastic zone and its effect would be decreased. Therefore, although the mesh used cannot model the high local stress gradient it should be reasonable for the purpose of studying the effect of loading on welding residual stress.

8.2.2 Effect Of loading On Welding Residual Stress

If the T-joint specimen was stress-relieved before the fatigue test, the specimen would be essentially loaded elastically by the load levels applied. Very localized yielding at the weld toe occurs as a result of the high stress concentration. Since this zone is very small and the plastic strain is contained by surrounding elastic material, the strain effectively returns to zero upon unloading. Compressive residual stress is the result as shown in the analyses. Clearly, further loadings create only elastic stresses. This process is known as 'shakedown'.

Since the T-joint specimen was tested in the as welded condition with residual stress of yield strength magnitude around the weld zone, any loading would cause yielding in a greater amount of material. The effect of shakedown is more wide spread as seen in the analyses. However, the welding residual stress is not totally relaxed after shakedown as assumed by some researchers. The same effect is also observed by Allen et al. [70] in their neutron diffraction measurement of similar T-joint specimen.

The largest reduction of stress occurs in a very localized region within 3 to 4 mm of the weld toe. This is also the region where significant plastic yielding has occurred. In areas that remain elastic throughout the loading, residual stress is also reduced to re-establish equilibrium, but the magnitude of reduction is much smaller. The amount of stress relaxation depends on the applied load with greater reductions resulting from higher loads. For loading greater than 25 MPa on the 26 mm specimen, the transverse tensile residual stress near the weld toe can be reduced to zero or to compression while the longitudinal residual stress can be reduced by a half.

8.2.3 Effect On Fatigue Life Of The T-joint Specimen

Fatigue predictions for the T-joint specimen are beyond the scope of this study, however, based on the results of this study, qualitative comments can be made on the possible effects of welding residual stresses on the fatigue behavior of the T-joint specimen.

Effect On Initiation Life

The formation of a fatigue crack is a complex process. It is believed that the shearing action of the cyclic loads causes dislocations to entangle [80]. Since the material surface is usually weaker than the interior, notches (intrusions) and ridges (extrusions) of atomic scale are formed. Under the action of the cyclic stresses, these surface defects eventually deepen to form microcracks. With further cyclic loading, these microcracks coalesce to form one dominant surface crack (macrocrack). The point at which initiation of the fatigue crack is considered finished and propagation has begun is arbitrary, but for typical steel components, initiation usually makes up the majority of the total fatigue life. However, for welded components and structures, initiation is usually a very small portion of the total life. Weld defects such as undercuts and porosities along the toe of the weld are perfect sites for the initiation of fatigue cracks. In fact, some researchers have considered fatigue of welded structures as a propagation problem only.

Since initiation is a result of the cyclic shearing action, residual stress which only modifies the mean stress, is thought to have only a small effect. A compressive mean stress tends to prevent microcracks from opening. This retards microcracks from growing into fatigue cracks. Of course, the opposite is true with tensile mean stress which tends to open microcracks and accelerates the formation of macrocracks. As observed in the results of the analysis using similar loading range as in the fatigue test, tensile transverse residual stresses still exist on the surface near the weld toe after shakedown. The residual stress is small (about 50 MPa) on the surface, so the effect on initiation is probably small. However, if an overload is used for shakedown, high compressive residual stress can be set up on the surface and delay the initiation of fatigue cracks.

Effect On Propagation Of Fatigue Crack

A fatigue crack can propagate in three modes, Mode I (opening or tensile), Mode II (in-plane shear) and Mode III (out- of-plane shear). For the T-joint specimen in three point bending, the dominant mode of crack propagation is Mode I. The propagation rate of a fatigue crack can be predicted reasonably well with linear elastic fracture mechanics. The simplest model is the direct integration of the Paris equation [81],

$$\frac{da}{dN} = C(\Delta K)^m \tag{8.1}$$

where da/dN is the change of crack depth per load cycle; C and m are experimentally determined material properties; ΔK is the stress intensity factor range which is a function of the stress range.

Some researchers have used shakedown to explain the effect (or no effect) of welding residual stresses on the fatigue life of welded structures. The usual assumption is that welding residual stresses of tensile yield stress level exist near the weld and are constant through the thickness. Thus, any tensile loading will cause yielding of the material and reduce the residual stresses to a lower level upon unloading. Further cyclic loading will be elastic up to but not beyond the yield stress. The actual stress level will be different from the nominal applied stress, however, the stress range will be the same which will give the same stress intensity factor range. The values of the material properties, C and m, are modified to compensate for the higher mean stress.

The above assumption of constant stress through the plate thickness, is probably true for thinner specimens or for full penetration butt welds. However, as observed in this study and similar results of Holden et al. [63] and Allen et al. [70], the residual stress in the direction normal to crack growth (transverse) is not constant through the horizontal plate thickness in the 26 mm T-joint specimen. In fact, about one third through the plate thickness, the residual stress is compressive. Shakedown does not occur throughout the plate thickness. Therefore, shakedown of the welding residual stresses through the whole plate thickness at the weld toe would not occur. As observed in the analysis, shakedown only affects the welding residual stresses in the top 1 mm around the weld toe of the horizontal plate and relatively high residual stresses remain elsewhere. These observations are contrary to the theory described above and the welding residual stresses can have various effects on fatigue crack propagation depending on the size of the crack. Since the transverse residual stresses are tensile in the top third of the plate, the crack growth rate could be faster than if the T-joint specimen had been heat treated to relief the welding residual stresses. The crack growth rate could decrease or even arrest when compressive residual stresses exists, but this was not observed in the fatigue tests [5,6] when the fatigue crack has penetrated into the transverse compressive residual stress zone. The reason for this is because the crack would be about 8 to 10 mm deep when it reached the compressive stress zone. A crack this size would probably have altered the whole stress field and removed any residual stresses. Therefore, the compressive residual stresses do not have any beneficial effect on crack growth.

One interesting observation in the fatigue test [6] was that the surface crack in the 26 mm and thinner specimens did not reach the edges and only grew as a semi-elliptical crack; while for thicker specimens, flat fronted cracks across the whole width developed very early. One suggested explanation is that compressive transverse residual stresses still existed at the edges in the thinner specimens even though one inch was removed from each end after welding. These compressive residual stresses prevented cracks from growing across the whole plate. Unfortunately, the present study cannot predict the residual stresses in this region of the specimen due to the three dimensional effects near the ends of the weld.

Effects On Final Fracture

After a large number of loading cycles, the fatigue crack may have grown to a point at which the remaining uncracked section cannot support the applied stress and final fracture of the component occurs. According to fracture mechanics, final fracture occurs after the stress intensity factor, K, which is a function of the geometry, loading condition and crack size, reaches the critical fracture toughness, K_{Ic}, of the material. K is directly proportional to the applied stress, and therefore, the maximum stress controls the fracture process. Tensile residual stresses which increase the actual stress in the component tend to cause fast fracture earlier than a stress free component; while the opposite is true for a compressive residual stress.

In the fatigue test of the 26 mm T-joint specimen [5, 6], final fracture did not occur until the fatigue crack penetrated over half of the plate thickness. This is well within the transverse compressive residual stress zone. As mentioned in the last section, the welding residual stresses are most likely being relaxed by the large propagating crack. Therefore, the residual stresses probably have little or no effect on fast fracture. However, the residual stresses may have a significant role in the thicker specimens in which fast fracture occurred when the crack is very shallow, especially with a low applied stress [5-7]. Assuming the through thickness residual stress distribution is similar for both thin and thick specimens. With low applied stress, will cause only small reductions in residual stresses during shakedown. The high tensile residual stress near the weld toe can raise the actual stress in the specimen to a very high level and cause fast fracture to occur even with a very shallow crack.

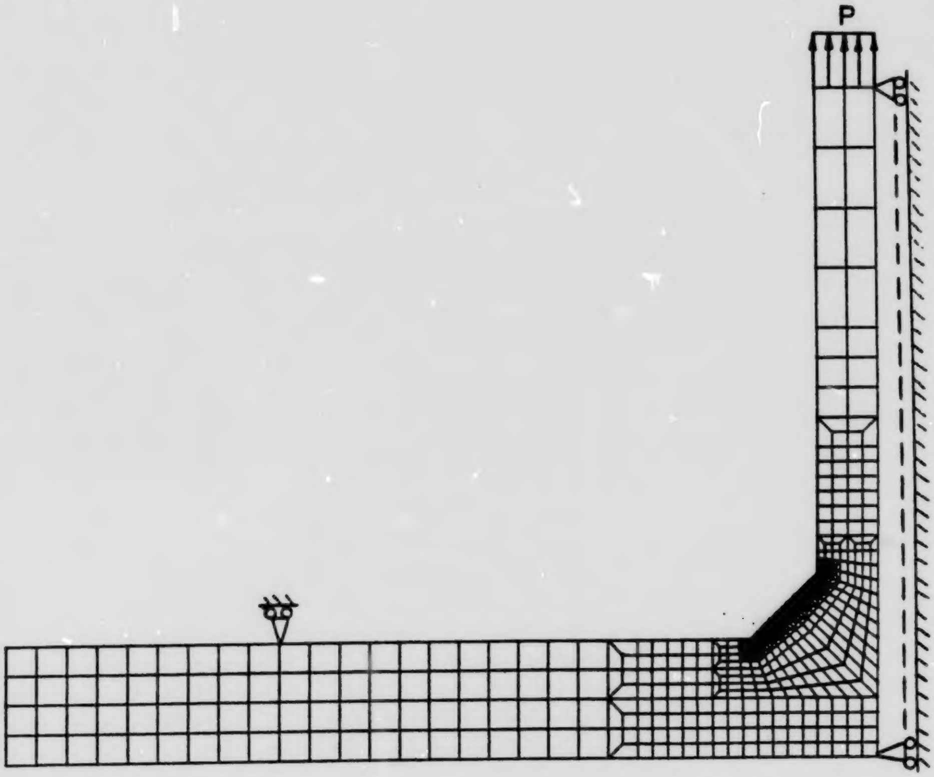

Figure 8.1: Kinematic boundary conditions for loading analysis

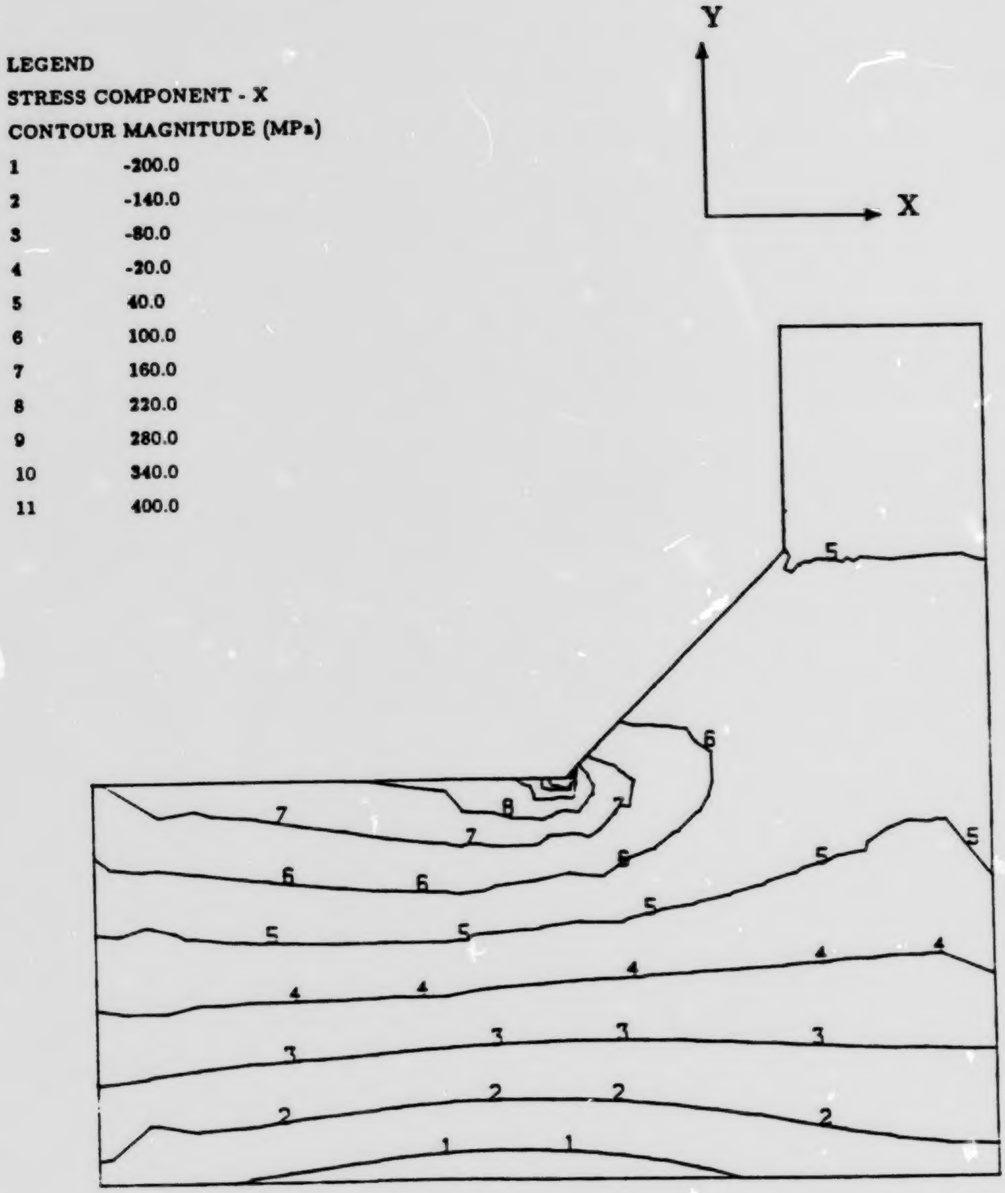

LEGEND

STRESS COMPONENT - X

CONTOUR MAGNITUDE (MPa)

1	-200.0
2	-140.0
3	-80.0
4	-20.0
5	40.0
6	100.0
7	160.0
8	220.0
9	280.0
10	340.0
11	400.0

Figure 8.2: X-stress distribution with 25 MPa load (stress free condition)

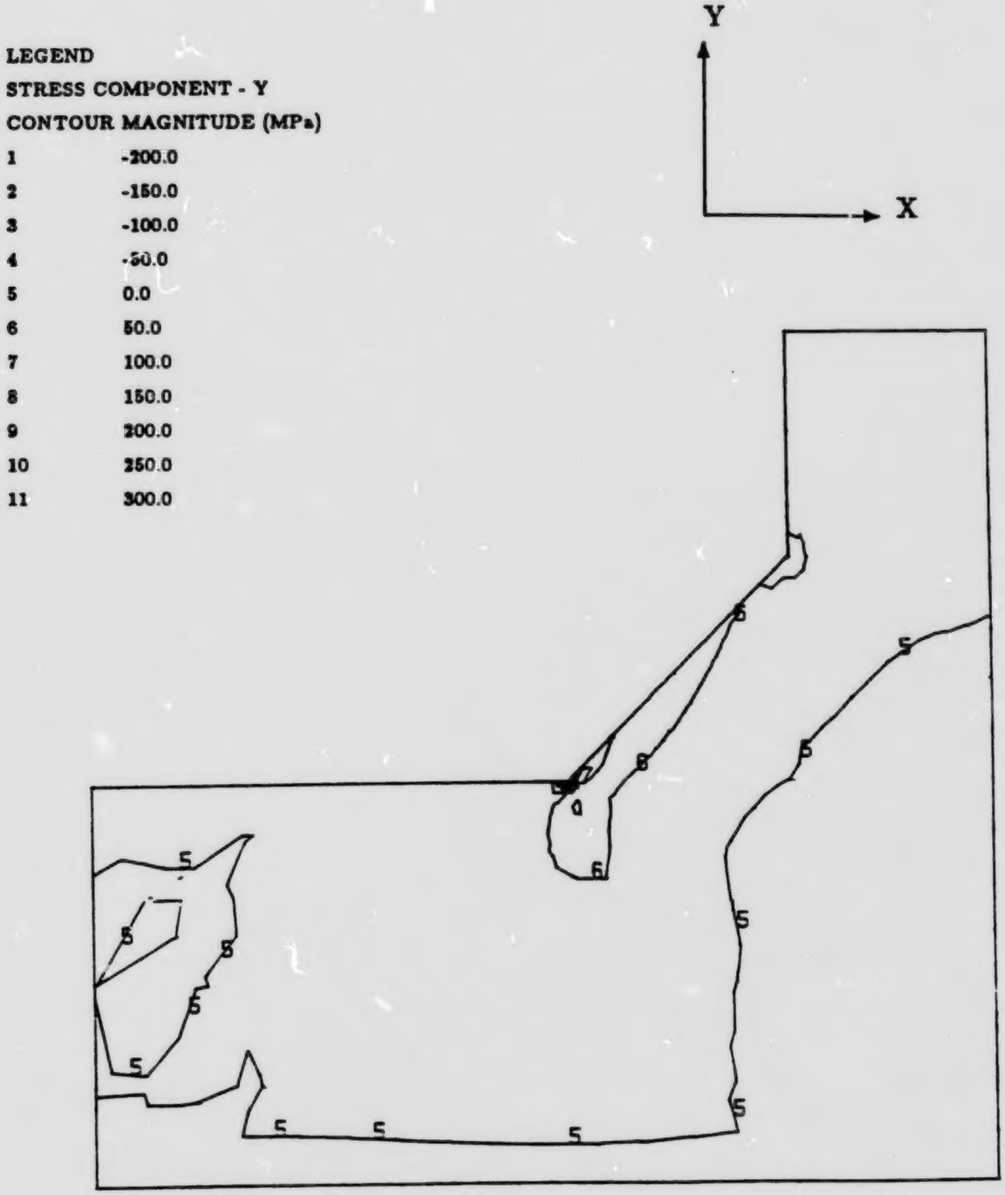

Figure 8.3: Y-stress distribution with 25 MPa load (stress free condition)

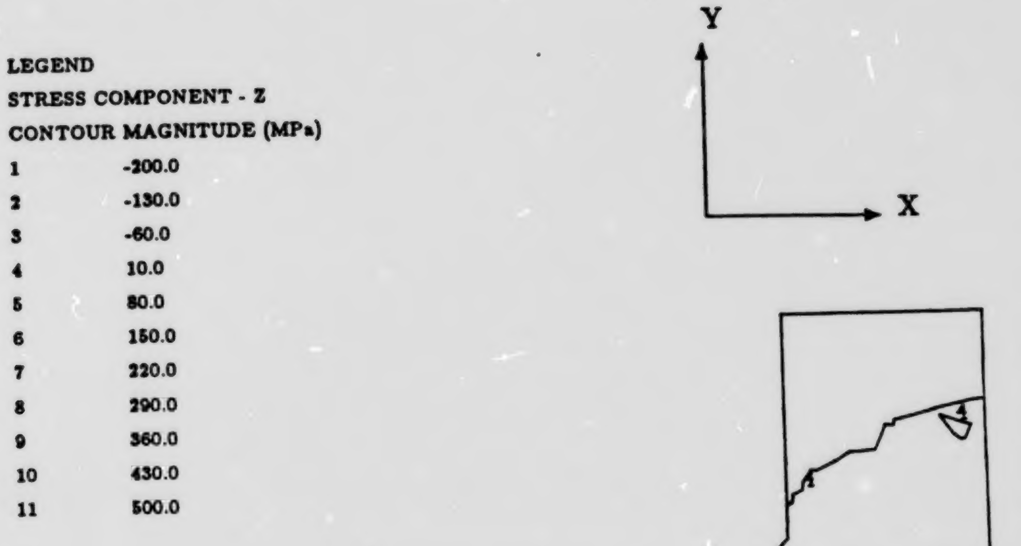

Figure 8.4: Z-stress distribution with 25 MPa load (stress free condition)

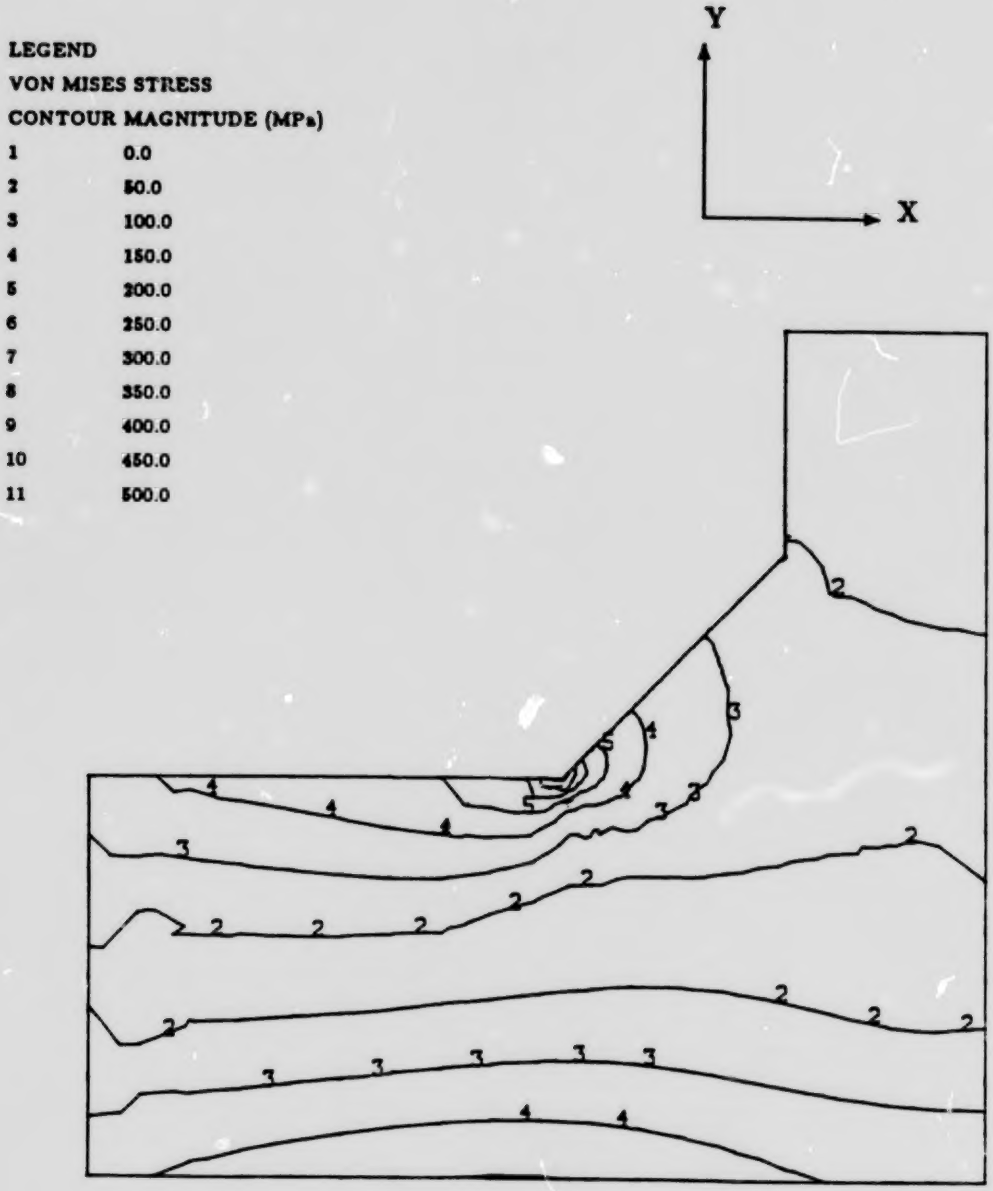

Figure 8.5: Von Mises stress distribution with 25 MPa load (stress free condition)

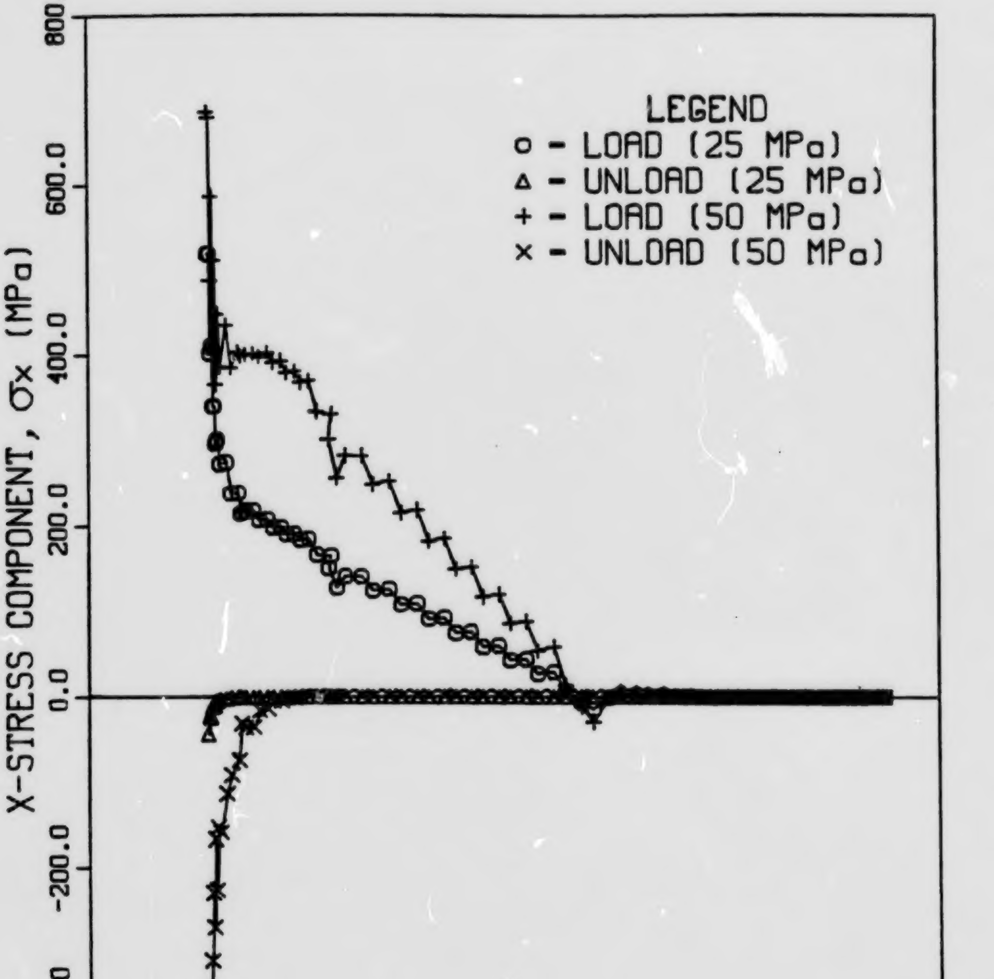

Figure 8.6: X-stress distribution along the top surface after one loading cycle (stress free condition)

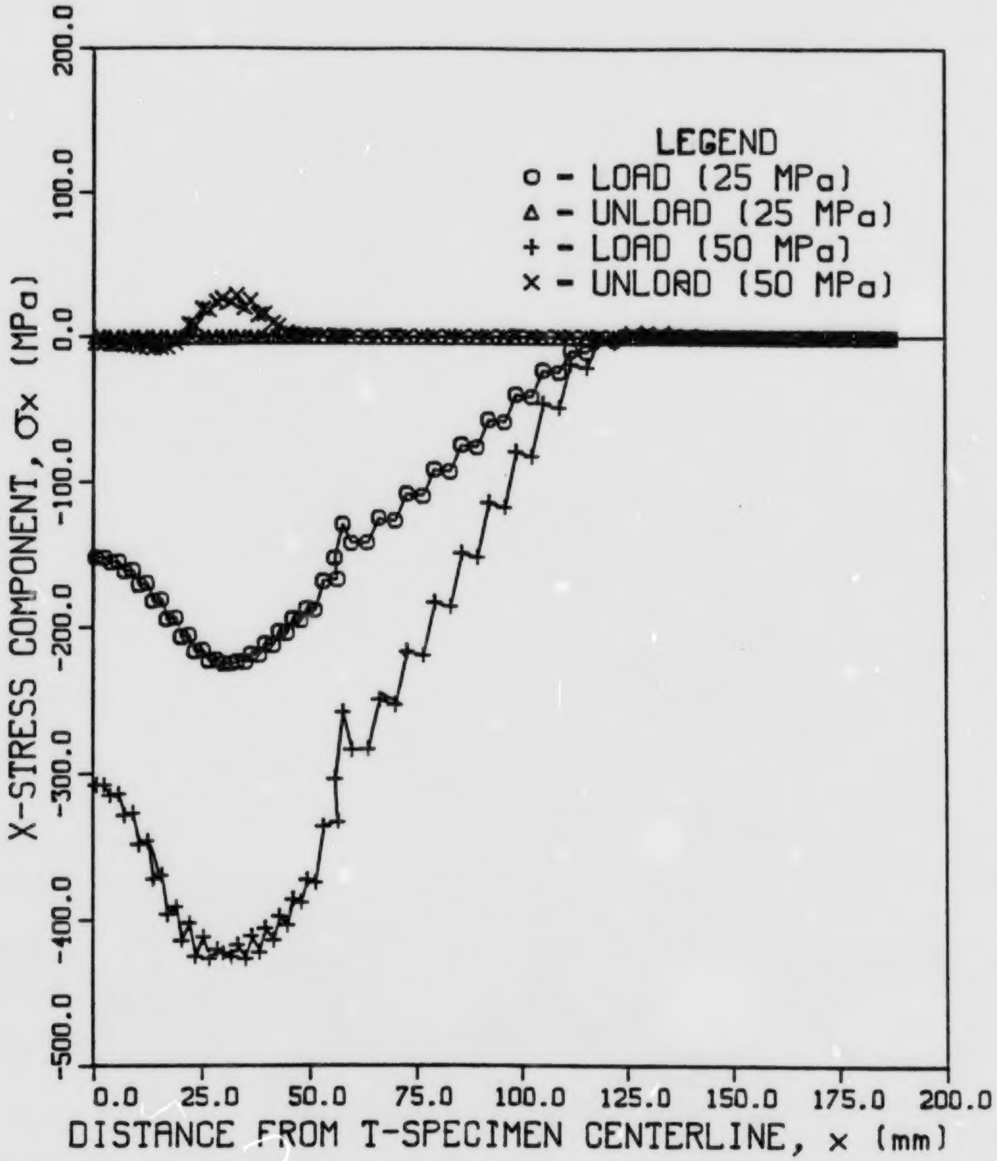

Figure 8.7: X-stress distribution along the bottom surface after one loading cycle (stress free condition)

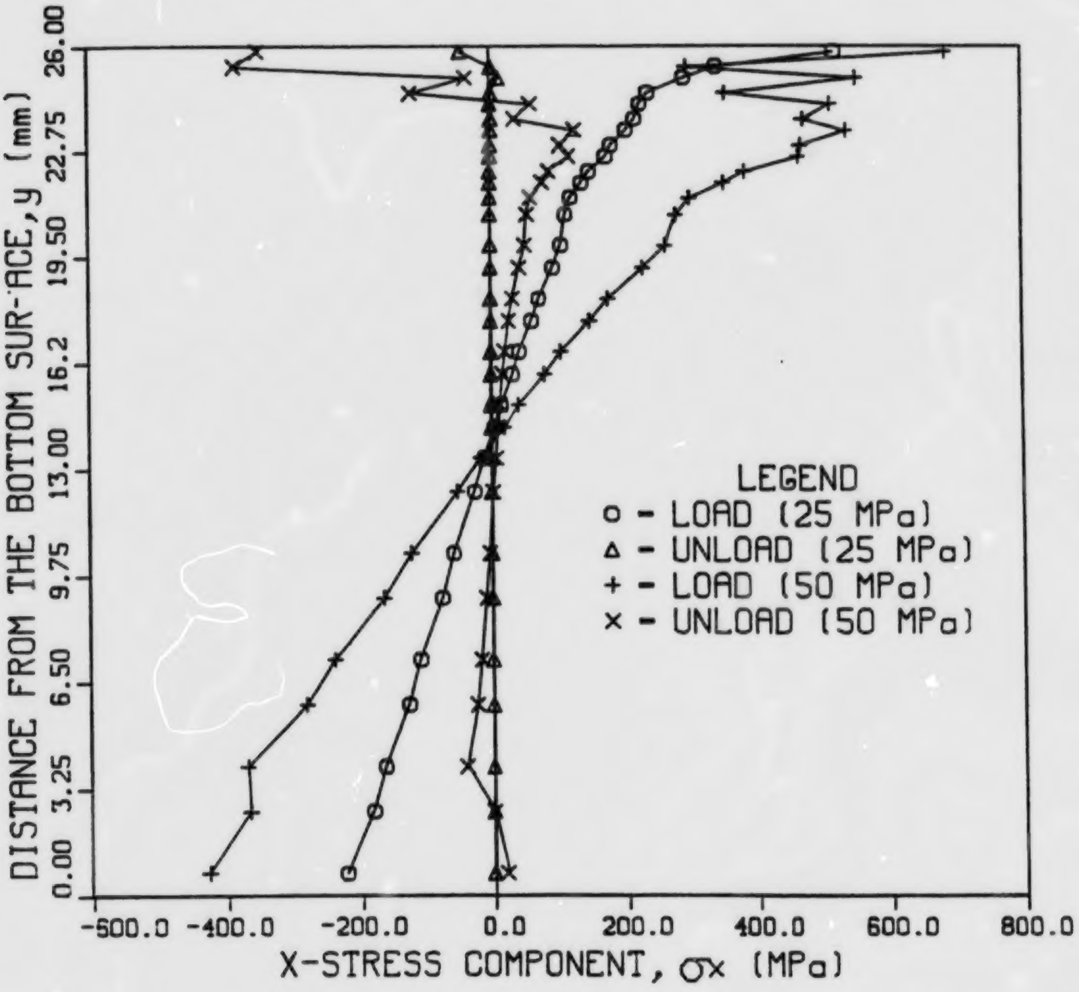

Figure 8.8: X-stress distribution through the palte thickness below the weld toe after one loading cycle (stress free condition)

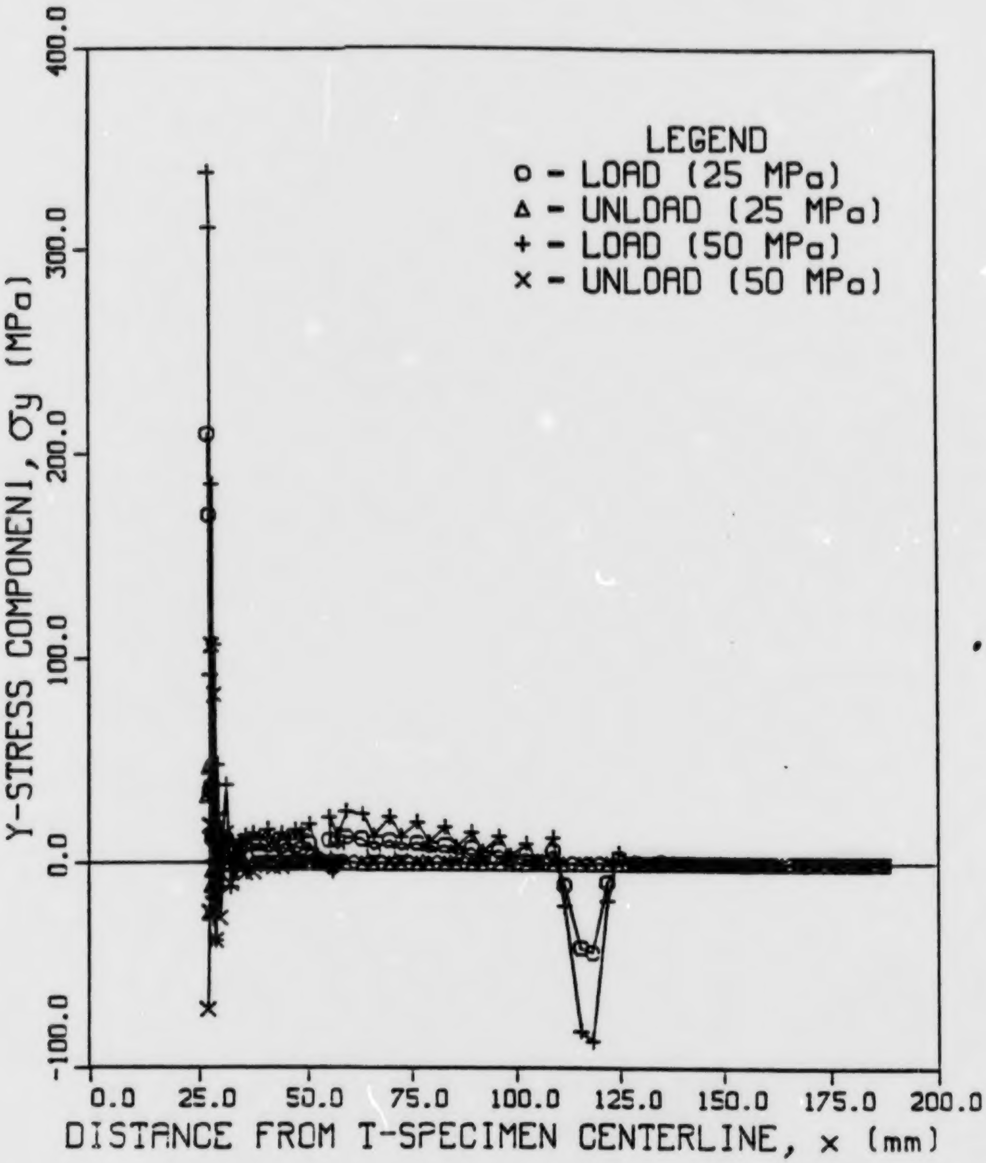

Figure 8.9: Y-stress distribution along the top surface after one loading cycle (stress free condition)

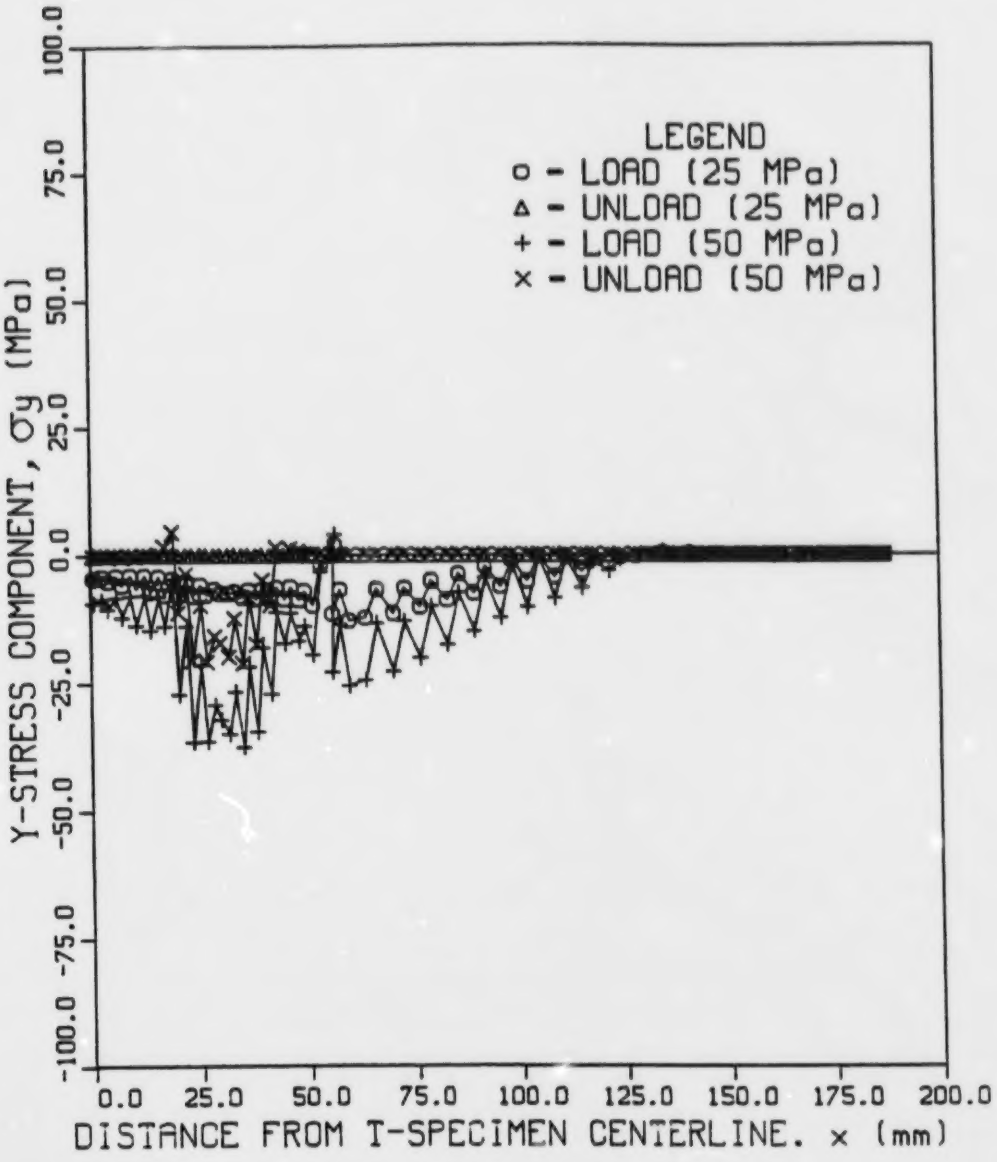

Figure 8.10: Y-stress distribution along the bottom surface after one loading cycle (stress free condition)

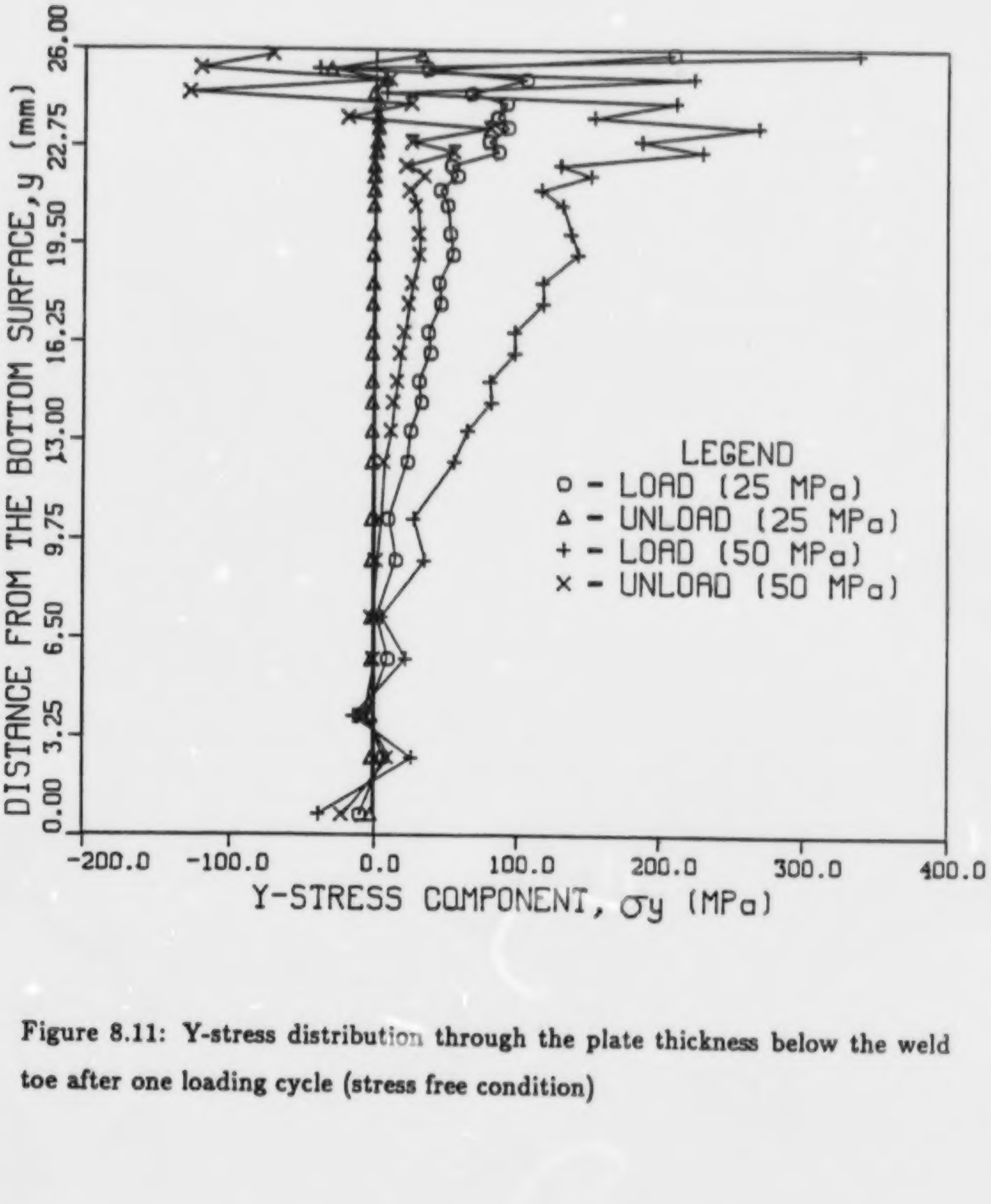

Figure 8.11: Y-stress distribution through the plate thickness below the weld toe after one loading cycle (stress free condition)

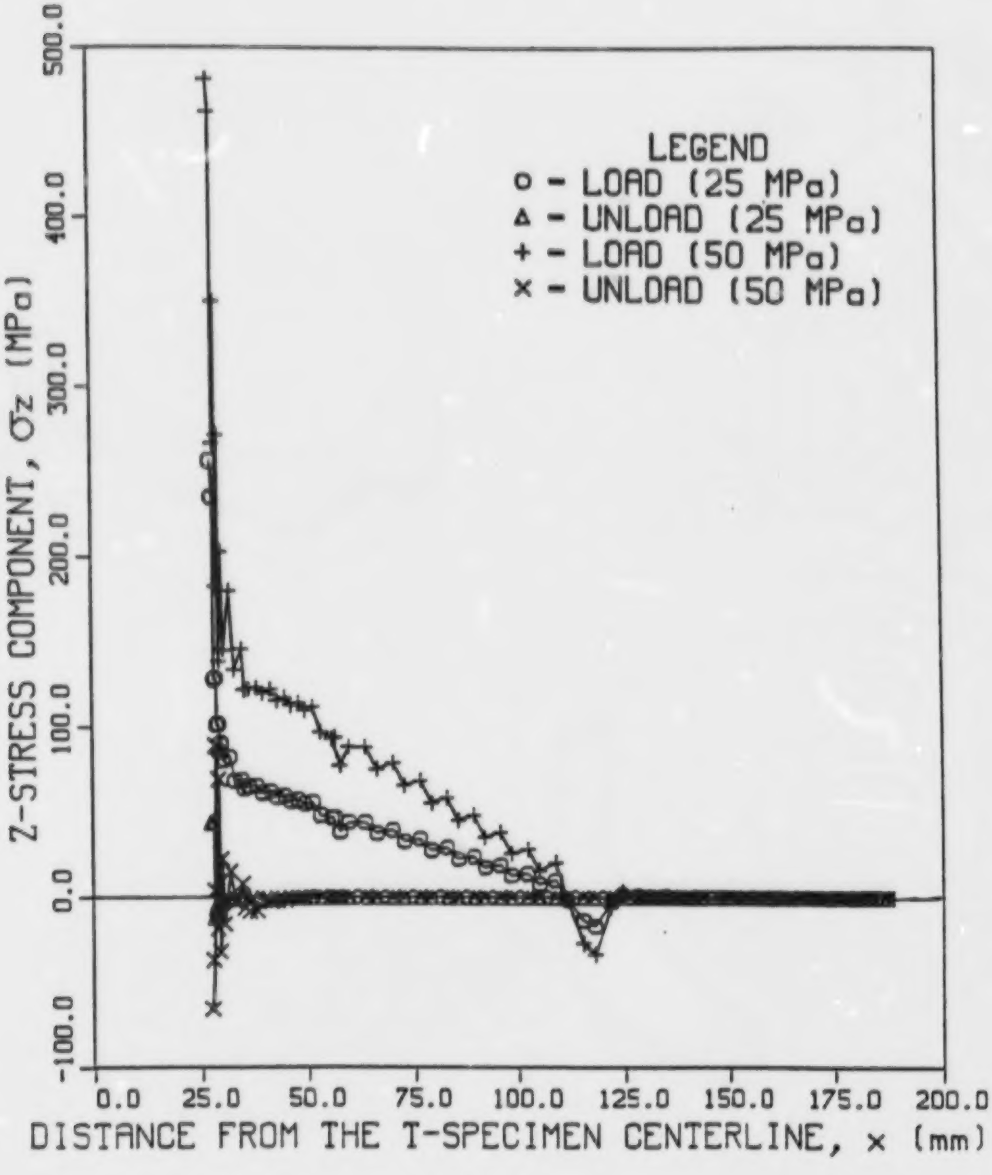

Figure 8.12: Z-stress distribution along the top surface after one loading cycle (stress free condition)

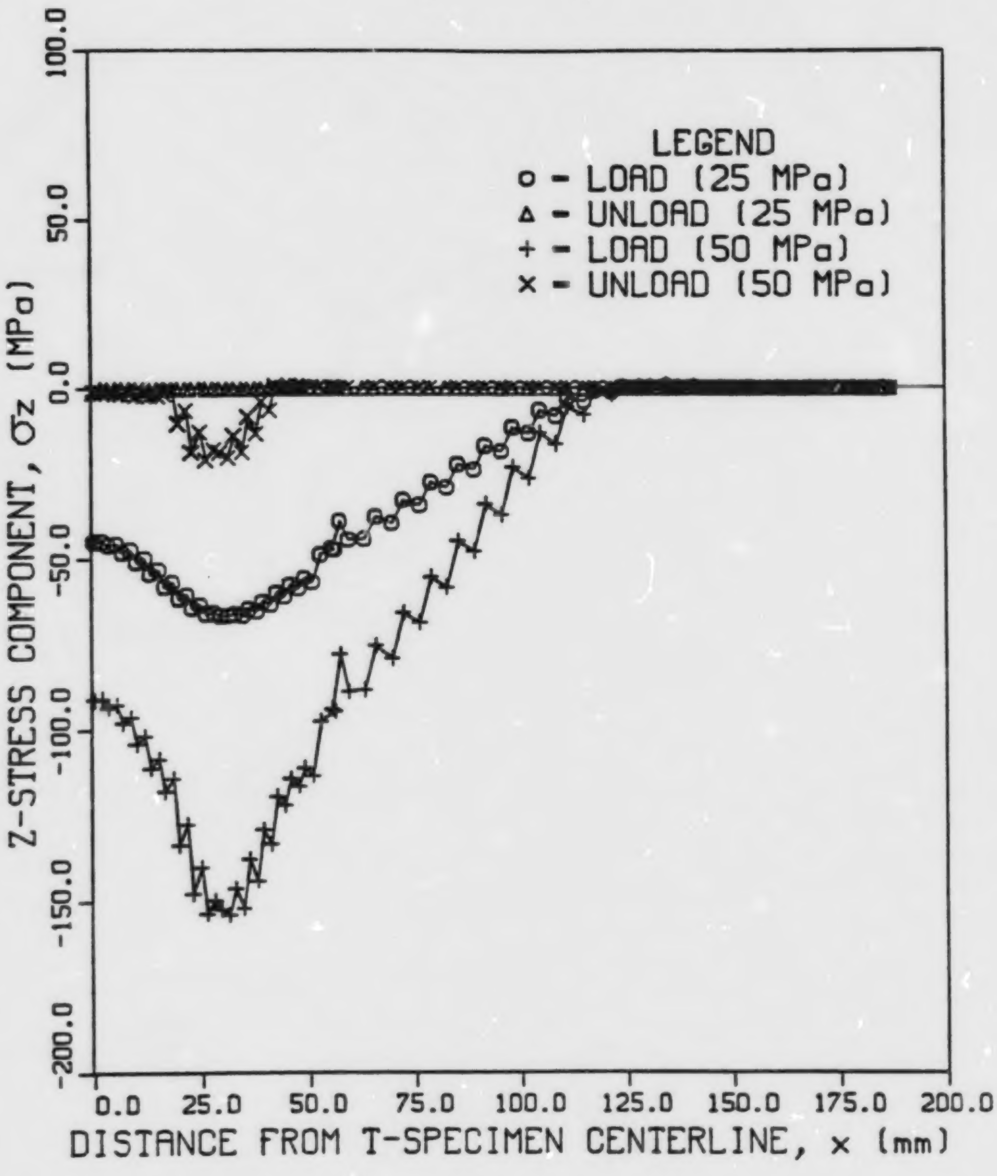

Figure 8.13: Z-stress distribution along the bottom surface after one loading cycle (stress free condition)

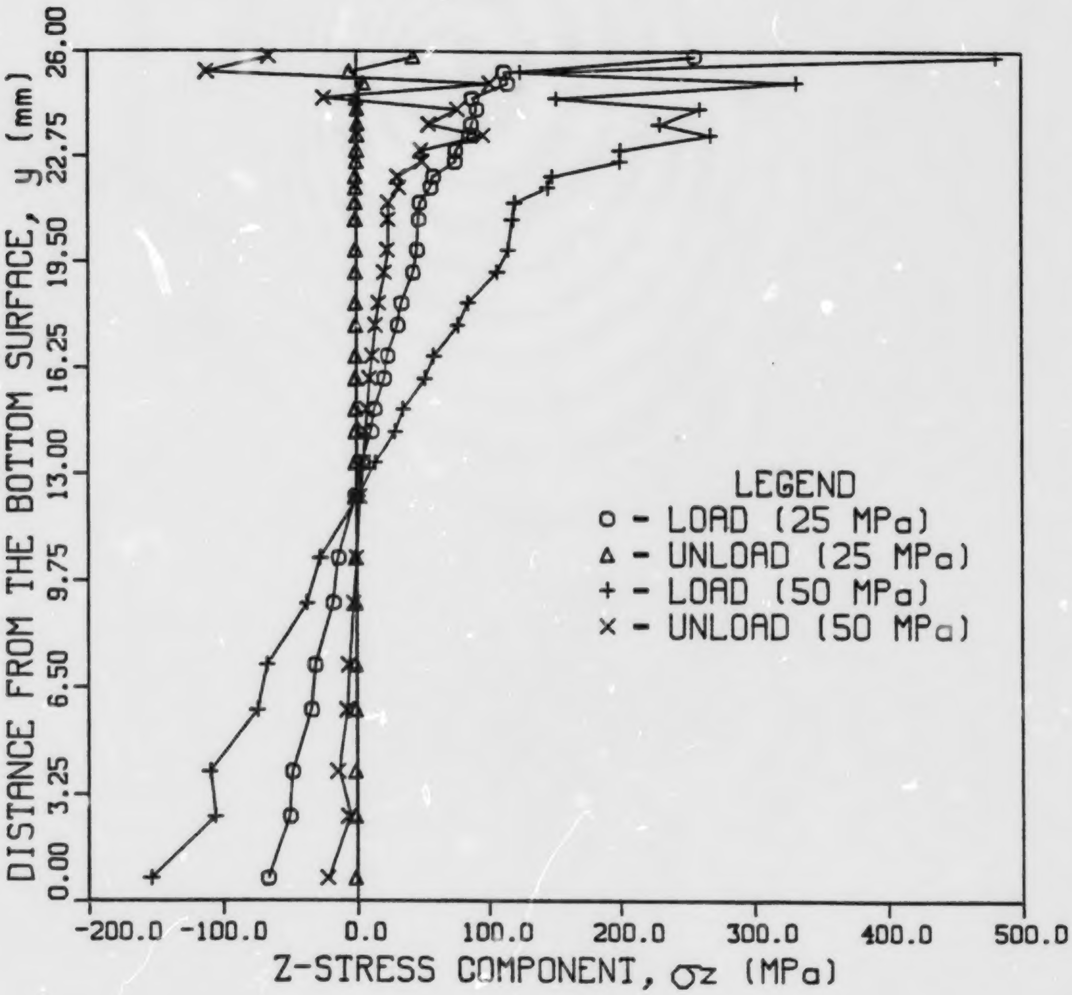

Figure 8.14: Z-stress distribution through the plate thickness below the weld toe after one loading cycle (stress free condition)

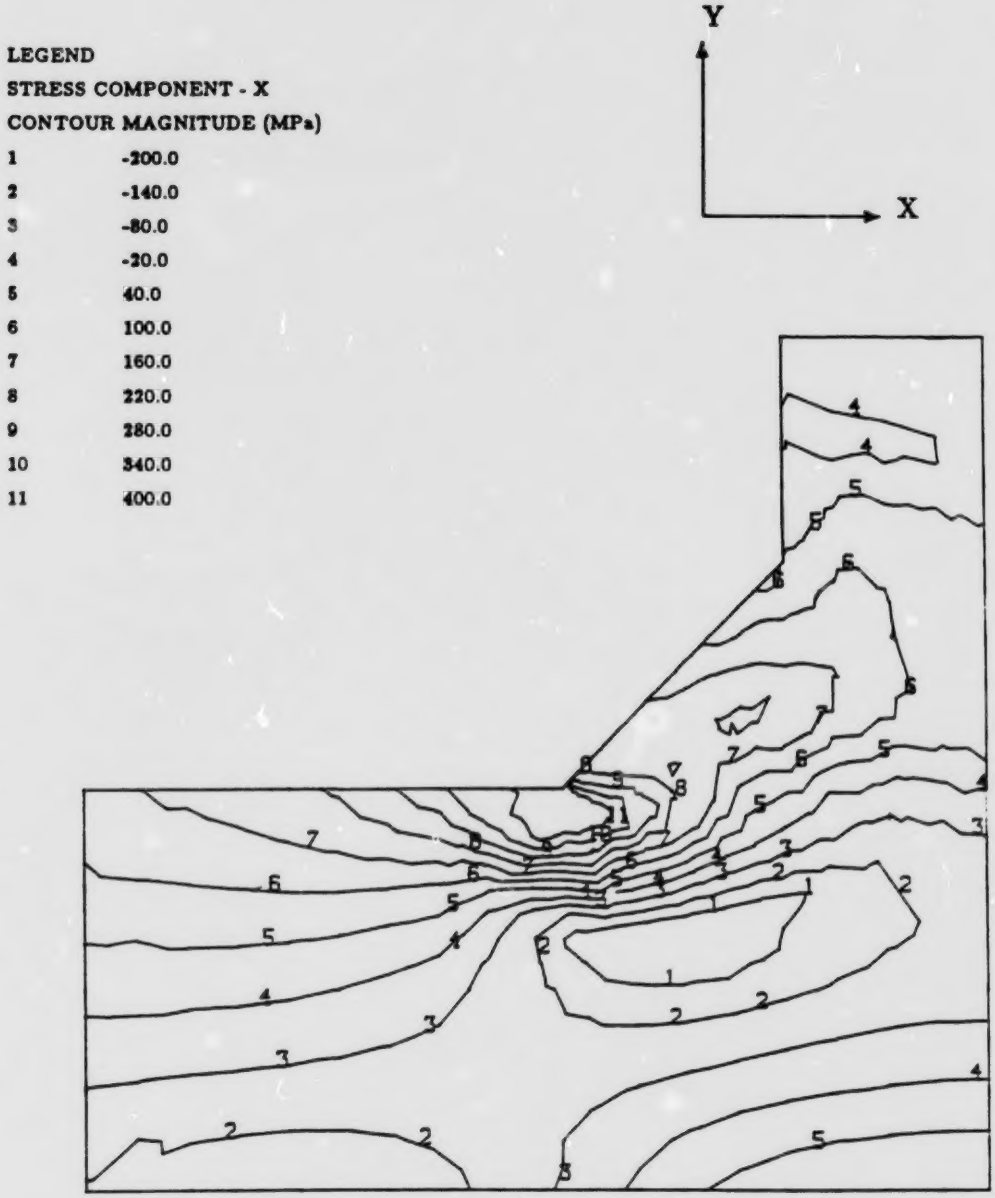

LEGEND

STRESS COMPONENT - X

CONTOUR MAGNITUDE (MPa)

1	-200.0
2	-140.0
3	-80.0
4	-20.0
5	40.0
6	100.0
7	160.0
8	220.0
9	280.0
10	340.0
11	400.0

Figure 8.15: X-stress distribution with 25 MPa load (as welded condition)

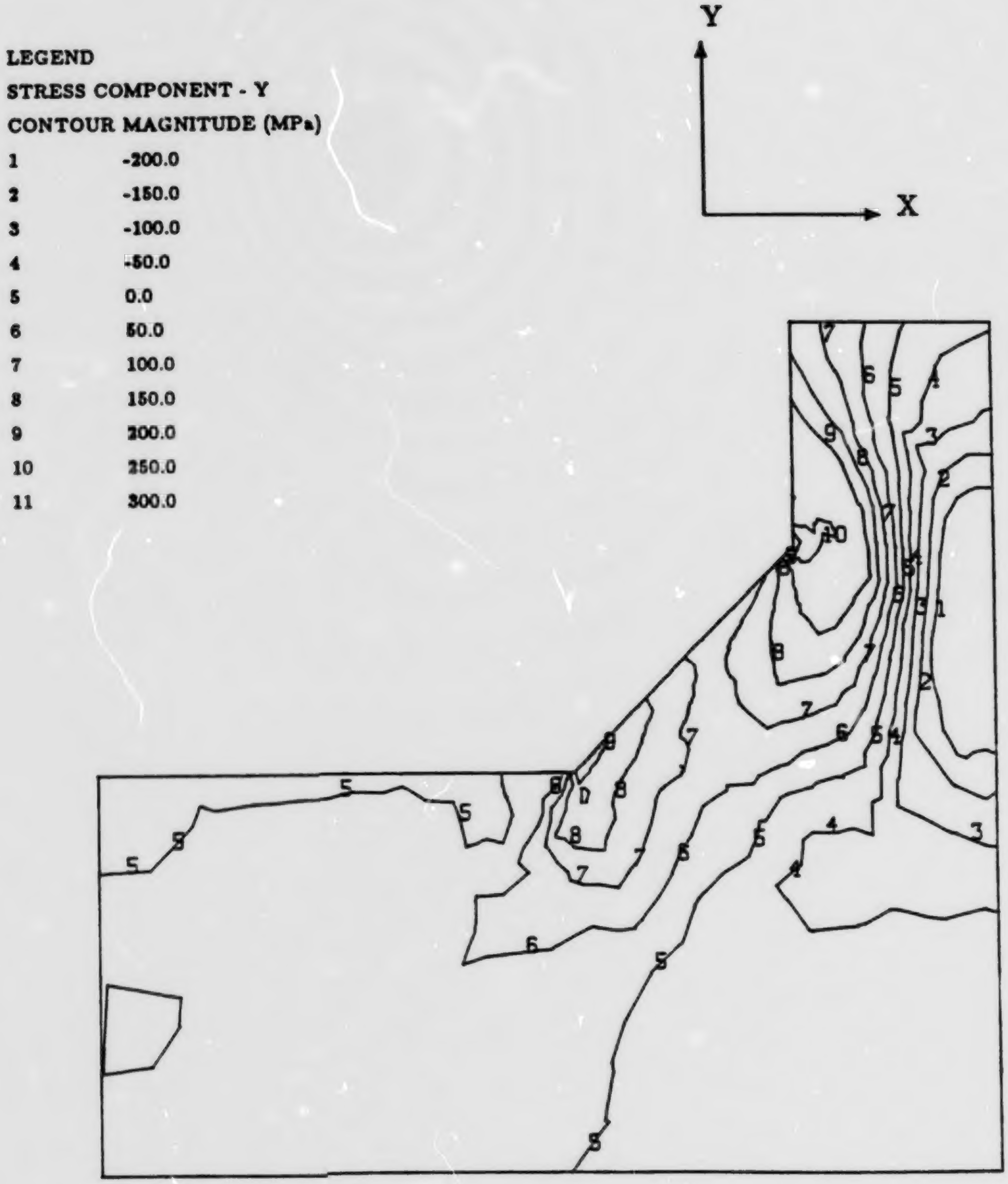

Figure 8.16: Y-stress distribution with 25 MPa load (as welded condition)

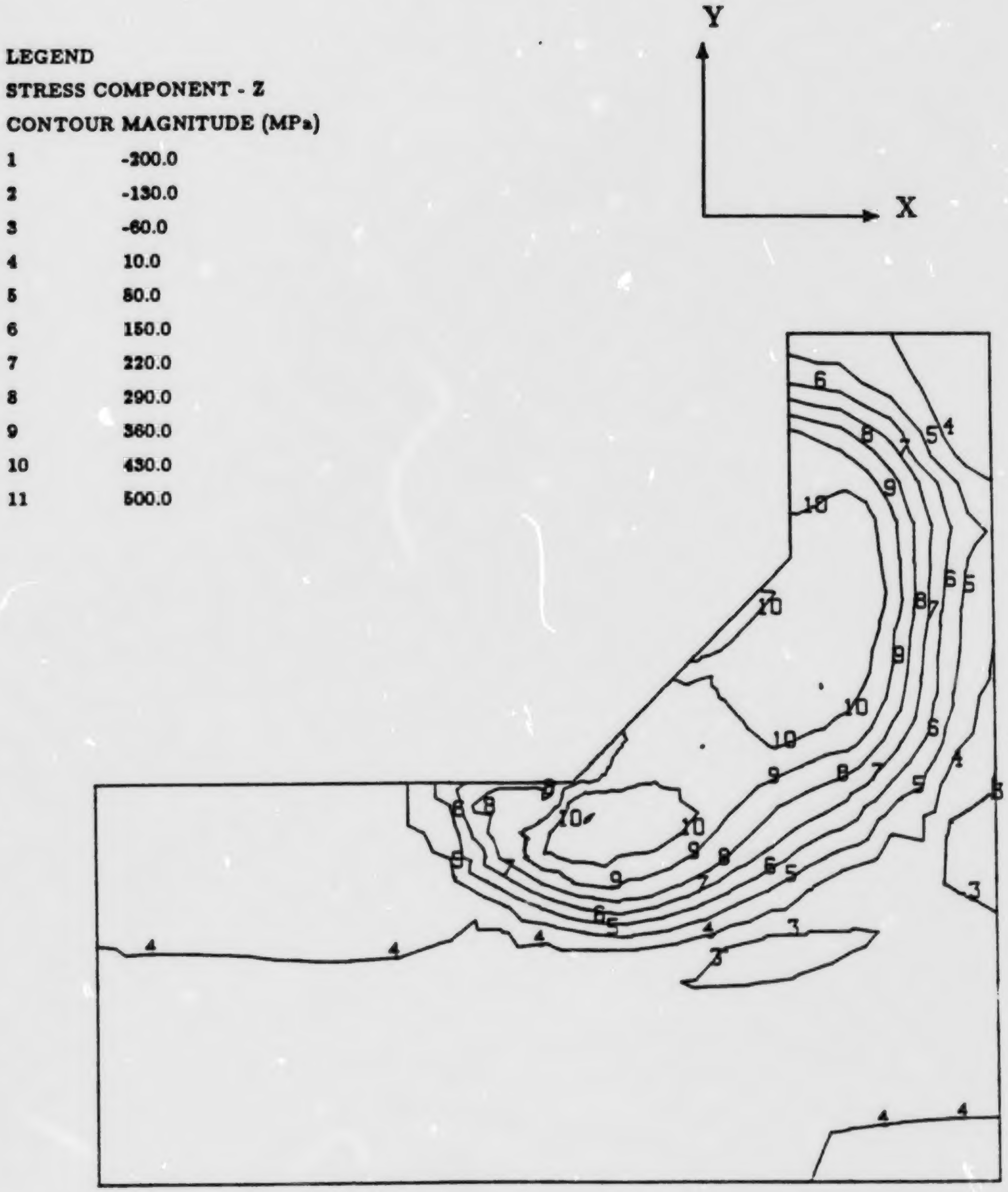

LEGEND

STRESS COMPONENT - Z

CONTOUR MAGNITUDE (MPa)

1	-200.0
2	-130.0
3	-60.0
4	10.0
5	80.0
6	150.0
7	220.0
8	290.0
9	360.0
10	430.0
11	500.0

Figure 8.17: Z-stress distribution with 25 MPa load (as welded condition)

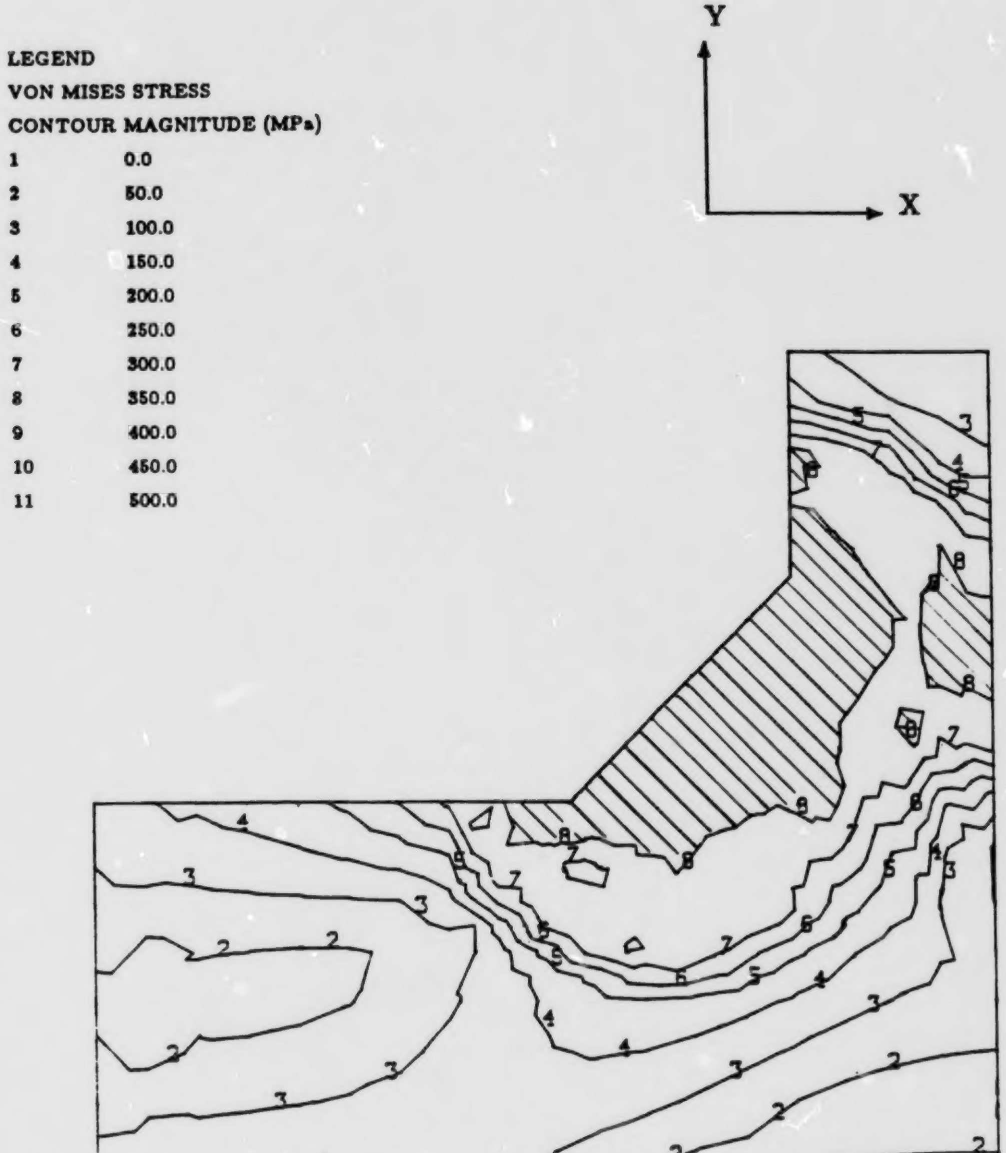

Figure 8.18: Von Mises stress distribution with 25 MPa load (as welded condition)

LEGEND
STRESS COMPONENT - X
CONTOUR MAGNITUDE (MPa)

1	-200.0
2	-140.0
3	-80.0
4	-20.0
5	40.0
6	100.0
7	160.0
8	220.0
9	280.0
10	340.0
11	400.0

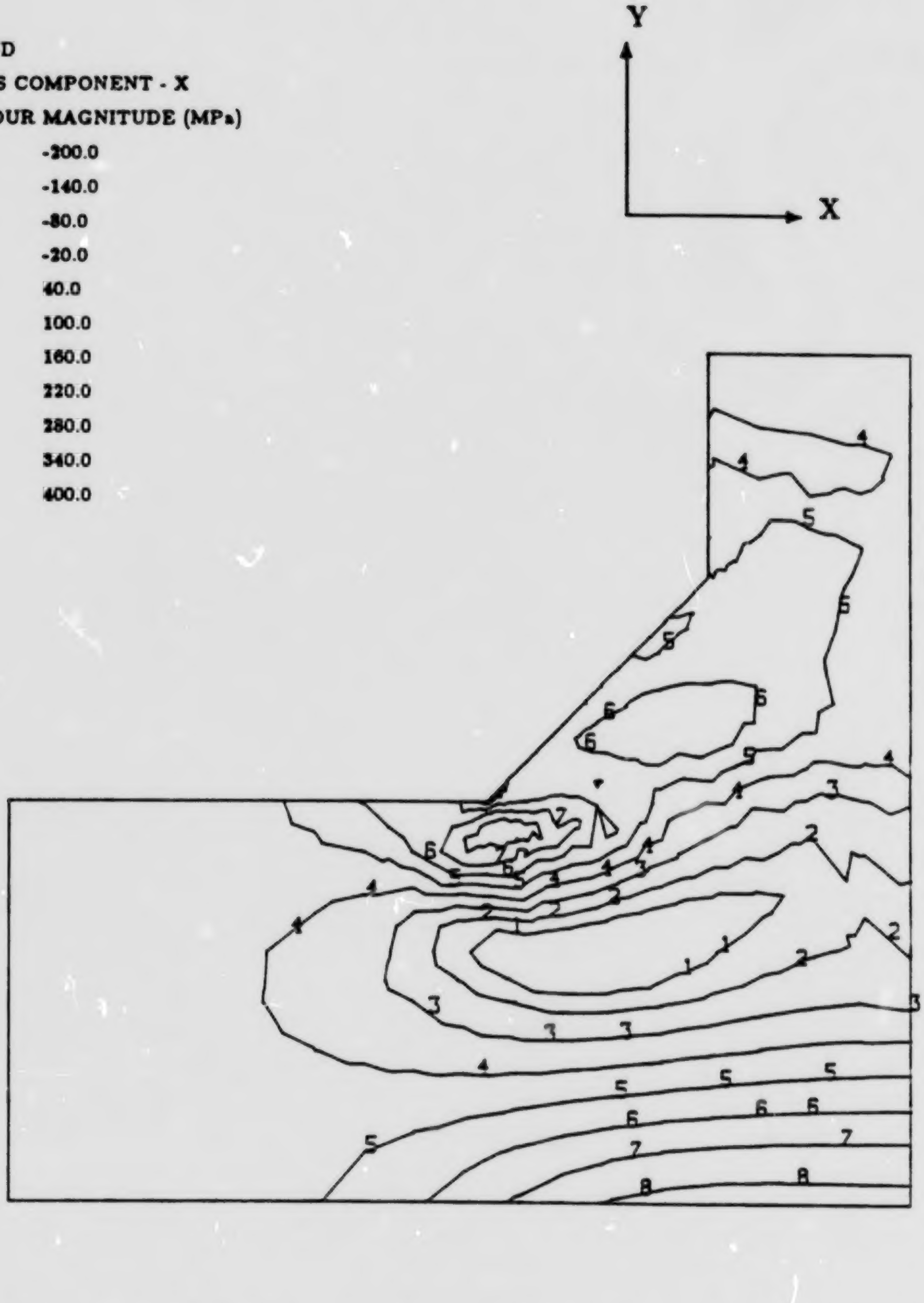

Figure 8.19: X-stress distribution after one 25 MPa loading cycle (as welded condition)

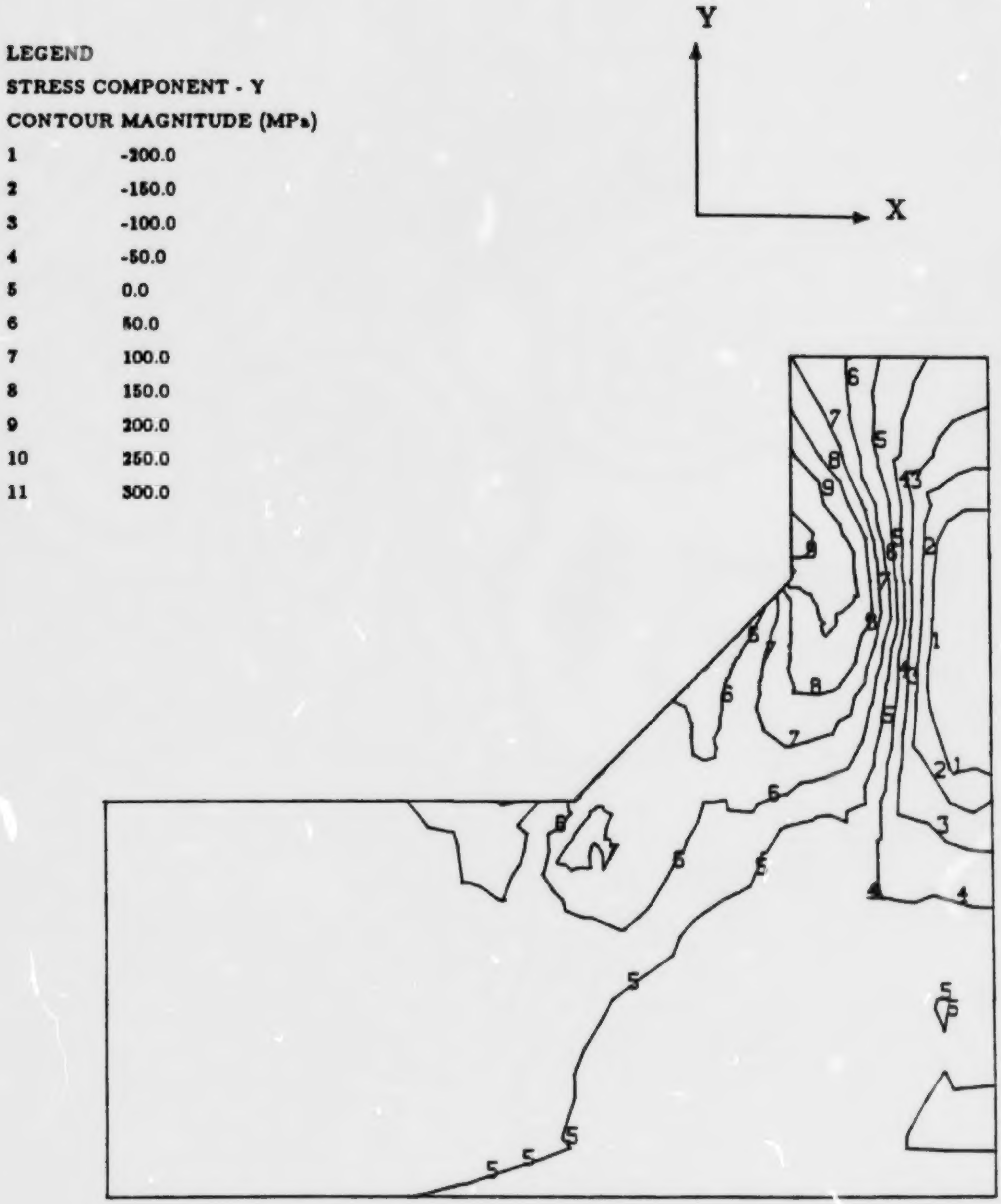

Figure 8.20: Y-stress distribution after one 25 MPa loading cycle (as welded condition)

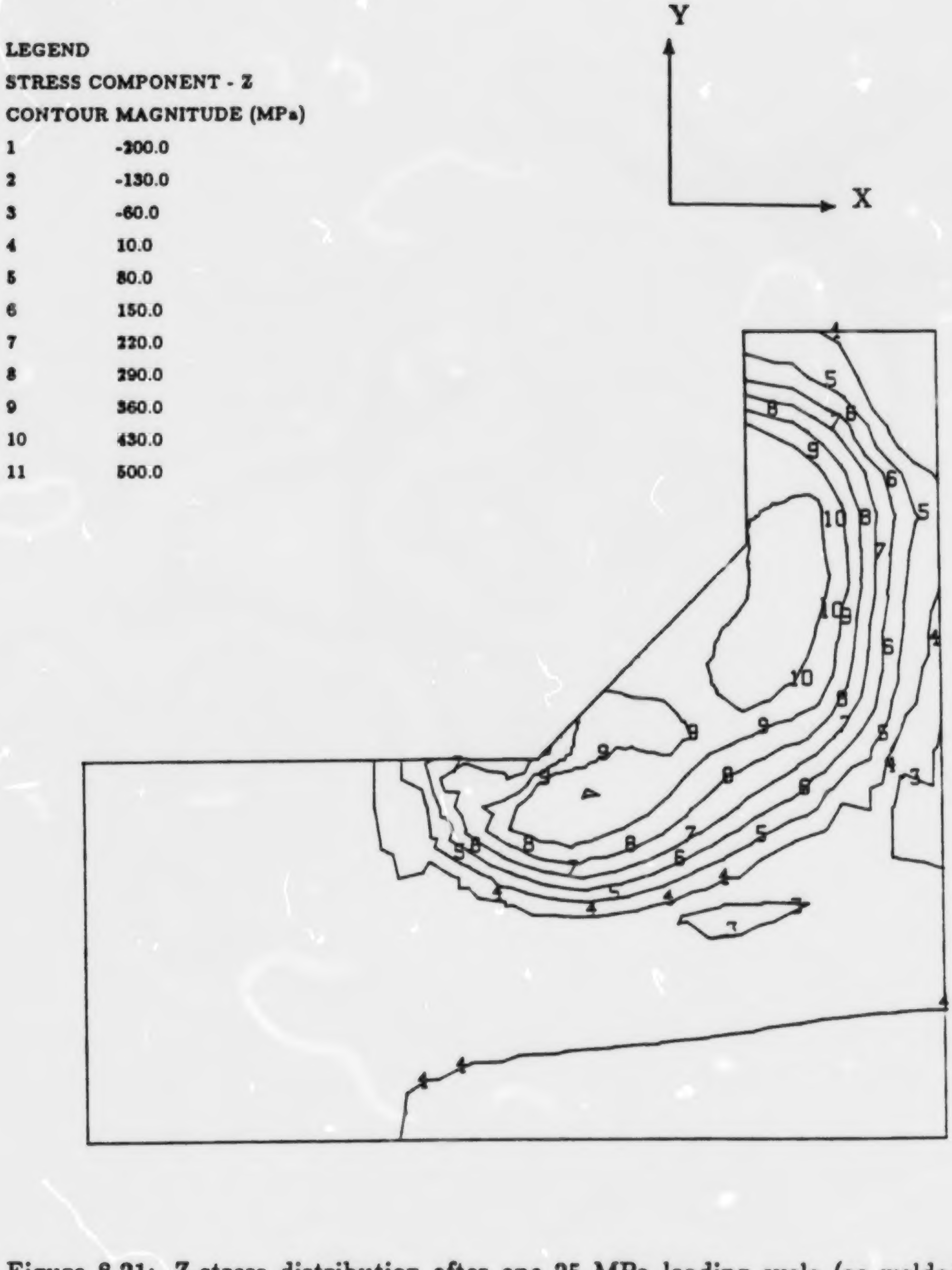

Figure 8.21: Z-stress distribution after one 25 MPa loading cycle (as welded condition)

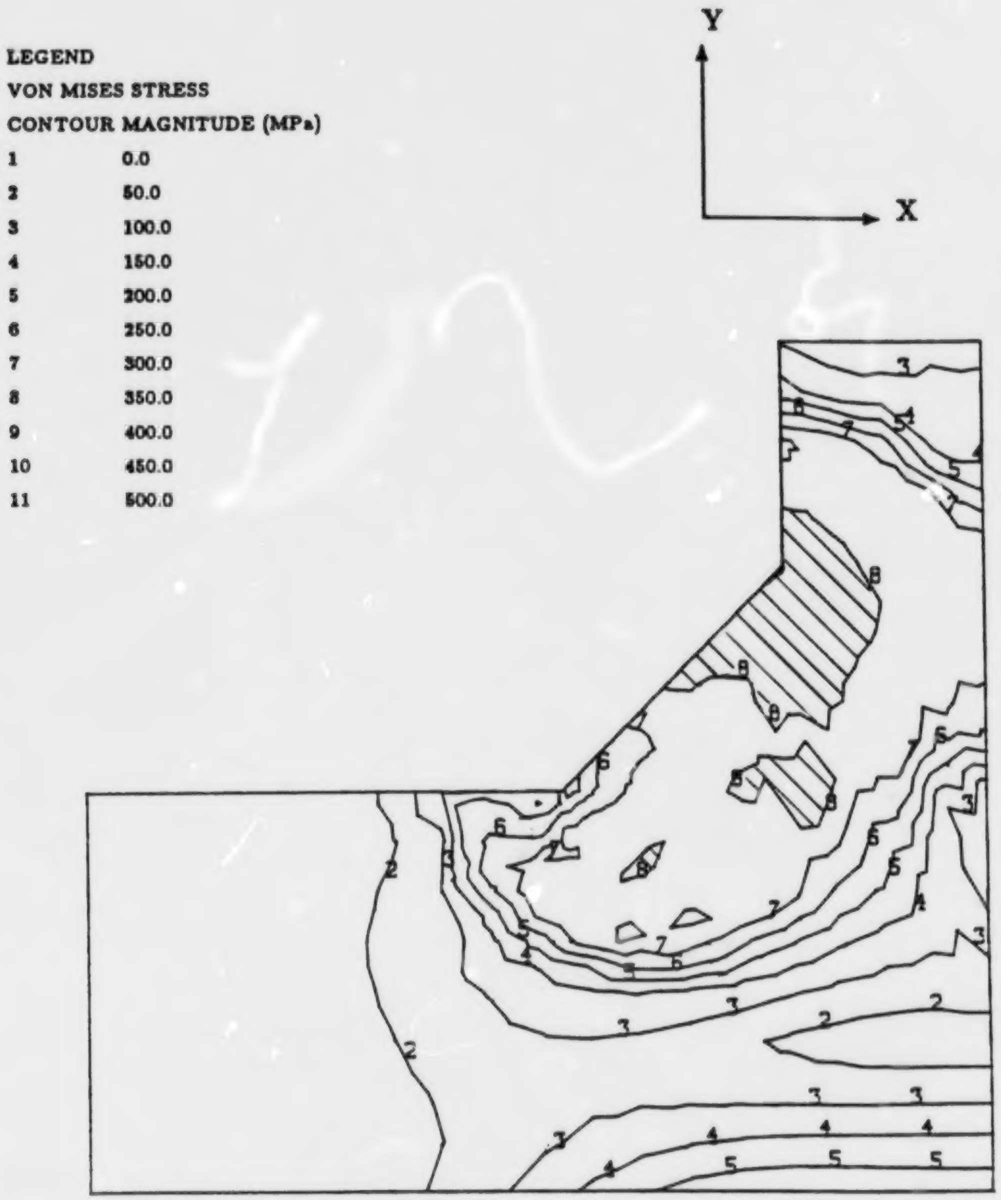

LEGEND

VON MISES STRESS

CONTOUR MAGNITUDE (MPa)

1	0.0
2	50.0
3	100.0
4	150.0
5	200.0
6	250.0
7	300.0
8	350.0
9	400.0
10	450.0
11	500.0

Figure 8.22: Von Mises stress distribution after one 25 MPa loading cycle (as welded condition)

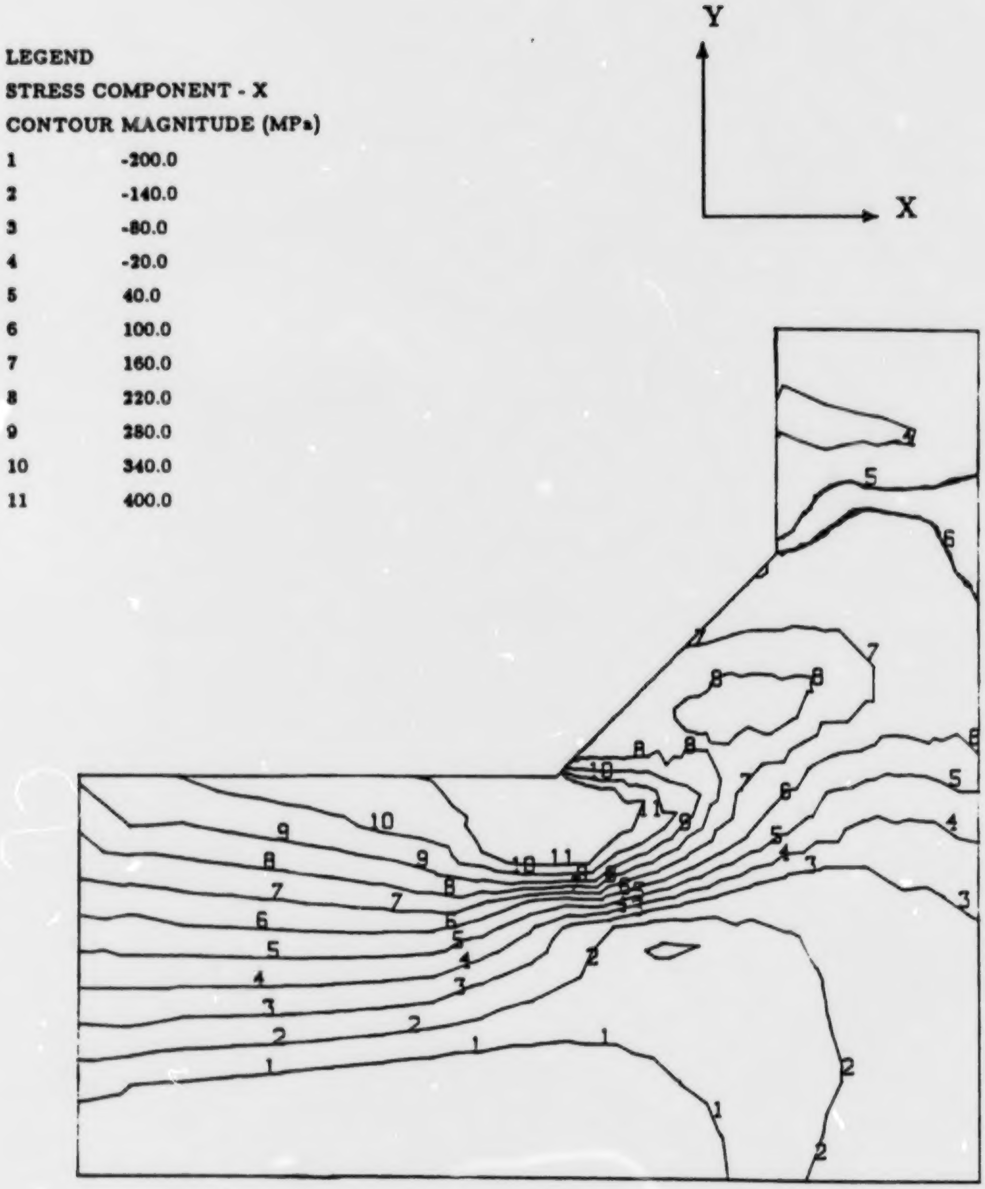

LEGEND

STRESS COMPONENT - X

CONTOUR MAGNITUDE (MPa)

1	-200.0
2	-140.0
3	-80.0
4	-20.0
5	40.0
6	100.0
7	160.0
8	220.0
9	280.0
10	340.0
11	400.0

Figure 8.23: X-stress distribution with 50 MPa load (as welded condition)

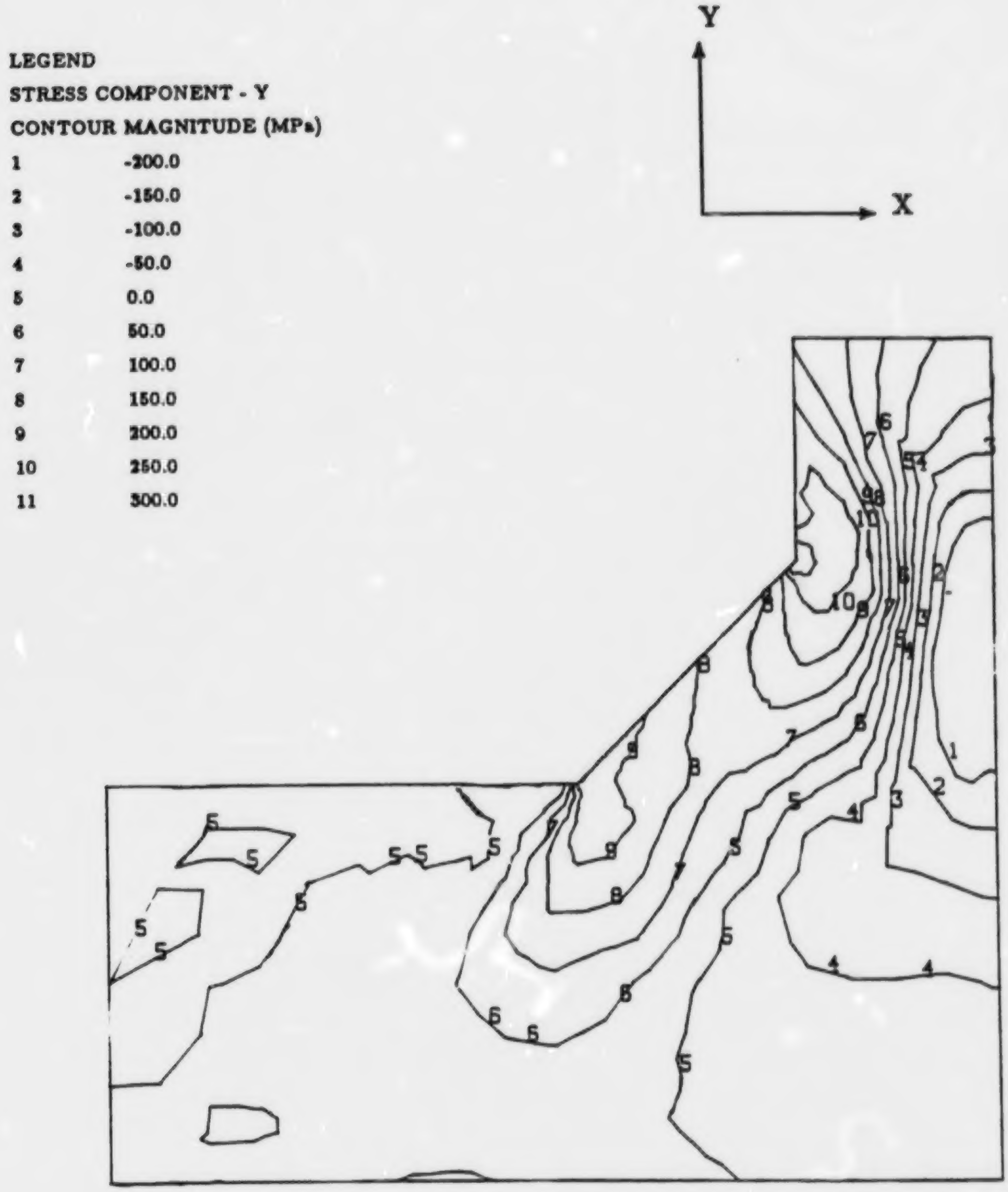

LEGEND

STRESS COMPONENT - Y

CONTOUR MAGNITUDE (MPa)

1	-200.0
2	-150.0
3	-100.0
4	-50.0
5	0.0
6	50.0
7	100.0
8	150.0
9	200.0
10	250.0
11	300.0

Figure 8.24: Y-stress distribution with 50 MPa load (as welded condition)

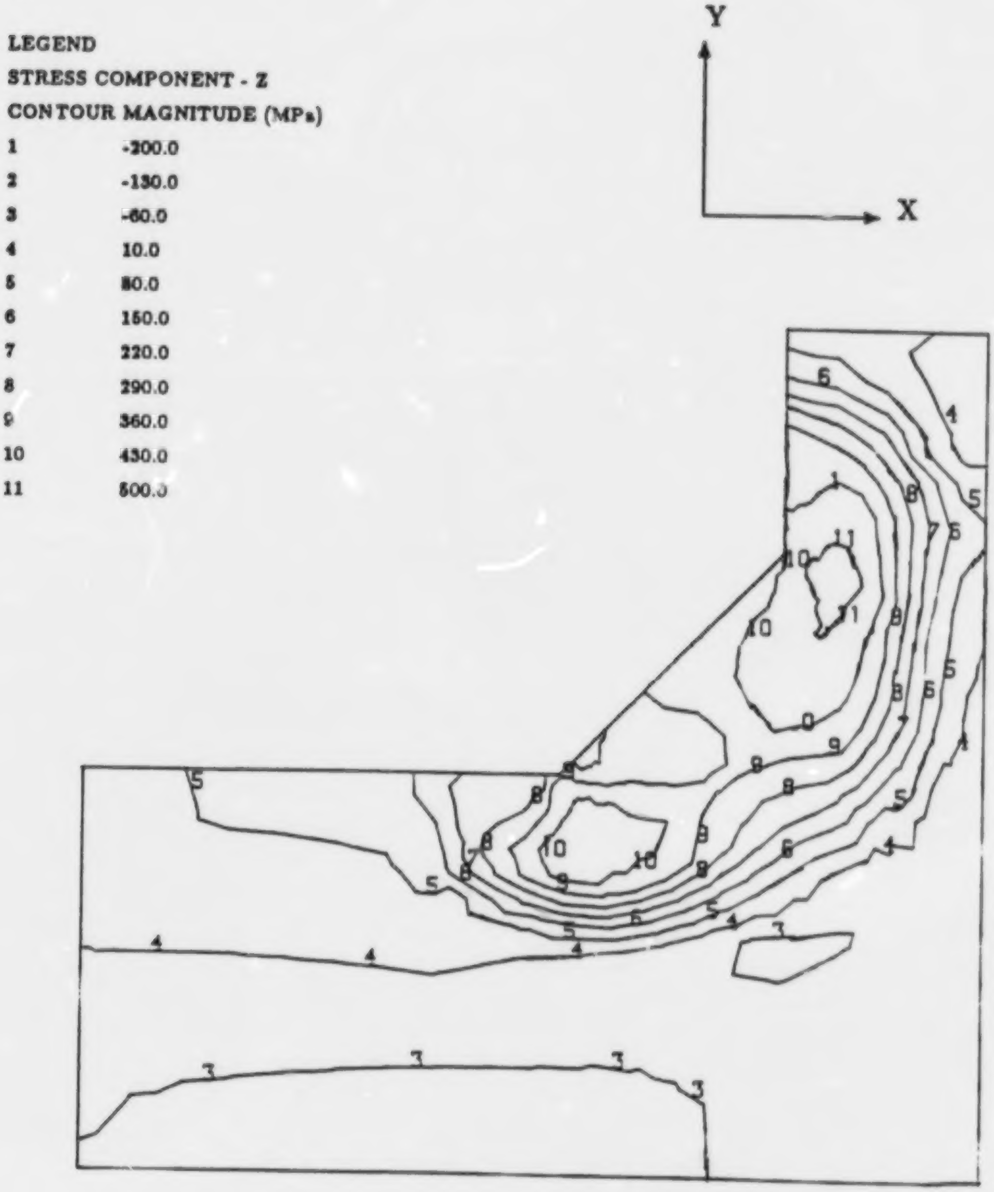

LEGEND

STRESS COMPONENT - Z

CONTOUR MAGNITUDE (MPa)

1	-200.0
2	-130.0
3	-60.0
4	10.0
5	80.0
6	150.0
7	220.0
8	290.0
9	360.0
10	430.0
11	500.0

Figure 8.25: Z-stress distribution with 50 MPa load (as welded condition)

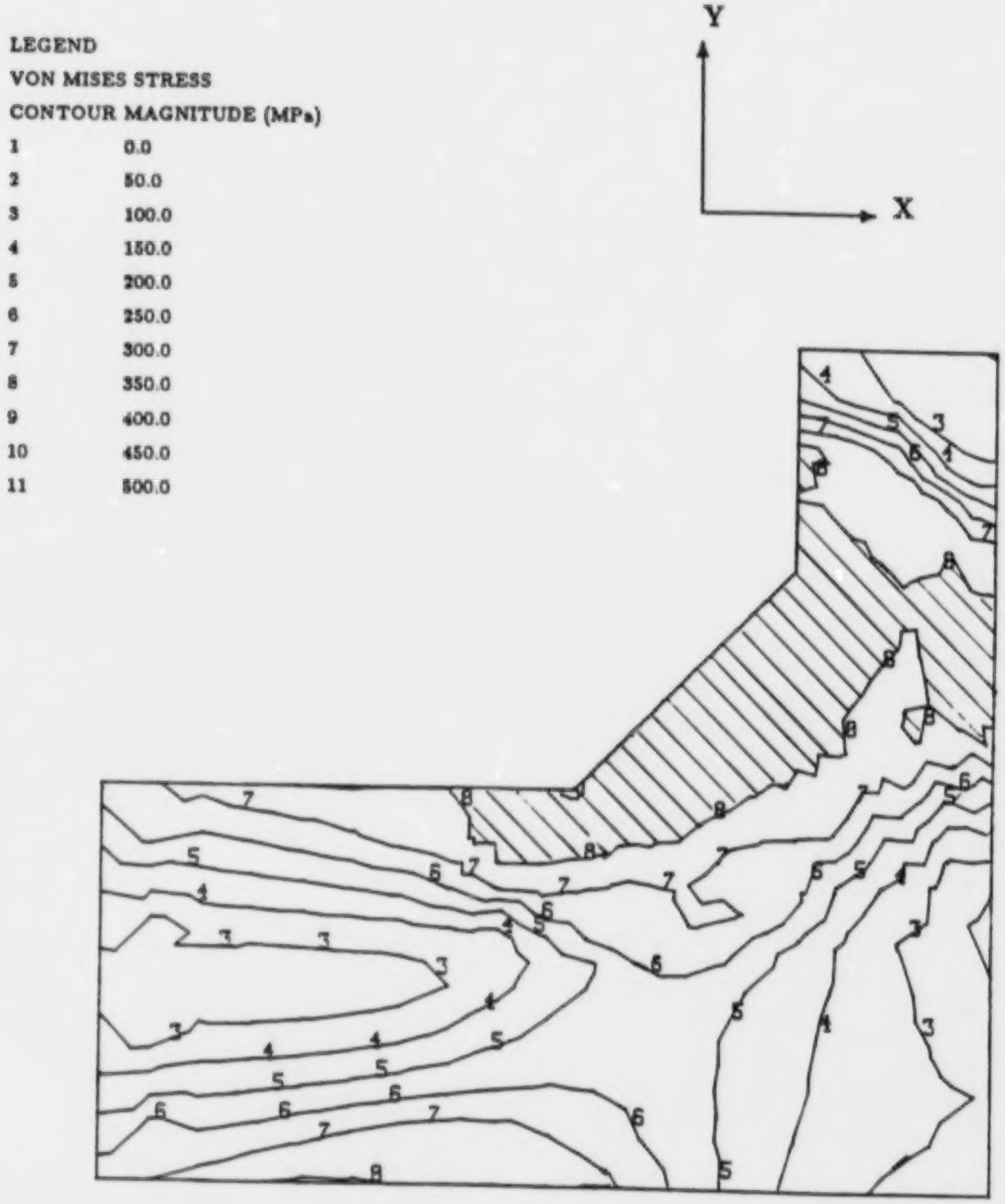

LEGEND

VON MISES STRESS

CONTOUR	MAGNITUDE (MPa)
1	0.0
2	50.0
3	100.0
4	150.0
5	200.0
6	250.0
7	300.0
8	350.0
9	400.0
10	450.0
11	500.0

Figure 8.26: Von Mises stress distribution with 50 MPa load (as welded condition)

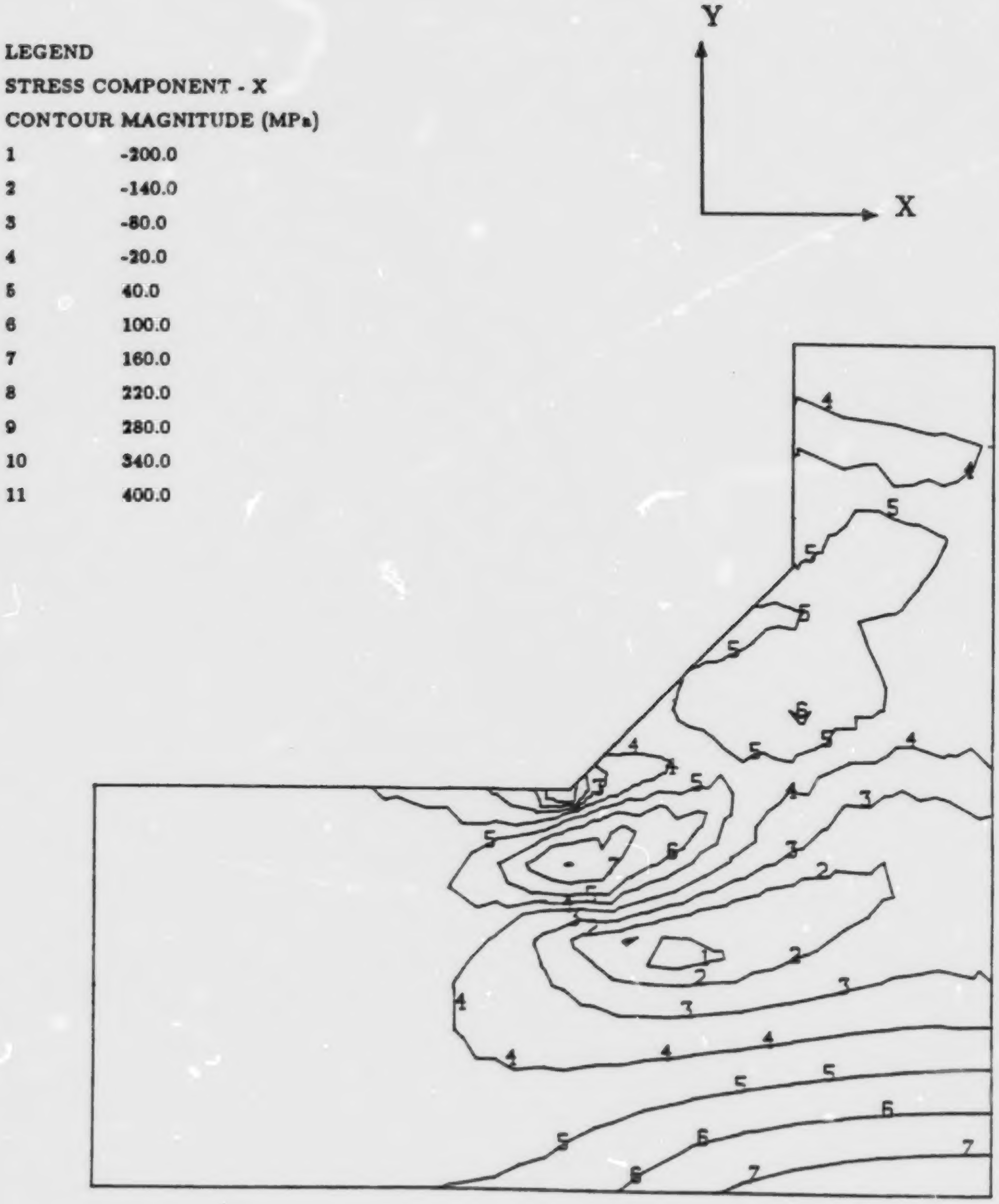

Figure 8.27: X-stress distribution after one 50 MPa loading cycle (as welded condition)

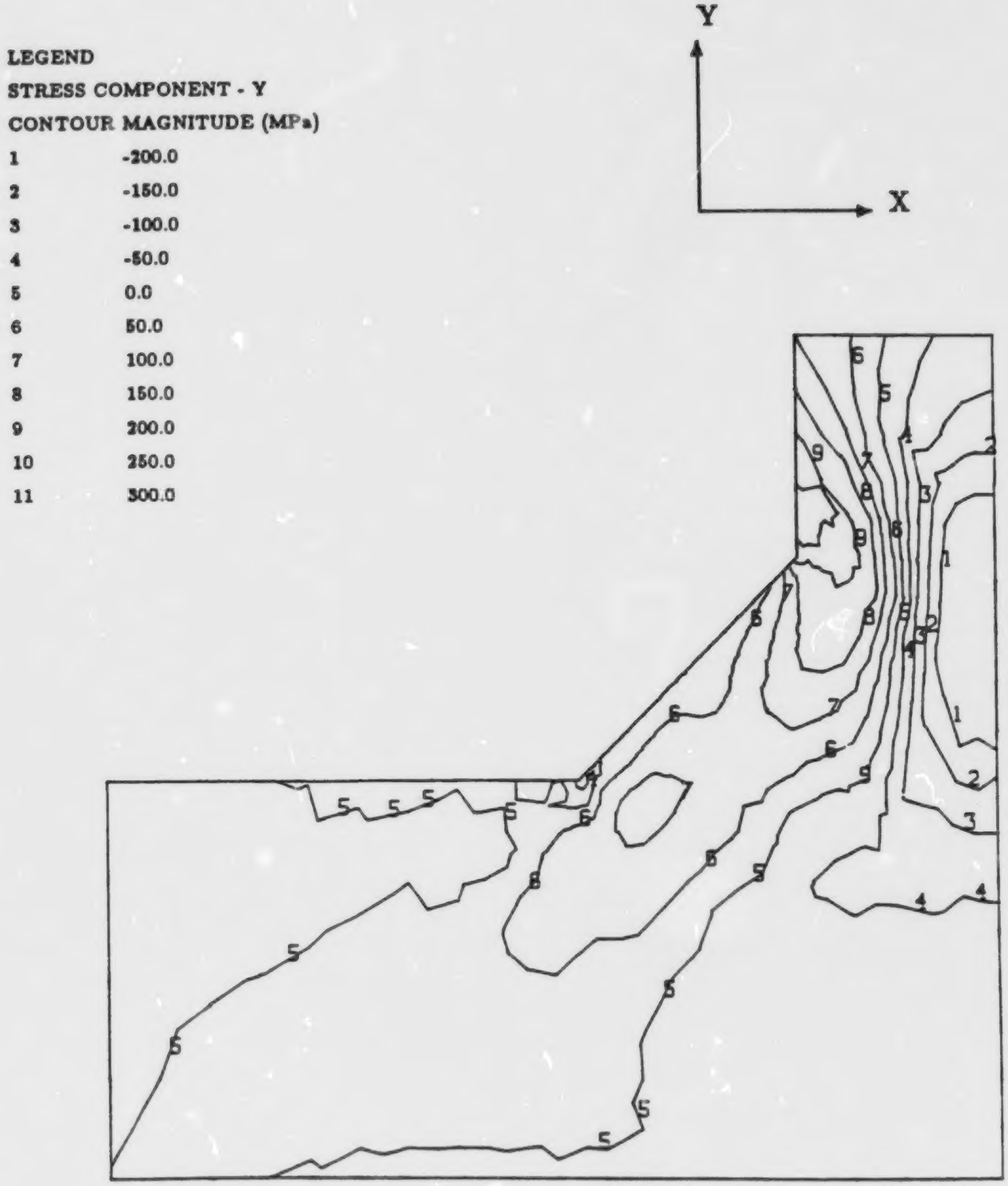

Figure 8.28: Y-stress distribution after one 50 MPa loading cycle (as welded condition)

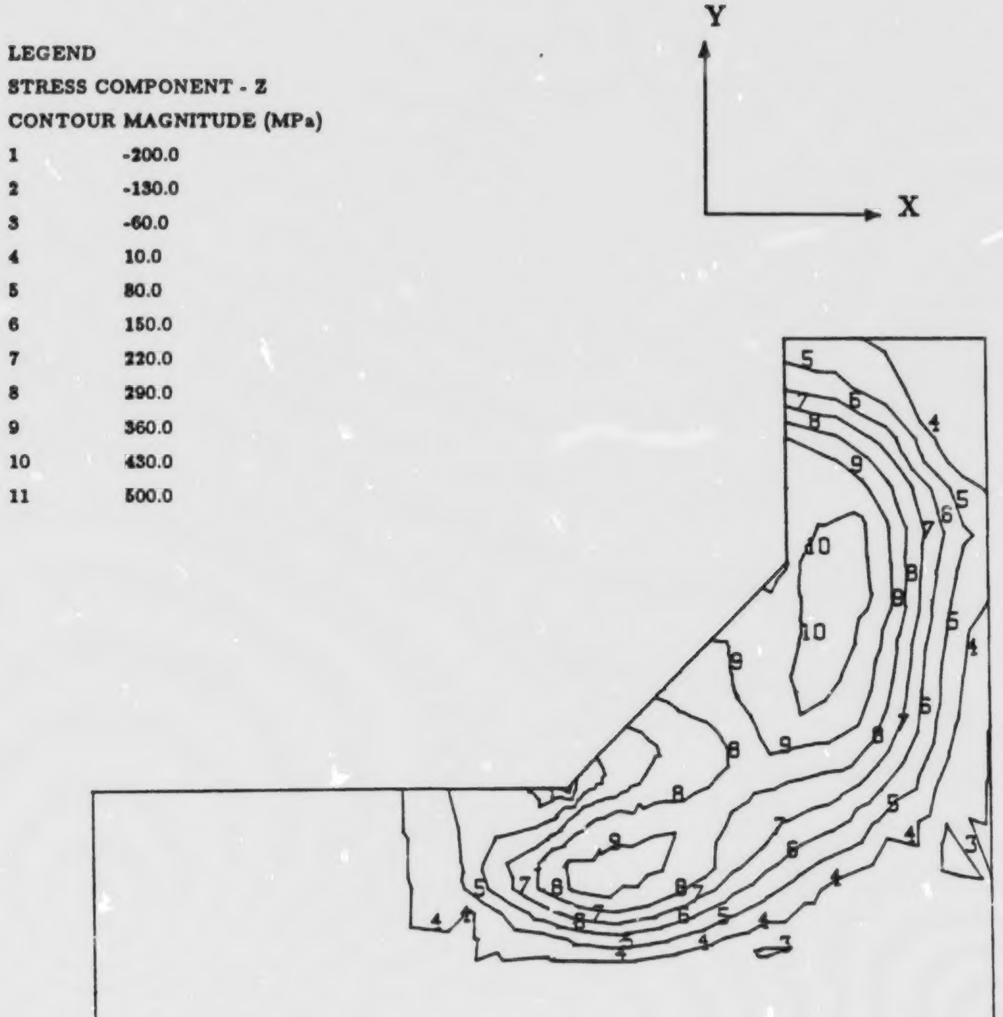

Figure 8.29: Z-stress distribution after one 50 MPa loading cycle (as welded condition)

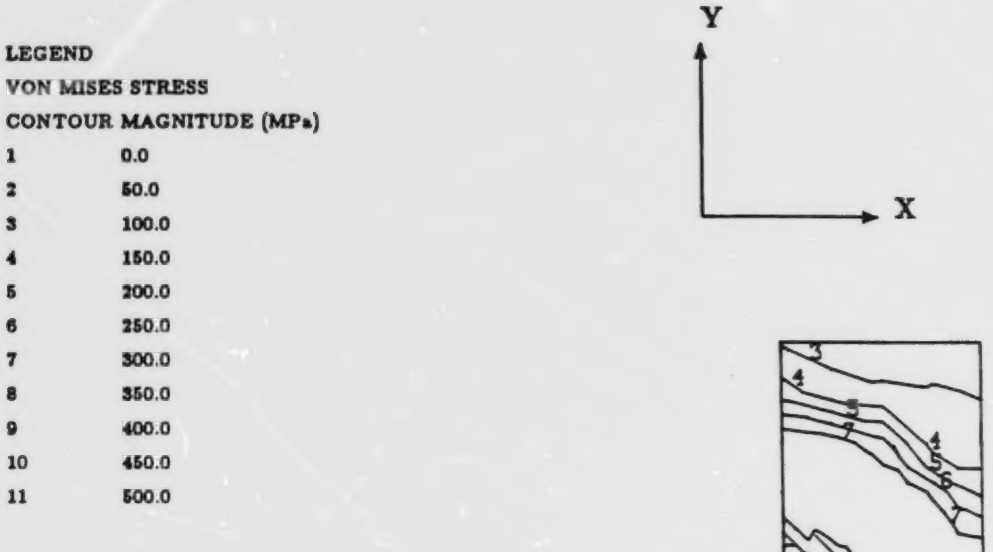

Figure 8.30: Von Mises stress distribution after one 50 MPa loading cycle (as welded condition)

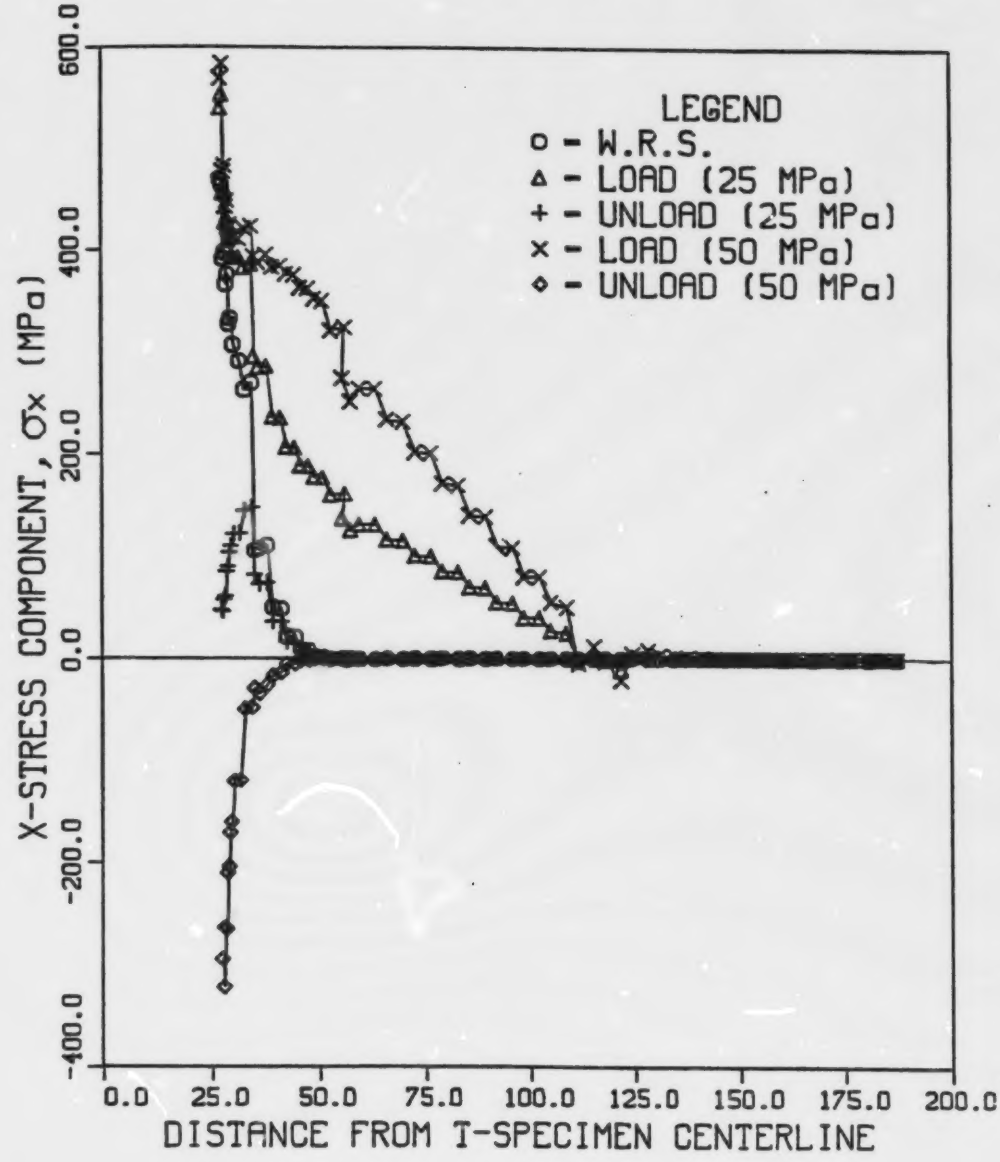

Figure 8.31: Distribution of the X-stress component along the top surface (as welded condition)

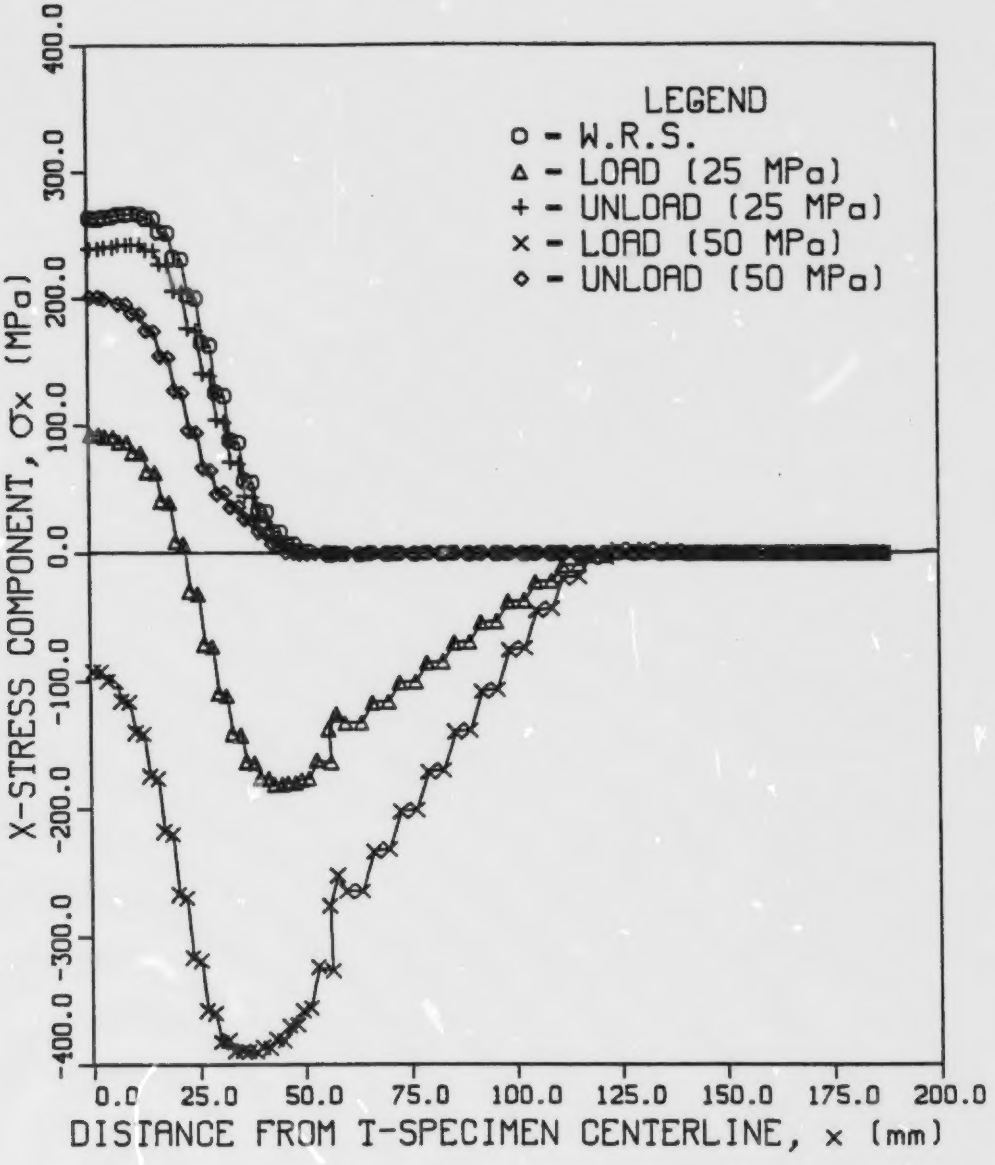

Figure 8.32: Distribution of the X-stress component along the bottom surface (as welded condition)

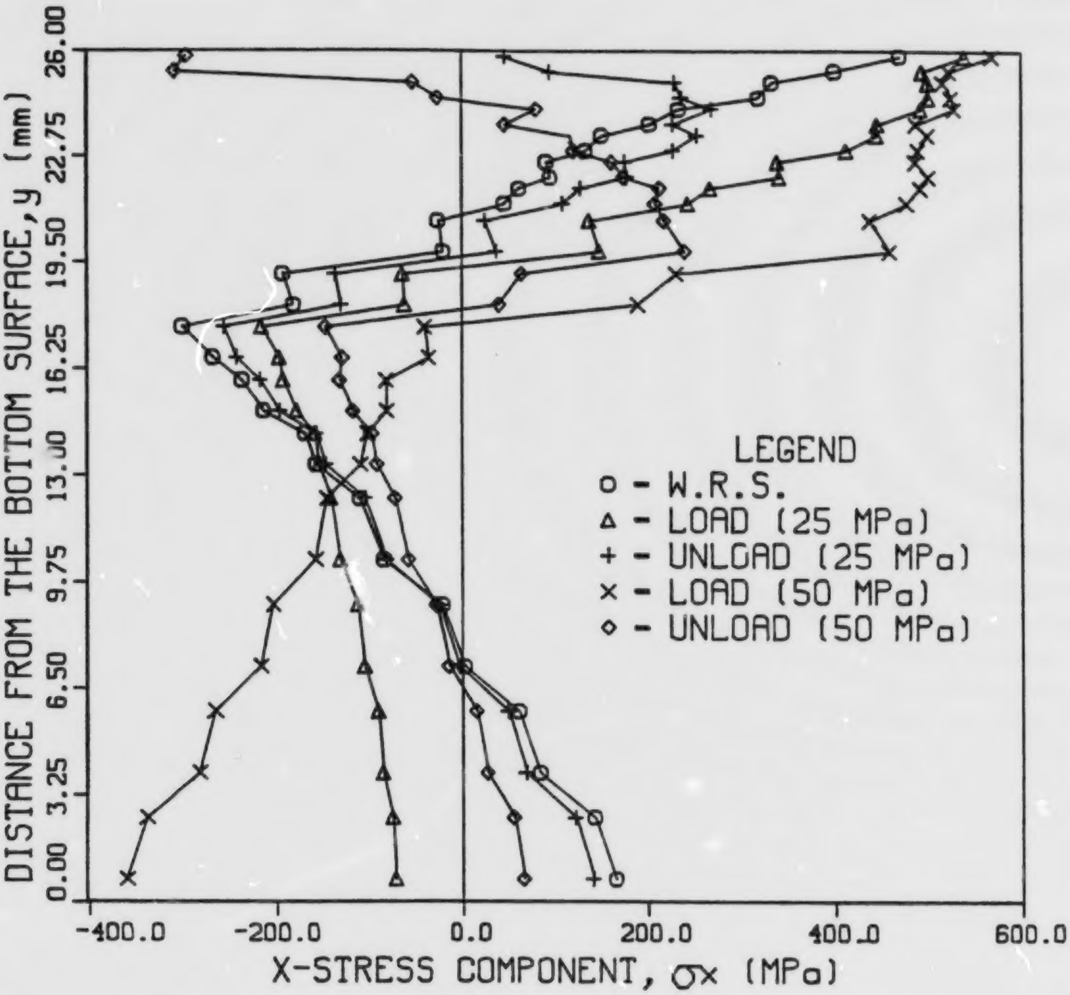

Figure 8.33: Distribution of the X-stress component through the plate thickness below the weld toe (as welded condition)

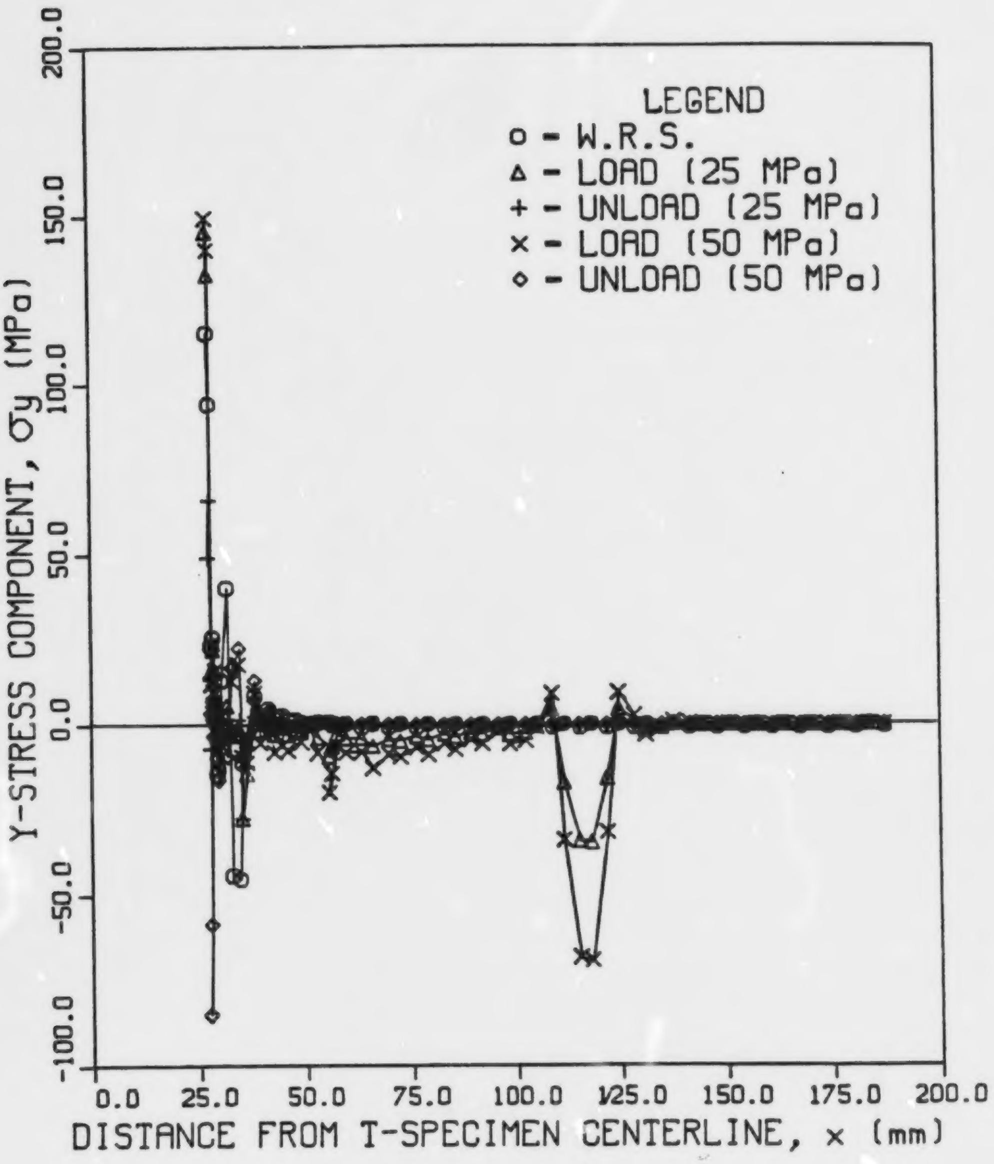

Figure 8.34: Distribution of the Y-stress component along the top surface (as welded condition)

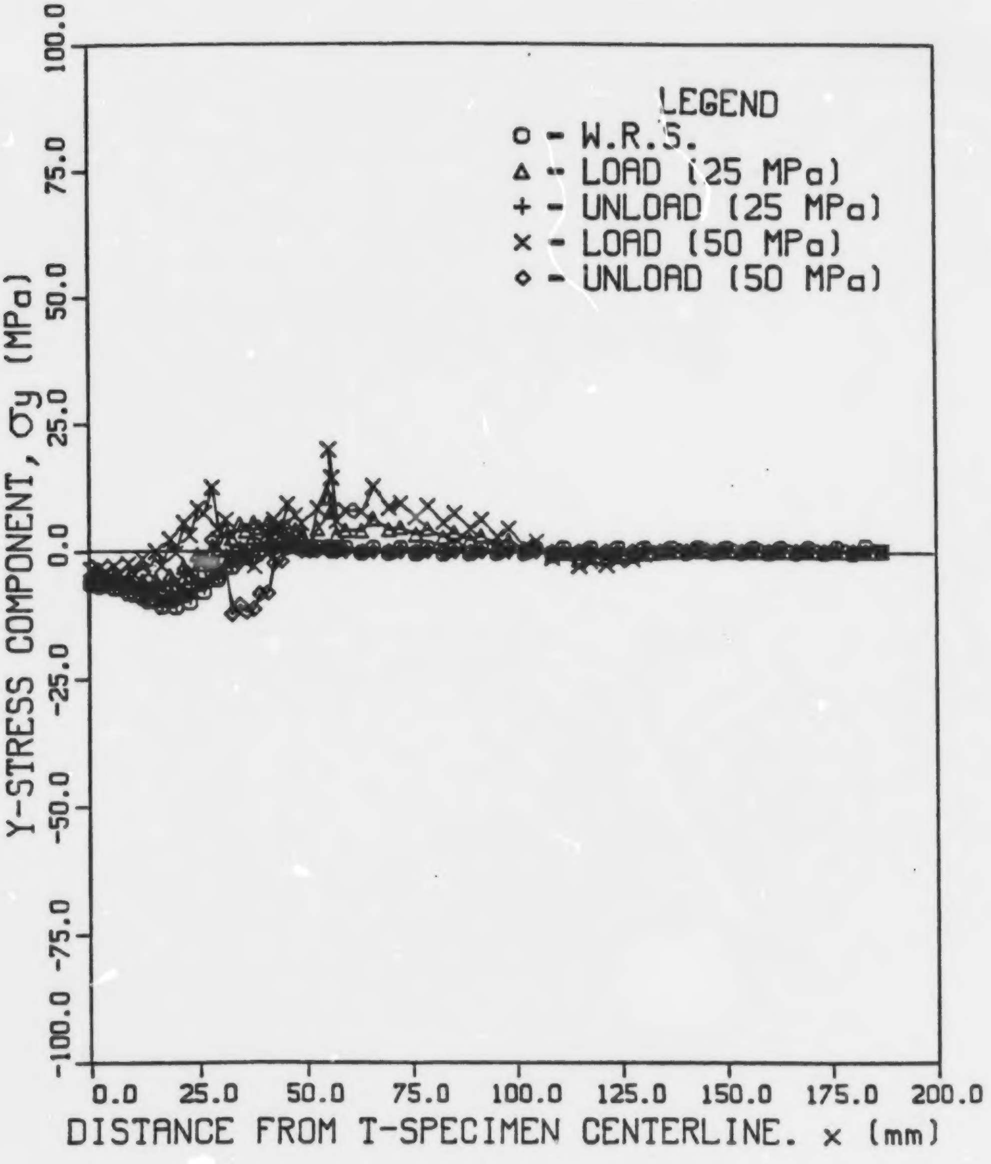

Figure 8.35: Distribution of the Y-stress component along the bottom surface (as welded condition)

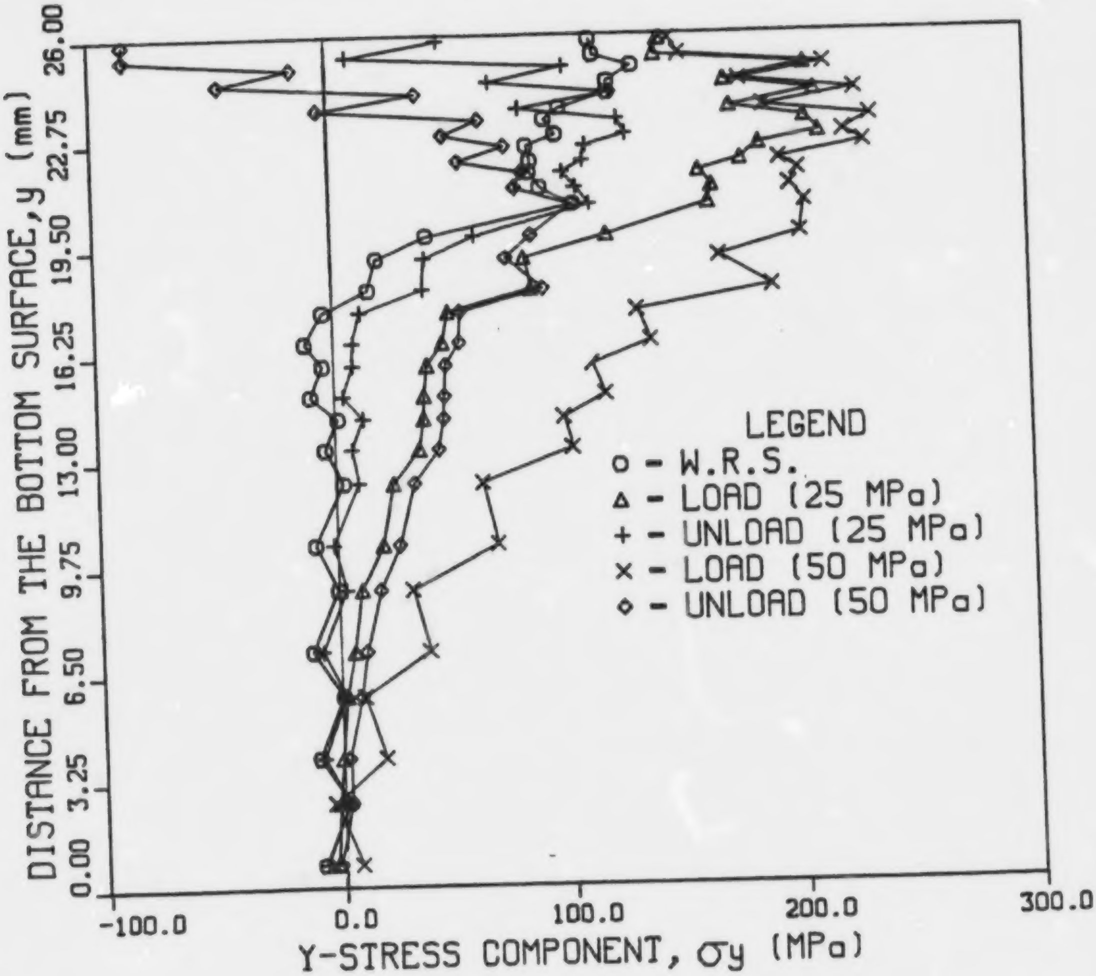

Figure 8.36: Distribution of the Y-stress component through the plate thickness below the weld toe (as welded condition)

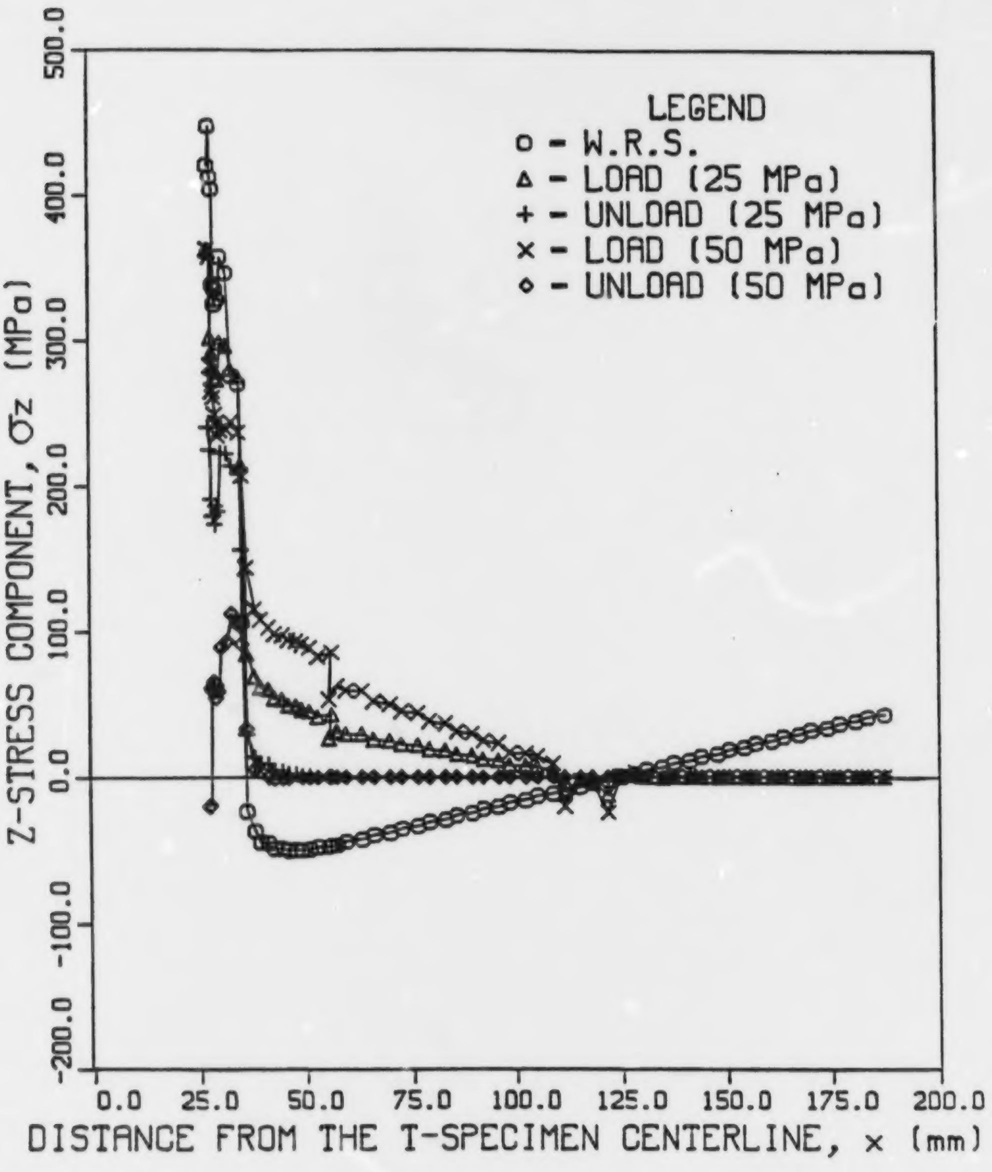

Figure 8.37: Distribution of the Z-stress component along the top surface (as welded condition)

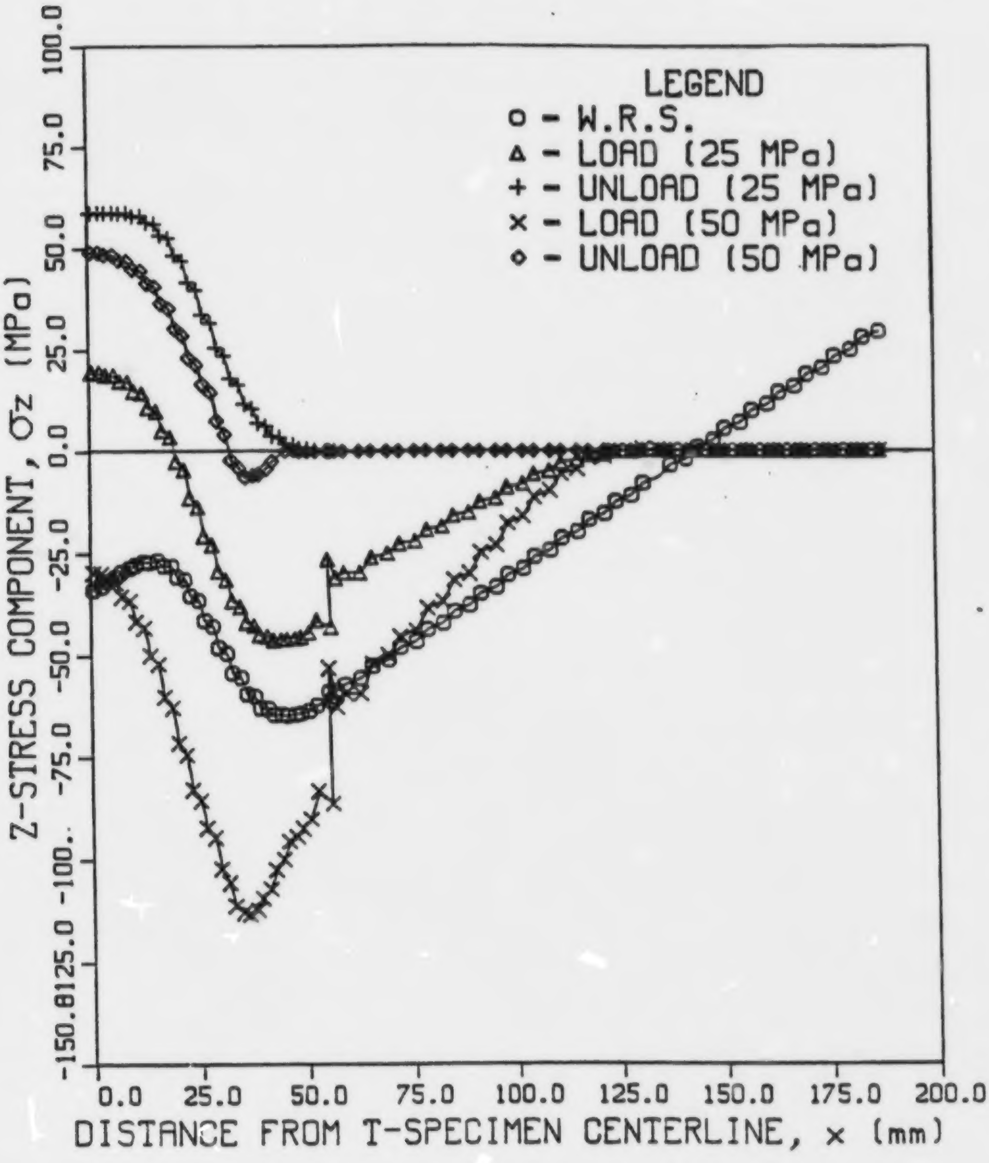

Figure 8.38: Distribution of the Z-stress component along the bottom surface (as welded conditon)

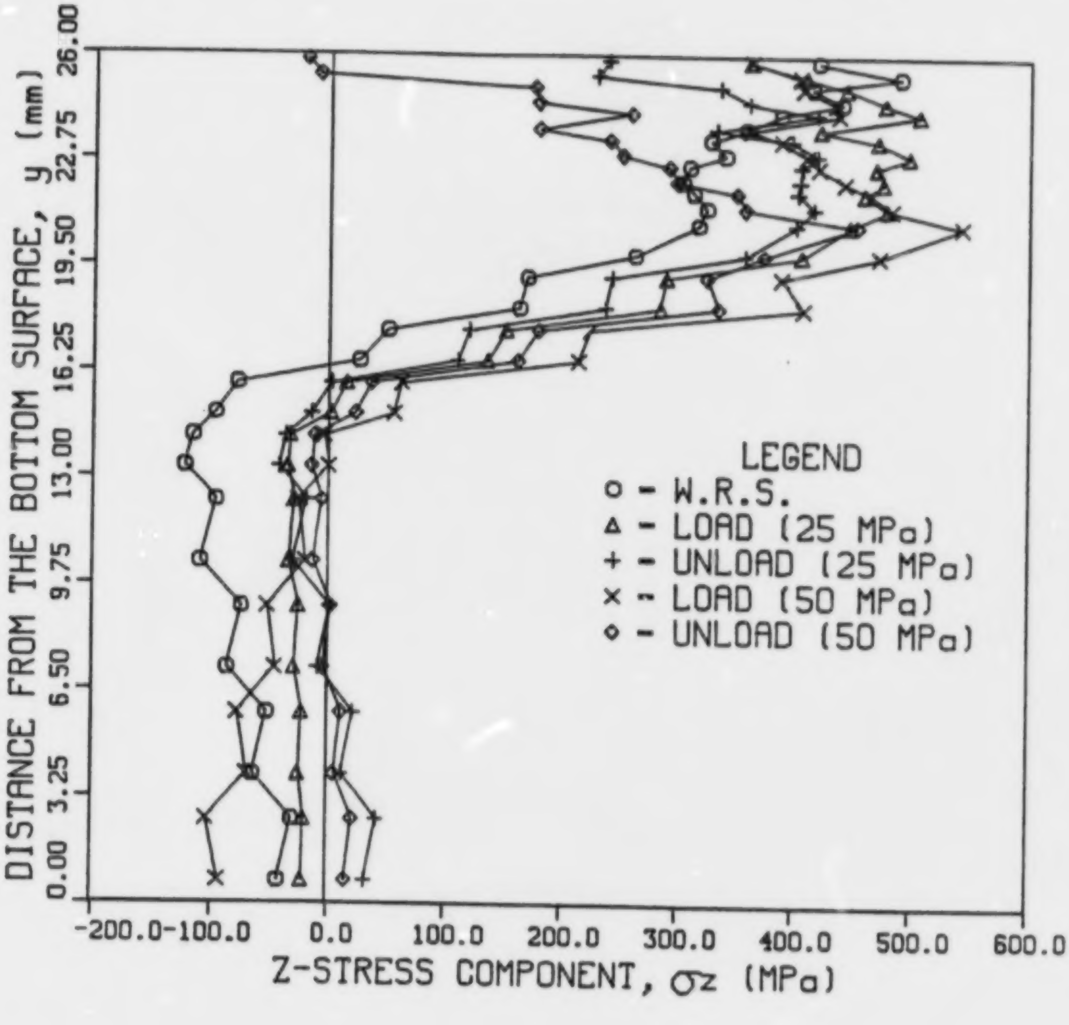

Figure 8.39: Distribution of the Z-stress component through the plate thickness below the weld toe (as welded condition)

Chapter 9

Conclusions

9.1 Phase Transformation Effect

In the first part of this Report, a model based on Leung's single weld pass model [1] was developed to determine the effect of allotropic phase transformations and the accompanying volumetric strains on welding residual stress.

The welding residual stress was predicted using a transformation strain of 0.5% and transformation temperature of 650°C. The results were compared to an analysis without the phase transformation effect and only a very small difference in the predicted welding residual stresses were observed.

A parametric study of the effects of transformation temperatures were carried out with transformation temperature of 450°C, 650°C and 850°C. The results of analyses with a phase transformation that takes place at 650°C or higher were identical. The predicted residual stresses were lower by less than 10 MPa in the analysis with a phase transformation that starts at 450°C.

The effect of the magnitude of the volumetric strain was also studied. Volumetric strains of 0.5% and 2.0% were used with the transformation taking place at 650°C. The predicted welding residual stresses for the analysis with the higher volumetric strain were lower by about 20 MPa.

Based on the results of this study, it can be concluded that that the phase transformation effect is very small when realistic volumetric strains and transformation temperatures for ferrite steels are used. Furthermore, the transformation temperature affects the residual stress magnitude only in the fusion region where the transformation takes place. Transformations at high temperature appear to have no significant effect in residual stress. Whereas, a small decrease of residual stress magnitude can be expected for transformations at lower temperatures. Only if the volumetric strain is comparable to the thermal contraction strain (which is unrealistic), will a significant decrease in residual stress magnitude occur. When a transformation reduces residual stresses, the general trend of the stress distribution does not change, however the overall distortion of the welded structure will be affected. Small local perturbations in the residual stress may occur in the HAZ, however this is a function of both the phase transformation and local metallurgy.

It can be further concluded that the model developed by Leung [1,2] for stainless steel is adequate for predicting welding residual stress for most ferritic steels and other materials that exhibit allotropic phase transformations, providing that the volumetric expansion is small compared to the thermal contraction strain.

9.2 Analysis Of The 26 mm T-Joint Specimen

In the second part of this Report, the welding residual stresses in a 26 mm T-joint fatigue specimen was predicted. The effect of mechanical loading on the welding residual stresses was also investigated.

9.2.1 Heat Transfer Analysis

In the heat transfer analysis, the thermal history for the capping passes of the T-joint specimen were calculated. The heat input from the electrode was simulated using a modified version of Goldak's double ellipsoidal heat source model [48]. Convective and radiative heat transfer were assumed on all surfaces except on the surface of the weld pool which was assumed to be adiabatic. Half of the horizontal plate was not modelled in order to reduce computation time. The heat flow into this part of the specimen was replaced by surface convection. Temperature dependent material properties were used and a latent heat of fusion was assumed. Latent heats due to allotropic phase transformation were neglected. The temperature distribution before the laying of the first capping pass was assumed to be room temperature which would introduce some error in the predicted thermal history because an interpass temperature of 230°C was maintained during welding.

Based on the results, this model appears to predict the temperature history quite accurately. The predicted weld pool shapes compared reasonably well with measurements and the fast cooling rate expected in the fillet weld was also observed. A maximum temperature of 2800°C was predicted which indicates the cooling effect due to weld pool convection was underestimated. However, this is expected to cause only a minor error in the calculation of residual stresses as the temperatures are modified such that the maximum temperature does not exceed 1550°C.

In addition, it can be concluded that Goldak's double ellipsoidal heat source model [48] is applicable to fillet type of weld joints just as well as for butt welds of flat plates.

9.2.2 Welding Residual Stress Prediction

After the temperature history was calculated, it was supplied to the stress analysis as thermal loading. A two dimensional analysis was carried out with generalized plane strain elements capable of modelling longitudinal displacements. No restraint was applied during welding of the T-joint specimen, therefore, all degrees of freedom were set free. A time independent, thermo-elastic-plastic constitutive model was assumed. The strain hardening and the Bauschinger effect were modelled by using a kinematic hardening model.

Analyses were was carried out with and without the symmetry assumption. The predicted residual stresses showed no difference between the two analyses. This indicates that the residual stress distribution is symmetrical about the specimen center-line which is consistent with observations by other researchers [56].

Welding residual stresses due to the capping passes were predicted without the inclusion of residual stresses from previous passes. The calculated results were compared to neutron diffraction measurements by Holden et al. [63]. In general, the predicted residual stresses achieved reasonable agreement with the measured results with differences usually less than 50 MPa.

The first capping pass was simulated with the inclusion of residual stresses from previous passes and were compared with the simulation without previous stresses. The predicted residual stresses around the weld region were very similar for both analyses which indicates that the residual stresses in this region can be attributed to the capping passes alone. In regions away from the weld zone, the predicted results appeared to be closer to the measurements with the inclusion of existing residual stresses. Based on this observation, it can be concluded that the predicted residual stresses due to the capping passes, without existing stresses from previous passes, are accurate at the weld toe region. Improvement in the predicted results in regions away from the weld zone can be achieved by including the effect of previous passes either by simulating all passes or by providing a reasonable estimation as in this study.

9.2.3 Loading Of The T-Joint Specimen

Mechanical loading of the 26 mm T-joint specimen was simulated in both the stress free and as welded conditions. The load was applied through the vertical plate of the T-joint specimen which loaded the horizontal plate in a three point bending configuration. This loading configuration is symmetrical about the center-line and plane strain exists in most part of the specimen. By applying a load similar to that in the fatigue test, 25 MPa, in the stress free condition, some yielding was predicted at the weld toe which left a small region of compressive residual stress when the load was removed. A stress concentration factor of 2.3 was predicted at the weld toe. This is smaller than values reported in the literature which indicates the finite element mesh used near the weld toe was not fine enough to capture the stress gradient.

In the simulation of loading in the as welded condition, the results showed that the welding residual stress is dominant in the weld zone and the bending stress is dominant in the rest of the specimen. Shakedown of the residual stress was observed. However, this effect was found only in the weld toe region and not through the whole plate thickness as assumed by some researchers. With an applied load of 25 MPa (250 MPa 'hot spot' stress), tensile transverse residual stress still exists near the weld toe after shakedown. This tensile residual stress can lead to faster fatigue crack growth than a specimen that has been stress relief.

References

[1] Leung, C.K., and Pick, R.J., **Study of Finite Element Modelling of Multipass Welds - Final Report**, *WRI Project No. 208-12, DSS File No. 01st.23440-2-9060*, University of Waterloo, Waterloo, Ontario, Mar. 1986.

[2] Leung, C.K., **Study of Finite Element Modelling of Multipass Welds**, *Ph.D. Thesis*, University of Waterloo, Waterloo, Ontario, 1986.

[3] Hibbitt, Karlsson, and Sorenson, *ABAQUS Users Manual*, Hibbitt, Karisson and Sorenson Inc., Providence, Rhode Island.

[4] Mair, D., **A Study of Residual Stresses in a Welded Plate**, *MASc. Thesis*, University of Waterloo, Waterloo, Ontario, 1987.

[5] Mohaupt, U.H., Burns, D.J., Kalbfleisch, J.C., Vosikovsky, O., and Bell, R., **Fatigue Crack Development, Thickness and Corrosion Effects in Welded Plate to Plate Joints**, *Proceedings of the International Offshore Conference "Steels In Marine Structures 1987"*, Delft, The Netherlands, 1987.

[6] Yee, R., Burns, D.J., Mohaupt, U.H., Bell, R., and Vosikovsky, O., **Thickness Effect and Fatigue Crack Development in Welded Joints**, *Pro-*

ceedings of The 7th International Conference on Offshore Mechanics and Arctic Engineering, Houston, Texas, Feb. 7-12 1988, Pg. 447-457.

[7] Tyson, W.R., Vosikovsky, O., Faucher, B., and Burns, D.J., **Brittle Fracture in Heavy Section Welded T-Joints: Correlation Between Stress Intensity At Fracture and Small- Specimen Toughness Tests**, *Proceedings of the 7th International conference on Offshore Mechanics and Arctic Engineering*, Houston, Texas, Feb. 7-12, 1988, Pg. 219-224.

[8] Macherauch, E., and Wohlfahrt, H., **Different Sources of Residual Stress As a Result of Welding**, *Proceedings of An International Conference on Residual Stresses in Welded Construction and Their Effects*, London, Nov. 15-17, 1977, The Welding Institute, Pg. 267-282.

[9] Macherauch, E., and Kloos, K.H., **Origin, Measurement and Evaluation of Residual Stresses**, *Residual Stresses in Science and Technology - Proceedings of the International Conference on Residual Stresses*, Garmisch-Partenkirchen (FRG), 1986, Vol. 2, Pg. 3-26.

[10] Heeschen, J., Nitschke, T., and Wohlfahrt, H., **New Results on the Formation of Residual Stresses Due to Phase Transformations in the Welded Structural Steels St 52-3 and StE 690**, *Residual Stresses in Science and Technology - Proceedings of the International Conference on Residual Stresses*, Garmisch-Partenkirchen (FRG), 1986, Vol. 2, Pg. 1005-1013.

[11] Clark, S.D., and Varney, W.R., *Physical Metallurgy for Engineers, 2nd ed.*, D. Van Nostrand Company, 1962.

[12] Inoue, T., and Tanaka, K., **An Elastic-Plastic Analysis of Quenching When Considering a Transformation**, *International Journal of Mechanical Science*, Vol. 17, 1975, Pg. 361-367.

[13] Rammerstorfer, F.G., Fischer, D.F., Mitter, W., Bathe, K.J., and Snyder, M.D., **On Thermo-Elastic-Plastic Analysis of Heat- Treatment Processes Including Creep and Phase Changes**, *Computers & Structures*, Vol. 13, 1981, Pg. 771-779.

[14] Leblond, J.B., Mottet, G., Devaux, J., and Devaux, J.C., **Mathematical Models for Description of Anisothermal Phase Transformations in Steels and Their Consequences on the Plastic Behavior**, *Proceedings of International Symposium on the Calculation of Internal Stresses in Heat Treatment of Metallic Materials*, Linköping, May 23-25 1984, Vol. 2, Pg. 191-220.

[15] Leblond, J.B., Mottet, G., and Devaux, J.C., **A Theoretical and Numerical Approach to the Plastic Behavior of Steels During Phase Transformations - I. Derivation of General Relations**, *Journal of Mechanics and Physics of Solids*, Vol. 34, No. 4, 1986, Pg. 395-409.

[16] Leblond, J.B., Mottet, G., and Devaux, J.C., **A Theoretical and Numerical Approach to the Plastic Behavior of Steels During Phase Transformations - II. Study of Classical Plasticity for Ideal-Plastic Phases**, *Journal of Mechanics and Physics of Solids*, Vol. 34, No. 4, 1986, Pg. 411-432.

[17] Denis, S., Sjöstrom, S., and Simon, A., **Coupled Temperature, Stress, Phase Transformation Calculation Model. Application to the Pre-**

diction of Phase Transformation During Cooling of An Eutectoid Carbon Steel, *Residual Stresses in Science and Technology - Proceedings of the International Conference on Residual Stresses*, Garmisch-Partenkirchen (FRG), 1986, Vol. 2, Pg. 595-602.

[18] Denis, S., and Simon, A., **Discussion on the Role of Transformation Plasticity in the Calculation OF Quenching Stresses in Steels,** *Residual Stresses in Science and Technology - Proceedings of the International Conference on Residual Stresses*, Garmisch-Partenkirchen (FRG), 1986, Vol. 2, Pg. 565-572.

[19] Denis, S., Sjöstrom, S., and Simon, A., **Coupled Temperature, Stress, Phase Transformation Calculation Model Numerical Illustration of The Internal Stresses Evolution During During Cooling of a Eutectoid Carbon Steel Cylinder,** *Metallurgical Transactions A*, Vol. 18A, July 1987, Pg. 1203-1212.

[20] Jones, W.K.C., and Alberry, P.J., **The Role of Phase Transformation in the Development of Residual Welding Stresses,** Central Electricity Generating Board Research Division, Marchwood Engineering Laboratories, February 1977.

[21] Jones, W.K.C., and Alberry, P.J., **A Model for Stress Accumulation in Steels During Welding,** *Proceedings of An International Conference on Residual Stresses in Welded Construction and Their Effects*, London, Nov. 15-17, 1977, The Welding Institute, Pg. 15-26.

[22] Masubuchi, K., **The Analysis of Thermal Stresses and Metal Movement During Welding,** *Proceedings of An International Conference on*

Control of Distortion and Residual Stresses in Weldments, Chicago, Nov. 16-17, 1976, Pg. 1-21.

[23] Masubuchi, K., **Thermal Stresses and Metal Movement During Welding Structural Materials, Especially High Strength Steels,** *Proceedings of An International Conference on Residual Stresses in Welded Construction and Their Effects*, London, Nov. 15-17, 1977, The Welding Institute, Pg. 1-13.

[24] Masubuchi, K., **Model of Stresses and Deformation Due to Welding - A Review,** *Modeling of Casting and Welding Processes*, 1981, Pg. 223-237.

[25] Satoh, K., Ueda, Y., and Kihara, H., **Recent Trend of Researches on Restraint Stresses and Strains for Weld Cracking,** *Transactions of Japanese Welding Research Institute*, Vol. 1, No. 1, 1972, Pg. 53-68.

[26] Friedman, E., **Thermomechanical Analysis of The Welding Process Using the Finite Element Method,** *Transaction of the ASME, Journal of Pressure Vessel Technology*, Aug. 1975, Pg. 206-213.

[27] Friedman, E., **Numerical Simulation of the Gas Tungsten-Arc Welding Process,** Westinghouse Electric Corporation Bettis Atomic Power Laboratory, West Mifflin, Pennsylvania.

[28] Muraki, T., Bryan, J.J., and Masubuchi, K., **Analysis of Thermal Stresses and Metal Movement During Welding - Part I Analytical Study,** *Transaction of the ASME, Journal of Engineering Materials and Technology*, Jan. 1975, Pg. 81-84.

[29] Muraki, T., Bryan, J.J., and Masubuchi, K., **Analysis of Thermal Stresses and Metal Movement During Welding - Part II Comparison of Experimental Data and Analytical Data**, *Transaction of the ASME, Journal of Engineering Materials and Technology*, Jan. 1975, Pg. 85-91.

[30] Rybicki, E.F., Schmueser, D.W., Stonesifer, R.W., Groom, J.J., and Mishler, H.W., **A Finite-Element Model for Residual Stresses and Deflections in Girth-Butt Welded Pipe**, *Transaction of the ASME, Journal of Pressure Vessel Technology*, Vol. 100, Aug. 1978, Pg. 256-262.

[31] Rybicki, E.F., and Stonesifer, R.B., **Computation of Residual Stresses Due to Multipass Welds in Piping Systems**, *Transaction of the ASME, Journal of Pressure Vessel Technology*, Vol. 101, May 1979, Pg. 149-154.

[32] Ueda, Y., and Yamakawa, T., **Thermal Stress Analysis of Metals with Temperature Dependent mechanical Properties**, *Proceedings of International Conference on Mechanical Behavior of Materials*, Vol. III, 1972, Pg. 10-20.

[33] Masubuchi, K., *Analysis of Welded Structures - Residual Stresses, Distortion, and Their Consequences*, Pergamon Press, 1980.

[34] Hibbitt, H.D., **A Numerical, Thermo-Mechanical Model for the Welding and Subsequent Loading of a Fabricated Structure**, *Ph.D. Thesis*, Brown University, June 1972.

[35] Hibbitt, H.D., and Marcal, P.V., **A Numerical, Thermo-Mechanical Model for the Welding and Subsequent Loading of a Fabricated**

Structure, *Computers & Structures*, Vol. 3, 1973, Pg. 1145-1174.

[36] Argyris, J.H., Szimmat, J., and Willam, K.J., **Computational Aspect of Welding Stress Analysis**, *Computer Methods In Applied Mechanics and Engineering*, Vol. 33, 1982, Pg. 635-666.

[37] Dubois, D., Devaux, J., and Leblond, J.B., **Numerical Simulation of a Welding Operation: Calculation of Residual Stresses and Hydrogen Diffusion**, *Proceedings of the 5th International Conference on Pressure Vessel Technology*, San Francisco, Sept. 9-14, 1984, Pg. 1210-1239.

[38] Andersson, B.A.B., **Thermal Stresses in a Submerged-Arc Welded Joint Considering Phase Transformation**, *Transaction of the ASME, Journal of Engineering Materials and Technology*, Vol. 100, Oct. 1978, Pg. 356-362.

[39] Andersson, B., and Karlsson, L., **Thermal Stresses in Large Butt-Welded Plates**, *Journal of Thermal Stresses*, Vol. 4, No. 3-4, 1981, Pg. 491-500.

[40] Ueda, Y., Fukuda, K., and Nakacho, N., **Basic Procedures In Analysis and Measurement of Welding Residual Stresses By the Finite Element Method**, *Proceedings of An International Conference on Residual Stresses in Welded Construction and Their Effects*, London, Nov. 15-17 1977, The Welding Institute, Pg. 27-37.

[41] Josefson, B.L., **Residual Stresses and Their Redistribution During Annealing of a Girth-Butt Welded Thin-Walled Pipe**, *Transaction of the ASME, Journal of Pressure Vessel Technology*, Vol. 104, 1982, Pg. 245-250.

[42] Josefson, B.L., **Effects of Transformation Plasticity of The Welding Residual Stress Field in Thin-Walled Pipes And Thin Plates,** *Proceedings of International Symposium on the Calculation of Internal Stresses in Heat Treatment of Metallic Materials*, Linköping, May 23-25 1984, Vol. 2, Pg. 487-497.

[43] Josefson, B.L., **Stress Redistribution During Annealing of A Multi-Pass Butt-Welded Pipe,** *Transaction of the ASME, Journal of Pressure Vessel Technology*, Vol. 105, May 1983, Pg. 165-170.

[44] Jonsson, M., Karlsson, L., and Lindgren, L.E., **Thermal Stresses and Plate Motion in Butt-Welding,** *Proceedings of the 3rd International Conference on Numerical Methods in Thermal Problems*, Swansea, U.K., Aug. 2-5 1983, Pineridge Press, Pg. 270-279.

[45] Wang, Z.G., and Inoue, T., **A Viscoplastic Constitutive Relationship with Phase Transformation and the Application to the Process of Welding,** *International Symposium on the Calculation of Internal Stresses in Heat Treatment of Metallic Materials*, Linköping, May 23-25 1984, Vol. 2, Pg. 474-486.

[46] Papazoglou, V.J., **Analytical Techniques for Determining Temperatures, Thermal Strains, and Residual Stresses During Welding,** *Ph.D. Thesis*, M.I.T., 1981.

[47] Papazoglou, V.J., and Masubuchi, K., **Numerical Analysis of Thermal Stresses During Welding Including Phase Transformation Effects,** *Transaction of the ASME, Journal of Pressure Vessel Technology*, Vol. 104, Aug. 1982, Pg. 198-203.

[48] Goldak, J., Chakravarti, A., and Bibby, M., **An Advanced Finite Element Model for Welding Heat Sources**, Department of Mechanical and Aeronautical Engineering, Carleton University, Ottawa, Canada, Jan. 1983.

[49] Mok, D.H.B., Pick, R.J., and Hoff, R., **A Study of the Effect of Phase Transformations on the Formation of Weld Residual Stress - Progress Report**, *WRI Project No. 1097701, EMR Contraction No. 2340-6-9168/01-ST*, University of Waterloo, Waterloo, Ontario, Oct. 1987.

[50] Bowker, J., *Private communication.*

[51] Pates, M.J., *Private communication.*

[52] CSA Standard W48.3-M1982.

[53] Rosenthal, D., **The Theory of Moving Sources of Heat and Its Application to Metal Treatments**, *Transactions of the ASME*, Nov. 1946, Pg. 849-866.

[54] Boulton, N.S., and Lance Martin, H.E., **Residual Stresses in Arc-Welded Plates**, *Proceedings of the Institute of Mechanical Engineers, London*, Vol. 133, 1936, Pg. 295-347.

[55] Tall, L., **Residual Stresses in Welded Plates - A Theoretical Study**, *Welding Research Supplement*, Jan. 1964, Pg. 10s-23s.

[56] Nagaraja Rao, N.R., Estuar, F.R., and Tall, L., **Residual Stresses in Welded Shapes**, *Welding Journal Research Supplement*, Vol. 43, 1964, Pg. 295s-306s.

[57] Odar, E., Nishino, F., and Tall, L., **Residual Stresses in Welded Built-Up "T-1" Shapes**, *Welding Research Council Bulletin No. 121*, 1967.

[58] McFalls, R.K., and Tall, L., **A Study of Welded Columns Manufactured from Flame-Cut Plates**, *Welding Journal Research Supplement*, Vol. 48, Apr. 1969, Pg. 141s-153s.

[59] Alpsten, G.A., and Tall, L., **Residual Stresses in Heavy Welded Shapes**, *Welding Journal Research Supplement*, Vol. 49, Mar. 1970, Pg. 93s-105s.

[60] Bjørhovde, R., Brozzetti, J., Alpsten, G.A., and Tall, L., **Residual Stresses in Thick Welded Plates**, *Welding Journal Research Supplement*, Vol. 51, 1972, Pg. 392s-405s.

[61] Kihara, H., Suzuki, H., and Tamura, H., *The Society of Naval Architects of Japan - 60th Anniversary Series, Vol. 1*, The Society of Naval Architects of Japan, 1957, Tokyo.

[62] Paley, Z., and Hibbert, P.D., **Computation of Temperatures in Actual Weld Designs**, *Welding Journal Research Supplement*, Nov. 1975, Pg. 385s-391s.

[63] Holden, T.M., Root, J.H., Holt, R.A., and Roy, G., **Neutron Diffraction Measurements of the Residual Strain State of a Tubular T-Joint**, *Proceedings of the 7th International conference on Offshore Mechanics and Arctic Engineering*, Houston, Texas, Feb. 7-12, 1988, Pg. 127-131.

[64] Holden, T.M., Root, J.H., Fidleris, V., Holt, R.A., and Roy, G., **Application of Neutron Diffraction to Engineering Problems**, Atomic En-

ergy of Canada Limited, Chalk River Nuclear Laboratories, Chalk River, Ontario.

[65] Roy, G., *Private communication.*

[66] Ueda, Y., Fukuda, K., Nakacho, K., Takahashi, E., and Sakamoto, K., **Transient and Residual Stresses from Multipass Weld in Very Thick Plates and Their Reduction from Stress Relief Annealing**, *Proceedings of the 3rd International Conference on Pressure Vessel Technology*, Tokyo, Japan, 1977, Vol. 2, Pg. 925-933.

[67] Ueda, Y., and Nakacho, K., **Simplifying Methods for Analysis of Transient Residual Stresses and Deformations Due to Multipass Welding**, *Transactions of the Japan Welding Research Institute*, Osaka University, Japan, Vol. 11, No. 1, 1982, Pg. 95-103.

[68] Gurney, T.R., *Fatigue of Welded Structures, 2nd ed.*, Cambridge University Press, 1979.

[69] Lawrence, F.V., Ho, N.J., and Mazumdar, P.N., **Predicting the Fatigue Resistance of Welds**, Ann. Review Material Science, 1981, Pg. 401-425.

[70] Allen, A.J., Hutchings, M.T., and Rainey, V., **Measurement of Through-Thickness Stress in Offshore Steels Using the Neutron Diffraction Technique**, *AERE R 12178*, Atomic Energy Research Establishment, Harwell Laboratory, U.K., May 1986.

[71] Goldak, J., McDill, M., Oddy, A., House, R., Chi, X., and Bibby, M., **Computational Heat Transfer for Weld Mechanics**, *Advances in Welding Science and Technology - Proceedings of an International Conference on*

Trends in Welding Research, Gatlinburg, Tennessee, U.S.A., May 12-18 1986, Pg. 15-20.

[72] Friedman, E., **On the Calculation of Temperature Due to Arc Welding**, Westinghouse Electric Corporation, Bettis Atomic Power Laboratory, West Mifflin, Pa. 15122.

[73] Christensen, N., Davis, V. De L., and Gjermundsen, K., **Distribution of Temperatures in Arc Welding**, *British Welding Journal*, Feb. 1965, Pg. 54-75.

[74] Incropera, F.P., and DeWitt, D.P., *Fundamentals of Heat Transfer*, John Wiley & Sons, New York, 1981.

[75] Touloukian, Y.S., and DeWitt, D.P., *Thermophysical Properties of Matter, Volume 7 - Thermal Radiative Properties, Metallic Elements and Alloys*, IFI/Plenum, New York, 1970.

[76] Pehlke, R.D., Jeyarajan, A., and Wada, H., **Summary of Thermal Properties for Casting Alloys and Mold Materials**, *NSF/MEA-82028*, Dec. 1982.

[77] DeGarmo, E.P., Meriam, J.L., and Jonassen, F., **The Effect of Weld Length Upon the Residual Stresses of Unrestrained Butt Welds**, *Welding Journal Research Supplements*, Vol. 25, Aug. 1946, Pg. 485s-487s.

[78] Touloukian, Y.S., Kirby, R.K., Taylor, R.E., and Desai, P.D., *Thermophysical Properties of Matter, Volume 12 - Thermal Expansion, Metallic Elements and Alloys*, IFI/Plenum, New York, 1970.

[79] Goldsmith, A., Waterman, T.E., Hirschhorn, H.J., and Armour Research Foundation, *Handbook of Thermophysical Properties of Solid Materials, Revised Edition, Volume II: Alloys*, The MacMillan Company, New York, 1961.

[80] Dieter, G.E., *Mechanical Metallurgy, 3rd ed.*, McGraw-Hill Book Company, New York, 1986.

[81] Hertzberg, R.W., *Deformation and Fracture Mechanics of Engineering Materials, 2nd ed.*, John Wiley & Sons, New York, 1983.

Appendix A

Test Problem For Volumetric Expansion Model

As mentioned in section 3.2, the most convenient method to implement the volumetric strain produced by allotropic phase transformation is to use the SWELLING option in the commercial finite element code ABAQUS [A.1]. However, SWELLING option was originally designed for material swelling under radiation, which is a time and temperature dependent phenomenon. This option requires the volumetric strain rate as an input. Therefore, the the phase transformation expansion has to be inputted as a peusdo-strain rate. This is accomplished in a user defined subroutine. In order to verify this approach, a test problem was solved and is described in the following section.

A.1 Test Problem

The objective of the test problem is to verify the implementation of transformation strain by using the SWELLING option in ABAQUS. The problem is chosen such that the transformation strain is isolated from the thermal strain. More importantly, an analytical solution does exist so that the finite element results can be compared.

The chosen problem is a solid sphere with heat generation near the bore for a short time duration. With this heating cycle, only the material near the bore would reach an abitrary chosen transformation temperature. Using the same assumption as in welding, no phase transformation was assumed for heating. In order to isolate the transformation strain from thermal strain, the linear thermal expansion coefficient was set equal to zero. No nonlinearities such as plasticity or temperature dependent properties were assumed so that an analytical solution could be obtained.

A.1.1 Analytical Solution

This problem is essentially the same as shrink fitting a hollow sphere onto a solid sphere. The analytical solution can be found in [A.2]. The radial and tangential stress distributions are as followed:

$$\sigma_r = \begin{cases} -P & \text{for } r \leq a \\ \frac{Pa^3}{(a^3+b^3)}\left(\frac{b^3}{r^3} - 1\right) & \text{for } a < r \leq b \end{cases}$$

and

$$\sigma_\theta = \begin{cases} -P & \text{for } r \leq a \\ \frac{-Pa^3}{(a^3+b^3)}\left(\frac{b^3}{2r^3} + 1\right) & \text{for } a < r \leq b \end{cases}$$

where

$$P = \frac{\epsilon_\theta E}{(1-2\nu) + \frac{a^3}{(a^3+b^3)}\left[\frac{b^3}{2a^3}(1+\nu) + (1-2\nu)\right]}$$

$$\epsilon_\theta = \text{volumetric strain } / \ 3$$

where a and b are the defined as in Figure A.1. The volumetric expansion near the bore is constrained by the rest of the sphere. Thus, compressive stress results in the material that undergoes the transformation. Outside this zone, the radial stress decreases gradually to zero. In the tangential direction, the expansion causes the sphere to go into tension. Therefore, a large stress reversal is observed at the interface between the two zones.

A.1.2 FEM Solution

Both the heat transfer analysis and stress analysis were solved with the same finite element mesh (Figure A.2). Due to symmetry, only a wedge of the sphere has to be modelled. The kinematic constraints are shown in Figure A.3. The 8-noded axisymmetric element was used. The material's thermal and mechanical properties are listed in Table A.1.

A.1.3 Comparisons Of Results

The radial stress and tangential stress distribution for both analytical and FEM solution are presented in Figure A.4 and A.5 respectively. The FEM solution agrees exactly with the analytical solution. This suggests that the SWELLING option [A.1] is a viable scheme for implementing the volumetric expansion due to phase transformations.

References

[A.1] Hibbitt, Karlsson, and Sorenson, *ABAQUS Users Manual*, Hibbitt, Karlsson and Sorenson Inc., Providence, Rhode Island.

[A.2] Timoshenko, S.P., and Goodier, J.N., *Theory Of Elasticity, 3rd ed.*, McGraw-Hill Book Company, 1970.

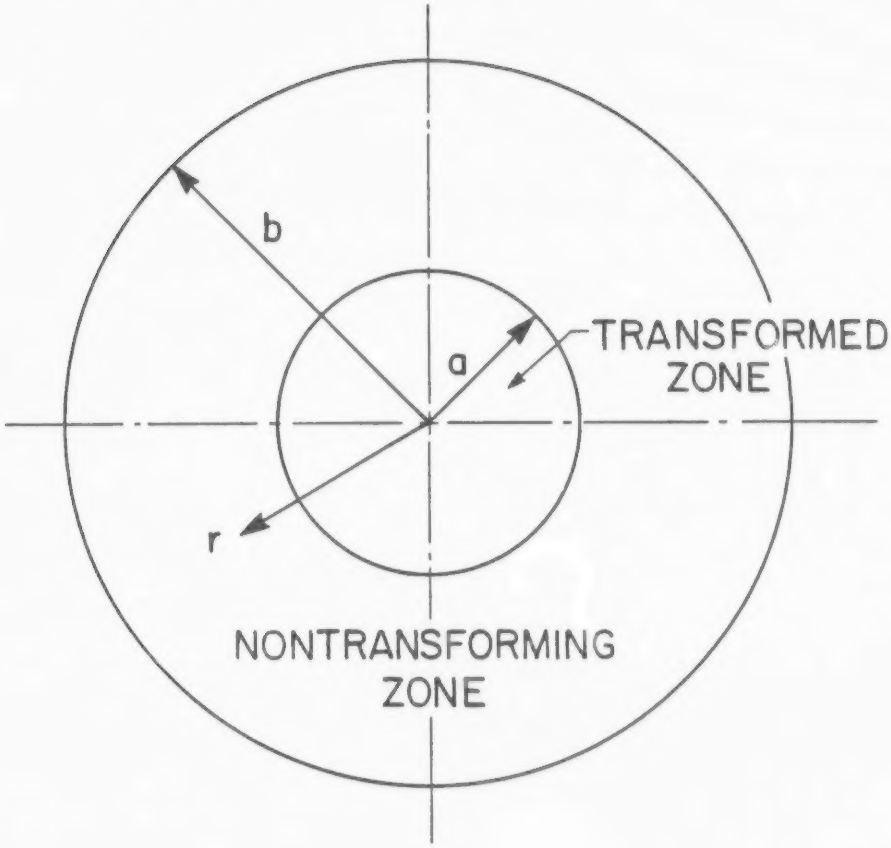
b
a
TRANSFORMED ZONE
r
NONTRANSFORMING ZONE

Figure A.1: Test problem configuration

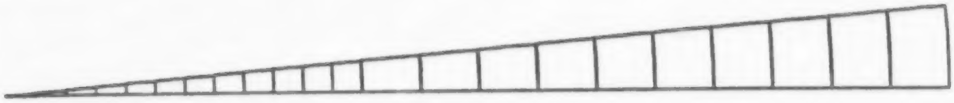

Figure A.2: Finite element mesh for test problem

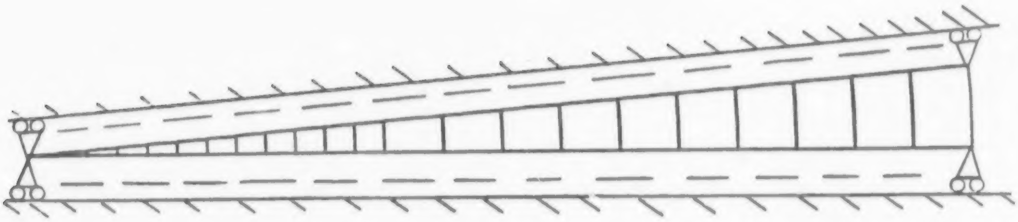

Figure A.3: Kinematic constraints for test problem

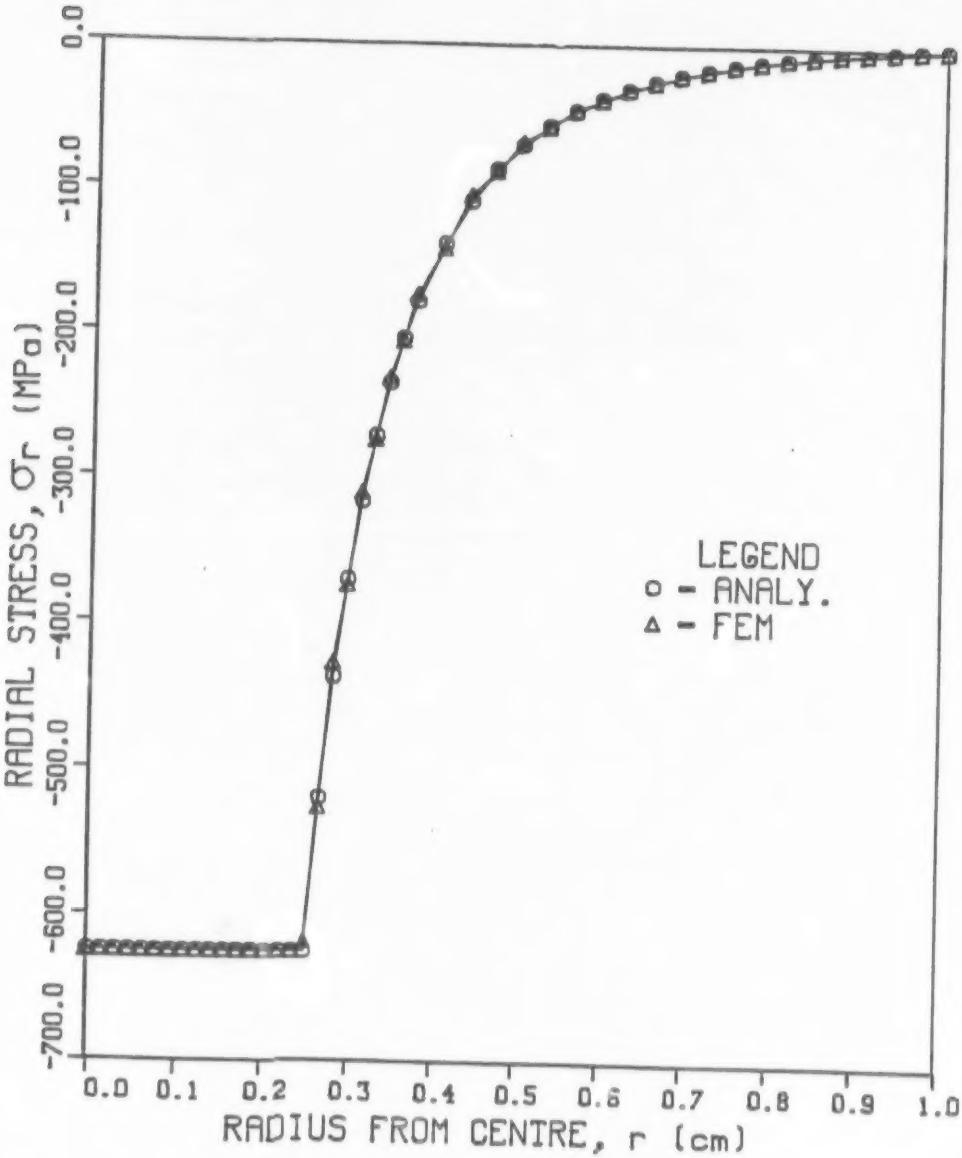

Figure A.4: Comparison between analytical and FEM solution (radial stress distribution)

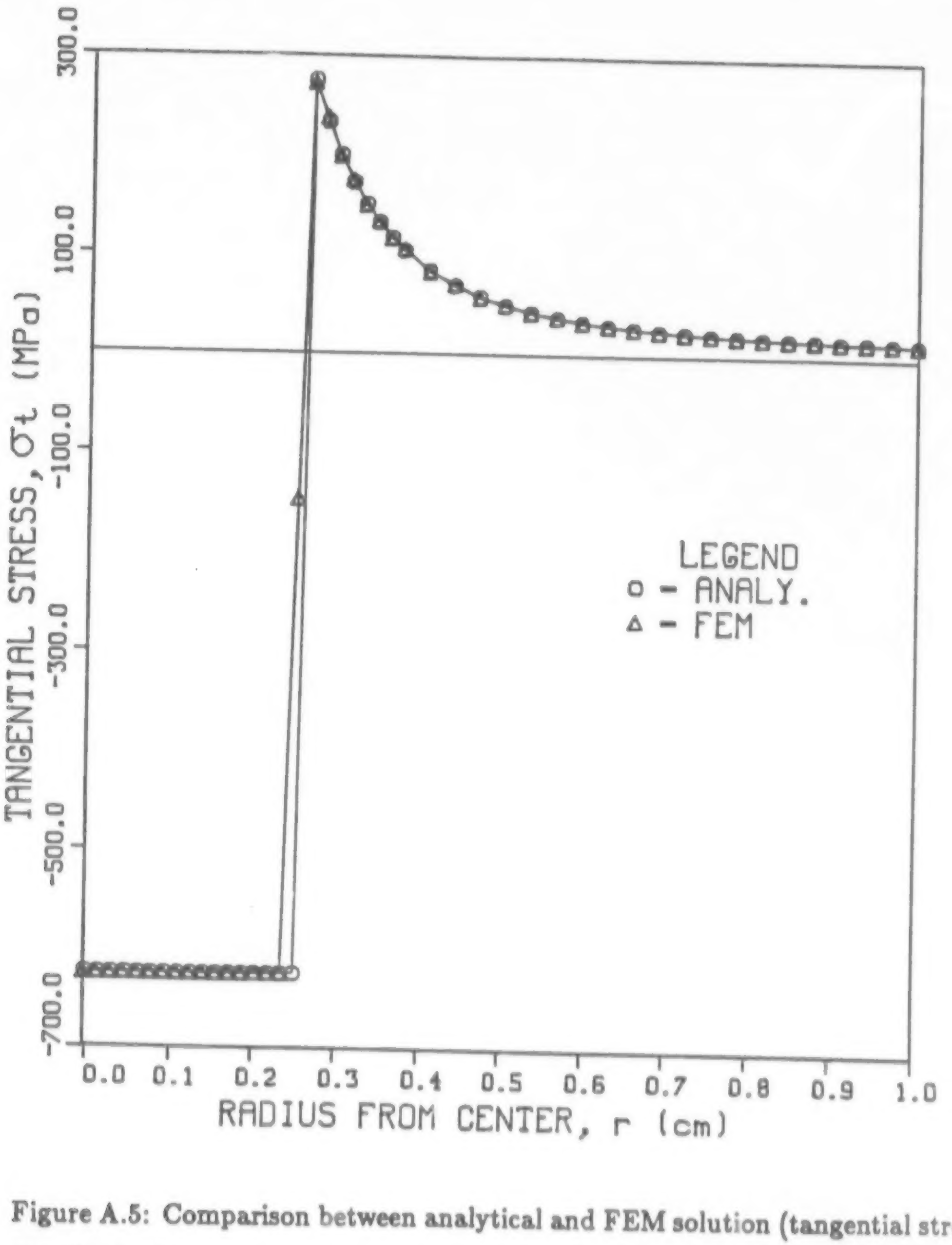

Figure A.5: Comparison between analytical and FEM solution (tangential stress distribution)

Appendix B

ABAQUS Input Data And Subroutines For Heat Transfer Analysis

B.1 ABAQUS Input Data

B.1.1 First Capping Pass

```
**********************************************************
**
**  FINITE ELEMENT MODEL OF THE T-JOINTED FATIGUE SPECIMEN
**  HEAT TRANSFER ANALYSIS FOR THE CAPPING PASSES
**
*HEADING
 HEAT TRANSFER MODEL FOR T-SPECIMEN
**
*************************
**                     **
**  NODAL DEFINITIONS  **
**                     **
*************************
**
*NODE,NSET=ALL
    4   6.50000   0.00000
   84 136.50000   0.00000
  120 195.00000   0.00000
 8120 195.00000  13.00000
 8140 195.00000  45.50000
12120 180.37500  27.62500
13633 185.25000  38.18750
14120 177.12500  30.87500
14128 181.76786  35.75000
14133 184.25915  38.36585
14134 185.25000  39.40625
16004   6.50000  26.00000
16084 136.50000  26.00000
16098 159.25000  26.00000
16099 160.87500  26.00000
16100 162.50000  26.00000
16102 164.93750  26.00000
16106 167.37500  26.00000
16116 170.62500  29.25000
16122 173.87500  32.50000
16128 177.12500  35.75000
16133 182.00000  40.62500
16138 182.00000  43.87500
16140 182.00000  45.50000
```

```
29113 183.62500  47.12500
29119 193.37500  47.12500
30112 182.00000  48.75000
30120 195.00000  48.75000
46112 182.00000  74.75000
46120 195.00000  74.75000
90112 182.00000 146.25000
90120 195.00000 146.25000
**
** NODES FOR THE RIGHT HALF OF TEE
**
  128 222.62500   0.00000
 2121 198.45313   3.25000
 4128 222.62500   6.50000
 6121 198.45313   9.75000
18120 195.00000  13.00000
18128 222.62500  13.00000
22128 222.62500  26.00000
26128 208.00000  40.62500
28120 195.00000  45.50000
28128 208.00000  45.50000
30128 208.00000  48.75000
32126 204.75000  52.00000
40122 198.25000  65.00000
90128 208.00000 146.25000
*NGEN,NSET=ALL
    4   84    4
   84  120    2
  120 8120 2000
 8120 8140    2
1600416084    4
1608416098    2
1610216106    1
1610616116    1
1611616122    1
1612216128    1
1612816133    1
1613316138    1
    416004 4000
   8416084 4000
 4004 4084    4
 8004 8084    4
1200412084    4
   8616086 2000
 2086 2120    2
 4086 4120    2
 6086 6120    2
 8086 8120    2
 810016100 1000
1008610100    2
```

```
1208612100    2
1408614100    2
 8098 8100    1
 809916099 1000
 810216102 1000
 810416104 1000
 810616106 1000
1310213104    1
1310413106    1
1310316103  500
1310416104  500
1310516105  500
1310616106  500
 812012120 1000
1212014120  500
 9106 9120    2
1010610120    2
1110611120    2
1210612120    2
1310613120    2
1360613620    1
1410614120    1
 813414134 1000
1313414134  500
1413416134  500
 813816138 1000
1313814138  500
 814016140 1000
1363413638    1
1413414138    1
1413516135  500
 813614136 1000
1413616136  500
1413716137  500
 9120 9134    2
1012010134    2
1112011134    2
1212012134    2
1312013134    2
1412014128    1
1412814133    1
1312814128  500
1313214132  500
1362013628    1
1362813633    1
1411616116  500
1412216122  500
1412816128  500
1413316133  500
1460614616    1
```

```
1461614622    1
1462214628    1
1462814633    1
1510615116    1
1511615122    1
1512215128    1
1512815133    1
1560615616    1
1561615622    1
1562215628    1
1562815633    1
3011246112 2000
4611290112 4000
3012046120 2000
4612090120 4000
2911329119    1
3011230120    2
4411244120    2
4611246120    4
9011290120    4
3011444114 2000
3011644116 2000
3011844118 2000
4611690116 4000
4612090120 4000
  120  128    2
 4120 4128    2
 2121 6121 2000
1812018128    2
1812018122    1
1812028120 1000
1812822128 2000
2012020128    2
2212022128    2
2212022122    1
1812122121 1000
2212826128 2000
2412024128    2
2612026128    2
2612026122    1
2212126121 1000
2612828128 1000
2712027128    2
2812028128    2
3012030128    2
9012090128    4
3012240122 2000
3012490124 4000
3012890128 4000
3012834128 2000
```

```
**
***************************
**                       **
**  ELEMENT DEFINITIONS  **
**                       **
***************************
**
*ELEMENT,TYPE=DC2D4,ELSET=TEE
   41    4    8 4008 4004
  841   84 2086 4086 4084
  842 4084 4086 6086 6084
  843 8084100861208612084
  84412084120861408616084
  861   84   88 2088 2086
  862 2086 2088 4088 4086
  863 4086 4088 6088 6086
  864 6086 6088 8088 8084
  881   88   90 2090 2088
  981   98  100 2100 2098
  985 8098 90991009910098
  98610098100991109912098
  98712098130991409914098
  98814098140991509916098
  991 8098 8100 9100 9099
  992 9099 91001010010099
  99310099101001110011099
  99411099111001210012098
 1005 8100 8102 9102 9100
 101013100131021410214100
 103013102131041360413603
 103113102136031410314102
 103214102141031460315102
 103315102156031610316102
 103613603136041410414103
 103714103141041460414603
 103814603146041510415102
 103915102151041560415603
 104015603156041610416103
 105013104131061360513604
 105113604136051410514104
 105214104141051460514604
 105613605131061410614105
 105714105141061460614605
 137214136141371463714636
 137314636146371513815136
 137415136151381563715636
 137515636156371613716136
 137714137141381513814637
 137815637151381613816137
 139013138131401414014138
```

```
2800115140291133011216140
2800214140291142911315140
2800313140291152911414140
2800412140301162911513140
2800511140291173011612140
2800610140291182911711140
28007 9140291192911810140
28008 81403012029119 9140
2900129114301143011229113
2900229115301163011429114
2900329118301183011629117
2900429119301203011829118
3000130114321143211230112
4200142114441144611242112
4200242116441164411442114
4200342118441184411642116
4200442120461204411842118
4400144116461164611244114
4400244118461204611644116
4600146116501165011246112
5800158116661166611258112
 1401  120  122 2121 2120
 1402 2120 2121 4121 4120
 1403 2121  122 4122 4121
 1404  122  124 4124 4122
 1411 4120 4121 6121 6120
 1412 6120 612118122 8120
 1413 4121 412218122 6121
 1414 4122 412418124 18122
 1421 81201812219121 8122
 1422 81221912120121 8124
 1423191211812220122 20121
 1424181221812420124 20122
 1431 81242012121121 8126
 1432 81262112122122 8128
 1433201212012222122 21121
 144122122 23121 8130 8128
 144223121 24121 8132 8130
 1443221222412224121 23121
 1444221242412424122 22122
 145124121 25121 8134 8132
 145225121 26122 8136 8134
 1453241222612225121 24121
 146126122 27122 8138 8136
 1464261242712427122 26122
 147127122 28122 8140 8138
28009281223012230120 8140
2801028124301243012228122
3000530122321223212030120
3000630124341243212230122
```

```
3000730126321263412430124
3000830128321283212630126
3200532122341243412032120
3200632128341283412432126
3400534124361223612034120
3600536122381223812036120
3600634124381243812236122
3600734128381283812434124
3800538122401224012038120
3800638124421244012238122
3800738128421284212438124
4000540122421244212040120
4200542124461244612042120
4600346124501245012046120
5800358124661246612058120
*ELGEN,ELSET=TEE
   41    4 4000    1   20    4   40
  861    2 8000    4
  862    2 8000    4
  863    2 8000    4
  864    2 8000    4
  881    8 2000    1    5    2   20
  981    4 2000    1   11    2   20
  991    2 4000    4
  992    2 4000    4
  993    2 4000    4
  994    2 4000    4
 1005    5 1000    1   20    2   20
 1010    3 1000    1
 1030    9    4   40
 1031    9    4   40
 1036    9    4   40
 1050    9    4   40
 1051    9    4   40
 1052    4  500    1   16    2   20
 1056    9    4   40
 1057    4  500    1   16    2   20
 1390    3 1000    1
30001    4    2    1    6 2000 2000
46001    2    4    1    3 4000 4000
58001    2    4    1    4 8000 8000
 1404    3    2    1
 1414    3    2    1
 1424    3    2    1    2 2000   10
 1444    3    2    1    2 2000   10
 1464    3    2    1    2 1000   10
28010    3    2    1
42005    2    4    1
46003    2    4    1    3 4000 4000
58003    2    4    1    4 8000 8000
```

```
**
*********************************
**                             **
**   ELEMENT SET DEFINITION    **
**                             **
*********************************
**
*ELSET,ELSET=PASS,GENERATE
 1172 1332    20
 1173 1333    20
 1174 1334    20
 1175 1335    20
 1177 1317    20
 1178 1318    20
 1179 1319    20
 1180 1320    20
**
*ELSET,ELSET=HEAT1,GENERATE
 1050 1060     1
 1070 1080     1
 1090 1100     1
 1110 1120     1
 1130 1140     1
 1150 1160     1
*ELSET,ELSET=HEAT1
 1170 1171 1176
**
*ELSET,ELSET=HEAT2,GENERATE
 1150 1160     1
 1170 1180     1
 1190 1200     1
 1210 1220     1
*ELSET,ELSET=HEAT2
 1230 1231 1236
**
*ELSET,ELSET=HEAT3,GENERATE
 1210 1220     1
 1230 1240     1
 1250 1260     1
 1270 1280     1
*ELSET,ELSET=HEAT3
 1290 1291 1296
**
*ELSET,ELSET=HEAT4,GENERATE
 1270 1280     1
 1290 1300     1
 1310 1320     1
 1330 1340     1
 1350 1360     1
**
```

```
*ELSET,ELSET=FACE1,GENERATE
   41  801   40
  861 1181   20
 1404 1406    1
 1446 1476   10
4600458004 4000
6600482004 8000
*ELSET,ELSET=FACE1
 1401230123000832006360073800742006
**
*ELSET,ELSET=FACE2
8200182002
8200382004
**
*ELSET,ELSET=FACE3,GENERATE
   44  804   40
  868  968   20
 1335 1375   20
2800142001 2000
4600158001 4000
6600182001 8000
*ELSET,ELSET=FACE3
  998 1012 1033 1040 1055 1060 1340 1360 1378 1392
**
*ELSET,ELSET=FACE4,GENERATE
   41   44    1
**
*ELSET,ELSET=PAF4,GENERATE
 1337 1340    1
**
*ELSET,ELSET=P1F3,GENERATE
 1171 1311   20
 1176 1616   20
**
*ELSET,ELSET=P2F3,GENERATE
 1075 1155   20
 1080 1160   20
 1231 1311   20
 1236 1316   20
**
*ELSET,ELSET=P3F3,GENERATE
 1075 1215   20
 1080 1220   20
*ELSET,ELSET=P3F3
 1291 1296 1311 1316
**
*ELSET,ELSET=P4F3,GENERATE
 1075 1275   20
 1080 1280   20
**
```

```
*ELSET,ELSET=WELD,GENERATE
  841  844     1
  861  868     1
  881  888     1
  901  908     1
  921  928     1
  941  948     1
  961  968     1
  981  988     1
  991  998     1
 1001 1012     1
 1021 1033     1
 1036 1200     1
 1205 1220     1
 1225 1240     1
 1245 1260     1
 1265 1280     1
 1285 1300     1
 1305 1320     1
 1325 1340     1
 1345 1360     1
 1365 1378     1
 1385 1392     1
2800128008     1
2900129004     1
3000130004     1
3200132004     1
 1401 1406     1
 1411 1416     1
 1421 1426     1
 1431 1436     1
 1441 1446     1
 1451 1456     1
 1464 1466     1
 1474 1476     1
2800928012     1
3000530008     1
*ELSET,ELSET=WELD
 1461 14713200532006
**
****************************
**                        **
**  MATERIAL PROPERTIES   **
**                        **
****************************
**
*MATERIAL,ELSET=TEE
**
*CONDUCTIVITY
**
```

```
** W/mm C
**
    0.0482       0.0
    0.0435     274.0
    0.0262     912.0
    0.0331    1504.0
    0.1655    1528.0
**
*DENSITY
**
** Kg/mm**3
**
  7.85D-06
**
*SPECIFIC HEAT
**
** J/Kg K
**
     460.0       0.0
     477.0     100.0
     510.0     200.0
     544.0     300.0
     594.0     400.0
     653.0     500.0
     745.0     600.0
     837.0     700.0
    1456.0     750.0
     820.0     800.0
     536.0     900.0
     602.0    1000.0
     619.0    1100.0
     636.0    1200.0
     644.0    1300.0
**
*LATENT HEAT
**
** J/Kg
**
  277000.0    1504.0    1528.0
**
**************************
**                      **
**  INITIAL CONDITIONS  **
**                      **
**************************
**
*INITIAL CONDITIONS,TYPE=TEMPERATURE
**
** PREHEAT TEMPERATURE (C)
**
```

```
  ALL      15.0
**
*RESTART,WRITE,FREQ=10
**
************************
**                    **
**  HEATING HISTORY   **
**                    **
************************
**
**  FIRST CAPPING PASS
**
*STEP,AMP=STEP
*HEAT TRANSFER,TEMPTOL=5.0,END=PERIOD,DELTMX=500.0
   0.00001   0.00001
*MODEL CHANGE,REMOVE
 PASS
**
*END STEP
**
*STEP,AMP=STEP,INC=150,CYC=10
*HEAT TRANSFER,TEMPTOL=5.0,END=PERIOD,DELTMX=500.0
      0.10     4.725
**
** HEAT INPUT
**
*DFLUX,OP=NEW
HEAT1 BFNU
**
** BOUNDARY CONDITIONS
**
*FILM
FACE1 F1NU
FACE2 F2NU
FACE3 F3NU
 P1F3 F3NU
FACE4 F4NU
 PAF4 F4NU
**
*RADIATE,ZERO=-273.16
FACE1   R1      20.0  3.12E-14
FACE2   R2      20.0  3.12E-14
FACE3   R3      20.0  3.12E-14
 P1F3   R3      20.0  3.12E-14
FACE4   R4      20.0  3.12E-14
 PAF4   R4      20.0  3.12E-14
**
** OUTPUT RESULTS
**
*NODE PRINT,NSET=ALL,FREQ=150
```

```
    2    1    1    1    1
**
*NODE FILE,NSET=ALL,FREQ=1
    2    1    1    1    1
*END STEP
**
*STEP,AMP=STEP,INC=50
*HEAT TRANSFER,TEMPTOL=2.0,END=PERIOD,DELTMX=200.0
      0.50   295.275
*DFLUX,OP=NEW
HEAT1   3F       0.0
*FILM,OP=MOD
*RADIATE,OP=MOD,ZERO=-273.16
**
** OUTPUT RESULTS
**
*NODE PRINT,NSET=ALL,FREQ=50
    2    1    1    1    1
**
*NODE FILE,NSET=ALL,FREQ=1
    2    1    1    1    1
*END STEP
```

B.1.2 Second Capping Pass

```
***********************************************************
**
**  RESTART FROM THE END OF THE FIRST CAPPING PASS
**
*RESTART,READ,STEP=3,INC=17,WRITE,FREQ=10
**
** SECOND CAPPING PASS
**
*STEP,AMP=STEP
*HEAT TRANSFER,TEMPTOL=5.00,END=PERIOD,DELTMX=500.0
0.0001,0.0001
*MODEL CHANGE,REMOVE
 1332 1333 1334 1335
*MODEL CHANGE,INCLUDE
 1172 1173 1174 1175 1177 1178 1179 1180
 1192 1193 1194 1195 1197 1198 1199 1200
 1212 1213 1214 1215 1217 1218 1219 1220
*NODE FILE
    2    1    1    1    1
*NODE PRINT
    2    1    1    1    1
*END STEP
**
*STEP,AMP=STEP,INC=150,CYC=10
*HEAT TRANSFER,TEMPTOL=5.0,END=PERIOD,DELTMX=500.0
      0.10     4.725
**
** HEAT INPUT
**
*DFLUX,OP=NEW
HEAT2 BFNU
**
** BOUNDARY CONDITIONS
**
*FILM,OP=NEW
FACE1 F1NU
FACE2 F2NU
FACE3 F3NU
 P2F3 F3NU
FACE4 F4NU
 PAF4 F4NU
**
```

```
*RADIATE,ZERO=-273.16
FACE1   R1       20.0  3.12E-14
FACE2   R2       20.0  3.12E-14
FACE3   R3       20.0  3.12E-14
 P2F3   R3       20.0  3.12E-14
FACE4   R4       20.0  3.12E-14
 PAF4   R4       20.0  3.12E-14
**
** OUTPUT RESULTS
**
*NODE PRINT,NSET=ALL,FREQ=150
    2    1    1    1    1
**
*NODE FILE,NSET=ALL,FREQ=1
    2    1    1    1    1
*END STEP
**
*STEP,AMP=STEP,INC=50
*HEAT TRANSFER,TEMPTOL=2.0,END=PERIOD,DELTMX=200.0
       0.50   295.275
*DFLUX,OP=NEW
HEAT2    BF        0.0
*FILM,OP=MOD
*RADIATE,OP=MOD,ZERO=-273.16
**
** OUTPUT RESULTS
**
*NODE PRINT,NSET=ALL,FREQ=50
    2    1    1    1    1
**
*NODE FILE,NSET=ALL,FREQ=1
    2    1    1    1    1
*END STEP
```

B.1.3 Third Capping Pass

```
***********************************************************
**
**  RESTART FROM THE END OF THE THIRD CAPPING PASS
**
*RESTART,READ,STEP=9,INC=17,WRITE,FREQ=10
**
** LAST CAPPING PASS
**
*STEP,AMP=STEP
*HEAT TRANSFER,TEMPTOL=5.00,END=PERIOD,DELTMX=500.0
0.0001,0.0001
*MODEL CHANGE,INCLUDE
 1292 1293 1294 1295 1297 1298 1299 1300
 1312 1313 1314 1315 1317 1318 1319 1320
 1332 1333 1334 1335
*NODE FILE
    2    1    1    1    1
*NODE PRINT
    2    1    1    1    1
*END STEP
**
*STEP,AMP=STEP,INC=150,CYC=10
*HEAT TRANSFER,TEMPTOL=5.0,END=PERIOD,DELTMX=500.0
      0.10      4.725
**
** HEAT INPUT
**
*DFLUX,OP=NEW
HEAT4 BFNU
**
** BOUNDARY CONDITIONS
**
*FILM,OP=NEW
FACE1 F1NU
FACE2 F2NU
FACE3 F3NU
 P4F3 F3NU
FACE4 F4NU
**
*RADIATE,ZERO=-273.16
FACE1   R1      20.0  3.12E-14
FACE2   R2      20.0  3.12E-14
FACE3   R3      20.0  3.12E-14
```

```
 P4F3   R3       20.0  3.12E-14
FACE4   R4       20.0  3.12E-14
**
** OUTPUT RESULTS
**
*NODE PRINT,NSET=ALL,FREQ=150
    2    1    1    1    1
**
*NODE FILE,NSET=ALL,FREQ=1
    2    1    1    1    1
*END STEP
**
*STEP,AMP=STEP,INC=50
*HEAT TRANSFER,TEMPTOL=2.0,END=PERIOD,DELTMX=200.0
      0.50   295.275
*DFLUX,OP=NEW
HEAT4   BF       0.0
*FILM,OP=MOD
*RADIATE,OP=MOD,ZERO=-273.16
**
** OUTPUT RESULTS
**
*NODE PRINT,NSET=ALL,FREQ=50
    2    1    1    1    1
**
*NODE FILE,NSET=ALL,FREQ=1
    2    1    1    1    1
*END STEP
**
** RETURN TO ROOM TEMPERATURE
**
*STEP,AMP=STEP,INC=50
*HEAT TRANSFER,TEMPTOL=1.0,END=PERIOD,DELTMX=10.0
       5.0    3000.0
**
*TEMPERATURE
  ALL      20.0
**
*FILM,OP=MOD
*RADIATE,OP=MOD,ZERO=-273.16
**
** OUTPUT RESULTS
**
*NODE PRINT,NSET=ALL,FREQ=50
    2    1    1    1    1
**
*NODE FILE,NSET=ALL,FREQ=1
    2    1    1    1    1
*END STEP
```

B.1.4 Last Capping Pass

```
***********************************************************************
**
**  RESTART FROM THE END OF THE THIRD CAPPING PASS
**
*RESTART,READ,STEP=9,INC=17,WRITE,FREQ=10
**
** LAST CAPPING PASS
**
*STEP,AMP=STEP
*HEAT TRANSFER,TEMPTOL=5.00,END=PERIOD,DELTMX=500.0
0.0001,0.0001
*MODEL CHANGE,INCLUDE
 1292 1293 1294 1295 1297 1298 1299 1300
 1312 1313 1314 1315 1317 1318 1319 1320
 1332 1333 1334 1335
*NODE FILE
    2    1    1    1    1
*NODE PRINT
    2    1    1    1    1
*END STEP
**
*STEP,AMP=STEP,INC=150,CYC=10
*HEAT TRANSFER,TEMPTOL=5.0,END=PERIOD,DELTMX=500.0
      0.10      4.725
**
** HEAT INPUT
**
*DFLUX,OP=NEW
HEAT4 BFNU
**
** BOUNDARY CONDITIONS
**
*FILM,OP=NEW
FACE1 F1NU
FACE2 F2NU
FACE3 F3NU
 P4F3 F3NU
FACE4 F4NU
**
*RADIATE,ZERO=-273.16
FACE1    R1       20.0  3.12E-14
FACE2    R2       20.0  3.12E-14
FACE3    R3       20.0  3.12E-14
```

```
 P4F3   R3       20.0  3.12E-14
FACE4   R4       20.0  3.12E-14
**
** OUTPUT RESULTS
**
*NODE PRINT,NSET=ALL,FREQ=150
    2    1    1    1    1
**
*NODE FILE,NSET=ALL,FREQ=1
    2    1    1    1    1
*END STEP
**
*STEP,AMP=STEP,INC=50
*HEAT TRANSFER,TEMPTOL=2.0,END=PERIOD,DELTMX=200.0
      0.50   295.275
*DFLUX,OP=NEW
HEAT4   BF         0.0
*FILM,OP=MOD
*RADIATE,OP=MOD,ZERO=-273.16
**
** OUTPUT RESULTS
**
*NODE PRINT,NSET=ALL,FREQ=50
    2    1    1    1    1
**
*NODE FILE,NSET=ALL,FREQ=1
    2    1    1    1    1
*END STEP
**
** RETURN TO ROOM TEMPERATURE
**
*STEP,AMP=STEP,INC=50
*HEAT TRANSFER,TEMPTOL=1.0,END=PERIOD,DELTMX=10.0
       5.0    3000.0
**
*TEMPERATURE
  ALL       20.0
**
*FILM,OP=MOD
*RADIATE,OP=MOD,ZERO=-273.16
**
** OUTPUT RESULTS
**
*NODE PRINT,NSET=ALL,FREQ=50
    2    1    1    1    1
**
*NODE FILE,NSET=ALL,FREQ=1
    2    1    1    1    1
*END STEP
```

B.2 User Defined Subroutines

```
CCCCCCCCCCCCCCCCCCCCCCCCCCCCCCCCCCCCCCCCCCCCCCCCCCCCCCCCCCC
C
C  SUBROUTINE TO CALCULATE POWER DENSITY DISTRIBUTION
C  USING GOLDAK'S MODEL - CAPPING PASSES IN T-JOINT
C  SPECIMEN
C
CCCCCCCCCCCCCCCCCCCCCCCCCCCCCCCCCCCCCCCCCCCCCCCCCCCCCCCCCCC

      SUBROUTINE DFLUX(FLUX,TEMP,KSTEP,KINC,TIME,NOEL,
     *                NPT,COORDS,JLTYP)
      IMPLICIT DOUBLE PRECISION (A-H,O-Z)
      DIMENSION COORDS(3)

C---- WELDING PARAMETERS

      AETA=0.65D0
      VOLT=20.0D0
      CURR=125.0D0
      VEL=127.0D0/60.0D0

C---- FRONT QUADRANT (ZETA.GE.0.0)

      FF=0.8
      A1=4.4
      B1=4.4
      C1=4.0

C---- REAR QUADRANT (ZETA.LT.0.0)

      FR=0.2
      A2=4.4
      B2=4.4
      C2=6.0

C---- ORIGIN OF HEAT SOURCE (LOCATION AND ORIENTATION)

      IF (TIME .LE. 300.0D0) GOTO 100
      IF (TIME .LE. 600.0D0) GOTO 200
      IF (TIME .LE. 900.0D0) GOTO 300
      IF (TIME .LE. 1200.0D0) GOTO 400

C---- FIRST CAPPING PASS
```

```
100    XC=171.00D0
       YC=28.8D0
       ANG=-25.0D0/180.0D0*3.141592654D0
       TI=TIME
       GOTO 600

C----  SECOND CAPPING PASS

200    XC=174.0D0
       YC=31.9D0
       ANG=-25.0D0/180.0D0*3.141592654D0
       TI=TIME-300.0D0
       GOTO 600

C----  THIRD CAPPING PASS

300    XC=177.5D0
       YC=35.2D0
       ANG=-25.0D0/180.0D0*3.141592654D0
       TI=TIME-600.0D0
       GOTO 600

C----  LAST CAPPING PASS

400    XC=180.50D0
       YC=38.250D0
       ANG=-55.0D0/180.0D0*3.141592654D0
       TI=TIME-900.0D0

C----  HEAT SOURCE MODEL COORDINATES (X,Y,ZETA)

600    XX=COORDS(1)-XC
       YY=COORDS(2)-YC

C----  ROTATION OF AXIS (CLOCKWISE POSITIVE)

       X=XX*COS(ANG)-YY*SIN(ANG)
       Y=XX*SIN(ANG)+YY*COS(ANG)
       ZETA=C1-VEL*TI

C----  CALCULATE POWER DENSITY

       Q=AETA*VOLT*CURR
       IF (ZETA .LT. 0.0D0) GOTO 700
       CALL HEAT(FF,A1,B1,C1,Q,X,Y,ZETA,FLUX)
       GOTO 800
700    CALL HEAT(FR,A2,B2,C2,Q,X,Y,ZETA,FLUX)
800    RETURN
       END
C
```

```
CCCCCCCCCCCCCCCCCCCCCCCCCCCCCCCCCCCCCCCCCCCCCCCCCCCCCCCCCC
C
C  SUBROUTINE TO CALCULATE POWER DENSITY
C
C  (THIS SUBROUTINE IS CALLED BY DFLUX)
C
CCCCCCCCCCCCCCCCCCCCCCCCCCCCCCCCCCCCCCCCCCCCCCCCCCCCCCCCCC
C
      SUBROUTINE HEAT(F,A,B,C,Q,X,Y,ZETA,FLUX)
      IMPLICIT DOUBLE PRECISION (A-H,O-Z)
C
      PIE=3.141592654D0
      PP=-3.0D0*((X/A)**2+(Y/B)**2+(ZETA/C)**2)
      FLUX=12.0D0*DSQRT(3.0D0)*F*Q*DEXP(PP)/
     1     (A*B*C*PIE*DSQRT(PIE))
      IF (PP .LT. -3.0D0) FLUX=0.0D0
      RETURN
      END
C
CCCCCCCCCCCCCCCCCCCCCCCCCCCCCCCCCCCCCCCCCCCCCCCCCCCCCCCCCC
C
C  SUBROUTINE TO CALCULATE CONVECTIVE FILM COEFFICIENTS
C
C  (THIS SUBROUTINE IS CALLED BY ABAQUS DIRECTLY)
C
CCCCCCCCCCCCCCCCCCCCCCCCCCCCCCCCCCCCCCCCCCCCCCCCCCCCCCCCCC
C
      SUBROUTINE FILM(H,SINK,TEMP,KSTEP,KINC,TIME,NOEL,
     1                NPT,COORDS,JLTYP)
      IMPLICIT DOUBLE PRECISION (A-H,O-Z)
      DIMENSION COORDS(3)
      SINK=20.0D0

C---- FILM COEFFICIENT

      H=(0.006*TEMP+4.9)/1.0D+06
      IF (TEMP .GT. 400.0D0) H=7.3D-06
      IF (TEMP .LT. 100.0D0) H=5.5D-06
C
      RETURN
      END
```

Appendix C

ABAQUS Input Data For Residual Stress Calculation

C.1 First Capping Pass

```
***********************************************************
**
**  FINITE ELEMENT MODEL OF THE T-JOINTED FATIGUE SPECIMEN
**  THERMAL STRESS ANALYSIS FOR THE CAPPING PASSES WITHOUT
**  RESIDUAL STRESSES FROM PREVIOUS PASSES
**
*HEADING
 THERMAL STRESS MODEL FOR T-SPECIMEN
**
*************************
**                     **
**  NODAL DEFINITIONS  **
**                     **
*************************
**
*NODE,NSET=ALL
    4   6.50000   0.00000
   84 136.50000   0.00000
  120 195.00000   0.00000
 8120 195.00000  13.00000
 8140 195.00000  45.50000
12120 180.37500  27.62500
13633 185.25000  38.18750
14120 177.12500  30.87500
14128 181.76786  35.75000
14133 184.25915  38.36585
14134 185.25000  39.40625
16004   6.50000  26.00000
16084 136.50000  26.00000
16098 159.25000  26.00000
16099 160.87500  26.00000
16100 162.50000  26.00000
16102 164.93750  26.00000
16106 167.37500  26.00000
16116 170.62500  29.25000
16122 173.87500  32.50000
16128 177.12500  35.75000
16133 182.00000  40.62500
16138 182.00000  43.87500
16140 182.00000  45.50000
29113 183.62500  47.12500
29119 193.37500  47.12500
30112 182.00000  48.75000
```

```
30120 195.00000  48.75000
46112 182.00000  74.75000
46120 195.00000  74.75000
90112 182.00000 146.25000
90120 195.00000 146.25000
*NGEN,NSET=ALL
    4   84    4
   84  120    2
  120 8120 2000
 8120 8140    2
1600416084    4
1608416098    2
1610216106    1
1610616116    1
1611616122    1
1612216128    1
1612816133    1
1613316138    1
    416004 4000
   8416084 4000
 4004 4084    4
 8004 8084    4
1200412084    4
   8616086 2000
 2086 2120    2
 4086 4120    2
 6086 6120    2
 8086 8120    2
 810016100 1000
1008610100    2
1208612100    2
1408614100    2
 8098 8100    1
 809916099 1000
 810216102 1000
 810416104 1000
 810616106 1000
1310213104    1
1310413106    1
1310316103  500
1310416104  500
1310516105  500
1310616106  500
 812012120 1000
1212014120  500
 9106 9120    2
1010610120    2
1110611120    2
1210612120    2
1310613120    2
```

```
1360613620    1
1410614120    1
 813414134 1000
1313414134  500
1413416134  500
 813816138 1000
1313814138  500
 814016140 1000
1363413638    1
1413414138    1
1413516135  500
 813614136 1000
1413616136  500
1413716137  500
 9120 9134    2
1012010134    2
1112011134    2
1212012134    2
1312013134    2
1412014128    1
1412814133    1
1312814128  500
1313214132  500
1362013628    1
1362813633    1
1411616116  500
1412216122  500
1412816128  500
1413316133  500
1460614616    1
1461614622    1
1462214628    1
1462814633    1
1510615116    1
1511615122    1
1512215128    1
1512815133    1
1560615616    1
1561615622    1
1562215628    1
1562815633    1
3011246112 2000
4611290112 4000
3012046120 2000
4612090120 4000
2911329119    1
3011230120    2
4411244120    2
4611246120    4
9011290120    4
```

```
3011444114 2000
3011644116 2000
3011844118 2000
4611690116 4000
4612090120 4000
**
** NODE DEFINITION FOR GENERALIZE PLANE STRAIN ELEMENT
**
*NODE,NSET=CGPE
     1 195.00000    0.00000
     2 195.00000    0.00000
**
******************************
**                          **
**  NODE SET DEFINITIONS    **
**                          **
******************************
**
*NSET,NSET=NSP1,GENERATE
     4    88     4
    90   120     2
  2086  2120     2
  4004  4084     4
  4086  4120     2
  6086  6120     2
  8004  8088     4
  8090  8140     2
  909911099 1000
  9100  9140     2
1008610140     2
1110011140     2
1200412084     4
1208612140     2
1309915099 1000
1310013140     2
1360313605     1
1360713609     1
1361113613     1
1361913621     1
1362313625     1
1362713629     1
1363113633     1
1363513637     1
1408614100     2
1410214116     1
1413314138     1
1414016140 2000
1460314616     1
1463314637     1
1510015116     1
```

```
1513315135     1
1513615140     2
1560315616     1
1563315637     1
1600416088     4
1609016102     2
1610316116     1
1613316138     1
2911329115     1
2911729119     1
3011230120     2
3211232120     2
3411234120     2
3611236120     2
3811238120     2
4011240120     2
4211242120     2
4411444118     2
4611246120     4
5011250120     4
5411254120     4
5811258120     4
6611266120     4
7411274120     4
8211282120     4
9011290120     4
*NSET,NSET=NSP2,GENERATE
1411614122     1
1461614622     1
1511615122     1
1561615622     1
1611616122     1
**
*NSET,NSET=NSP3,GENERATE
1412214128     1
1462214628     1
1512215128     1
1562215628     1
1612216128     1
**
*NSET,NSET=NSP4,GENERATE
1412814133     1
1462814633     1
1512815133     1
1562815633     1
1612816133     1
**
*NSET,NSET=CENTL,GENERATE
  120 8120 2000
 8120 8140    2
```

```
3012042120 2000
4612058120 4000
6612090120 8000
**
*****************************
**                         **
**   ELEMENT DEFINITIONS   **
**                         **
*****************************
**
*ELEMENT,TYPE=CGPE6H,ELSET=TEE
    41    4    8 4008 4004    1    2
   841   84 2086 4086 4084    1    2
   842 4084 4086 6086 8084    1    2
   843 808410086120861208 4    1    2
   844120841208614086160 84    1    2
   861   84   88 2088 2086    1    2
   862 2086 2088 4088 4086    1    2
   863 4086 4038 6088 6086    1    2
   864 6086 6088 8088 8084    1    2
   881   88   90 2090 2088    1    2
   981   98  100 2100 2098    1    2
   985 8098 90991009910098    1    2
   98610098100991109912098    1    2
   98712098130991409914098    1    2
   98814098140991509916098    1    2
   991 8098 8100 9100 9099    1    2
   992 9099 91001010010099    1    2
   99310099101001110011099    1    2
   99411099111001210012098    1    2
  1005 8100 8102 9102 9100    1    2
  101013100131021410214100    1    2
  103013102131041360413603    1    2
  103113102136031410314102    1    2
  103214102141031460315102    1    2
  103315102156031610316102    1    2
  103613603136041410414103    1    2
  103714103141041460414603    1    2
  103814603146041510415102    1    2
  103915102151041560415603    1    2
  104015603156041610416103    1    2
  105013104131061360513604    1    2
  105113604136051410514104    1    2
  105214104141051460514604    1    2
  105613605131061410614105    1    2
  105714105141061460614605    1    2
  137214136141371463714636    1    2
  137314636146371513815136    1    2
  137415136151381563715636    1    2
  137515636156371613716136    1    2
```

```
     13771413714138151381463    1    2
     13781563715138161381613    1    2
     13901313813140141401413    1    2
    280011514029113301121614    1    2
    280021414029114291131514    1    2
    280031314029115291141414    1    2
    280041214030116291151314    1    2
    280051114029117301161214    1    2
    280061014029118291171114    1    2
    28007 91402911929118101 4    1    2
    28008 8140301202911 9140    1    2
    290012911430114301122911    1    2
    290022911530116301142911    1    2
    290032911830118301162911    1    2
    290042911930120301182911    1    2
    300013011432114321123011    1    2
    420014211444114461124211    1    2
    420024211644116441144211    1    2
    420034211844118441164211    1    2
    420044212046120441184211    1    2
    440014411646116461124411    1    2
    440024411846120461164411    1    2
    460014611650116501124611    1    2
    580015811666116661125811    1    2
*ELGEN,ELSET=TEE
   41    4 4000    1   20    4   40
  861    2 8000    4
  862    2 8000    4
  863    2 8000    4
  864    2 8000    4
  881    8 2000    1    5    2   20
  981    4 2000    1   11    2   20
  991    2 4000    4
  992    2 4000    4
  993    2 4000    4
  994    2 4000    4
 1005    5 1000    1   20    2   20
 1010    3 1000    1
 1030    9    4   40
 1031    9    4   40
 1036    9    4   40
 1050    9    4   40
 1051    9    4   40
 1052    4  500    1   16    2   20
 1056    9    4   40
 1057    4  500    1   16    2   20
 1390    3 1000    1
30001    4    2    1    6 2000 2000
46001    2    4    1    3 4000 4000
58001    2    4    1    4 8000 8000
```

```
**
******************************
**                          **
**  ELEMENT SET DEFINITION  **
**                          **
******************************
**
*ELSET,ELSET=PASS,GENERATE
 1172 1332   20
 1173 1333   20
 1174 1334   20
 1175 1335   20
 1177 1317   20
 1178 1318   20
 1179 1319   20
 1180 1320   20
**
*ELSET,ELSET=WELD,GENERATE
  841  844    1
  861  868    1
  881  888    1
  901  908    1
  921  928    1
  941  948    1
  961  968    1
  981  988    1
  991  998    1
 1001 1012    1
 1021 1033    1
 1036 1200    1
 1205 1220    1
 1225 1240    1
 1245 1260    1
 1265 1280    1
 1285 1300    1
 1305 1320    1
 1325 1340    1
 1345 1360    1
 1365 1378    1
 1385 1392    1
2800128008    1
2900129004    1
3000130004    1
3200132004    1
*ELSET,ELSET=WELD
 1461 14713200532006
**
*************************
**                     **
**  ELEMENT THICKNESS  **
**                        **
***************************
**
*ATTRIBUTE
**
      1.0
**
*****************************
**                         **
**  MATERIAL PROPERTIES    **
**                         **
*****************************
**
*MATERIAL,ELSET=TEE
**
** TEMPERATURE DEPENDENT ELASTIC MATERIAL PROPERTIES
** YOUNG'S MODULUS (N/mm**2), POISSON'S RATIO
**
*ELASTIC
**
  2.10E+02    0.2875       0.0
  2.10E+05    0.2875      10.0
  2.10E+05    0.2875      15.0
  1.65E+05    0.3000     400.0
  1.75E+04    0.3000    1000.0
  1.00E+04    0.3000    1600.0
**
** TEMPERATURE DEPENDENT PLASTIC MATERIAL PROPERTIES
** YIELD STRESS (N/mm**2) AND CORRESPONDING PLASTIC STRAIN
**
*PLASTIC,HARD=KIN
**
      0.01       0.00       0.0
      0.01       0.10       0.0
    346.25       0.00      10.0
    567.47       0.10      10.0
    346.25       0.00      15.0
    567.47       0.10      15.0
    250.00       0.00     400.0
    435.39       0.10     400.0
     43.75       0.00     700.0
     43.75       0.10     700.0
     12.50       0.00    1000.0
     12.50       0.10    1000.0
      1.00       0.00    1600.0
      1.00       0.10    1600.0
**
** TEMPERATURE DEPENDENT THERMAL EXPANSION COEFFICIENT
** (1/C)
**
```

```
*EXPANSION,ZERO=20.0
**
      0.00        0.0
      0.00       14.9
  10.9E-06       15.0
  12.8E-06      127.0
  14.2E-06      227.0
  15.2E-06      327.0
  15.9E-06      427.0
  16.2E-06      527.0
  16.2E-06      627.0
  16.3E-06      727.0
  20.8E-06     1000.0
  23.3E-06     1500.0
  23.3E-06     1600.0
**
***************************
**                       **
**  INITIAL CONDITIONS   **
**                       **
***************************
**
*INITIAL CONDITIONS,TYPE=TEMPERATURE
**
** PREHEAT TEMPERATURE (C)
**
  ALL      15.0
**
****************************
**                        **
**  BOUNDARY CONDITIONS   **
**                        **
****************************
**
*BOUNDARY
CENTL    1    1       0.0
  120    2    2       0.0
**
*RESTART,WRITE,FREQ=10
**
**********************************************************
**                                                      **
**  REMOVING THE ELEMENTS FOR THE CAPPING PASSES        **
**                                                      **
**********************************************************
**
*STEP,AMP=RAMP,INC=1,CYC=10
*STATIC,PTOL=1.0
   0.00001   0.00001
*MODEL CHANGE,REMOVE
```

```
 PASS
**
*EL PRINT
    1    1    1    1    1
    1    1    1    1    1
    1    1    1    1    1    1    1    1
*NODE PRINT
    1    1    1    1    1    1    1    1
*END STEP
**
*************************************************
**                                             **
**  THERMAL LAODING OF THE FIRST CAPPING PASS  **
**                                             **
*************************************************
**
*STEP,AMP=RAMP,INC=150,CYC=10
*STATIC,PTOL=200.0
    0.1000  300.0000   0.00001
**
**  READ IN THE TEMPERATURE HISTORY
**
*TEMPERATURE,FILE=18,BSTEP=2(INC=1),ESTEP=3(INC=17)
  NSP1
*EL PRINT,FREQ=100
    1    1    1    1    1
    1    1    1    1    1
    1    1    1    1    1    1    1    1
*NODE PRINT,FREQ=100
    1    1    1    1    1    1    1    1
*END STEP
```

C.2 Second And Third Capping Pass

```
***********************************************************
**
** RESTART FROM THE END OF THE FIRST CAPPING PASS
**
*RESTART,READ,ENDSTEP,STEP=2,INC=62,WRITE,FREQ=10
**
************************************
**                                **
**  APPLYING THE CAPPING PASSES  **
**                                **
************************************
**
**  THE SECOND AND THIRD CAPPING PASS
**
*STEP,AMP=RAMP,INC=20,CYC=10
*STATIC,PTOL=10.0
   1.0E-06   1.0E-05   1.0E-07
*MODEL CHANGE,INCLUDE
 1172 1173 1174 1175 1177 1178 1179 1180
 1192 1193 1194 1195 1197 1198 1199 1200
 1212 1213 1214 1215 1217 1218 1219 1220
 1232 1233 1234 1235 1237 1238 1239 1240
 1252 1253 1254 1255 1257 1258 1259 1260
 1272 1273 1274 1275 1277 1278 1279 1280
**
*BOUNDARY,OP=MOD
1,1,1,1.1500E-04
2,1,1,-1.7000E-07
2,2,2,-2.5394E-07
14116,1,1,-5.0075E-02
14116,2,2,-5.1253E-03
14117,1,1,-3.2438E-02
14117,2,2,-2.0360E-02
14118,1,1,-2.4266E-02
14118,2,2,-1.7127E-02
14119,1,1,-2.0538E-02
14119,2,2,-1.0489E-02
14120,1,1,-1.7916E-02
14120,2,2,-3.2417E-03
14121,1,1,-1.6361E-02
14121,2,2,2.0599E-03
14122,1,1,-1.5576E-02
14122,2,2,4.9414E-03
14123,1,1,-1.3505E-02
```

```
14123,2,2,7.0616E-03
14124,1,1,-1.2477E-02
14124,2,2,8.1972E-03
14125,1,1,-1.1289E-02
14125,2,2,8.5871E-03
14126,1,1,-1.0463E-02
14126,2,2,9.0658E-03
14127,1,1,-9.5258E-03
14127,2,2,9.8690E-03
14128,1,1,-8.7825E-03
14128,2,2,1.0608E-02
14616,1,1,-4.9016E-02
14616,2,2,9.0504E-02
15116,1,1,-4.8558E-02
15116,2,2,0.1493
15616,1,1,-3.9548E-02
15616,2,2,0.2180
16116,1,1,-5.5178E-02
16116,2,2,0.2407
*TEMPERATURE,OP=MOD
 NSP2       1.00
 NSP3       1.00
*EL PRINT
    1    1    1    1    1
    1    1    1    1    1
    1    1    1    1    1    1    1    1
*NODE PRINT
    1    1    1    1    1    1    1    1
*END STEP
**
*STEP,AMP=RAMP,INC=10,CYC=10
*STATIC,PTOL=5.0
   0.5E-05   1.0E-05   0.1E-05
**
*BOUNDARY,OP=NEW
CENTL     1    1        0.0
  120     2    2        0.0
**
*EL PRINT
    1    1    1    1    1
    1    1    1    1    1
    1    1    1    1    1    1    1    1
*NODE PRINT
    1    1    1    1    1    1    1    1
*END STEP
**
*STEP,AMP=RAMP,INC=10,CYC=10
*STATIC,PTOL=5.0
   0.00001   0.00001
**
*TEMPERATURE,FILE=18,BSTEP=4(INC=1),ESTEP=4(INC=1)
```

```
 NSP1
 NSP2
 NSP3
**
*EL PRINT,FREQ=10
    1    1    1    1    1
    1    1    1    1    1
    1    1    1    1    1    1    1    1
*NODE PRINT,FREQ=10
    1    1    1    1    1    1    1    1
*END STEP
**
*STEP,AMP=RAMP,INC=150,CYC=10
*STATIC,PTOL=200.0
    0.1000  300.0000   0.00001
**
**  READ IN THE TEMPERATURE HISTORY
**
*TEMPERATURE,FILE=18,BSTEP=5(INC=1),ESTEP=6(INC=17)
 NSP1
 NSP2
 NSP3
*EL PRINT,FREQ=150
    1    1    1    1    1
    1    1    1    1    1
    1    1    1    1    1    1    1    1
*NODE PRINT,FREQ=150
    1    1    1    1    1    1    1    1
*END STEP
```

C.3 Last Capping Pass

```
**********************************************************
**
** RESTART FROM THE END OF THE THIRD CAPPING PASS
**
*RESTART,READ,ENDSTEP,STEP=6,INC=72,WRITE,FREQ=10
**
***********************************
**                               **
**  APPLYING THE CAPPING PASSES  **
**                               **
***********************************
**
**  THE LAST CAPPING PASS
**
*STEP,AMP=RAMP,INC=20,CYC=10
*STATIC,PTOL=10.0
  1.25E-06   1.0E-05   1.0E-07
*MODEL CHANGE,INCLUDE
 1292 1293 1294 1295 1297 1298 1299 1300
 1312 1313 1314 1315 1317 1318 1319 1320
 1332 1333 1334 1335
**
*BOUNDARY,OP=MOD
1,1,1,3.9080E-04
2,1,1,3.8182E-07
2,2,2,-9.0544E-07
14128,1,1,-4.9147E-02
14128,2,2,-1.6558E-02
14129,1,1,-3.3334E-02
14129,2,2,-1.4744E-02
14130,1,1,-2.9018E-02
14130,2,2,-8.3818E-03
14131,1,1,-2.4670E-02
14131,2,2,-1.6322E-03
14132,1,1,-1.8923E-02
14132,2,2,7.4410E-03
14133,1,1,-1.7032E-02
14133,2,2,1.6799E-02
14628,1,1,-8.2103E-02
14628,2,2,1.4599E-02
14633,1,1,-1.5087E-02
14633,2,2,2.1596E-02
15128,1,1,-7.9148E-02
15128,2,2,6.8615E-02
```

```
15133,1,1,-1.4882E-02
15133,2,2,2.2979E-02
15628,1,1,-6.6611E-02
15628,2,2,0.1453
15633,1,1,-1.4625E-02
15633,2,2,2.4422E-02
16128,1,1,-8.2989E-02
16128,2,2,0.1664
16133,1,1,-1.4664E-02
16133,2,2,2.5382E-02
*TEMPERATURE,OP=MOD
 NSP4       1.00
*EL PRINT,FREQ=20
    1    1    1    1    1
    1    1    1    1    1
    1    1    1    1    1    1    1    1
*NODE PRINT,FREQ=20
    1    1    1    1    1    1    1    1
*END STEP
**
*STEP,AMP=RAMP,INC=10,CYC=10
*STATIC,PTOL=5.0
   0.5E-05   1.0E-05   0.1E-05
**
*BOUNDARY,OP=NEW
CENTL     1    1         0.0
  120     2    2         0.0
**
*EL PRINT,FREQ=10
    1    1    1    1    1
    1    1    1    1    1
    1    1    1    1    1    1    1    1
*NODE PRINT,FREQ=10
    1    1    1    1    1    1    1    1
*END STEP
**
*STEP,AMP=RAMP,INC=10,CYC=10
*STATIC,PTOL=5.0
   0.00001   0.00001
**
*TEMPERATURE,FILE=18,BSTEP=10(INC=1),ESTEP=10(INC=1)
  ALL
**
*EL PRINT,FREQ=10
    1    1    1    1    1
    1    1    1    1    1
    1    1    1    1    1    1    1    1
*NODE PRINT,FREQ=10
    1    1    1    1    1    1    1    1
*END STEP
**
```

```
*STEP,AMP=RAMP,INC=150,CYC=10
*STATIC,PTOL=200.0
    0.1000 3300.0000   0.00001
**
**  READ IN THE TEMPERATURE HISTORY
**
*TEMPERATURE,FILE=18,BSTEP=11(INC=1),ESTEP=13(INC=13)
  ALL
*EL PRINT,FREQ=150
    1    1    1    1    1
    1    1    1    1    1
    1    1    1    1    1    1    1    1
*NODE PRINT,FREQ=150
    1    1    1    1    1    1    1    1
*END STEP
**
*STEP,AMP=RAMP,INC=10,CYC=10
*STATIC,PTOL=200.0
     800.0    1800.0
**
**  RETURN TO ROOM TEMPERATURE
**
*TEMPERATURE
  ALL      15.0
*EL PRINT,FREQ=10
    1    1    1    1    1
    1    1    1    1    1
    1    1    1    1    1    1    1    1
*NODE PRINT,FREQ=10
    1    1    1    1    1    1    1    1
*END STEP
```